Variabilität und Veränderung der polaren Ozonschicht und ihre Bedeutung im Klimasystem

Habilitationsschrift

zur Erlangung des akademischen Grades

Dr. rerum naturalium habilitatus
(Dr. rer. nat. habil.)

des Fachbereichs Physik/Elektrotechnik
der Universität Bremen

vorgelegt von

Markus Rex
geboren am 28.11.1966 in Braunschweig

Potsdam, Januar 2013

Inhaltsverzeichnis

Vorwort 3

1 Einleitung 5
  1.1 Polare Ozonvariabilität: Die antreibenden Prozesse 6

2 Grundlagen 9
  2.1 Ozonbildungs- und Verlustprozesse 9
  2.2 Anthropogene polare Ozonverluste 10

3 Chemischer Ozonabbau 13
  3.1 Quantifizierung chemischer Ozonverluste 13
    3.1.1 Match 13
    3.1.2 Wirbelmittelansatz 17
    3.1.3 Ozon/Tracerrelation 20
  3.2 Theoretisches Verständnis des polaren Ozonverlustprozesses 21
    3.2.1 Die Chloraktivierungsphase 22
    3.2.2 Die Deaktivierungsphase 23
      3.2.2.1 Der Einfluss von Denitrifizierung 24
    3.2.3 Der Ozonabbauprozess 25
      3.2.3.1 Analyse von Ozonsondenmatchereignissen 27
      3.2.3.2 Unsicherheiten modellierter Ozonabbauraten 31
      3.2.3.3 Selfmatch-Flugpattern 32
  3.3 Sommerprozesse 37

4 Dynamische Variabilität 39
  4.1 Statistische Modellierung 39
  4.2 Mechanistische Modellierung 42
    4.2.1 Gesamtbudget und Antrieb der Variabilität 43
    4.2.2 Die Rolle der stratosphärischen Residualzirkulation 43
  4.3 Die Rolle solarer Variabilität 45

5 Die Rolle der tropischen Tropopausenregion für die polare Ozonschicht 47
  5.1 Grundsätzliche Prozesse 48
  5.2 Lagrangesche Modellierung der tropischen Tropopause 49
  5.3 Diagnose tropischer Tropopausenprozesse in Chemie-Klimamodellen 53

6 Interaktion zwischen Ozonschicht und Klimaänderungen 55
  6.1 Empirische Quantifizierung der Klimasensitivität des Ozonabbaus 55
  6.2 Beobachtete langfristige Änderungen 57
  6.3 Empirisch gestützte Szenarien für die zukünftige Entwicklung 58
  6.4 Defizite derzeitiger Chemie-Klimamodelle 59
  6.5 Das semi-empirische Modell SWIFT 60
  6.6 Das vollständig lagrangesche Chemie-/Transportmodell ATLAS 61

7 Zusammenfassung und Ausblick 65

Literatur 67

Ausgewählte Veröffentlichungen 75

Vorwort

Die Erforschung der Rolle stratosphärischer Prozesse im Klimasystem der Erde ist ein aktives Forschungsgebiet, in dem in den letzten Jahren große Fortschritte erzielt wurden. Insbesondere konnten die Prozesse, welche die Verteilung von Ozon in der Stratosphäre bestimmen, weiter aufgeklärt werden und ihr quantitatives Verständnis verbessert werden. Ein Fokus der Forschung lag dabei auf der Aufklärung der Auswirkungen menschlichen Handelns und globaler Klimaveränderungen auf die Ozonschicht. Damit gewinnen numerische Modelle der globalen Ozonverteilung in der Atmosphäre der Erde zunehmend an Reife.

Die vorliegende Schrift stellt eine Übersicht der Beiträge des Autors zu diesem Forschungsfeld dar. Sie beginnt mit einer kurzen Monografie, der eine Zusammenstellung einiger Veröffentlichungen des Autors und der von ihm geleiteten Arbeitsgruppe folgt. Die Monografie ist als Zusammenfassung der zitierten wissenschaftlichen Veröffentlichungen gedacht und stellt dar, wie diese einzelnen Arbeiten in einer kohärenten Forschungsstrategie zusammenhängen. Der wesentliche wissenschaftliche Fortschritt wird themenbezogen aus den einzelnen Veröffentlichungen synthetisiert.

Die Monografie erhebt nicht den Anspruch, die wissenschaftlichen Entwicklungen des dargestellten Forschungsfelds umfassend darzustellen und stellt damit ausdrücklich kein Review der Literatur des Forschungsfelds dar. Sie zeigt vielmehr den Beitrag des Autors zum wissenschaftlichen Fortschritt in diesem Feld und stützt sich daher im wesentlichen auf die Arbeiten des Autors und der von ihm geführten Arbeitsgruppe. Einige Referenzen anderer Autoren werden jedoch ebenfalls angeführt. Um eine Unterscheidung dieser von den Beiträgen des Autors zu erlauben, sind diese im Haupttext kursiv gesetzt. Die Abbildungen sind alle den Arbeiten des Autors und denen seiner Arbeitsgruppe entnommen. Eine umfassende Betrachtung der Literatur im Forschungsbereich befindet sich in den zitierten und in Auswahl beiliegenden wissenschaftlichen Veröffentlichungen.

KAPITEL 1

EINLEITUNG

Die Ozonschicht ist ein wichtiger Bestandteil des globalen Atmosphäre/Umweltsystems. Die Absorption solarer UV-Strahlung in der Ozonschicht schützt zum einen die Biosphäre vor diesen schädlichen energiereichen Strahlen und wirkt zum anderen als effektive Heizung der Stratosphäre. Damit haben Änderungen der Ozonverteilung in der Stratosphäre direkte Auswirkungen nicht nur auf die Intensität der UV-Einstrahlung an der Erdoberfläche, sondern auch auf die thermische Struktur der Atmosphäre und damit auf das globale Klimasystem. Gleichzeitig wirken Änderungen der atmosphärischen Zirkulation und Temperatur sowie Änderungen der Emissionen anthropogener und biogener Substanzen auf die Ozonschicht ein. Sie ist damit integraler Teil des globalen Klimasystems und ein detailliertes Verständnis der Prozesse, welche die Verteilung von Ozon in der Atmosphäre regulieren, ist fundamental für eine korrekte Klimavorhersage und für jede Prognose der zukünftigen UV-Belastung der Biosphäre.

Die Ozonbilanz der Stratosphäre wird von chemischen und von dynamischen Prozessen reguliert. Daher ist ein vollständiges Verständnis beider Beiträge zu Variabilität und langfristigen Änderungen erforderlich, um die zukünftige stratosphärische Ozonverteilung im sich ändernden Klimasystem vorherzusagen.

Abbildung 1 zeigt den saisonalen Verlauf der Ozonschichtdicke über der Arktis und der Antarktis. In der Antarktis kommt es durch inzwischen gut verstandene chemische Prozesse jeweils im Frühjahr zu einem deutlichen Einbruch der Ozonschichtdicke - dem antarktischen Ozonloch. Demgegenüber nimmt in der Arktis die Ozonschichtdicke im Verlauf des Winters im klimatologischen Mittel zu und erreicht in vielen Jahren ein Maximum in den Monaten Februar bis April.

Während sowohl die kurzfristige als auch die interannuale Variabilität im Sommer und Herbst der jeweiligen Hemisphäre verhältnismäßig gering ist, fällt insbesondere in der Arktis eine ausgeprägte Zunahme der Variabilität im Verlauf des Winters auf. In einigen Jahren bleibt das oben erwähnte arktische Frühjahrsmaximum der Ozonschichtdicke sogar im wesentlichen aus.

Im dieser Arbeit werden die Ursachen für die in Abbildung 1 gezeigte ausgeprägte interannuale Variabilität der Ozonschichtdicke insbesondere in der Arktis beleuchtet, die antreibenden Prozesse werden quantifiziert und unser theoretisches Verständnis dieser Prozesse wird überprüft und verbessert.

1.1 Polare Ozonvariabilität: Die antreibenden Prozesse

Abbildung 2 zeigt im oberen Bereich die sich im Winter aufbauende interannuale Variabilität der Ozongesamtsäule (Tegtmeier et al., 2008b). Während im gezeigten Zeitraum im Oktober die Ozongesamtsäule sehr stabil war (grau schraffierter Bereich in Abbildung 2), variierte sie am Ende des arktischen Winters zwischen 0 und nahezu 200DU über dem Oktoberwert. Sie stieg also in einigen Jahren um zwei Drittel an, während sie in anderen Jahren nahezu konstant blieb. Die Prozesse, welche im polaren Winter die Ozonschichtdicke beeinflussen und diese enorme Variabilität verursachen, sind der variable anthropogene chemische Verlust und der ebenfalls variable dynamisch bedingte Eintrag von Ozon in den polaren Bereich.

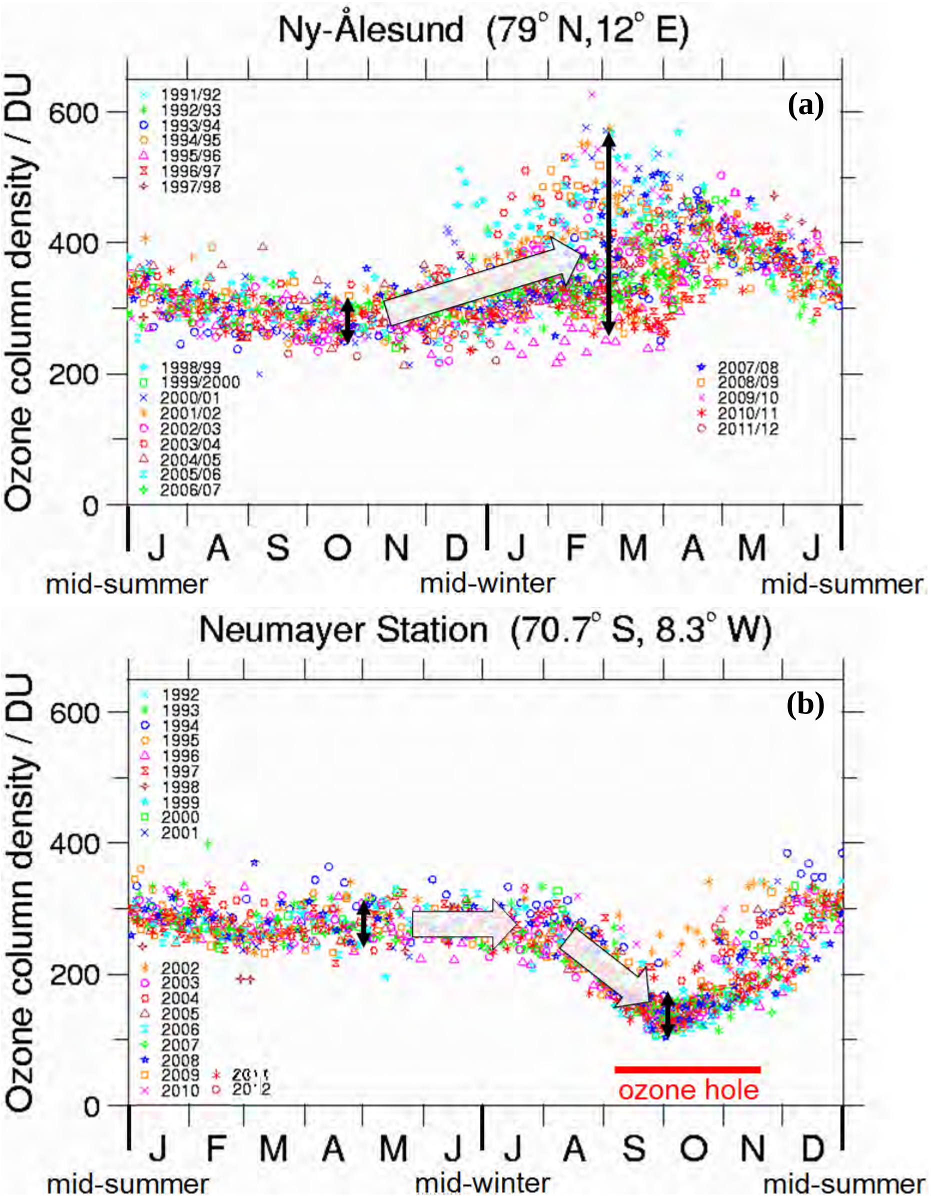

Abbildung 1: Saisonaler Verlauf der Ozonschichtdicke über den angegebenen Stationen in der Arktis (a) und der Antarktis (b) basierend auf Ozonsondendaten der Jahre 1991-2012. Aktualisiert nach Rex et al. (2000).

Es wurden in dieser Arbeit Verfahren entwickelt, beide Beiträge zur Variabilität zu quantifizieren, damit das Gesamtbudget der Variabilität (gestrichelte schwarze Linie) aufzustellen und den Beobachtungen gegenüberzustellen. Als Synthese der Ergebnisse der folgenden Kapitel sind in Abbildung 2 bereits die Beiträge von Chemie (rot) und Dynamik (blau) zur Gesamtänderung der Ozonschichtdicke im Verlauf des Winters enthalten.

Die hier gezeigte Quantifizierung des chemischen Verlusts wird in Kapitel 3 erläutert und diskutiert. Die Quantifizierung des dynamisch bedingten Eintrags von Ozon wird in Kapitel 4 beschrieben und dabei auch die in Abbildung 2 sichtbare deutliche Korrelation zwischen dem chemischen und dem dynamischen Term diskutiert. Die Rolle solarer Variabilität wird im Abschnitt 4.3 behandelt. Kapitel 5 widmet sich der wichtigen Rolle der tropischen Tropopausenregion für die Zusammensetzung der polaren Stratosphäre und damit für die polare

Ozonchemie. In Kapitel 6 werden die Auswirkungen von Klimaänderungen auf die polare Ozonvariabilität untersucht und quantifiziert und im Kapitel 7 folgen Zusammenfassung und Ausblick.

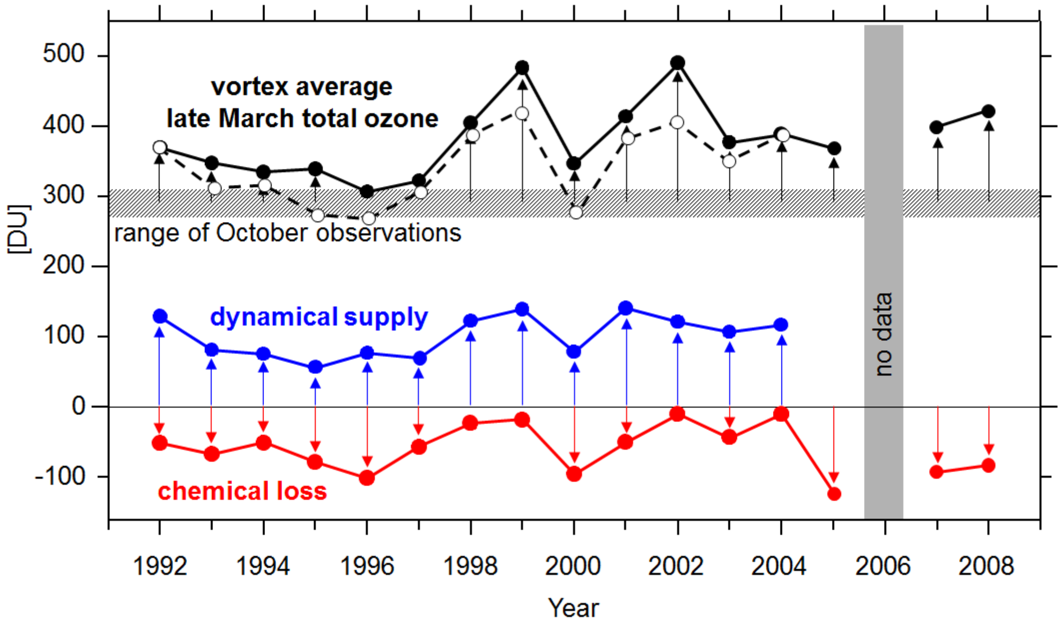

Abbildung 2: Interannuale Variabilität der über den Polarwirbel gemittelten Ozonschichtdicke am Ende des arktischen Winters (Ende März, schwarz, durchgezogen). Der schraffierte Bereich stellt den Bereich der Ozonvariabilität jeweils zu Beginn des Winters (Oktober) dar. Schwarze Pfeile illustrieren die Änderung der Ozonschichtdicke während des jeweiligen Winters. In der vorliegenden Arbeit wurden Methoden entwickelt, die chemischen und dynamischen Beiträge zu diesen Änderungen zu quantifizieren und damit das Gesamtbudget der winterlichen Ozonbilanz aufzustellen. Die Ergebnisse dieser Rechnungen sind hier rot (chemischer Anteil) und blau (dynamisch bedingter Anteil) eingetragen. Die schwarze gestrichelte Linie zeigt die Summe beider Anteile und des relativ konstanten Oktoberwerts. Aktualisiert nach Rex et al. (2004b), Tegtmeier et al. (2008b), WMO-Assessment 2010: Douglass et al. (2011).

KAPITEL 2

GRUNDLAGEN

2.1 Ozonbildungs- und Verlustprozesse

Im Bereich der stratosphärischen Ozonschicht wird Ozon hauptsächlich durch die Photolyse von Sauerstoffmolekülen mit nachfolgender Reaktion der enstehenden Sauerstoffatome mit Sauerstoffmolekülen gebildet:

$$O_2 + h\nu \longrightarrow 2\,O \qquad (1)$$

$$O + O_2 + M \longrightarrow O_3 + M \qquad (2)$$

Ozon photolysiert recht effizient selbst im sichtbaren Wellenlängenbereich. Daher liegt die Lebensdauer eines Ozonmoleküls tagsüber auch bei den niedrigen Sonnenständen der Polarregionen im Bereich unterhalb von Stunden. Die bei der Photolyse entstehenden Sauerstoffatome reagieren jedoch fast alle mit Sauerstoffmolekülen und bilden dabei erneut Ozon. Um diese für die Ozonbilanz nicht sehr wesentliche schnelle Zirkulation zwischen O und O_3 aus unseren Betrachtungen herauszuhalten, wird sinnvollerweise statt der Ozonkonzentration die Konzentration der Stoffgruppe O_x betrachtet, welche aus der Summe von O_3 und O besteht. Der Vorteil ist, dass O_x durch die Ozonphotolyse nicht abgebaut wird und dieser schnelle Umwandlungszyklus zwischen O_3 und O in der Betrachtung nicht weiter auftaucht. Im Sprachgebrauch hat sich der Begriff „Ozonabbau“ für den Abbau von O_x durchgesetzt. Wird in den folgenden Kapiteln daher von der Ozonabbaurate gesprochen, ist im eigentlichen Sinne die Abbaurate von O_x gemeint und nicht die viel schnellere Rate der Photolyse der Ozonmoleküle.

Im Allgemeinen findet der Abbau von O_x in der Stratosphäre über vier Gruppen von Prozessen statt. Die folgende bereits von Chapman beschriebene Reaktion ist die älteste bekannte O_x-Abbauraktion:

$$O + O_3 \longrightarrow O_2 + O_2 \qquad (3)$$

In den 1970er Jahren wurden zusätzliche katalytische Ozonabbaureaktionen gefunden, die sich nach den beteiligten Katalysatoren einordnen lassen als Ozonabbau durch NO_x-Verbindungen, HO_x-Verbindungen oder durch Halogenverbindungen (ClO_x, BrO_x).

Dabei bezeichnen NO_x, HO_x, ClO_x und BrO_x jeweils Gruppen kurzlebiger, größtenteils radikalischer Verbindungen, die verschiedene Oxide des jeweiligen Elements darstellen. Jeweils ein oder mehrere Vertreter dieser Stoffgruppen reagieren sehr effizient mit Ozon und/oder Sauerstoffatomen. Das so oxidierte Produkt reagiert dann in katalytischen Zyklen mit weiteren Vertretern der gleichen oder einer anderen dieser Stoffgruppen (im letzteren Fall spricht man von einem gemischten Zyklus) und geht aus diesen Reaktionen wieder in seiner Ausgangsform hervor, so dass es erneut mit Ozon oder O reagieren kann.

Wird bei diesen Reaktionen die O-O Bindung wiederhergestellt und O_2 freigesetzt, kommt es in dem Gesamtzyklus zum Verlust von zwei O_x Molekülen und es handelt sich um einen katalytischen Ozonverlustzyklus. Während die HO_x und NO_x-Zyklen zum großen Teil auf natürlichen Verbindungen beruhen, beruhen die ClO_x-Zyklen bei derzeitiger Chlorbelastung der Stratosphäre zu mehr als 80% auf anthropogenen Chlorverbindungen. Ozonabbau durch BrO_x erlangt im polaren Winter nur in einem gemischten ClO_x/BrO_x-Zyklus wesentliche Bedeutung. Da ein Großteil des für diesen gemischten Zyklus benötigten ClO_x anthropogen ist, muss daher auch der Ozonabbau durch BrO_x als im wesentlichen anthropogen angesehen werden, obwohl mehr als die Hälfte des stratosphärischen Broms aus natürlichen Quellen stammt. Für den Polarwinter trägt dieser natürliche Hintergrund an Bromverbindungen in der Stratosphäre aber ohne anthropogen erhöhte Chlorbelastung nicht wesentlich zum Ozonabbau bei.

Je nach Bereich der Stratosphäre sind verschiedene dieser katalytischen Ozonabbauzyklen für den Gesamtozonabbau relevant. Dabei dominieren fast überall entweder HO_x- oder NO_x-Zyklen, während die Halogenzyklen und die Chapmanreaktion eine untergeordnete, jedoch nicht vernachlässigbare Rolle spielen.

Alle kurzlebigen Verbindungen der NO_x-, HO_x- und ClO_x-Gruppen stehen in der Stratosphäre in Balance mit ihren jeweiligen langlebigen Reservoirverbindungen. Dies ist für NO_x das HNO_3-Molekül, für HO_x das H_2O-Molekül und für ClO_x die Moleküle HCl und $ClONO_2$. BrO_x besitzt kein wirklich langlebiges Reservoir und macht immer einen Großteil des gesamten Brombudgets der Stratosphäre aus.

In der unteren und mittleren Stratosphäre sind die ClO_x-Konzentrationen unter normalen Bedingungen sehr gering, da die Reservoire HCl und $ClONO_2$ recht stabile Moleküle sind. Daher liegen im Bereich des Hauptteils der Ozonschicht nur wenige Prozent des gesamten Chlors in der Stratosphäre in den ozonzerstörenden ClO_x-Verbindungen vor und der anthropogene Ozonabbau beschränkt sich auf die obere Stratosphäre und die obersten Ausläufer der Ozonschicht, wo durch intensivere Photolyse des $ClONO_2$ ein etwas größerer Anteil des Gesamtchlors als ClO_x vorliegt.

2.2 Anthropogene polare Ozonverluste

Seit den 60er und 70er Jahren des letzten Jahrhunderts hat die Menschheit große Mengen an Fluorchlorkohlenwasserstoffen (FCKW) und bromhaltigen Halonen produziert und in die Atmosphäre emittiert. In der Troposphäre sind diese Substanzen extrem stabil und erreichen hier eine Lebensdauer von Jahrhunderten. Sie vermischen sich daher in der Troposphäre gleichmäßig und steigen dann langsam bis in die Stratosphäre auf. Dort werden sie abgebaut und setzen dabei Chlor- und Bromradikale frei, was zu einer Erhöhung der ClO_x-und BrO_x-Konzentrationen der Stratosphäre führt (obere Hälfte der Abbildung 3).

Wie oben erwähnt werden die ClO_x-Verbindungen aber zumindest in der unteren und mittleren Stratosphäre glücklicherweise sehr schnell in die reaktionsträgeren Reservoirverbindungen eingebunden, welche die Ozonschicht nicht direkt schädigen (untere Hälfte der Abbildung 3). Damit ist unter nicht polaren Bedingungen die ozonschädigende Wirkung der FCKW-Emissionen hauptsächlich auf die obere Stratosphäre begrenzt und führt nur zu wenigen Prozent Abnahme der Ozonschichtdicke (*WMO-Assessment 2010: Douglass et al., 2011*).

In den Polarregionen kommt es jedoch jeweils im Winter zu einer drastischen Verstärkung des anthropogenen Ozonabbaus. Zunächst bildet sich im Herbst in der polaren Stratosphäre der Arktis und der Antarktis jeweils ein ausgeprägtes Tiefdruckgebiet. Luftmassen rotieren in diesem sogenannten Polarwirbel um dessen Zentrum in der Nähe des Pols. Diese vorwiegend zonale Strömung unterdrückt meridionale Transporte. Dadurch bleiben einerseits die Luftmassen im Innern des Polarwirbels für lange Zeit von der Umgebung isoliert und können sich chemisch weitgehend unabhängig von den Prozessen in mittleren Breiten entwickeln, andererseits bleiben diese Luftmassen auch lange Zeit im Bereich der Polarnacht und kühlen strahlungsbedingt stark ab. Bei Temperaturen unter ca. -78°C (ca. 195K) kondensieren Gemische aus natürlich vorkommender Salpetersäure, Schwefelsäure und Wasser zu Tröpfchen oder zu kleinen Kristallen. Diese bilden die in der polaren Stratosphäre schon seit langem bekannten und bereits auf Gemälden der vorletzten Jahrhundertwende belegten (*Lowe und MacKenzie, 2008*) polaren stratosphäri-

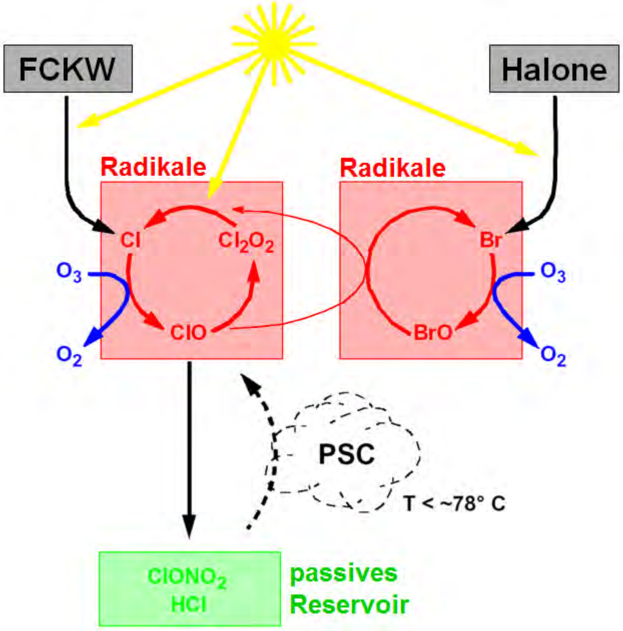
FCKW
Halone
Radikale
Radikale
Cl
Cl_2O_2
ClO
Br
BrO
O_3
O_2
O_3
O_2
PSC
T < ~78° C
$ClONO_2$
HCl
passives Reservoir

Abbildung 3: Illustration des polaren Ozonabbauprozesses. Nach Frieler et al., (2006) entfallen auf die dargestellten ClO_x und BrO_x Zyklen ca. 85% des winterlichen polaren Ozonabbaus.

schen Wolken (Polar Stratospheric Clouds; PSC) - im Zwielicht des polaren Winters in allen Farben schillernde Wolken, die aufgrund ihres Aussehens auch als Perlmutterwolken bekannt sind (Abbildung 4).

Früher harmlos, sind PSCs durch die Präsenz der Abbauprodukte der FCKW in der Stratosphäre heutzutage Auslöser für schwere Ozonverluste. An den Oberflächen der einzelnen Partikel oder Tröpfchen laufen heterogene chemische Reaktionen ab, die innerhalb von wenigen Stunden die harmlosen chlorhaltigen Reservoirverbindungen vollständig zerlegen können und daraus ClO_x

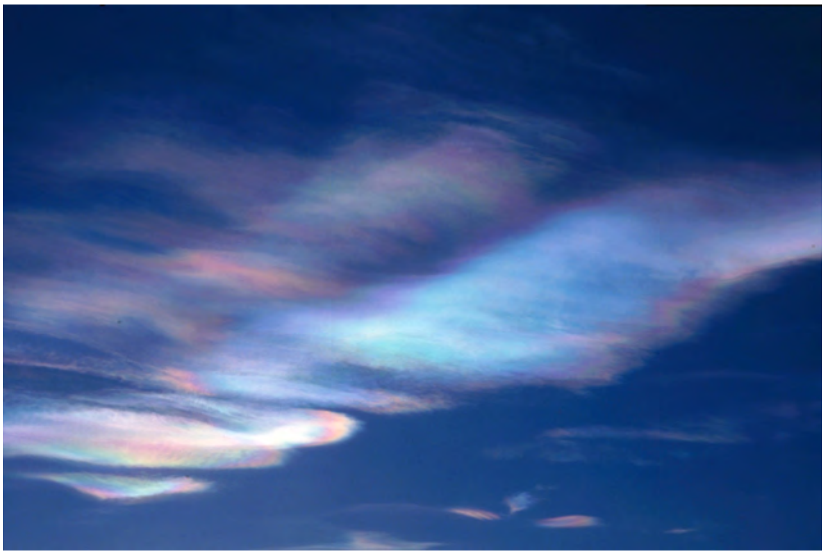

Abbildung 4: Polare stratosphärische Wolke, Kiruna, Schweden, 27.1.2000 (Foto: M. Rex).

freisetzen. Im folgenden Polarfrühling können die ClO_x-Verbindungen dann im Zusammenwirken mit Sonnenlicht und zum Teil auch mit Bromradikalen sehr effizient Ozon zerstören. In der Antarktis führt dies seit ca. drei Jahrzehnten nahezu alljährlich zum saisonalen Ozonloch im antarktischen Frühjahr. Unsere Messungen an der Antarktisstation Neumayer (Abbildung 1) zeigen diesen Effekt als dramatischen Einbruch der Ozonschichtdicke in praktisch allen Jahren am Ende des antarktischen Winters in den Monaten September bis November. Als Ausnahme sticht das Jahr 2002 hervor, in der Abbildung mit orangen Sternen dargestellt, in dem durch eine dynamisch bedingte Anomalie der Polarwirbel frühzeitig zusammengebrochen ist, und die Bedingungen für die Bildung eines scharf abgegrenzten Ozonlochs daher nicht gegeben waren.

KAPITEL 3

CHEMISCHER OZONABBAU

Der chemisch bedingte polare Ozonabbau spielt eine Schlüsselrolle für Variabilität und dekadische Veränderungen der polaren Ozonschicht. Als Grundlage aller weiteren Arbeiten zum theoretischen Verständnis des Ozonverlustprozesses ist eine möglichst genaue Quantifizierung des gesamten Ozonverlustes und insbesondere der chemischen Ozonverlustraten unter möglichst weit variierenden Umgebungsbedingungen erforderlich. Die Arbeiten konzentrieren sich daher zunächst auf eine Entwicklung von Methoden, Ozonabbau und chemische Abbauraten in der polaren Stratosphäre zu bestimmen.

3.1 Quantifizierung chemischer Ozonverluste

Die zeitliche Veränderung der Ozonkonzentration an einem Ort in der polaren Stratosphäre wird durch die Kontinuitätsgleichung beschrieben. Neben den chemisch bedingten Quellen- und Senkentermen enthält die Kontinuitätsgleichung transportbedingte Terme. Instantan betrachtet, ist die Größenordnung der Transportterme dabei in der Regel viel größer als die der chemisch bedingten Änderungsraten (siehe z.B. Rex, 1993 und Rex, 1997 für eine genaue Darstellung der Terme der Kontinuitätsgleichung und eine Abschätzung ihrer jeweiligen Größenordnung). Jedes Verfahren, chemisch bedingte Änderungen auf der Basis von Ozonmessungen zu quantifizieren, muss daher die chemischen Terme von den Transporttermen trennen. Teilweise gelingt dies schon durch die Betrachtung größerer zeitlicher und/oder räumlicher Mittel, da die Transportterme die Tendenz haben, sich auf größeren Skalen teilweise aufzuheben. Solche simplen Verfahren bleiben jedoch immer unbefriedigend, da systematische Anteile der Transportterme nicht entfernt werden und diese oft trotz der Mittelungen in der Größenordnung der chemischen Änderungsraten liegen (z.B. Tegtmeier et al., 2008b). Die folgenden Abschnitte geben einen Überblick über die drei wichtigsten Verfahren zur Quantifizierung der chemischen Terme, Diese Verfahren wurden in den letzten Jahren entwickelt und immer weiter verfeinert.

3.1.1 Match

Das sogenannte Matchverfahren ist ein lagrangesches Messverfahren, dessen Grundlagen in Rex (1993) und Rex (1997) entwickelt wurden. Das Verfahren basiert auf dem koordinierten Start einer Vielzahl von Ozonsonden. Ozonsonden sind elektrochemische Ozonsensoren, die an heliumgefüllten Ballonen bis ca. 30km Höhe aufsteigen können und ihre Messdaten dabei per Funk zur Bodenstation übertragen (siehe z.B. Rex, 1993 und Rex, 1997).

Die Grundidee des Match-Verfahrens beruht darauf, Messungen am festen Ort zu ersetzen durch wiederholte Messungen in bestimmten Luftmassen, die mit der stratosphärischen Strömung im Polarwirbel im wesentlichen zonal über die Polargebiete driften. Für das Verfahren wurden die in Arktis und Antarktis befindlichen Ozonsondenstationen zu eng kooperierenden Netzwerken integriert, die durch eine enge Koordinierung der Messungen in Realzeit auf beiden Erdhalbkugeln jeweils wie ein integriertes Messsystem hemisphärischen Ausmaßes agieren. So stehen heutzutage während einer Matchkampagne in der Arktis über 30 Stationen zur Verfügung, von denen Ozonsonden gestartet werden können. Während einer Winterkampagne werden von diesem Netzwerk zwischen 500 und 1200 Ozonsonden derart koordiniert gestartet, dass hunderte bis tausende von Luftmassen jeweils zweimal im Abstand von drei bis zehn Tagen beprobt werden.

Mittels einer statistischen Auswertung wird aus den gemessenen Ozondifferenzen und der Zeit, die die jeweilige Luftmasse zwischen den Messungen in der Sonne verbracht hat, ein genaues, zeitlich und vertikal aufgelöstes Bild der chemischen Ozonabbauraten und ihrer Unsicherheiten in der jeweiligen Polarregion und dem jeweiligen Winter rekonstruiert (Rex et al., 1998, Rex et al., 1999).

In den letzten zwei Jahrzehnten wurden 15 Matchkampagnen in der Arktis und zwei Kampagnen in der Antarktis durchgeführt.

In den kältesten arktischen Wintern 1999/2000, 2004/2005 und 2010/2011 wurde sehr starker chemischer Ozonabbau nachgewiesen. Die Einordnung als „kälteste" Winter bezieht sich dabei auf die stratosphärischen Temperaturen und dem daraus folgenden PSC-Bildungspotenzial (Details siehe Abschnitt 6.1). Abbildung 5 und Abbildung 6 zeigen ein detailliertes Bild des chemischen Ozonabbaus während des Winters 1999/2000 (Rex et al., 2002). In 2004/2005 dehnte sich schwerer Ozonverlust über einen noch weiteren Höhenbereich nach unten aus (Abbildung 7), was in der Gesamtsäule zu signifikant größerem Verlust führte als 1999/2000. Damit galt der in 2004/2005 erreichte Ozonverlust als die bis dahin größte nachgewiesene Ozonzerstörung in der Arktis (Rex et al., 2006; WMO-Assessment 2006: Newman und Rex, 2007).

2010/2011 erreichte der Ozonverlust jedoch ein erneut vergrößertes Ausmaß. Abbildung 8 zeigt die mit der Matchmethode gemessenen Ozonverlustraten im Verlauf des Winters und vergleicht diese mit dem Bereich der Verlustraten in früheren Wintern sowie mit dem Verlauf des Ozonverlusts in einem typischen antarktischen Winter.

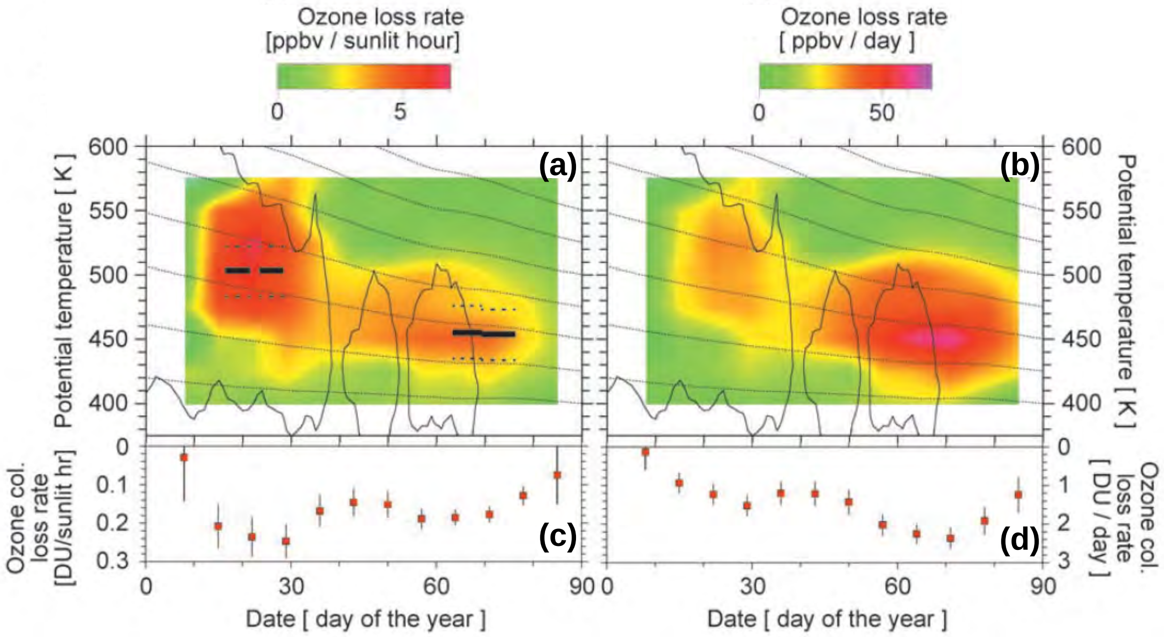

Abbildung 5: Obere Panel: Vertikale Verteilung und saisonaler Verlauf des Ozonabbaus pro Stunde Sonnenlichts (a) und pro Tag (b) für Januar bis März 2000. Schwarze Konturen zeigen die $4 \cdot 10^6 km^2$ Isolinie von A_{PSC}, der Ausdehnung des Bereichs über der Arktis, in dem aufgrund niedriger Temperaturen PSC-Bedingungen herrschen. Gepunktete Linien deuten das berechnete Absinken von Luftmassen im Laufe des Winters an. Untere Panel: Vertikal integrierter chemischer Ozonverlust pro Stunde Sonnenlichts (c) und pro Tag (d). Nach Rex et al. (2002).

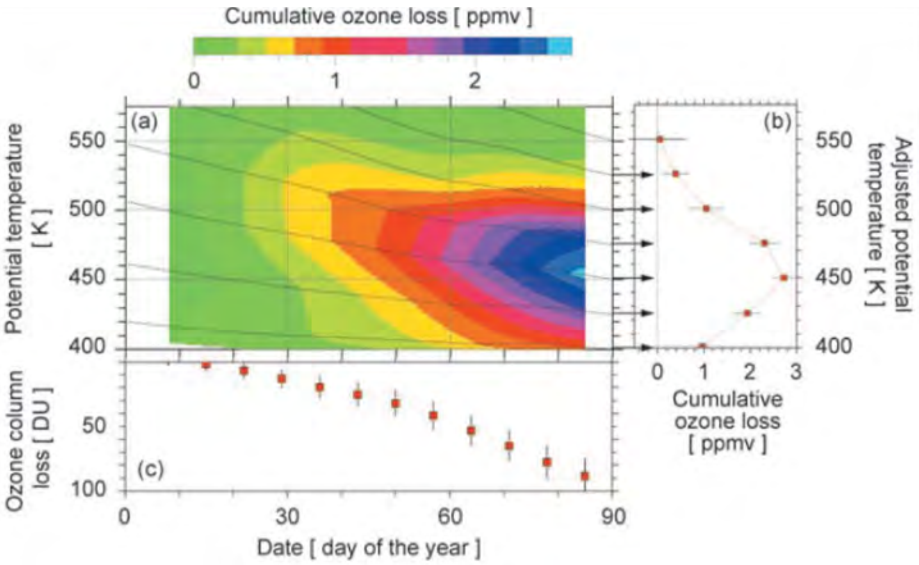

Abbildung 6: (a) Vertikale Verteilung und saisonaler Verlauf des kumulativen Ozonverlusts im Winter 1999/2000. Gepunktete Linien deuten das berechnete Absinken von Luftmassen im Laufe des Winters an. (b) Vertikalprofil des akkumulierten chemischen Ozonverlusts am Ende des Winters. (c) Vertikal integrierter kumulativer Ozonverlust in der Gesamtsäule. Nach Rex et al. (2002), WMO-Assessment 2002: Newman et al, 2003.

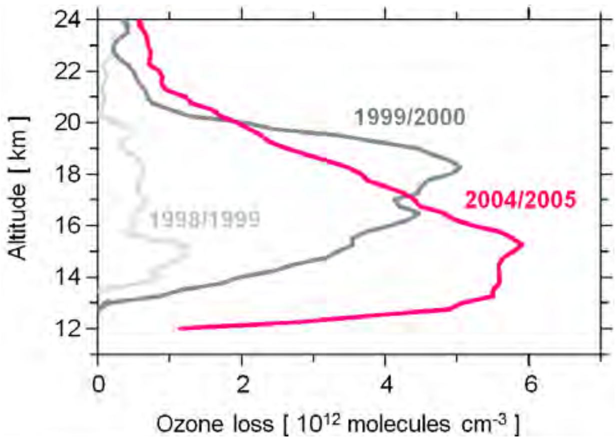

Abbildung 7: Ozonverlustprofile der Winter 1999/2000 und 2004/2005. Zum Vergleich zu diesen kalten arktischen Wintern ist auch der für den warmen Winter 1998/1999 abgeleitete Ozonverlust eingetragen. In dieser Abbildung sind im Unterschied zu den anderen Abbildungen dieses Abschnitts Ozonkonzentrationen dargestellt, statt der sonst verwendeten Mischungsverhältnisse. Die Konzentrationen sind direkter mit der Ozonschichtdicke verknüpft (welche sich als vertikale Integration der Konzentrationsprofile ergibt), während die Mischungsverhältnisse invariant gegenüber Transporten sind und sich daher zur Diagnose chemischer Verluste besonders eigenen. Nach Rex et al. (2006), WMO-Assessment 2006: Newman und Rex, 2007.

Es wird deutlich, dass die arktischen Ozonverlustraten im März 2011 einen neuen Rekord erreicht haben und im gesamten Verlauf über den Winter sehr nah dem Verlauf der Ozonverlustraten in der Antarktis folgen. In den folgenden Abschnitten wird gezeigt, dass auch in der vertikalen Verteilung des aufakkumulierten chemischen Ozonverlusts kein wesentlicher Unterschied zwischen dem Rekordozonverlust im arktischen Winter 2010/2011 und typischen antarktischen Ozonlöchern besteht. Dieser Ozonverlust führte zu einem scharf abgegrenzten Minimum in der Ozongesamtsäule im Bereich des Polarwirbels, mit minimalen Ozonschichtdicken im Bereich von 220DU (Manney et al., 2011). Es kann daher für März/April 2011 erstmals von einem „Ozonloch“ über der Arktis gesprochen werden.

Im Vergleich zur Antarktis erfolgen in der Arktis jedoch wesentlich ausgeprägtere Transporte von Ozon von niedrigeren zu hohen Breiten. Daher ist die Ozonschicht dort generell dicker und die Ozonschichtdicke im Bereich des arktischen Ozonlochs lag noch ca. 100DU über der Dicke der Ozonschicht in modernen antarktischen Ozonlöchern (Manney et al., 2011).

Insgesamt besteht der Matchdatensatz inzwischen aus tausenden von einzelnen Matchereignissen, die ein breites Spektrum an meteorologischen Bedingungen, Luftmassenhistorien und solarer Einstrahlung abdecken. Dies reicht von den kältesten antarktischen Bedingungen mit kontinuierlichem PSC-Bildungspotenzial bis zu Bedingungen in warmen arktischen Wintern ohne jegliche PSC-Bildungsmöglichkeit. Der Datensatz deckt weiterhin den ganzen Bereich von vollständig dunklen Bedingungen in der Mitte des Winters bis zu verhältnismäßig starker Sonneneinstrahlung im polaren Frühjahr ab. Dabei sind durch die bekannten Luftmassentrajektorien für jeden einzelnen Datenpunkt die Randbedingungen (wie z.B. Druck, Temperatur, Sonnenzenitwinkel) für chemische Modellierung genau bekannt. Dies gilt für den Abschnitt der Trajektorie zwischen den jeweils zwei Ozonsondenmessungen als auch für die Luftmassenhistorie, die durch Rückwärtstrajektorienrechungen ebenfalls bis etwa zwei Wochen vor dem Matchereignis hinreichend genau bekannt ist. Dies macht den Matchdatensatz zu einem idealen Beobachtungsdatensatz für den Antrieb detaillierter Modellstudien des polaren Ozonabbauprozesses (siehe Abschnitt 3.2).

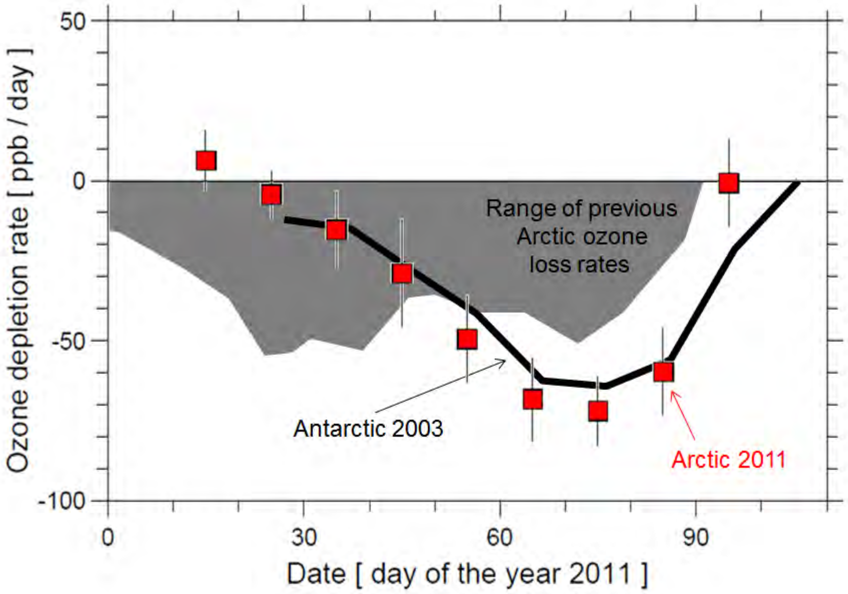

Abbildung 8: Vergleich der mit dem Matchansatz bestimmten Ozonabbauraten im Winter 2010/2011 (rot) mit den Abbauraten aus früheren arktischen Wintern (graue Schraffur). Rex et al., 2011a.

Eine Beurteilung des theoretischen Verständnisses von chemischen Ozonabbauprozessen mittels solch einer Modellierung erfordert eine genaue Quantifizierung der statistischen und systematischen Unsicherheiten jedes einzelnen Datenpunktes. Nur im Zusammenhang mit ihrer jeweiligen Unsicherheit sind Messungen der chemischen Ozonabbaurate als Grundlage von Modellierung und Beurteilung der sich ergebenden Modellergebnisse sinnvoll einsetzbar.

Die Unsicherheiten von Matchergebnissen wurden detailliert analysiert. In mehreren Studien wurden die Unsicherheiten entweder aus einer Bilanz aller Beiträge zur Unsicherheit quantifiziert (Rex et al., 1998; Rex et al., 1999) oder durch Vergleich mit Ergebnissen unabhängiger Arbeiten abgeschätzt (Harris et al., 2002; Newman und Rex, 2007). Abbildung 9 zeigt als Beispiel einen Vergleich der Matchergebnisse mit anderen unabhängigen Studien für eine bestimmte Periode während des Winters 1999/2000.

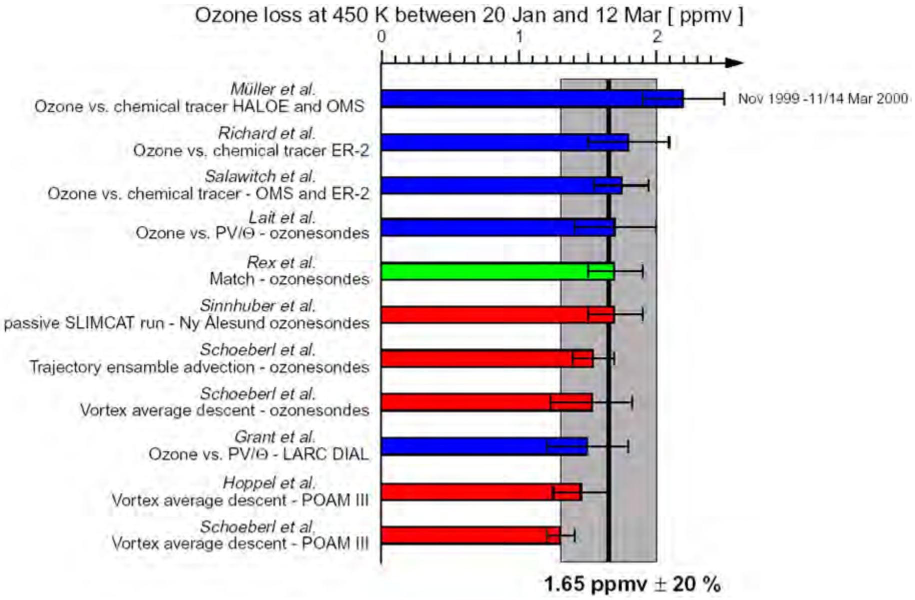

Abbildung 9: Vergleich der aus verschiedenen Ozonbeobachtungen mittels unterschiedlicher Verfahren abgeleiteten chemischen Ozonverluste auf dem eΘ=450K level zwischen dem 20. Januar und dem 12. März 2000. Nach WMO Assessment 2002: Newman et al., 2003.

Lehmann et al. (2005) analysieren die genaue statistische Beschaffenheit der Matchdatensätze, daraus resultierende Kovarianzen zwischen den statistischen Unsicherheiten der einzelnen Matchpaare und den darauf beruhenden Einfluss auf die Fehlerberechnungen. Alle Matchergebnisse enthalten Fehlerbalken, welche die so ermittelten sehr variablen statistischen Fehler wiedergeben. In der Gesamtheit der Arbeiten ergibt sich als mögliche zusätzliche systematische Abweichung maximal 20%.

3.1.2 Wirbelmittelansatz

Rex et al. (2002) und Hoppel et al. (2002) entwickelten den sogenannten Wirbelmittelansatz zur Abschätzung chemischer Ozonverluste in der polaren Atmosphäre weiter, der erstmals von *Bevilacqua et al. (1997)* verwendet wurde. Dieses Verfahren beruht auf der Annahme, dass der Austausch von Luftmassen über eine geeignet definierte Grenze des Polarwirbels gering ist und das Ozonfeld im Polarwirbel nur unwesentlich beeinflusst. Generell kommt es aber immer zu einem gewissen Maß an Durchmischung über jede fest definierte hypothetische Oberfläche des Wirbelvolumens - siehe z.B. Rex et al., (1999a) welche eine Methode entwickeln, diese Einmischung aus der Kombination verschiedener Tracermessungen zu quantifizieren.

Das Ausmaß der Durchmischung ist in der Regel ausreichend klein, so dass es den Ozongehalt im Polarwirbel nur unwesentlich beeinflusst. Die Gültigkeit dieser Annahme wurde in Rex et al. (2002) eingehend untersucht. Basierend auf der Analyse vielfältiger Tracermessungen kommen Rex et al. (2002) dabei zu dem Schluss, dass Austauchprozesse über den Polarwirbelrand zumindest im kalten arktischen Winter 1999/2000 vernachlässigbar waren. Rex et al. (2004a) zeigen zusätzlich, dass die Erhaltung des Ozonfeldes in den warmen arktischen Wintern 1997/1998 und 1998/1999 belegt, dass auch in diesen dynamisch aktiveren Wintern mit gestörteren Polarwirbeln Durchmischung über die Polarwirbelgrenze keine dominierende Rolle spielte.

Grundsätzlich nehmen die Durchmischungsprozesse über den Polarwirbelrand in den unteren Schichten der Stratosphäre zu. Rex et al., (2006) zeigen jedoch mittels Transportmodellrechnungen, dass im kalten Polarwirbel des Winters 2004/2005 die Voraussetzungen für die Gültigkeit des Wirbelmittelansatzes zumindest bis zu einer potentiellen Temperatur von 360K nach unten hin gültig waren.

Reversible und schnelle horizontale Transporte werden im Wirbelmittelverfahren dadurch ausgeglichen, dass der geografische Mittelungsbereich dem Polarwirbel folgt. Kurzfristige vertikale Transportprozesse werden unterdrückt, indem die Analyse auf potentiellen Temperaturniveaus durchgeführt wird, die auf der Zeitskala von ein paar Tagen den kurzfristigen vertikalen Bewegungen der Luftmassen folgen. Langfristig sinken die Luftmassen im Polarwirbel durch strahlungsbedingte Abkühlung jedoch über die potentiellen Temperaturniveaus ab. Rex et al. (2002) beschreiben ein Konzept, den Einfluss dieser systematischen vertikalen Bewegung zu erfassen, indem die Analyse auf Flächen konstanter sogenannter „spring equivalent potential temperature“ (eΘ) durchgeführt wird. eΘ gibt dabei die potentielle Temperatur an, die eine gegebene Luftmasse zu einem Stichdatum am Ende des Winters erreicht.

Verglichen mit den Ergebnissen der in den letzten beiden Abschnitten beschriebenen Verfahren muss jedoch bei der Wirbelmittelmethode aufgrund des immerhin begrenzt möglichen Einflusses von Durchmischung von einer größeren Unsicherheit der Ergebnisse ausgegangen werden. Diese Unsicherheit ist aufgrund von Unterschieden in der Dynamik der Stratosphäre von Winter zu Winter sehr verschieden und ist im Einzelfall oft schwer abzuschätzen. Aus einem Vergleich der Ergebnisse dieses Verfahrens mit Matchergebnissen (Abbildung 10) und anderen Verfahren (Abbildung 9) ergibt sich, dass der Fehler der so bestimmten Ozonverluste für kalte, stabile Polarwirbel im Bereich von 20DU liegt (Newman und Rex, 2007).

Da zur Wirbelmittelanalyse keine logistisch aufwändigen Messkampagnen nötig sind und sie sich zur Analyse von Satellitendaten genauso eignet wie für unkoordiniert durchgeführte Ozonsondenmessungen, kann mit diesem Verfahren eine vollständigere Zeitreihe der chemischen Ozonverluste rekonstruiert werden. Der Wirbelmittelansatz versagt jedoch, wenn der Polarwirbel sich im Zuge einer mittwinterlichen Stratosphärenerwärmung auflöst. Daher können Winter nicht erfasst werden, in denen eine Periode chemischer Ozonverluste mit einer Stratosphärenerwärmung überlappt. Bislang konnte noch kein Verfahren entwickelt werden, das es erlaubt, in diesen komplizierten dynamischen Lagen chemische Ozonverluste zu bestimmen. Diese glücklicherweise seltenen Bedingungen werden also weiterhin in Zeitreihen der chemischen Ozonverluste in der Arktis fehlen.

Abbildung 11 zeigt einen Vergleich des zeitlichen Verlaufs der Ozonverluste einiger arktischer und antarktischer Winter und Abbildung 12 vergleicht die vertikale Verteilung des arktischen Ozonverlusts in 2010/2011 mit früheren arktischen und antarktischen Wintern. In beiden Ab-

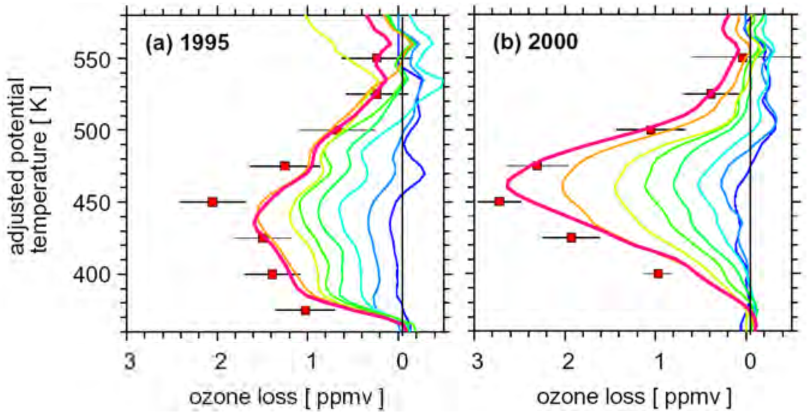

Abbildung 10: Vergleich der vertikalen Verteilung des mittels des Wirbelmittelverfahrens bestimmten Ozonabbaus (farbige Linien) und des Ozonabbaus aus aufakkumulierten Match-Ozonabbauraten (rote Symbole) für die arktischen Winter 1995 (a) und 2000 (b). Die Ergebnisse des Wirbelmittelansatzes sind während des Winters alle zehn Tage in verschiedenen Farben eingezeichnet (von Anfang Januar in blau bis Ende März in rot). Nach Rex et al., (2002).

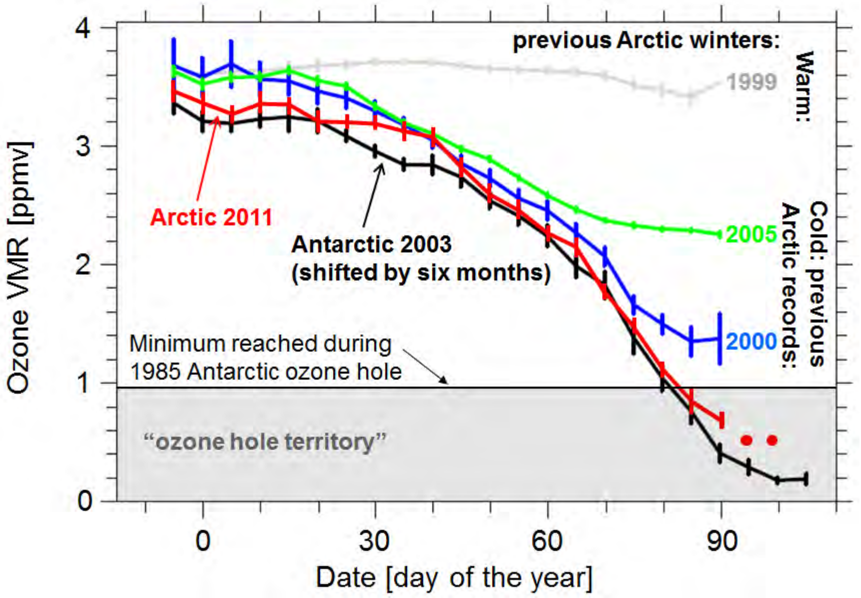

Abbildung 11: Zeitlicher Verlauf des über den Polarwirbel gemittelten Ozonmischungsverhältnisses auf einer mit der gemittelten vertikalen Bewegung absinkenden Fläche während verschiedener arktischer und einem antarktischen Winter. Zum Vergleich ist das minimale Ozonmischungsverhältnis eingezeichnet, welches im Verlauf des antarktischen Ozonlochs 1985 erreicht wurde. Nach Rex et al., 2011a und Manney et al., 2011.

bildungen stellt sich der arktische Ozonverlust in 2010/2011 als kaum von den Ozonverlusten der Antarktis unterscheidbar dar und liegt weit außerhalb des Bereichs der bislang in der Arktis beobachteten Ozonverluste.

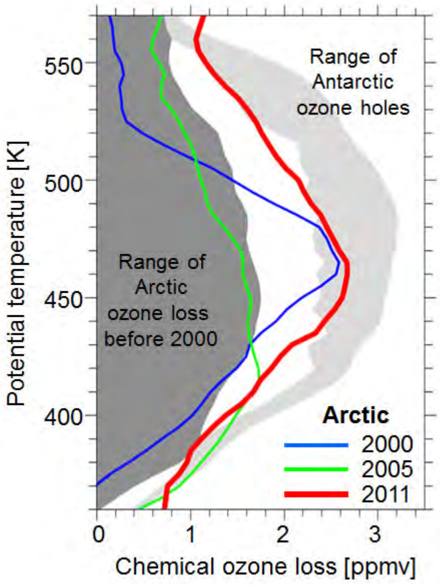

Abbildung 12: Vertikale Verteilung des über den Polarwirbel gemittelten chemisch bedingten Ozonabbaus für die drei kalten arktischen Winter seit 2000 verglichen mit der Variabilität der Ozonverluste in der Arktis vor dem Jahr 2000 und dem Bereich antarktischer Ozonverluste. Nach Rex et al., (2011a), Manney et al. (2011).

3.1.3 Ozon/Tracerrelation

Profitt et al. (1990) entwickelte einen Ansatz, chemische Ozonverluste aus der Relation zwischen Ozon und einem langlebigen chemischen Tracer zu bestimmen. Relationen zwischen langlebigen Spurengasen werden nach Etablierung des Polarwirbels im Herbst durch Durchmischung innerhalb des Wirbels und weitgehender Isolation des Polarwirbels verhältnismäßig kompakt. Da Ozon ab dem Herbst in den Polarregionen bis zum Einsetzen des heterogen initiierten chemischen Ozonverlusts sehr langlebig ist, weist es innerhalb des Polarwirbels gegen Mittwinter eine relativ kompakte Relation zu allen anderen langlebigen Spurengasen auf. In Abwesenheit von Durchmischung mit Luft von außerhalb des Polarwirbels (wo aufgrund der dort aktiven Ozonchemie eine andere Relation zwischen Ozon und dem jeweiligen Tracer herrscht) und in Abwesenheit chemischer Prozesse im Polarwirbel bleibt diese Relation unverändert. Abweichungen von dieser einmal etablierten mittwinterlichen Referenzrelation sind daher Folge chemischer Ozonverluste. Somit erlaubt eine Analyse der zeitlichen Entwicklung von Ozon/Tracerrelationen die Quantifizierung chemischer Ozonverluste.

Durchmischungsprozesse zwischen Luft aus dem Polarwirbel und Luft von außerhalb des Wirbels führen dabei zu charakteristischen linearen Mischungslinien in den gemessenen Tracerrelationen, welche die Innerwirbelrelation mit der Außerwirbelrelation verbinden. Rex et al. (1999a) konnten unter der Annahme eines einzelnen Mischungsevents z.B. durch eine Stratosphärenerwärmung ein Vorgehen entwickeln, mit dem der Einfluss von Durchmischung auf die Ergebnisse von Tracerrelationsstudien korrigiert werden kann. Dieses Verfahren beruht auf der Analyse von mehreren Tracern, die untereinander nichtlineare Relationen aufweisen müssen.

Rex et al. (2002) und Salawitch et al. (2002) verwenden die Tracerrelationsmethode, um den Ozonverlust im Winter 1999/2000 unabhängig von den in den letzten Abschnitten beschriebenen Verfahren zu bestimmen. Dabei zeigen Rex et al. (2002) einige der charakteristischen, auf

Durchmischung beruhenden Mischungslinien in gemessenen Ozon/N_2O-Relationen (Abbildung 13). Rex et al. (2002) finden aber, dass die niedrige Frequenz des Auftretens dieser Mischungslinien in den Messungen darauf hinweist, dass Einmischung von Luft von außerhalb des Polarwirbels keine wesentliche Änderung der Ozon- oder Tracerfelder verursachen konnte.

Die Ergebnisse von Rex et al. (2002) und Salawitch et al. (2002) vervollständigen das Bild der chemischen Ozonverluste in dem außergewöhnlich kalten arktischen Winter 1999/2000.

3.2 Theoretisches Verständnis des polaren Ozonverlustprozesses

Ein genaues theoretisches Verständnis der chemischen Mechanismen, die zum polaren Ozonverlust führen, ist eine grundlegende Voraussetzung dafür, diesen Prozess in globalen Modellen korrekt wiederzugeben und somit die gegenseitigen Wechselwirkungen zwischen polarer Ozonchemie und den anderen Komponenten des Klimasystems in Klimavorhersagen berücksichtigen zu können.

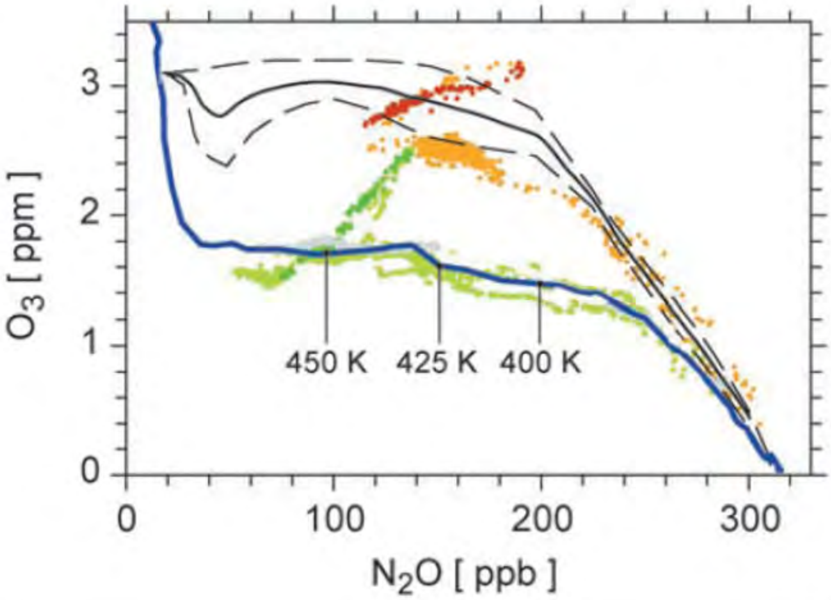

Abbildung 13: Mischungsverhältnisse von O_3 gegen N_2O basierend auf Messungen verschiedener Ballon- und ER-Flüge. Zwei Ballonmessungen vom 19.11.1999 und vom 3.12.1999 (gestrichelte Linien) wurden gemittelt um die mittwinterliche Referenzrelation zwischen O_3 und N_2O zu erhalten (obere durchgezogene schwarze Linie). Eine Ballonmessung am 5.3.2000 ergab die untere schwarze Linie. Die Differenz zu der Referenzrelation ist im Wesentlichen durch chemischen Ozonabbau verursacht. ER-2 Messungen am 23.1.2000 (orange/rot) und am 7.3.2000 (hellgrün, dunkelgrün) zeigen außer des verbreiteten und während des Winters zunehmenden Ozonverlusts auch zwei klare Mischungslinien zwischen der O_3/N_2O-Relation innerhalb des Polarwirbels und der hier nicht gezeigten Relation außerhalb des Wirbels (da diese nicht gemessen wurde). Die Relation außerhalb des Wirbels verläuft qualitativ ähnlich wie die Referenzrelation, jedoch noch etwas oberhalb dieser. Die Mischungslinien sind in rot bzw. dunkelgrün markiert. Nach Rex et al., (2002).

Im Abschnitt 2.2 wurde ein qualitativer Überblick über den polaren Ozonabbaumechanismus gegeben. Im Detail besteht der Ozonabbauprozess während eines polaren Winters aus drei Phasen, über die mit Hilfe der im Abschnitt 3.1 vorgestellten Messungen quantitative Aussagen gemacht werden können: Die Chloraktivierungsphase, die Deaktivierungsphase und der eigentliche Ozonverlustprozess. Diese Phasen werden im Folgenden betrachtet.

3.2.1 Die Chloraktivierungsphase

Durch den Mangel an solarer Einstrahlung unter den Bedingungen der winterlichen Polarnacht verschwinden HO_x, NO_x und ClO_x in der unteren polaren Stratosphäre fast komplett in ihren Reservoiren. Auch der Ozonverlust über den Chapman Mechanismus kommt nahezu zum Erliegen. Demzufolge ist die Lebensdauer von O_x dort unter normalen Umständen sehr lang.

Dies ändert sich schlagartig mit dem Auftreten polarer stratosphärischer Wolken. Diese entstehen wenn die fallenden Temperaturen im Bereich der Polarnacht die Grenztemperatur für die Kondensation von Salpetersäure unterschreiten. Die Kondensation erfolgt auf den immer vorhandenen Hintergrundaerosoltröpfchen der Junge-Schicht, welche aus Schwefelsäure- und Wassermolekülen bestehen. Die entstehenden ternären Gemische aus Schwefelsäure, Salpetersäure und Wasser können jeweils unterhalb bestimmter Grenztemperaturen unter noch ungeklärten Umständen in verschiedene kristalline Formen von Salpetersäure (Nitric Acid Trihydrate, NAT; Nitric Acid Dihydrate, NAD) oder Schwefelsäure (Sulfuric Acid Tetrahydrate, SAT) übergehen. Bislang ist jedoch von diesen verschiedenen thermodynamisch stabilen Zuständen nur NAT in der Stratosphäre nachgewiesen worden (*Voigt et al., 2000*) und es muss bezweifelt werden, dass NAD oder SAT sich unter normalen stratosphärischen Bedingungen tatsächlich bilden.

Die Aufnahme signifikanter Salpetersäureanteile in die Schwefelsäuretröpfchen des Hintergrundaerosols, also die Bildung der ternären Lösungen, beginnt bei etwa -78^oC. Ab etwa der gleichen Temperatur sind auch NAT-Kristalle thermodynamisch stabil, und zwar tatsächlich stabiler als die ternären Tröpfchen. Die Tröpfchen existieren demnach als unterkühlte Lösungen, welche die Nukleationsbarriere zu den eigentlich stabileren NAT-Kristallen nicht überwinden. Bei den typischen stratosphärischen Wasserdampfkonzentrationen findet die Kondensation von Wassereiskristallen ab etwa -85^oC statt, wobei die Überwindung der Nukleationsbarriere bei der erstmaligen Bildung von Wassereiskristallen ebenfalls einige Grad Unterkühlung voraussetzt.

Das Auftreten von PSCs hat für die Chemie der polaren winterlichen Stratosphäre zwei wichtige Konsequenzen: Auf den Oberflächen aller oben angesprochenen Tröpfchen oder festen Partikel laufen in unterschiedlicher Effizienz verschiedene heterogene chemische Reaktionen ab, die in der Gasphase nicht stattfinden können. Einige dieser Reaktionen brechen Chlorreservoirverbindungen auf und setzen ClO_x frei, zum Teil über den Umweg weiterer schnell in ClO_x-Verbindungen photolysierender Substanzen. Von größter Bedeutung ist dabei die Reaktion der beiden Chlorreservoirgase HCl und $ClONO_2$ miteinander:

$$HCl + ClONO_2 \longrightarrow Cl_2 + HNO_3 \qquad (4)$$

wobei das entstehende Cl_2 beim ersten Sonnenlicht in zwei Chlorradikale und damit zu ClO_x photolysiert. Eine vollständige Liste der Reaktionen findet sich zum Beispiel in Wohltmann et al. (2010).

Allgemein hängt die Geschwindigkeit der heterogenen Reaktionen stark von der Zusammensetzung und dem Typ des Tröpfchens oder der Oberfläche ab und ist extrem temperaturabhängig. Die Lebensdauer des Chlorreservoirs sinkt bereits bei der ersten Existenz von PSC auf wenige

Stunden und reduziert sich bei weiter fallenden Temperaturen auf Minuten. Dabei kommt es mehr auf die genaue Temperatur an, als auf die genaue Beschaffenheit der Partikel oder Tröpfchen. Daher kann unabhängig von den Details der komplizierten Mikrophysik, welche die jeweils entstehende Partikelsorte bestimmt, eine recht einheitliche Temperaturgrenze angegeben werden, bei der praktisch schlagartig das gesamte verfügbare Chlorreservoir bis zur Erschöpfung eines der beiden Reaktionspartner (HCl oder $ClONO_2$) in ClO_x überführt wird.

Da anfänglich weniger $ClONO_2$ als HCl existiert, bleibt nach dieser ersten sehr schnellen Chloraktivierung HCl zurück. In den nächsten Wochen wird durch HNO_3-Photolyse NO_2 freigesetzt, welches in Reaktion mit ClO neues $ClONO_2$ bildet, welches nun bei fortbestehender oder erneuter PSC-Existenz in heterogener Reaktion mit dem verbliebenen HCl schrittweise das restliche Chlor aktiviert (z.B. Harris et al., 2010). Während des Zeitraums derartig erhöhter ClO_x-Konzentrationen kann bei gleichzeitiger Sonneneinstrahlung sehr effizient Ozon zerstört werden.

Basierend auf den Match-Messungen (Abschnitt 3.1.1) wurde gezeigt, dass chemischer Ozonabbau sowohl auf die Bereiche des Polarwirbels (Schulz et al., 2000; Schulz et al., 2001) als auch auf die individuellen Luftmassen (Schulz, 2001) beschränkt ist, die Temperaturen unterhalb der Grenze für mögliche PSC-Existenz ausgesetzt waren, d.h. in etwa Temperaturen unterhalb von 195K (siehe Abbildung 14). Die Robustheit und globale Gültigkeit dieser Temperaturgrenze legt nahe, dass die Details der PSC-Zusammensetzung relativ unerheblich für die Effektivität der Chloraktivierung auf PSC-Partikeln sind.

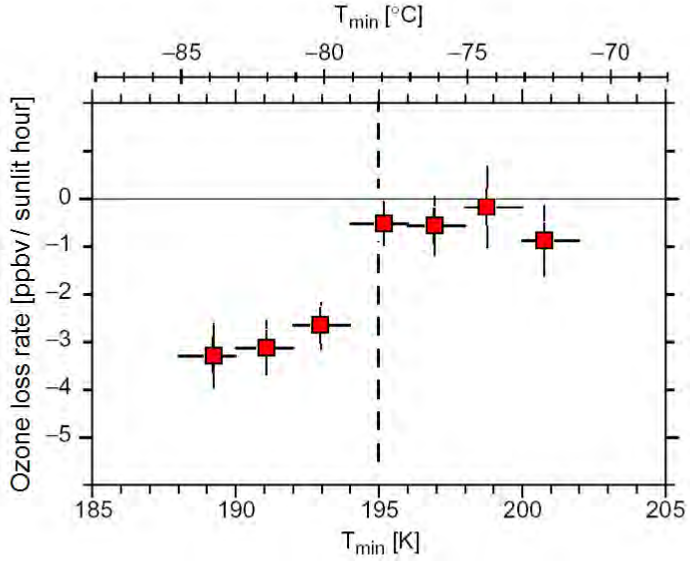

Abbildung 14: Abhängigkeit der Ozonverlustrate von der minimalen Temperatur, welche für eine Luftmasse innerhalb der jeweils letzten zwei Wochen erreicht wurde. Nach Schulz, (2001).

3.2.2 Die Deaktivierungsphase

Bei zunehmender Sonneneinstrahlung im polaren Spätwinter/Frühjahr gewinnt die Photolyse von HNO_3 zunehmend an Bedeutung, welche bei höher steigender Sonne im Frühjahr immer effizienter NO_2 erzeugt. Dieses bildet über die Reaktion

$$ClO + NO_2 + M \longrightarrow ClONO_2 + M \qquad (5)$$

das Chlorreservoir $ClONO_2$ zurück. Damit wird das ozonzerstörende ClO_x in eine der beiden reaktionsträgeren Reservoirsubstanzen überführt und somit die Ozonabbauperiode mit einem $ClONO_2$-Burst beendet. Im Verlauf der nächsten Wochen normalisiert sich dann das $ClONO_2$/ HCl-Verhältnis durch langsamere Reaktionen wieder.

Wird jedoch wie oft in der Antarktis bereits vorher das Ozon nahezu komplett zerstört, fehlt im ClO_x-Ozonabbauzyklus der Reaktionspartner für Cl (siehe Abbildung 3) und der Zyklus wird unterbrochen. Die Cl-Konzentration nimmt dabei sprunghaft zu und die Reaktion

$$Cl + CH_4 \longrightarrow HCl + CH_3 \qquad (6)$$

gewinnt an Bedeutung. Dadurch kommt es in der Antarktis mit der kompletten Ozonzerstörung zu einem HCl-Burst, welcher das $ClONO_2$-Maximum am Ende des arktischen Winters ersetzt.

Manney et al (2011) zeigen, dass es im Frühjahr 2011, bedingt durch das erste arktische „Ozonloch“ erstmals auch in der Arktis zu einem HCl-Maximum statt des sonst in der Arktis üblichen $ClONO_2$-Maximums gekommen ist.

Die Chlordeaktivierung steht in Konkurrenz zum Ozonabbau selbst. Beide Prozesse werden in ihrer Geschwindigkeit durch Photolysereaktionen bestimmt. Für die Chlordeaktivierung ist dies die oben beschriebene Photolyse von HNO_3 und für den Ozonverlust ist die Geschwindigkeit der Photolyse des ClOOCl-Moleküls (siehe Abschnitt 2.2) ratenbestimmend. Beide Substanzen photolysieren im nahen UV und der Abfall ihrer Photolysequerschnitte zum sichtbaren Bereich hin verläuft verhältnismäßig ähnlich.

Daher ist unabhängig von der solaren Einstrahlung im Wesentlichen nur die Menge des im Winter insgesamt aktivierten Chlors für den Gesamtozonabbau ausschlaggebend (Harris et al., 2010). Findet die Aktivierung früh im Winter bei weitgehender Dunkelheit statt, ist sowohl die Deaktivierung als auch die Ozonzerstörung langsam und es kommt zu einer ausgedehnten Phase langsamen Ozonabbaus. Bei Aktivierung später im Winter und intensiverer solarer Einstrahlung sind Ozonabbau und Chlordeaktivierung beide schnell und es kommt zu einer kurzen Phase sehr schnellen Ozonabbaus. Harris et al. (2010) zeigen, dass die Gesamtmengen an Ozon, die in beiden Situationen zerstört werden, sich bei gleicher Menge aktivierten Chlors nur um wenige Prozent unterscheiden (Abbildung 15).

Obwohl sich der Katalysator ClO_x bei der Ozonzerstörung nicht verbraucht, verläuft der Abbau von ClO_x eng gekoppelt an die Ozonzerstörung. Die Rate der Deaktivierung ist durch den qualitativ ähnlichen Verlauf der HNO_3- und der ClOOCl-Photolysequerschnitte dabei sogar nahezu proportional zur Ozonzerstörungsrate. Daher ist die Dynamik des Ozonverlustprozesses vergleichbar der eines Prozesses, bei dem die ozonzerstörende Substanz von der Ozonzerstörung selbst verbraucht wird. Genau wie bei so einem nicht katalytischen Prozess wird beim katalytischen Ozonabbau pro Katalysatormolekül eine recht genau vorbestimmte Menge an Ozon zerstört, bevor der Katalysator durch parallel laufende Prozesse abgebaut ist. Der Unterschied zu einem nicht katalytischen Prozess ist allerdings der weitaus größere Hebel: Harris et al. (2010) zeigen, dass im Gesamtzyklus aus Aktivierung-Ozonverlust-Deaktivierung pro ClO_x-Molekül etwa 330-400 Ozonmoleküle zerstört werden. Dieser Hebel vergrößert sich wenn es im Verlauf des Winters zu dem ozonverlustverstärkenden Effekt der Denitrifizierung kommt.

3.2.2.1 Der Einfluss von Denitrifizierung

Neben den im letzten Abschnitt beschriebenen chemischen Prozessen kann es durch PSC-Bildung auch zu sogenannter Denitrifizierung oder Dehydrierung kommen. Wenn die PSC-Partikel bei länger anhaltenden tiefen Temperaturen oder Temperaturen unter der Wassereisbildungsgrenze groß genug wachsen, beginnen sie zu sedimentieren. Dabei entziehen

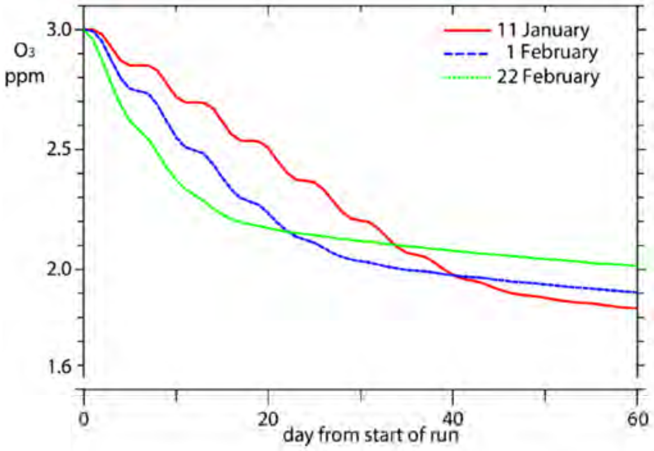

Abbildung 15: Ozonmischungsverhältnisse berechnet mit einem Boxmodell für typische Luftmassen im arktischen Polarwirbel mit einer anfänglichen Chloraktivierung von 3ppbv ClO_x am 11. Januar, 1. Februar und 22. Februar. Trotz der sehr unterschiedlichen solaren Einstrahlung zum Zeitpunkt der Chloraktivierung variiert der Gesamtozonverlust am Ende der Läufe in diesen Fällen nur um wenige Prozent. Bemerkenswert ist, dass der Lauf mit der geringsten solaren Einstrahlung sogar letztlich etwas mehr Ozonverlust produziert als Läufe mit intensiverer Einstrahlung (Harris et al., 2010).

sie der Luft, in denen ihre Kondensation stattgefunden hat, die Bestandteile, die in den PSC-Partikeln kondensiert sind. Hier ist insbesondere der Entzug von HNO_3 (Denitrifizierung) wesentlich. Falls bei sehr tiefen Temperaturen wesentliche Wassereisbestandteile in den PSC-Partikeln enthalten sind, findet auch signifikanter Entzug von Wasserdampf (Dehydrierung) statt.

Der Entzug von HNO_3 hat erhebliche Auswirkungen auf die Chlordeaktivierungsphase im Spätwinter/Frühjahr. In denitrifizierten Luftmassen steht weniger HNO_3 zur Photolyse zur Verfügung, es wird daher weniger NO_2 gebildet und die Chlordeaktivierung über Reaktion (5) ist verzögert. Dieser Prozess trägt in der Antarktis erheblich zur Bildung des Ozonlochs bei.

Rex et al. (1997) haben gezeigt, dass erhebliche Denitrifizierung im sehr kalten Winter 1995/1996 auch in der Arktis stattgefunden hat. Erstmals wurde in dieser Arbeit gezeigt, dass die Ozonabbauperiode in den denitrifizierten Luftmassen erheblich verlängert wurde und es daher in den denitrifizierten Luftmassen insgesamt zu einem deutlich verstärkten Ozonabbau gekommen ist. Rex et al. zeigen, dass sich die Beobachtungen der Ozonverlustraten am besten erklären lassen, wenn ca. 80% Denitrifizierung in etwa der Hälfte der Luftmassen stattgefunden hat. Unterhalb des denitrifizierten Bereichs wurde eine Zone verminderten Ozonabbaus gefunden, was eine Renitrifizierung durch Verdampfen der PSC-Partikel in diesem Bereich andeutet.

3.2.3 Der Ozonabbauprozess

Sobald durch die oben beschriebenen Chloraktivierungsprozesse signifikante Mengen an ClO_x in der polaren Stratosphäre zur Verfügung stehen, setzt unter Einfluss solarer Einstrahlung der eigentliche Ozonabbauprozess ein. Ziel der Forschung ist es, diesen Prozess möglichst genau in chemischen Modellen zu repräsentieren, so dass er als Modul in globale Klimamodelle eingebaut werden kann. Der Grad unseres theoretischen Verständnisses des polaren Ozonabbauprozesses ergibt sich im Vergleich der in einem numerischen Modell berechneten Ozonabbauraten mit atmosphärischen Messungen dieser Raten.

Jedes Chemiemodell basiert auf einem Satz an chemischen Reaktionen, die als relevant für die untersuchten Prozesse angenommen werden. Die Geschwindigkeit dieser Reaktionen beruht auf reaktionskinetischen Parametern, welche durch Labormessungen bestimmt werden müssen. Ein Expertenpanel empfiehlt basierend auf der Gesamtheit dieser vielen hundert Labormessungen Werte für diese reaktionskinetischen Parameter und ihrer jeweiligen Unsicherheiten. Diese Empfehlungen wurden in den Veröffentlichungen JPL 2002 (*Sander et al., 2003*), JPL 2006 (*Sander et al., 2006*), JPL 2009 (*Sander et al., 2009*) und JPL 2010 (*Sander et al., 2011*) alle paar Jahre aktualisiert.

Modellierung des chemischen Ozonabbauprozesses und der Vergleich der Modellergebnisse mit Messungen des Ozonabbaus erlauben es, zu ermitteln ob das im Modell verwendete Reaktionssystem vollständig ist und ob die im Labor bestimmten kinetischen Parameter mit diesem Reaktionssystem den beobachteten Ozonverlust hervorbringen. Dies ist eine notwendige Bedingung dafür, dass das Modell auf einer hinreichend vollständigen Theorie des polaren Ozonabbaus beruht.

Stellt sich darüber hinaus heraus, dass ein so gestaltetes Modell den beobachteten Ozonabbau unter einem weiten Spektrum an meteorologischen und chemischen Bedingungen reproduzieren kann, wächst die Zuversicht, das unsere Theorie vollständig ist, zumindest für das Spektrum der in der Stratosphäre vorkommenden Bedingungen, und die Übereinstimmung für einzelne Datenpunkte nicht nur zufällig auf sich gegenseitig aufhebenden Fehlern beruht.

Abbildung 3 (oben links) zeigt eine Illustration des sogenannten Chlordimerzyklusses, auf den in der Arktis etwa 50-60% des winterlichen Ozonverlusts zurückgehen und in der Antarktis ein noch etwas größerer Anteil (Frieler et al., 2006; Newman und Rex, 2007):

$$2\text{x} (\mathrm{Cl} + \mathrm{O_3} \longrightarrow \mathrm{ClO} + \mathrm{O_2}) \tag{7}$$

$$\mathrm{ClO} + \mathrm{ClO} + \mathrm{M} \longrightarrow \mathrm{ClOOCl} + \mathrm{M} \tag{8}$$

$$\mathrm{ClOOCl} + h\nu \longrightarrow \mathrm{ClOO} + \mathrm{Cl} \tag{9}$$

$$\mathrm{ClOO} + \mathrm{M} \longrightarrow \mathrm{Cl} + \mathrm{O_2} + \mathrm{M} \tag{10}$$

$$2\mathrm{O_3} \longrightarrow 3\mathrm{O_2}$$

Der zweitwichtigste Ozonabbauzyklus des polaren Winters ist der gekoppelte ClO/BrO-Zyklus (oben rechts in Abbildung 3):

$$\mathrm{Cl} + \mathrm{O_3} \longrightarrow \mathrm{ClO} + \mathrm{O_2} \tag{11}$$

$$\mathrm{Br} + \mathrm{O_3} \longrightarrow \mathrm{BrO} + \mathrm{O_2} \tag{12}$$

$$\mathrm{ClO} + \mathrm{BrO} \longrightarrow \mathrm{Br} + \mathrm{ClOO} \tag{13}$$

$$\mathrm{ClOO} + \mathrm{M} \longrightarrow \mathrm{Cl} + \mathrm{O_2} + \mathrm{M} \tag{14}$$

$$2\mathrm{O_3} \longrightarrow 3\mathrm{O_2}$$

dabei kann statt Reaktion (13) und (14) auch

$$\mathrm{ClO} + \mathrm{BrO} \longrightarrow \mathrm{BrCl} + \mathrm{O_2} \tag{15}$$

$$\mathrm{BrCl} + h\nu \longrightarrow \mathrm{Br} + \mathrm{Cl} \tag{16}$$

ablaufen.

Die zu (13) und (14) alternativen Reaktionen:

$$\mathrm{ClO} + \mathrm{BrO} \longrightarrow \mathrm{Br} + \mathrm{OClO} \tag{17}$$

$$\mathrm{OClO} + h\nu \longrightarrow \mathrm{O} + \mathrm{ClO} \tag{18}$$

stellt die O-O Bindung nicht wieder her und erzeugt im Gesamtzyklus genausoviel O_x wie es zerstört - es wird ein O_3 zerstört aber ein O erzeugt, welches in der Folge sofort mit O_2 zu O_3 weiterreagiert - und stellt daher eine Konkurrenz zum Ozonabbauzyklus dar.

3.2.3.1 Analyse von Ozonsondenmatchereignissen

Der Matchdatensatz (Abschnitt 3.1.1) ist ideal geeignet, die genaue Kinetik des Ozonabbauprozesses zu untersuchen. Bei anderen Methoden, Ozonabbau in der polaren Stratosphäre zu bestimmen, erhält man typischerweise den gesamten Ozonabbau über große räumliche und zeitliche Mittel, ohne genaue Information, welchen Bedingungen die Gesamtheit der betrachteten Luftvolumina jeweils individuell ausgesetzt waren. Match hingegen misst Ozonabbauraten in individuellen sehr genau charakterisierten Luftmassen. Es wurden detaillierte Modellansätze entwickelt, die gerade diesen Vorteil von Match ausnutzen.

Becker et al. (1998) verwenden ein chemisches Boxmodell, um entlang der Trajektorien aller Matchereignisse des arktischen Winters 1991/1992 Ozonverlustraten zu bestimmen. Die größten von Match bestimmten Ozonabbauraten im Januar dieses Winters konnten dabei nicht erreicht werden.

Die größten Unsicherheiten in dieser Studie liegen in der korrekten Modellierung der Chloraktivierungsprozesse. Die enorme Temperaturabhängigkeit der heterogenen Reaktionen, große Unsicherheiten bei der Abschätzung der für die heterogene Chemie zur Verfügung stehenden reaktiven Oberfläche der PSC-Partikel und große Unsicherheiten der reaktionskinetischen Parameter der heterogenen Chemie führen zu großen Unsicherheiten bei der Berechnung des für den Ozonabbauprozess zur Verfügung stehenden ClO_x.

Woyke et al. (1999) verwenden ClO und BrO Messdaten eines Ballonaufstiegs im Winter 1994/1995 um die Unsicherheit der Modellierung von ClO_x im Modell zu verringern. Modellierte Ozonabbauraten basierend auf diesen Messungen erreichen jedoch wiederum nicht die von Match in diesem Winter bestimmten Ozonverlustraten (Woyke et al., 1999).

Becker et al. (2000) analysieren den im Vergleich zu 1991/1992 viel umfangreicheren Matchdatensatz des Winters 1994/1995 in einer Modellstudie, die dem gleichen Ansatz wie in Becker et al. (1998) folgt. Erstmals wird in dieser Studie auch ein breiter Höhenbereich in die Analyse mit einbezogen und ein Höhen-/Zeitschnitt der Modellergebnisse mit den Messungen verglichen. Auch hier zeigt sich ein erhebliches Defizit des Modells, welches die gemessenen Ozonabbauraten in keiner der umfangreichen Sensitivitätsläufe erreichen kann.

Rex et al. (2003) führen einen neuen Modellansatz ein, um die Unsicherheiten durch die heterogene Chemie aus den Ergebnissen herauszuhalten und robustere Aussagen über die Kinetik des in der Gasphase ablaufenden eigentlichen Ozonabbauprozesses machen zu können. Statt eines vollständigen Modells der stratosphärischen Chemie setzen Rex et al. (2003) ein sehr schlankes Modell ausschließlich des Ozonverlustprozesses ein. Statt des Versuchs ClO_x aus der komplizierten Interaktion aus heterogener Aktivierung und folgender Deaktivierung zu berechnen, wird dieses Modell dazu verwendet, aus den gemessenen Ozonabbauraten auszurechnen, welche Konzentration an ClO_x im Modell erforderlich wäre, um die Messungen nach dem Stand der Kenntnis des Ozonabbauprozesses zu erklären.

Da mit dem konstanten Gesamtbudget des stratosphärischen Chlorgehalts (Cl_y) eine robuste Obergrenze für ClO_x existiert, können mit diesem Modellansatz sehr robuste Aussagen gemacht werden, sobald die berechnete ClO_x-Menge diese Obergrenze überschreitet. Rex et al.

(2003) untersuchten das sich in den vorherigen Arbeiten abzeichnende Modellproblem mit diesem Ansatz in einer umfassenden Studie, die alle Winter bis zu diesem Zeitpunkt und alle Höhenbereiche einschließt.

Es zeigt sich, dass mit der bekannten Theorie und den zu diesem Zeitpunkt in JPL 2002 empfohlenen reaktionskinetischen Parametern sehr konsistent der beobachtete Ozonabbau in allen untersuchten kalten arktischen Januaren nicht erklärt werden konnte (Abbildung 16). Da die im Modell benötigte Menge an ClO_x für diese Perioden regelmäßig über der Obergrenze des zur Verfügung stehenden Cl_y liegt, ist diese Aussage robust und unabhängig von den großen Unsicherheiten der heterogenen Chemie und Chloraktivierung.

Rex et al. (1999c) schlugen als Beitrag zur Lösung des Problems höhere Photolysequerschnitte des ClOOCl Moleküls vor, insbesondere bei den längeren Wellenlängen. Im Winter 1999/2000 wurde mit THESEO2000/SOLVE in der arktischen Stratosphäre die bis dahin umfangreichste Messkampagne zur Untersuchung des arktischen Ozonverlusts durchgeführt. Während des Winters wurden umfangreiche Messungen von Spurengasen und PSC-Eigenschaften von Höhenforschungsballonen und mehreren Flugzeugen einschließlich des amerikanischen Höhenforschungsflugzeugs ER-2 durchgeführt. Erstmals wurde dabei während acht Missionen der ER-2 in der Stratosphäre sowohl ClO als auch ClOOCl in-situ gemessen. *Stimpfle et al. (2004)* fanden basierend auf diesen Messungen, dass sich das ClO/ClOOCl Verhältnis und seine Variation mit dem Sonnenzenitwinkel tatsächlich nur mit größeren Photolysequerschnitten von ClOOCl im nahen UV erklären lässt.

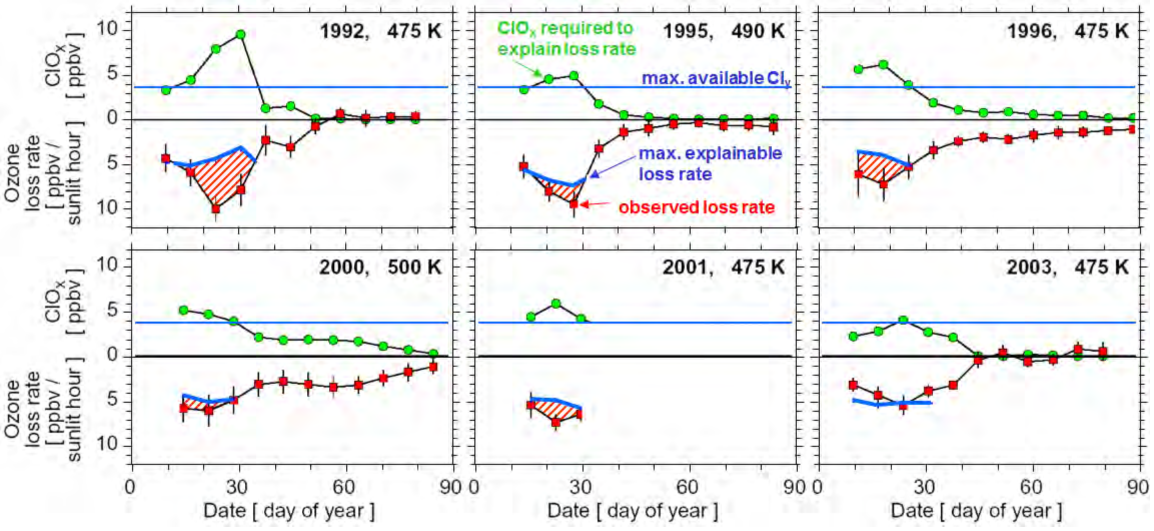

Abbildung 16: Auf dem Matchverfahren basierende chemische Ozonverlustraten im Polarwirbel (rot) für verschiedene arktische Winter mit jeweils kalten Januaren. Das Mischungsverhältnis von ClO_x, welches basierend auf Modellrechnungen erforderlich wäre, die beobachtete Ozonabbaurate zu erklären, ist grün eingezeichnet und liegt oftmals über der insgesamt verfügbaren Menge an stratosphärischem Chlor (dünne blaue horizontale Linie). Die mit dieser maximal verfügbaren Menge an stratosphärischen Chlor maximal erklärbaren Ozonabbauraten (d.h. unter der Annahme vollständiger Chloraktivierung) sind als dicke blaue Linien eingezeichnet. Die rot schraffierten Ozonabbauraten lassen sich mit dem verwendeten Modell nicht erklären und weisen auf Defizite im Modell hin. Diese Defizite sind inzwischen behoben (siehe z.B. Abbildung 17). Nach Rex et al., (2003).

Darauf aufbauend waren Frieler et al. (2006) erstmalig in der Lage, eine konsistente und vollständige Theorie des polaren Ozonabbaus zu präsentieren. Zunächst wurden mit der Methode von Rex et al. (2003) die Matchdaten des Winters 1999/2000 untersucht und die aus den gemessenen Ozonverlustraten berechneten ClO_x-Konzentrationen mit den ClO_x-Messungen der ER-2 verglichen (Abbildung 17).

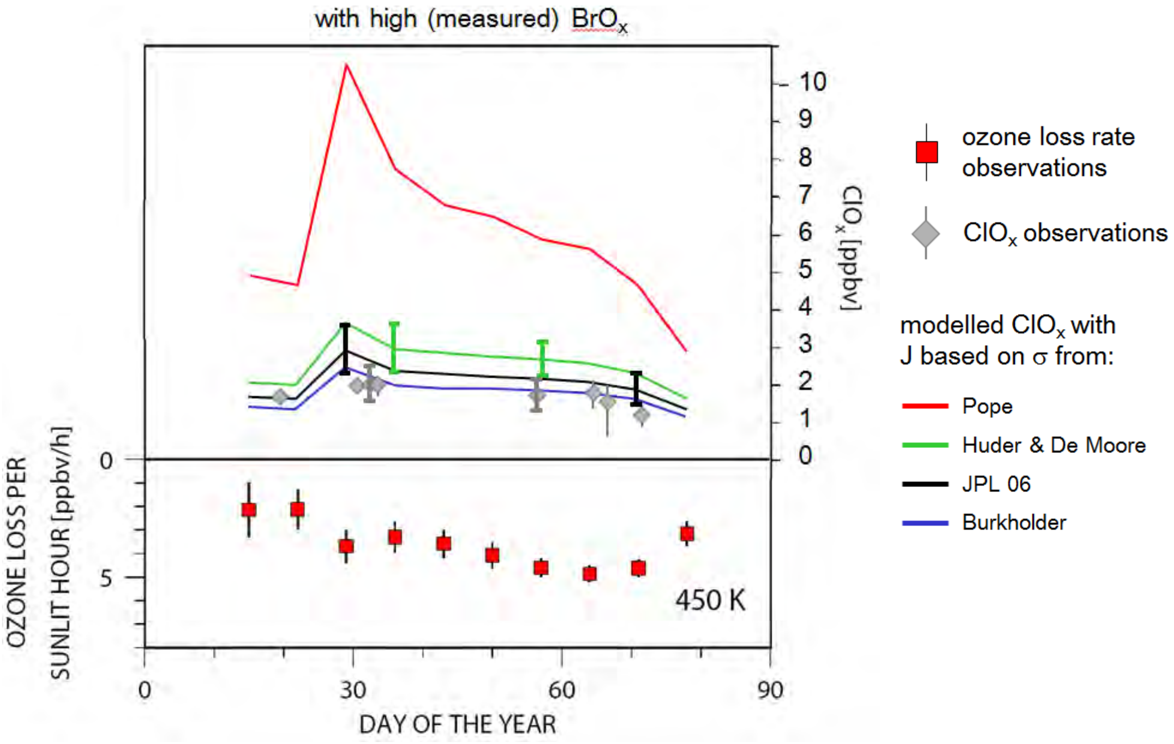

Abbildung 17: Ozonverlustrate im Winter 1999/2000 basierend auf Match (rote Symbole) und mit verschiedenen Modellannahmen berechnete Mischungsverhältnisse von ClO_x, die im Modell erforderlich sind um die beobachteten Ozonabbauraten zu erklären. Aus direkten Messungen von ClO und ClOOCl abgeleitete Mischungsverhältnisse von ClO_x sind als graue Symbole eingezeichnet. Nach Frieler et al., (2006), WMO-Assessment 2006: Newman und Rex (2007).

Frieler et al. (2006) fand hervorragende Übereinstimmung zwischen den Messungen der Ozonabbauraten, der darauf beruhenden modellierten Menge an ClO_x und den gemessenen ClO_x-Konzentrationen, wenn im Modell zwei Annahmen gemacht wurden:

Erstens wurden statt der auf den Labormessungen beruhenden Empfehlung für die ClOOCl Photolysequerschnitte größere Querschnitte verwendet, die konsistent mit dem von *Stimpfle et al. (2004)* berichteten ClO/ClOOCl-Verhältnis sind. Diese Querschnitte folgen der Labormessung von *Burkholder et al. (1990),* welche zu dem Zeitpunkt die größten im Labor gemessenen Photolysequerschnitte darstellten. Die kleinere Empfehlung in JPL 2002 beruhte auf dem Gesamtbild der Labormessungen zu diesem Zeitpunkt, die auch Messungen kleinerer Werte einschlossen. Die in Frieler et al. (2006) verwendeten Werte von *Burkholder et al. (1990)* liegen jedoch gerade noch im Unsicherheitsbereich der Empfehlungen von JPL 2002.

Zweitens wurde ein Beitrag von sehr kurzlebigen Bromverbindungen zum Gesamtbudget des Stratosphärischen Broms angenommen, welches durch diesen zunächst spekulativen Beitrag größer angenommen wurde als zuvor (siehe Kapitel 5).

Mit diesen beiden Annahmen ergab sich erstmals eine konsistente quantitative Theorie des arktischen Ozonverlusts, welche auch die in Rex et al. (2003) bemerkten hohen Ozonverlustraten in kalten arktischen Januaren erklären konnte (Frieler et al., 2006).

In dieser Theorie macht der Chlordimerzyklus und der gekoppelte ClO/BrO-Zyklus zusammen etwa 85% des gesamten Ozonverlustes aus. Der Rest entfällt fast ausschließlich auf den hier nicht weiter beschriebenen ClO+O Zyklus (Frieler et al., 2006). Beide Zyklen profitieren durch die Vergrößerung der ClOOCl-Photolysequerschnitte. Durch den erhöhten Anteil an stratosphärischem Brom gewinnt der Anteil des Ozonverlusts über den gekoppelten BrO/ClO-Zyklus jedoch gegenüber dem Chlordimerzyklus an Bedeutung und löst diesen unter bestimmten arktischen Bedingungen sogar als den effizientesten Ozonabbauzyklus ab (Abbildung 18; Frieler et al., 2006; WMO-Assessment 2006: Newman und Rex, 2007). Dies unterstreicht die große Bedeutung des stratosphärischen Broms und seiner Variabilität und langfristigen Trends für den polaren Ozonabbau (siehe auch Kapitel 5).

Sowohl die durch Match gezeigte Temperaturabhängigkeit des Ozonverlusts (Abbildung 14) als auch die aus Matchmessungen abgeleitete Abhängigkeit von solarer Einstrahlung (Abbildung 19) stützen solide die Theorie des Ozonabbauprozesses und lassen wenig Raum für spekulative alternative chemische Prozesse. Diese beiden empirisch sicheren Befunde erlangen große Relevanz insbesondere da eine Laborstudie (*Pope et al., 2007*) Zweifel am grundlegenden Verständnis des chemischen Ozonabbauprozesses begründet (*Schiermeier, 2007*; Details siehe Abschnitt 3.2.3.3).

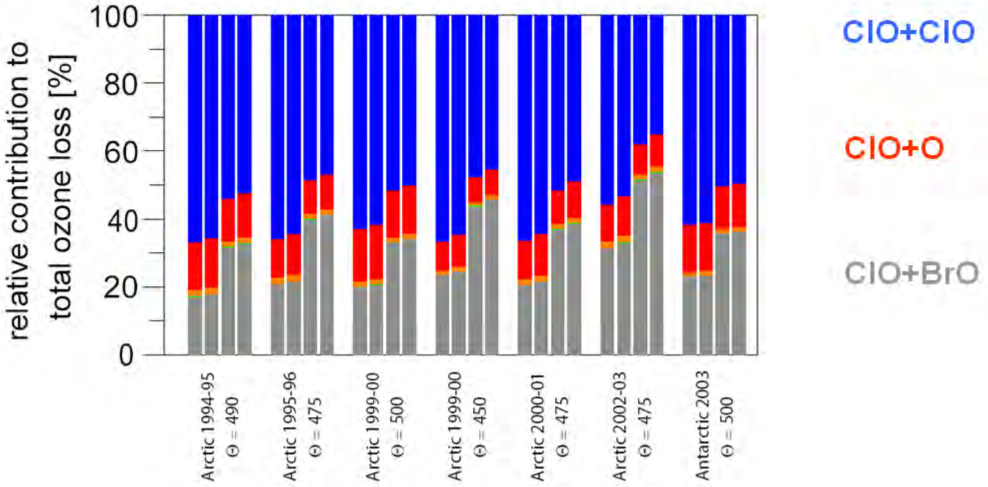

Abbildung 18: Anteil des ClO_x- (blau), des ClO+O- (rot) und des gekoppelten ClO_x/BrO_x-Ozonabbauzyklusses (grau) am gesamten Ozonabbau für verschiedene arktische und einen antarktischen Winter. Für jeden Winter sind die Ergebnisse verschiedener Modellannahmen gezeigt: Links: JPL 2002-Kinetik, Mitte links: erhöhte ClOOCl Photolyserate nach den Ergebnissen von Abbildung 17, Mitte rechts: erhöhte BrO_x-Konzentrationen nach Frieler et al. (2006), rechts: ClOOCl Photolyserate und BrO_x-Konzentrationen erhöht, welches nach Abbildung 17 mit Beobachtungen konsistente Ergebnisse ergibt. Nach Frieler et al., (2006), WMO-Assessment 2006: Newman und Rex, (2007).

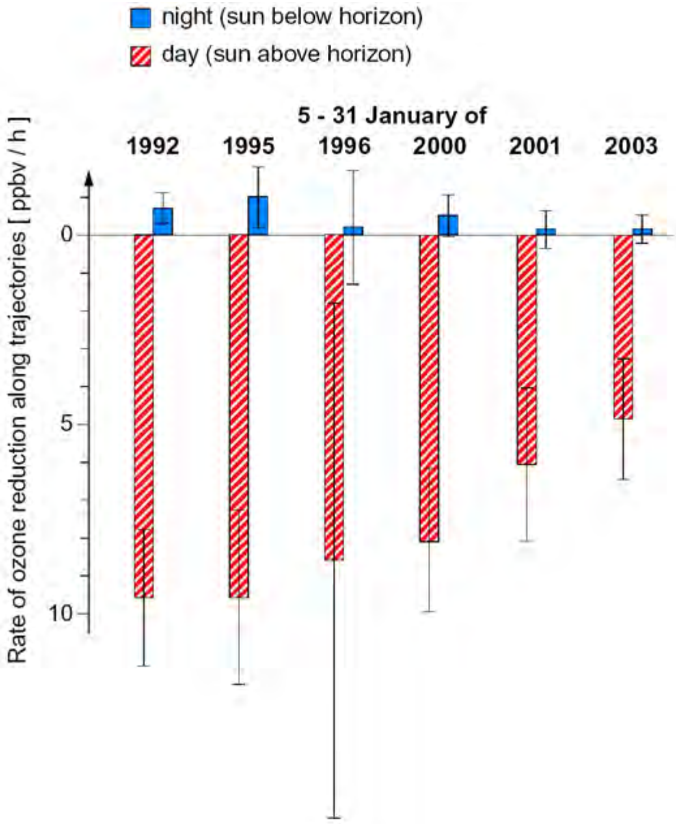

Abbildung 19: Mittels bivariater Regressionsanalyse aus Matchdaten ermittelte Ozonabbauraten für sonnenbeschienene Bedingungen (rot, „day“) und in Bereichen, in denen die Sonne vollständig unter dem geometrischen Horizont liegt (blau, „night“). Nach Rex et al., (2003).

3.2.3.2 Unsicherheiten modellierter Ozonabbauraten

Aufgrund des hohen numerischen Aufwands der Modellierung stratosphärenchemischer Prozesse werden die Unsicherheiten der reaktionskinetischen Parameter bei der Modellierung in der Regel nicht durch das Modell propagiert und auf die Angabe der Unsicherheiten von Modellergebnissen wird in praktisch allen Studien verzichtet. In globaler 3d-Modellierung ist eine Propagation der hunderten von Unsicherheiten in den antreibenden Parametern durch das Modell tatsächlich leider derzeit noch faktisch unmöglich. Die Vernachlässigung der Modellfehler behindert den wissenschaftlichen Fortschritt allerdings erheblich, da bei Diskrepanzen zwischen Modellergebnissen und Messungen nicht ohne weiteres ersichtlich ist, ob diese größer oder kleiner als die kombinierte Unsicherheit von Modell und Messung sind.

In Frieler (2005) und Kawa et al. (2009) wurde ein Monte-Carlo-Ansatz entwickelt, um die Unsicherheiten der reaktionskinetischen Parameter zumindest in Modellen des polaren Ozonverlustprozesses durch die Modellrechnung hindurch zu propagieren. Wegen des begrenzten numerischen Aufwands ist dies besonders erfolgreich in dem vereinfachten Modellansatz, der in Rex et al. (2003) und Frieler et al. (2006) zum Einsatz kam. Abbildung 20 zeigt die enorme Unsicherheit in den berechneten Ozonabbauraten, die sich allein aus den Unsicherheiten der reaktionskinetischen Parameter ergibt (basierend auf den zum Zeitpunkt der Studie aktuellen JPL 2002 Empfehlungen für die reaktionskinetischen Parameter).

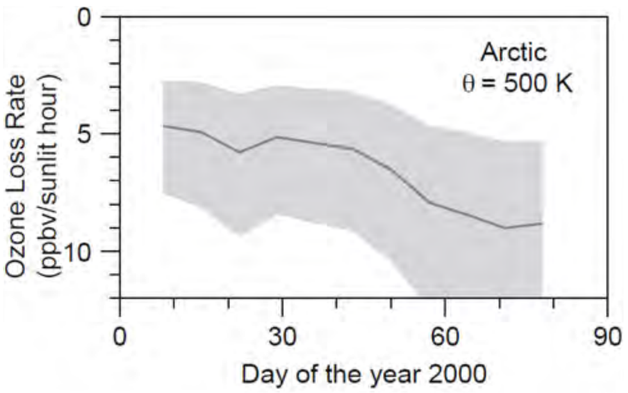

Abbildung 20: Median der mit einem chemischen Modell berechneten Ozonverlustraten für das Ensemble von Match-Trajektorien des Winters 1999/2000 (graue Linie). Die Unsicherheiten der reaktionskinetischen Parameter wurden mittels eines Monte-Carlo-Verfahrens durch das chemische Modell propagiert und als graue Schraffur dargestellt (+/- 34% der Verteilung der Ergebnisse der Monte Carlo Simulation, d.h. 68% der Ergebnisse der Monte Carlo Simulationen verlaufen im schraffierten Bereich). Nach Kawa et al. (2009).

Der Monte-Carlo-Ansatz erlaubt es auch, die relativen Beiträge der einzelnen reaktionskinetischen Parameter zu der gesamten Unsicherheit zu bestimmen. Mit ca. 70% Beitrag zum gesamten Unsicherheitsbereich trägt die Unsicherheit der ClOOCl-Photolysequerschnitte den größten Anteil bei. Dieser ist gefolgt von dem Beitrag der Unsicherheit in den kinetischen Parametern, die Reaktion (13) beschreiben.

3.2.3.3 Selfmatch-Flugpattern

Abschnitt 3.2.3.2 hat die Relevanz der genauen Kinetik der Reaktionen der ClO_x-Spezies für unser Verständnis des polaren Ozonabbaus deutlich gemacht. In der Vergangenheit wurde die Kinetik dieser Reaktionen ausschließlich in Labormessungen bestimmt. Dies führt jedoch wegen der enormen Schwierigkeiten, die Bedingungen der winterlichen polaren Stratosphäre im Labor zu erzeugen, oft zu unbefriedigenden Ergebnissen und sehr großen Fehlergrenzen für die bestimmten Parameter.

Es wurde daher nach einem Verfahren gesucht, Information über die Kinetik der ClO_x-Reaktionen direkt durch Messungen in der Stratosphäre zu erlangen. Dazu wurde basierend auf dem lagrangeschen Messkonzept der Ozonsonden-Matchkampagnen ein spezielles Flugpattern für Stratosphärenflugzeuge entwickelt, welches so entworfen wurde, dass die Kinetik dieser Reaktionen durch in-situ Messungen in der Stratosphäre selbst bestimmt werden kann. Das Verfahren nutzt aus, dass der Verlust von ClOOCl und damit die Bildung von ClO tagsüber vollständig durch die Photolyse dominiert ist, während er nachts nur durch die thermische Zersetzung von ClOOCl stattfindet. Damit ist das Verhältnis von ClO/ClOOCl tagsüber sensitiv auf die Photolyserate und verhältnismäßig unsensitiv auf die Rate der thermischen Zersetzung, während sich diese Verhältnisse nachts umkehren.

Im Gleichgewicht gilt sogar formal:

$$\text{tagsüber:} \quad [\mathrm{ClO}]^2 / [\mathrm{ClOOCl}] = J_{\mathrm{ClOOCl}} / k_f \qquad \text{(i)}$$
$$\text{nachts:} \quad [\mathrm{ClO}]^2 / [\mathrm{ClOOCl}] = k_b / k_f \qquad \text{(ii)}$$

wobei J die Photolysefrequenz von ClOOCl, k_f die Reaktionskonstante der ClOOCl-Bildungsreaktion (8) und k_b die Reaktionskonstante der thermischen Zersetzung von ClOOCl sind. Eckige Klammern stehen für die Konzentration des jeweiligen Stoffs.

Die Lebensdauer von ClOOCl bezüglich der thermischen Zersetzung liegt jedoch bei den Temperaturen im polaren Winter bei vielen Stunden, so dass nachts in der Regel nicht von einem Gleichgewicht zwischen ClO und ClOOCl ausgegangen werden kann.

Tagsüber ist die Lebensdauer von ClOOCl bezüglich der Photolyse eine steile Funktion des Sonnenzenitwinkels, da die Photolyse im UV Bereich liegt. Bei den typischerweise großen Sonnenzenitwinkeln im polaren Winter ist auch hier die Lebensdauer kurz vor oder kurz nach Sonnenauf- bzw. untergang so lang, dass nicht vom Erreichen des Gleichgewichts ausgegangen werden kann. Dennoch veranschaulichen Gleichungen (i) und (ii) den Übergang von einem J/k_f-dominierten Verhältnis von ClO zu ClOOCl vor Sonnenuntergang zu einem k_b/k_f-dominierten Verhältnis nach Sonnenuntergang.

Diese schnelle Änderung eines messbaren Verhältnisses von der Sensitivität auf einen kinetischen Parameter zur Sensitivität auf einen anderen Parameter bildet die Basis des sogenannten Selfmatch-Verfahrens. Hierbei wird der Flugpfad eines Stratosphärenflugzeugs so geplant, das auf dem Hinweg Luftmassen im Sonnenlicht kurz vor Sonnenuntergang beprobt werden, das Flugzeug bei Sonnenuntergang wendet und auf dem Rückweg entlang eines Flugpfades gesteuert wird, der den zwischenzeitlich verdrifteten Positionen der auf dem Hinweg beprobten Luftmassen entspricht. Dadurch erhält man Paarungen von Luftmassen, die jeweils vor und nach Sonnenuntergang vom Flugzeug beprobt wurden (Abbildung 21a).

Das Selfmatch Verfahren wurde in der EUPLEX-Kampagne Anfang 2003 mit dem Stratosphärenflugzeug Geophysika zum ersten Mal und sehr erfolgreich eingesetzt (Schofield et al., 2008) und dann während der RECONCILE-Kampagne Anfang 2010 mehrfach und in verschiedenen Konfigurationen auch zu Sonnenaufgang wiederholt (Suminska-Ebersoldt et al., 2012). Die Planung des Flugpfades beruht dabei auf Trajektorienrechnungen, die mittels meteorologischer Vorhersagedaten in der Zukunft gerechnet werden und die Verdriftung der Luftmassen zwischen den beiden Beprobungen vorhersagen. Das Konzept war so erfolgreich, dass auf dem Rückflug mehrmals der Abgasstrahl des Hinfluges berührt wurde, was durch Spikes in den Partikelmessungen an Bord der Geophysika belegt wurde (Abbildung 21b).

In der Analyse der Selfmatch-Messungen kommt das in Rex et al. (2003) beschriebene Modell der $\mathrm{ClO_x}$-Chemie zum Einsatz. Es kann dabei entweder sowohl auf die ClO als auch auf die gleichzeitig erfolgten ClOOCl-Messungen zurückgegriffen werden, oder es kann auf die Verwendung der erheblich unsichereren ClOOCl-Messungen verzichtet werden. In beiden Fällen wird das Modell entlang von Trajektorien betrieben, die ausgehend von der jeweils ersten Messung einen Tag zurückreichen und von der Messung vorwärts bis zur zweiten Messung durch die Geophysika reichen.

Das Modell erkundet nun den Parameterraum aus J, k_b und k_f. Wird die ClOOCl-Messung nicht verwendet, ist $\mathrm{ClO_x}$ ebenfalls Parameter, ansonsten wird es aus der Summe ClO + 2xClOOCl berechnet und vorgegeben. Dabei werden die Unsicherheiten für ClOOCl aus den Messunsicherheiten für ClO und ClOOCl abgeleitet und gehen in die Fehlerrechnung mit ein.

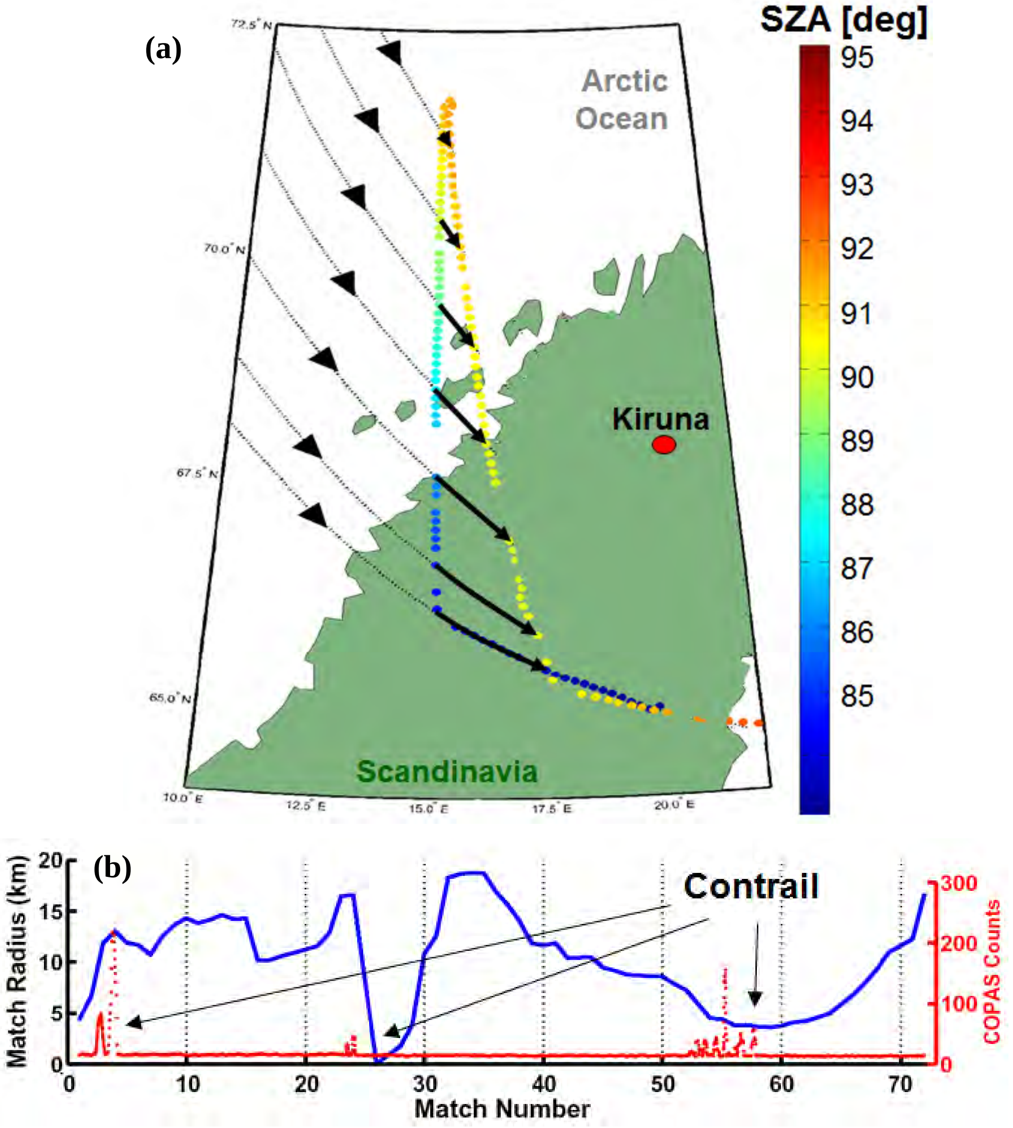

Abbildung 21: Oben: Darstellung des Flugpfades des ersten Selfmatch-Fluges. Pfeile deuten Trajektorien an, die die Messungen des Hinfluges (links) mit denen des Rückfluges (rechts) verknüpfen. Farben geben den Sonnenzenitwinkel während der Messungen an. Unten: In einer nachträglichen, auf meteorologischen Analysedaten (anstatt auf Vorhersagen wie bei der Flugplanung) beruhenden Berechnung bestimmter Abstand zwischen verdrifteten Luftmassen des Hinflugs und Messungen während des Rückflugs (blau). Messungen des Partikelinstruments COPAS zeigen in drei Bereichen des Rückflugs klare Zeichen der Abgasspur des Hinflugs, jeweils dort, wo der berechnete Abstand zu den verdrifteten Luftmassen besonders gering ist. Nach Schofield et al. (2008).

Innerhalb des so aufgespannten Parameterraums berechnet das Modell die ClO Konzentrationen an den beiden Messpunkten entlang der Trajektorie. Die Summe der Abweichungen zwischen berechnetem und gemessenen ClO über alle Trajektorien und jeweils über beide Messpunkte ist ein Maß für die Plausibilität der entsprechenden Kombination von Parametern. Die Kombination, welche die geringste Abweichung ergibt, stellt im Sinne der Messungen die optimalen Werte der kinetischen Parameter dar. Das Volumen im Parameterraum, welches Abweichungen unterhalb der Messungenauigkeit von ClO ergibt, stellt die Gesamtheit der Parameterkombinationen dar, welche konsistent mit den Messungen sind - es repräsentiert also das „Unsicherheitsvolumen“ um das eigentliche Minimum herum.

Die Identifizierung des absoluten Minimums im Parameterraum ist eine nichtlineare Optimierungsaufgabe mit dem verwendeten chemischen Modell als Vorwärtsmodell und kann mit numerischen Lösungsverfahren für solche Aufgaben gelöst werden, wie zum Beispiel mit der „optimal estimation“-Technik.

Eine Charakterisierung des Unsicherheitsvolumens würde jedoch durch die hohe Nichtlinearität des Problems die vierdimensionale Abtastung des vollständigen Parameterraumes in einem engmaschigen Gitter erfordern und wäre numerisch kaum durchführbar. Schofield et al. (2008) verwendeten eine Kombination aus dem jeweils eindimensionalen Abtasten des Parameterraums in Richtung der größten Nichtlinearität und einem „optimal estimation“-Ansatz in dem jeweiligen lineareren dreidimensionalen Unterraum, um das Unsicherheitsvolumen mit begrenztem numerischen Aufwand vollständig zu charakterisieren und dabei die Hauptnichtlinearitäten zu berücksichtigen.

Als wichtigste Ergebnisse finden Schofield et al. (2008), dass die Selfmatch-Messungen einen kleineren Wert für k_{eq} ($k_{eq}=k_f/k_b$) und einen größeren Wert für J nahelegen als in JPL 2006 empfohlen, falls k_f annähernd im empfohlenen Bereich liegt (Abbildung 22a und b). Der Wert von k_b ist dabei zwar für das Verständnis der Nacht-Balance zwischen ClO und ClOOCl relevant, hat aber nur minimale Auswirkungen auf den berechneten Ozonabbau. Gegenüber JPL 2006 erhöhte Werte für J sind konsistent mit den auf den THESEO2000/SOLVE-Daten beruhenden Ergebnissen von *Stimpfle et al. (2004)*, und führen im Modell zu erheblich realistischeren Ozonabbauraten (vergleiche z.B. mit Frieler et al., 2006).

Die Ergebnisse von Rex et al. (1999c), Frieler et al. (2006), *Stimpfle et al. (2004)*, Schofield et al. (2008) und einiger weiterer Arbeiten, die auf eine schnellere Photolyse des ClOOCl-Moleküls hinwiesen, zusammen mit der letztlich in Kawa et al. (2010) veröffentlichten Erkenntnis, dass die großen Unsicherheiten in der ClOOCl-Photolyseeffizienz es fast unmöglich machen, polaren Ozonabbau sinnvoll zu modellieren, führten zu neuen Labormessungen der ClOOCl-Photolysequerschnitte.

Ein großes Problem in früheren Labormessungen der ClOOCl-Photolysequerschnitte war die Anwesenheit von Nebenprodukten in der Absorptionszelle, welche aus der ClOOCl-Synthese stammen. Da diese Nebenprodukte die Gesamtabsorption oft komplett dominieren, stellen sie eine Hauptunsicherheit für die Messung dar. *Pope et al. (2007)* entwickeln einen erheblich verbesserten Versuchsaufbau zur Darstellung deutlich reineren ClOOCls, welches in dieser Arbeit vor Einleitung in die Absorptionszelle aus einer Kältefalle abdestilliert wird. Basierend auf diesem Versuchsaufbau berichten *Pope et al. (2007)* Absorptionsquerschnitte, welche fast eine Größenordnung unter den in JPL 2006 berichteten Werten liegen (siehe z.B. Linie für *Pope et al., 2007* in Abbildung 22b).

Zusammen mit der Modellierung von z. B. Rex et al. (2003) oder Frieler et al. (2006), siehe die Linie für *Pope et al., 2007* im oberen Panel von Abbildung 17, wurde sofort klar, dass - sollten diese Messungen korrekt sein - unser Bild des Ozonabbaumechanismus unvollständig sein müsste (z.B. Rex et al, 2007 und dem darauf beruhenden Nature-News Artikel *Schiermeier et al., 2007*). Diese Erkenntnis löste erhebliche Aktivität in der Ozonforschungsgemeinschaft aus.

Zum einen wurde die Möglichkeit der Existenz alternativer Ozonabbaumechanismen eingehend untersucht. Rex et al. (2008) argumentieren jedoch in einem systematischen Ausschlussverfahren, dass es aufgrund der über die letzten beiden Jahrzehnte gesammelten Messungen der Ozon-

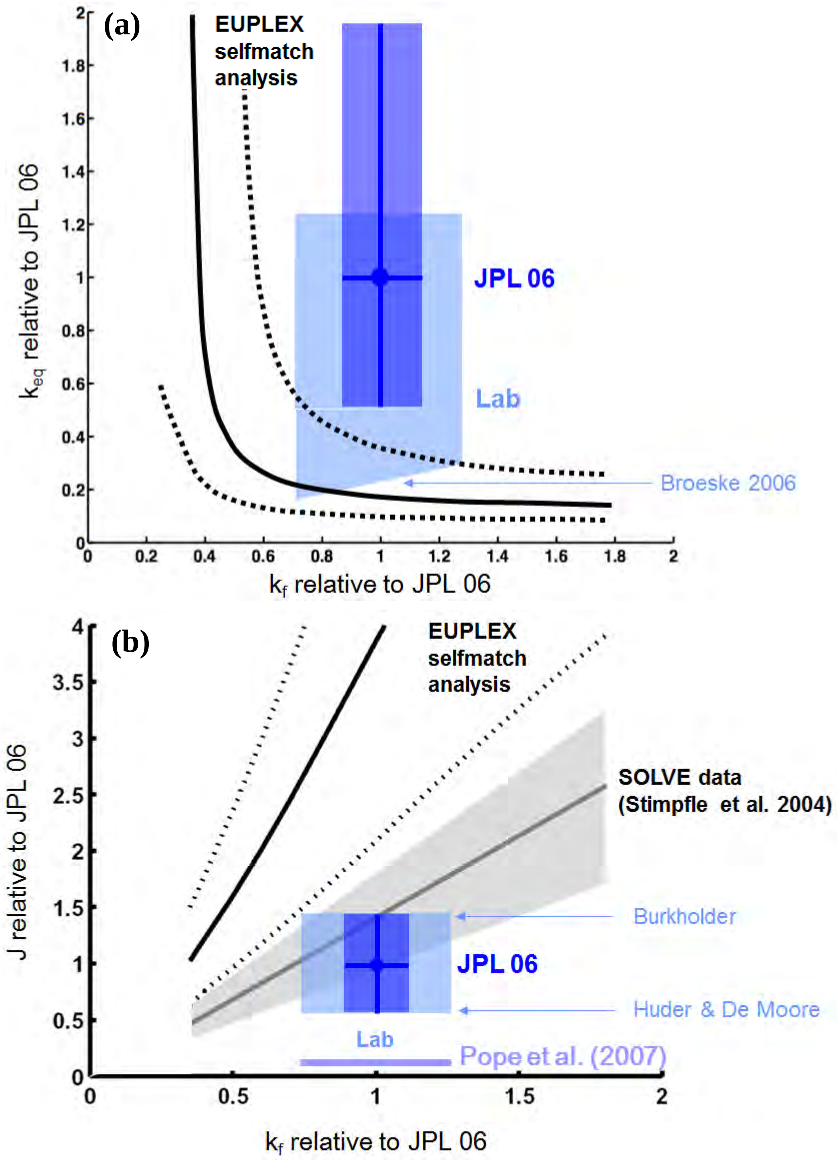

Abbildung 22: (a) Kombinationen von k_{eq} *und* k_f*, welche mit den Ergebnissen des Selfmatch-Fluges konsistent sind (schwarze Linie mit durch gepunktete Linien angedeutetem Unsicherheitsbereich). Der Bereich der Labormessungen dieser Parameter ist hellblau eingezeichnet und die JPL 2006 Empfehlungen dunkelblau. (b) wie (a), aber für die mit den Daten des Selfmatch-Fluges konsistenten Kombinationen von J und* k_f*. Hier sind zusätzlich Ergebnisse von Stimpfle et al. (2004) eingezeichnet (grau), basierend auf Daten der SOLVE-Kampagne. Nach Schofield et al., (2008).*

abbauraten bei einem weiten Spektrum an Bedingungen sowie der zahlreichen remote sensing und in-situ Messungen weiterer relevanter Spurengase praktisch keinen Raum gibt für alternative Mechanismen des polaren Ozonabbaus.

Zum Anderen begannen noch im gleichen Jahr eine Reihe Laborgruppen, neue Messaufbauten für Messungen der ClOOCl-Absorptionsquerschnitte zu entwickeln und aufzubauen. Mittlerweile sind die ersten Ergebnisse einiger dieser Messungen veröffentlicht (z.B. *Chen et al., 2009; Papanastasiou et al., 2009)*.

Aus der Gesamtheit der bereits bekannten neuen Messungen ergibt sich, dass die Absorptionsquerschnitte von ClOOCl vermutlich tatsächlich größer sind als in JPL 2006 und wohl recht nahe bei den in Frieler et al. (2006) aufgrund der beobachteten Ozonverlustraten geforderten Querschnitte von *Burkholder et al. (1990)* liegen. So empfiehlt JPL 2010 nunmehr ebenfalls größere Absorptionsquerschnitte von *Papanastasiou et al., 2009,* welche den Messungen von *Burkholder et al. (1990)* sehr ähnlich sind.

Die Ergebnisse von *Pope et al. (2007)* werden mittlerweile auf eine Fehlinterpretation der eigentlichen Messdaten zurückgeführt, die durch das in *Pope et al. (2007)* verwendete spezielle Auswerteverfahren verursacht wurde - dies missinterpretierte ein wohl tatsächlich vorhandenes Absorptionsmerkmal des ClOOCl im nahen UV als eine in ihren spektralen Eigenschaften unglücklicherweise sehr ähnliche Absorption durch Cl_2-Verunreinigung und entfernte diese daher aus den gemessenen Spektren.

3.3 Sommerprozesse

Die oben beschriebenen Prozesse spielen sich im polaren Winter ab. Aufgrund ihrer hohen Temperatursensitivität tragen sie im Zusammenspiel mit sehr variablen Temperaturen in der arktischen winterlichen Stratosphäre, deren Ursache in Abschnitt 4.2.2 erläutert wird, zum Aufbau interannualer Variabilität über den Winter hinweg bei.

Für den Sommer zeigt Abbildung 1 einen Rückgang der interannualen Variabilität, welche im Spätsommer/Herbst nahezu verschwindet. Toon et al. (1999) zeigen, dass das Verschwinden des Variabilitätssignals im arktischen Sommer auf die dann dort sehr aktive Chemie zurückzuführen ist. Durch die Absinkbewegung im Verlauf des vorangegangenen Winters sind hohe Konzentrationen von Stickstoffoxidverbindungen (NO_y) bis in den Bereich der unteren Stratosphäre abgesunken.

Nach der kurzen Periode der Zirkulationsumstellung von West- auf Ostwinde am Ende des arktischen Winters ist die sommerliche arktische Stratosphäre nun dynamisch recht ruhig. Die vorherrschenden langsamen Ostwinde erlauben keine vertikale Ausbreitung von planetaren Wellen in die Stratosphäre und die langsame Ostrotation findet daher ruhig und wenig durchmischt statt. Die in der sommerlichen arktischen Stratosphäre im globalen Vergleich höheren NO_y Konzentrationen bleiben demnach dort erhalten und werden nicht vollständig durch Durchmischung ausgeglichen. Rex et al. (1999a) zeigen, dass sich Bereiche mit Luftmasseneigenschaften aus dem winterlichen Polarwirbel und damit auch erhöhtem NO_y noch recht unvermischt auch in Messungen am 30. Juni, also bereits nach Mittsommer, in der arktischen Stratosphäre nachweisen lassen. Aus Tracerkorrelationsanalysen schließen Rex et al. (1999a), dass diese Luftmassen noch zu zwischen 50 und 70% aus Polarwirbelluft bestehen und nur 30%-50% Extrawirbelluft eingemischt wurde. Dies führte dazu, dass in diesen Luftmassen NO_y um etwa die Hälfte höher liegt als in Luftmassen aus mittleren Breiten in gleicher Höhe (Rex et al., 1999a).

In dem vorherrschenden Polartag verschiebt sich innerhalb des NO_y die Balance zwischen HNO_3 und NO_x in Richtung NO_x. Dies liegt zum einen daran, dass eine wesentliche Bildungsreaktion von HNO_3 im Polartag ausfällt: Die Bildung von N_2O_5 aus der Reaktion von NO_2 mit NO_3 und folgende heterogene Reaktion des N_2O_5 mit H_2O zu HNO_3. Durch die schnelle Photolyse des NO_3 und auch des N_2O_5 kann diese Reaktion im permanenten Sonnenlicht des Polartages nicht ablaufen. Zum anderen nimmt durch die permanente Verfügbarkeit von Sonnenlicht auch die tagesgemittelte Lebensdauer von HNO_3 aufgrund der ständig andauernden Photolyse ab.

Das hohe NO_x/NO_y-Verhältnis zusammen mit den erhöhten NO_y-Konzentrationen führt zu einer großen Menge verfügbaren NO_x. Der NO_x-Ozonabbauzyklus wird daher im Bereich des Polartages sehr effizient und kann wegen des ständig verfügbaren Sonnenlichts permanent ablaufen (Toon et al., 1999).

Diese Kombination aus dynamischen und chemischen Mechanismen führt im Bereich des Polartags im polaren Sommer zu einer bis in die untere Stratosphäre hinein deutlich reduzierten Lebensdauer von Ozon. Daher relaxiert die Ozongesamtsäule während des Sommers in Richtung des chemisch bestimmten Gleichgewichts und erreicht dieses bis Ende des Sommers auch. Da die Ostströmung die vertikale Ausbreitung von Wellen in die Stratosphäre effizient unterdrückt, ist auch die dynamisch induzierte Variabilität gering. Daher wird das chemische Gleichgewicht in der dynamisch ruhigen spätsommerlichen Stratosphäre kaum gestört und neue Variabilität wird im Verlauf des Sommers kaum erzeugt.

KAPITEL 4

DYNAMISCHE VARIABILITÄT

In Abbildung 1 fällt insbesondere der Kontrast der Variabilität der arktischen Ozonschichtdicke zwischen Herbst und Frühjahr auf. Während die Ozongesamtsäule im Herbst nur eine geringe Variabilität aufweist, baut sich die enorme Variabilität im Frühjahr offensichtlich durch Prozesse im arktischen Winter auf. Die diese Variabilität erzeugenden Prozesse spielen für die polare Ozonbilanz und ihre Wechselwirkungen mit dem globalen Klima eine wesentliche Rolle. Ein Verständnis aller Prozesse, die zu dieser Variabilität beitragen, ist unabdingbar um die Rolle der polaren Ozonschicht im Klimasystem zu verstehen. Die folgenden Abschnitte befassen sich mit den dynamisch bedingten Beiträgen zu dieser Variabilität.

Eine genaue Betrachtung von Abbildung 1 zeigt, dass ein erheblicher Teil der Variabilität im Frühjahr auf interannualer Variabilität beruht, während die Anomalie jeweils während einer Saison relativ persistent ist. Eine quantitativere Aufteilung in kurzfristige Fluktuationen und interannuale Variabilität erfolgt in Wohltmann et al. (2007). Abbildung 1 und Wohltmann et al. (2007) beruhen auf den Daten an jeweils einem festen Punkt und beinhalten somit die kurzfristigen Fluktuationen, die durch die Bewegung des Polarwirbels erzeugt werden. Diese Gesamtvariabilität wird im folgenden Abschnitt 4.1 untersucht. Im Abschnitt 4.2 wird der von den kurzfristigen Schwankungen bereinigte persistente Teil der Variabilität als Mittel über den Polarwirbel betrachtet.

4.1 Statistische Modellierung

Ein bewährtes Verfahren, die Gesamtvariabilität in Beobachtungsdaten einzelnen antreibenden Faktoren zuzuordnen, ist die multivariate statistische Analyse der Beobachtungszeitreihe. Hierbei wird jedem Prozess, von dem angenommen wird, dass er einen Einfluss auf die Beobachtungsgröße hat, ein Proxy zugeordnet, der die Stärke des jeweiligen Prozesses zu jedem Zeitpunkt beschreibt. In einer multivariaten statistischen Analyse werden nun für jede Proxyzeitreihe Faktoren so bestimmt, dass die über alle Messpunkte aufsummierte quadratische Abweichung aus der Summe der mit den Faktoren multiplizierten Proxyzeitreihen und den Messdaten minimiert wird. Im optimalen Fall geben dann die mit den Faktoren multiplizierten Proxyzeitreihen den Einfluss des jeweiligen Prozesses auf die Messgröße an.

Der Schwachpunkt dieses Verfahrens ist, dass man eine vollständige Kenntnis aller Prozesse benötigt, welche die Messgröße beeinflussen. Wird ein Prozess nicht erkannt und daher kein Proxy für diesen Prozess verwendet, führt das nur idealerweise dazu, dass der Einfluss dieses Prozesses vollständig in den Residuen auftaucht und dort sichtbar wird, weil die Residuen dann größer als die Messungenauigkeit werden.

In der Praxis treten jedoch fast immer Kovarianzen zwischen den beteiligten Prozessen auf. Das liegt oft an der Natur der Prozesse, die nicht orthogonal sind (Beispiel: Einfluss der horizontalen Advektion und schichtdickenverändernder Konvergenz in der Strömung sind durch physikalische Gesetze verknüpft und daher nicht orthogonal, siehe Wohltmann et al., 2005, für eine detaillierte Diskussion). Kovarianz tritt in zeitlich begrenzten Datensätzen auch zufällig zwischen an sich unabhängigen Prozessen auf. Eine gewisse Kovarianz zwischen den beteiligten Prozessen ist eigentlich kein Problem, solange diese nicht parallel sind und die Kovarianz in der durchaus komplizierten Fehlerrechnung korrekt berücksichtigt wird (Wohltmann et al., 2007).

Kovarianz stellt aber ein erhebliches Problem dar, wenn der Satz an Proxies nicht vollständig ist. In dem Falle wird vom statistischen Modell der Einfluss eines fehlenden Prozesses zu einem erheblichen Anteil einem Prozess zugeordnet, welcher eine Kovarianz mit dem fehlenden Prozess aufweist. Dieser Effekt kann leicht zu Fehlinterpretationen der Ergebnisse eines statistischen Modells führen.

In vielen Ansätzen zur statistischen Modellierung von Variabilitäten und Trends der Ozonschichtdicke wurde in der Vergangenheit ein sehr begrenzter Satz an Proxies verwendet, die in vielen Fällen nicht einmal jeweils sauber einem bestimmten Prozess zuzuordnen sind sondern vielmehr selbst das kombinierte Ergebnis verschiedener zugrundeliegender Prozesse sind. Als Beispiel kann hier die Tropopausentemperatur dienen, die hoch mit der Gesamtozonschichtdikke korreliert ist und daher in vielen statistischen Modellen als Proxy herangezogen wird. Für sich genommen, in einer prozessorientierten Betrachtung, hat die Tropopausentemperatur jedoch keinen nennenswerten Einfluss auf die Ozonschichtdicke. Selbst der denkbare direkte Einfluss auf die Kinetik der Chemie im Tropopausenbereich sollte keinen erheblichen Effekt auf die Ozonschichtdicke haben, da die Ozonkonzentration an der Tropopause gering ist und keinen deutlichen Einfluss auf die Gesamtschichtdicke entfalten kann. Die hohe Korrelation der Tropopausentemperatur mit der Ozonschichtdicke kommt vielmehr dadurch zustande, dass die Tropopausentemperatur auf kurzer Zeitskala in ähnlicher Weise auf die eigentlich zugrundeliegenden dynamischen Prozesse reagiert wie die Ozonschichtdicke. Bei diesen Prozessen handelt es sich im wesentlichen um Konvergenzen in der Strömung, die den Druck an der Tropopause erhöhen, diese damit in einen wärmeren Bereich verschieben und gleichzeitig die Ozonschichtdicke durch die Konvergenz in der ozonreichen unteren Stratosphäre erhöhen. Wird nun statt eines Proxies für diesen eigentlich dynamischen Prozess einfach die Tropopausentemperatur in einem statistischen Modell verwendet, drohen erhebliche Fehlschlüsse: Anhand der großen Dynamik in den kurzfristigen Fluktuationen bestimmt das Modell ein hohes Gewicht für den Proxy Tropopausentemperatur. Ändert sich die Tropopausentemperatur jetzt langfristig aufgrund völlig anderer Prozesse, zum Beispiel aufgrund des Strahlungseffekts zunehmender Treibhausgaskonzentrationen, schließt das statistische Modell daraus auf einen entsprechend großen treibhausgasbedingten Effekt auf die Ozonschichtdicke. Da diese Änderungen der Tropopausentemperatur strahlungsgetrieben sind und nichts mit Konvergenzen in der Strömung zu tun haben, kann der Effekt von zunehmenden Treibhausgaskonzentrationen auf die Ozonschichtdicke aber so natürlich nicht ermittelt werden.

Aufgrund dieser Überlegungen wurde ein neues, global anwendbares statistisches Modell der Ozonschichtdicke entwickelt. Im Gegensatz zu früheren Ansätzen (Übersicht zum Beispiel in Harris et al., 2008) wurde dieses Modell streng prozessorientiert aufgebaut. Aufgrund des problematischen Einflusses von Kovarianzen zwischen individuellen Prozessen auf nicht vollständige statistische Modelle wurde große Sorgfalt darauf verwendet, alle Prozesse in das Modell aufzunehmen, obwohl dies aufgrund der vielen zu fittenden Parameter in der Regel die statistischen Fehlerbalken der Ergebnisse vergrößert. Dazu wurde zunächst eine möglichst vollständige Liste aller Prozesse aufgestellt, welche Einfluss auf die Ozonschichtdicke haben und dann für jeden dieser Prozesse ein Proxy definiert (Wohltmann et al., 2005; Wohltmann et al., 2007).

Im Gegensatz zu früheren Modellen enthält dieses Modell nun explizite Terme zum Beispiel für den Einfluss der kurzfristigen Dynamik (Konvergenz, kurzfristige reversible Advektion), der Variabilität der stratosphärischen Brewer-Dobson-Zirkulation, und des Einflusses des chemischen polaren Ozonverlusts auf die Ozonschichtdicke sowohl in polaren als auch in mittleren Breiten. Zeitreihen dieser Proxies wurden aus meteorologischen Reanalysedatensätzen bestimmt.

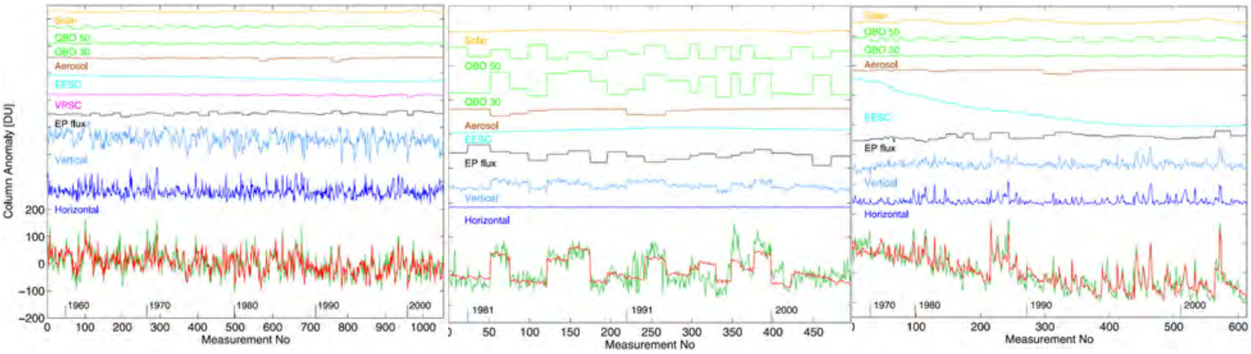

Abbildung 23: Ergebnisse der multiplen Regression für Arosa (47^{o}N) für den Monat März (links) Singapur (1^{o}N) für den Monat September (Mitte) und Syowa (69^{o}S) ebenfalls für den Monat September. Die gemessene Ozonanomalie ist mit einer grünen Linie jeweils im unteren Bereich dargestellt. Die sehr ähnliche rote Linie ist das Ergebnis der Rekonstruktion durch das statistische Modell. Die einzelnen Beiträge zur Variabilität sind im oberen Bereich durch farbige Linien eingetragen. Die Variabilität in nördlichen mittleren Breiten (links) wird stark durch den „Equivalente-Breite-Proxy" (Summe aus hell- und dunkelblau) dominiert, welcher dynamische Prozesse beschreibt. Demgegenüber überwiegt in den Tropen (Mitte) der Einfluss der Quasi-Biennial-Oszillation (Summe der beiden grün dargestellten Beiträge). In der Antarktis (rechts) dominiert erwartungsgemäß der Beitrag des anthropogenen Ozonabbaus, welcher durch den EESC-Proxy erfasst wird (cyan). Nach Wohltmann et al. (2007).

Die Ergebnisse des neuen Modells sind vielfältig (Beispiele in Abbildung 23 und Abbildung 24). Es ist erstmalig in der Lage, auch die teilweise reversiblen Tag zu Tag Variationen der Ozonschichtdicke schlüssig den zugrundeliegenden dynamischen Prozessen zuzuordnen (Wohltmann et al., 2005; 2007).

Für Monatsmittel der Daten ergibt sich, dass die Variabilität der stratosphärischen Residualzirkulation die dominierende Rolle für die interannuale Variabilität der Ozonschichtdicke in hohen Breiten ab etwa 50^{o} Breite spielt.

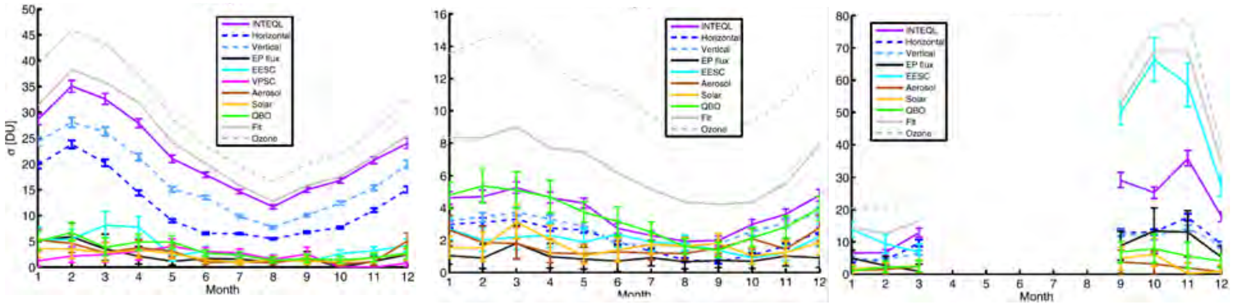

Abbildung 24: Beiträge der verschiedenen Prozesse zur Ozonvariabilität in Europa (links), den Tropen (Mitte) und der Antarktis (rechts) als Funktion der Jahreszeit. Die gestrichelte graue Linie gibt die beobachtete Variabilität wieder und die durchgezogene graue Linie die aus den Proxis mittels des statistischen Modells rekonstruierte Variabiliät. Nach Wohltmann et al. (2007).

Für die nördlichen mittleren Breiten zeigt sich, dass ein erheblicher Teil der Erholung der Ozonschichtdicke seit den 1990er Jahren nicht auf den Rückgang der FCKW-Konzentrationen zurückzuführen ist, sondern auf eine Verstärkung der stratosphärischen Residualzirkulation in diesem Zeitraum (Dhomse et al., 2006; Wohltmann et al., 2007; Newman und Rex, 2007; Harris et al., 2008). Dennoch bleibt die langfristige Variation der stratosphärischen Chlorbelastung für den langfristigen Trend der dominierende Faktor.

Der Beitrag polarer Ozonzerstörung auf den Ozontrend in nördlichen mittleren Breiten wurde erstmalig quantifiziert und ergibt in den Frühjahrsmonaten einen signifikanten Anteil am Gesamttrend. In den restlichen Monaten ist er erwartungsgemäß nicht relevant (Wohltmann et al., 2007; Newman und Rex, 2007; Harris et al., 2008).

In den Tropen ist die Modifikation der Aufstiegsraten in der unteren Stratosphäre durch die Sekundärzirkulation der Quasi Biennalen Oszillation (QBO) der dominierende Faktor für die Variabilität der Ozonschichtdicke (Wohltmann et al., 2007). In den Extratropen spielt die QBO eine untergeordnete Rolle für die Variabilität.

Vulkanausbrüche verursachen temporär einen erheblichen Rückgang der Ozonschichtdicke insbesondere in den Extratropen und können das Signal dort für ein paar Jahre dominieren.

Der Einfluss der Schwankung der UV-Einstrahlung mit dem solaren Zyklus ist in den Tropen erwartungsgemäß deutlich ausgeprägt, wird jedoch durch die erheblich größere Variabilität durch die anderen oben angesprochenen Prozesse in den Extratropen weitgehend verdeckt und spielt dort keine wesentliche Rolle für die Variabilität der Ozonschichtdicke. Bei der Analyse kürzerer Zeitreihen kann eine zufällige Kovarianz mit dem Vulkanproxy zu einem erheblichen Überschätzen des Einflusses des solaren Zyklusses führen, insbesondere wenn das statistische Modell nicht vollständig formuliert wird oder die Fehlerrechnung in einem vollständigen Modell die Kovarianzen der Proxies nicht korrekt berücksichtigt, was leider oftmals der Fall ist.

4.2 Mechanistische Modellierung

Die im letzten Abschnitt beschriebene statistische Modellierung erlaubt zwar oft die Zuordnung von beobachteten Variabilitätsmustern oder langfristigen Veränderungen zu den zugrundeliegenden physikalischen Mechanismen und ist somit ein wesentliches Rückgrat dieses wichtigen, Attribution genannten Prozesses. Diese Art der Analyse von Beobachtungszeitreihen kann jedoch allein nicht ausreichen. Erstens können aus den oben beschriebenen Gründen Fehlzuordnungen zwischen kovariierenden Prozessen auftreten. Zweitens trägt diese Analyse nicht zu einem physikalischen Verständnis der zugrundeliegenden Prozesse bei. Hierzu müssen diese Prozesse direkt und mechanistisch modelliert werden.

Rex et al. (1999b), Rex et al. (2002) und viele weitere Analysen haben ergeben, dass die Polarwirbelkante als eine sehr effiziente Barriere gegen Durchmischung wirkt, die Durchmischungsterme eine untergeordnete Rolle für das Ozonbudget im Polarwirbel spielen und in der Bilanzbetrachtung oft vernachlässigt werden können (siehe auch Abschnitt 3.1.2). Der Eintrag von Ozon in die Polargebiete ist im Winter vielmehr dominiert von der systematischen Advektion mit der Residualzirkulation.

Durch die im Sommer in hohen Breiten aktivere Photochemie und insbesondere durch den aktiven NO_X-katalysierten Ozonabbau dort (Abschnitt 3.3) hat sich im Verlauf des Sommers ein Ozonminimum über den Polargebieten ausgebildet. In dem Gradienten zwischen niedrigem polaren Ozon und ozonreicherer Luft mittlerer Breiten führt die in der mittleren und oberen Stratosphäre systematisch polwärts gerichtete Advektion zum Eintrag von Ozon in die polare Luftsäule. Diese Advektion von Luft findet dabei zu einem großen Teil oberhalb des für die Gesamtozonsäule besonders relevanten Bereichs der unteren Stratosphäre statt. Durch die im Polarwirbel absinkende Luftmassenbewegung und der damit einhergehenden Kompression dieser Luft führt dieser Prozess letztlich aber auch im Bereich der unteren Stratosphäre zu großen Ozonkonzentrationen und einer deutlichen Vergrößerung der Gesamtsäule.

Wohltmann und Rex (2008) und Tegtmeier et al. (2008a) haben ein Verfahren entwickelt, den polaren Zweig der Residualzirkulation sowohl in seiner Stärke als auch in seiner meridionalen Verteilung aus einer Kombination von Messdaten und Modellierung zu charakterisieren und seine interannuale Variation abzuleiten. Mit Hilfe dieses Modells ist es auch möglich, den variablen Einfluss der Residualzirkulation auf die winterliche Zunahme der Ozongesamtsäule zu berechnen (Tegtmeier et al., 2008b). Die so berechneten dynamischen Einträge von Ozon sind in ihrer Wirkung auf die Gesamtozonsäule in Abbildung 2 als blaue Linie dargestellt.

4.2.1 Gesamtbudget und Antrieb der Variabilität

Abbildung 2 zeigt erstmals das Gesamtbudget der interannualen Variabilität der arktischen Ozonsäule (Tegtmeier et al., 2008b). Die Summe aus dynamischem Eintrag und chemischem Verlust, bezogen auf die Oktober-Ozonsäule, ist als gestrichelte schwarze Linie eingetragen. Die gute Übereinstimmung dieses Budgets aus abgeleitetem chemischen Verlust und dynamischen Eintrag mit den beobachteten Ozonänderungen während des Winters (durchgezogene schwarze Linie in Abbildung 2) zeigt, dass beide Terme in den jeweiligen Modellansätzen gut quantifiziert werden konnten und dass sie das Budget der winterlichen Änderung der Ozonschichtdicke gut beschreiben.

Die kleine systematische Unterschätzung der tatsächlich im Frühjahr beobachteten Ozonschichtdicke ist vermutlich auf schlecht verstandene Transportprozesse im Tropopausenbereich zurückzuführen, die aber offensichtlich keine dominierende Rolle für das Gesamtbudget spielen.

In Abbildung 2 ist eine deutliche Korrelation der chemischen und dynamischen Terme erkennbar, die auf eine gemeinsame Ursache für die Variabilität beider Terme hinweist. Diese gemeinsame Ursache liegt in der Variabilität der Stärke des Wellenantriebs der stratosphärischen Residualzirkulation, welche auf einer Kombination von variabler troposphärischer Dynamik und variablen Wellenausbreitungsbedingungen in der untersten Stratosphäre beruht.

4.2.2 Die Rolle der stratosphärischen Residualzirkulation

Durch nachlassende Sonneneinstrahlung kühlt im Herbst die polare Luftsäule aus. Durch zunehmende Dichte sackt sie nach unten und führt zu einem Tiefdruckgebiet in der Stratosphäre - dem Polarwirbel. Luftmassen, die von der Druckgradientenkraft in Richtung des polaren Tiefdrucks beschleunigt werden, spüren die mit zunehmender Geschwindigkeit zunehmende ablenkende Wirkung der Corioliskraft und enden schließlich auf einer Kreisbahn um den Tiefdruck herum, in der die Druckgradientenkraft durch die Corioliskraft gerade balanciert wird. In diesem geostrophischen Gleichgewicht hätte eine Bewegung in Richtung Tiefdruck eine Beschleunigung durch die Druckgradientenkraft zur Folge, wodurch die zunehmende Corioliskraft die Luftmasse wieder vom Tiefdruck weg beschleunigen würde - Nettomeridionaltransport in das Tiefdruckgebiet hinein ist in dieser Situation nicht möglich.

Ungestört würde sich nun auf einer Zeitskala von wenigen Wochen ein strahlungsbedingtes Temperaturgleichgewicht in der stratosphärischen polaren und äquatorialen Luftsäule einstellen, mit sehr niedrigen polaren und hohen äquatorialen Temperaturen und hohen Westwindgeschwindigkeiten des thermischen Winds in diesem Temperaturkontrast.

Planetare Wellen, die sich von der Troposphäre vertikal bis in die Stratosphäre ausbreiten und dort dissipieren, stellen jedoch eine Impulskopplung zwischen dem Erdboden und der stratosphärischen Zirkulation her. Sie tragen den Impuls ihres Ausgangspunktes - in der Regel des Erdbodens - mit sich und lagern diesen in der Westwindströmung ab, wenn sie in der Stratosphäre dissipieren. Die dadurch bewirkte Abbremsung des Westwindes erlaubt eine meridionale Strömungskomponente in Richtung Tiefdruck und führt zu einem Nettomassefluss von niedrigen zu hohen Breiten.

Die zusätzliche Masse über der polaren Luftsäule komprimiert und erhitzt diese adiabatisch und treibt die Temperaturen über das kalte Strahlungsgleichgewicht. Dies hat ein strahlungsbedingtes Auskühlen der Luftmassen zur Folge, welches gleichbedeutend mit einem Absinken über Isentropen hinweg ist.

Der gegenteilige Effekt findet in den Tropen statt - hier werden die Luftmassen expandiert, adiabatisch abgekühlt und es kommt zu strahlungsgetriebener Erwärmung und Aufsteigen. Dieser Prozess hat eine sehr langsame meridionale Zirkulation der Stratosphäre zur Folge, die Ozon in hohe Breiten „hineinpumpt“.

Starker Wellenantrieb aus der Troposphäre hat demnach eine verstärkte Residualzirkulation zur Folge und damit auch einen verstärkten Eintrag von Ozon in polare Breiten. Gleichzeitig führt die verstärkte Residualzirkulation jedoch auch dazu, dass die damit verbundene dynamisch bedingte Aufheizung der polaren Luftsäule die Temperatur weiter über das kalte Strahlungsgleichgewicht anhebt und es insgesamt in der polaren Stratosphäre wärmer wird. Es können sich dann weniger PSC bilden und es kommt zu weniger Ozonabbau.

Abbildung 25 zeigt deutlich, wie beide Terme, der dynamische Eintrag von Ozon in polare Breiten (blau) und der chemische Ozonverlust (rot) im wesentlichen durch den Wellenantrieb aus der Troposphäre gesteuert werden und daher hoch miteinander korreliert sind. Bei heutiger Ha-

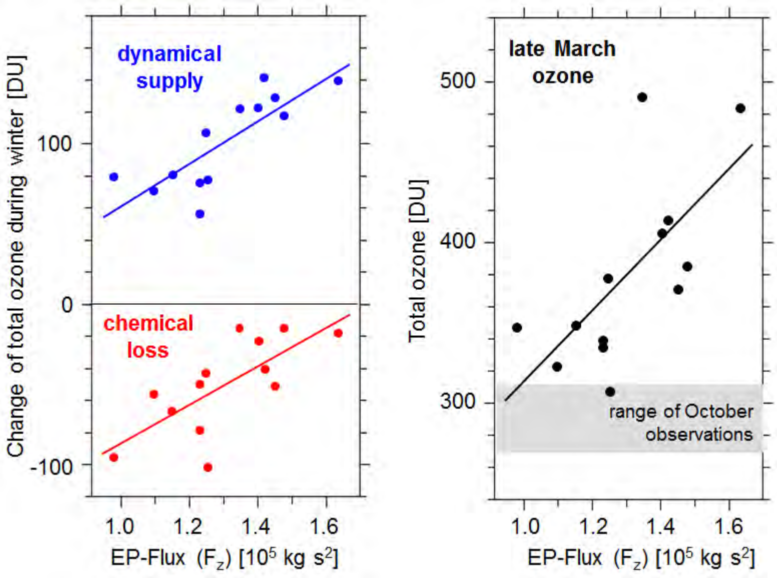

Abbildung 25: Rechts: Ozonschichtdicke im Bereich des Polarwirbels in Abhängigkeit der über den Winter gemittelten Vertikalkomponente des Eliassen-Palm Flusses (EP-Fluss) bei 100hPa (im Bereich der Tropopause). Diese Größe ist ein Maß für die wellengetriebene Anregung der stratosphärischen Residualzirkulation. Links: Chemischer Ozonverlust und dynamisch bedingter Eintrag von Ozon im Verlauf des Winters in Abhängigkeit vom wintergemittelten EP-Fluss. Nach Rex et al. (2004b), Tegtmeier et al. (2008b).

logenbelastung der Stratosphäre tragen beide Terme etwa gleich viel zur beobachteten interannualen Variabilität bei (schwarz). Der anthropogene Ozonverlust verstärkt also zur Zeit die natürliche dynamisch bedingte interannuale Variabilität der arktischen Ozonsäule im Frühjahr um etwa einen Faktor zwei (Tegtmeier et al., 2008b).

4.3 Die Rolle solarer Variabilität

Die Sonne ist ein sehr dynamisches und variables System. Interne Prozesse in der Sonne selbst und auch die Rotation der Sonne führen zu verschiedenen, zum Teil periodischen Variabilitäten. Für die hier betrachteten Zeitskalen sind insbesondere von Bedeutung die 27-tägige Variabilität, die aus der Kombination aus der Eigenrotation der Sonne mit der Erdumlaufbahn folgt, und der etwa 11-jährige Aktivitätszyklus der Sonne, der intern in der Sonne generiert wird.

Während der 27-tägige Zyklus in der Stratosphäre nur minimale Auswirkungen hat, ist der etwa 11-jährige Zyklus in vielen Parametern deutlich erkennbar. Die Hauptwirkung des 11-jährigen Zyklusses auf das Erdsystem liegt in einer geringfügigen Variation der solaren Einstrahlung, welche bei den kürzeren Wellenlängen ausgeprägter ist und im kurzwelligeren UV-Bereich die Größenordnung von einigen Prozent erreicht.

Die Variation der solaren UV-Einstrahlung mit dem 11-jährigen Zyklus der Sonne hat sowohl chemische wie auch dynamische Auswirkungen auf die Stratosphäre und damit auch auf die Ozonschicht. Diese können generell mit den statistischen Modellen wie in Abschnitt 4.1 beschrieben gut quantifiziert werden. So finden zum Beispiel Wohltmann et al. (2007) statistisch signifikante Auswirkungen des solaren Zyklusses auf die Ozonschichtdicke, die jedoch äußerst gering sind und generell 1% nicht deutlich übersteigen. Diese geringe Variabilität ist nur in den Tropen durch die dort allgemein deutlich geringere Variabilität sichtbar und wird in den Extratropen durch die große Variabilität aufgrund anderer Prozesse überlagert.

Neben der Schwankung der solaren Einstrahlung im UV hat der 11-jährige Aktivitätszyklus der Sonne auch eine periodische Veränderung des äußeren Magnetfelds der Erde zur Folge, die durch die Wechselwirkung des variablen Sonnenwinds mit dem Erdmagnetfeld hervorgerufen wird. Dies bewirkt eine zyklische Variation der Einfallsbedingungen für sehr energiereiche relativistische Elektronen aus der kosmischen Hintergrundstrahlung. Sinnhuber et al. (2006) zeigen, dass eine über 10% liegende dekadische Variabilität der mittwinterlichen Ozonkonzentration in der oberen arktischen Stratosphäre mit dem Fluss relativistischer Elektronen korreliert, der gegenüber dem 11-jährigen Aktivitätszyklus der Sonne etwa 90^{o} phasenverschoben auftritt. Dies wäre mit Abstand das größte durch den solaren Zyklus induzierte Signal in der unteren und mittleren Atmosphäre und hätte, wenn es sich langfristig bestätigt, bedeutende Implikationen für die Wirkung des solaren Zyklusses auf das Erdklima.

KAPITEL 5

DIE ROLLE DER TROPISCHEN TROPOPAUSENREGION FÜR DIE POLARE OZONSCHICHT

Die chemischen Prozesse, welche die Ozonbilanz in der polaren Stratosphäre beeinflussen, hängen von der Verfügbarkeit der sie antreibenden Spurengase ab. Für die in Kapitel 3 besprochene polare Ozonchemie ist dabei insbesondere das Gesamtbudget des inorganischen Chlors (Cl_y) und des inorganischen Broms (Br_y) relevant. Dabei stellte lange Zeit nach allgemeiner Auffassung der Abbau langlebiger organischer chlor- und bromhaltiger Substanzen in der Stratosphäre die einzige Quelle von Cl_y und Br_y dar. Für Cl_y sind das die anthropogenen FCKW und das teilweise anthropogene und teilweise biogene Methylchlorid. Für Br_y galten diese lange als einzige Quelle. Derzeit ergibt sich damit für Chlor ein anthropogener Anteil von etwa 17% am Cl_y und für Brom ein anthropogener Anteil von etwa 58% am Br_y (*WMO-Assessment 2010: Douglass et al., 2011*).

Für die Gesamtbilanz des Cl_y haben alle Messungen von Chlorverbindungen in der Stratosphäre dieses Bild bislang eindeutig bestätigt. Inzwischen können alle wesentlichen Komponenten des Cl_y in der Stratosphäre gemessen werden und es stellt sich heraus, dass die Summe der Mischungsverhältnisse aller Cl_y-Substanzen plus der ebenfalls gut messbaren FCKW und des Methylchlorids in der Stratosphäre konstant ist und genau der Summe der Mischungsverhältnisse von FCKW plus Methylchlorid im Bereich der tropischen Troposphäre entspricht, die die Quellregion für stratosphärische Luftmassen darstellt (siehe Abbildung 26). Damit ist die Bilanz des stratosphärischen Chlors geschlossen.

Br_y kann mit gewissen Unsicherheiten mit einem chemischen Modell aus stratosphärischen Messungen von BrO rekonstruiert werden. Diese Messungen im Bereich weniger ppt sind sehr schwierig und sind ebenfalls mit erheblichen Unsicherheiten behaftet, die durch die Unsicherheit des chemischen Modells bei der Bestimmung von Br_y noch vergrößert werden.

Dennoch mehren sich zunehmend Hinweise darauf, dass die Gesamtmenge an stratosphärischem Brom konsistent und signifikant größer ist als die Summe von Halonen und Methylbromid in der tropischen Troposphäre (WMO 2007). Frieler et al. (2006) weist auf die große Bedeutung eines genauen Verständnisses des stratosphärischen Brombudgets für unser theoretisches Verständnis des polaren Ozonabbauprozesses hin und zeigt, dass ein entsprechend der stratosphärischen BrO Messungen nach oben korrigiertes Brombudget erforderlich ist, um die gemessenen Ozonabbauraten zu verstehen.

Dies zeigt, dass ein genaues Verständnis des Eintrags von Luft in die Stratosphäre und der Prozesse, die dabei die Zusammensetzung der eingetragenen Luft bestimmen, erforderlich ist, um die Chemie der polaren Stratosphäre zu verstehen. Insbesondere ist dies im Hinblick auf mögliche Klimaänderungen erforderlich, die diese Prozesse verändern können und damit zu einer veränderten Zusammensetzung der Stratosphäre führen können. Dies kann über den daraus resultierenden Einfluss auf die Ozonschicht erhebliche Rückkopplungseffekte auf das Klimasystem haben.

Die Prozesse, die den Eintrag von Spurengasen in die Stratosphäre regulieren, bestimmen ebenfalls den Eintrag von Wasserdampf. Dieser scheint erheblichen langfristigen Veränderungen zu unterliegen. Diese langfristigen Schwankungen des stratosphärischen Wasserdampfgehalts sind für eine deutliche Modulation des treibhausgasbedingten globalen Erwärmungstrends verantwortlich gemacht worden *(Solomon et al., 2010)*.

5.1 Grundsätzliche Prozesse

Abbildung 26 fasst die grundsätzlichen Prozesse beim Eintrag von Spurengasen in die Stratosphäre zusammen. An der Erd- oder Ozeanoberfläche werden hunderte organische Verbindungen biogen und einige zusätzliche Verbindungen anthropogen oder durch geologische Prozesse freigesetzt. Fast alle diese Verbindungen sind durch eine effiziente Reaktion mit OH oder durch schnelle Photolyse recht kurzlebig und werden dabei in der Regel in wasserlösliche Abbauprodukte umgewandelt. Diese werden in der Troposphäre relativ schnell ausgewaschen, damit der Atmosphäre entzogen und erreichen stratosphärische Höhen nahezu nicht.

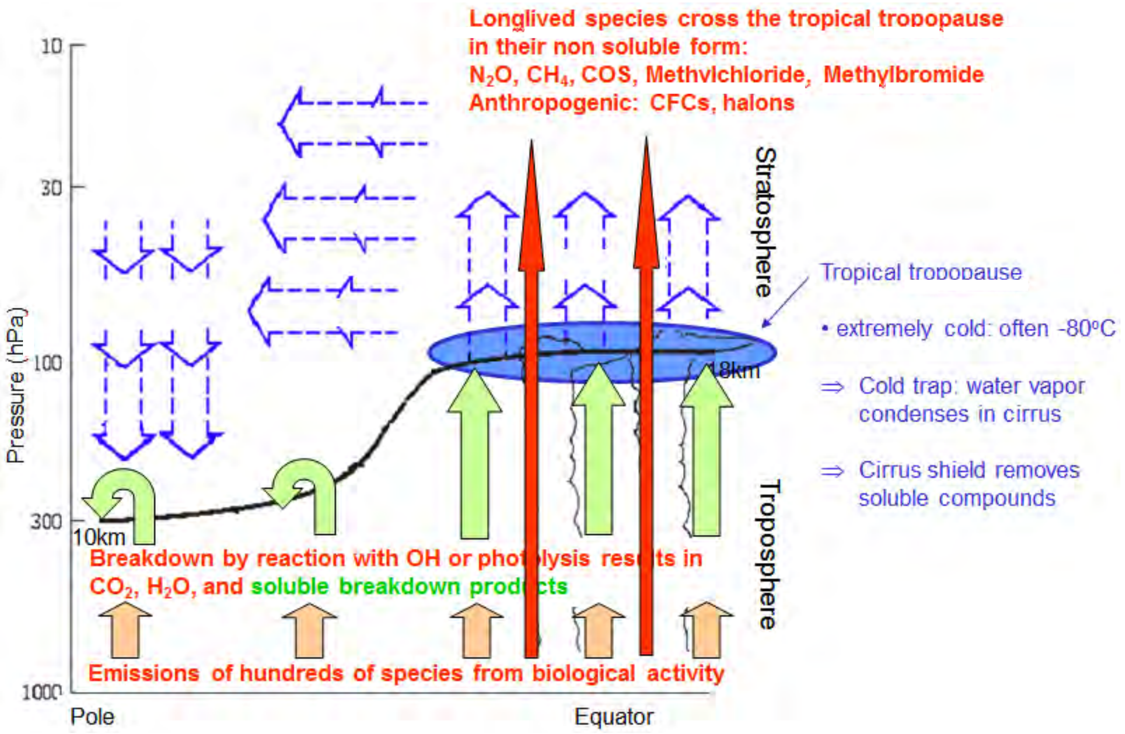
Longlived species cross the tropical tropopause
in their non soluble form:
N_2O, CH_4, COS, Methylchloride, Methylbromide
Anthropogenic: CFCs, halons
10
30
100
300
1000
Pressure (hPa)
Stratosphere
Tropical tropopause
• extremely cold: often -80°C
⇒ Cold trap: water vapor condenses in cirrus
⇒ Cirrus shield removes soluble compounds
18km
10km
Breakdown by reaction with OH or phot lysis res ts in
CO_2, H_2O, and soluble breakdown prod cts
Troposphere
Emissions of hundreds of species from biological activity
Pole
Equator

Abbildung 26: Illustration des Eintrags von Spurengasen in die Stratosphäre.

Der Eintrag von Luft in die Stratosphäre erfordert aufsteigende Bewegung. Aufgrund der stratosphärischen Residualzirkulation sinken die Luftmassen in der Stratosphäre in den mittleren und hohen Breiten jedoch generell ab. Aufsteigende Bewegung herrscht nur in den Tropen vor und der Eintrag von Luft tief in die Stratosphäre ist daher nur dort möglich.

Nur im Bereich der Subtropenjets, wo die Isentropen die Tropopause schneiden, ist ein isentroper (also quasi-horizontaler) Eintrag von Luft aus der tropischen oberen Troposphäre in die unterste extratropische Stratosphäre möglich, was hier aber nicht weiter betrachtet werden soll, da diese Luft aufgrund des generellen Absinkens von dort nicht tiefer in die Stratosphäre vordringen kann.

Der Schlüsselbereich für den Eintrag von Luft und der enthaltenen Spurengase in die Stratosphäre ist also die tropische Tropopause. Diese stellt eine der kältesten Regionen der gesamten Atmosphäre dar und wirkt beim Eintrag von Luft in die Stratosphäre als eine gewaltige Kältefalle. Bei den tiefen Temperaturen kondensiert nahezu der gesamte Wasserdampf in Zirren und die Sedimentation der Eiskristalle entzieht der Luft den Wasserdampf bis auf den kleinen Anteil, der auch bei den niedrigen Temperaturen der tropischen Tropopause in der Gasphase verbleibt.

Bei diesem Prozess werden der Luft die wasserlöslichen Bestandteile zum größten Teil zusammen mit den Eiskristallen entzogen. Nur die Substanzen, die beim letzten Kontakt individueller Luftmassen mit der Eisphase in einer nicht wasserlöslichen Form vorliegen, können in größerem Umfang in die Stratosphäre eingetragen werden. Dies sind in jedem Falle die langlebigen Spurengase Methan, Lachgas, FCKWs, Methylchlorid, Halone und Methylbromid. Diese Substanzen werden in der Stratosphäre abgebaut und sind die Quelle der dort stattfindenden chemisch aktiven Spurengase. Der Abbau von Methan trägt zum stratosphärischen Wasserdampf bei, der von Lachgas bildet das stratosphärische NO_y, der von FCKWs und Methylchlorid das Cl_y und der von Halonen und Methylbromid das Br_y. Andere Substanzen wie SF_6, Perfluorkarbone oder CO_2, die auch in der Stratosphäre nicht abgebaut werden, spielen für die Stratosphärenchemie eine geringere Rolle.

Die Erkenntnis, dass in der Stratosphäre wohl größere Konzentrationen an Br_y vorhanden sind als durch die Quellen aus Halonen und Methylbromid allein erklärt werden kann, hat eine ganze Reihe biogener kurzlebigerer bromhaltiger Substanzen in den Mittelpunkt aktiver Forschung gestellt. Es muss dringend untersucht werden, ob Teile dieser Substanzen in die Stratosphäre gelangen können, welchen Anteil sie an der stratosphärischen Brombilanz haben und ob ihre schlecht bekannten Quellen oder ihr Eintrag in die Stratosphäre sich durch Klimaänderungen verändern können.

Soweit bekannt, werden viele dieser Substanzen durch Algen in nährstoffreichen Küstengewässern und Flussmündungsgebieten in den Tropen erzeugt. Änderungen von Niederschlagsverteilung und daraus folgende Änderung des Nährstoffeintrags durch Auswaschung von den Landgebieten können hier erhebliche Änderungen in der Verteilung der Quellen zur Folge haben. Auch die Eintragsprozesse in die Stratosphäre sind, wie im folgenden Abschnitt deutlich werden wird, sehr sensitiv auf kleine Änderungen der Konvektion und der dynamischen und thermischen Struktur der Tropopause in den Tropen und können daher sehr empfindlich auf Klimaänderungen reagieren.

5.2 Lagrangesche Modellierung der tropischen Tropopause

Das Ziel der Forschung im tropischen Tropopausenbereich ist es, das komplizierte Zusammenspiel zwischen horizontalen und vertikalen Transportprozessen mit Mikrophysik und Chemie so weit zu verstehen, dass ein Weg gefunden werden kann, diese Prozesse in globale Modelle aufzunehmen. Es wurde daher ein lagrangesches Modellsystem entwickelt, welches geeignet ist, die beteiligten Prozesse im Detail zu untersuchen.

Abbildung 27 illustriert, wie einzelne Trajektorienrechnungen den Eintrag von Luft in die Stratosphäre auflösen können. Im unteren Bereich der tropischen Troposphäre bis etwa 15km Höhe herrscht bei clear-sky-Bedingungen strahlungsgetriebenes Absinken vor. Hier findet der Vertikaltransport nach oben ausschließlich durch latente Wärmefreisetzung in Konvektionsgebieten statt. Der Großteil des Ausflusses aus der Konvektion findet unterhalb des „zero radiative heating“-Niveaus statt und diese Luftmassen sinken wieder ab. Einige hochreichende Konvektionszellen durchbrechen aber dieses Niveau und deponieren Masse im Bereich des

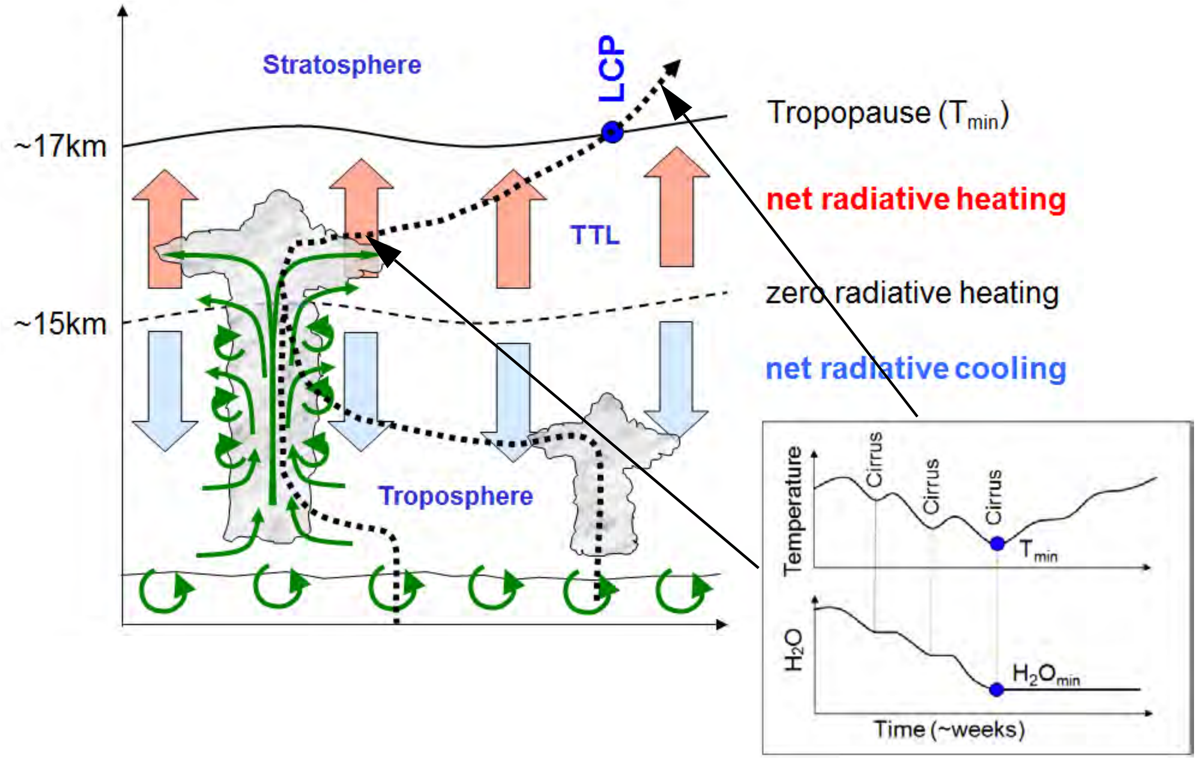

Abbildung 27: Illustration der vertikalen Transportprozesse in der tropischen Troposphäre und der tropischen Tropopausenregion (TTL) sowie der Dehydrierung von Luftmassen in diesem Bereich.

strahlungsgetriebenen Aufsteigens darüber. Diese Luftmassen steigen dann langsam durch die cold-point-Tropopause hindurch auf, gelangen dabei in immer kältere Bereiche und unterliegen zusätzlich immer wieder Temperaturfluktuationen durch Kelvinwellen. Bei jedem neuen Temperaturminimum, oft in der negativen Temperaturanomalie im Bereich einer Kelvinwelle (Immler et al., 2008), wird erneut Wasserdampfübersättigung erreicht und überschüssiger Wasserdampf kondensiert in Zirren, die die Luftmasse weiter dehydrieren. Dabei wird für jedes individuelle Luftpaket irgendwann im Bereich der cold-point-Tropopause einmal die absolut niedrigste Temperatur erreicht, wo zum letzten Mal Zirrenbildung stattfindet. Dieser für den ganzen Prozess sehr wesentliche Punkt wird der Lagrangesche Cold Point (LCP) genannt. Nach Erreichen des LCP gelangt die Luftmasse bei weiter aufsteigender Bewegung in den Bereich des positiven Temperaturgradienten der Stratosphäre. Die Erwärmung hier ist im Wesentlichen eine Folge der einsetzenden Ozonbildung und der Absorption solarer Strahlung durch das neu gebildete Ozon.

Die Temperatur des LCPs bestimmt den Anteil an Wasserdampf, der in dieser Luftmasse in der Gasphase in die Stratosphäre gelangt. Die chemische Zusammensetzung der Luft im LCP bestimmt, welche Spurengase in die Stratosphäre gelangen. Was dort in wasserlöslicher Form vorliegt wird zu einem großen Teil aus der Gasphase entfernt und sinkt mit den Eispartikeln ab, während die wasserunlöslichen Bestandteile ungehindert in die Stratosphäre gelangen.

Die meteorologischen und chemischen Bedingungen in der Gesamtheit der LCPs bestimmen die mittlere Zusammensetzung der Luft, die in die Stratosphäre gelangt. Durch die inhomogenen Bedingungen im Bereich der tropischen Tropopause und die erheblichen Temperaturkontraste sowohl in longitudinaler als auch in meridionaler Richtung ist ein korrektes

Zusammenspiel aus horizontalen und vertikalen Transporten in einem Modell der tropischen Tropopause Vorraussetzung für eine realistische Darstellung dieser komplizierten und kleinskaligen Prozesse im Modell. Werden zum Beispiel die vertikalen Transportgeschwindigkeiten überschätzt, können erheblich mehr Luftmassen in wärmeren Bereichen der Tropopause in die Stratosphäre gelangen bevor sie zonal durch die extrem kalte Tropopause über dem Bereich des westlichen Pazifiks driften und dort noch stärker dehydrieren. Außerdem bestimmt die Verweildauer der Luft vom konvektiven Outflow bis zum Erreichen des LCP, welche Zeit für chemische Prozesse zur Verfügung steht, welche die in der Regel unlöslichen organischen Quellverbindungen in zum Teil lösliche Abbauprodukte umwandeln und wie sich das Verhältnis zwischen den löslichen und unlöslichen Abbauprodukten in der Luftmasse einstellt.

Wohltmann und Rex (2008) entwickelten einen neuen Ansatz, Vertikalgeschwindigkeiten aus meteorologischen Assimilationsdaten abzuleiten. Dieser beruht auf der Lösung der thermodynamischen Gleichung und der Berechnung der dafür notwendigen diabatischen Terme aus Strahlungstransportrechnungen. Die sich aus diesem Ansatz ergebenden Vertikalgeschwindigkeiten erhalten alle großräumigen Strukturen der Originalgeschwindigkeitsfelder des Assimilationsmodells, entfernen aber große Teile kleinräumiger Strukturen, die das Ergebnis von lokalen Modellungleichgewichten sind, die durch die Assimilation der mit dem freilaufenden Modell nicht konsistenten Beobachtungsdaten entstehen (Abbildung 28).

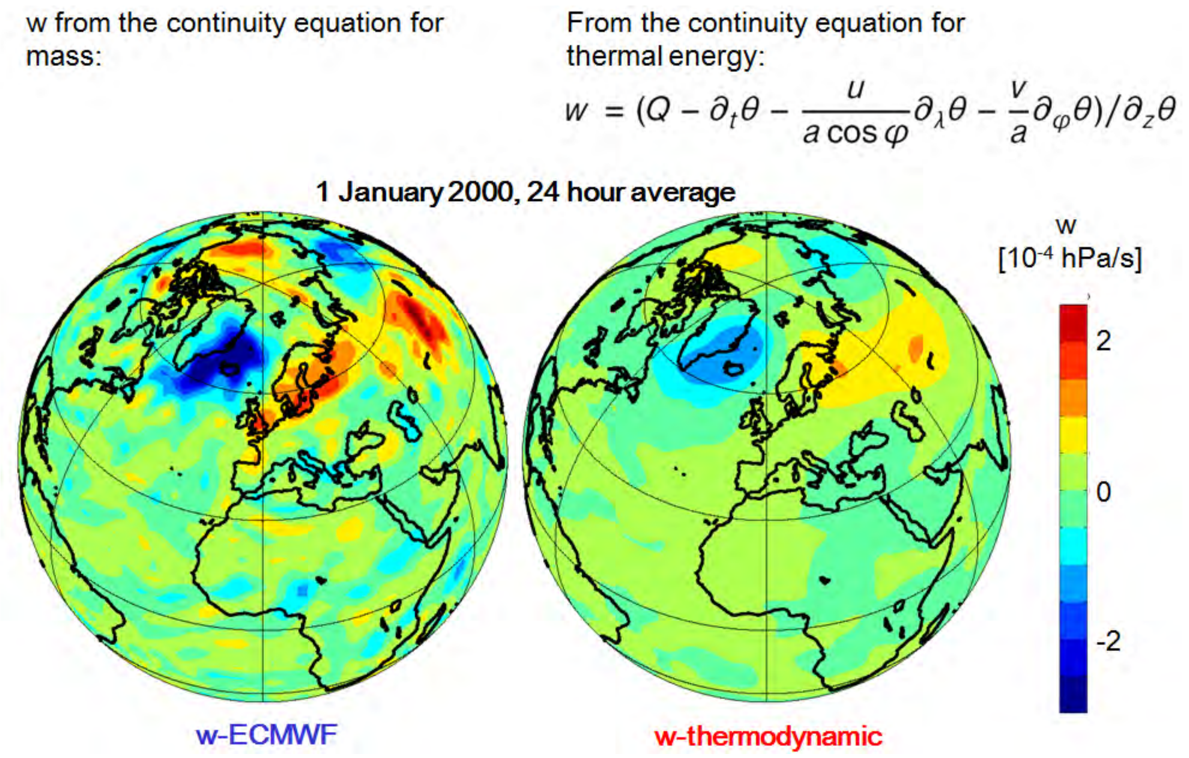
w from the continuity equation for mass:
From the continuity equation for thermal energy:
$w = (Q - \partial_t\theta - \frac{u}{a\cos\varphi}\partial_\lambda\theta - \frac{v}{a}\partial_\varphi\theta)/\partial_z\theta$
1 January 2000, 24 hour average
w
[10^{-4} hPa/s]
2
0
-2
w-ECMWF
w-thermodynamic

Abbildung 28: V24 Stundenmittel der Vertikalwinde von ECMWF ERA-40 Reanalysen für den 1.1.2000 auf 50hPa mit zwei unterschiedlichen Methoden berechnet: Links: Basierend auf der Kontinuitätsgleichung für Masse (wie in den standardmäßig vom ECMWF zur Verfügung gestellten Windfeldern). Rechts: Mit der angegebenen thermodynamischen Gleichung und einem in Wohltmann und Rex (2008) beschriebenen lagrangeschen Verfahren aus diabatischen Heizraten (Q) berechneter Vertikalwind. Q wird dazu mittels Strahlungstransportrechnungen basierend auf den Temperaturfeldern bestimmt. Nach Wohltmann und Rex (2008).

Diese beiden Vertikalwindfelder stimmen nicht überein, da das ECMWF-Modell als Assimilationsmodell nicht physikalisch konsistent frei läuft. Durch die Assimilationsinkremente erhält es ständig zusätzliche kleine Impulse, was zu Rauschkomponenten in den meteorologischen Feldern führt.

Wohltmann und Rex (2008) zeigen, dass die originalen Vertikalgeschwindigkeitsfelder aus meteorologischen Assimilationssystemen im Bereich der tropischen unteren Stratosphäre tatsächlich viel zu verrauscht sind, und bei Verwendung in Transportmodellen einen völlig unrealistischen Vertikaltransport erzeugen, der zwar im Mittel bei einigen Assimilationssystemen recht realistisch sein kann, welcher aber durch eine um Größenordnungen zu große vertikale Diffusion dominiert wird (Abbildung 29). Der Modellansatz, die Vertikalgeschwindigkeit über die thermodynamische Gleichung zu bestimmen, führt dagegen zu erheblich realistischeren vertikalen Diffusionsraten (Wohltmann und Rex, 2008).

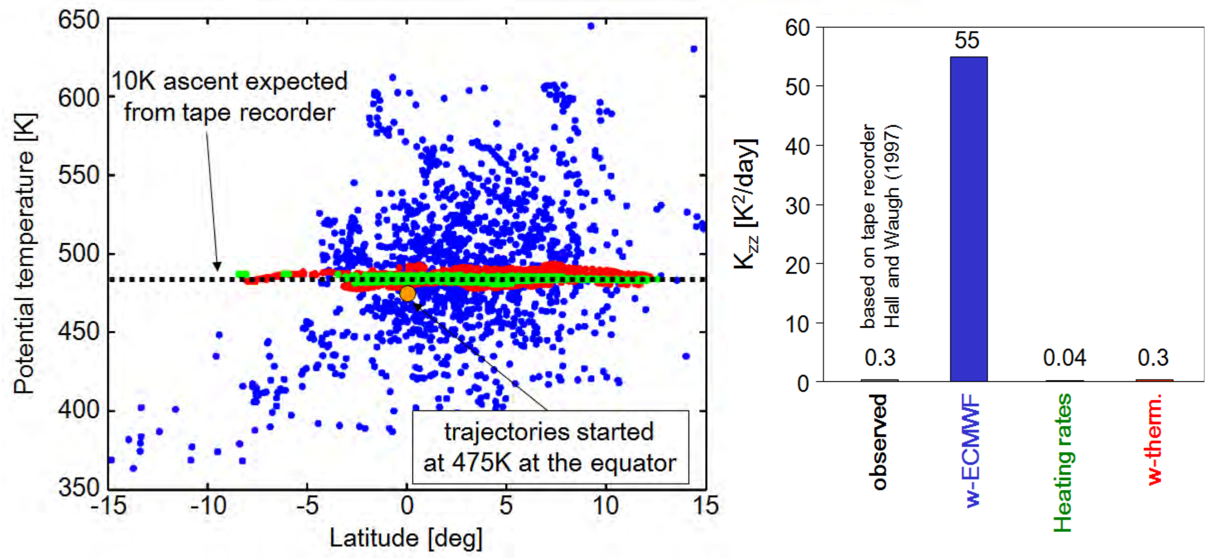

Abbildung 29: Links: Ergebnisse von Trajektorienrechnungen basierend auf verschiedenen Annahmen für den vertikalen Transport. Alle Trajektorien wurden am 1.1.2000 auf Θ=475K gestartet (orange Markierung) und 20 Tage integriert. Die Endpunkte der Rechnungen basierend auf ECMWF-Vertikalwinden (blau), diabatischen Heizraten (grün) und thermodynamisch berechneten Vertikalwinden (rot) sind dargestellt. Die sich aus diesen Rechnungen ergebenden vertikalen Diffusivitäten sind rechts einer Abschätzung der vertikalen Diffusivität im Bereich der unteren tropischen Stratosphäre gegenübergestellt. Es wird deutlich, dass die sich aus ECMWF-Vertikalwindfeldern ergebende vertikale Diffusivität um mehr als zwei Größenordnungen zu groß ist. Nach Wohltmann und Rex (2008).

Obwohl der mittlere vertikale Massefluss auch bei Verwendung der originalen Vertikalwindfelder in der richtigen Größenordnung liegen kann, wird der vertikale Transport von Spurengasen dann durch die diffusiven Terme dominiert und ist daher viel zu schnell. Wohltmann und Rex (2008) zeigen, dass die mittleren Verweildauern im Bereich der tropischen Tropopause deutlich zu klein sind, wenn diese Windfelder in Transportmodellierung verwendet werden. Dies hat wichtige Auswirkungen auf unser Verständnis der chemischen Prozessierung von Luftmassen vor dem Erreichen des LCP und damit für den Eintrag chemisch aktiver Spurengase in die Stratosphäre.

Basierend auf dem Konzept thermodynamisch berechneter Vertikalgeschwindigkeiten entwickelt Krüger et al. (2008) ein lagrangesches Modell der Transportprozesse an der tropischen Tropopause. Es werden die geografische Verteilung der LCP sowie die Verteilung der Aufenthaltsdauern in der TTL untersucht. Während sich die geografische Verteilung der LCP als relativ robust gegenüber dem verwendeten Ansatz für den Vertikaltransport erweist, ist die Aufenthaltsdauer erwartungsgemäß sehr empfindlich gegenüber den verschiedenen Verfahren und liegt bei Verwendung von thermodynamisch bestimmten Aufstiegsraten deutlich über den Ergebnissen früherer Studien. Damit steht im oberen Bereich der Troposphäre längere Zeit für chemische Prozessierung zur Verfügung, als es in Standardmodellen der Fall ist.

Schofield et al. (2011) entwickelt ein konzeptionelles Modell, welches es erlaubt die Beiträge der verschiedenen Transportprozesse im Bereich der tropischen Tropopause zur stratosphärischen Brombilanz zu untersuchen und unter verschiedenen Annahmen zu quantifizieren.

5.3 Diagnose tropischer Tropopausenprozesse in Chemie-Klimamodellen

Üblicherweise wird die Auswirkung von Klimaänderungen auf die Zusammensetzung der Stratosphäre mit Chemie/Klima-Modellen (Chemistry Climate Models, CCMs; siehe auch Abschnitt 6.4) untersucht. Aufgrund der im letzten Abschnitt beleuchteten Unsicherheiten bei der Formulierung vertikaler Transportprozesse im tropischen Tropopausenbereich stellt sich die Frage, wie realistisch diese Modelle den Eintragsprozess von Luft in die Stratosphäre und die chemische Umwandlung von Spurenstoffen während dieses Prozesses wiedergeben.

Kremser et al. (2009) nutzt das im letzten Abschnitt entwickelte lagrangesche Transportmodell zur Diagnose dieser Prozesse in CCMs. Abbildung 30 zeigt die Verteilung der Aufenthaltszeiten von Luftmassen in der oberen TTL (im Bereich von 385-395K potentieller Temperatur) in den CCMs (rechts) verglichen mit Aufenthaltszeiten abgeleitet von Daten des Europäischen Zentrums für Mittelfristige Wettervorhersage (ECMWF, links). Dabei wurden die Aufenthalts-

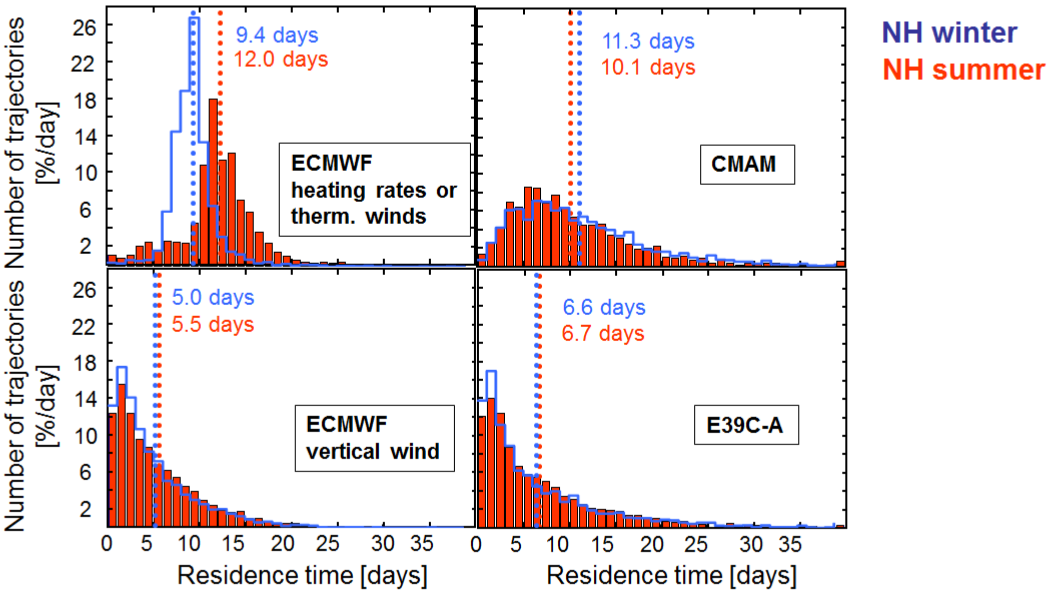

Abbildung 30: Verteilung der Aufenthaltszeiten in der oberen TTL (Θ=385-395K) für Luftmassen, die in die Stratosphäre eingetragen werden, basierend auf den jeweils angegebenen Daten. Die Abbildung zeigt Ergebnisse für den nordhemisphärischen Sommer (rot) und den nordhemisphärischen Winter (blau). Nach Kremser et al. (2009), Gettelmann et al. (2010).

dauern aus ECMWF-Daten zum einen basierend auf thermodynamischen Vertikalwinden bestimmt (oberes Panel) als auch basierend auf den Vertikalwinden des ECMWFs (welche auf der Kontinuitätsgleichung beruhen, unteres Panel).

Aufgrund der Betrachtungen im Abschnitt 5.2 gelten die mittels thermodynamischer Vertikalwinde bestimmten Aufenthaltsdauern (Panel oben links) als realistisch und werden hier als Referenz verwendet. Nur bei diesen zeigen sich die erwarteten Unterschiede zwischen dem nordhemisphärischen Sommer und Winter, mit kürzeren Aufenthaltsdauern im Winter. Da diese zwingend aus der saisonalen Variabilität der Residualzirkulation folgen, ist ein Fehlen dieser Differenz ein klarer Hinweis darauf, dass die Transporte durch vertikale Diffusion im Modell dominiert sind. Dies ist bei Verwendung von Vertikalwinden des ECMWFs genauso der Fall wie bei beiden untersuchten CCMs, deren Advektionsschemen ebenfalls durch Vertikalwinde angetrieben werden.

Obwohl bei CMAM die mittlere Aufenthaltsdauer nicht zu kurz ist, ist die Verteilung der Aufenthaltsdauern bei beiden CCMs unrealistisch. Bei beiden durchquert ein erheblicher Teil der Luftmassen die obere TTL in weniger als fünf Tagen, was im Referenzlauf fast gar nicht vorkommt. Diese Luftmassen gelangen dann in den CCMs chemisch erheblich weniger prozessiert in die Stratosphäre, als es in der Referenz (und sehr wahrscheinlich in der Natur) der Fall ist.

Diese Ergebnisse zeigen, dass derzeitige CCMs große Schwierigkeiten haben, die dynamischen Prozesse an der tropischen Tropopause korrekt zu beschreiben. Diese Prozesse bestimmen die Zusammensetzung der globalen Stratosphäre und koppeln damit direkt an die polare Ozonchemie. Da sie dem Einfluss von Klimaänderungen unterliegen, müssen zukünftig Modelle entwikkelt werden, die eine realistischere Darstellung der Transporte im Bereich der tropischen Tropopause erlauben und es ermöglichen, den Einfluss von Klimaänderungen auf diese Transporte und damit auf die Zusammensetzung der Stratosphäre zu untersuchen. Die Arbeiten im Abschnitt 6.6 leisten einen Beitrag dazu.

KAPITEL 6

INTERAKTION ZWISCHEN OZONSCHICHT UND KLIMAÄNDERUNGEN

Die Ozonschicht ist integraler Bestandteil des globalen Klimasystems der Erde. Die chemischen Prozesse, welche die Ozonschicht regulieren, sind temperaturabhängig und reagieren damit auf Veränderungen im Klimasystem. Die durch die Residualzirkulation der Stratosphäre angetriebenen Transporte von Ozon sowie von für die Ozonchemie relevanten Spurenstoffen und Aerosolen reagieren ebenfalls auf Veränderungen im Klimasystem. Andersherum beeinflusst die Ozonschicht aufgrund ihrer Absorption und Emission von Strahlung die Temperaturstruktur der Atmosphäre, wodurch jede Veränderung der Ozonschicht auf das Klimasystem rückkoppelt.

6.1 Empirische Quantifizierung der Klimasensitivität des Ozonabbaus

Die Zeitreihe der bislang in der Arktis gemessenen chemischen Ozonverluste geht bis Anfang der 1990er Jahre zurück. Abbildung 31 zeigt die mit dem Wirbelmittelansatz (Abschnitt 3.1.2) bestimmten Ozonverluste der Winter seit 1993. In diesem Zeitraum variierte die stratosphärische Chlorbelastung nur um einige Prozent, da gerade das Maximum der Chlorbelastung überschritten wurde. Auf der in Abbildung 31 gezeigten Zeitskala ist das Bild der beobachteten Ozonverluste durch sehr starke interannuale Variabilität geprägt, die jedes eventuell vorhandene Signal einer langfristigen Veränderung überdeckt.

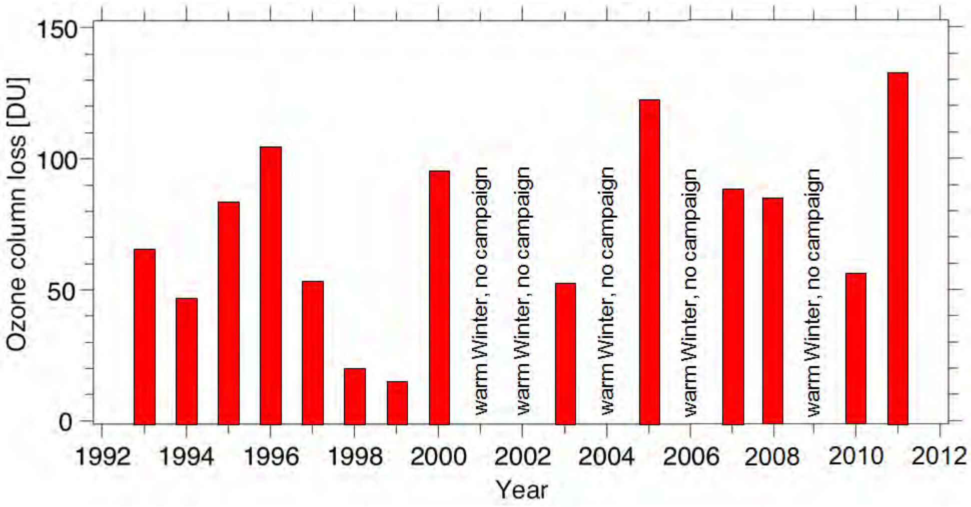

Abbildung 31: Zeitreihe der chemischen Ozonverluste in der Arktis. Aktualisiert nach Rex et al. (2004a), WMO-Assessment 2002: Newman et al. (2003).

Aufgrund der im Kapitel 3 beschriebenen Prozesse geht die interannuale Variabilität im Wesentlichen auf die Variabilität der stratosphärischen Temperaturen zurück. Rex et al. (2004a) führen den Parameter V_{PSC} ein, welcher das aufgrund der variablen Temperaturen variable Ozonabbaupotential eines Winters beschreibt. V_{PSC} ist das aus Temperaturfeldern berechnete und über den Winter gemittelte stratosphärische Volumen, in welchem die Temperaturen unterhalb der Temperaturgrenze lagen, die PSC-Bildung erlaubt. In Tilmes et al. (2006) wurde statt der absoluten Größe von V_{PSC} der Anteil des Volumens des Polarwirbels betrachtet, der PSC-Bedingungen ausgesetzt war (V_{PSC}/V_{vortex}). Dies hat den Vorteil, dass das leicht variable Volumen des Polarwirbels berücksichtigt wird und beide Hemisphären miteinander verglichen werden können, in denen die Polarwirbel sehr unterschiedliche Größen haben.

Abbildung 32 zeigt die Ozonverlustdaten aufgetragen gegen den Parameter V_{PSC}/V_{vortex} (aktualisiert nach Rex et al., 2004a; 2006). Es ergibt sich eine kompakte und nahezu lineare Relation. Tilmes et al. (2006) verwendeten Tracerrelationen (Abschnitt 3.1.3) zur Bestimmung der Ozonverluste und fanden diese kompakte, lineare Beziehung zu V_{PSC}/V_{vortex} bestätigt. Weiterhin zeigten Tilmes et al. (2006), dass diese Relation sich bis zu antarktischen Bedingungen hin erstreckt.

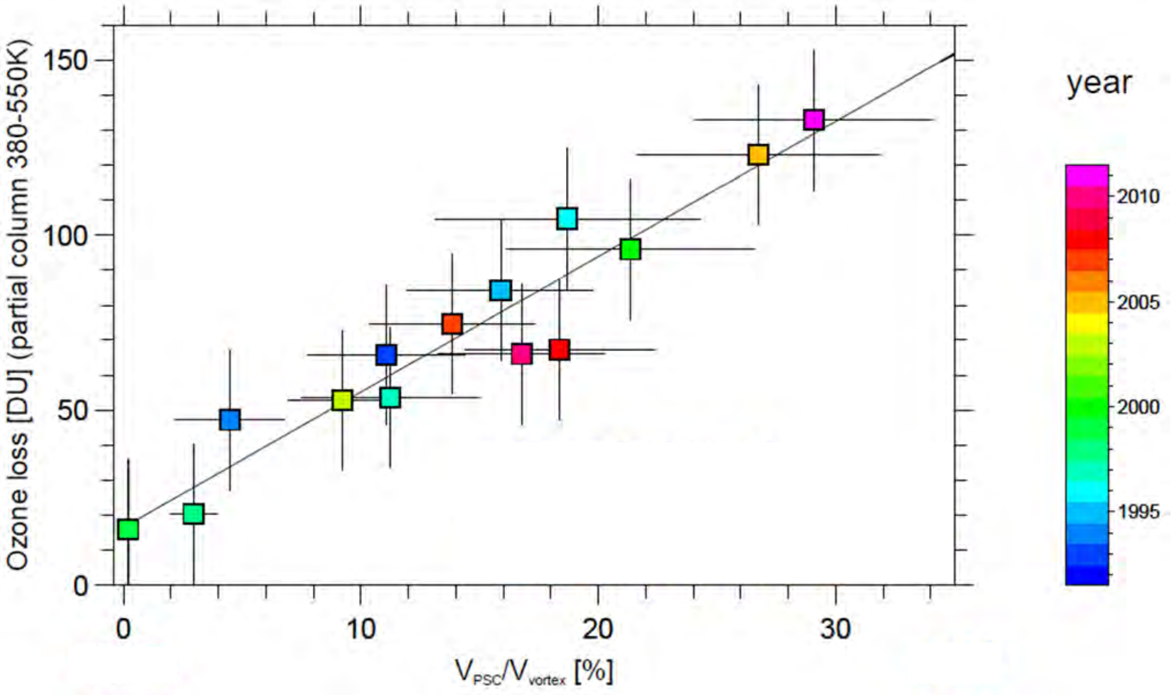

Abbildung 32: Chemische Ozonverluste der Arktis aufgetragen gegen den Parameter V_{PSC}/V_{vortex} (siehe Text). Aktualisiert nach Rex et al. (2004a), Rex et al. (2006), WMO-Assessment 2002: Newman et al., (2003), WMO-Assessment 2006: Newman und Rex (2007).

Harris et al. (2010) erklären die Kompaktheit der Relation basierend auf fundamentalen Eigenschaften der atmosphärischen Prozesse, die zum Ozonabbau führen. Es wird dort gezeigt, dass die Wirkung vieler Prozesse, die zu einer größeren Variabilität in dieser Relation führen könnten, sich gegenseitig gerade aufhebt, was zu der beobachteten Kompaktheit beiträgt.

Eine wichtige Eigenschaft der in Abbildung 32 gezeigten Relation zwischen Ozonverlust und V_{PSC}/V_{vortex} ist, dass sie für die derzeitige Chlorbelastung der Stratosphäre die Sensitivität des Ozonverlustes auf Temperaturänderungen empirisch quantifiziert - der Parameter V_{PSC} kann ja allein aus Temperaturfeldern berechnet werden. Rex et al. (2004a) und Rex et al. (2006) zeigen, dass die Steigung der in Abbildung 32 gezeigten Relation einer Temperatursensitivität des Ozonverlusts von 15DU pro Kelvin entspricht. Diese empirische Quantifizierung der Klimasensitivität des arktischen Ozonabbaus ist die zur Zeit robusteste Abschätzung dieses Schlüsselparameters und wird auch zur Validierung von Modellen der Ozon/Klima-Wechselwirkung verwendet (CCMval report: *Eyring et al., 2010;* WMO-Assessment 2010: *Douglass et al, 2011*).

6.2 Beobachtete langfristige Änderungen

Ansteigende Treibhausgaskonzentrationen in der Atmosphäre führen im globalen Mittel strahlungsbedingt zu einer Abkühlung der Stratosphäre. In polaren Breiten wird die Temperatur der Stratosphäre aber gerade im Winter erheblich durch dynamische Prozesse modifiziert (siehe Abschnitt 4.2.2). Es ist derzeit unklar, wie diese komplizierten dynamischen Prozesse auf Klimaänderungen reagieren und daher ist eine Prognose der Temperaturen in der polaren Stratosphäre im Winter derzeit nicht robust möglich.

Für die Vergangenheit sind die Temperaturen in der unteren Stratosphäre auf der Nordhemisphäre aber recht zuverlässig seit etwa Mitte der 1960er Jahre bekannt, aufgrund der ab dann in hoher Frequenz durchgeführten Radiosondierungen und darauf basierenden Analysen der stratosphärischen Temperaturfelder.

Im letzten Abschnitt wurde gezeigt, dass V_{PSC}/V_{vortex} der Schlüsselparameter für den arktischen Ozonverlust eines gegebenen Winters ist und das sich der zu erwartende Ozonverlust (bei derzeitiger Chlorbelastung der Stratosphäre) nahezu vollständig aus der Größe dieses meteorologisch bestimmten Parameters ergibt.

Rex et al. (2004a) und Rex et al. (2006) berechnen V_{PSC}/V_{vortex} aus mehreren stratosphärischen Analysedatensätzen und untersuchen die langfristigen Veränderungen (Abbildung 33). Es zeigt sich die bereits aus den Ozonverlusten bekannte enorme interannuale Variabilität. Warme Winter mit sehr kleinen V_{PSC}-Werten (und daher geringem Ozonverlust) treten in unregelmäßigen Abständen über die gesamte Periode auf. Gegen Ende der Zeitreihe scheinen sehr kleine Werte von V_{PSC} jedoch auszubleiben, was aber derzeit noch nicht statistisch signifikant ist.

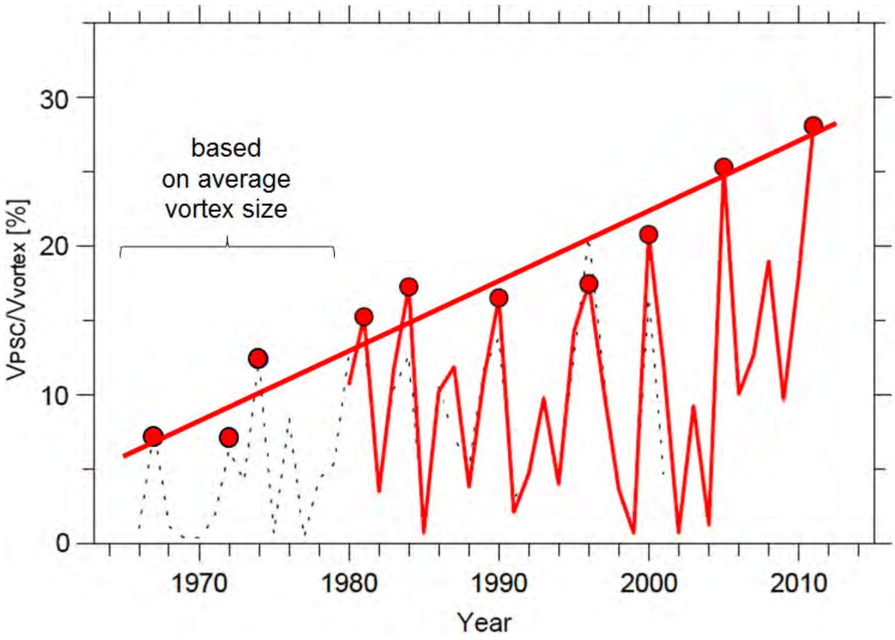

Abbildung 33: Zeitreihe von V_{PSC}/V_{vortex}. Der jeweils größte Wert jedes Fünfjahresintervalls ist hervorgehoben. Aktualisiert nach Rex et al. (2004a), Rex et al. (2006), WMO-Assessment 2006: Newman und Rex (2007), WMO-Assessment 2010: Douglass et al. (2011).

Im langjährigen Mittel treten kalte Winter mit V_{PSC}-Werten im oberen Bereich der Variabilität etwa bei einem von fünf Jahren auf. Diese Winter (definiert als jeweils der kälteste Winter in jedem 5-Jahres-Intervall) sind in Abbildung 33 durch Punktmarkierungen hervorgehoben. Für diese Winter zeigt sich über den dargestellten Zeitraum eine sehr ausgeprägte Abkühlung, welche zu einer Verdreifachung der maximal erreichten V_{PSC}/V_{vortex}-Werte seit den 1960er und frühen 1970er Jahren geführt hat.

Basierend auf einem Monte-Carlo-Ansatz zeigen Rex et al. (2006), dass die langfristige, nunmehr fast fünf Jahrzehnte andauernde Änderung der Maximalwerte von V_{PSC} bereits bis zum Jahr 2005 statistisch weit über 99.9% signifikant war und robust gegenüber Unsicherheiten in den zugrundeliegenden Radiosondenmessungen und den daraus abgeleiteten stratosphärischen Temperaturfeldern ist. Seit der ersten Veröffentlichung dieser Beobachtung durch Rex et al. (2004a), beruhend auf Daten bis 2003, hat sich die langfristige Änderung bereits seit fast einem weiteren Jahrzehnt fortgesetzt und es wurden mit den Werten für 2005 und 2011 neue Rekorde erreicht.

6.3 Empirisch gestützte Szenarien für die zukünftige Entwicklung

Eine Vorhersage zukünftiger Entwicklungen im nichtlinear gekoppelten Klimasystem erfordert immer eine mechanistische Modellierung aller relevanten Prozesse in einem gekoppelten Chemie-/Klimamodell. Extrapolationen vergangener Trends oder Veränderungen sind in dem nichtlinearen System als Vorhersage nicht geeignet.

Solange eine mechanistische Vorhersage jedoch noch nicht möglich ist oder noch mit sehr großen Unsicherheiten behaftet ist, kann eine Betrachtung nützlich sein, was in der Zukunft geschehen würde, sollten sich die in der Vergangenheit beobachteten Veränderungen fortsetzen. Solch eine Betrachtung trägt dazu bei, die Bandbreite möglicher zukünftiger Entwicklungen auszuloten und stellt ausdrücklich keine Vorhersage der erwarteten Entwicklung dar.

Die in Abschnitt 6.1 aus Beobachtungen abgeleitete Temperatursensitivität des arktischen Ozonabbaus von 15DU pro K gilt für die derzeitige Chlorbelastung der Stratosphäre. Da die für 85% des Ozonverlusts verantwortlichen Abbauzyklen in der Summe nahezu linear von ClO_x abhängen (z.B. Harris et al., 2010), ist davon auszugehen, dass diese Sensitivität linear mit der Chlorbelastung skaliert.

Damit kann der Ozonabbau in einem zukünftigen arktischen Winter im Wesentlichen aus der dann vorherrschenden Chlorbelastung der Stratosphäre und dem V_{PSC}-Wert dieses Winters abgeschätzt werden.

Die zukünftige Chlorbelastung der Stratosphäre kann aufgrund der Maßgaben des Montrealer Protokolls verhältnismäßig gut vorhergesagt werden (WMO-Assessment 2010: *Douglass et al., 2011*). Die Hauptunsicherheit in Vorhersagen zukünftiger arktischer Ozonverluste liegt damit in der zukünftigen Entwicklung von V_{PSC}.

Knudsen et al. (2004) betrachten, wie sich der arktische Ozonverlust zukünftig verhalten würde, wenn die in der Vergangenheit beobachtete Veränderung von V_{PSC} sich in die Zukunft fortsetzt. Es ergibt sich dann in der Zukunft ein Wettlauf aus weiter zunehmenden Maximalwerten von V_{PSC} und langsam abnehmender Chlorbelastung der Stratosphäre. In diesem Spannungsfeld nimmt der maximale, jeweils für kalte Winter erreichte Ozonabbau in der Arktis bis etwa 2015 zu und beginnt dann langsam abzunehmen (Knudsen et al., 2004). Damit wird aufgrund der angenommenen weiteren Abkühlung der kalten Winter das Maximum des arktischen Ozonabbaus

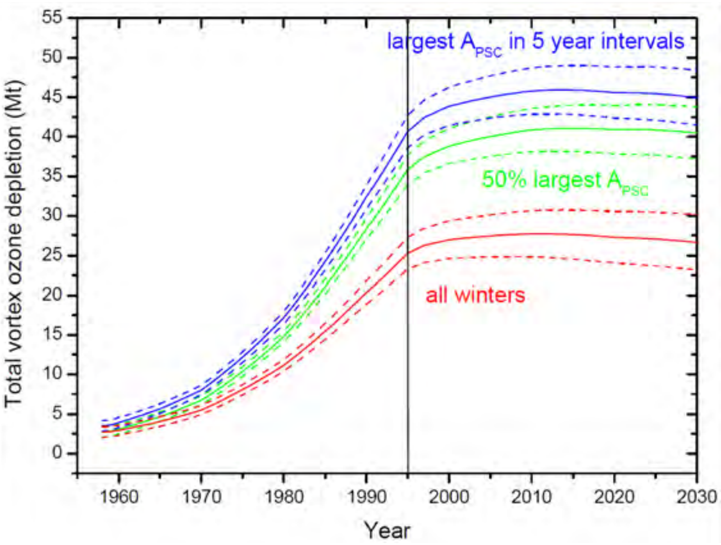

Abbildung 34: Zukünftige Entwicklung des arktischen Ozonabbaus für die Winter mit der maximalen PSC-Ausdehnung in Fünfjahresintervallen (blau), alle Winter (rot) und die 50% kältesten Winter (grün), jeweils unter der Annahme, dass sich der für diese Gruppen in der Vergangenheit beobachtete Trend der PSC-Ausdehnung in die Zukunft fortsetzt. Nach Knudsen et al. (2004).

gegenüber dem Maximum der stratosphärischen Chlorbelastung um fast zwei Jahrzehnte nach hinten verschoben (Abbildung 34). Die bisherige Entwicklung seit Knudsen et al. (2004) bestätigt diese Abschätzungen.

6.4 Defizite derzeitiger Chemie-Klimamodelle

Letztlich kann die vielfältige nichtlineare Interaktion zwischen der Ozonschicht und anderen Komponenten des Klimasystems der Erde nur in globalen Modellen vollständig verstanden und vorhergesagt werden, die alle wesentlichen Prozesse quantitativ korrekt enthalten. Aufgrund der Komplexität des Klimasystems und der extrem großen Bandbreite der involvierten räumlichen und zeitlichen Skalen wird dabei jede Modellbeschreibung nur eine mehr oder minder gute Annäherung an die Realität bleiben müssen. Daraus folgt, dass eine objektive Betrachtung der Modellunsicherheiten untrennbar mit jedem Modellergebnis einhergehen muss, um Fehlinterpretationen zu vermeiden.

Die meisten für Klimavorhersagen verwendeten globalen Klima- oder Erdsystemmodelle enthalten keine gut aufgelöste Stratosphäre und in diesen Modellen ist keine stratosphärische Chemie und keine interaktive Ozonschicht enthalten. Daher sind diese Modelle nicht geeignet, die Wechselwirkungen zwischen Klimaänderungen und Veränderungen der Ozonschicht zu untersuchen und die Klimaprognosen dieser Modelle enthalten die Auswirkungen der interaktiven Wechselwirkungen nicht.

Im Gegensatz dazu enthalten Chemie/Klimamodelle (Chemistry Climate Models - CCMs) eine gut aufgelöste Stratosphäre sowie detaillierte stratosphärische Chemie mit interaktiver Ozonschicht. Diese Modelle haben jedoch derzeit noch große Defizite.

Die meisten CCMs enthalten keinen interaktiven Ozean. Damit sind diese Modelle nicht für Vorhersagen des Klimas an der Erdoberfläche geeignet und erlauben es nicht, die Auswirkungen von Veränderungen in der Ozonschicht auf das Oberflächenklima interaktiv zu erfassen.

Eyring et al. (2005) beschreibt eine Strategie, CCMs prozessorientiert zu validieren. Es zeigt sich, dass CCMs gerade in der Darstellung der Polarwirbel und der chemischen Prozesse, die zum polaren Ozonabbau führen, große Schwierigkeiten haben. Gerade in der Arktis repräsentieren CCMs den chemischen Ozonabbau nur schlecht. Einige CCMs erhalten in der Arktis keinerlei Ozonabbau und die meisten anderen unterschätzen den beobachteten Abbau erheblich. Eine realistische Darstellung der Klimasensitivität des Ozonabbaus nach Abbildung 32 gelingt nahezu keinem CCM (Abbildung 6-37 in *Eyring et al, 2010*).

Auch in der Antarktis gelingt die Darstellung des Polarwirbels und des Ozonlochs in derzeitigen CCMs nicht zufriedenstellend. Durch die in Gitterpunktsmodellen unvermeidliche numerische Diffusion des verwendeten Advektionsverfahrens werden die scharfen Gradienten von Ozon und vielen Spurengasen an der Polarwirbelkante verwischt, so dass in den meisten CCMs nur im Zentrum des Polarwirbels sehr niedrige Ozonkonzentrationen auftreten, während diese in der Natur über den ganzen Wirbel hinweg vorliegen.

Ein weiteres Problem von CCMs ist ihr großer numerischer Aufwand. Auch auf modernen Hochleistungsrechnern können diese Modelle nur mit größtem Aufwand über ein Jahrhundert integriert werden. Die für IPCC-Studien notwendigen vielen Szenarienläufe und nach Möglichkeit auch von mehreren Ensembleläufen können nicht durchgeführt werden.

Für eine realistische und robuste Berücksichtigung der Ozon/Klimawechselwirkung und Klimavorhersagen müssen also numerisch effizientere Modelle entwickelt werden, die zudem die polaren Ozonverlustprozesse realistischer beschreiben.

6.5 Das semi-empirische Modell SWIFT

Ein Ansatz für eine erheblich effizientere Beschreibung der stratosphärischen Chemie ist die Verwendung semi-empirischer Methoden (Huck et al., 2012). Rex et al. (2011b) entwickeln für die polare Ozonchemie das semi-empirische Modell SWIFT.

SWIFT ist ein extrem schnelles Modul zur Berechnung des wirbelgemittelten chemischen Ozonverlusts im polaren Winter. Die Architektur von SWIFT ist ähnlich der eines vollständigen Chemiemodells. Es löst ein Differentialgleichungssystem für die wesentlichen chemischen Komponenten und wird durch meteorologische Parameter angetrieben. Statt in den Differentialgleichungen jedoch Terme für alle individuellen chemischen Reaktionen zu enthalten, basiert es auf dem Nettoeffekt ganzer chemischer Mechanismen auf die wirbelgemittelten Konzentrationen der Spurenstoffe.

In SWIFT ersetzen Zeitkonstanten für die enthaltenen chemischen Mechanismen die reaktionskinetischen Daten der einzelnen Reaktionen eines vollständigen Chemiemodells, welche üblicherweise im Labor bestimmt werden. In SWIFT werden die Zeitkonstanten in einem nichtlinearen multidimensionalen Optimierungsprozess so gewählt, dass das Modell die Reproduktion der beobachteten saisonalen Verläufe der enthaltenen Spurengase und der Ozonverlustraten ergibt. Dabei ist wichtig, dass die in SWIFT empirisch angepassten Zeitkonstanten direkt auf die Kinetik der in den jeweiligen Mechanismen enthaltenen chemischen Reaktionen zurückgehen. D.h. es handelt sich um universelle Parameter, welche nicht an meteorologische Prozesse gebunden sind und die sich durch Klimaänderungen daher nicht verändern werden.

Das Differentialgleichungssystem in SWIFT ist nicht steif und kann mit einem Zeitschritt von einem Tag gelöst werden. Damit ist SWIFT extrem schnell und erlaubt die Prozessierung hunderter von Jahren pro Sekunde. Das Modell repräsentiert die jahreszeitlichen Verläufe der chemischen Spezies im Polarwirbel sehr gut, und zwar für den weiten Bereich an meteorologischen Bedingungen von den wärmsten und dynamisch stark gestörten arktischen Wintern bis zu den sehr kalten und stabilen antarktischen Polarwirbeln (Abbildung 35).

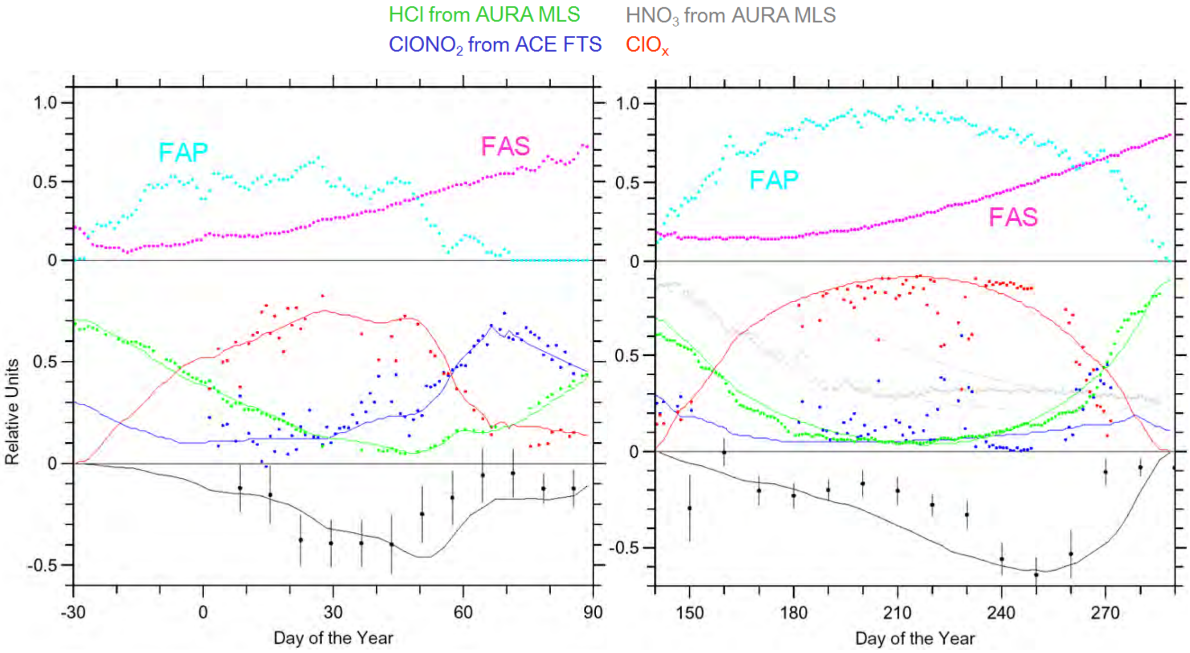

Abbildung 35: Ergebnisse von SWIFT: Links: Für den arktischen Winter 2004/2005. Rechts: Für den antarktischen Winter 2006. Obere Panel: Die antreibenden meteorologischen Parameter FAS (magenta; 24-Stundenmittel des Anteils der Vortexfläche im Sonnenlicht) und FAP (cyan; Anteil der Vortexfläche in dem PSC-Bedingungen herrschen). Mittlere Panel: HCl (grün), $ClONO_2$ (blau) und ClO_x (rot) von SWIFT (Linien) und den am oberen Bildrand angegebenen Messungen (Punkte). Untere Panel: Chemische Ozonverlustraten von SWIFT (Linie) und Match (Symbole). Nach Rex et al. (2011b).

SWIFT reproduziert auch die ausgeprägte interannuale Variabilität des Ozonabbaus in der Arktis sehr gut (Abbildung 36).

SWIFT stellt somit einen erfolgversprechenden Ansatz dar, die polaren Ozonverlustprozesse und damit auch die Klimawechselwirkungen des Ozonlochs interaktiv und numerisch effizient in volle Erdsystemmodelle aufzunehmen.

6.6 Das vollständig lagrangesche Chemie-/Transportmodell ATLAS

In den Abschnitten 5.3 und 6.4 hat sich gezeigt, dass derzeitige globale Modelle stratosphärischer Chemie oft unter den Auswirkungen exzessiver numerischer Diffusion leiden. Das Problem ist besonders ausgeprägt bei CCMs. Diese werden aufgrund des Anspruchs, sie über ein Jahrhundert integrieren zu können, oft in geringerer Auflösung formuliert als detaillierte Chemie-/Transportmodelle, welche oft zum Studium einzelner Jahre verwendet werden. Das Problem wird besonders dort manifest, wo große Spurengasgradienten herrschen, so dass die numerische Diffusion dort zu erheblichen numerisch bedingten Spurengasflüssen führen kann. Diese numerischen Effekte übertreffen die tatsächlichen Transporte in diesen Bereichen oft weit. Die Folge ist, dass Modelle die ausgeprägten Spurenstoffgradienten im Bereich der Polar-

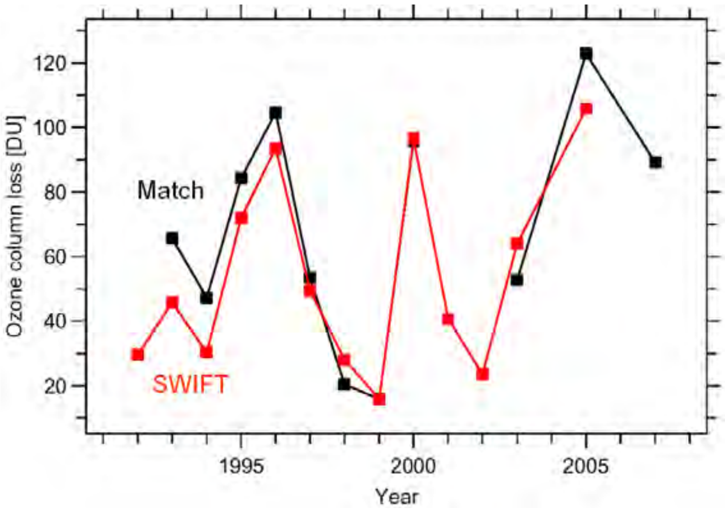

Abbildung 36: Interannuale Variabilität des chemischen Ozonabbaus in der Arktis von SWIFT (rot) und aus Beobachtungen (schwarz). Nach Rex et al. (2011b).

wirbelgrenze oder im Bereich der tropischen Tropopause oft nicht aufrecht erhalten können (*Eyring et al., 2010*), was dort zu einer unrealistischen Darstellung atmosphärischer Prozesse führen kann.

Die Entwicklung des vollständig lagrangeschen Chemie-/Transportmoduls ATLAS (Wohltmann und Rex, 2008; Wohltmann et al., 2009) soll einen Beitrag dazu leisten, diese Limitierung der Modellierung zu überwinden. Dies ist besonders relevant im Bereich der beiden oben erwähnten atmosphärischen Schlüsselregionen der Polarwirbel und der tropischen Tropopause.

Der Vertikaltransport in ATLAS beruht auf thermodynamisch berechneten Vertikalgeschwindigkeiten (Wohltmann et al., 2008, siehe auch Abschnitt 5.2), kann aber zu Testzwecken auf normale Vertikalwinde umgeschaltet werden. In einem Übergangsbereich in der mittleren Troposphäre geht das Modell nach unten auf die Verwendung von Vertikalwinden über. Zur Zeit läuft ATLAS als ein eigenständiges Chemie-/Transportmodell, soll aber in Zukunft als ein Modul für CCMs und Erdsystemmodelle zur Verfügung stehen.

ATLAS ist ein vollständig lagrange formuliertes Modell und verzichtet auf jegliche vertikale oder horizontale Gitterstruktur. Die vollständig lagrangesche Formulierung des Modelltransports ist frei von jeglicher numerischer Diffusion. Die tatsächliche subskalige Durchmischung der Atmosphäre kann daher basierend auf physikalischen Grundsätzen im Modell parametrisiert werden. Eine solche Parametrisierung erfolgt in eulerschen Gitterpunktmodellen üblicherweise nicht, da die unphysikalische numerische Diffusion in diesen Modellen die tatsächliche Diffusivität der Atmosphäre ohnehin weit übertrifft. In ATLAS werden die Parameter der physikalisch begründeten Diffusionsparametrisierung anhand von Beobachtungsdaten angepasst (Wohltmann und Rex, 2008).

ATLAS folgt in einigen Konzepten der Formulierung von CLaMS (*McKenna et al., 2002a: 2002b*), dem ersten und neben ATLAS weltweit einzigen lagrangeschen globalen Chemie-/ Transportmodell. Gegenüber CLaMS ist jedoch die atmosphärische Durchmischung auch in der Vertikalen unabhängig von einer festen Levelstruktur formuliert, während CLaMS in der vertikalen feste Level aufweist. Der levelfreie Ansatz von ATLAS resultiert in einer weiteren Reduzierung der vertikalen Diffusivität (Wohltmann und Rex, 2008).

ATLAS enthält einen vollständigen Satz der für stratosphärische Prozesse relevanten chemischen Spurenstoffe (46 explizit behandelte Spezies) und chemischen Reaktionen (171 Gasphasenreaktionen und sieben heterogene Reaktionen auf drei verschiedenen Partikeltypen). Das Differentialgleichungssystem, welches die Modellchemie beinhaltet, wird mit adaptivem Zeitschritt explizit gelöst und es werden keine vereinfachenden Annahmen über das Vorliegen instantaner Gleichgewichte in chemischen Familien gemacht.

Großer Wert wird auf eine genaue Darstellung der für die Prozesse im Polarwirbel wichtigen Mikrophysik gelegt. Die Bildung von Partikeln erfolgt in zwei Klassen, einer für die Chemie relevanten kleinen Größenklasse und einer Klasse, in welcher der volle Lebenszyklus größerer Partikel aus Nukleation, diffusionsbegrenztem Wachstum in übersättigten Bereichen und diffusionsbegrenzter Evaporation in Untersättigung im Wechselspiel mit Sedimentation durch die Atmosphäre modelliert wird (basierend auf dem bei *Carslaw et al., 2002* beschriebenen Ansatz). Für diese Partikelklasse werden im Modell individuelle, aufgrund der tatsächlichen aktuellen Größe der Partikel sedimentierende Partikeltrajektorien berechnet. Diese detaillierte Behandlung der Mikrophysik ist für eine realistische Darstellung des Denitrifikationsprozesses im Modell und damit für eine realistische Temperatursensitivität der modellierten Ozonverluste unerlässlich (Chipperfield et al., 2005).

Modellrechnungen von ATLAS wurden für eine Reihe arktischer Winter umfassend mit Beobachtungsdaten von vielen verschiedenen Instrumenten (Satelliten-, Flugzeug- und Ballondaten) verglichen (Wohltmann und Rex, 2009; Wohltmann et al., 2010; Wohltmann et al., 2012). Es zeigt sich eine sehr gute Fähigkeit von ATLAS, auch die Details der beobachteten chemischen Felder und Mechanismen zu reproduzieren.

Abbildung 37 und Abbildung 38 zeigen zum Beispiel den von ATLAS modellierten Ozonverlust im arktischen Polarwirbel im Vergleich mit Ozonmessungen für die Winter 1999/2000 und 2010/2011. Bemerkenswert ist neben dem allgemein sehr gut reproduzierten Ausmaß des Ozon-

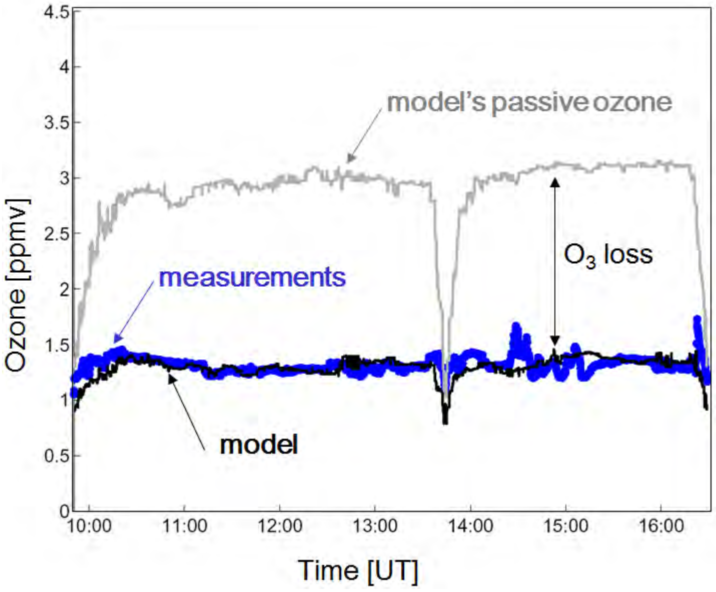

Abbildung 37: Ozon (blau) und passiver Ozontracer (grau) am 12. März 2000 ausgelesen aus ATLAS entlang des Flugpfades der ER-2 an diesem Tag. Die Differenz zwischen passivem Ozontracer und Ozon gibt das Ausmaß des chemischen Ozonverlusts an (Pfeil). Die Ozonmessung der ER-2 ist schwarz eingezeichnet. Nach Wohltmann et al., (2010).

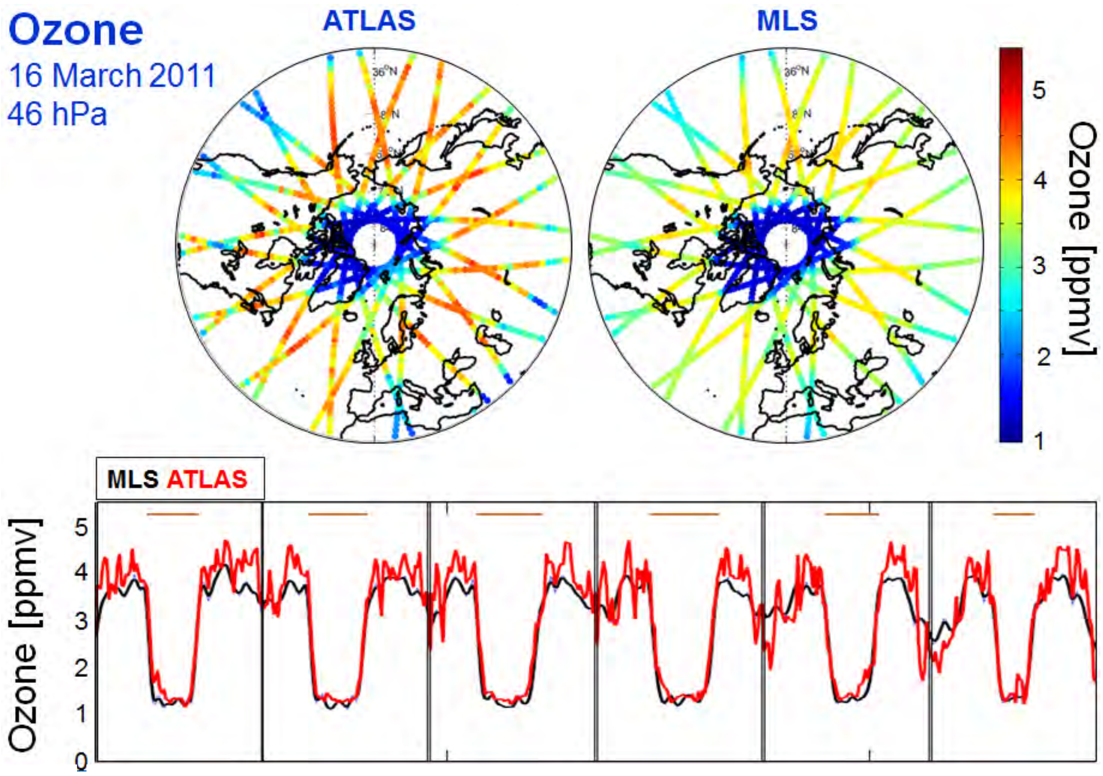

Abbildung 38: Obere Panel: Links: Ozonmischungsverhältnis ausgelesen aus ATLAS für den 16.3.2011 auf 46hPa am Ort der MLS-Messungen. Rechts: Entsprechende MLS-Ozonmessungen. Untere Panel: Ozon von ATLAS (rot) und MLS (schwarz) entlang von sechs zufällig ausgewählten Orbits der oberen Panel. Nach Rex et al. (2011a; Darstellung von Ergebnissen der Modellläufe für Manney et al., 2011).

verlusts insbesondere die exzellente Erhaltung des steilen Ozongradienten an der Polarwirbelaußengrenze, der sich durch den massiven Ozonverlust im Winter 2010/2011 herausgebildet hat (Abbildung 38 untere Panel).

KAPITEL 7

ZUSAMMENFASSUNG UND AUSBLICK

Die Variabilität und langfristige Veränderung der Ozonschicht ist ein wichtiger Bestandteil der Veränderungen im Klimasystem der Erde. In der vorliegenden Arbeit werden diese Beiträge quantifiziert, die sie jeweils antreibenden Prozesse untersucht und Methoden entwickelt, diese Prozesse in globalen Modellen der Erdatmosphäre zu repräsentieren.

Die Ergebnisse zeigen, dass eine Hauptquelle von Variabilität und Veränderung der Ozonschicht Prozesse sind, die sich im polaren Winter abspielen, wobei das größte Ausmaß von interannualer Variabilität in der Arktis erreicht wird. Die vorliegende Arbeit entwickelt Methoden, die verschiedenen Beiträge zu dieser Variabilität aus Beobachtungsdatensätzen und mittels angepasster Messstrategien zu bestimmen.

Es zeigt sich, dass die Kombination von so bestimmtem natürlichen, dynamisch bedingten Eintrag von Ozon in hohe Breiten und anthropogenem, chemisch bedingten Ozonverlust die beobachtete Variabilität der Ozonschichtdicke in der Arktis vollständig erklären kann. Somit ist es erstmalig gelungen, ein geschlossenes Gesamtbudget der Beiträge der verschiedenen Prozesse zur Variabilität der polaren Ozonschicht aufzustellen.

Die gemessenen chemischen Ozonverluste in der Arktis waren seit Beginn der 1990er Jahre extrem variabel, und erreichten dabei jeweils im Frühjahr 1996, 2000, 2005 und schließlich 2011 neue Rekordwerte. Im Verlauf dieser Entwicklung zunehmender Ozonverluste erreichte die Ozonzerstörung in der Arktis 2011 erstmals das Ausmaß antarktischer Ozonlöcher.

Unser theoretisches Verständnis des chemischen Ozonverlustprozesses wurde mit detaillierten Modellrechnungen und durch gezielte Flugzeugmesskampagnen in der arktischen Stratosphäre überprüft und weiterentwickelt. Zunächst vorhandene Defizite wurden auf eine Unterschätzung der Photolyserate von ClOOCl und des stratosphärischen Bromgehalts zurückgeführt. Nach Verbesserungen in diesen Bereichen liegt nun erstmals eine mit Beobachtungen der Ozonverlustrate und der Konzentration der ozonabbauenden Spurengase vollständig konsistente Beschreibung des Ozonverlustprozesses vor.

Der aus einer Kombination aus Beobachtungsdaten und Transportmodellrechnungen abgeleitete dynamisch bedingte Eintrag von Ozon in die Arktis ist ebenfalls sehr variabel und im Betrag in der Regel größer als der chemische Verlust. Somit nimmt in der Arktis mit wenigen Ausnahmen die Ozonschichtdicke im Verlauf des Winters zu. Es wird gezeigt, dass der ursprüngliche Antrieb der Variabilität beider Terme in dem variablen Wellenantrieb der stratosphärischen Residualzirkulation liegt. Die Residualzirkulation bestimmt sowohl die Ozontransporte als auch, durch ihren dynamisch bedingten Einfluss auf die stratosphärischen Temperaturfelder, das Ausmaß des chemischen Ozonverlusts. Daher korrelieren in Wintern mit geringem Wellenantrieb tiefe Temperaturen und demzufolge ausgeprägter chemischer Ozonverlust mit geringem Eintrag von Ozon in die Arktis.

Bei derzeitiger Chlorbelastung der Stratosphäre tragen die Variabilität des chemischen Ozonverlusts und des dynamisch bedingten Eintrags von Ozon in die Arktis etwa gleich viel zu den beobachteten Anomalien der Ozonschichtdicke bei. Damit verstärkt der anthropogene Ozonverlust die natürliche, dynamisch bedingte Variabilität der arktischen Ozonschicht derzeit etwa um einen Faktor zwei.

Zur Untersuchung der Kopplung zwischen Ozonschicht- und Klimaänderungen definiert die vorliegende Arbeit ein auf Temperaturanalysen beruhendes Maß der „Kälte“ eines Winters, dessen Variabilität die Variabilität arktischer Ozonverluste nahezu vollständig erklärt. Es wird gezeigt, dass seit fast fünf Jahrzehnten die so definierten „kalten“ arktischen Winter kontinuierlich erheblich „kälter“ geworden sind und sich die maximal erreichten Werte dieses Parameters dabei mehr als verdreifacht haben. Diese Veränderung der klimatischen Bedingungen in der arktischen Stratosphäre sind die Ursache für zunehmende Ozonverluste dort und letztlich für die Bildung eines Ozonlochs über der Arktis im Frühjahr 2011.

Obwohl eine generelle Abkühlung der Stratosphäre aufgrund steigender Treibhausgaskonzentrationen erwartet wird, ist das Ausmaß der Abkühlung gerade der „kalten“ arktischen Winter bislang nicht verstanden und eine Vorhersage zukünftiger Ozonverluste daher zur Zeit nicht robust möglich.

Diese Ergebnisse verdeutlichen die Notwendigkeit, die Wechselwirkungen zwischen der Ozonschicht und anderen Komponenten des Klimasystems in gekoppelten Modellen vollständig zu erfassen und als Teil von Klima- und Ozonsvorhersagen zu berücksichtigen. In der vorliegenden Arbeit werden für diesen Zweck mit SWIFT und ATLAS zwei neue Modellsysteme geschaffen. Während bei SWIFT der Schwerpunkt der Entwicklung auf numerischer Effizienz liegt, erfasst ATLAS alle Prozesse möglichst detailliert. SWIFT basiert auf einem neuartigen semi-empirischen Ansatz und erlaubt eine robuste Modellierung polarer Ozonverluste beider Hemisphären in bislang nicht erreichter numerischer Effizienz. ATLAS ist ein vollständig lagrangesches Modell der stratosphärischen Chemie ohne jegliches festes Modellgitter. Es vermeidet durch diesem Ansatz Probleme numerischer Diffusion, welche in klassischen Modellen der Chemie insbesondere in den Schlüsselbereichen der stratosphärischen Polarwirbel und der tropischen Tropopause zu erheblichen Artefakten führen. ATLAS ist in der Lage, die Chemie der Stratosphäre detailliert zu modellieren und erreicht bei der Repräsentation polarer Ozonverluste eine exzellente Übereinstimmung mit Beobachtungen. So reproduziert ATLAS unter anderem das Auftreten des ersten arktischen Ozonlochs im Frühjahr 2011 vollständig. ATLAS kann daher die chemischen Prozesse, die zu diesem Ereignis geführt haben, vollständig charakterisieren.

Der Schwerpunkt zukünftiger Arbeiten wird auf der interaktiven Kopplung von SWIFT und ATLAS an Erdsystemmodelle liegen, um die Wechselwirkungen zwischen Klimasystem und Ozonschicht schließlich auf allen Zeitskalen in voll gekoppelten Modellsystemen untersuchen zu können. Dabei wird die Einbettung von SWIFT in solche Modellsysteme diese nicht erheblich verlangsamen und es erlauben, verschiedene Emissionsszenarien zu prozessieren und Ensembleläufe durchzuführen. Das Ziel dieser Entwicklungen ist es, die Ozon/Klimawechselwirkungen zu einem festen Bestandteil von Prognosen des Klimas unseres Planeten zu machen.

Literatur

Becker, G., Müller, R., McKenna, D. S., Rex, M., Carslow, K. S. (1998). Ozone loss rates in the Arctic stratosphere in the winter 1991/92: Model calculations compared with Match results, Geophysical Research Letters, 25/23, 4325-4328.

Becker, G., Müller, R., McKenna, D. S., Rex, M., Carslaw, K. S., Oelhaf, H. (2000). Ozone loss rates in the Arctic stratosphere in the winter 1994/95: Model simulations underestimate results of the Match analysis, Journal of Geophysical Research, 105, 15175-15184.

Carslaw, K. S., Kettleborough, J. A., Northway, M. J., Davies, S., Gao, R.-S., Fahey, D. W., Baumgardner, D. G., Chipperfield, M. P., and Kleinböhl, A. (2002). A vortex-scale simulation of the growth and sedimentation of large nitric acid hydrate particles, J. Geophys. Res., 107, 8300, doi:10.1029/2001JD000467.

Chen, H.-Y., C.-Y. Lien, W.-Y. Lin, Y.T. Lee, and J.J. Lin (2009). UV absorption cross sections of ClOOCl are consistent with ozone degradation models, Science, 324, 781-784, doi: 10.1126/science.1171305.

Chipperfield, M. P., Feng, W., Rex, M. (2005). Arctic ozone loss and climate sensitivity: Updated threedimensional model study, Geophysical research letters, 32, L11813. DOI: 10.1029/2005GL022674.

Dhomse, S., Weber, M., Wohltmann, I., Rex, M., Burrows, J. (2006). On the possible causes of recent increases in northern hemispheric total ozone from a statistical analysis of satellite data from 1979 to 2003, Atmospheric chemistry and physics, 6(5), 1165-1180. SREF: 1680-7324/acp/2006-6-1165.

Douglass, A., Fioletov, V., Godin-Beekmann, S., Müller, R., Stolarski, R. S., Webb, A., Arola, A., Burkholder, J. B., Burrows, J. P., Chipperfield, M. P., Cordero, R., David, C., den Outer, P. N., Diaz, S. B., Flynn, L. E., Hegglin, M., Herman, J. R., Huck, P., Janjai, s., Janosi, I. M., Kryscin, J. W., Liu, Y., Logan, J., Matthes, Katja, McKenzie, R. L., Muthama, N. J., Petropavlovskikh, I., Pitts, M., Ramachandran, S., Rex, M., Salawitch, R. J., Sinnhuber, B.-M., Staehelin, J., Strahan, S., Tourpali, K., Valverde-Canossa, J., Vigouroux, C., Bodeker, G. E., Canty, T., De Backer, H., Demoulin, P., Feister, U., Frith, S. M., Grooß, J.-U., Hase, F., Klyft, J., Koide, T., Kurylo, M. J., Loyola, D., McLinden, C. A., Megretskaia, I. A., Nair, P. J., Palm, M., Papanastasiou, D., Poole, L. R., Schneider, M., Schofield, R., Slaper, H., Steinbrecht, W., Tegtmeier, Susann, Terao, Y., Tilmes, S., Vyushin, D. I., Weber, M. und Yang, E.-S. (2011) Stratospheric Ozone and Surface Ultraviolet Radiation, Scientific Assessment of Ozone Depletion: 2010, Chapter 2. World Meteorological Organization, Geneva, Switzerland, pp. 1-80.

Eyring, V., Harris, N. R. P., Rex, M., Sheperd, T. G., Fahey, D. W., Amanatidis, G. T., Austin, J., Chipperfield, M. P., Dameris, M., Forster, P. M. De F., Gettleman, A., Graf, H. F., Nagashima, T., Newman, P. A., Pawson, S., Prather, M. J., Pyle, J. A., Salawitch, R. J., Santer, B., Waugh, D. W. (2005). A Strategy for Process-Oriented Validation of Coupled Chemistry-Climate Models, Bulletin of the american meteorological society, Vol. 86, No. 8, 11171133. DOI: 10.1175/BAMS-86-8-1117.

Erying, V., Shepherd, T., Waugh, D. (2010). Chemistry-Climate Model Validation, SPARC Report N°5,WCRP - 30 WMO/TD - No. 40, available at http://www.sparc-climate.org/publications/sparc-reports/sparc-report-no5.

Frieler, K. (2005). "Beitrag zum theoretischen Verständnis polarer stratosphärischer Ozonver-

luste - Modellrechnungen basierend auf Labormessungen und in situ Beobachtungen.", Dissertation, Freie Universität Berlin, Fachbereich Geowissenschaften.

Frieler, K., Rex, M., Salawitch, R. J., Canty, T., Streibel, M., Stimpfle, R., Pfeilsticker, K., Dorf, M., Weisenstein, D. K., Godin-Beekman, S. (2006). Towards a better quantitative understanding of polar stratospheric ozone loss, Geophysical Research Letters, 33, L10812, doi:10.1029/2005GL025466.

Gettelman, A., Hegglin, M.I., Son, S.-W., Kim, J., Fujiwara, M., Birner, T., Kremser, S., Rex, M., Anel, J.A., Akiyoshi, H., Austin, J., Bekki, S., Braesike, P., Brühl, C., Butchart, N., Chipperfield, M., Dameris, M., Dhomse, S., Garny, H., Hardiman, S.C., Jöckel, P., Kinnison, D.E., Lamarque, J.F., Mancini, E., Marchand, M., Michou, M., Morgenstern, O., Pawson, S., Pitari, G., Plummer, D., Pyle, J. A., Rozanov, E., Scinocca, J., Shepherd, T.G., Shibata, K., Smale, D., Teyssèdre, H., Tian, W.(2010).Multimodel assessment of the upper troposphere and lower stratosphere: Tropics and global trends, Journal of Geophysical Research, 115, D00M08., doi:10.1029/2009JD013638 .

Harris, N.R.P., Rex, M., Goutail, F., Knudsen, B.M., Manney, G.L., Müller, R., von der Gathen, P. (2002). Comparison of Empirically Derived Ozone Loss Rates in the Arctic Vortex, Journal of Geophysical Research, 107/D20, 8264, doi:10.1029/2001JD000482.

Harris, N. R. P., Kyrö, E., Staehelin, J., Brunner, D., Andersen, S. -B., Godin-Beekmann, S., Dhomse, S., Hadjinicolaou, P., Hansen, G., Isaksen, I., Jrrar, A., Karpetchko, A., Kivi, R., Knudsen, B., Krizan, P., Lastovicka, J., Maeder, J., Orsolini, Y., Pyle, J. A., Rex, M., Vanicek, K., Weber, M., Wohltmann, I., Zanis, P., Zerefos, C. (2008). Ozone trends at northern mid- and high latitudes - a European perspective, Annales Geophysicae, 26, 1207-1220.

Harris, N.R.P., Lehmann, R., Rex, M., von der Gathen, P.(2010).A closer look at Arctic ozone loss and polar stratospheric clouds, Atmospheric Chemistry and Physics, 10, 8499-8510., doi:10.5194/acp-10-8499-2010 .

Hoppel, K., Bevilacqua, R., Nedoluha, G., Deniel, C., Lefèvre, F., Lumpe, J., Fromm, M., Randall, C., Rosenfield, J., Rex, M. (2002). POAM III Observations of Arctic Ozone Loss for the 1999/2000 winter, Journal of Geophysical Research, 107/D20, 8262, doi:10.1029/2001JD000476.

Huck, P. E., Bodeker, G. E., Kremser, S., McDonald, A. J., Rex, M., and Struthers, H. (2012). Semi-empirical models for chlorine activation and ozone depletion in the Antarctic stratosphere: proof of concept, Atmos. Chem. Phys. Discuss., 12, 28451-28466, doi:10.5194/acpd-12-28451-2012.

Immler, F., Krüger, K., Fujiwara, M., Verver, G., Rex, M., Schrems, O. (2008). Correlation between equatorial Kelvin waves and the occurrence of extremely thin ice clouds at the tropical tropopause, Atmospheric Chemistry and Physics, 8, 4019-4026.

Kawa, S.R., Stolarski, R.S., Newman, P.A., Douglass, A.R., Rex, M., Hofmann, D.J., Santee, M.L., Frieler, K.(2009).Sensitivity of polar stratospheric ozone loss to uncertain-ties in chemical reaction kinetics, Atmospheric Chemistry and Physics, 9, 8651-8660.

Knudsen, B.M., Harris, N.R.P., Andersen, S.B., Christiansen, B., Larsen, N., Rex, M., Naujokat, B. (2004). Extrapolating future Arctic Ozone Losses, Atmospheric Chemistry and Physics, Vol. 4, pp 1849-1856, SREF: 1680-7324/acp/2004-4-1849

Kremser, S., Wohltmann, I., Rex, M., Langematz, U., Dameris, M., Kunze, M. (2009). Water vapour transport in the tropical tropopause region in coupled Chemistry-Climate Models and ERA-40 reanalysis data, Atmospheric Chemistry and Physics, 9(8), 2679-2694.

Krüger, K., Tegtmeier, S., Rex, M. (2008). Long-term climatology of transport processes in the Tropical Tropopause Layer (TTL) during NH winter, Atmospheric Chemistry and Physics, 8, 813-823.

Krüger, K., Tegtmeier, S., Rex, M.(2009).Variability of residence time in the Tropical Tropopause Layer during Northern Hemisphere winter, Atmospheric Chemistry and Physics, 9, 6717-6725.

Lehmann, R., Gathen, P. von der, Rex, M., Streibel, M. (2005). Statistical analysis of the precision of the Match method, Atmospheric chemistry and physics, 5, 2713-2727. SREF: 1680-7324/acp/2005-5-2713.

Lowe, D, MacKenzie, R. (2008) Review of Polar Stratospheric Cloud Microphysics and Chemistry. Journal of Atmospheric and Solar-Terrestrial Physics, 70 (1). pp. 13-40. ISSN 1364-6826.

Manney, G. L., M. L. Santee, M. Rex, N. J. Livesey, M. C. Pitts, P. Veefkind, E. R. Nash, I. Wohltmann, R. Lehmann, L. Froidevaux, L. R. Poole, M. R. Schoeberl, D. P. Haffner, J. Davies, V. Dorokhov, H. Gernandt, B. Johnson, R. Kivi, E. Kyrö, N. Larsen, P. F. Levelt, A. Makshtas, C. T. McElroy, H. Nakajima, M. C. Parrondo, D. W. Tarasick, P. von der Gathen, K. A. Walker, N. S. Zinoviev, Unprecedented Arctic ozone loss in 2011, (2011), Nature, 478, 7370, 469, DOI: 10.1038/nature10556.

McKenna, D. S., P. Konopka, J.-U. Grooß, G. Günther, R. Müller, R. Spang, D. Offerman and Y. Orsolini (2002a). A new Chemical Lagrangian Model of the Stratosphere (ClaMS), 1, Formulation of advection and mixing, J. Geophys. Res., 107(D16), doi:10.1029/2000JD000114.

McKenna, D. S., J.-U. Grooß, G. Günther, P. Konopka, R. Müller, G. Carver, and Y. Sasano (2002b). A new Chemical Lagrangian Model of the Stratosphere (CLaMS), 2 Formulation of chemistry scheme and initialization, J. Geophys. Res., 107(D15), doi:10.1029/2000JD000113.

Newman, P., Pyle, J.A., Austin, J., Braathen, G., Canzini, P., Carslaw, K., Forster, P., Godin, S., Knudsen, B., Kreher, K., Nakane, H., Pawson, S., Ramaswamy, V., Rex, M., Salawitch, R., Shindell, D., Tabazadeh, A., Toohey, D. (2003) Polar Stratospheric Ozone, Scientific Assessment of Ozone Depletion: 2002 chapter 3, Global Ozone Research and Monitoring Project, Report No. 47, 498 pp., Geneva, ISBN: 92-807-2261-1.

Newman, P. A., Rex, M. (2007). Polar Ozone, Scientific Assessment of Ozone Depletion: 2006, World Meteorological Organization Global Ozone Research and Monitoring Project-Report No. 50. Geneva, ISBN 978-92-807-2756-2.

Papanastasiou, D.K., V.C. Papadimitriou, D.W. Fahey, and J.B. Burkholder (2009). UV absorption spectrum of the ClO dimer (Cl2O2) between 200 and 420 nm, J. Phys. Chem. A, 113, 13711-13726, doi: 10.1021/jp9065345.

Pope, F. D., J. C. Hansen, K. D. Bayes, R. R. Friedl, and S. P. Sander (2007), Ultraviolet Absorption Spectrum of Chlorine Peroxide, ClOOCl, J. Phys. Chem. A, 111, 4322-4332, doi:10.1021/jp067660w.

Rex, M. (1993). Stratosphärische Ozonabbauraten aus den Ozonsondendaten der EASOE-Kampagne im Winter 1991/92, Diploma thesis, Fachbereich Physik, Georg-August-Universität zu Göttingen.

Rex, M. (1997). Der Ozonabbau in der arktischen Stratosphäre: Ergebnisse einer neuen Meßstrategie (Match), Dissertation, Fachbereich für Geowissenschaften, Freie Universität Berlin.

Rex, M., Harris, N. R. P., Gathen, P. von der, Lehmann, R., Braathen, G. O., Reimer, E., Beck, A., Chipperfield, M. P., Alfier, R., Allaart, M., O’Connor, F., Dier, H., Dorokhov, V., Fast, H., Gil, M., Kyrö, E., Litynska, Z., Mikkelsen, I. S., Molyneux, M. G., Nakane, H., Notholt, J., Rummukainen, M., Viatte, P., Wenger, J. (1997). Prolonged stratospheric ozone loss in the 1995/96 Arctic winter, Nature, 389, 835-838.

Rex, M., Gathen, P. von der, Harris, N. R. P., Lucic, D., Knudsen, B. M., Braathen, G. O., Reid, S. J., Backer, H. De, Claude, H., Fabian, R., Fast, H., Gil, M., Kyrö, E., Mikkelsen, I. S., Rummukainen, M., Smit, H. G., Stähelin, J., Varotsos, C., Zaitcev, I. (1998). In-situ measurements of stratospheric ozone depletion rates in the Arctic winter 1991/1992: A Lagrangian approach, Journal of Geophysical Research, 103/D5, 5843-5853.

Rex, M., Salawitch, R. J., Toon, G. C., Sen, B., Margitan, J. J., Osterman, G. B., Balvier, J-F., Gao, R. S., Donelly, S., Keim, E., Neumann, J., Fahey, D. W., Webster, C. R., Scott, D. C., Herman, R. L., May, R. D., Moyer, E. J., Gunson, M. R., Irion, F. W., Chang, A. Y., Rinsland, C. P., Bui, T. P. (1999a). Subsidence, mixing and denitrification of Arctic polar vortex air measured POLARIS, Journal of Geophysical Research, 104, 26611-26623.

Rex, M., Gathen, P. von der, Braathen, G. O., Harris, N. R. P., Reimer, E., Beck, A., Alfier, R., Krüger-Carstensen, R., Chipperfield, M., Backer, H. De, Balis, D., O‘Connor, F., Dier, H., Dorokhov, V., Fast, H., Gamma, A., Gil, M., Kyrö, E., Litynska, Z., Mikkelsen, S., Molyneux, M., Murphy, G., Reid, S. J., Rummukainen, M., Zerefos, C. (1999b). Chemical ozone loss in the Arctic winter 1994/95 as determined by the Match technique, Journal of Atmospheric Chemistry, 32/1, 35-59.

Rex, M., Salawitch, R.J. (1999c). Does Cl_2O_2 photolyse in the visible?, SOLVE planning meeting, Lancaster, California, USA.

Rex, M., Dethloff, K., Handorf, D., Herber, A., Lehmann, R., Neuber, R., Notholt, J., Rinke, A., Gathen, P. von der, Weisheimer, A., Gernandt, H. (2000). Arctic and Antarctic ozone layer observations - chemical and dynamical aspects of variability and long-term changes in the polar stratosphere, Polar Research 19(2), 193-204.

Rex, M., Salawitch, R.J., Harris, N.R.P., Gathen, P. von der, Braathen, G.O., Schulz, A., Deckelman, H., Chipperfield, M., Sinnhuber, B.M., Reimer, E., Alfier, R., Bevilacqua, R., Hoppel, K., Fromm, M., Lumpe, J., Küllmann, H., Kleinböhl, A., Bremer, H., von König, M., Künzi, K., Toohey, D., Vömel, H., Richard, E., Aikin, K., Jost, H., Greenblatt, J.B., Loewenstein, M., Podolske, J.R., Webster, C.R., Flesch, G.J., Scott, D.C., Herman, R.L., Elkins, J.W., Ray, E.A., Moore, F.L., Hurst, D.F., Romashkin, P., Toon, G.C., Sen, B., Margitan, J.J., Wennberg, P., Neuber, R., Allart, M., Bojkov, R.B., Claude, H., Davies, J., Davies, W., De Backer, H., Dier, H., Dorokhov, V., Fast, H., Kondo, Y., Kyrö, E., Litynska, Z., Mikkelsen, I.S., Molyneux, M.J., Moran, E., Murphy, G., Nagai, T., Nakane, H., Parrondo, C., Ravegnani, F., Skrivankova, P., Viatte, P., Yushkov, V. (2002). Chemical depletion of Arctic ozone in winter 1999/2000, Journal of Geophysical Research, 107/D20, 8276, doi:10.1029/2001JD000533.

Rex, M., Salawitch, R. J., Santee, M. L., Waters, J. W., Hoppel, K., Bevilacqua, R. (2003). On the unexplained stratospheric ozone losses during cold Arctic Januaries, Geophysical Research Letters, 30/1, 1008, doi 10.1029/2002GL016008.

Rex, M., Salawitch, R.J., von der Gathen, P., Harris, N.R.P., Chipperfield, M.P., Naujokat, B. (2004a). Arctic ozone loss and climate change, Geophysical Research Letters, Vol. 31, L04116, doi: 10.1029/2003GL018844

Rex, M., Salawitch, R.J., von der Gathen, P., Harris, N.R.P., Chipperfield, M.P., Naujokat, B., Frieler, K., Streibel, M., Wohltmann, I., Tegtmeier, S., the Match ozonesonde team (2004b). Arctic ozone loss and climate change, SPARC General Assembly, Victoria, Kanada.

Rex, M., Salawitch, R. J., Deckelmann, H., von der Gathen, P., Harris, N. R. P., Chipper-field, M. P., Naujokat, B., Reimer, E., Allaart, M., Andersen, S. B., Bevilacqua, R., Braathen, G. O., Claude, H., Davies, J., De Backer, H., Dier, H., Dorokov, V., Fast, H., Gerding, M., Hoppel, K., Johnson, B., Kyrö, E., Litynska, Z., Moore, D., Nagai, T., Par-rondo, M. C., Risley, D., Skrivankova, P., Stübi, R., Trepte, C., Viatte, P., Zerefos, C. (2006). Arctic winter 2005: Implications for stratospheric ozone loss and climate change, Geophysical Research Letters, 33, L23808.

Rex, M., Schofield, R., Lehmann, R., Frieler, K., Wohltmann, I., von Hobe, M., Stroh, F., Koch, G., Peter, T., Salawitch, R.J., Canty, T. (2007). Is a major fraction of polar ozone loss due to a currently unknown mechanism ?, SPARC workshop Bremen.

Rex, M., Frieler, K., Schofield, R., Salawitch R., Canty T. (2008). On Our Understanding of Ozone Loss Rates in the Polar Vortex: Models and Measurements, SPARC Meeting The Role of Halogen Chemistry in Polar Stratospheric Ozone Depletion, Cambridge, UK.

Rex, M., Wohltmann, I., Deckelmann, H., von der Gathen, P., Manney, G.L., Santee, M.L., Livesey, N.J., Davies, J., Dorokhov, V., Gernandt, H., Johnson, B., Kivi, R., Kyrö, E., Larsen, E., Makshtas, A., McElroy, C.T., Nakajima, H., Conception Parrando, M., Tarasick, D.W., Walker, K.A., Zinoviev, N.S. (2011a). Record Arctic ozone loss in spring 2011 compared with Antarctic ozone hole conditions, American Geophysical Union, Fall Meeting, San Francisco, USA.

Rex, M., Huck, P. E., Kremser, S., Bodeker, G., Santee, M.L., Bernath P. (2011b). SWIFT - An Extremely Fast Semi-empirical Module for Including Polar Ozone Loss in Climate Model Systems, International Union of Geodesy and Geophysics, General Assembly, Melbourne, Australia.

Salawitch, R.J., Margitan, J.J., Sen, B., Toon, G.C., Rex, M., Osterman, G.B., Elkins, J.W., Ray, E.A., Moore, F.L., Richard, E., Romashkin, P., Hurst, D., Brune, W. (2002). Chemical Loss of Ozone During Arctic Winter of 1999-2000: An Analysis Based on Balloon-borne Observations, Journal of Geophysical Research, 107/D20, 8269, doi:10.1029/2001JD000620.

Sander, S.P., R.R. Friedl, D.M. Golden, M.J. Kurylo, R.E. Huie, V.L. Orkin, G.K. Moortgat, A.R. Ravishankara, C.E. Kolb, M.J. Molina, and B.J. Finlayson-Pitts, (2003). Chemical Kinetics and Photochemical Data for Use in Atmospheric Studies: Evaluation No. 14, JPL Publication 02-25, Jet Propulsion Laboratory, Pasadena, California, USA, available at http://jpldataeval.jpl.nasa.gov.

Sander, S.P., R.R. Friedl, D.M. Golden, M.J. Kurylo, G.K. Moortgat, H. Keller-Rudek, P.H. Wine, A.R. Ravishankara, C.E. Kolb, M.J. Molina, B.J. Finlayson-Pitts, R.E. Huie, and V.L. Orkin, (2006). Chemical Kinetics and Photochemical Data for Use in Atmospheric Studies: Evaluation No. 15, JPL Publication 06-2, Jet Propulsion Laboratory, Pasadena, California, USA, available at http://jpldataeval.jpl.nasa.gov.

Sander, S.P., J. Abbatt, J.R. Barker, J.B. Burkholder, R.R. Friedl, D.M. Golden, R.E. Huie, C.E. Kolb, M.J. Kurylo, G.K. Moorgat, V.L. Orkin, and P.H. Wine, (2009). Chemical Kinetics and Photochemical Data for Use in Atmospheric Studies: Evaluation Number 16, JPL Publication 09-31, Jet Propulsion Laboratory, Pasadena, California, USA, available at http://jpldataeval.jpl.nasa.gov.

Sander, S. P., J. Abbatt, J. R. Barker, J. B. Burkholder, R. R. Friedl, D. M. Golden, R. E. Huie, C. E. Kolb, M. J. Kurylo, G. K. Moortgat, V. L. Orkin and P. H. Wine (2011). "Chemical Kinetics and Photochemical Data for Use in Atmospheric Studies, Evaluation No. 17," JPL Publication 10-6, Jet Propulsion Laboratory, Pasadena, California, USA, available at http://jpldataeval.jpl.nasa.gov.

Schiermeier, Q. (2007). Chemists poke holes in ozone theory, Nature 449, 382-383, doi:10.1038/449382a

Schofield, R., Frieler, K., Wohltmann, I., Rex, M., von Hobe, M., Stroh, F., Koch, G., Peter, T., Canty, T., Salawitch, R., Volk, C. M. (2008). Polar stratospheric chlorine kinetics from a self-match flight during SOLVE-II/EUPLEX, Geophysical Research Letters, 35, L01807.

Schofield, R., Fueglistaler, S., Wohltmann, I., Rex, M.(2011).Sensitivity of stratospheric Bry to uncertainties in very short lived substance emissions and atmospheric transport, Atmospheric Chemistry and Physics, 11, 4, 1379-1392, DOI: 10.5194/acp-11-1379-2011.

Schulz, A., Rex, M., Steger, J., Harris, N. R. P., Braathen, G. O., Reimer, E., Alfier, R., Beck, A., Alpers, M., Cisneros, J., Claude, H., Backer, H. De, Dier, H., Dorokhov, V., Fast, H., Godin, S., Hansen, G., Kanzawa, H., Kois, B., Kondo, Y., Kosmidis, E., Kyrö, E., Litynska, Z., Molyneux, M. J., Murphy, G., Nakane, H., Parrondo, C., Ravegnani, F., Varotsos, C., Vialle, C., Viatte, P., Yushkov, V., Zerefos, C., Gathen, P. von der (2000). Match observations in the Arctic winter 1996/97: High stratospheric ozone loss rates correlate with low temperatures deep inside the polar vortex, Geophysical Research Letters, 27/2, 205-208.

Schulz, A., (2001). Bestimmung des Ozonabbaus in der arktischen und subarktischen Stratosphäre, Dissertation, Fachbereich Geowissenschaften, Freie Universität Berlin.

Schulz, A., Rex, M., Harris, N. R. P., Braathen, G. O., Reimer, E., Alfier, R., Kilbane-Dawe, I., Eckermann, S., Allaart, M., Alpers, M., Bojkov, B., Cisneros, J., Claude, H., Cuevas, E., Davies, J., De Backer, H., Dier, H., Dorokhov, V., Fast, H., Godin, S., Johnson, B., Kois, B., Kondo, Y., Kosmidis, E., Kyrö, E., Litynska, Z., Mikkelsen, I. S., Molyneux, M. J., Murphy, G., Nagai, T., Nakane, H., O'Connor, F., Parrondo, C., Schmidlin, F. J., Skrivankova, P., Varotsos, C., Vialle, C., Viatte, P., Yushkov, V., Zerefos, C., Gathen, P. von der (2001). Arctic ozone loss in threshold conditions: Match observations in 1997/1998 and 1998/1999, Journal of Geophysical Research.

Sinnhuber, B.-M., Gathen, P. von der, Sinnhuber, M., Rex, M., König-Langlo, G., Oltmans, S. J. (2006). Large decadal scale changes of polar ozone suggest solar influence, Atmospheric chemistry and physics, 6, 1835–1841, SRef-ID: 1680-7324/acp/2006-6-1835.

Solomon, S., Rosenlof, K.H., Portmann R.W., Daniel, J.S., Davis, S.M., Sanford, T.J., Plattner, G.K. (2010). Contributions of Stratospheric Water Vapor to Decadal Changes in the Rate of Global Warming, Science 327, 1219, DOI: 10.1126/science.1182488.

Stimpfle, R. M., D. M. Wilmouth, R. J. Salawitch, and J. G. Anderson (2004), First measurements of ClOOCl in the stratosphere: The coupling of ClOOCl and ClO in the Arctic polar vortex, J. Geophys. Res., 109, D03301, doi:10.1029/2003JD003811.

Suminska-Ebersoldt, O., Lehmann, R., Wegner, T., Grooß, J.-U., Hösen, E., Weigel, R., Frey, W., Griessbach, S., Mitev, V., Emde, C., Volk, C. M., Borrmann, S., Rex, M., Stroh, F.; von Hobe, M. (2012). ClOOCl photolysis at high solar zenith angles: analysis of the RECONCILE self-match flight, Atmospheric Chemistry and Physics 12 3, 1353 - 1365, 10.5194/acp-12-1353-2012, http://dx.doi.org/10.5194/acp-12-1353-2012.

Tegtmeier, S., Krüger, K., Wohltmann, I., Schoellhammer, K., Rex, M. (2008a). Variations of the residual circulation in the northern hemispheric winter, Journal of Geophysical Research, 113, D16109.

Tegtmeier, S., Rex, M., Wohltmann, I., Krüger, K. (2008b). Relative importance of dynamical and chemical contributions to Arctic wintertime ozone, Geophysical Research Letters, 35, L17801.

Tilmes, S., Müller, R., Engel, A., Rex, M., Russel III, J.M. (2006). Chemical ozone loss in the Arctic and Antarctic stratosphere between 1992 and 2005, Geophysical Research Letters, 33, L20812.

Toon, G. C., Blavier, F-F., Sen, B., Salawitch, R. J., Osterman, G. B., Notholt, J., Rex, M., McElroy, G. T., Russell. III, J. M. (1999). Ground-based observations of Arctic Ozone loss during spring and summer 1997, Journal of Geophysical Research, 104/D21, 26497-26510.

Voigt C, Schreiner J, Kohlmann A, Zink P, Mauersberger K, Larsen N, Deshler T, Kröger C, Rosen J, Adriani A, Cairo F, Di Donfrancesco G, Viterbini M, Ovarlez J, Ovarlez H, David C, Dörnbrack A. (2000). Nitric acid trihydrate (NAT) in polar stratospheric clouds, Science, Vol. 290 no. 5497 pp. 1756-1758, DOI: 10.1126/science.290.5497.1756.

Wohltmann, I., Rex, M., Brunner, D., Maeder, J. (2005). Integrated equivalent latitude as a proxy for dynamical changes in ozone column, Geophysical research letters, 32, 9, L09811. DOI: 10.1029/2005GL022497.

Wohltmann, I., Lehmann, R., Rex, M., Brunner, D., Mäder, J. A. (2007). A process-oriented regression model for column ozone, Journal of Geophysical Research-Atmospheres, 112, D12304.

Wohltmann, I., Rex, M. (2008). Improvement of vertical and residual velocities in pres-sure or hybrid sigma-pressure coordinates in analysis data in the stratosphere, Atmos-pheric chemistry and Physics, 8(2), 265-272.

Wohltmann, I., Rex, M.(2009). The Lagrangian chemistry and transport model ATLAS: validation of advective transport and mixing, Geoscientific Model Development, 2, 153-173.

Wohltmann, I., Lehmann, R., Rex, M.(2010).The Lagrangian chemistry and transport model ATLAS: Simulation and validation of stratospheric chemistry and ozone loss in the winter 1999/2000, Geoscientific Model Development, 3, 585-601., http://www.geosci-model-dev.net/3/585/2010/.

Woyke, T., Müller, R., Stroh, F., McKenna, D. S., Engel, A., Margitan, J., Rex, M., Carslaw, K. S. (1999). A test of our understanding of the ozone chemistry in the Arctic polar vortex based on in-situ measurements of ClO, BrO and O3 in the 1994/95 winter, Journal of Geophysical Research, 104, D15, 18755-18768.

Ausgewählte Veröffentlichungen

1. Rex, M., Harris, N. R. P., Gathen, P. von der, Lehmann, R., Braathen, G. O., et al. (1997). Prolonged stratospheric ozone loss in the 1995/96 Arctic winter, Nature, 389, 835-838.
2. Rex, M., Salawitch, R. J., Toon, G. C., Sen, B., Margitan, J. J., et al. (1999). Subsidence, mixing and denitrification of Arctic polar vortex air measured POLARIS, Journal of Geophysical Research, 104, 26611-26623.
3. Rex, M., Dethloff, K., Handorf, D., Herber, A., Lehmann, R., et al. (2000). Arctic and Antarctic ozone layer observations - chemical and dynamical aspects of variability and long-term changes in the polar stratosphere, Polar Research 19(2), 193-204.
4. Rex, M., Salawitch, R.J., Harris, N.R.P., Gathen, P. von der, Braathen, G.O., et al. (2002). Chemical depletion of Arctic ozone in winter 1999/2000, Journal of Geophysical Research, 107/D20, 8276, doi:10.1029/2001JD000533.
5. Rex, M., Salawitch, R. J., Santee, M. L., Waters, J. W., Hoppel, K., et al. (2003). On the unexplained stratospheric ozone losses during cold Arctic Januaries, Geophysical Research Letters, 30/1, 1008, doi 10.1029/2002GL016008.
6. Rex, M., Salawitch, R.J., von der Gathen, P., Harris, N.R.P., Chipperfield, M.P., et al. (2004). Arctic ozone loss and climate change, Geophysical Research Letters, Vol. 31, L04116, doi: 10.1029/2003GL018844.
7. Frieler, K., Rex, M., Salawitch, R. J., Canty, T., Streibel, M., et al. (2006). Towards a better quantitative understanding of polar stratospheric ozone loss, Geophysical Research Letters, 33, L10812, doi:10.1029/2005GL025466.
8. Rex, M., Salawitch, R. J., Deckelmann, H., von der Gathen, P., Harris, N. R. P., et al. (2006). Arctic winter 2005: Implications for stratospheric ozone loss and climate change, Geophysical Research Letters, 33, L23808.
9. Schofield, R., Frieler, K., Wohltmann, I., Rex, M., von Hobe, M., et al. (2008). Polar stratospheric chlorine kinetics from a self-match flight during SOLVE-II/EUPLEX, Geophysical Research Letters, 35, L01807.
10. Tegtmeier, S., Rex, M., Wohltmann, I., Krüger, K. (2008). Relative importance of dynamical and chemical contributions to Arctic wintertime ozone, Geophysical Research Letters, 35, L17801.
11. Wohltmann, I., Rex, M. (2008). Improvement of vertical and residual velocities in pressure or hybrid sigma-pressure coordinates in analysis data in the stratosphere, Atmospheric chemistry and Physics, 8(2), 265-272.
12. Wohltmann, I., Rex, M.(2009). The Lagrangian chemistry and transport model ATLAS: validation of advective transport and mixing, Geoscientific Model Development, 2, 153-173.
13. Wohltmann, I., Lehmann, R., Rex, M.(2010).The Lagrangian chemistry and transport model ATLAS: Simulation and validation of stratospheric chemistry and ozone loss in the winter 1999/2000, Geoscientific Model Development, 3, 585-601., http://www.geosci-model-dev.net/3/585/2010/.
14. Manney, G. L., Santee M.L., Rex, M., Livesey N.J.,Pitts, M.C., et al. (2011), Unprecedented Arctic ozone loss in 2011, Nature, 478, 7370, 469, DOI: 10.1038/nature10556.

8. White, J. L., Beck, L. W. & Haw, J. F. Characterization of hydrogen bonding in zeolites by proton solid-state NMR. *J. Am. Chem. Soc.* **114,** 6182–6189 (1992).
9. Cleland, W. W. & Kreevoy, M. M. Low-barrier hydrogen bonds and enzymic catalysis. *Science* **264,** 1887–1890 (1994).
10. Hibbert, F. & Emsley, J. Hydrogen bonding and chemical reactivity. *Adv. Phys. Org. Chem.* **26,** 255–379 (1990).
11. Munson, E. J. & Haw, J. F. NMR observation of trimethyloxonium formation from dimethyl ether on zeolite HZSM-5. *J. Am. Chem. Soc.* **113,** 6303–6305 (1991).
12. Munson, E. J., Kheir, A. A. & Haw, J. F. An in situ solid-state NMR study of the formation and reactivity of trialkylonium ions in zeolites. *J. Phys. Chem.* **97,** 7321–7327 (1993).
13. Chang, C. D. Hydrocarbons from methanol. *Catal. Rev. Sci. Eng.* **25,** 1–118 (1983).
14. Blaszkowski, S. R. & van Santen, R. A. Theoretical study of C–C bond formation in the methanol-to-gasoline process. *J. Am. Chem. Soc.* **119,** 5020–5027 (1997).
15. Krossner, M. & Sauer, J. Interactions of water with Brønsted acidic sites of zeolite catalysts. Ab initio study of 1 : 1 and 2 : 1 surface complexes. *J. Phys. Chem.* **100,** 6199–6211 (1996).
16. Zygmunt, S. A., Curtiss, L. A., Iton, L. E. & Erhardt, M. K. Computational studies of water adsorption in the zeolite HZSM-5. *J. Phys. Chem.* **100,** 6663–6671 (1996).
17. Nusterer, E., Blochl, P. E. & Schwarz, K. Interactions of water and methanol with a zeolite at high coverages. *Chem. Phys. Lett.* **253,** 448–455 (1996).
18. Parr, R. G. & Yang, W. *Density-Functional Theory of Atoms and Molecules* (Oxford Univ. Press, New York, 1989).
19. Andzelm, J. in *Density Functional Methods in Chemistry* (eds Labanowski, J. & Andzelm, J.) 155 (Springer, New York, 1991).
20. Vosko, S. J., Wilk, L. & Nussair, M. Accurate spin-dependent electron liquid correlation energies for local spin density calculations: a critical analysis. *Can. J. Phys.* **58,** 1200–1211 (1980).
21. Godbout, N., Salahub, D. R., Andzelm, J. & Wimmer, E. Optimization of gaussian-type basis sets for local spin density functional calculations. 1. Boron through neon, optimization technique and validation. *Can. J. Chem.* **70,** 560–571 (1992).
22. Miertus, S. & Tomasi, J. Approximate evaluation of the electrostatic free energy and internal energy changes in solution processes. *Chem. Phys.* **65,** 239–248 (1982).
23. Frisch, M. J. *et al. Gaussian94* (Gaussian, Inc., Pittsburgh, PA, 1995).

Acknowledgements. This work was supported by the US Department of Energy. Computer resources were provided by the National Energy Research Supercomputer Center, Berkeley, CA, the Texas A&M University Supercomputing Facility, the National Science Foundation and the National Center for Supercomputing Applications, Champaign, IL, USA.

Correspondence and requests for materials should be addressed to J.F.H. (e-mail: haw@chemvx.tamu.edu) or J.B.N. (e-mail: jb_nicholas@pnl.gov).

Prolonged stratospheric ozone loss in the 1995–96 Arctic winter

Markus Rex[1], Neil R. P. Harris[2,3], Peter von der Gathen[1], Ralph Lehmann[1], Geir O. Braathen[4], Eberhard Reimer[5], Alexander Beck[5], Martyn P. Chipperfield[3], Reimond Alfier[5], Marc Allaart[6], Fiona O'Connor[7], Horst Dier[8], Valery Dorokhov[9], Hans Fast[10], Manuel Gil[11], Esko Kyrö[12], Zenobia Litynska[13], Ib Steen Mikkelsen[14], Mike G. Molyneux[15], Hideaki Nakane[16], Justus Notholt[1], Markku Rummukainen[12], Pierre Viatte[17] & John Wenger[18]

[1] Alfred Wegener Institute for Polar and Marine Research, PO Box 60 01 49, D-14401 Potsdam, Germany. [2] European Ozone Research Coordinating Unit, Union Road, Cambridge, CB2 1HE, UK. [3] Centre for Atmospheric Science, Department of Chemistry, University of Cambridge, Cambridge, CB2 1EW, UK. [4] NILU, PO Box 100, Instituttveien 18, N-2007 Kjeller, Norway. [5] Meteorological Institute, Free University Berlin, Carl-Heinrich-Becker-Weg 6-10, D-12165 Berlin, Germany. [6] Royal Netherlands Meteorological Institute, Section of Climate Scenarios and Ozone, PO Box 201, 3730 AE De Bilt, The Netherlands. [7] Physics Department, University of Wales, Aberystwyth, SY23 3BZ, UK. [8] Meteorological Observatory Lindenberg, D-15864 Lindenberg, Germany. [9] Central Aerological Observatory, Pervomajskaya street 3, Dolgoprudny, Moscow region, 141700, Russia. [10] Atmospheric Environment Service, 4905 Dufferin Street, North York ON, M3H 5T4, Canada. [11] Instituto Nacional de Técnica Aerospacial, Torrejón de Ardoz, 28850 Madrid, Spain. [12] Finnish Meteorological Institute, Ilmala, FIN-99600 Sodankylä, Finland. [13] Institute of Meteorology and Water Management, Centre of Aerology, Zegrzynska Str. 38, 95–119 Legionowo, Poland. [14] Danish Meteorological Institute, Lyngbyvej 100, DK-2100 Copenhagen Ø, Denmark. [15] The Meteorological Office, London Road, Bracknell, Berkshire, RG12 2SZ, UK. [16] National Institute for Environmental Studies, Onogawa, Tsukuba, Ibaraki 305, Japan. [17] Swiss Meteorological Institute, Station aerologique Payerne, Les Invuardes, CH-1530 Payerne, Switzerland. [18] University College Dublin, Department of Chemistry, Belfield, Dublin 4, Ireland.

It is well established that extensive depletion of ozone, initiated by heterogenous reactions on polar stratospheric clouds (PSCs) can occur in both the Arctic and Antarctic lower stratosphere[1–9]. Moreover, it has been shown that ozone loss rates in the Arctic region in recent years reached values comparable to those over the Antarctic[8,9]. But until now the accumulated ozone losses over the Arctic have been the smaller, mainly because the period of Arctic ozone loss has not—unlike over the Antarctic—persisted well into springtime[8–10]. Here we report the occurrence—during the unusually cold 1995–96 Arctic winter—of the highest recorded chemical ozone loss over the Arctic region. Two new kinds of behaviour were observed. First, ozone loss at some altitudes was observed long after the last exposure to PSCs. This continued loss appears to be due to a removal of the nitrogen species that slow down chemical ozone depletion. Second, in another altitude range ozone loss rates decreased while PSCs were still present, apparently because of an early transformation of the ozone-destroying chlorine species into less active chlorinenitrate. The balance between these two counteracting mechanisms is probably a fine one, determined by small differences in wintertime stratospheric temperatures. If the apparent cooling trend in the Arctic stratosphere[11] is real, more dramatic ozone losses may occur in the future.

The polar lower stratosphere in winter is characterized by a cyclonic wind circulation (the polar vortex) encompassing a relatively isolated low-temperature region where PSCs can form. The cold surfaces provided by PSCs allow a number of reactions to proceed. The main effect of these reactions is to convert the longer-lived chlorine reservoir species HCl and $ClONO_2$ into temporary reservoir species such as Cl_2 which are readily photolysed into the species involved in ozone destruction cycles (Cl, ClO, $Cl_2O_2 = ClO_x$). Fast chemical ozone loss can occur in the presence of sunlight while ClO_x is present[12,13]. When the temperatures rise so that the PSCs evaporate activation of chlorine is no longer possible. In the Arctic, deactivation occurs primarily through $ClONO_2$ formation by the reaction of ClO with NO_2, which is produced mainly by the photolysis of HNO_3 or by reaction with OH (refs 14, 15).

Here we report results of the Match 95–96 experiment conducted from mid-January to early April 1996. During this experiment coordinated ozonesonde launches were used to determine chemical ozone loss rates in the Arctic polar vortex.

Trajectory calculations were used to trigger the launches of ~600 ozonesondes in such a way that the ozone concentrations in a large number of air parcels were each measured twice, a few days apart ('matches'). The differences in ozone, when averaged, are interpreted as being caused by chemical processes, as dynamic processes are assumed to be allowed for in the trajectories used. Similar experiments in 1991–92[4,8] and 1994–95[9] found significant ozone loss rates during and immediately after (<14 days) periods of PSC existence. A full description of the Match approach can be found in Rex *et al.*[9] As in the previous experiments[8,9] the area-weighted sampling of different intervals of potential vorticity inside the vortex with match events was again quite homogeneous. This implies a relative uniform coverage of the vortex air so that the results can be interpreted as vortex averages.

The winter 1995–96 was one of the coldest in the 30-year record of analyses by the Free University of Berlin[16] and the coldest in the 18-year NCEP (National Centers for Environmental Predictions) record[17]. Temperatures in the Arctic polar vortex were continuously low enough to form Type I PSCs from early December 1995 to early March 1996. After 11 March, the minimum temperature in the data from the European Centre for Medium Range Weather Forecasts (ECMWF) stayed at least 4 K above the equilibrium temperature of nitric acid trihydrate (used here as indicator for Type I PSC formation; see Rex *et al.*[8] for details). PSCs were observed by lidars at Ny-Ålesund, Spitsbergen (Norway) and Andøya (Norway) in nearly all measurements between 1 January and 29 February, but no PSC observation was reported during March although measurements continued[18,19]. The Microwave Limb Sounder (MLS) on the Upper Atmosphere Research Satellite observed a persistent local minimum of gas-phase HNO_3 from the end of January to 3 March, which also indicates that PSCs occurred throughout this period[20]. The cold temperatures and the

Nature © Macmillan Publishers Ltd 1997

Nature © Macmillan Publishers Ltd 1997

local HNO_3 minimum were located over the Atlantic sector of the polar vortex, stretching from the vortex core to the vortex edge. Owing to the circulation of air masses in the vortex, a large fraction of the vortex air mass passed through this region every few days. During January the temperatures at an altitude of ~21 km stayed below the threshold for ice-particle (Type II PSC) formation for 3 weeks, the longest period ever observed in the Arctic[16]. The vortex, as defined by large values of potential vorticity and a steep gradient of this quantity at the vortex edge, still existed at the end of March.

Extensive and pervasive photochemical ozone loss occurred over a wide altitude range for several weeks in January–February 1996 (Fig. 1a). In early March the vortex warmed above the PSC threshold and the ozone loss rate dropped rapidly, reaching insignificant values at most altitudes after a few days. The maximum loss rates occurred in January, and these rates are similar to those found during 1991–92[4,8] and 1994–95[9]. Where comparable (during February on the 465 K potential temperature surface) our loss rates are in good quantitative agreement with those derived from observations of MLS[17]. Substantial ozone losses were also derived from observations of the Halogen Occultation Experiment (HALOE)[7] and from lidar data[6].

A closer look at Fig. 1a reveals three additional features. (1) Ozone loss persisted throughout March over a limited altitude range

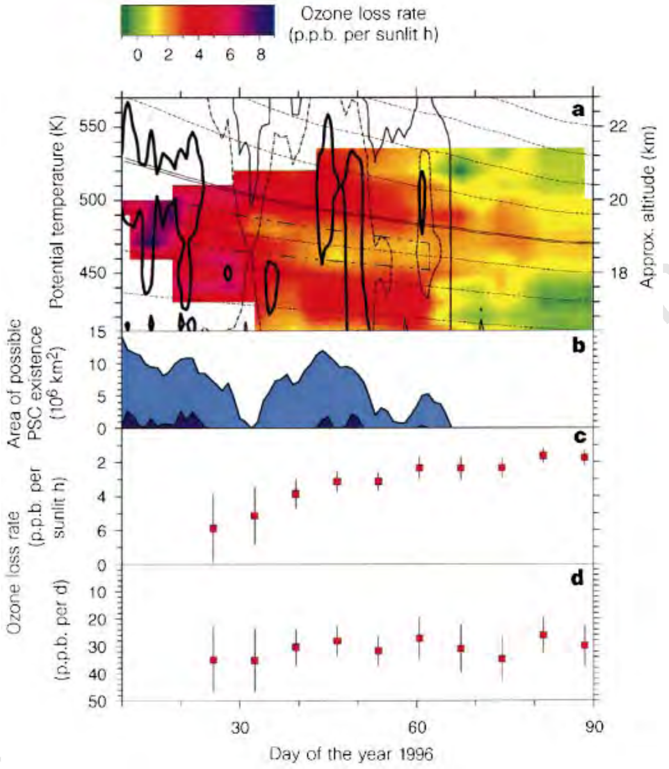

Figure 1 Ozone loss rate and PSC probability in the Arctic atmosphere during January–March 1996. **a**, Contour plot showing the ozone loss rate in p.p.b. per sunlit hour as a function of time and altitude. Potential temperature is used as a measure of altitude. The approximate geometric height of the various potential temperature levels is given on the right-hand scale. 667 matches inside the polar vortex contributed to the plot. The vortex edge was chosen at a scaled potential vorticity of 136 s^{-1} which corresponds to 36×10^{-6} K m^2 kg^{-1} s^{-1} in 475 K (ref. 8). The thin contour lines are the 0.3×10^6 km^2 (solid lines) and 4×10^6 km^2 (dash-dotted) isolines of the geographical area covered with temperatures low enough for Type I PSCs to form. The heavy solid contour line is the 0.3×10^6 km^2 isoline of the area covered with temperatures below the ice frost point. The dashed lines correspond to surfaces that follow the diabatic descent of the air masses during the winter. The vertical motion of the air masses inside the vortex was calculated from modelled diabatic cooling/heating rates[9]. See text for the meaning of the dash-dot-dotted box. **b**, **c**, Data as a section along the double line in **a**, reflecting the situation in a subsiding layer of air which started at 535 K potential temperature on 1 January and reached 470 K on 31 March. For this layer **b** shows the geographical area covered with temperatures low enough for the formation of Type I PSCs (light blue) and Type II PSCs (dark blue). **c**, Ozone loss rate in p.p.b. per sunlit hour. **d**, Ozone loss rate in p.p.b. per day. The error bars in **c** and **d** denote the 1σ uncertainty.

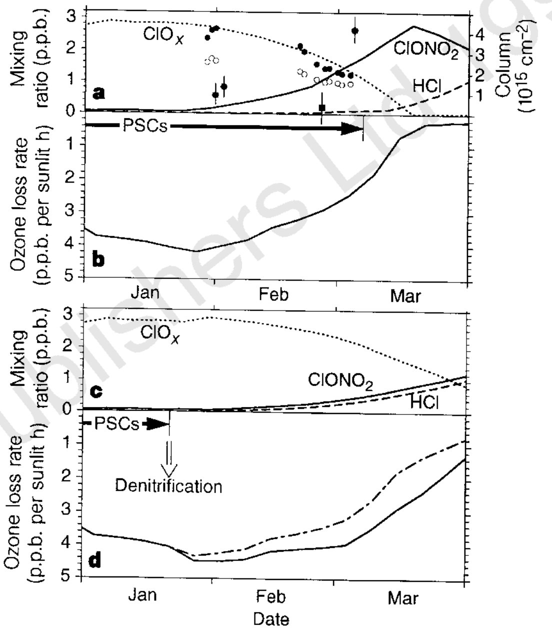

Figure 2 Results from a box model run on an idealized trajectory at 20 km height, oscillating between 60° and 80° N with a period of 6 days. The model was initialized at the beginning of December. **a**, **b**, Results of a model run where 8% PSC probability was assumed between 1 December and 7 March, which led to a total activation of chlorine until 1 January. **a**, Mixing ratios (by volume) of $ClONO_2$ (solid line), HCl (dashed line), ClO_x (dotted line). The model results are compared with ClO_x vortex averages (filled circles without error bars) calculated from MLS ClO measurements (open circles)[20]. For this, only ClO measurements at solar zenith angles <87° were used and only those days are shown when the vortex was sufficiently covered by such measurements. For the calculation of the ratio ClO/ClO_x ECMWF temperatures and reaction constants from De More *et al.*[29] were used. The comparison with the simulation shows that the model reproduces the decline of ClO_x inside the vortex surprisingly well. The model shows that the chlorine partitioning is shifted to $ClONO_2$ although PSCs still exist. This is qualitatively confirmed by $ClONO_2$ column measurements with a Fourier transform infrared (FTIR) instrument (using the method described in ref. 30) at Ny-Ålesund (78.9° N, 11.9° E)[30] even though these measurements represent only a single location. All FTIR measurements (filled circles with error bars) were performed deep inside the polar vortex, and back trajectory calculations show that the probed air masses around 475 K encountered temperatures below the Type I PSC threshold a few days before each measurement. Simultaneous FTIR measurements of the HCl column show that it is constantly very low in early February and early March. The square symbol shows an ASUR observation of the HCl mixing ratio inside the vortex (68.6° N, –6.0° E) at 18 km altitude[28]. **b**, Ozone destruction per sunlit hour as calculated by the model. The model reproduces the decline of the ozone destruction rate during February, which occurs despite the existence of PSCs, and reveals the underlying mechanism of the 'trapping' of chlorine in $ClONO_2$. **c**, **d**, Results (mixing ratios by volume) of a model run where 80% denitrification (for consistency with observations during the slightly warmer winter 1988–89[22]) was assumed in late January. No further PSC formation was assumed thereafter owing to a lack of HNO_3 in the denitrified air parcels. In fact, the air parcels in the small denitrified layer inside the vortex and therefore those probed by Match encountered different degrees of denitrification. For example, the dash-dotted line in **d** shows the average ozone loss rate if denitrification is assumed in 50% of the air parcels.

Nature © Macmillan Publishers Ltd 1997

(around the 470 K potential temperature level). This is shown more clearly in Fig. 1b to d. (2) The magnitude of the ozone loss rates generally declined during February by about a factor of two although PSCs were still present. (3) Just below the air in which prolonged ozone loss occurred, a narrow band can be identified (outlined by the dash-dot-dotted box in Fig. 1a) where the decline in the loss rate was more rapid than above and below.

The persistence of ozone loss four weeks after the last PSC occurrence mentioned above (feature (1)) differs completely from the behaviour observed in previous Arctic winters when the ozone loss stopped within ~14 days after the last exposure to PSCs[4,8,9]. Diabatic cooling calculations (double solid line in Fig. 1a) suggest that in January the air parcels probed in March at around 470 K had been at around 530–550 K. This is the upper part of the region where temperatures were below the threshold for formation of Type II PSCs. Indeed, such clouds were observed at Andøya in three of four measurements during the time period 10–25 January[19], predominantly in the altitude range 525–585 K, and at Sodankylä, Finland, in the altitude ranges 430–454 K and 487–547 K on the 22 January[21]. Vömel *et al.*[21] have shown that this intensive Type II PSC formation caused a redistribution of water by sedimentation of the ice particles. They concluded that water was permanently removed in a layer with a vertical extent of ~500 m around the 550 K potential temperature level, exactly the air mass in which we later observe the prolonged ozone loss. Although some indications exist that dehydration might take place without denitrification under certain special conditions[22], it is accepted that most incidences of dehydration are accompanied by a removal of HNO_3 which is dissolved in the settling Type II PSC particles. Some indications of the removal of gaseous HNO_3 are visible in HNO_3 data measured by MLS[20]. But because of the limited vertical resolution, any denitrification in a 500-m-thick layer does not appear clearly in the MLS data. The effect of vertical redistribution of water and HNO_3 is common in the Antarctic[12], and measured HNO_3 profiles indicate that it also took place in recent cold winters in the Arctic polar vortex[22–25]. In a region of severely reduced HNO_3 concentrations the transformation of ClO_x into $ClONO_2$, and hence the decline of the ozone loss, takes longer as the amount of NO_2 produced by photolysis of HNO_3 is reduced. This effect is illustrated in Fig. 2c and d. We are not aware of any reasonable explanation for the unusual persistence of the ozone loss in the air mass mentioned above other than the assumption that a considerable number of air parcels probed by Match during March around 470 K were denitrified. The observed dehydration in this layer strongly supports this explanation.

A reduction in the magnitude of ozone loss rates in air exposed to Type I PSC for a long time (feature (2) above) has been considered before[26], but it has not been observed. Chemical simulations (Fig. 2a and b) show that the first exposure of air to PSCs effectively converts the HCl and the $ClONO_2$ into ClO_x as they react together on PSC surfaces. In agreement with previous results of similar model studies (see, for example, Müller *et al.*[27]) any excess HCl reacts on the second or third exposure as, in the interim, $ClONO_2$ is reformed by the reaction of ClO with NO_2. The simulation suggests that in the extremely cold winter 1995–96 all HCl was consumed. Observations from the Airborne-Submillimeter-SIS-Radiometer (ASUR)[28] (Fig. 2a) and from HALOE[7] support this. Once all the initial HCl has reacted, the fast Cl activation by the reaction of HCl with $ClONO_2$ is impossible. The most efficient alternative seems to be the reaction of $ClONO_2$ with H_2O on cold sulphuric acid aerosol (or Type II PSC) surfaces. The reaction rate is strongly temperature dependent, and the sticking coefficients are not well determined (see references in DeMore *et al.*[29]). The observed decline of the ozone loss rates during February supports the idea that it was hard to recycle $ClONO_2$ back to ClO_x during this phase of the winter although Type I PSCs persisted. The decline in the ozone loss rate coincides with a decrease of vortex-averaged ClO_x (Fig. 2a) and a strong increase of the $ClONO_2$ column inside the polar vortex (Fig. 2a). All observations and the simulation suggest that at the end of February a significant part of the chlorine was trapped in $ClONO_2$ and could not be recycled by the persisting PSCs.

But in Fig. 1a there is a hint that the ozone loss temporarily accelerates after the second period of possible Type II PSC exposure in the second half of February (in the lower part of the dash-dot-dotted box), consistent with an acceleration in the reaction of $ClONO_2 + H_2O$ due to the colder temperatures.

The more rapid decrease of the ozone loss rate during late January and February mentioned above (feature (3)) occurred in the air mass which was at the base of the Type II PSC region in January (around 490 K), so it is reasonable to suggest that falling Type II PSC particles would have evaporated here. This would enhance the HNO_3 concentrations in this layer. As soon as the Sun shines on this region again, this would lead to enhanced NO_2 concentrations formed by the photolysis of the additional HNO_3. The faster deceleration of the ozone loss rate in this air mass could therefore be caused by an acceleration of the trapping of chlorine in $ClONO_2$ in this air mass. Because no direct observations of the involved evaporation processes are available this suggestion is in no way proven.

Our results show that prolonged ozone loss, presumably due to denitrification, occurred long after the last exposure to PSCs in the 1995–96 Arctic winter. Features consistent with renitrification of air below this region were found. The cumulative ozone loss in the air mass with prolonged ozone loss reached 2.4 ± 0.3 p.p.m. (~64%) between 20 January and 9 April 1996, the largest loss ever observed in the Arctic. The earlier termination of the ozone loss in the Arctic spring compared to the Antarctic spring (see, for example, refs 8, 10) has been the main difference between the Northern and Southern Hemispheres in the past, and the prolongation of the loss in a limited height region in the 1995–96 Arctic winter is one more step toward the formation of an Arctic ozone hole. However, the spatial non-uniformity of the presented ozone loss rates show also that the balance between the different mechanisms determining the ozone loss rates in the Arctic spring is a fine one, and depends rather sensitively on small differences in the temperature history of the air masses. Predictions of ozone losses in a particular future winter are, therefore, not possible at present. Larger ozone losses over the Arctic could be expected in future, if the apparent cooling trend in the Arctic stratospheric temperatures[11] is real. ☐

Received 2 June; accepted 2 September 1997.

1. Hofmann, D. J. & Deshler, T. Evidence from balloon measurements for chemical depletion of stratospheric ozone in the Arctic winter of 1989–90. *Nature* **349,** 300–305 (1991).
2. Manney, G. L. *et al.* Chemical depletion of ozone in the Arctic lower stratosphere during winter 1992–93. *Nature* **370,** 429–434 (1994).
3. Manney, G. L., Zurek, R. W., Froidevaux, L. & Waters, J. W. Evidence for Arctic ozone depletion in late February and early March 1994. *Geophys. Res. Lett.* **22,** 2941–2944 (1995).
4. von der Gathen, P. *et al.* Observational evidence for chemical ozone depletion over the Arctic in winter 1991–92. *Nature* **375,** 131–134 (1995).
5. Müller, R. *et al.* Chlorine activation and ozone depletion in the Arctic vortex: Observations by the Halogen Occultation Experiment on the Upper Atmosphere Research Satellite. *J. Geophys. Res.* **101,** 12531–12554 (1996).
6. Hansen, G. *et al.* Evidence of substantial ozone depletion in winter 1995–1996 over northern Norway. *Geophys. Res. Lett.* **24,** 799–802 (1997).
7. Müller, R. *et al.* Severe chemical ozone loss in the Arctic during the winter of 1995–96. *Nature* **389,** 709–712 (1997).
8. Rex, M. *et al.* In-situ measurements of stratospheric ozone depletion rates in the Arctic winter 1991/92: a Lagrangian approach. *J. Geophys. Res.* (submitted).
9. Rex, M. *et al.* Chemical ozone loss in the Arctic winter 1994/95 as determined by the Match technique. *J. Atmos. Chem.* (submitted).
10. Santee, M. L. *et al.* Interhemispheric differences in polar stratospheric HNO_3, H_2O, ClO, and O_3. *Science* **267,** 849–852 (1995).
11. Gelman, M. E. *et al.* Stratospheric temperature trends derived from SPARC Datasets. in *Proc. 1st SPARC General Assembly* (Cooperative Research Center for Southern Hemisphere Meteorology, Clayton, Australia, 1996).
12. *Scientific Assessment of Ozone Depletion: 1994* (ed. Ennis, C. A.) (Rep. 37, WMO, Geneva, 1995).
13. *European Research in the Stratophere—The Contribution of EASOE and SESAME to our Current Understanding of the Ozone Layer* (EC Rep. EUR16986, Office for Official Publ. of the European Communities, Luxembourg, 1997).
14. Jones, R. L., McKenna, D. S., Poole, L. R. & Solomon, S. On the influence of polar stratospheric cloud formation on chemical composition during the 1988/89 Arctic winter. *Geophys. Res. Lett.* **17,** 545–548 (1990).
15. Webster, C. R. *et al.* Chlorine chemistry on polar stratospheric cloud particles in the Arctic winter. *Science* **261,** 1130–1133 (1993).

Nature © Macmillan Publishers Ltd 1997

16. Naujokat, B. & Pawson, S. The cold stratospheric winters 1994/95 and 1995/96. *Geophys. Res. Lett.* **23,** 3703–3706 (1997).
17. Manney, G. L. *et al.* Polar vortex conditions during the 1995–96 Arctic winter: meteorology and MLS ozone. *Geophys. Res. Lett.* **23,** 3203–3206 (1996).
18. Stebel, K. *et al.* Polar stratospheric clouds above Spitsbergen. in *Proc. XVIII Quadrenn. Ozone Symp.* (in the press).
19. Hansen, G. & Hoppe, U.-P. Lidar observations of polar stratospheric clouds and stratospheric temperature in winter 1995/96 over northern Norway. *Geophys. Res. Lett.* **24,** 131–134 (1997).
20. Santee, M. L. *et al.* Polar vortex conditions during the 1995–1996 Arctic winter: MLS ClO and HNO_3. *Geophys. Res. Lett.* **23,** 3207–3210 (1996).
21. Vömel, H. *et al.* Dehydration and sedimentaiton of ice particles in the Arctic stratospheric vortex. *Geophys. Res. Lett.* **24,** 795–798 (1997).
22. Fahey, D. W. *et al.* Observations of denitrification and dehydration in the winter polar stratospheres. *Nature* **344,** 321–324 (1990).
23. Hübler, G. *et al.* Redistribution of reactive odd nitrogen in the lower Arctic stratosphere. *Geophys. Res. Lett.* **17,** 453–456 (1990).
24. Arnold, F., Gollinger, K. & Spreng, S. in *Polar Stratospheric Ozone* (eds Pyle, J. A. *et al.*) 175–178 (Rep. 56, Commissions of the European Communities, DG-XII, Brussels, 1996).
25. Oelhaf, H. *et al.* in *Polar Stratospheric Ozone* (eds Pyle, J. A. *et al.*) 187–193 (Rep. 56, Commissions of the European Communities, DG-XII, Brussels, 1996).
26. Salawitch, R. J. *et al.* Chemical loss of ozone in the Arctic polar vortex in the winter of 1991–1992. *Science* **261,** 1146–1149 (1993).
27. Müller, R. *et al.* Chlorine chemistry and the potential for ozone depletion in the arctic stratosphere in the winter 1991/92. *Geophys. Res. Lett.* **21,** 1427–1430 (1994).
28. Urban, J. *et al.* Observations of stratospheric ClO, HCl, O_3, N_2O, and HO_2 at high latitudes during the winters of 1995 and 1996 with the Airborne-Submillimeter-SIS-Radiometer. in *Proc. XVII Quadrenn. Ozone Symp.* (in the press).
29. De More, W. B. *et al.* Chemical kinetics and photochemical data for use in stratospheric modeling. (Evaluation No. 11, Publ. 94-26, Jet Propulsion Lab., Pasadena, 1994).
30. Notholt, J. *et al.* Seasonal variations of atmospheric trace gases in the high Arctic at 79° N. *J. Geophys. Res.* **102,** 12855–12861 (1997).

Acknowledgements. We thank the following for cooperation and for providing ozonesonde data: H. De Backer, Royal Meteorol. Inst.; D. Balis and I. Ziomas, Univ. Thessaloniki; H. Claude, Meteorol. Obs. Hohenpeißenberg; S. Godin and M. Guirlet, CNRS, Univ. Paris; B. Kois, Inst. of Meteorol. and Water Management; G. Murphy, Irish Meteorol. Service; S. J. Reid, Univ. Wales; F. H. Sigurdsson, Icelandic Meteorol. Office; C. Varotsos, Univ. Athens; V. Yushkov, Central Aerol. Obs.; National Space Development Agency of Japan and all others involved in Match. We also thank G. L. Manney and M. L. Santee for providing the MLS data, and the ECMWF and the German Weather Service for providing meteorological data. The chemistry model used was based on a model from G. Brasseur (NCAR, USA). This work was supported by the Environment and Climate Program of DG-XII of the EC, the UK DETR and the German BMBF.

Correspondence and requests for materials should be addressed to M.R. (mrex@awi-potsdam.de).

Timing of the Ethiopian flood basalt event and implications for plume birth and global change

C. Hofmann*†, V. Courtillot*, G. Féraud†, P. Rochette‡, G. Yirgu§, E. Ketefo§ & R. Pik‡

* *Institut de Physique du Globe, 4 Place Jussieu, 75252 Parix Cedex 05, France*
† *UMR Géosciences Azur (Université de Nice, CNRS), Parc Valrose, 06108 Nice Cedex 2, France*
‡ *CEREGE, Univesité d'Aix-Marseille 3, BP 81, 13545 Aix en Provence Cedex 4, France*
§ *Department of Geology and Geophysics, University of Addis Ababa, Addis Ababa, Ethiopia*

Continental flood basalts are often considered as fossil evidence of mantle plume heads impinging on the lithosphere[1,2] and have been related to continental breakup[3–5]. Many of these flood basalts erupted within a short time span—of the order of 1 Myr—and were apparently synchronous with crises in global climate and with mass extinctions[6]. Here we present geochronological ($^{40}Ar/^{39}Ar$) and magnetostratigraphic results for the Ethiopian traps, one of the last remaining flood basalts for which few such data were available. The bulk of the traps, which have been inferred to mark the appearance of the Ethiopian-Afar plume head at the Earth's surface, erupted approximately 30 Myr ago, over a period of 1 Myr or less. This was about the time of a change to a colder and drier global climate, a major continental ice-sheet advance in Antarctica, the largest Tertiary sea-level drop and significant extinctions.

The Ethiopian traps occur near the triple junction of the Red Sea, Gulf of Aden and East African rifts, and have long been associated with the Afar hotspot[2,7] (Fig. 1). Most of the province lies over the African plate where our study was concentrated. Prolific outpourings of (mainly) basalts have built a subaerial pile which originally covered an area in excess of 500,000 km^2 (ref. 8), with total thickness locally exceeding 2,000 m. The northwestern traps consist of a series of Late Eocene and Oligocene fissure basalts, covered by Miocene shield volcanoes. Conventional K/Ar ages measured in basalts, rhyolites and ignimbrites from the plateau to the north of Addis Ababa range from[9] 14 to 40 Myr (Fig. 2). Berhe *et al.*[10] have distinguished three prolonged stages of volcanism at 50–40, 40–30 and 30–21 Myr ago, whereas Ebinger *et al.*[11] have proposed that the main phase of volcanism occurred between 45 and 35 Myr ago in the southern part of the Ethiopian rift.

We have investigated three sections of the province. The main section, called the Lima–Limo (LL) section, consists of 2,000 m of lava (Fig. 3) and is located 450 km to the north of Addis Ababa (Fig. 1). A lower 900-m-thick sequence of basaltic lavas ends with 150 m of differentiated products, forming a significant regional terrace level. A second 1,000-m-thick section follows, with an acidic tuff forming another erosional surface at the top of the plateau. This morphology indicates two main volcanic episodes separated by a probable period of quiescence. More recent shield-building volcanism with much smaller volumes ends the LL section. The second section comprises 500 m of the top of the basaltic pile and a capping of ignimbrites and rhyolites at Wegel Tena (WT), 200 km to the north of Addis Ababa (Fig. 1). Another 100 km further north is the third section along the Woreta-Waldia or 'Chinese Road'. The petrology and geochemistry of the sampled formations are described in ref. 12. Samples (50) of whole rocks and plagioclase bulk samples from the basalts, and bulk samples and single grains of feldspars from ignimbrites, rhyolites and tuffs were analysed by the $^{40}Ar/^{39}Ar$ step-heating or total fusion method. A magnetostratigraphy was performed on two of the sections (LL and WT). A more complete description is given elsewhere[13].

Because the basalts were very fine-grained, it was often not possible to obtain mineral separates, and whole rocks had to be analysed for dating purposes; whenever possible, these were constrained by mineral analyses. The procedure is described and the

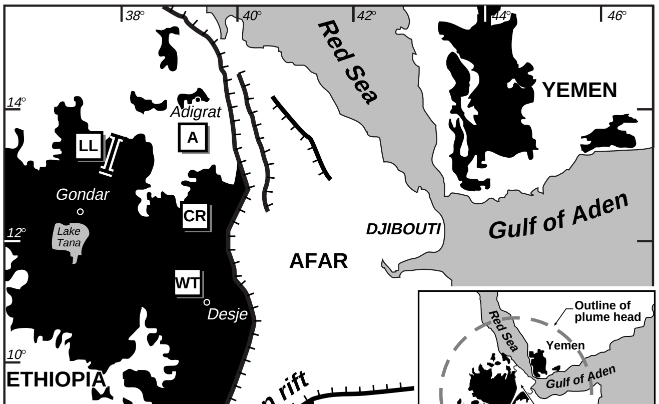

Figure 1 Location map of the northern Ethiopia and Yemen (Oligocene) volcanic province and East African triple junction (after ref. 9, 38). The sections discussed in the text are Wegel Tena (WT), Lima-Limo (LL), Adigrat (A) and 'Chinese Road' (CR).

Nature © Macmillan Publishers Ltd 1997

Nature © Macmillan Publishers Ltd 1997

JOURNAL OF GEOPHYSICAL RESEARCH, VOL. 104, NO. D21, PAGES 26,611-26,623, NOVEMBER 20, 1999

Subsidence, mixing, and denitrification of Arctic polar vortex air measured During POLARIS

M. Rex[1], R. J. Salawitch[1], G. C. Toon[1], B. Sen[1], J. J. Margitan[1], G. B. Osterman[1],
J.-F. Blavier[1], R. S. Gao[1], S. Donnelly[2], E. Keim[2], J. Neuman[2], D. W. Fahey[2],
C. R. Webster[1], D. C. Scott[1], R. L. Herman[1], R. D. May[1], E. J. Moyer[1],
M. R. Gunson[1], F. W. Irion[1], A. Y. Chang[1], C. P. Rinsland[3], and T. P. Bui[4]

Abstract. We determine the degree of denitrification that occurred during the 1996-1997 Arctic winter using a technique that is based on balloon and aircraft borne measurements of NO_y, N_2O, and CH_4. The NO_y/N_2O relation can undergo significant change due to isentropic mixing of subsided vortex air masses with extravortex air due to the high nonlinearity of the relation. These transport related reductions in NO_y can be difficult to distinguish from the effects of denitrification caused by sedimentation of condensed HNO_3. In this study, high-altitude balloon measurements are used to define the properties of air masses that later descend in the polar vortex to altitudes sampled by the ER-2 aircraft (i.e., ~20 km) and mix isentropically with extravortex air. Observed correlations of CH_4 and N_2O are used to quantify the degree of subsidence and mixing for individual air masses. On the basis of these results the expected mixing ratio of NO_y resulting from subsidence and mixing, defined here as NO_y**, is calculated and compared with the measured mixing ratio of NO_y. Values of NO_y and NO_y** agree well during most parts of the flights. A slight deficit of NO_y versus NO_y** is found only for a limited region during the ER-2 flight on April 26, 1997. This deficit is interpreted as indication for weak denitrification (~2-3 ppbv) in that air mass. The small degree of denitrification is consistent with the general synoptic-scale temperature history of the sampled air masses, which did not encounter temperatures below the frostpoint and had relatively brief encounters with temperatures below the nitric acid trihydrate equilibrium temperature. Much larger degrees of denitrification would have been inferred if mixing effects had been ignored, which is the traditional approach to diagnose denitrification. Our analysis emphasizes the importance of using other correlations of conserved species to be able to accurately interpret changes in the NO_y/N_2O relation with respect to denitrification.

1. Introduction

Rapid loss of ozone in the Arctic vortex during winter and spring is caused by catalytic cycles driven by active chlorine species (ClO_x = Cl, ClO, Cl_2O_2) [e.g., *Salawitch et al.*, 1990; *Waters et al.*, 1993]. Elevated levels of ClO_x result from heterogeneous reactions of HCl and $ClONO_2$ on polar stratospheric cloud (PSC) particles, which form at low temperatures during winter in the Arctic region [e.g., *Brune et al.*, 1990; *Webster et al.*, 1993; *Notholt et al.*, 1995]. Following the evaporation of PSCs, the lifetime of elevated ClO_x, and hence the time period of rapid ozone loss, is mainly controlled by the amount of NO_2 in the vortex [e.g., *Brune et al.*, 1991; *Salawitch et al.*, 1993]. Levels of NO_2 are quite small during the Arctic winter due to heterogeneous conversion of NO_x (NO, NO_2) to HNO_3 [e.g., *Kawa et al.*, 1992]. In spring, the production rate of NO_2 from the photolysis of HNO_3 rises due to the increase in the intensity of solar UV irradiance in the lower stratosphere. The released NO_2 reacts rapidly with ClO to form the passive reservoir species $ClONO_2$ [e.g., *Toon et al.*, 1992; *Roche et al.*, 1994]. This mechanism effectively slows down the Arctic ozone loss rate in spring and limits the overall loss of ozone in the Arctic vortex [e.g., *Brune et al.*, 1991; *Salawitch et al.*, 1993].

Denitrification, the permanent removal of NO_y (total reactive nitrogen) by the sedimentation of HNO_3-bearing PSC particles, leads to reduced production of NO_2 during spring [*Toon et al.*, 1986]. Widespread severe denitrification is common in the Antarctic [e.g., *Toon et al.*, 1989; *Fahey et al.*, 1990; *Santee et al.*, 1995] because of the extremely low wintertime temperatures. In the warmer Arctic, patches of denitrified air have also been observed after exceptionally cold winters [e.g., *Fahey et al.*, 1990; *Huebler et al.*, 1990; *Oelhaf et al.*, 1996; *Arnold et al.*, 1998; *Hintsa et al.*, 1998]. For the Arctic winter of 1995-1996, the coldest on record, the period of ozone destruction was so prolonged by denitrification that the overall ozone loss reached record values in the layer of air that experienced the longest period of cold conditions (favorable for denitrification) [*Rex et al.*, 1997]. Recent model calculations have shown that higher degrees of Arctic denitrification in the future, related perhaps to stratospheric cooling due to the build-up of greenhouse gases, would lead to larger seasonal ozone depletion despite the projected decline in inorganic chlorine [*Waibel et al.*, 1999].

The degree of denitrification in a given air mass has been typically estimated by comparison of measured mixing ratios of NO_y with the expected abundance of NO_y (defined as NO_y*) calculated

---

[1] Jet Propulsion Laboratory, California Institute of Technology, Pasadena, California.

[2] Aeronomy Laboratory, NOAA, Boulder, Colorado.

[3] NASA Langley Research Center, Hampton, Virginia.

[4] NASA Ames Research Center, Moffett Field, California.

Copyright 1999 by the American Geophysical Union.

Paper number 1999JD900463.
0148-0227/99/1999JD900463$09.00

from simultaneous observations of N_2O and well-established correlations between the mixing ratios of NO_y and N_2O [e.g., *Toon et al.*, 1989; *Fahey et al.*, 1990; *Rinsland et al.*, 1999]. This method is based on the assumption that the mixing ratios of two long-lived tracers (i.e., chemical lifetime long compared to mixing lifetime) develop a compact relationship independent of altitude and latitude [*Plumb and Ko*, 1992]. Severe denitrification is common throughout the Antarctic vortex and can be inferred in a straightforward manner by examination of the NO_y versus N_2O relation [e.g., *Fahey et al.*, 1990]. This method can also be used in the Arctic provided that mixing does not change the tracer relations prior to denitrification. For instance, the observation of a patchy structure of severe NO_y deficits and the nearby presence of air masses with the established NO_y/N_2O correlation indicates that mixing did not change the NO_y/N_2O relation prior to the onset of denitrification for the winter of 1988-1989 [*Fahey et al.*, 1990].

In contrast to the picture of well-preserved tracer/tracer relationships that can be changed only by chemistry or denitrification, *Waugh et al.* [1997], *Michelsen et al.* [1998] and *Kondo et al.* [1999] have recently shown that mixing of subsided innervortex with extravortex air masses can lead to substantial changes in the NO_y/N_2O relationship without denitrification. *Michelsen et al.* [1998] and *Kondo et al.* [1999] have also suggested that dynamically induced changes in the NO_y/N_2O correlation can be mistaken for denitrification. The NO_y versus N_2O relation is highly nonlinear, making it particularly sensitive to changes induced by descent and mixing [*Waugh et al.*, 1997; *Michelsen et al.*, 1998; *Kondo et al.*, 1999] (discussed in more detail in section 3.1.). *Waugh et al.* [1997] has noted more generally that the unique tracer/tracer relationships in the *Plumb and Ko* [1992] framework are not preserved under the special conditions of the polar vortices where redistribution of tracers by vertical transport is comparably fast to isentropic (quasi-horizontal) mixing. *Waugh et al.* [1997] showed examples of a change in the relationship of several pairs of long-lived tracers that was connected with mixing processes in the vicinity of the polar vortex. In the Arctic vortex, severe denitrification is rare [e.g., *Santee et al.*, 1995; *Rinsland et al.*, 1999], and changes in the NO_y/N_2O relationship caused by descent and isentropic mixing can easily mask changes caused by moderate denitrification.

The focus of this paper is to account for changes in the NO_y/N_2O relationship due to descent and isentropic mixing so that the degree of denitrification can be accurately quantified. The tracer/tracer relationship of a pair of long-lived tracers that does not include NO_y is first examined to quantify the dynamically induced changes that affect the measured airmasses. The selected pair of tracers should have a long chemical lifetime in the stratosphere. Dynamically induced changes can only be quantified if the tracer/tracer relationship prior to isentropic mixing are nonlinear. *Michelsen et al.* [1998] and *Kondo et al.* [1999] have shown that the CH_4/N_2O relationship can be used to assess the influence of descent and mixing because the extravortex correlation of these gases exhibits significant curvature [*Herman et al.*, 1998; *Michelsen et al.*, 1998] and because both gases are long-lived (the lifetime of CH_4 is longer than 1 year below 40 km and ~250 days at 50 km, the lifetime of N_2O is longer than 1 year below 35 km, ~200 days at 40 km and ~2 months at 50-55 km; the lifetimes have been estimated for 60°N during mid-October, using the model described by *Osterman et al.* [1997]. During the Photochemistry of Ozone Loss in the Arctic Region in Summer (POLARIS) campaign measurements of CH_4 and N_2O gases have been obtained by instruments onboard the ER-2 as well as by the balloon-borne MkIV and ALIAS II instruments at high latitude.

As will be shown in sections 3.2. and 3.7., the in situ observations obtained during POLARIS clearly show distinct "mixing lines" in the CH_4/N_2O relationship on individual isentropic surfaces. A mixing line refers to the tracer/tracer correlation pattern that results from various mixtures of two air masses, at the same potential temperature level, with distinctly different composition resulting from their dynamical histories (e.g. a midlatitude air parcel with high values of N_2O and CH_4 and a vortex air parcel with low values of N_2O and CH_4). Our approach for estimating denitrification differs somewhat from the method used by *Michelsen et al.* [1998] in which mixing lines in tracer/tracer plots were assembled over a wide range of potential temperatures from points along a vertical profile. The end points of these lines cannot be interpreted as end-members of isentropic mixing processes because they have not been at similar potential temperatures at any time during the winter. Recently, R. A. Plumb et al. (The effects of mixing on tracer relationships in the polar vortices, submitted to *Journal of Geophysical Research*, 1999) (hereinafter referred to as Plumb et al., submitted manuscript, 1999) have shown that relatively straight lines can evolve in profile measurements of tracer/tracer relationships that cover a wide range of potential temperatures if there is continuous mixing into the polar vortex concurrent with descent inside the vortex. Quantification of the influence of mixing under these circumstances remains difficult. In this paper, however, we show how changes in the NO_y/N_2O relationship due to mixing can be accurately quantified, given that isentropic mixing lines (rather than lines covering a wide range of potential temperatures) can be identified from the CH_4/N_2O relation. Our quantitative results are contingent on the assumption that the change in the tracer/tracer relations due to mixing took place following the bulk of the descent inside the polar vortex. The validity of this assumption is discussed in sections 3.4 and 4.

2. Data Sets

In this work, we utilize observations obtained by instruments aboard the NASA ER-2 aircraft and several balloon borne instruments during the POLARIS mission. Instruments aboard the ER-2 provided in situ measurements of many important stratospheric gases for a wide range of latitudes and altitudes near 20 km. During POLARIS, balloon-borne observations complemented the ER-2 measurements by providing vertical profiles of stratospheric gas concentrations using both in situ and remote sensing techniques.

Measurements aboard the ER-2 of N_2O and CH_4 were made by the Aircraft Laser Infrared Absorption Spectrometer (ALIAS). ALIAS is a scanning tunable diode laser spectrometer that measures CH_4, N_2O, HCl, and CO using high-resolution laser absorption in the 3-8 μm wavelength region [*Webster et al.*, 1994]. ALIAS II provided in situ measurements of CH_4 and N_2O from the Observations from the Middle Stratosphere (OMS) in situ balloon gondola. ALIAS and ALIAS II measure N_2O and CH_4 with an estimated 5% accuracy and precisions of 1% and 5%, respectively [*Herman et al.*, 1998]. ER-2 measurements of NO_y were made by the National Oceanic and Atmospheric Administration (NOAA) Aeronomy Laboratory reactive nitrogen instrument. The instrument measures total nitrogen by catalytically reducing NO_y to NO then detecting NO through chemiluminescent reaction with O_3. NO_y is measured with a total 1σ uncertainty of <15% [*Fahey et al.*, 1989]. Here we examine ER-2 observations obtained on the two poleward flights from Fairbanks, Alaska (65°N, 148°W), that encountered polar vortex air (April 26 and June 30, 1997) and the OMS observations obtained on June 30, 1997, from a balloon flight over Fairbanks.

The MkIV Fourier Transform Infra-Red (FTIR) spectrometer [*Toon*, 1991] obtains remote measurements of the composition of the atmosphere using the solar occultation technique. The bright-

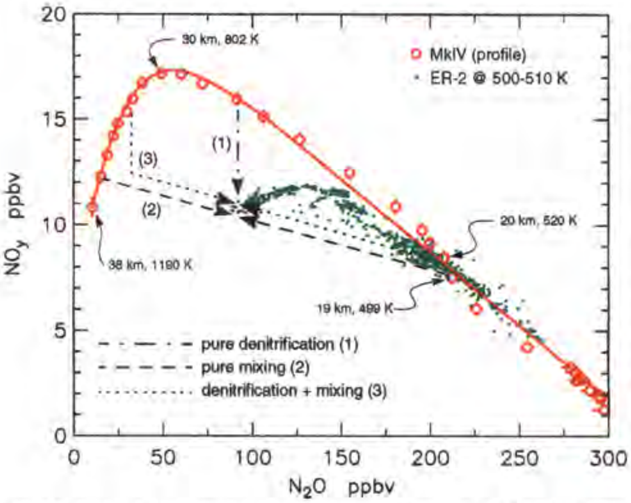

Plate 1. NO_y/N_2O correlations measured during the MkIV flight on May 8, 1997 and during the ER-2 flight on April 26, 1997. The MkIV data represent a vertical profile between 8 and 38 km altitude. The potential temperatures of some data points are indicated in the plot. The spacing between points is 1 km. The error bars denote the 1σ precision of the MkIV measurements. The red line is a composed polynomial fit to the MkIV data (4th-order fit for N_2O volume mixing ratios (vmrs) < 125 ppbv, linear fit for N_2O vmrs > 125 ppbv). All ER-2 data points have been measured between potential temperatures of 500 and 510 K. The ER-2 NO_y measurements were obtained by the NOAA chemiluminescent instrument with a 1σ total uncertainty of better than 10%; the ER-2 N_2O measurements were made by the ALIAS diode laser instrument with a 1σ total uncertainty of 5% (1% precision). The dashed, dotted, and dash-dotted lines illustrate scenarios with different degrees of denitrification and descent that could explain the low mixing ratios of NO_y observed by the ER-2 at mixing ratios of N_2O below 100 ppbv.

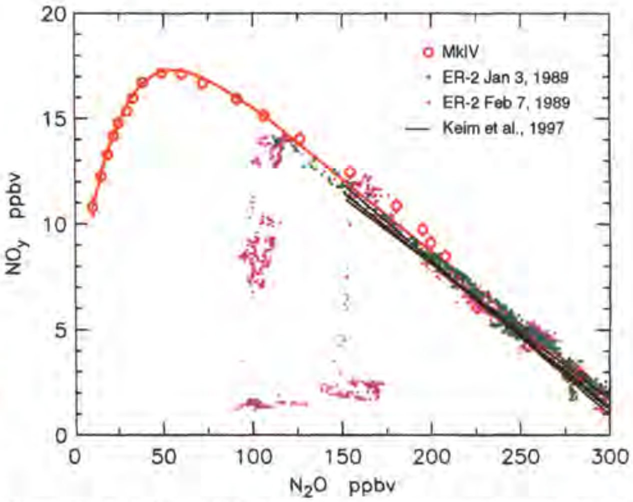

Plate 2. As in Plate 1, but for ER-2 data measured during an early winter and a mid-winter flight during the Airborne Arctic Stratospheric Experiment (AASE) in 1989. The ER-2 data has not been filtered by Θ. The ER-2 observations of N_2O were obtained by the ATLAS instrument with a 1σ total uncertainty of 3%. They were obtained for temperatures above T_{NAT} (see text for an explanation of T_{NAT}). However, the average temperature near 20 km during January 1989 was lower than observed during the 26 years prior to 1989 and the minimum temperature in the vortex was persistently below T_{NAT} and reached the frostpoint during late January 1989. Fits to ER-2 observations in northern midlatitudes in various years and seasons [*Keim et al.*, 1997] are also shown (black lines). The ER-2 data was normalized to 1997, assuming an increasing trend in the N_2O and NO_y mixing ratios of 0.2% per year.

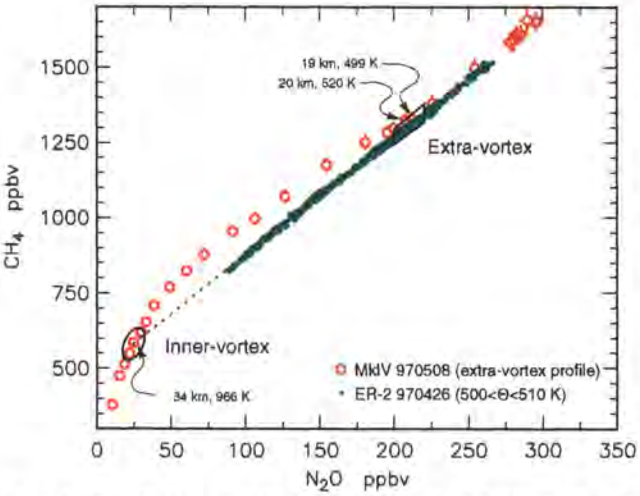

Plate 3. CH_4/N_2O correlation measured by the MkIV on May 8, 1997, and the ER-2 ALIAS instrument on the same flight as in Plate 1. The 1σ total uncertainty of both the ALIAS CH_4 and N_2O measurements is 5% (1% precision). The error bars for the MkIV measurement denote the 1σ precision. The mixing line for the ER-2 measurements is indicated by the dotted line. The regions where the mixing line intersects the extravortex reference correlation denote the air masses that have mixed to produce the properties observed by the ER-2 along the mixing line. The innervortex and extravortex mixing end-members are indicated. The altitudes and potential temperatures of the MkIV measurements in these regions are shown.

ness and stability of the Sun allow high signal-to-noise ratio spectra with broad coverage (650-5650 cm^{-1}) to be obtained at high-spectral resolution (0.01 cm^{-1}), allowing the abundances of a large number of gases to be measured simultaneously. The retrieval algorithm, spectroscopic parameters, and measurement uncertainties are discussed by *Sen et al.* [1996, 1998]. Gases measured by MkIV relevant to this work include O_3, N_2O and CH_4. The MkIV instrument also provides a complete determination of NO_y by measuring NO, NO_2, HNO_3, HNO_4, N_2O_5 and $ClONO_2$ individually. The measurement of CH_4 and N_2O have an accuracy and precision of 5%. The precision of NO_y for 20 km is ~5% with an accuracy of 15%, values which are confirmed by the comparisons between MkIV balloon and ER-2 measurements [*Toon et al.*, this issue]. Here we examine profiles obtained by the MkIV instrument on the May 8, 1997, balloon flight near Fairbanks.

3. Data Analysis and Results

3.1. NO_y/N_2O Relationship

Plate 1 shows the NO_y/N_2O relationship measured at high latitude during POLARIS by the MkIV infrared spectrometer between 8 and 38 km at a vertical resolution of ~2 km on May 8, 1997 and by the NO_y and ALIAS instruments on board the ER-2 on an isentropic level (500-510 K) near 20 km on April 26, 1997. Potential vorticity analyses and the relation between N_2O and potential temperature (e.g. N_2O= 200 ppbv at 500 K: typical values of N_2O inside the vortex at 500 K are much lower) indicate that the MkIV profile was obtained outside of the polar vortex.

In Plate 2 we compare the MkIV measurements to other (non-POLARIS) ER-2 NO_y/N_2O measurements [*Loewenstein et al.*, 1993] to demonstrate that the differences shown in Plate 1 are

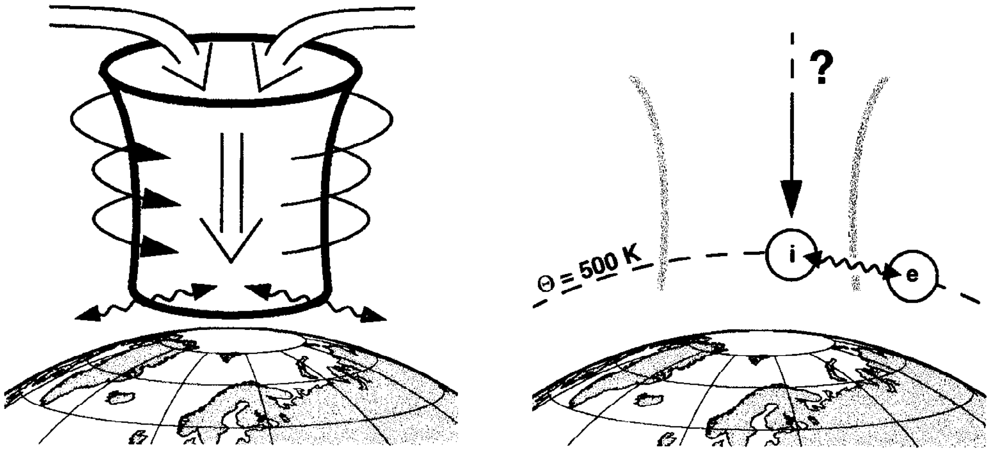

Figure 1. Illustration of the large scale descent in the polar vortex, which brings air masses from high altitudes to low potential temperature levels where they can mix with extravortex air mainly during the late vortex and vortex break up period. The descended innervortex mixing member is marked by an "i" and the extravortex mixing member is marked by an "e". To predict the properties of the mixed air masses, the original level of the air mass "i" has to be estimated.

not platform or instrument related. The MkIV measurements of NO_y and N_2O are similar to the well established reference relationship between these tracers at mid-latitudes [e.g., *Chang et al.*, 1996; *Sen et al.*, 1998; *Keim et al.*, 1997 (black lines in Plate 2)] and agree well with earlier measurements obtained by ER-2 instruments at similar latitudes during the Arctic winter (e.g. the flight on January 3, 1989, green points in Plate 2). For mixing ratios of N_2O below ~100 ppbv, the relation between NO_y/N_2O is highly nonlinear and exhibits a peak near 30 km due to rapid loss of NO_y at high altitudes due to the reaction N+NO [e.g., *Russell et al.*, 1988; *Nevison and Holland*, 1997]. The NO_y/N_2O relationship measured by MkIV (Plate 1) is used in this work to represent the conditions in the vortex prior to denitrification, descent, and isentropic mixing. Compared with this reference relation, severe NO_y deficits were observed in the Arctic during a number of ER-2 flights in February 1989 (e.g. the flights on February 7, 1989, magenta points in Plate 2). In contrast, the ER-2 observations obtained inside the Arctic vortex on April 26, 1997 during POLARIS show only moderate deficits of NO_y compared to the reference NO_y/N_2O relationship for air with mixing ratios of N_2O below ~200 ppbv (Plate 1).

The moderate deficit of NO_y observed during POLARIS could be due to one of several processes: (1) denitrification, (2) descent followed by isentropic mixing, and (3) a combination of 1 and 2. Denitrification (process 1) is illustrated by the dot-dashed arrow in Plate 1: Starting from the MkIV NO_y/N_2O reference correlation, this process could have reduced the NO_y mixing ratio without changing the N_2O mixing ratio. The process of descent followed by isentropic mixing (process 2) is illustrated schematically in Figure 1. During winter large scale subsidence takes place inside the vortex, which is relatively well isolated from extravortex air [e.g., *Abrams et al.*, 1996]. As the vortex weakens and finally breaks up during spring, vortex air masses irreversibly mix with air outside the vortex along surfaces of constant potential temperature [e.g., *Waugh et al.*, 1997]. The effect of process 2 on the NO_y/N_2O correlation is illustrated by the dashed arrow in Plate 1. Mixing of two air masses at the same potential temperature in varying degrees (one air mass from inside the vortex, the other from outside) would lead to a linear relationship between NO_y and N_2O. If the reference tracer/tracer relation is nonlinear, the mixing between these air masses can produce a new tracer/tracer relation quite different than the reference relation [*Waugh et al.*, 1997; *Herman et al.*, 1998; *Michelsen et al.*, 1998; *Kondo et al.*, 1999]. The combination of denitrification and mixing (process 3) is illustrated by the dotted arrow in Plate 1. In this scenario, denitrification first reduces the NO_y mixing ratio at constant N_2O (illustrated by the part of the dotted arrow that is parallel to the NO_y axis). Subsequent mixing with extravortex air (illustrated by the rest of the dotted arrow) then would produce the observed air mass properties. Recently, Plumb et al. (submitted manuscript, 1999) have shown that continuous isentropic mixing during descent could lead to the development of anomalous tracer/tracer relationships inside the vortex. This possibility is also discussed.

3.2. CH_4/N_2O Relationship

Michelsen et al. [1998] and *Herman et al.* [1998] showed that mixing of subsided innervortex air with extravortex air tends to reduce the curvature of the CH_4/N_2O relation. We use straight isentropic mixing lines in the CH_4/N_2O relation at specific potential temperature levels to quantify the amount of descent that has occurred inside the vortex and the degree of mixing between vortex and extravortex air for the regions sampled by the ER-2. MkIV measurements of the CH_4/N_2O correlation (red circles in Plate 3) obtained near 65 N on May 8, 1997, for extravortex air are used as the extravortex reference correlation. The MkIV CH_4/N_2O correlation agrees well with that measured by ATMOS in November 1994 between 40° and 50°N [*Chang et al.*, 1996]. A pronounced curvature is visible in the extravortex CH_4/N_2O correlation for mixing ratios of N_2O below 250 ppbv. In contrast, observations obtained on April 26, 1997 near 20 km by the ER-2 ALIAS instrument reveal a nearly linear correlation between CH_4 and N_2O (green dots in Plate 3) that deviates significantly from the extravortex correlation. The low mixing ratios of N_2O between 500 and 510 K potential temperature indicate that subsided polar vortex air masses were sampled by the ER-2 during this flight.

Since the correlation between the mixing ratios of these long-lived tracers cannot be changed by reversible transport or chemistry, the most obvious explanation for the ER-2 observations is mixing of extravortex air with polar vortex air that has subsided from higher altitudes [e.g., *Waugh et al.*, 1997]. The two air masses that must have mixed isentropically to produce the observed CH_4/N_2O relations along the linear mixing line are referred to as the "innervortex end-member" and the "extravortex end-member". It is reasonable to assume that the bulk of the mixing took place in spring, following the strongest descent within the vortex (this assumption is discussed in section 4). Therefore the composition of the extravortex end-member (the trapezoid marked in Plate 3) is defined by the ambient mixing ratios of CH_4 and N_2O observed outside of the vortex by the ER-2 and by the MkIV instrument at the same potential temperature level of the ER-2 flight. The composition of the innervortex end-member is defined by the intersection of the extrapolated ER-2 mixing line and the MkIV reference correlation (oval region in Plate 3). Since the CH_4/N_2O relation is nearly linear between 15 and 40 ppbv N_2O, inhomogeneous descent inside the polar vortex (provided that the air masses originate from this near-linear region) followed by isentropic mixing of these vortex air masses with each other would not change the CH_4/N_2O relationship in the innervortex end-member considerably. The fractional contribution of the innervortex and the extravortex end-members to specific ER-2 observations along the CH_4/N_2O mixing line is determined from the relative distance of the observed N_2O mixing ratio to that of both end-members.

3.3. Calculation of NO_y**

We use the notation NO_y** to refer to the mixing ratio of NO_y that would have been present in the absence of denitrification, after accounting for the effects of descent and isentropic mixing. For the limit of unmixed air masses this quantity is identical to NO_y* [*Fahey et al.*, 1989] which is based only on the reference correlation and does not account for descent and mixing. The value of NO_y** is calculated on a point-by-point basis along the flight track of the ER-2 by considering isentropic mixing between the innervortex and extravortex end-members derived from our analysis of simultaneous measurements of CH_4 and N_2O. As described in section 3.2, the mixing ratio of N_2O associated with the innervortex end-member (here defined as $[N_2O]_i$) was calculated based on the intersection with the reference relation of a straight line passing through two points: one defined by the measured mixing ratios of CH_4 and N_2O and the other defined by the extravortex end-member. The composition of the extravortex end-member used for all ER-2 observations considered here, which were obtained for potential temperatures between 500 and 530 K, is defined by the trapezoid in Plate 3. The NO_y mixing ratios of both end-members can be estimated from the respective mixing ratios of N_2O and the NO_y/N_2O correlation measured by the MkIV instrument on May 8, 1997. Values of NO_y** have been calculated from the NO_y mixing ratios of both end-members and their fractional contribution to the mixed air mass:

$$NO_y^{**} = \frac{[N_2O]-[N_2O]_i}{[N_2O]_e-[N_2O]_i}[NO_y]_e + \left(1-\frac{[N_2O]-[N_2O]_i}{[N_2O]_e-[N_2O]_i}\right)[NO_y]_i \qquad (1)$$

where $[N_2O]$ denotes the mixing ratio of N_2O of the respective air mass and the variables with indices e and i denote the properties of the extravortex and innervortex mixing end-members, respectively. The uncertainties of the calculated parameters including NO_y** have been estimated based on the uncertainty of the composition of the extravortex end-member (indicated by the size of the trapezoid in Plate 3) and the precisions of the measurements.

3.4. Underlying Assumptions

Two critical assumptions for our analysis are (1) the ability to directly combine remote (MkIV) and in situ (ER-2 and OMS) observations of NO_y, CH_4, and N_2O acquired by vastly different techniques without corrections for possible systematic differences and (2) the validity of using the NO_y/N_2O and CH_4/N_2O reference relations that have been measured outside the polar vortex to represent the innervortex end-member for the mixing processes analyzed here. Assumption (1) is supported by the remarkably good agreement between the MkIV reference correlation for NO_y/N_2O and the ER-2 observations obtained in the Arctic vortex during January and February 1989 (Plate 2). Comparisons of MkIV and ER-2 observations of NO_y and N_2O obtained at mid-latitudes [*Sen et al.*, 1998, Figure 2] and of ATMOS and ER-2 observations of NO_y, CH_4, and N_2O ([*Chang et al.*, 1996, Figure 3] ATMOS acquires observations using solar occultation in a manner similar to the MkIV instrument) lend further confidence in the agreement of the different sources of data. *Toon et al.* [1999] conclude that the bias between the MkIV and ALIAS measurements of N_2O is only 2%. Finally, the excellent agreement between the MkIV CH_4/N_2O reference relation and ALIAS II observations obtained at high latitude during POLARIS for extravortex air (discussed in section 3.7) provides additional support for the validity of assumption (1). Furthermore, the NO_y/N_2O and CH_4/N_2O relations measured at northern mid-latitudes during November 1994 by ATMOS [*Chang et al.*, 1996] agree well with the MkIV reference relations used here (the agreement between MkIV and ATMOS measurements of CH_4 and N_2O is discussed further in section 3.7).

Assumption (2) cannot be fully tested for the winter of 1996-1997 since tracer measurements inside the Arctic vortex are not available during the different phases of the winter. Measurements of CH_4 and N_2O obtained during February 1997 from two balloon flights over Kiruna, Sweden (68°N) [*Kondo et al.*, 1999] represent conditions near the vortex edge and therefore can not properly be interpreted as being representative of the polar vortex. Recently, Plumb et al. (submitted manuscript, 1999) have suggested that a small amount of continuous mixing across the vortex edge throughout the winter could lead to distinct innervortex tracer relations that differ considerably from the extravortex relations or that compact relations might be lost inside the polar vortex. However, assuming the validity of assumption (1), the in situ observations of NO_y and N_2O obtained near 20 km during January and February 1989 suggest that the MkIV NO_y/N_2O reference correlation was valid inside the vortex during the initial phase of denitrification in 1989 (Plate 2). We note that the remarkably good agreement between the MkIV and in situ observations of NO_y and N_2O supports the validity of both assumptions (1) and (2) because it would be highly unlikely that deviations from the assumptions would cancel in such a way to preserve the good agreement. However, it is not clear whether this agreement of innervortex and extravortex relations in January and February holds at higher altitudes and for all winters and whether it holds until mid-March, when diabatic descent inside the polar vortex commonly gets sufficiently slow [*Rex et al.*, 1998; *Knudsen et al.*, 1998; *Rex et al.*, 1999] that any mixing occuring after this time would be well represented by our approach. The results of *Michelsen et al.* [1998] indicate that in mid-April 1993 the innervortex tracer relations deviated considerably from the extravortex relations, but it is not clear when this discrepancy developed. The question of whether and when distinct innervortex tracer relations develop needs to be addressed by tracer measurements within the vortex throughout the winter. We note that our analysis is valid only under the assumption that for the 1996-1997 winter the bulk of the mixing across the vortex edge took place after descent slowed down sufficiently (i.e., after approximately mid-March; estimations of diabatic descent rates based on observed temperatures and radiation transport calculations show that at 500 K the total descent after mid-March was of the order of only 10 K [Knudsen et al., 1998]). In section 4 we will further discuss the validity of this assumption for the 1996-1997 winter in the light of our results.

3.5. ER-2 Flight on April 26, 1997

3.5.1. Descent and mixing. Plate 4b shows the mixing ratio of N_2O calculated with the method described in section 3.3 for the innervortex end-members along the ER-2 flight track on April 26, 1997. The mixing ratios of the innervortex end-member were found to be between 25 and 40 ppbv. The associated approximate altitudes from which the innervortex end-members subsided through the winter are ~32-34 km (Plate 4c). The altitudes have been estimated using the mixing ratios of N_2O measured by the ER-2 and the MKIV extravortex profile of N_2O. An overall subsidence of ~13 km for air masses ending near 500 K (~20 km) is suggested by our analysis. This value agrees well with the overall descent of 13.8 km for air ending at 20 km that was derived by *Abrams et al.* [1996] for the Arctic winter 1992-1993 from ATMOS/ATLAS-2 data. *Abrams et al.* [1996] showed that this descent is consistent with the theoretical results of *Manney et al.* [1994] and *Rosenfield et al.* [1994]. The ratio between innervortex air and extravortex air in the sampled air masses has been calculated as described above and is shown in Plate 4d. For the observations discussed here, this ratio varies between 0.3 and 0.6 with higher fractions of innervortex air present at higher latitudes. As expected, high fractions of innervortex air correlate with high values of potential vorticity (Plate 4a).

3.5.2. Denitrification. Plate 4e compares observations of NO_y to NO_y* (NO_y based on the measured N_2O and the reference correlation between N_2O and NO_y) and NO_y** (NO_y calculated from the reference correlation, allowing for descent and isentropic mixing). Large differences between observed NO_y and NO_y* are apparent. In contrast, observations of NO_y agree well with NO_y** during most parts of the flight. This result suggests that most of the NO_y deficit found along the ER-2 flight track was caused by descent followed by isentropic mixing. However, during the northernmost part of the ER-2 flight on April 26, 1997, the mixing ratios of NO_y were smaller than NO_y**, indicating that some denitrification had taken place.

This is further illustrated in Plate 5, where the observed NO_y/N_2O correlation, the NO_y**/N_2O correlation, and the extravortex reference correlation are shown. Measured NO_y agrees well with NO_y** for N_2O mixing ratios larger than 125 ppbv. For N_2O levels below 100 ppbv, a deficit of measured NO_y compared to NO_y** is visible. We interpret this 1-2 ppbv deficit in NO_y as the result of weak irreversible denitrification that occurred earlier in the winter. Since the denitrification probably occurred before the bulk of the mixing, it is reasonable to suggest that the deficit of NO_y originally caused by denitrification was diluted by subsequent mixing. Back projection of the NO_y deficit to pre-mixing conditions (dashed lines in Plate 5) shows that the original average degree of denitrification must have been approximately 2-3 ppbv (solid arrow in Plate 5) to cause the NO_y deficit observed in late April. Most likely the denitrification inside the polar vortex was characterized by patchy regimes of higher denitrified areas and areas without denitrification (as was observed on February 7, 1989; see Plate 2). In the weeks following the denitrification events, comparatively fast mixing inside the vortex probably led to an averaging of the degree of denitrification throughout the vortex yielding the 2-3 ppbv value reported above.

The weak denitrification reported here is consistent with the temperature structure of the 1996-1997 winter. PSC particles must grow to large sizes (of the order of 1-2 μm) to sediment with appreciable velocities [e.g., *Salawitch et al.*, 1989]. Particle formation and growth models show that PSC particles reach sizes large enough to cause rapid denitrification once temperature falls below the frostpoint, due to efficient uptake of water [e.g., *Drdla and Turco*, 1991]. Differential growth may also lead to large particles for temperatures that are above the frostpoint but below the NAT (nitric acid trihydrate) equilibrium temperature (T_{NAT}) [*Salawitch et al.*, 1989]. However, *Santee et al.* [1998] show that the phase change required to initiate differential growth most likely requires suppression of temperature below T_{NAT} continuously for a period of at least several days. In the Arctic the cold temperature region is normally displaced from the center of the vortex. As air masses circulate in the vortex, they alternately pass through cold ($T < T_{NAT}$) and warm regions every few days, so that severe denitrification in the Arctic may require the minimum temperature to drop below the frostpoint. Temperature analysis from the European Centre for Medium Range Weather Forecast shows that the synoptic temperatures dropped below the frostpoint (assuming 4.6 ppmv H_2O) only in limited areas (largest area $>2\times10^6$ km^2 $\cong$ 10% of the vortex area) and only for two short periods, both only a couple of days long during mid and late February. The potential for formation of water ice PSCs during 1996-1997 was much smaller than in the winters of 1988-1989 and 1995-1996. Furthermore, in 1996-1997 the areas cold enough for synoptic water ice PSC formation were mainly at the 450 K level, which is below the air masses sampled by the ER-2 during its vortex flight. Considering some diabatic cooling during the late winter period, the air masses sampled by the ER-2 in late April at 500 K would have been even somewhat above 500 K during the cold periods in February. From vortex averaged radiative cooling rates calculated from the Universities' Global Atmospheric Modeling Programme (UGAMP), it was estimated that the subsidence between the coldest period and the April ER-2 flight was between 5-10 K potential temperature.

Our analyses have been based on ER-2 measurements of N_2O obtained by the ALIAS instrument. In situ measurements of the mixing ratio of N_2O are also obtained by the Airborne Tunable Laser Absorption Spectrometer (ATLAS) instrument for each ER-2 flight. There are slight differences between the ATLAS and ALIAS measurements of N_2O during limited segments of the two ER-2 flights considered here. However, we have repeated our entire analyses using the ATLAS measurements of N_2O, and we note that our overall conclusions are independent of which measurement of N_2O is used.

3.6. ER-2 Flight on June 30, 1997

During the ER-2 flight on June 30, 1997 remnants of the polar vortex were found at 510-530 K potential temperature, i.e., at slightly higher isentropic levels than during the flight of April 26. Plate 6 shows the CH_4/N_2O relation measured during this flight. The innervortex end-members that contributed to the air mass probed by the ER-2 had fairly constant N_2O mixing ratios of about 15-20 ppbv (Plate 7a). The associated initial altitude is ~37 km (Plate 7b), so that the overall descent for air masses ending at around 520 K in June is estimated to be ~16 km. Plate 7c shows that the fraction of innervortex air in the probed air masses varied between 20 and 70% for the air masses discussed here. The NO_y

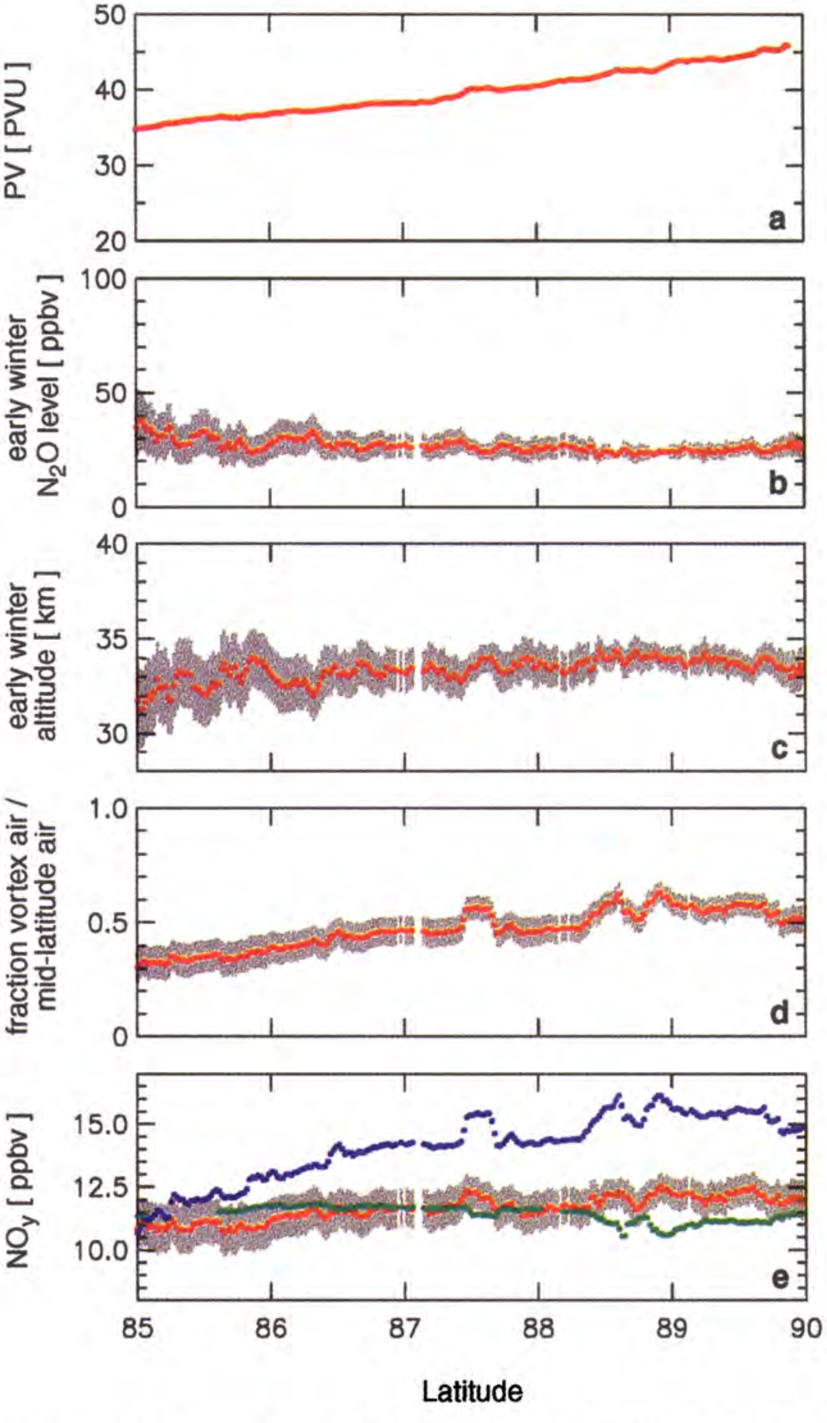

Plate 4. Measured and calculated quantities along the northbound track of the ER-2 flight on April 26, 1997. The gray shaded areas give an estimate of the uncertainty based on the errors in the measurements and the uncertainty in defining the properties of the extravortex mixing end-member. (a) Potential vorticity (1 Potential Vorticity Unit (PVU) = 10^{-6} K m^2 s^{-1} kg^{-1}), (b) calculated mixing ratio of N_2O for the innervortex mixing end-member, (c) corresponding approximate early winter altitude of the innervortex air, (d) fraction of innervortex air versus extravortex air in the mixed sample, (e) NO_y* which would have been predicted from the N_2O vmrs without considering mixing (blue), NO_y** predicted with consideration of mixing (red), and NO_y measured by the NOAA chemiluminescence instrument aboard the ER-2 (green).

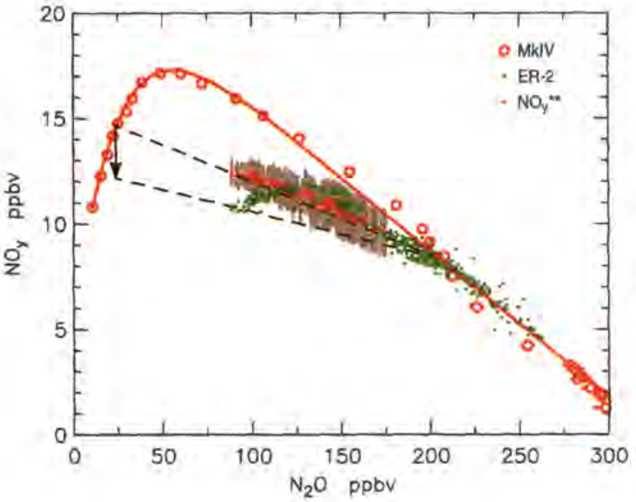

Plate 5. MkIV and ER-2 measurements as in Plate 1. The NO$_y$** predicted for the air masses sampled by the ER-2 (red) and its uncertainty (gray, c.f. Plate 4) are compared with the measured NO$_y$ (green). NO$_y$** was calculated from the degree of descent and mixing derived from the CH$_4$/N$_2$O correlation. The NO$_y$ versus NO$_y$** deficit at low N$_2$O levels is interpreted as a signature of irreversible denitrification. The premixing degree of denitrification in the air masses is estimated by a backprojection of the measured properties of the mixed sample to the properties of the innervortex mixing end-member (dashed lines). The estimated average premixing degree of denitrification in the sampled air masses is indicated by the arrow. Since the air masses inside the vortex are rapidly mixed and the denitrification typically occurs inhomogeneously, this degree of denitrification is likely the result of mixing of more heavily denitrified air masses with less or nondenitrified innervortex air.

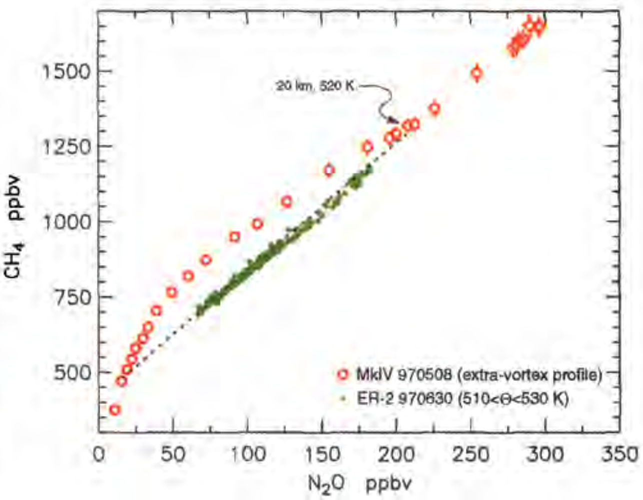

Plate 6. As Plate 3, but for the portion of the ER-2 flight at potential temperatures of 510-530 K near 65°N on June 30.

observations agree very well with NO$_y$** throughout the flight (Plate 8). This analysis reveals that the large deficits of NO$_y$ compared with the extravortex reference can be explained entirely by descent and mixing. No indication for denitrification was found.

The vortex air masses sampled during the June 30, 1997, ER-2 flight were at higher potential temperature levels than those encountered during the April 26, 1997, flight. These air masses were well above the cold temperature region in February, and synoptic temperatures never dropped below the frostpoint in these air masses for the entire winter. Our finding that these air masses have not been significantly denitrified is consistent with the temperature structure of the 1996-1997 winter.

3.7. OMS Flight on June 30, 1997

On the same day as the latter ER-2 flight, the OMS balloon borne platform measured a profile of several trace species and encountered polar vortex remnants in two altitude regions around 500-520 K and 615-637 K potential temperature [*Herman et al.*, 1998]. The measured CH$_4$/N$_2$O mixing ratios obtained during the balloon descent are plotted in Plate 9 together with the extravortex reference measured by the MkIV instrument. The ALIAS II observations are grouped into potential temperature ranges that are shown in different colors.

The mixing ratios of CH$_4$ and N$_2$O found in the vortex air masses around 495-520 K (blue points in Plate 9) lie along a mixing line very similar to that formed by the ER-2 observations obtained on the same day. The measurements of CH$_4$ and N$_2$O in air masses that have not been influenced by the polar vortex (black points in Plate 9) agree remarkably well with measurements made by the MkIV instrument on May 8, 1997 [see, also, Herman et al., 1998]. These observations strongly support the assumption that the measurements from the different platforms may be compared directly without bias.

We now focus on the air masses probed between 615 and 637 K potential temperature (green in Plate 9). The CH$_4$/N$_2$O relation of these air masses form a mixing line with a steeper slope than those indicated by the ER-2 and OMS measurements at lower altitudes. The mixing line meets the CH$_4$/N$_2$O reference correlation at mixing ratios that correspond to the MkIV measurement obtained at 615 K potential temperature. This level coincides well with the potential temperature range probed by the OMS platform for the mixing line. The slope of the mixing line indicates that the innervortex end-member originated from well above the altitude region sampled by the MkIV instrument (dashed arrow in Plate 9). We used data from ATMOS/ATLAS-3 obtained during November of 1994 to identify the intersection of the extended mixing line with the reference correlation of CH$_4$/N$_2$O (Plate 10). The intersection of the dashed line in Plate 10 with the extravortex reference indicates that the innervortex mixing member originated at an extremely low mixing ratio of N$_2$O and at a CH$_4$ mixing ratio of ~200 ppbv. Plate 11 shows that in autumn such low CH$_4$ levels are found between 40 and 60 km altitude, depending on latitude. Since the descending motion inside the vortex is coupled with a poleward motion at higher altitudes, it is not clear at which latitude and altitude the vortex air masses have been in autumn. According to Plate 11, it is possible that the vortex remnants at 615-637 K originated in the mesosphere.

The NO$_y$/CH$_4$ correlation measured by ATMOS/ATLAS-3 between 40 and 50° N (Plate 12, 50°N is the highest latitude sampled by the ATMOS instrument during the ATLAS-3 mission) has been used to calculate NO$_y$** from the estimated CH$_4$ mixing ratios of the innervortex end-member for the air masses probed by the OMS platform between 615 and 637 K potential temperatures (Plate 13). At 60°N, the lifetime of NO$_y$ is sufficiently long (during mid-October longer than 2 years below ~55 km; the lifetime has been estimated using the model described by *Osterman et al.* [1997] that probably no significant loss of NO$_y$ during the descent occurred). However, the lifetime of N$_2$O at 50-55 km is only about 2 months (compare section 1) so that the quantitative results of this calculation might be slightly influenced by possible chemical changes of

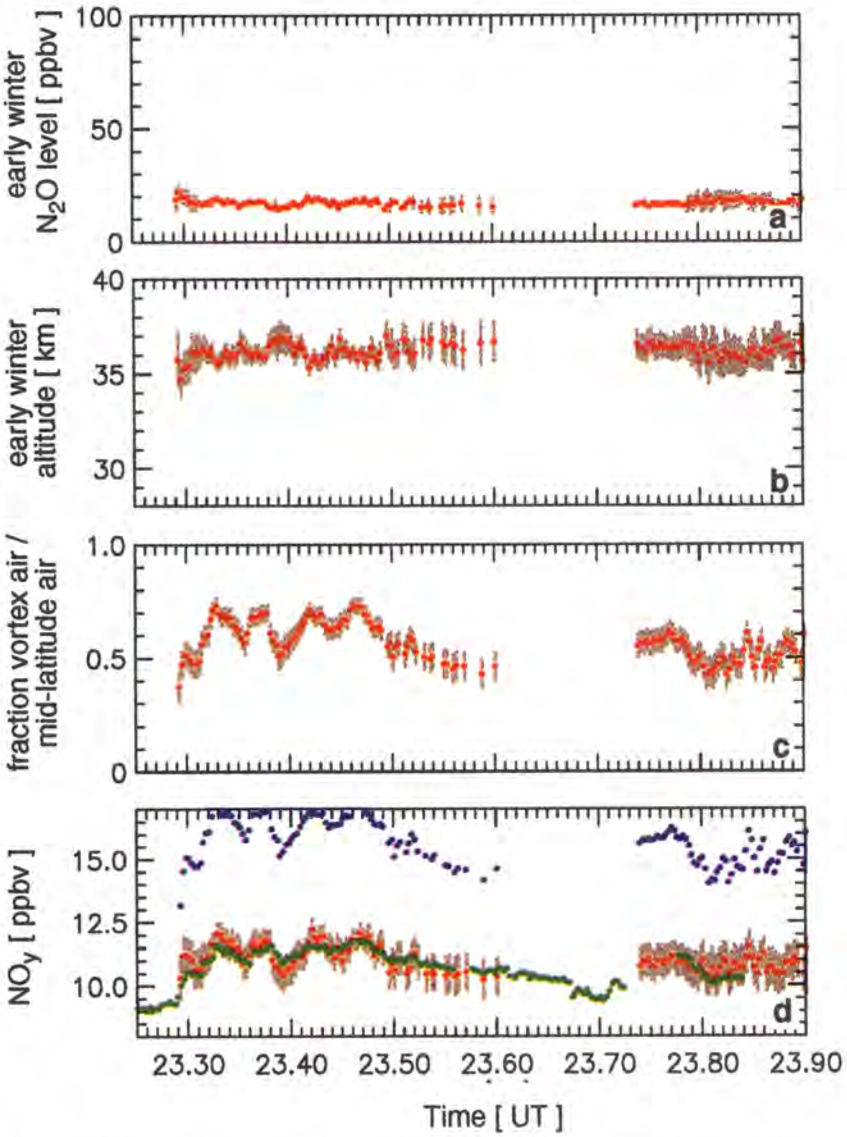

Plate 7. As Plate 4, but for the portion of the ER-2 flight at potential temperatures of 510-530 K near 65°N on June 30.

N_2O during the initial phase of the descent. Plate 13 shows that above 600 K, quite low NO_y/N_2O ratios can be produced purely by mixing processes between subsided mesospheric air masses with extravortex air. This result supports the hypothesis of *Kondo et al.* [1999] that for altitudes above 20 km, very low values of NO_y can easily be mistaken for severe denitrification if dynamical processes are neglected.

4. "Continuous Mixing" Versus "Late Mixing"

Plumb et al. (submitted manuscript, 1999) presented a theoretical study of the evolution of tracer relationships inside the polar vortex in the presence of continuous weak mixing across the vortex edge. Their results show that if mixing across the vortex edge during the main phase of descent is strong enough to change the innervortex tracer relations, then the approach used here would not be applicable in a quantitative manner. The critical aspect is the time at which mixing across the vortex edge first changes the tracer relations inside the polar vortex. If mixing changes the innervortex tracer relations during the main phase of the descent (approximately until early March), the results of Plumb et al. (submitted manuscript, 1999) demonstrate that transport properties inferred from one set of tracer relations should not be applied to a different set of tracer relations. If, however, the change in the tracer relations inside the vortex first occurs after descent has slowed sufficiently (i.e., after approximately mid-March), our approach is applicable, regardless of the precise nature of the isentropic mixing (i.e., whether it occurs as a single mixing event, a succession of a number of mixing events, or as continuous mixing after mid-March). We will refer to the latter scenario as "late mixing" and to the other scenario as "continuous mixing". In the following we discuss data from two winters to address whether indications for continuous mixing can be identified in the real atmosphere.

4.1. Winter 1992-1993

The representation of ATMOS data from the ATLAS-2 mission (April 8-16, 1993) by *Michelsen et al.* [1998] suggests that over a broad range of potential temperatures, single, distinct, and near linear relations between NO_y and N_2O and between CH_4 and N_2O ex-

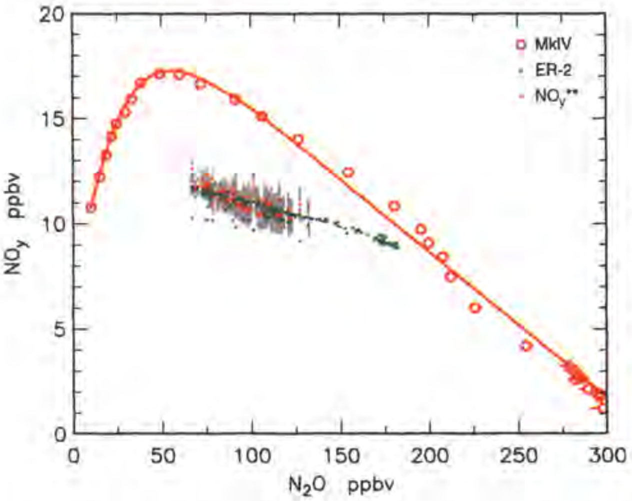

Plate 8. As in Plate 5, but for the ER-2 flight on June 30, 1997. The vortex remnants were encountered, while the ER-2 was between potential temperatures of 510 and 530 K; only ER-2 measurements between these levels have been plotted. No indication for denitrification is apparent.

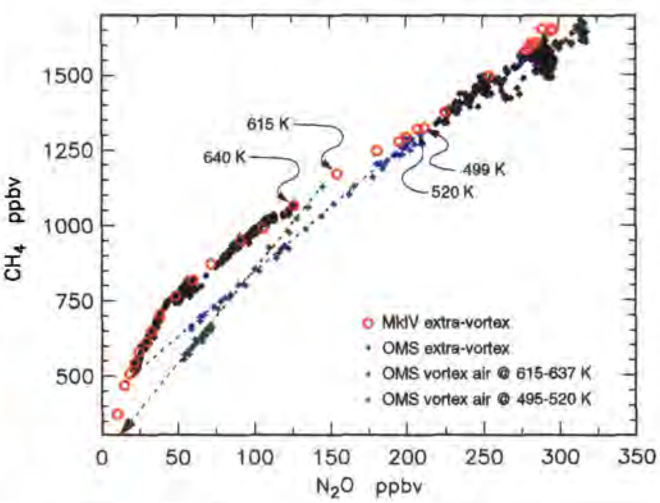

Plate 9. CH_4/N_2O correlation observed by the ALIAS II instrument during the descent portion of the OMS balloon flight on June 30, 1997, compared to the MkIV measurements on May 8, 1997. The ALIAS II OMS data has been grouped into extravortex samples (black) and measurements obtained during the penetration of two distinct layers of vortex air remnants (green: 615-637 K, blue: 495-520 K). The observations within the vortex remnants reveal distinct mixing lines (dashed) for both potential temperature regions. The MkIV measurements on May 8, 1997, are given in red. The potential temperatures of the MkIV data points at the intersections with the OMS mixing lines are indicated.

isted inside the Arctic vortex during that winter. The existence of distinct compact innervortex tracer relations over a broad range of potential temperatures would suggest that continuous mixing had occurred (Plumb et al., submitted manuscript, 1999). However, in *Michelsen et al.* [1998] the large number of ATMOS measurements of individual NO_y species were averaged on a number of vertical levels, and the NO_y mixing ratio at each level was calculated to give an innervortex profile. This binning and averaging procedure may mask individual isentropic mixing lines. Isentropic mixing lines in tracer/tracer plots are formed by various individual measurements obtained on one potential temperature level. Statistically some of these individual measurements occur in air masses that contain a larger fraction of end-member A (e.g. innervortex air), others in air masses with larger fractions of end-member B (e.g. extravortex air). The statistical scatter of measurements at one isentropic level is needed to identify mixing lines in tracer/tracer plots.

If our approach of analyzing isentropic mixing lines is applied to the ATMOS/ATLAS-2 data, various distinct isentropic mixing lines in the NO_y/N_2O relation are apparent. The isentropic analysis also reveals distinct mixing lines in the CH_4/N_2O relation that are not apparent as given in *Michelsen et al.* [1998, Plate 2] because their analysis focusses solely on a few number of measurements obtained deep inside the Arctic vortex. The CH_4/N_2O and NO_y/N_2O mixing lines we identify have slopes that rise with increasing potential temperature and intersect with the extravortex relation in a manner similar to the mixing lines shown in Plate 9. This picture is compatible with the late mixing scenario but does not rule out continuous mixing either. A comprehensive analysis of the ATMOS data from 1992 to 1993 using the approach of isentropic mixing lines will be the subject of a future publication.

4.2. Winter 1996-1997

As mentioned in section 3.4, we currently cannot completely rule out the possibility that continuous mixing during descent inside the 1996-1997 vortex changed the innervortex tracer relations in a way that would hamper our approach. However, the good agreement between NO_y^{**} and the measured NO_y shown in Plate 8 indicates that this is probably not the case. Plumb et al. (submitted manuscript, 1999) demonstrated that if mixing during the main phase of descent had changed the innervortex tracer relations, the mixing lines observed in a NO_y/N_2O plot and in a CH_4/N_2O plot would intersect with the respective extravortex relations at differ-

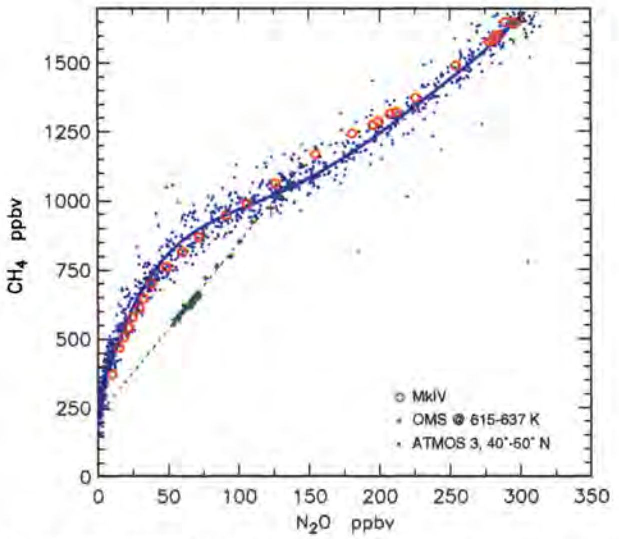

Plate 10. CH_4/N_2O correlation for the OMS encounter of vortex remnants at 615 - 637 K potential temperature (green) compared with an extravortex reference correlation established by ATMOS/ATLAS-3 measurements obtained between 40° and 50°N in early November 1994 (blue dots, a fit to the data is plotted as blue line). The MkIV reference correlation from May 8, 1997, is shown in red.

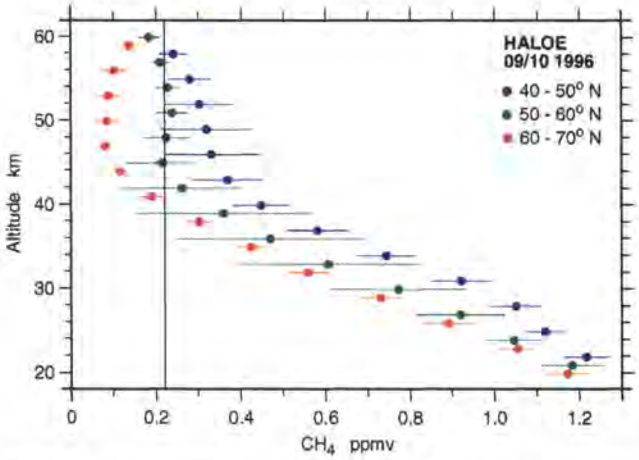

Plate 11. CH_4 profiles measured during September-October 1996 by the Halogen Occultation Experiment (HALOE)(data version 19) on the Upper Atmosphere Research Satellite between 40° and 70°N. The individual profiles were sorted into different latitude bands and were averaged into ±1.5 km vertical bins. The error bars reflect the 1σ variability. The vertical line denotes the mixing ratio of CH_4 of the innervortex end-member for the OMS mixing line observed at 615-637 K potential temperature.

ent mixing ratios of N_2O. In contrast to that scenario, the success of our approach to precisely reproduce measured NO_y as shown in Plate 8 demonstrates that the N_2O levels derived from both tracer plots agree very well. Given the temperature history of the air masses shown in Plate 8, it is unlikely that NO_y in these air masses was influenced by denitrification (compare section 3.6). It is highly unlikely that even if denitrification cannot be ruled out completely, the effect of denitrification would precisely cancel the effect of continuous early winter mixing to produce the good agreement between NO_y** and measured NO_y shown in Plate 8.

Measurements of CH_4 and N_2O from two balloon flights at 68°N on February 11 and 22, 1997, show a near linear relationship [*Kondo et al.*, 1999], which indicates considerably mixing early in the winter. However, these observations were obtained near the edge of the vortex and therefore may not be representative of conditions throughout the vortex.

We note that although our analysis indicates that any continuous mixing during the main phase of descent was probably not effective enough to influence the innervortex tracer relations in 1996-1997, this does not necessarily mean that such mixing could not influence the innervortex tracer relationships during other winters. The timing of mixing in a given winter is closely connected with the level of wave activity in the Northern Hemisphere during the respective winter. The temporal development of the wave activity throughout an Arctic winter varies tremendously from year to year, so that the tracer relationships inside the Arctic polar vortex may well be different from year to year. Plumb et al. (submitted manuscript, 1999) demonstrated the importance of detailed knowledge about the timing of any relevant mixing. The development of tracer/tracer relationships inside the Arctic polar vortex under a variety of meteorological conditions needs further research.

5. Conclusions

Mixing processes between subsided air masses from the polar vortex and midlatitude air can considerably alter otherwise well-established tracer correlations if their relationship is nonlinear. The combined measurements of NO_y, N_2O, and CH_4 obtained by the NOAA NO_y and the ALIAS instrument aboard the ER-2, the MkIV balloon-borne FTIR-spectrometer and the ALIAS II balloon borne tunable diode laser instrument during the POLARIS campaign provide detailed in situ tracer data in the mixed air masses as well as concurrently measured reference correlations for extravortex air.

A technique based on near linear isentropic mixing lines in the otherwise nonlinear correlation between CH_4 and N_2O has been used to quantify dynamically induced changes in the tracer relationships. The mixing lines at increasing potential temperature levels show an increasing slope and intersect with the reference correlation at their respective potential temperature. The informa-

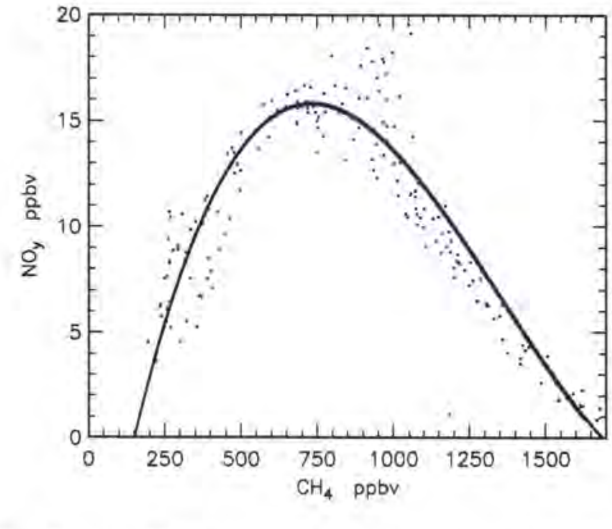

Plate 12. NO_y/CH_4 reference correlation measured by ATMOS/ATLAS-3 between 40° and 50°N in early November 1994. The fit to the data has been used to estimate the mixing ratio of NO_y of the innervortex mixing end-member based on the estimated mixing ratio of CH_4 of that air mass (compare Plate 9).

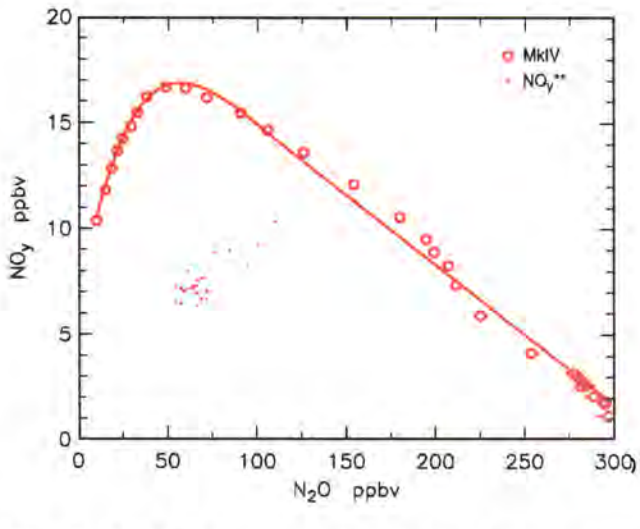

Plate 13. The NO_y**/N_2O correlation calculated for the air masses measured by OMS between 615 and 637 K on June 30 based on the degree of subsidence and mixing inferred from the CH_4 versus N_2O correlation. No denitrification has been assumed. MkIV data are the same as in Plate 1.

tion extracted from the CH_4/N_2O correlation has been used to calculate the abundance of NO_y^{**} (the expected mixing ratio of NO_y accounting for descent and isentropic mixing) for the mixed air masses. The degree of denitrification has been derived by comparing observed NO_y with NO_y^{**}. This approach is an extension of the approach of comparing NO_y with NO_y^{*} [*Fahey et al.*, 1990] to situations where the air masses have been subject to mixing across the vortex edge. Our analysis reveals evidence for only a small degree of denitrification in a limited region of the Arctic vortex sampled by the ER-2 flight on April 26, 1997, and no indication for denitrification for vortex air sampled at higher potential temperature levels during a flight on June 30, 1997. These findings are consistent with the synoptic-scale temperature history of the sampled air masses throughout the winter. The considerable deficit of NO_y compared with NO_y^{*} (the mixing ratio of NO_y derived from the abundance of N_2O without considering mixing) during both flights, which would have been incorrectly interpreted as the result of denitrification in the 'traditional' approach, is actually mainly the result of descent and end-member mixing.

Our analysis supports the conclusions of *Waugh et al.* [1997], *Kondo et al.* [1999], and *Michelsen et al.* [1998] that it is important to use measurements of additional conserved species to accurately interpret changes in the NO_y/N_2O relation with respect to denitrification. The main uncertainty in our work lies in the definition of the innervortex tracer/tracer reference correlations that represent the composition of the innervortex end-members of the isentropic mixing process. We assume that tracer/tracer relations measured outside of the vortex also represent the composition of the innervortex end-members. Recent results from Plumb et al. (submitted manuscript, 1999) suggest that even weak continuous entrainment of extravortex air into the polar vortex during the main phase of descent could lead to innervortex tracer relationships that differ considerably from extravortex relations. We present data obtained inside the vortex near 20 km during POLARIS and a previous winter to support the validity of our assumptions concerning the innervortex tracer relations. However, it is not clear whether this result holds for other winters because wave activity that could lead to mixing across the vortex edge is quite variable from year to year. Measurements of tracer profiles inside the vortex during different phases of winter, as are planned for the upcoming NASA SAGE III Ozone Loss and Validation Expedition (SOLVE), will largely reduce the uncertainty of this type of analysis.

Acknowledgments. We thank P. Newman and L. Lait for providing the potential vorticity data used in Plate 4, James M. Russell III for providing the HALOE data used in Plate 11, and R. A. Plumb and D. W. Waugh for making their results available to us prior to publication. We also appreciate the efforts of the many personnel who contributed to the balloon launches and the ER-2 flights. Part of the research described in this paper was carried out by the Jet Propulsion Laboratory, California Institute of Technology, under a contract with the National Aeronautics and Space Administration.

References

Abrams, M. C. et al., Trace gas transport in the Arctic vortex inferred from ATMOS ATLAS 2 observations during April 1993, *Geophys. Res. Lett.*, *23*, 2341-2344, 1996.

Arnold F., V. Burger, K. Gollinger, M. Roncossek, J. Schneider, and S. Spreng, Observations of nitric acid perturbations in the winter Arctic stratosphere: Evidence for PSC sedimentation, *J. Atmos. Chem.*, *30*, 49-59, 1998.

Brune, W. H., D. W. Toohey, J. G. Anderson, and K. R. Chan, In situ observations of ClO in the Arctic stratosphere: ER-2 aircraft results from 59°N to 80°N latitude, *Geophys. Res. Lett.*, *17*, 505-508, 1990.

Brune, W. H., J. G. Anderson, D. W. Toohey, D. W. Fahey, S. R. Kawa, R. L. Jones, D. S. McKenna, and L. R. Poole, The potential for ozone depletion in the Arctic polar stratosphere, *Science*, *252*, 1260-1266, 1991.

Chang, A. Y. et al., A comparison of measurements from ATMOS and instruments aboard the ER-2 aircraft: Tracers of atmospheric transport, *Geophys. Res. Lett.*, *23*, 2389-2392, 1996.

Drdla, K, and R. P. Turco, Denitrification through PSC formation - a 1-D model incorporating temperature oscillations, *J. Atmos. Chem.*, *12*, 319-366, 1991.

Fahey, D. W., K. K. Kelly, G. V. Ferry, L. R. Poole, J. C. Wilson, D. M. Murphy, M. Loewenstein, and K. R. Chan, In situ measurements of total reactive nitrogen, total water, and aerosol in a polar stratospheric cloud in the Antarctic, *J. Geophys. Res.*, *94*, 11299-11315, 1989.

Fahey, D. W., K. K. Kelly, S. R. Kawa, A. F. Tuck, M. Loewenstein, K. R. Chan, and L. E. Heidt, Observations of denitrification and dehydration in the winter polar stratospheres, *Nature*, *344*, 321-324, 1990.

Herman, R. L. et al., Tropical entrainment timescales inferred from stratospheric N_2O and CH_4 observations, *Geophys. Res. Lett.*, *25*, 2781-2784, 1998.

Hintsa, E. J. et al., Dehydration and denitrification in the Arctic polar vortex during the 1995-1996 winter, *Geophys. Res. Lett.*, *25*, 501-504, 1998.

Huebler, G., D. W. Fahey, K. K. Kelly, D. D. Montzka, M. A. Carroll, A. F. Tuck, L. E. Heidt, W. H. Pollock, G. L. Gregory, and J. F. Vedder, Redistribution of reactive odd nitrogen in the lower Arctic stratosphere, *Geophys. Res. Lett.*, *17*, 453-456, 1990.

Kawa S. R., D. W. Fahey, L. E. Heidt, W. H. Pollock, S. Solomon, D. E. Anderson, M. Loewenstein, M. H. Proffitt, J. J. Margitan, and K. R. Chan, Photochemical partitioning of the reactive nitrogen and chlorine reservoirs in the high-latitude stratosphere, *J. Geophys. Res.*, *97*, 7905-7923, 1992.

Keim, E. R. et al., Measurements of the NO_y-N_2O correlation in the lower stratosphere: Latitudinal and seasonal changes and model comparisons, *J. Geophys. Res.*, *102*, 13193-13212, 1997.

Knudsen, B. M. et al., Ozone depletion in and below the Arctic Vortex for 1997, *Geophys. Res. Lett.*, *25*, 627-630, 1998.

Kondo, Y. et al., NO_y-N_2O correlation inside the Arctic vortex in February 1997: Dynamical and chemical effects, *J. Geophys. Res.*, *104*, 8215-8224, 1999.

Loewenstein, M. et al., New observations of the NO_y/N_2O correlation in the lower stratosphere, *Geophys. Res. Lett.*, *20*, 2531-2534, 1993.

Manney, G. L., R. W. Zurek, A. O'Neill, and R. Swinbank, On the motion of air through the stratospheric polar vortex, *J. Atmos. Sci.*, *51*, 2973-2994, 1994.

Michelsen, H. A., G. L. Manney, M. R. Gunson, and R. Zander, Correlations of stratospheric abundances of NO_y, O_3, N_2O, and CH_4 derived from ATMOS measurements, *J. Geophys. Res.*, *25*, 2777-2780, 1998.

Nevison, C. D., and E. A. Holland, A reexamination of the impact of anthropogenically fixed nitrogen on atmospheric N_2O and the stratospheric O_3 layer, *J. Geophys. Res.*, *102*, 25519-25537, 1997.

Notholt, J., P. von der Gathen, and S. Peil, Heterogeneous conversion of HCl and $ClONO_2$ during the Arctic winter 1992/1993 initiating ozone depletion, *J. Geophys. Res.*, *100*, 11269-11274, 1995.

Oelhaf, H., G. et al., Correlative balloon measurements of the vertical distribution of N_2O, NO, NO_2, NO_3, HNO_3, N_2O_5, $ClONO_2$, and total reactive NO_y inside the polar vortex during SESAME, in Polar Stratospheric Ozone, edited by J. A. Pyle, et al., pp.175-178, Comm. of the Eur. Communities, Brussels, 1996.

Osterman, G. B., R. J. Salawitch, B. Sen, G. C. Toon, R. A. Stachnik, H. M. Pickett, J. J. Margitan, J.-F. Blavier, and D. B. Peterson, Balloon-borne measurements of stratospheric radicals and their precursors: Implications for the production and loss of ozone, *Geophys. Res. Lett.*, *24*, 1107-1110, 1997.

Plumb, R. A., and M. W. K. Ko, Interrelationships between mixing ratios of long-lived stratospheric constituents, *J. Geophys. Res.*, *97*, 10145-10156, 1992.

Rex, M. et al., Prolonged stratospheric ozone loss in the 1995/96 Arctic winter, *Nature*, *389*, 835-838, 1997.

Rex, M. et al., In-situ measurements of stratospheric ozone depletion rates in the Arctic winter 1991/92: A Lagrangian approach, *J. Geophys. Res.*, *103*, 5843-5853, 1998.

Rex, M. et al., Chemical ozone loss in the Arctic winter 1994/95 as determined by the Match technique, *J. Atmos. Chem.*, *35*, 35-59, 1999.

Rinsland, C. P., R. J. Salawitch, M. R. Gunson, S. Solomon, R. Zander, E. Mahieu, A. Goldman, M. J. Newchurch, F. W. Irion, and A. Y. Chang, Polar stratospheric descent of NO_y and CO and Arctic denitrification during winter 1992-93, *J. Geophys. Res.*, *104*, 1847-1861, 1999.

Roche, A. E., J. B. Kummer, J. L. Mergenthaler, R. W. Nightingale, W. G.

Uplinger, G. A. Ely, J. F. Potter, D. J. Wuebbels, P. S. Connel, and D. E. Kinnison, Observations of lower-stratospheric $ClONO_2$, HNO_3, and aerosol by the UARS CLAES experiment between January 1992 and April 1993, *J. Atmos. Sci.*, *51*, 2877-2902, 1994.

Rosenfield, J. E., P. A. Newman, and M. R. Schoeberl, Computations of diabatic descent in the stratospheric polar vortex, *J. Geophys. Res.*, *99*, 16677-16689, 1994.

Russell, J. M., III, C. B. Farmer, C. P. Rinsland, R. Zander, L. Froidvaux, G. C. Toon, B. Gao, J. Shaw, and M. Gunson, Measurements of odd nitrogen-compounds in the stratosphere by the ATMOS experiment on Spacelab-3, *J. Geophys. Res.*, *93*, 1718-1736, 1988.

Salawitch, R. J., G. P. Gobbi, S. C. Wofsy, and M. B. McElroy, Denitrification in the Antarctic stratosphere, *Nature*, *339*, 525-527, 1989.

Salawitch, R. J. et al., Loss of ozone in the Arctic vortex for the winter of 1989, *Geophys. Res. Lett.*, *17*, 561-564, 1990.

Salawitch, R. J. et al., Chemical loss of ozone in the Arctic polar vortex in the winter of 1991-1992, *Science*, *261*, 1146-1149, 1993.

Santee, M. L., W. G. Reed, J. W. Waters, L. Froidvaux, G. L. Manney, D. A. Flower, R. F. Jarnot, R. S. Harwood, and G. E. Peckham, Interhemispheric differences in polar stratospheric HNO_3, H_2O, ClO, and O_3, *Science*, *267*, 849-852, 1995.

Santee, M. L., A. Tabazadeh, G. L. Manney, R. J. Salawitch, L. Froidvaux, W. G. Read, and J. W. Waters, UARS Microwave Limb Sounder HNO_3 observations: Implications for Antarctic polar stratospheric clouds, *J. Geophys. Res.*, *103*, 13285-13313, 1998.

Sen, B., G. C. Toon, J. -F. Blavier, E. L. Fleming, and C. H. Jackman, Balloon-borne observations of midlatitude fluorine abundance, *J. Geophys. Res.*, *101*, 9045-9054, 1996.

Sen, B., G. C. Toon, G. B. Osterman, J. -F. Blavier, J. J. Margitan, and R. J. Salawitch, Measurements of reactive nitrogen in the stratosphere, *J. Geophys. Res.*, *103*, 3571-3585, 1998.

Toon G. C., The JPL MkIV interferometer, *Opt. and Photonic News*, *2*, 19-21, 1991.

Toon G. C., C. B. Farmer, L. L. Lowes, P. W. Schaper, J. F. Blavier, and R. H. Norton, Infrared aircraft measurements of stratospheric composition over Antarctica during September 1987, *J. Geophys. Res.*, *94*, 16571-16596, 1989.

Toon, G. C., C. B. Farmer, P. W. Schaper, L. L. Lowes, and R. H. Norton, Composition measurements of the 1989 Arctic winter stratosphere by airborne infrared solar absorption spectroscopy, *J. Geophys. Res.*, *97*, 7939-7961, 1992.

Toon, G. C. et al., Comparison of MkIV balloon and ER-2 aircraft measurements of atmospheric trace gases, *J. Geophys. Res.*, this issue.

Toon, O. B., P. Hamill, R. P. Turco, and J. Pinto, Condensation of HNO3 and HCl in the winter polar stratospheres, *Geophys. Res. Lett.*, *13*, 1284-1287, 1986.

Waibel, A. E., T. Peter, K. S Carslaw, H. Oelhaf, G. Wetzel, P. J. Crutzen, U. Poschl, A. Tsias, E. Reimer, and H. Fischer, Arctic ozone loss due to denitrification, *Science*, *283*, 2064-2069, 1999.

Waters, J. W., L. Froidevaux, W. G. Read, G. L. Manney, L. S. Elson, D. A. Flower, R. F. Jarnot, and R. S. Harwood, Stratospheric ClO and ozone from the Microwave Limb Sounder on the Upper Atmosphere Research Satellite, *Nature*, *362*, 597-602, 1993.

Waugh, D. W. et al., Mixing of vortex air into middle latitudes as revealed by tracer-tracer scatterplots, *J. Geophys. Res.*, *102*, 13119-13134, 1997.

Webster, C. R., R. D. May, D. W. Toohey, L. M. Avallone, J. G. Anderson, P. Newman, L. Lait, M. R. Schoeberl, J. W. Elkins, and K. R. Chan, Chlorine chemistry on polar stratospheric cloud particles in the Arctic winter, *Science*, *261*, 1130-1133, 1993.

Webster, C. R., R. D. May, C. A. Trimble, R. G. Chave, and J. Kendall, Aircraft (ER-2) laser infrared absorption spectrometer (ALIAS) for in situ stratospheric measurements of HCl, N_2O, CH_4, NO_2 and HNO_3, *Appl. Opt.*, *33*, 454-472, 1994.

J.-F. Blavier, A. Y. Chang, M. R. Gunson, R. L. Herman, F. W. Irion, J. J. Margitan, R. D. May, E. J. Moyer, G. B. Osterman, M. Rex, R. J. Salawitch, D. C. Scott, B. Sen, G. C. Toon, C. R. Webster, Jet Propulsion Laboratory, California Institute of Technology, 4800 Oak Grove Drive, Pasadena, CA 91109-8009.

T. P. Bui, Ames Research Center, National Aeronautics and Space Administration, Moffett Field, CA 94035.

S. Donnelly, D. W. Fahey, R. S. Gao, E. Keim, J. Neuman, Aeronomy Laboratory, National Oceanic and Atmospheric Administration, Boulder, CO 80303.

C. P. Rinsland, Langley Research Center, National Aeronautics and Space Administration, Mail Stop 401A, Hampton, VA 23681-2199.

(Received December 31, 1998; revised June 1, 1999; accepted June 23, 1999.)

Arctic and Antarctic ozone layer observations: chemical and dynamical aspects of variability and long-term changes in the polar stratosphere[1]

Markus Rex, Klaus Dethloff, Dörthe Handorf,
Andreas Herber, Ralph Lehmann, Roland Neuber,
Justus Notholt, Annette Rinke, Peter von der Gathen,
Antje Weisheimer & Hartwig Gernandt

The altitude dependent variability of ozone in the polar stratosphere is regularly observed by balloon-borne ozonesonde observations at Neumayer Station (70°S) in the Antarctic and at Koldewey Station (79°N) in the Arctic. The reasons for observed seasonal and interannual variability and long-term changes are discussed. Differences between the hemispheres are identified and discussed in light of differing dynamical and chemical conditions. Since the mid-1980s, rapid chemical ozone loss has been recorded in the lower Antarctic stratosphere during the spring season. Using coordinated ozone soundings in some Arctic winters, similar chemical ozone loss rates have been detected related to periods of low temperatures. The currently observed cooling trend of the stratosphere, potentially caused by the increase of anthropogenic greenhouse gases, may further strengthen chemical ozone removal in the Arctic. However, the role of internal climate oscillations in observed temperature trends is still uncertain. First results of a 10 000 year integration of a low order climate model indicate significant internal climate variability, on decadal time scales, that may alter the effect of increasing levels of greenhouse gases in the polar stratosphere.

M. Rex, K. Dethloff, D. Handorf, A. Herber, R. Lehmann, R. Neuber, J. Notholt, A. Rinke, P. von der Gathen, A. Weisheimer & H. Gernandt, Alfred Wegener Institute, Box 60 01 49, D-14401 Potsdam, Germany.

Since the mechanisms of the formation of the Antarctic ozone hole were discovered, a question of prime concern has been whether comparable chemical losses of ozone can also occur in the Arctic. During winter/spring, Arctic stratospheric air masses regularly drift above mid-latitudes. Any considerable ozone depletion in these air masses would influence the densely populated areas of North America, Europe and northern Asia and could have severe consequences for the biosphere in these regions (van der Leun 1998).

The rapid ozone loss in the polar lower stratosphere is due to chlorine and bromine catalysed reaction cycles (WMO 1999). Nearly all of the chlorine and a substantial fraction of the bromine in the stratosphere originates from the breakdown of man-made chlorofluorocarbons (CFCs) and halons (WMO 1999). The most effective ozone destruction cycles involve active chlorine radicals and can proceed only if sunlight is present. However, in mid- and low latitude stratospheric conditions a large fraction of the chlorine is in the form of passive compounds that are not effective in destroying ozone. The ozone destroying effect of enhanced chlorine levels in mid-latitudes is therefore limited, though probably an important reason for the observed negative trend of the thickness of the ozone layer in mid-latitudes (WMO 1999).

---

[1] This paper was originally submitted in connection with the International Symposium on Polar Aspects of Global Change, Tromsø, Norway, 24–28 August 1998. – The Editor.

At polar latitudes the particular meteorological conditions can lead to a situation in which nearly all available chlorine is in its active form and ozone can be destroyed very rapidly. During polar winter the stratospheric temperatures fall and large low pressure systems form over the polar regions. These so-called polar vortices are encompassed by strong jet streams that isolate the air masses inside the vortices from air at mid-latitudes. Breaking atmospheric waves apply a drag on the jet stream

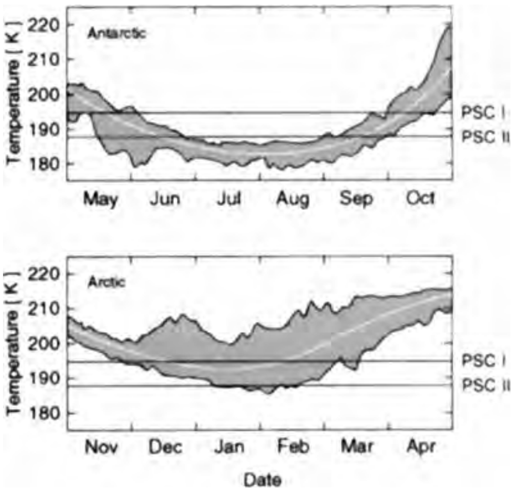

Fig. 1. Wintertime variation of the daily hemispheric minimum temperatures in 50 hPa based on NMC analysis between 1978 and 1994. The shaded area gives the spread of the curves for the individual years. The approximate threshold temperatures for PSC I and PSC II existence are marked by horizontal lines. (Reproduced from WMO 1995.)

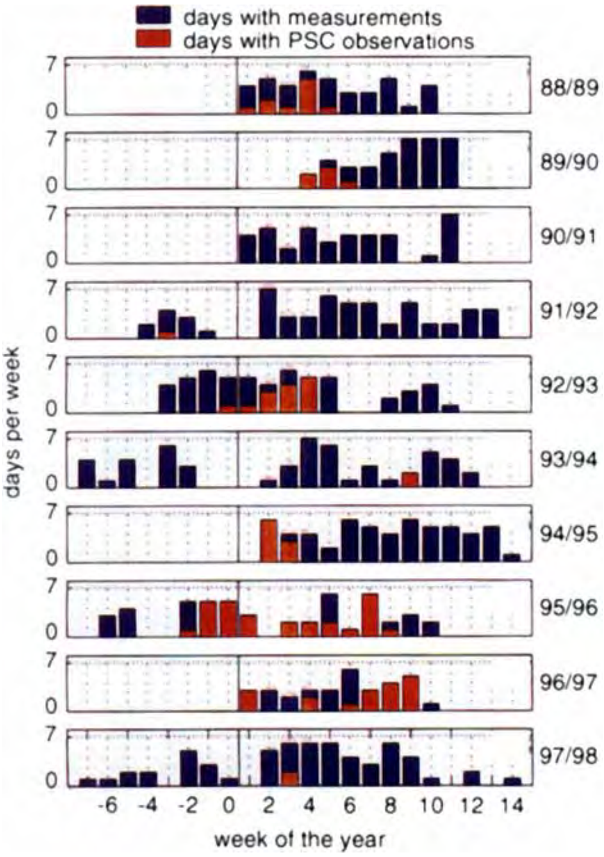

Fig. 2. Frequency of PSC I observations above Spitsbergen, as detected by a multi-wavelength lidar installed at the NDSC Station in Ny-Ålesund (78.9° N, 11.9° E).

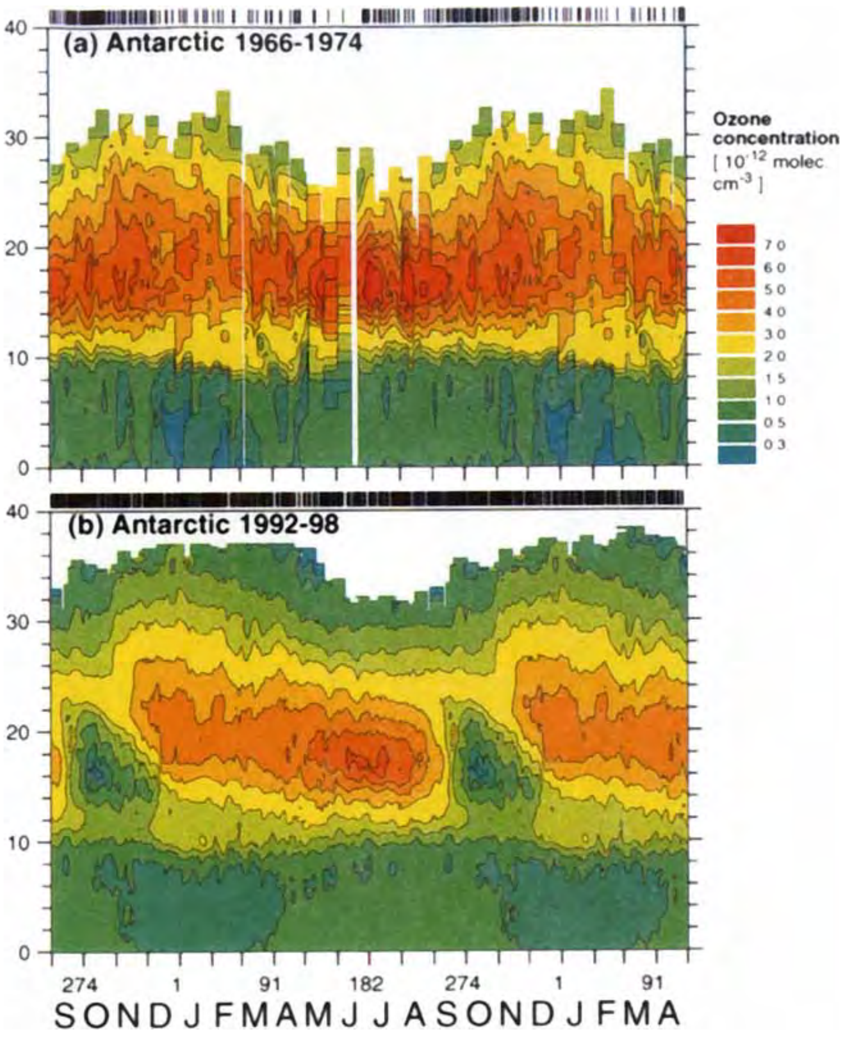

Fig. 3 (left). (a) Altitude-time section of the mean seasonal variation of the ozone concentration above Syowa Station (69.0° S, 39.4° E) between 1966 and 1974. The time axis denotes the day of the year, with the initial letters of the months also given. The months September to April are repeated on both sides of the diagram. 155 ozonesondes contributed to the plot. Each sonde is marked by a vertical black bar at the upper edge of the figure. (b) Altitude-time section of the mean seasonal variation of the ozone concentration above Neumayer Station (70.6° S, 8.2° E) between 1992 and 1998. 492 ozonesondes contributed to (b); all other information is the same as for (a).

Fig. 4 (below). Altitude-time section of the mean seasonal variation of the ozone concentration above Koldewey Station (78.9° N, 11.9° E) between 1992 and 1998. The time axis is shifted by six months compared to Fig 3: otherwise the information is the same. 693 ozone sondes contributed to the plot. For colour key, see Fig. 3.

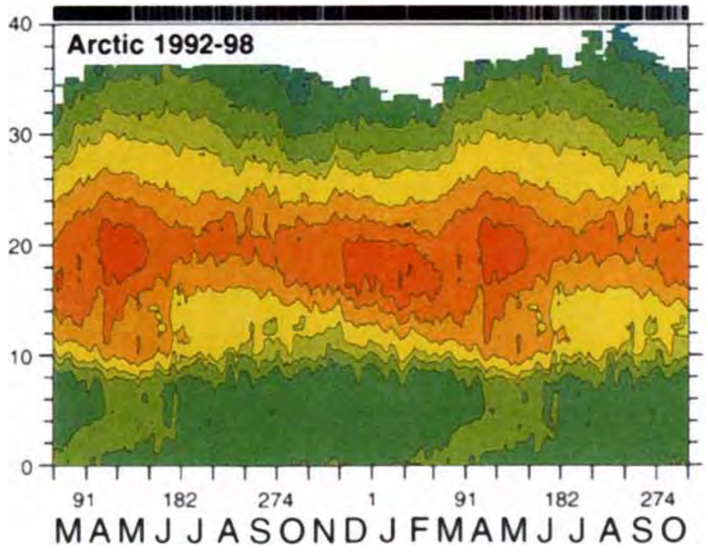

and, against the purely geostrophic motion of the air, allow the air to move slowly poleward. This process leads to subsidence and diabatic cooling of air inside the polar vortex. The degree of subsidence in a given winter is controlled by the respective wave activity. A stronger wave drag leads to higher temperatures inside the vortex, larger diabatic cooling rates and faster subsidence (Holton 1997).

Dramatic ozone losses can take place in the isolated polar vortices. When temperatures fall below approximately −78°C (at 475 K), condensed aerosol particles consisting of mixtures of H_2O, H_2SO_4 and HNO_3 may form Type I Polar Stratospheric Clouds (PSC I). Rapid heterogeneous reactions on the surface of PSC I particles convert passive chlorine compounds into active chlorine radicals. The most effective mechanism to deactivate the chlorine radicals once they have formed requires the presence of gas phase HNO_3. However, when temperatures during the polar winter fall below ca. −85°C (at 475 K), the PSC I particles quickly take up water ice, grow much larger and form Type II PSCs. These particles can sediment with considerable velocities and can irreversibly remove water and HNO_3 from the stratosphere. In these so-called denitrified air masses, rapid ozone loss can proceed for longer periods of time, leading to more severe depletion (e.g. Rex et al. 1997; Waibel et al. 1999).

The wave activity in the Arctic is much stronger than in the Antarctic, and the Arctic polar vortex is less stable, warmer and breaks up earlier. Temperatures and vortex strength show a pronounced year to year variability (e.g. Pawson et al. 1995). In some Arctic winters the vortex breaks up in midwinter, causing dramatic increases in polar temperatures in those years (e.g. Scherhag 1952; Naujokat 1992). Figure 1 shows the development of the minimum temperature for both hemispheres. In the Antarctic, the temperatures fall below the PSC I and PSC II thresholds over many weeks in each winter. In the Arctic, PSC I temperatures are reached in most of the winters, but the length of the PSC I period and the area covered by PSC I temperatures is variable. PSC II temperatures are rarely reached in the Arctic. However, during the extremely cold Arctic winter of 1995/96, minimum temperatures fell below the PSC II threshold for about three weeks (Naujokat & Pawson 1996).

Figure 2 shows the frequency of PSC I observations above Spitsbergen, as detected by a multi-wavelength lidar installed at the NDSC Station in Ny Ålesund (78.9° N, 11.9° E). As this site is not directly influenced by orographical effects, the observation statistic can be regarded as representative of the inner stratospheric vortex. Figure 2 reveals PSC "poor" winters in 1990/91, 1991/92, 1993/94 and 1997/98. Otherwise the occurrence of PSCs is highly variable, including periods when every measurement detected PSCs as during the cold periods of the winters of 1995/96 and 1996/97, as well as others, when PSCs occurred transiently, as in January 1989 and 1993.

Ozone observations in the Arctic and Antarctic

Ozone profiles

We have used balloon-borne electrochemical ozonesondes to measure ozone profiles in the Antarctic since 1985 and in the Arctic since 1988. The ozone sensors are launched with standard radiosondes. During ascent up to 30–38 km altitude, in situ measurements of ozone partial pressure and meteorological parameters are transmitted on-line. Ozone concentrations or ozone mixing ratios can be calculated from the measurements with a vertical resolution of ca. 150 m. Ozonesondes are currently the only instruments capable of measuring profiles of ozone with detailed vertical resolution throughout the year (including polar night and polar day) and during nearly all weather conditions. Between 1985 and early 1992 the measurements in the Antarctic were taken at Georg Forster Station (70.8° S, 11.8° E) (Gernandt et al. 1989). In 1992 the soundings have been moved to Neumayer Station (70.6° S, 8.2° E) (Gernandt et al. 1996). For comparison we also show measurements from Syowa Station (69.0° S, 39.4° E) between 1966 and 1974 (Gernandt et al. 1996). Due to the similar latitude of all three stations and the high zonal symmetry of the mean ozone field in the Antarctic the three data sets can be compared directly. The soundings in the Arctic have been made at Koldewey Station (78.9° N, 11.9° E) (Gernandt et al. 1996). In winter the measurements of all stations reflect the conditions inside the polar vortex.

Figures 3 and 4 show vertical sections of the ozone concentrations in the Antarctic and Arctic throughout the year. The ozone concentrations in the Antarctic are plotted for two different time periods: (a) shows the measurements from Syowa Station between 1967 and 1979, i.e. before the Antarctic ozone hole formed; (b) shows the measurements at Neumayer Station between 1992 and 1998.

In both hemispheres the stratospheric ozone concentrations increase below about 24 km after the formation of the respective polar vortex in fall (about September in the Arctic, March in the Antarctic). This is caused by the diabatic subsidence of air inside the vortex. In the lower stratosphere ozone mixing ratios systematically increase with altitude. Air masses with higher ozone mixing ratios descend and compression leads to higher ozone concentrations. This effect is limited to the region below ca. 24 km, since the vertical gradient of ozone mixing ratios is weak above this altitude.

In the Antarctic soundings from Neumayer Station (Fig. 3b) the ozone concentrations in the vertical region of the ozone maximum dramatically drop during the months August to December. The older data from Syowa Station (Fig. 3a) show no decrease in the ozone concentrations during these months. Figure 5 shows a number of recent profiles from these months. The ozone concentrations drop below the detection limit of the sonde in a broad vertical region. This effect, clearly caused by halogen catalysed ozone destruction (WMO 1999), is one of the strongest anthropogenic signals in the atmosphere. A profile from the mid-1980s is also shown in Fig. 5. In a smaller vertical region the ozone was nearly completely destroyed even in this early profile. Since then a further decrease of ozone concentrations occurred mainly at the upper and lower edge of the depleted region.

In the Northern Hemisphere no comparable decrease of the ozone concentrations in late winter is discernible. Instead, averaged over many years, the concentrations continue to increase until the polar vortex breaks up in spring. At this time air from mid-latitudes, where subsidence is weak and ozone concentrations are therefore lower, spreads into the polar region contributing to the observed decrease in the ozone concentrations during May to July. Part of this decrease may also be due to natural slow photochemical ozone destruction.

Figure 6a shows ozone profiles taken in the Arctic during late March of different years. The profiles from 1995, 1996 and 1997 show considerable ozone deficits in the region of the ozone maximum. In these years the Arctic winter was exceptionally cold. However, in the Arctic the dynamically induced variability of the ozone layer is too large to allow a straightforward interpretation of these deficits in terms of chemical ozone loss. Figure 6b shows one example of a dynamically driven ozone fluctuation above Koldewey Station. The short-term drop in the ozone concentration and subsequent recovery is caused by advection of air masses with different histories and is a common natural phenomenon in the Arctic. Given the large dynamical variability, more sophisticated approaches have to be used to detect and quantify chemically induced ozone loss in the Arctic. We will show that substantial chemically induced ozone loss did occur in recent Arctic winters and that even in 1992 some chemical ozone loss occurred which is not apparent in Fig. 6a.

Ozone column densities

A vertical integration of the ozonesonde profiles allows the calculation of ozone column densities. For the integration the ozone mixing ratios above the burst level of the balloon is assumed to be constant. To reduce the error introduced by this assumption, only ozone profiles that reached at least 25 km altitude have been used for the calculations of column densities. The estimated residual ozone above this level is generally smaller than 10% of the total ozone column.

Figures 7 and 8 show the variation of the ozone column density for different years above Neumayer Station, Antarctica, and Koldewey Station, the Arctic, respectively. In the Arctic (Fig. 8) the ozone column density reaches its maximum in spring. The general increase of the ozone column during winter is due to subsidence of air in the polar vortex. Air with high ozone mixing ratios replaces the subsided air masses at high altitudes, whereas air with lower ozone mixing ratios leaves the polar vortex in its lowest parts. The large year-to-year variability of the column densities in spring is mainly caused by the varying times of the vortex break-up in different years. After the break-up of the vortex, mid-latitude air masses with lower ozone column densities mix into the Arctic. Extremely high column densities in March/April were only reached in years when the vortex still existed during these months. In the winters of 1995, 1996 and 1997, the ozone column densities remained at low values, although the vortex still existed during March. During January to March

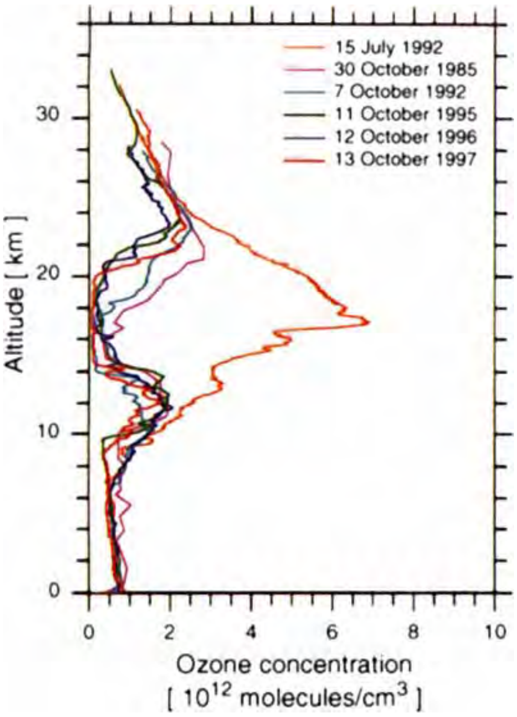

Fig. 5 (left). Ozone profiles measured during October at Georg Forster Station in 1985 and Neumayer Station in 1992–97. One early winter profile, July 1992, is also plotted.

Fig. 6 (below). Ozone profiles measured at Koldewey Station (78.9° N, 11.9° E): (a) profiles measured in late March during four different years; (b) profiles measured within four days in 1992.

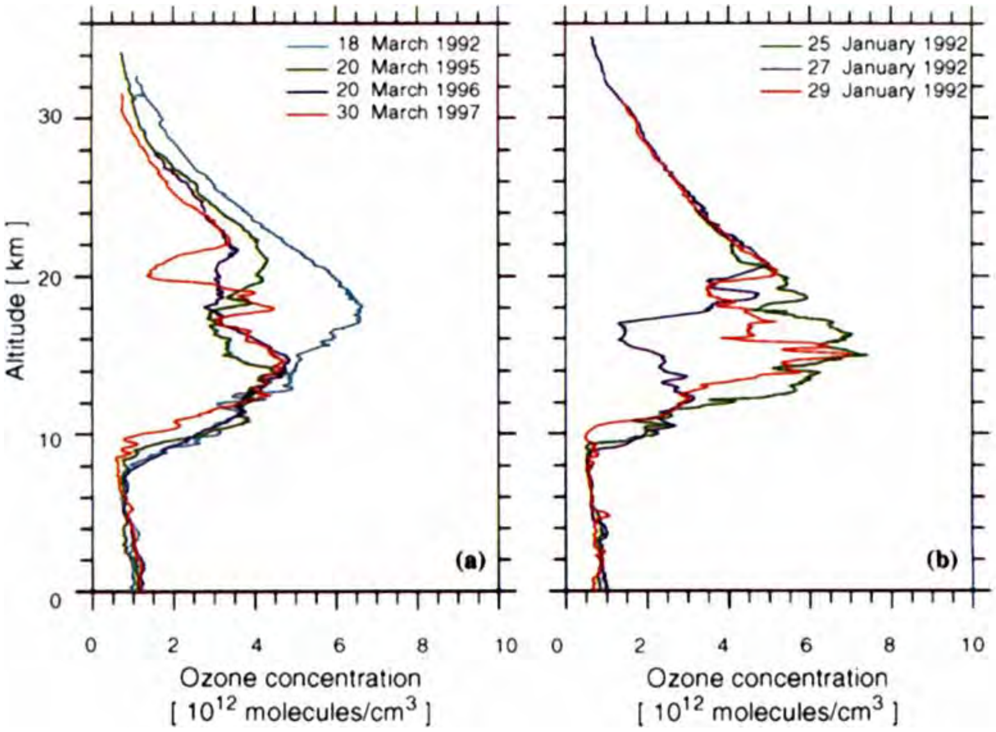

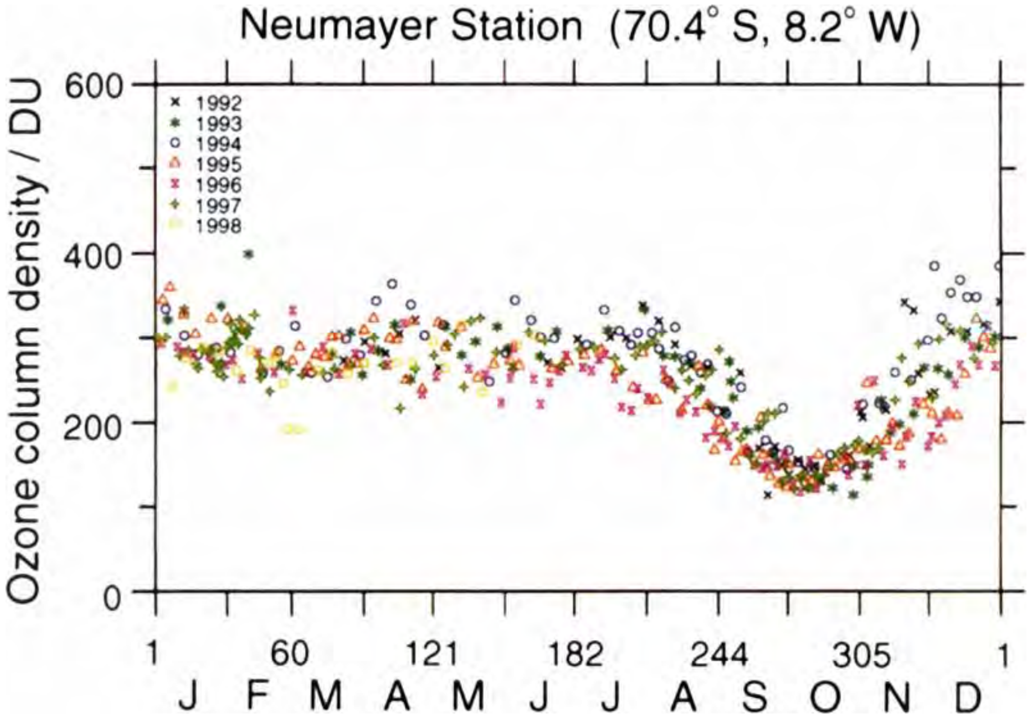

Fig. 7. Neumayer Station (70.6° S, 8.2° E). Data from the years from 1992 to 1998 are marked with different symbols and colours (see key). The time axis denotes the day of the year and the initial letters of the months are also given.

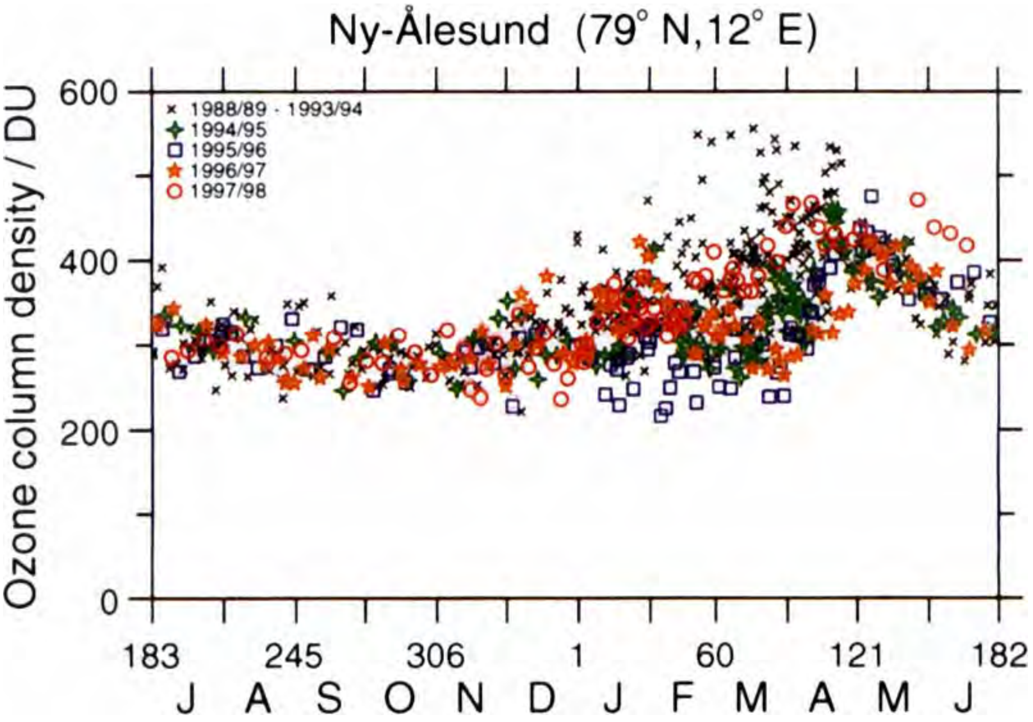

Fig. 8. Seasonal variation of the ozone column density above Koldewey Station (78.9° N, 11.9° E). See caption with Fig. 7.

1996, the lowest ozone column densities ever measured above Koldewey Station were reported. Possible explanations for the low ozone column densities during these years are: a weak wave activity connected with less subsidence in the polar vortex; chemical destruction of ozone; or a combination of both. The cold stable vortices of these years indicate that the wave activity was indeed weak. So it is reasonable to attribute a part of the unusually low ozone column densities during spring to a weaker diabatic circulation in these years. This is particularly true for the winter 1996/97, when the wave activity was exceptionally weak. However, we will demonstrate that a considerable fraction of the negative ozone anomaly in these Arctic springs was due to extensive chemical loss of ozone.

In the Antarctic no increase of the ozone column during winter is observed. This may partly be due to early chemical ozone loss, but is also caused by the weaker wave activity in the Southern Hemisphere resulting in a weaker diabatic circulation and less transport of ozone into the polar region during the southern winter. In late winter and spring rapid chemical destruction of ozone leads to a sharp drop in the ozone column densities. During these periods ozone column densities as low as 130 Dobson Units (1 DU = $2.69 \cdot 10^6\,\mathrm{cm}^{-2}$) are common.

Chemical ozone loss in the Arctic

Since the large variability of the Arctic ozone layer makes it difficult to detect chemical ozone loss, we developed the so-called Match approach. The technique is based on the statistical analysis of a large number of "matches." A match is defined as a pair of ozonesonde measurements, where both sondes probed the same air parcel at different times as it passed over their respective stations. The basic idea of the Match approach is illustrated in Fig. 9. To identify the matches, calculated air parcel trajectories that take into account modelled diabatic cooling rates were used to track the motion of the air parcels between the measurements. The approach can be applied in two ways: (1) for post campaign analysis of a very large number of uncoordinated ozonesonde soundings by selecting soundings which are linked by chance based on calculated trajectories (von der Gathen et al. 1995; Rex et al. 1998); or (2) much more effectively as a joint effort by a large number of stations that perform coordinated ozonesonde launches during a "Match campaign" (Rex et al. 1997; Rex et al. 1999; Schulz et al. 2000, in press). The analysis includes various quality controls on ozonesonde data as well as trajectory data. The main advantage of this Lagrangian approach is that chemical and dynamical effects can be separated to a high degree. The ability of the Match technique to account for dynamical changes in ozone without introducing a systematic bias is demonstrated by a statistical analysis that shows that no inferred chemical loss of ozone occurs during periods of darkness along the trajectories (Rex et al. 1998; Rex et al. 1999). Match results, based on the coordinated launches of 600 to 1400 ozonesondes per winter, are currently available for five winters between 1991/92 and 1997/98. A map showing the locations of the participating stations is shown in Fig. 9.

To derive the spatial and seasonal variation of the ozone loss rate, various subsets of matches can be analysed. Figure 10 shows an overview over the chemical ozone loss rates measured with the Match technique during specific Arctic winters. Additionally the areas of the Northern Hemisphere were temperatures were cold enough to allow PSCs to exist are indicated. Chemical ozone loss was detected in all winters other than the relatively warm winter of 1997/98, when the measured rates of chemical loss are hardly significant. In all instances periods of significant chemical ozone loss rates were initiated by periods with temperatures below the PSC threshold. Usually the ozone loss stopped about two weeks after temperatures warmed above the PSC threshold. The winter 1995/96 is an exception and is discussed below. This pattern and the fact that the ozone loss occurs only in sunlight is in qualitative agreement with the current theory.

Figure 11 shows a vertical section of the ozone loss rates measured during January to March 1995. At all levels the observed ozone loss periods are closely related with periods of possible PSC formation. The low loss rates in early January are due to a lack of sunlight close to mid-winter. During this winter, maximum local losses of approximately 60% occurred at ca. 20 km altitude. Larger local ozone losses (approximately 65%) have been found in the colder winter of 1995/96. Chemical loss rates in the ozone column reached about 2.5 DU per day during two periods. The accumulated loss in the ozone column is 127 ± 14 DU (ca. 30%). The observed local ozone loss rates are similar to the loss rates observed over Antarctica (WMO 1999). The main differences between both hemispheres are the longer persistence and the larger vertical extent of the ozone loss in the Antarctic.

Although the qualitative pattern of the ozone loss rates agrees very well with model calculations, the rate of the measured ozone loss is considerably larger than found by models (Becker et al. 1998, 2000). This discrepancy reveals an important inability of chemical models to quantitatively reproduce the observed ozone losses and indicates that further research is needed to improve our understanding of the ozone loss mechanisms.

After the extremely cold Arctic winter of 1995/96, the ozone loss in a thin vertical layer continued long after temperatures warmed above the PSC threshold, causing the largest amounts of local ozone loss ever observed in the Arctic. Model studies and trace gas measurements suggest that this was probably due to denitrification, causing Antarctic-like conditions in these Arctic air masses (Rex et al. 1997). This shows how close Arctic conditions are to those in the Antarctic and that only slightly lower temperatures in the Arctic can lead to dramatic ozone losses there.

Future of the ozone layer

External effects

Due to the effective regulations of the CFC production the increase in stratospheric chlorine loading flattens. During the coming decades the large reservoir of CFCs in the atmosphere will continue to maintain high levels of stratospheric chlorine loading. Models predict a slow decrease of stratospheric chlorine loading, reaching "pre-ozone hole concentrations" around the year 2050 (WMO 1999). However, the results of the Match experiments show how sensitive the Arctic ozone loss is to small changes in stratospheric temperatures. During the next decades the effect of year-to-year variations of the Arctic stratospheric temperatures will have a far greater effect on the ozone loss in a given year than the slow variation of the total chlorine loading. Model calculations and observations indicate that climate changes connected with increased greenhouse forcing may lead to a cooling trend in the stratosphere, coupled with a trend towards more stable Arctic vortices (WMO 1999). This could lead to larger Arctic ozone losses in the near future and may substantially delay the recovery of the ozone layer (Shindell et al. 1998; Waibel et al. 1999).

During the next decades strong volcanic eruptions that lead to an increase in the stratospheric aerosol loading could increase the ozone loss by the enhanced chlorine loading (Solomon et al. 1996). Significant depletions of the ozone layer have been observed after the eruptions of El Chichon (1982) and Mt. Pinatubo (1991) (e.g. Rodriguez et al. 1994).

Internal variability

Predictions of the future of the ozone layer are complicated by the fact that observed trends of temperature and vortex strength in the Arctic can be attributed not only to changes in response to greenhouse gas forcing but is also possible due to oscillations as part of natural decadal climate changes. There is growing evidence that the Arctic stratospheric polar vortex is implicated in the long-term oscillations of Earth's climate. Perlwitz & Graf (1995), for example, showed a strong coupling between the strength of the Arctic polar vortex and the North Atlantic Oscillation. It is crucial to know the influence of internal long-term climate variability of Earth's climate before reliable predictions for the future can be made.

An approach to study the causes and physical mechanisms of long-term natural climate variability was developed by Dethloff et al. (1998). A nonlinear atmosphere-like dynamical system with a sparse horizontal resolution including orographical and thermal forcing in a long planetary wave and its interaction with both a baroclinic wave and the zonal flow has been constructed and integrated over 10 000 years. This long-term integration allows the determination of the dominating modes of atmospheric variability on decadal time scales with high statistical significance. Spectra of the prognostic variables show well-pronounced maxima at the decadal time scale, statistically significant at the 95% confidence level. An extension of this approach to a coupled atmosphere–ocean ice model of moderate complexity is underway.

The current poor knowledge of the complex nonlinear interactions in the tropospheric–stratospheric climate system coupled with ocean and sea ice makes assessment of future atmospheric trends difficult. The unknown long-term natural climate variability over decadal and centennial time scales

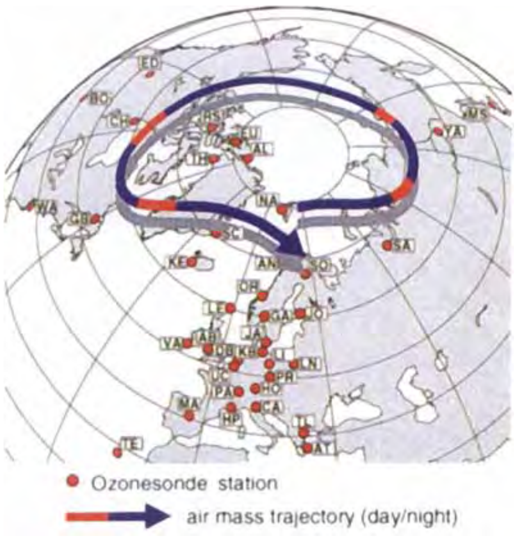
ED
BO
CH
RS
EU
AL
TH
MS
YA
WA
GB
NA
SC
SA
KE
AN
SO
OR
LE
GA
JO
JA
VA
AB
DB
KH
LI
LN
UC
PR
PA
HO
MA
CA
HP
TL
TE
AT
Ozonesonde station
air mass trajectory (day/night)

Fig. 9. Illustration of the Match technique and map of the participating ozonesonde stations.

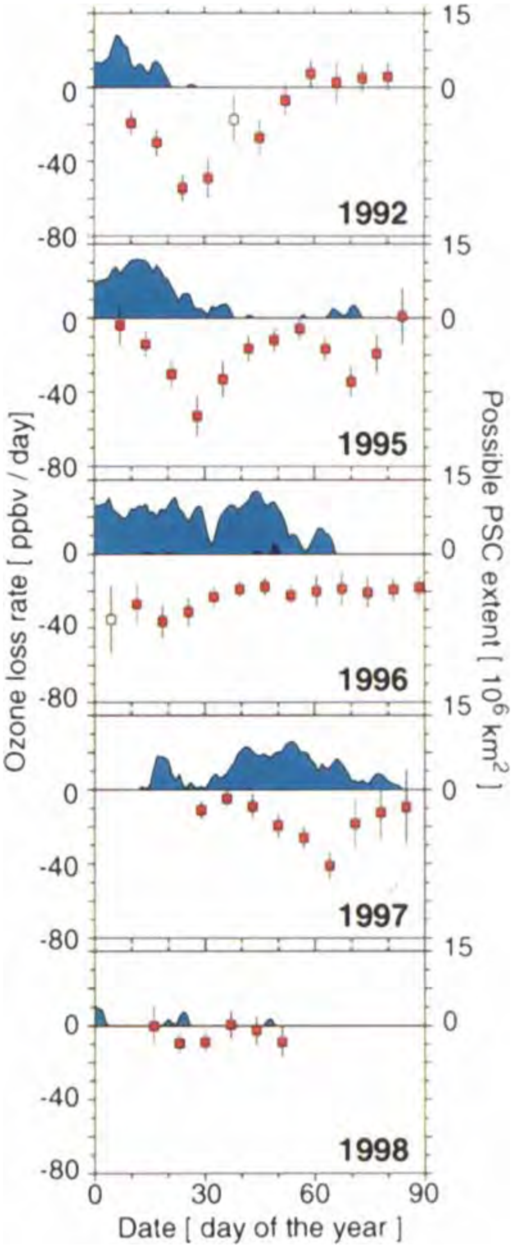

Fig. 10. Overview of the results of the different Match campaigns. The red points give the variation of the ozone loss rates through the different winters. The blue shaded curves give the potential PSC extent. Adapted from Rex et al. (1997, 1998, 1999) and Schulz et al. (2000).

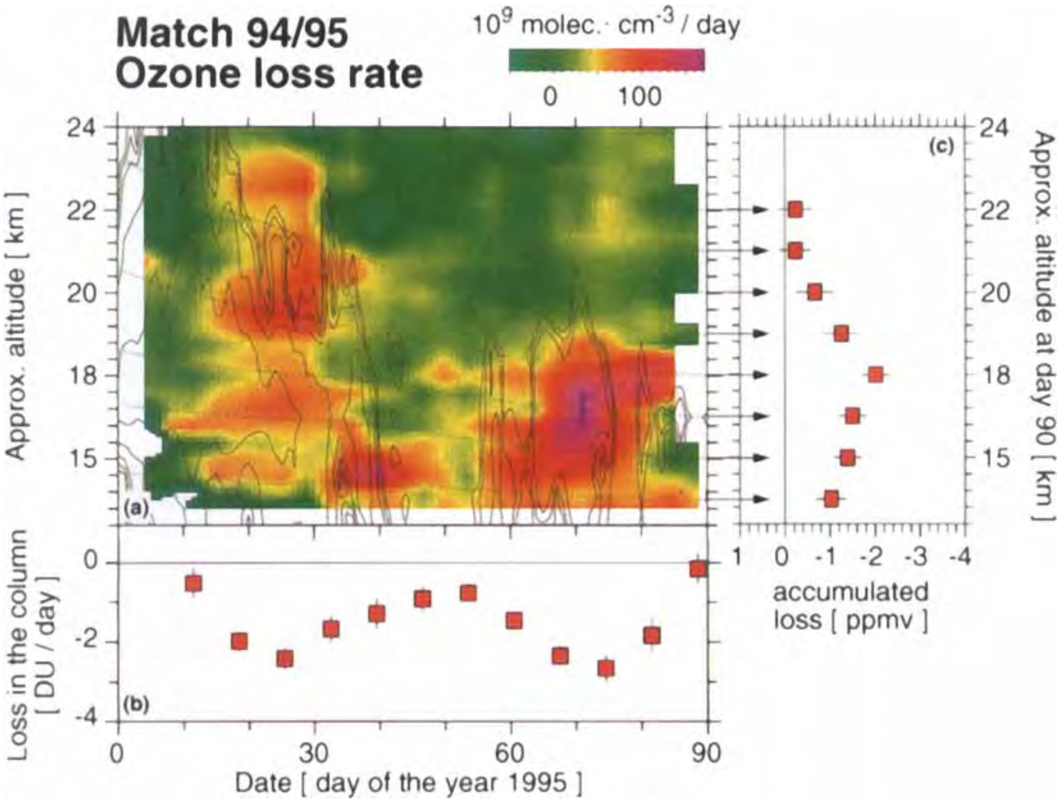

Fig. 11. (a) Altitude time section of the ozone loss rate during January to March 1995. 1470 matches contributed to the plot. The 0.3, 0.7 and 1.5 · 106 km^2 isolines of the potential PSC extent are plotted as thin black lines. The dotted lines give the descending motion of air masses through the plotted section. (b) Loss rates of the ozone column calculated by vertically integrating the local loss rates. The accumulated loss of the ozone column is 127 ± 14 DU (ca. 30%). (c) Accumulated ozone losses in subsiding layers of air as calculated by integrating the local loss rates along the dotted lines in panel (a).

may exert a significant impact on climate trends independent from greenhouse gases or coupled with them and has the potential for unexpected future changes.

References

Becker, G., Müller, R., McKenna, D. S., Rex, M. & Carslaw, K. S. 1998: Ozone loss rates in the Arctic stratosphere in the winter 1991/92: model calculations compared with Match results. *Geophys. Res. Lett. 25*, 4325–4328.

Becker, G., Müller, R., McKenna, D. S., Rex, M., Carslaw, K. S. & Oelhaf, H. 2000: Ozone loss rates in the Arctic stratosphere in the winter 1994/95: model calculations compared with Match results. *J. Geophys Res. 105(D12)*, 15175–15184.

Dethloff, K., Weisheimer, A., Rinke, A., Handorf, D., Kurgansky, M. V., Jansen, W., Maass, P. & Hupfer, P. 1998: Climate variability in a nonlinear atmosphere-like dynamical system. *J. Geophys. Res. 103(D20)*, 25957–25966.

Farman, J. C., Gardiner, B. G. & Shanklin, J. D. 1985: Large losses of total ozone in Antarctica reveal seasonal ClOx/NOx interaction. *Nature 315*, 207–210.

Gernandt, H., Gloede, P., Feister, U., Peters, G. & Thees, B. 1989: Vertical distributions of ozone in the lower stratosphere over Antarctica and their relations to the spring depletion. *Planet. Space Sci. 37(8)*, 915–933.

Gernandt, H., Herber, A., von der Gathen, P., Rex, M., Rinke, A., Wessel, S. & Kaneto, S. 1996: Variability of ozone and aerosols in the polar atmosphere. *Mem. Natl. Inst. Polar Res. 51*, 189–215.

Holton, J. 1997: Middle atmosphere dynamics. In G. Brasseur (ed.): *The role of the stratosphere in the climate system. NATO ASI Series.* Pp. 7–46. Hamburg: Springer.

Naujokat, B. 1992: Stratosphärenerwärmung: synoptik. (Stratospheric warming: synposis.) *Promet 2–4*, 81–89.

Naujokat, B. & Pawson, S. 1996: The cold stratospheric winters 1994/95 and 1995/96. *Geophys. Res. Lett. 23*, 3703–3706.

Pawson, S., Naujokat, B. & Labitzke, K. 1995: On the polar stratospheric cloud formation potential of the northern stratosphere. *J. Geophys. Res. 100(D11)*, 23215–23225.

Perlwitz, J. & Graf, H.-F. 1995: The statistical connection between tropospheric and stratospheric circulation of the Northern Hemisphere in winter. *J. Climate 8*, 2281–2295.

Rex, M. & 23 others, 1997: Prolonged stratospheric ozone loss in the 1995-96 Arctic winter. *Nature 389*, 835–838.

Rex, M. & 18 others, 1998: In-situ measurements of stratospheric ozone depletion rates in the Arctic winter 1991/92: a Lagrangian approach. *J. Geophys. Res. 103(D5)*, 5843–5853.

Rex, M. & 24 others, 1999: Chemical ozone loss in the Arctic winter 1994/95 as determined by the Match technique. *J. Atmos. Chem. 32*, 35–59.

Rodriguez, J. M., Ko, M. K. W., Sze, N. D., Heisey, C. W., Yue, G. K. & McCormick, M. P. 1994: Ozone response to enhanced heterogeneous processing after the eruption of Mt. Pinatubo. *Geophys. Res. Lett. 21*, 209–212.

Scherhag, R. 1952: Die explosionsartige Stratosphärenerwärmung des Spätwinters 1951–52. (The explosive warming of the stratosphere in late winter 1951–52.) *Ber. Deut. Wetterdienst 38*, 51–36.

Schulz, A. & 33 others, 2000: Match observations in the Arctic winter 1996/97: high stratospheric ozone loss rates correlate with low temperatures deep inside the polar vortex. *Geophys. Res. Lett. 27*, 205–208.

Schulz, A. & 40 others, in press: Match observations in the Arctic winter 1997/98 and 1998/99. *J. Geophys. Res.*

Shindell, D. T., Rind, D. & Lonergan, P. 1998: Increased polar stratospheric ozone losses and delayed eventual recovery owing to increasing greenhouse gas concentrations. *Nature 392*, 589.

Solomon, S., Portmann, R. W., Garcia, R. R., Thomason, L. W., Poole, L. R. & McCormick, M. P. 1996: The role of aerosol variations in anthropogenic ozone depletion at northern mid-latitudes. *J. Geophys. Res. 101(D3)*, 6713–6727.

van der Leun, J. C., Tang, X. & Tevini, M. 1998: Environmental effects of ozone depletion: 1998 assessment, *J. Photochem. Photobiol. B, Biol. 46*, 1–4.

von der Gathen, P. & 14 others, 1995: Observational evidence for chemical ozone depletion over the Arctic winter 1991–92. *Nature 375*, 131–134.

Waibel, A. E., Peter, T., Carslaw, K. S., Oelhaf, H., Wetzel, G., Crutzen, P. J., Poschl, U., Tsias, A., Reimer, E., Fischer, H. 1999: Arctic ozone loss due to denitrification. *Science 283*, 2046–2069.

WMO (World Meteorological Organization) 1995: *Scientific Assessment of ozone depletion: 1994*. Geneva: WMO.

WMO 1999: *Scientific assessment of ozone depletion: 1998*. Geneva: WMO.

JOURNAL OF GEOPHYSICAL RESEARCH, VOL. 107, NO. D20, 8276, doi:10.1029/2001JD000533, 2002

Chemical depletion of Arctic ozone in winter 1999/2000

M. Rex,[1] R. J. Salawitch,[2] N. R. P. Harris,[3] P. von der Gathen,[1] G. O. Braathen,[4]
A. Schulz,[1] H. Deckelmann,[1] M. Chipperfield,[5] B.-M. Sinnhuber,[5] E. Reimer,[6]
R. Alfier,[6] R. Bevilacqua,[7] K. Hoppel,[7] M. Fromm,[8] J. Lumpe,[8] H. Küllmann,[9]
A. Kleinböhl,[9] H. Bremer,[9] M. von König,[9] K. Künzi,[9] D. Toohey,[10] H. Vömel,[11]
E. Richard,[12] K. Aikin,[12] H. Jost,[13] J. B. Greenblatt,[13] M. Loewenstein,[13]
J. R. Podolske,[13] C. R. Webster,[2] G. J. Flesch,[2] D. C. Scott,[2] R. L. Herman,[2]
J. W. Elkins,[12] E. A. Ray,[12] F. L. Moore,[12] D. F. Hurst,[12] P. Romashkin,[12] G. C. Toon,[2]
B. Sen,[2] J. J. Margitan,[2] P. Wennberg,[14] R. Neuber,[1] M. Allart,[15] B. R. Bojkov,[4]
H. Claude,[16] J. Davies,[17] W. Davies,[18] H. De Backer,[19] H. Dier,[20] V. Dorokhov,[21]
H. Fast,[17] Y. Kondo,[22,23] E. Kyrö,[24] Z. Litynska,[25] I. S. Mikkelsen,[26] M. J. Molyneux,[27]
E. Moran,[28] T. Nagai,[29] H. Nakane,[30] C. Parrondo,[31] F. Ravegnani,[32] P. Skrivankova,[33]
P. Viatte,[34] and V. Yushkov[21]

Received 12 February 2001; revised 2 July 2001; accepted 7 July 2001; published 20 September 2002.

[1] During Arctic winters with a cold, stable stratospheric circulation, reactions on the surface of polar stratospheric clouds (PSCs) lead to elevated abundances of chlorine monoxide (ClO) that, in the presence of sunlight, destroy ozone. Here we show that PSCs were more widespread during the 1999/2000 Arctic winter than for any other Arctic winter in the past two decades. We have used three fundamentally different approaches to derive the degree of chemical ozone loss from ozonesonde, balloon, aircraft, and satellite instruments. We show that the ozone losses derived from these different instruments and approaches agree very well, resulting in a high level of confidence in the results. Chemical processes led to a 70% reduction of ozone for a region ~1 km thick of the lower stratosphere, the largest degree of local loss ever reported for the Arctic. The Match analysis of ozonesonde data shows that the accumulated chemical loss of ozone inside the Arctic vortex totaled 117 ± 14 Dobson units (DU) by the end of winter. This loss, combined with dynamical redistribution of air parcels, resulted in a 88 ± 13 DU reduction in total column ozone compared to the amount that would have been present in the

---

[1] Alfred Wegener Institute for Polar and Marine Research, Potsdam, Germany.

[2] Jet Propulsion Laboratory, California Institute of Technology, Pasadena, California, USA.

[3] European Ozone Research Coordinating Unit, University of Cambridge, Cambridge, UK.

[4] Norsk Institutt for Luftforskning, Kjeller, Norway.

[5] University of Leeds, Leeds, UK.

[6] Meteorological Institute, Free University of Berlin, Berlin, Germany.

[7] Naval Research Laboratory, Washington, D.C., USA.

[8] Computational Physics, Inc., Springfield, Virginia, USA.

[9] Institute of Environmental Physics, University of Bremen, Bremen, Germany.

[10] Program in Atmospheric and Oceanic Science, University of Colorado, Boulder, Colorado, USA.

[11] Cooperative Institute for Research in Environmental Sciences (CIRES), University of Colorado, Boulder, Colorado, USA.

[12] National Oceanic and Atmospheric Administration, Boulder, Colorado, USA.

[13] NASA Ames Research Center, Moffett Field, California, USA.

[14] Division of Geological and Planetary Sciences, California Institute of Technology, Pasadena, California, USA.

[15] Koninklijk Nederlands Meteorologisch Instituut, De Bilt, Netherlands.

[16] Deutscher Wetterdienst, Observatory Hohenpeißenberg, Hohenpeißenberg, Germany.

[17] Atmospheric Environment Service, Downsview, Ontario, Canada.

[18] Department of Physics, University of Wales, Aberystwyth, Wales, UK.

[19] Royal Meteorological Institute of Belgium, Brussels, Belgium.

[20] Meteorologisches Observatorium, Lindenberg, Germany.

[21] Central Aerological Observatory, Dolgoprudny, Moscow Region, Russia.

[22] Solar-Terrestrial Environment Laboratory, Nagoya University, Toyokawa, Aichi, Japan.

[23] Now at Research Center for Advanced Science and Technology, University of Tokyo, Tokyo, Japan.

[24] Sodankylä Meteorological Observatory, Sodankylä, Finland.

[25] Centre of Aerology, Legionowo, Poland.

[26] Danish Meteorological Institute, Copenhagen, Denmark.

[27] UK Met Office, Bracknell, Berkshire, UK.

[28] Valentia Observatory, Irish Meteorological Service, Cahirciveen, County Kerry, Ireland.

[29] Meteorological Research Institute, Tsukuba, Ibaraki, Japan.

[30] National Institute for Environmental Studies, Tsukuba, Ibaraki, Japan.

[31] Instituto Nacional de Técnica Aeroespacial, Torrejon de Argoz, Madrid, Spain.

[32] Fisbat Institute, Consiglio Nazionale delle Ricerche, Bologna, Italy.

[33] Czech Hydrometical Institute, Prague, Czech Republic.

[34] Swiss Meteorological Institute, Les Invuardes, Switzerland.

Copyright 2002 by the American Geophysical Union.
0148-0227/02/2001JD000533$09.00

absence of any chemical loss. The chemical loss of ozone throughout the winter was nearly balanced by dynamical resupply of ozone to the vortex, resulting in a relatively constant value of total ozone of 340 ± 50 DU between early January and late March. This observation of nearly constant total ozone in the Arctic vortex is in contrast to the increase of total column ozone between January and March that is observed during most years.

INDEX TERMS: 0341 Atmospheric Composition and Structure: Middle atmosphere—constituent transport and chemistry (3334); 1610 Global Change: Atmosphere (0315, 0325); 9315 Information Related to Geographic Region: Arctic region; 0322 Atmospheric Composition and Structure: Constituent sources and sinks; 0340 Atmospheric Composition and Structure: Middle atmosphere—composition and chemistry; *KEYWORDS:* ozone, stratosphere, Match

Citation: Rex, M., et al., Chemical depletion of Arctic ozone in winter 1999/2000, *J. Geophys. Res.*, *107*(D20), 8276, doi:10.1029/2001JD000533, 2002.

1. Introduction

[2] In autumn and early winter, stratospheric air at high northern latitudes cools and descends, and a westerly wind circulation (the Arctic vortex) develops. If the temperature within the vortex drops below a critical level, polar stratospheric clouds (PSCs) can form [e.g., *Solomon*, 1999, and references therein]. Reactions on the surface of these clouds convert stratospheric chlorine, that is supplied primarily by the breakdown of man-made chlorofluorocarbons, from benign forms into active forms and in the presence of sunlight chlorine monoxide (ClO) destroys ozone [e.g., *Solomon*, 1999]. The strength and temperature of the Arctic vortex varies considerably from winter to winter. Unlike the Antarctic vortex which is strong and cold every winter, resulting in the so-called Antarctic "ozone hole," the Arctic winter vortex varies considerably from year to year. Since the mean Arctic vortex temperatures are near the threshold for PSC occurrence, substantial differences in the degree of chemical loss of Arctic ozone for individual winters have been observed during the past decade [e.g., *Proffitt et al.*, 1990; *Schoeberl et al.*, 1990; *Hofmann and Deshler*, 1991; *Salawitch et al.*, 1993; *Manney et al.*, 1994; *von der Gathen et al.*, 1995; *Müller et al.*, 1997; *Rex et al.*, 1997, 1999]. Accurate quantification of the chemical and dynamical influences is required for a full understanding of the effects of human activity on Arctic ozone. A number of model studies that used either measured or calculated concentrations of ClO and observed rates for the important reactions have been unable to fully account for the observed chemical loss of Arctic ozone in a quantitative manner, particularly for winters with rapid chemical loss [e.g., *Hansen et al.*, 1997; *Becker et al.*, 1998, 2000]. Given the large sensitivity of Arctic ozone to temperature and the fact that the Arctic vortex is likely to cool due to rising concentrations of greenhouse gases, it is possible that there will be an increased frequency of winters where conditions are conducive for large amounts of chemical ozone loss [*Austin et al.*, 1992; *Shindell et al.*, 1998].

[3] During the winter of 1999/2000 the EU Third European Stratospheric Experiment on Ozone (THESEO 2000) and the NASA SAGE III Ozone Loss and Validation Experiment (SOLVE) were mounted as a collaborative field campaign to better quantify the chemical and dynamical factors that regulate Arctic ozone and thereby improve our predictive capability for future changes to Arctic ozone. Measurements of ozone, numerous other atmospheric gases, and the chemical and optical properties of PSCs were made using instruments on aircraft, balloons, ground-based stations and satellites. These concerted observations resulted in the most comprehensive set of measurements ever obtained in the Arctic winter stratosphere. The work described here resulted from these experiments. The total column abundance of ozone in the Arctic vortex stayed relatively constant during the winter, with values around 330 ± 38 Dobson units (DU) during January, 350 ± 48 DU during February and 332 ± 33 DU during March 2000 (1 Dobson unit equals 10^{-3} cm thickness of gas compressed to surface pressure and temperature). These values are based on a large number of ozonesonde observations inside the Arctic vortex (Figure 1). The chemical loss of ozone in the vortex is not straightforward to quantify from observations of ozone because the abundance of ozone is also strongly affected by atmospheric dynamics [e.g., *Rex et al.*, 2000]. For winters with little or no PSC activity, the column abundance of Arctic O_3 normally increases substantially (~100 DU) due to poleward, downward transport of ozone. The wintertime ozone build up is quite variable from year to year, depending on the meteorological situation [*Chipperfield and Jones*, 1999].

[4] In this paper, we use three techniques to quantify the chemical loss of ozone that occurred during the winter of 1999/2000. The "Match" technique [*von der Gathen et al.*, 1995; *Rex et al.*, 1997, 1999] relies on calculations of air parcel trajectories to isolate changes in ozone for many individual air parcels sampled at various times and places by a large number of coordinated ozonesonde soundings. The "tracer" technique [*Proffitt et al.*, 1990; *Müller et al.*, 1997] uses the temporal evolution of correlations of the volume mixing ratio (vmr) of ozone and a long-lived gas, such as nitrous oxide (N_2O) or methane (CH_4), that serves as a tracer of dynamical motions. The "vortex-averaged" technique [*Bevilacqua et al.*, 1997; *Knudsen et al.*, 1998] involves analysis of the temporal evolution of the mean profile of ozone within the vortex along surfaces of potential temperature that descend according to rates calculated by a radiative transfer model. These are considered in turn after a brief description of stratospheric conditions in the 1999/2000 winter.

2. Presence of PSCs in Winter 1999/2000

[5] The Arctic winter of 1999/2000 was exceptionally cold. Figure 2a shows a time series of the area of the vortex cold enough for PSCs to exist, denoted A_{PSC}, at a potential temperature (Θ) level of 475 K (~19 km altitude). A_{PSC} is

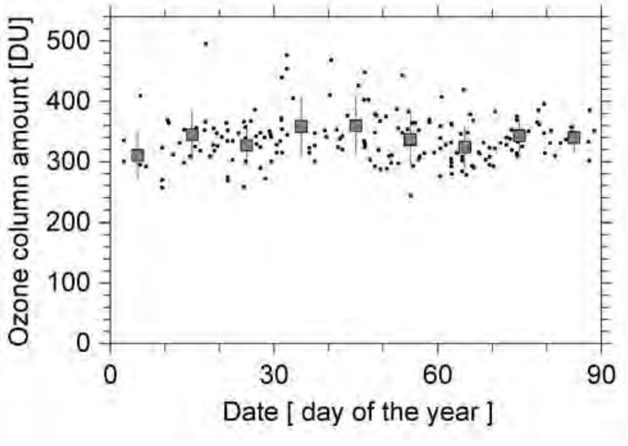

Figure 1. Evolution of the total ozone column inside of the Arctic vortex from January to March 2000 based on ozonesonde measurements. The ozone column between the surface and the termination altitude of the sounding was calculated from the measured ozone density, air pressure, and temperature profiles. The column above the termination altitude of the sounding was estimated assuming a constant ozone mixing ratio profile above. The total column was only derived from soundings that reached at least 25 km altitude. For all measurements included in the plot the estimated amount of ozone in the partial column of air above the measured profile contributes less than 15% to the total column. Due to the requirement that a minimum altitude of 25 km had to be reached by the sounding, the number of soundings included here is substantially smaller than the total number of sondes launched into the Arctic vortex during the SOLVE/THESEO 2000 campaign. Dots show the individual measurements and squares and error bars denote 10-day averages and the 1σ standard deviation.

calculated using temperatures from the European Centre for Medium-Range Weather Forecasts (ECMWF) and an assumption of thermodynamic equilibrium with nitric acid trihydrate (NAT), the most stable phase of PSCs that occur at temperatures above the water frost point [*Hanson and Mauersberger*, 1988]. Figure 2b shows the vertical distribution of A_{PSC} through December 1999 to March 2000. Significant areas with PSC-conditions first occurred around mid-December, covering a vertical region between potential temperatures of $\sim$450–600 K. This first period of low temperatures lasted until early February. During that time the vertical extent of significant A_{PSC} moved to lower altitudes and covered the region between $\sim$400 and 500 K at the beginning of February. A minor warming occurred during February and A_{PSC} dropped to low values around mid-February. A second cold spell started in the last days of February and lasted to about mid-March. During this period significant values of A_{PSC} were limited to the region below $\sim$450 K. Also shown in Figure 2b are observations of the location of PSCs obtained during the 1999/2000 winter season by the Polar Ozone Aerosol and Monitoring (POAM III) satellite instrument [*Lucke et al.*, 1999; *Hoppel et al.*, 2002] and by a ground-based lidar [*Beyerle et al.*, 1994]. These comparisons indicate that A_{PSC} provides a reasonable estimate of the height and times for which PSCs were actually observed. For much of the 1999/2000 winter, the area of PSCs in the Arctic vortex at $\Theta = 475$ K exceeded area estimates for the equivalent dates during any previous winter of the past two decades.

3. Chemical Ozone Loss Based on Match

[6] A Match campaign [*Rex et al.*, 1997, 1998, 1999], consisting of measurements of ozone from a total of 770 ozonesondes launched from 29 stations, was carried out to quantify the chemical loss of ozone during the winter of 1999/2000. The ozonesonde launches were coordinated in real time to probe several hundreds of air masses twice over a several-day interval (so-called "match events"). The coordination was based on calculations of air parcel trajectories (using wind fields from ECMWF) that allow for diabatic descent. The descent rates are calculated using the radiative transfer scheme of the SLIMCAT 3-D chemical transport model [*Chipperfield*, 1999], which uses UKMO analyses for stratospheric winds and temperatures and the ozone field that was calculated by SLIMCAT. Chemical loss rates are derived from a statistical analysis of many match events by subtracting the first measurement of ozone from the second. Further details of the Match technique, including a discussion of quality checks on the match events and on the ozonesonde data, are provided by *Rex et al.* [1999]. The quality checks as described by *Rex et al.* [1999] were applied unchanged, with the exception that the maximum "match radius" [cf. *Rex et al.*, 1999] was set to 400 km instead of 500 km. In winter 1999/2000 this reduction in the maximum match radius resulted in a reduced statistical uncertainty of the results. All results presented here are based on Match events that took place inside the Arctic polar vortex. We have chosen a value of 36 s^{-1} normalized potential vorticity to define the edge of the vortex [see *Rex et al.*, 1999]. This value is close to the maximum horizontal gradient in normalized PV, that varied between values of 35 and 40 s^{-1} between early January and late March. Due to the steep PV gradient at the edge of the vortex, the area enclosed by the narrow PV interval between 36 s^{-1} and the maximum horizontal gradient in PV is negligible and no Match events occurred in this area; that is, for Match, both definitions of the vortex edge are equivalent.

[7] Chemical ozone loss rates from Match are shown on three potential temperature surfaces in Figure 3. The loss rates are expressed in two ways: as ozone loss per sunlit time (Figures 3a, 3c, and 3e; see *Rex et al.* [1999] for the definition of the sunlit time) and as ozone loss per day (Figures 3b, 3d, and 3f). The evolution of A_{PSC} on the respective potential temperature surface is indicated in the upper part of each panel. The ozone loss per sunlit time reached a peak value of about 6 ppbv (parts per billion volume) per sunlit hour on the 500 and 550 K surfaces in late January. Due to the increasing sunlight in Arctic spring, the ozone loss per day peaked in early March, with rates of up to 61.6 ± 4.8 ppbv per day on the 450 K surface. All errors stated in this paper denote the 1σ uncertainty.

[8] The vertical distributions of the ozone loss rates from Match in the range from $\Theta = 400$ to $\Theta = 575$ K are given in Figures 4b (ppbv per sunlit hour) and 4c (ppbv per day). To allow a better comparison with Figure 2, the 4.10^6 km^2 isoline of A_{PSC} is also shown in these panels. A first period

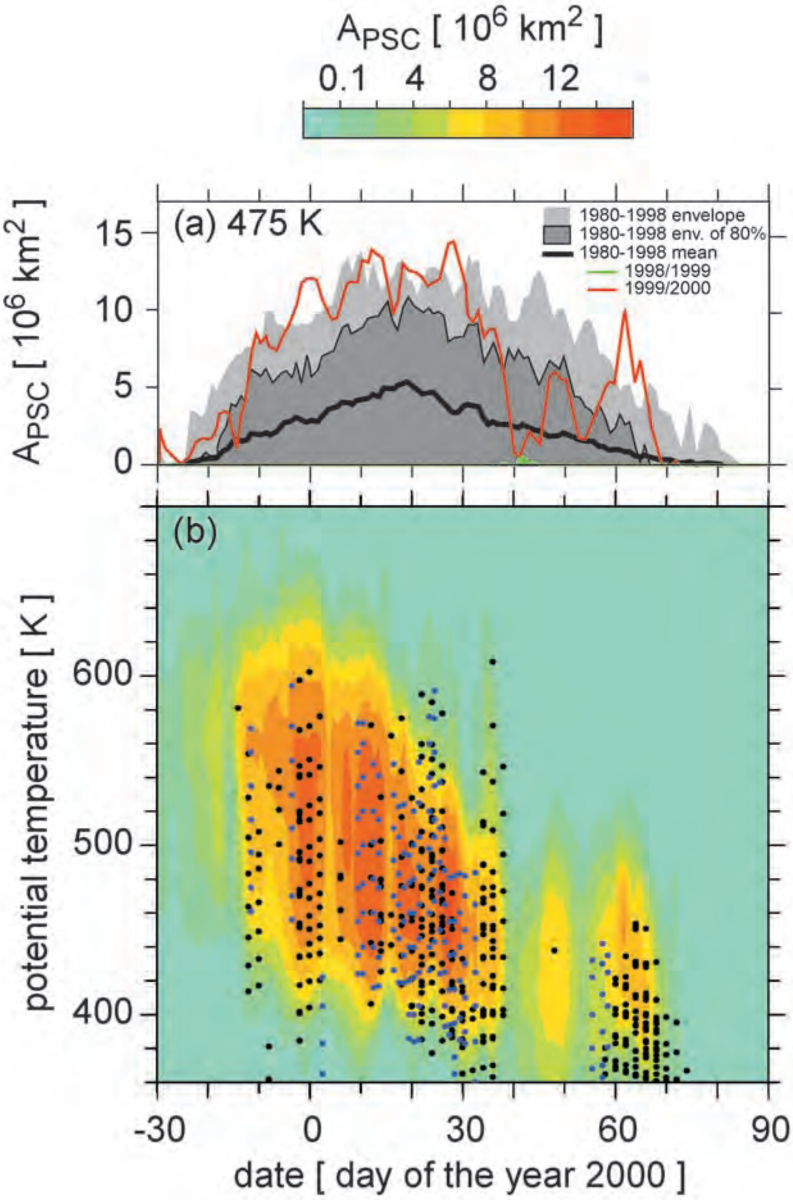

Figure 2. (a) The area of the Arctic at Θ = 475 K potentially populated by PSCs, A_{PSC}, based on temperatures from ECMWF and the thermodynamics of nitric acid trihydrate from *Hanson and Mauersberger* [1988] (see *Rex et al.* [1999] for details). Curves of A_{PSC} for winters of 1999/2000 (red) and 1998/1999 (green line near day 40) are shown. The mean, variance (envelope of 80% the data), and extreme of A_{PSC} for all winters between 1980/1981 and 1997/1998 are also shown. (b) Vertical distribution of A_{PSC} (values indicated on colorscale). The height of PSC appearance observed by POAM III on specific days between 63 and 68 N (black dots) and by a ground-based lidar at Ny Ålesund (79 N, 12 E) (blue dots). The lidar operated about 65% of the days due to weather, with significant gaps (longer than a couple of days) only during late December/early January, when about one observation per week was obtained.

of ozone loss occurred from mid-January to early February and had a vertical extent from Θ = 460 to 570 K, with the highest rates between 480 and 540 K. The ER-2 observations during the late January and early February 2001 were generally obtained at and below potential temperature levels of 430–465 K; therefore the finding of *Richard et al.* [2001] of insignificant chemical loss of ozone during this period is, within the error bars, consistent with the Match results shown in Figure 4b. A second period of rapid loss was observed from late February to late March. During this time the loss was limited to the region below 520 K. Figures 3 and 4 show that the vertical distribution and the time evolution of rapid ozone loss correlates well with the vertical distribution and evolution of A_{PSC}.

[9] Figure 4a shows the evolution of the vortex-averaged peak vmr of ClO observed by the Airborne Submillimeter

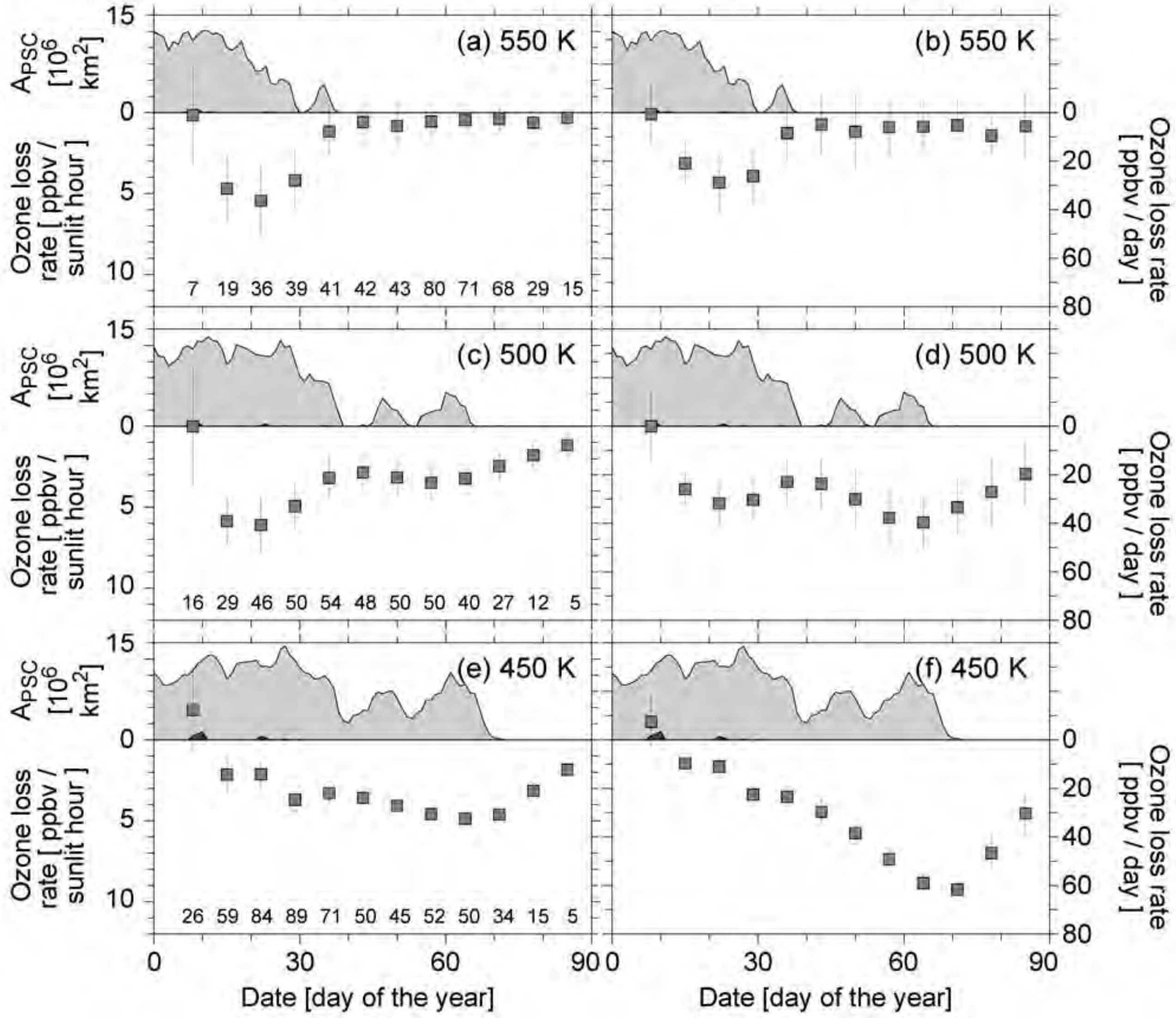

Figure 3. (a and b) Ozone loss rates from Match (squares) at Θ = 550, (c and d) 500 and (e and f) 450 K in ppbv per sunlit time (Figures 3a, 3c, and 3e), and ppbv per day (Figures 3b, 3d, and 3f). The loss rates represent the results of linear regressions over match events in ±10 day broad bins. The numbers at the lower part of Figures 3a, 3c, and 3e give the number of individual match events used in the respective linear regression. A_{PSC} is also indicated for each potential temperature surface as the shaded area in the upper part of the respective panels.

Radiometer (ASUR) [*Bremer et al.*, 2002, and references therein] on the DC-8 research aircraft. The absolute value of the peak vmr plotted in Figure 4a is influenced by the instrumental resolution (~6–10 km in the lower stratosphere; this corresponds approximately to 120–200 K in Θ coordinates). However, the relative change in the abundance of ClO is well represented by the ASUR measurements. Due to the vertical resolution of ASUR, the measurements of ClO shown in Figure 4a represent basically the average ClO vmr over the vertical region shown in Figure 4b. The vertically integrated loss of ozone in the partial column between 400 and 575 K is shown in Figure 4d (DU per sunlit hour) and Figure 4e (DU per day). Vortex-averaged profiles of pressure and temperature at the respective date, based on all ozone soundings inside the vortex within ±5 days around that date, were used to compute column loss from the profile of loss rates, given in vmr versus Θ. The ozone column loss per sunlit time reached a maximum in late January and then generally declined until late March, in concert with the evolution of ClO, which showed larger concentrations in late January and declined by a factor of 2–3 by mid-March. However, due to increasing sunlit time per day, the column loss per day peaked at 2.4 ± 0.3 DU per day during early March. The minimum of both loss rates in mid-February coincides with a warming of the vortex that is evident from the minimum for A_{PSC} during that time.

[10] The altitude of the maximum ClO vmr derived from the ASUR measurements (black bars in Figure 4b) was at ~500 K in January and ~450 K in March, which coincides with the respective altitudes of the maximum ozone loss

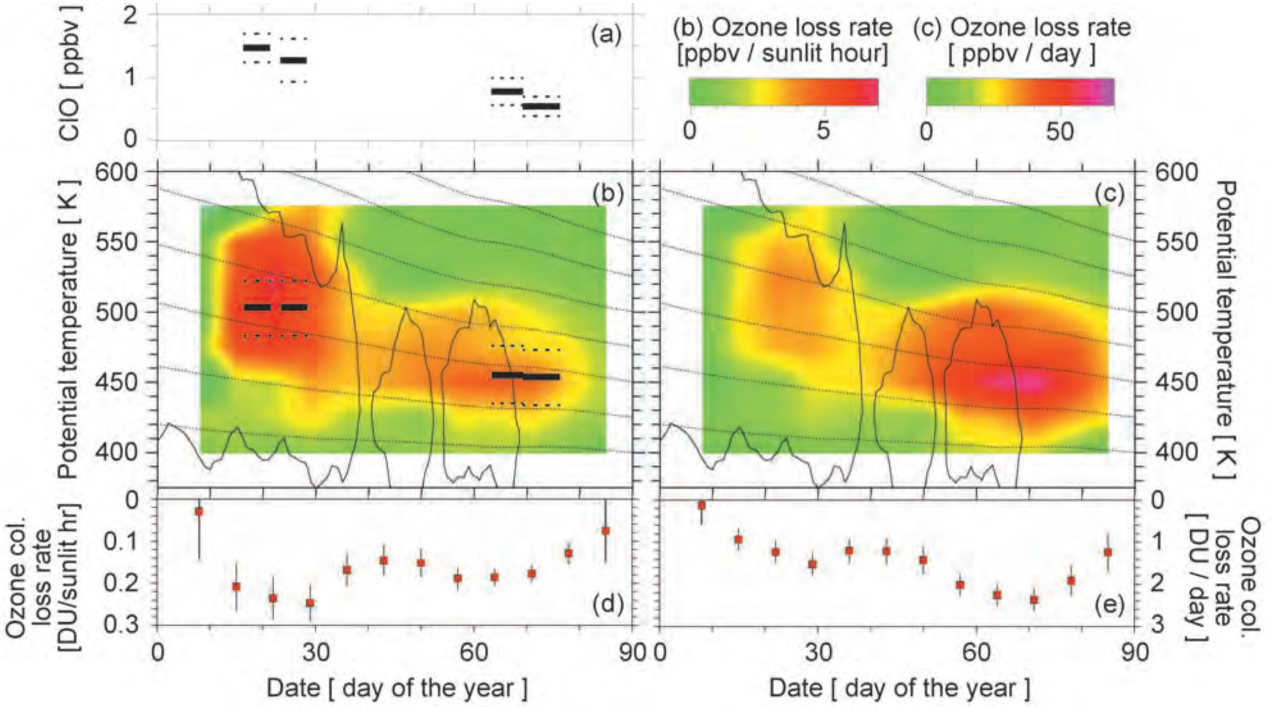

Figure 4. (a) The vortex-averaged peak vmr of ClO from ASUR. The data obtained by ASUR on several flights has been averaged into 5–7 day bins. Only measurements inside the polar vortex at solar zenith angles less than 87° have been used. Vertical distribution of the ozone loss (b) per sunlit time and (c) per day. The black contours show the 4.10^6 km^2 isoline of A_{PSC} (cf. Figure 2b). The black dotted lines show the subsidence of air masses as derived from SLIMCAT (see section 5 and *Rex et al.* [1999] for details). The altitudes of the peaks in the ClO profiles from ASUR are also shown (black bars in Figure 4b; the corresponding dotted lines represent the estimated uncertainties of the retrieval, under the assumption of a sufficiently symmetric ClO profile). Vertically integrated chemical ozone loss rate in the column of air between $\Theta = 400$ and 575 K in loss (d) per sunlit hour and (e) per day.

rates during these periods. Figure 5 compares the vertical distribution of the ozone loss rate derived from Match for early March with a profile of the ClO mixing ratio measured in situ inside the vortex on 1 March by an resonance fluorescence balloon-borne instrument (HALOZ) [*Vömel et al.*, 2001].

[11] The vertical region of fast ozone loss coincides reasonably well with the region of high concentrations of ClO observed by HALOZ, given that the ozone loss rates are vortex averages and the measurements of ClO represent conditions at one particular location in the Arctic vortex. This observation is consistent with observations from previous winters [*Pierson et al.*, 1999; *Woyke et al.*, 1999] and strongly supports the notion that the ozone loss in the Arctic is caused by elevated concentrations of active chlorine. A more quantitative analysis of the relation of chemical loss of ozone and the ClO vmr as measured by HALOZ is given by *Vömel et al.* [2001].

[12] We now turn to the accumulated chemical losses of ozone in particular layers of air within the Arctic vortex. In the vortex during winter, diabatic cooling results in subsidence and the potential temperature of air parcels is not conserved. The subsidence of air parcels must be accounted for in the calculation of integrated chemical loss of ozone. We do this by examining the change in ozone along surfaces of "adjusted potential temperature" ("$a\Theta$"), where $a\Theta$ is defined as the potential temperature a parcel would achieve on 31 March using vortex average descent rates. As above, descent rates are calculated using the radiative transfer scheme of the SLIMCAT model. For the period and vertical extent considered, diabatic subsidence derived from inert tracer observations obtained during SOLVE/THESEO 2000 agrees to better than $\Theta = 10$ K with the calculated subsidence [*Greenblatt et al.*, 2002b].

[13] The time evolution of the vortex-averaged accumulated ozone loss in subsiding layers is given in Figure 6a. During January to mid-March, when sufficient POAM III ozone measurements inside the polar vortex are available, the evolution, the vertical structure and the degree of chemical ozone loss shown in Figure 6a are in good quantitative agreement (better 20% throughout) with the accumulated ozone losses derived from POAM data [*Hoppel et al.*, 2002, Figure 5]. The accumulated loss from 9 January (day 8) through 26 March (day 85) is plotted versus $a\Theta\Theta$ in Figure 6b. It peaks at 2.7 ± 0.24 ppmv (parts per million volume) for air at $\Theta = 453$ K on 26 March. This is the largest local chemical ozone loss ever observed during Arctic winter. This result agrees well with results from *Sinnhuber et al.* [2000], who reported chemical ozone loss of 2.5 ppmv at 450 K for one particular station inside the Arctic vortex, and shows that this large loss of ozone was representative of the whole vortex. It is

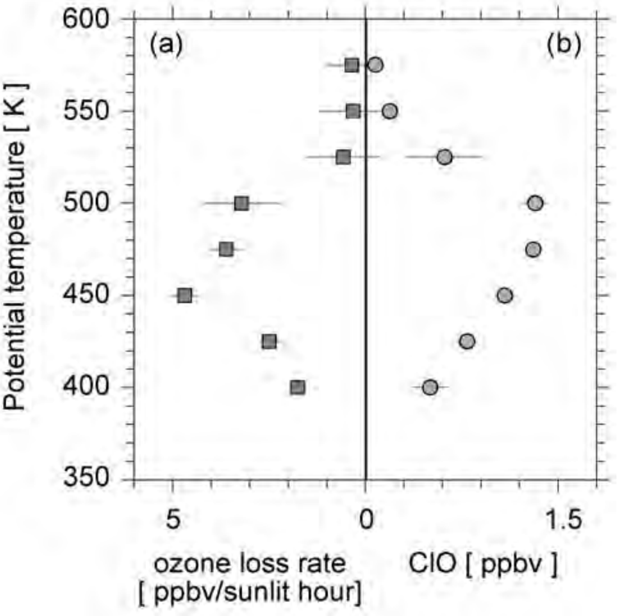

Figure 5. (a) Vertical profile of ozone loss rates on 1 March 2000 (±10 days) from Match. (b) The ClO profile measured by HALOZ on 1 March 2000 close to local noon. For better comparison with the Match data, the original data has been averaged into 25 K bins. The error bars are based on the scatter of the individual data points.

also generally consistent with reports of significant ozone decreases inside the polar vortex by *Santee et al.* [2000]; however a quantitative comparison with that study is not possible because the effect of diabatic subsidence on ozone change was not taken into account by *Santee et al.* [2000].

[14] In the previous paragraphs the results from Match have been regarded as average values over the Arctic vortex. We now analyze how well different parts of the vortex are represented by the Match results. Figure 7 shows the distribution of match events in potential vorticity space for the three isentropic surfaces shown in Figure 3 (low values of relative PV correspond to the inner most region of the vortex; see caption). Throughout most of the observing time the vortex was fully covered by match events, with a generally slight under representation of the outer part of the vortex. This is particularly true during March at the lower potential temperature levels, where the outer 50% of the vortex area was not sampled.

[15] Figure 8 shows the ozone loss rates in different parts of the polar vortex for two different periods, i.e., January/early February (squares) and late February/March (crosses). Generally the ozone loss rate at the edge of the vortex tended to be smaller than the vortex average. Otherwise the ozone loss was relatively homogenous within the polar vortex. During March no results could be obtained for the outer 50% of the vortex at $\Theta = 450$ K because this area was not sufficiently sampled by match events (cf. Figure 7)

[16] Based on theoretical considerations [e.g., *Solomon*, 1999, and references therein] and experimental results [*Rex et al.*, 1999] we know that Arctic ozone loss occurs exclusively in sunlit air masses. Therefore any oversampling or undersampling of the southern and more sunlit parts of the vortex or the darker northern regions may lead to differences between the ozone loss inferred from the Match observations and the true vortex average. Since low PV areas do not always correspond to the southernmost and most sunlit parts of the vortex, it may not be sufficient to look at the sampling of the vortex in PV space to assess the representativeness of the results. Figure 9 compares the vortex-averaged sunlit time per day with the same quantity along the trajectories used in the Match analysis. The exposure to sunlight along the Match trajectories generally reflects average conditions throughout the vortex very well. Only in January, particularly at the higher potential temperature levels, the average exposure to sunlight of the air parcels sampled by Match is slightly less than for the vortex

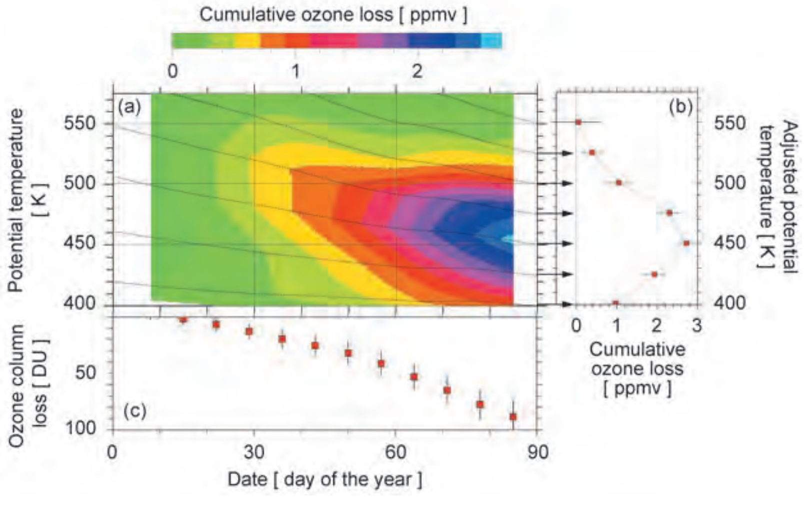

Figure 6. (a) Evolution of the accumulated ozone loss in subsiding air masses from Match. (b) Profile of the accumulated ozone loss on 26 March 2000 (day 85) from Match. (c) Accumulated chemical ozone loss in the partial column between $\Theta = 400$ and 575 K from Match (column [O_3*-O_3]; see section 6 for details).

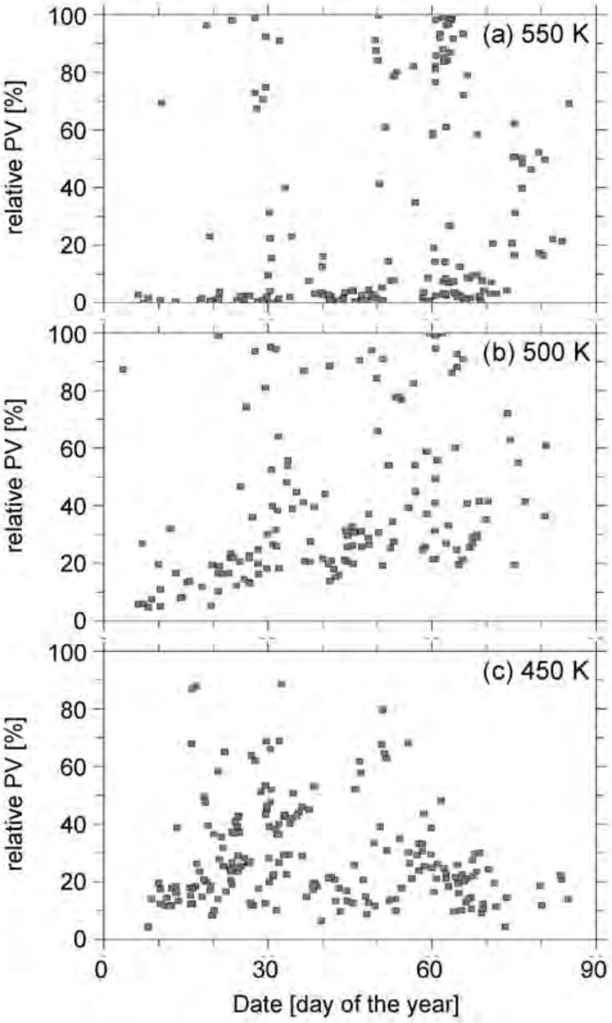

Figure 7. Sampling of the polar vortex with Match events at (a) $\Theta = 550$, (b) 500, and (c) 450 K. The PV value of each match event is plotted against date. To elucidate the homogeneity of the sampling, the PV values of the matches are mapped on a relative PV scale, which runs from 0 for the maximum PV value reached at the center of the vortex on a given day, to 1 at the vortex edge. The relation between PV and relative PV is chosen such that, for each day, equal intervals in the relative PV scale correspond to equal fractional areas of the polar vortex, i.e., a relative PV of 40% means that 0.4 of the vortex area is enclosed by the corresponding isoline of PV.

average and is more comparable to conditions for the inner 50% of the vortex area. Based on the data shown in Figure 7 and the comparisons shown in Figure 9, it is valid to consider the ozone loss rates from Match to be generally representative of the vortex average ozone loss.

4. Chemical Ozone Loss Based on Tracer Relations

[17] The change in the relation between mixing ratios of O_3 and long-lived tracers such as N_2O and CH_4 can also be used to quantify chemical loss of ozone [*Proffitt et al.*, 1990; *Müller et al.*, 1997]. Figure 10 shows the evolution of the O_3 versus N_2O relation observed by three flights in the Arctic vortex by the NASA Observations of the Middle Stratosphere (OMS) balloon-borne in situ and remote instrument payloads and for a few selected flights of the NASA ER-2 aircraft. Comprehensive discussions of chemical ozone loss rates based on the ER-2 observations is provided by *Richard et al.* [2001] and on the OMS observations by *Salawitch et al.* [2002]. Our focus is on chemical loss from the balloon observations and the use of the ER-2 observations to demonstrate that, for the winter of 1999/2000, transport of air across the edge of the vortex could not have been responsible for the dramatic change observed in the O_3 versus N_2O relation. A description of the OMS balloon-borne instruments and measurement sensitivities for observations used in our analysis is provided by *Salawitch et al.* [2002]. A similar description of ER-2 instruments and sensitivities is provided by *Richard et al.* [2001].

[18] Isolated descent of purely vortex air will preserve the initial O_3 versus N_2O relation [*Proffitt et al.*, 1990]. Neglecting for now any possible effects of transport on the O_3 versus N_2O relation, the reduction in the mixing ratio of O_3 during the course of the winter, for constant values of N_2O, signifies chemical loss of O_3. The largest source of uncertainty in the estimate of chemical loss from the tracer observations is the initial abundance of O_3 prior to chemical loss. Only two individual profiles are available to establish this initial relation, which differ by about ~20% in the relevant vertical region, probably due to true atmospheric variability [*Salawitch et al.*, 2002] The excellent agreement between the O_3 versus N_2O relation measured by the OMS in situ package on 5 March 2000 and by the ER-2 on this same date, for different geographic regions deep inside the vortex, demonstrates that this profile is representative of conditions in a broad region deep inside the vortex on this day. The balloon-borne observations shown in Figure 10 indicate that chemical reactions inside the vortex led to removal of 1.0 to 1.5 ppmv of O_3 for air sampled between $\Theta = 430$ and 460 K (~17–19 km) on 5 March 2000. This compares well with Match estimates for chemical loss of 1.1 ± 0.3 ppmv at $\Theta = 430$ K and 1.7 ± 0.3 ppmv at $\Theta = 460$ K for the same date. *Richard et al.* [2001] show, based on analysis of ER-2 data, that the accumulated chemical ozone loss reached 58 ± 4% near 450 K by 12 March 2000, which is also in good agreement with estimates from Match for that time and altitude.

[19] The validity of the chemical loss of ozone estimated in this manner is dependent on whether transport of air, particularly mixing across the vortex edge, changes the O_3 versus N_2O relation. *Michelsen et al.* [1998] and *Plumb et al.* [2000] have suggested that before chemical loss of ozone occurred, mixing between subsided inner vortex air with extravortex air may lead to a flattening out of the curved O_3/N_2O relation and thus may be mistaken as chemical loss of ozone. However, the effect of mixing on this relation largely depends on the shapes of the inner vortex and extravortex relations between O_3, N_2O and Θ throughout the winter. Observations of O_3 versus N_2O obtained by ER-2 instruments in the core of the vortex on 23 January (orange dots, Figure 10) and on 7 March (green dots, Figure 10) show evidence for some entrain-

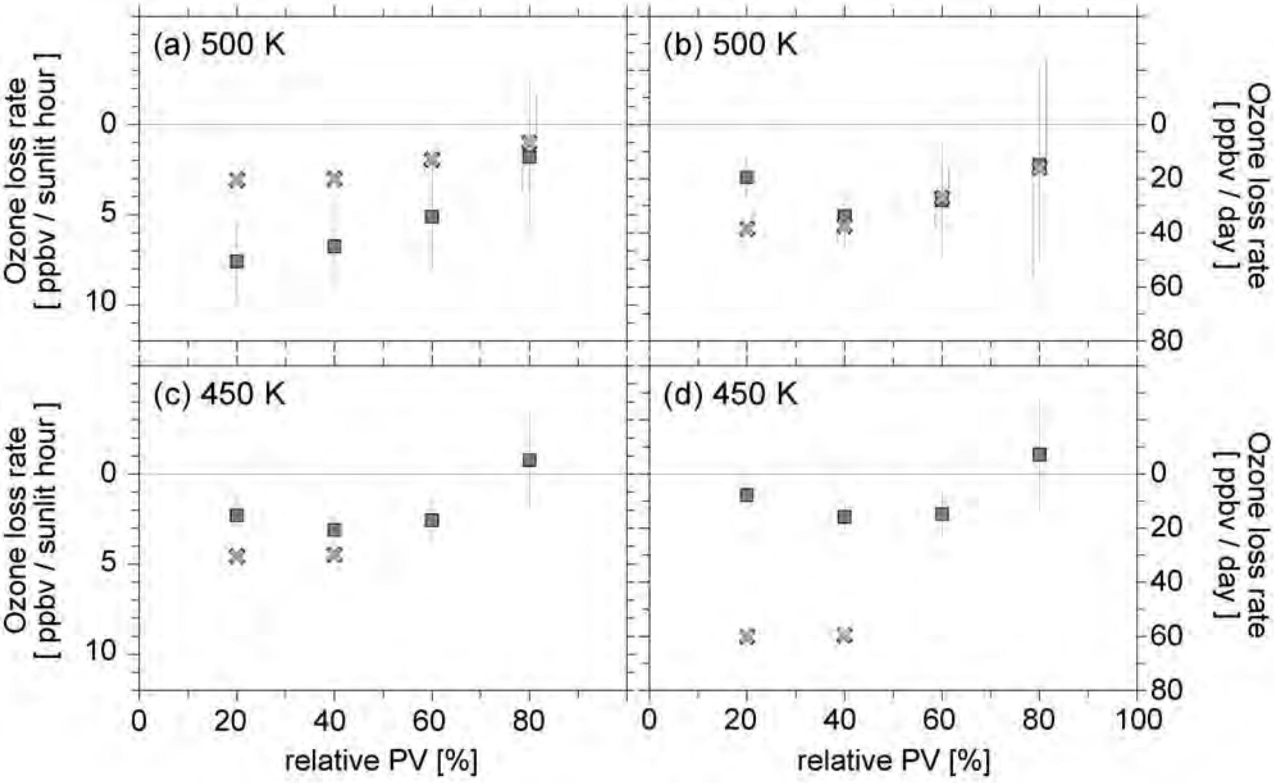

Figure 8. Ozone loss rates in different parts of the vortex for (a and b) Θ = 500 and (c and d) Θ = 450 K for the period 10 January to 5 February (red squares) and 25 February to 25 March (green crosses). Figures 8a and 8c show the ozone loss per sunlit hour, Figures 8b and 8d show the daily ozone loss. The ozone loss rates are plotted against relative PV (cf. caption of Figure 7).

ment of extravortex air into the core of the vortex during the winter, which allows us to assess the effect that such mixing had on the O_3/N_2O relation. The darker colored points in Figure 10 indicate measurements obtained in relatively narrow filaments of air along surfaces of near constant potential temperature (Θ = 462 ± 5 K for 23 January and Θ = 453 ± 3 K for 7 March). These observations indicate various degrees of mixing between air parcels originating from inside the vortex (O_3 versus N_2O close to the unmixed, vortex relation) and air originating outside the vortex (higher values of O_3 and N_2O). The measurements convincingly demonstrate that entrainment of extravortex air led to an increase in the mixing ratio of O_3 for a given value of N_2O, given the prevailing inner vortex and extravortex relations between O_3, N_2O, and Θ for January and March 2000. Although in section 6 we show that entrainment of extravortex air did not significantly alter the composition of the vortex (strong mixing lines inside the vortex were relative scarce during all the ER-2 flights; see *Greenblatt et al.* [2002a] for a statistic of mixing events during the ER-2 flights), whatever entrainment did occur during the time of chemical loss for this winter increased O_3 at a given level of N_2O inside the vortex. Thus the overall changes in the O_3 versus N_2O relation observed during the course of winter could not have been caused by transport, and rather represent a lower limit for the true chemical loss of ozone. Further demonstration that transport alone could not have led to the observed changes in the O_3 versus N_2O relation for the winter of 1999/2000 is provided by *Richard et al.* [2001], *Ray et al.* [2002], and *Salawitch et al.* [2002].

5. Chemical Ozone Loss Based on Vortex Average

[20] Changes in the vortex-averaged ozone vmr profile in aΘ coordinates can only be caused by either chemical loss or by transport of ozone across the edge of the vortex. Figure 11a shows the evolution of vortex-averaged ozone profiles in aΘ coordinates. To minimize the effects of transport, we used the maximum gradient of PV to define the vortex edge. Comparison of the black solid line (ozone in early January versus aΘ) to the dotted line (ozone in early January versus Θ) in Figure 11a illustrates the degree of subsidence computed by the SLIMCAT model. The accumulated chemical loss of ozone (the difference between the black solid and red solid lines) peaks at 2.6 ppmv for the aΘ = 460 K level.

[21] A critical test of chemical ozone loss based on the “vortex-averaged” technique is given in Figure 11b. The largest uncertainty of the vortex average approach is introduced by possible exchange of air across the vortex edge. In Match, synopticscale intrusions of extravortex air are explicitly accounted for and great care is taken to

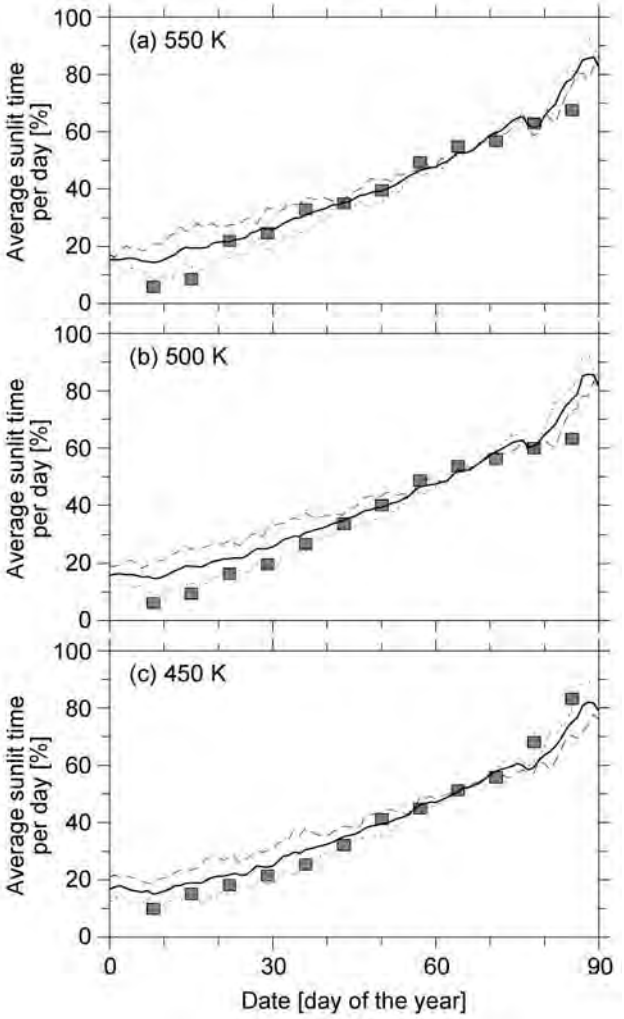

Figure 9. Comparison of the average sunlit time per day along the trajectories that have been used for the Match analysis (squares) with vortex average conditions (solid line) at (a) $\Theta = 550$, (b) 500, and (c) 450 K. The dotted and the dashed lines show the average sunlit time per day in the inner 50% area of the vortex (based on PV analyses) and the outer 50% area, respectively.

avoid areas of potential smallscale mixing [see *Rex et al.*, 1999]. A comparison between accumulated ozone loss from the Match analysis and from the vortexaveraged approach allows us to assess the potential influence of entrainment of extravortex air on the vortexaveraged ozone profile. The red points in Figure 11b show the accumulated ozone loss between early January and late March from Match (cf. Figure 6b). Differences between the vortex average profile of O_3 versus aΘ measured in early January and profiles measured at successive times are given by the colored lines in Figure 11b. The red solid line represents the total accumulated loss of ozone between early January and late March based on vortex average ozone in aΘ coordinates. The accumulated ozone loss found using these two approaches does not show significant discrepancies, indicating that the vortex-averaged ozone was not strongly influenced by transport of air across the edge of the vortex and that the observed reductions in ozone were predominantly due to chemistry.

6. Effects of Chemistry on Ozone Column

[22] Two different quantities can be used to describe the overall chemical loss of ozone in the total column of air. First, the amount of ozone that was lost during the winter is given by the number of ozone molecules that have been destroyed during the winter in a vertical column of air inside the polar vortex. This quantity is calculated as the time integral of the column loss rate of ozone and is here denoted $\int$column $[-dO_3/dt_{chem}]$. Second, the impact of the overall chemical loss on the actual column abundance of ozone can be described by the difference between the column ozone that would have been present in the absence of chemical loss

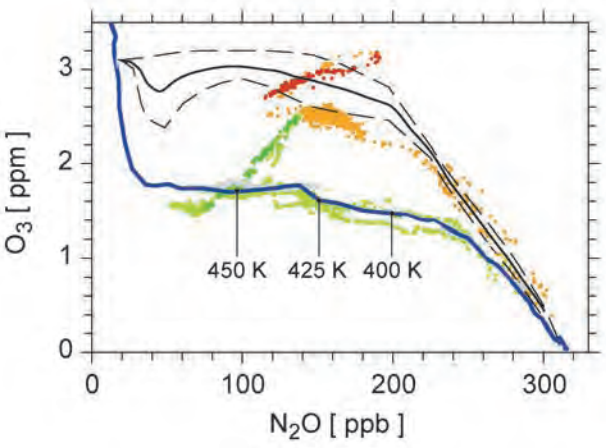

Figure 10. Measurements of the mixing ratio of O_3 versus N_2O obtained during various balloon and ER-2 flights. Measurements from the in situ (lower dashed line) and remote (upper dashed line) OMS balloon payloads on 19 November 1999 and 3 December 1999, respectively, and the average of these two relations (black solid line) are shown. Measurements from the in situ OMS balloon payload on 5 March 2000 are also shown (blue line). The balloon flights originated from a launch facility at Esrange, Sweden (68 N, 21E) and sampled the vortex based on analyses of PV [see *Salawitch et al.*, 2002]. The ER-2 measurements on 23 January 2000 (orange/red dots), 5 March 2000 (dashed gray line), and 7 March 2000 (light/dark green dots) were obtained for flights in the core of the vortex, based also on PV analyses. The ER-2 observations have been averaged onto a 10 s resolution time grid. For each time step, the average value of N_2O is computed from whichever observations are available from the ARGUS, ALIAS, and ACATS instruments. The averaging procedure places greater emphasis on data from the tunable diode laser ARGUS and ALIAS instruments, since measurements from these devices are reported at greater time resolution than are measurements from the ACATS gas chromatograph. High time resolution observations are critical for characterizing the mixing lines observed on 23 January 2000 at $\Theta = 462 \pm 5$ K and on 7 March 2000 at $\Theta = 452 \pm 2$ K, which are denoted by dark red and dark green color.

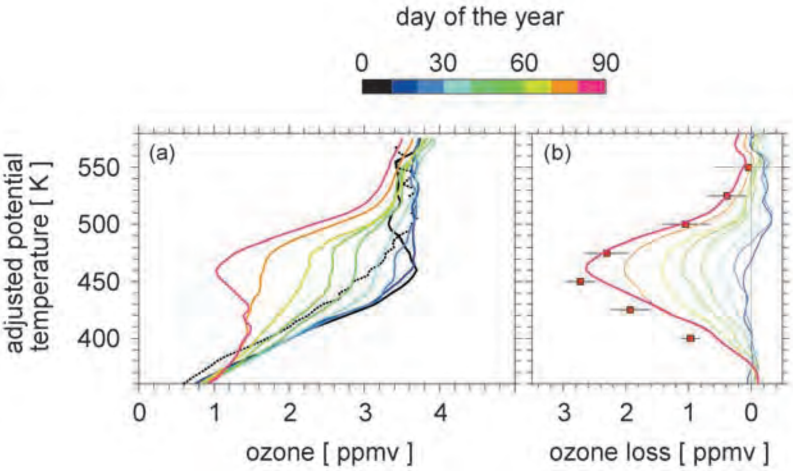

Figure 11. (a) Evolution of the average ozone profile inside the polar vortex in aΘ coordinates (see section 5). The data from all ozonesonde measurements inside the vortex have been averaged into 10 day bins, centered around the day indicated by the colorscale. The black dotted line shows the average profile for 5 January 2000 (±5 days) with Θ as the vertical coordinate (i.e., subsidence not applied). (b) Accumulated ozone loss from Match between 8 January 2000 and 26 March 2000 (red squares, cf. Figure 6b) and differences between the average profile of O_3 versus aΘ measured in early January and profiles measured at successive times (colored lines, as indicated by the scale). The last vortex-averaged ozone profile (red solid line) is for 26 March 2000, ±5 days.

(dynamics being equal), denoted column [O_3*], and the observed column abundance of ozone. We denote this second estimate of column loss as column [O_3*-O_3]. Due to subsidence and compression of air, the profile of O_3* (and hence column [O_3*]) changes with time. Several methods, as described below, are used to estimate column [O_3*].

[23] These measures of column ozone loss (e.g., $\int$column [$-dO_3/dt_{chem}$] and column [O_3*-O_3]) are different geophysical quantities. In the presence of subsidence in a non-cylindrical vortex; i.e., the presence of average poleward (or equatorward) motion, exchange of ozone depleted air masses across the surface of a cylindrical column occurs, even in the absence of exchange of air across the non-cylindrical vortex edge. The calculation of $\int$column [$-dO_3/dt_{chem}$] is insensitive to whether ozone depleted air masses later leave the cylindrical vertical column, or whether air masses that encountered ozone loss elsewhere enter this vertical column (this assumes, of course, that average conditions in the actual vortex are well sampled throughout the period of observation). However, column [O_3*-O_3], like the column amount of any chemical species, can be altered by dynamical processes. Simply put, column [O_3*-O_3] is not a dynamically conserved quantity, whereas $\int$column [$-dO_3/dt_{chem}$] is conserved. Both measures of column loss have physical meaning. The quantity $\int$column [$-dO_3/dt_{chem}$] represents the total number of ozone molecules destroyed by chemistry and is most appropriately compared to "book keeping" calculations of chemical loss, either from three-dimensional (3-D) model simulations or from model estimates constrained by measured ClO. Column [O_3*-O_3] is the true measure of the effect of chemical loss of ozone on the resulting radiative environment experienced at the ground underneath the Arctic vortex at the end of the winter and is most appropriately compared to the difference between "passive" ozone and "chemically active" ozone in 3-D model simulations.

[24] The quantity column [O_3*-O_3] is either calculated as the vertical integral of the difference between O_3 and estimates of O_3*, as derived from various approaches (see below), or as vertical integral of the accumulated ozone losses from Match (the vertical integral of the data in Figure 6b). The quantity $\int$column [$-dO_3/dt_{chem}$] is calculated by first vertically integrating the ozone column loss rates from the profiles of local ozone loss rates (data in Figure 4c) using the relation between aΘ and geometric altitude (z), as well as the density (ρ) profile at the respective time of the integration, and then accumulating these ozone column loss rates over the course of the winter (i.e., the time integral of the data in Figure 4e). Since the relation between aΘ and z, as well as the profile of ρ, are functions of time, the results of the two calculations are indeed different.

[25] Time integration of the data in Figure 4e yields $\int$column [$-dO_3/dt_{chem}$] = 117 ± 14 Dobson units (~35% of the total column present in March), similar to values of $\int$column [$-dO_3/dt_{chem}$] derived from Match experiments in previous cold Arctic winters (e.g., the winter of 1994/1995, as described by *Rex et al.* [1999]). Although chemical loss of ozone at Θ = 450 K during 1999/2000 was larger than found during any previous winter, the chemical loss extended over a broader vertical region during both 1994/1995 and 1995/1996, resulting in comparable amounts of column loss.

[26] The effect of this chemical loss on the column amount of O_3 during the Arctic winter of 1999/2000 is perhaps best visualized by comparing measured profiles of the concentration of O_3 to estimates of O_3*. Figure 12 compares profiles of O_3 measured in the Arctic vortex by different instruments (an in situ balloon photometer (Figure 12a) [*Salawitch et al.*, 2002], the POAM III satellite (Figure 12b) [*Hoppel et al.*,

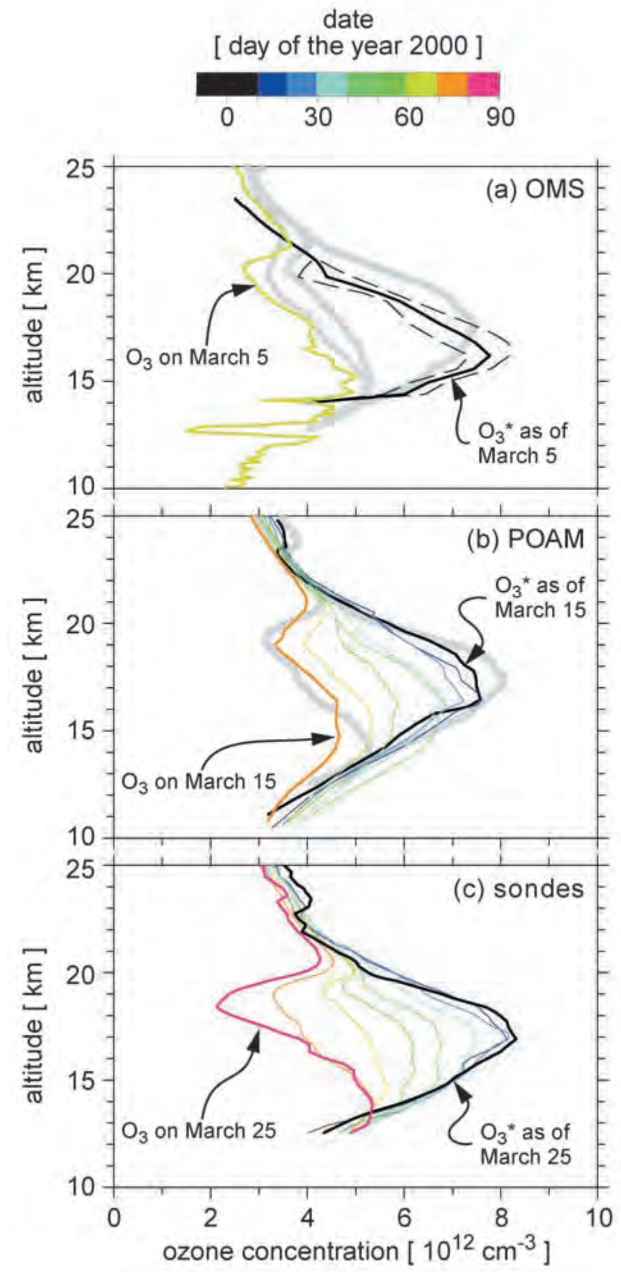

2002], and ozonesondes (Figure 12c)) to profiles of O_3* that are estimated in different ways from early winter measurements of the respective instruments. The different dates for which O_3 and O_3* are plotted in the various panels correspond to the day for which the last inner vortex O_3 profile could be determined from the respective data set. To facilitate comparisons of the sonde data with the OMS and POAM III measurements, profiles of O_3 and O_3* from the sondes for the indicated dates are shown by the solid gray lines on Figures 12a and 12b.

[27] The individual profiles for O_3 and O_3* plotted in Figure 12a reflect the local conditions in the air masses that have been sampled by the balloon instruments during the respective flights and do not necessarily represent vortex average conditions. Given this limitation, the agreement with the sonde data is reasonable. The balloon-borne observations specifically targeted the core of the vortex. Restricting the sonde profile of O_3 for 5 March to observations obtained only in the core of the vortex results in reasonably good agreement with the photometer profile. Average profiles of O_3 inside the vortex (gray dotted line, Figure 12a) were obtained by the POAM III satellite instrument until 15 March 2000 (Figure 12b) [*Hoppel et al.*, 2002]. Subsequently, the vortex was too close to the pole to be observed. Overall good agreement is found between profiles of O_3 and O_3* from POAM III for 15 March and the corresponding sonde profiles.

[28] For calculating column [O_3*-O_3] from the profiles of O_3 and O_3*, the vertical integral is evaluated between limits of 14 and 24 km. The upper limit reflects the approximate maximum altitude of PSC-initiated chemical loss. The lower limit corresponds to the Θ = 400 K surface, commonly considered to represent the bottom of the vortex circulation. Below this level, polar and extrapolar air parcels mix vigorously and it is unlikely that any of our methods for estimating chemical loss of ozone is valid.

[29] An overview over the different estimates of column [O_3*-O_3] as derived from ozone and tracer observations of the OMS balloon, the POAM III satellite measurements and the Match experiment is given in Table 1. The value of column [O_3*-O_3] derived from the tracer observations (Figure 12a) as of 5 March is 61 ± 14 DU. The largest source of error is uncertainty in the profile of O3*, which is due to observed variability in the initial O_3 versus N_2O relation (see *Salawitch et al.* [2002] for further details of this calculation). Column [O_3*-O_3] inferred from the sondes for that day is 51 DU and Column [O_3*-O_3] from Match is 53 ± 12 DU for the same day. We find column [O_3*-O_3] = 67 DU

Figure 12. (opposite) Concentration profiles of O_3 (thin colored lines) during late winter for observations from (a) the OMS balloon-borne in situ O_3 photometer on 5 March 2000; (b) the POAM III satellite instrument between 1 January and 20 March 2000; and (c) ozonesondes between 1 January and 30 March 2000. The profiles in Figures 12b and 12c represent vortex averages for 10 days centered on the indicated day of the year. The profile of O_3* (thin black line), the abundance of O_3 expected in the absence of any chemical loss, is estimated in Figure 12a by mapping the initial O_3 versus N_2O relation shown in Figure 5 onto a profile for N_2O measured by the balloon-borne LACE gas chromatograph in the core of the vortex on 5 March 2000 (see *Salawitch et al.* [2002] for details). Profiles of O_3* in Figures 12b and 12c are calculated by allowing the vortex average O_3 profiles from POAM III (see *Hoppel et al.* [2002] for details) and ozonesondes, respectively, to descend by amounts based on cooling rates from the SLIMCAT model (for this calculation, the mixing ratio of O_3 is assumed to be conserved during descent and is converted to concentration in the last step). All profiles are shown for the altitude and pressure the air would have been at on the date of the last measurement by each instrument. Profiles of O_3 and O_3* from the sondes, appropriate for the date indicated on each panel, are represented in the top two panels by gray solid lines. A second profile for O_3 from the sondes (gray dashed line) is given in Figure 12a, representing an average profile on 5 March 2000 for air in the core of the vortex.

Table 1. Comparisons of Chemical Loss of Column Ozone, Column [O_3^*-O_3], Inside the Arctic Vortex for Winter 1999/2000 as Indicated by Date

Data Source	OMS Balloon	POAM III Satellite	Ozonesondes
Method	tracer-tracer (O_3 versus N_2O)	vortex-averaged descent	Match trajectory analysis
Reference	*Salawitch et al.* [2001]	*Hoppel et al.* [2001]	this paper
5 March 2000	61 ± 13 DU	51 ± 11 DU	53 ± 11 DU
15 March 2000	na	67 ± 11 DU	71 ± 12 DU
28 March 2000	na	na	88 ± 13 DU

as of 15 March based on the POAM III observations. The sonde observations and Match yield column [O_3*-O_3] = 75 DU and column [O_3*-O_3] = 71 ± 12 DU, respectively, for this date, in good agreement with the satellite value. The good agreement between each of these estimates of column loss of O_3 due to chemistry increases our confidence in the validity of each approach.

[30] Ozonesonde observations (Figure 12c) reveal that significant loss of ozone occurred in the Arctic vortex during the winter of 1999/2000 after it was last sampled by the OMS balloons, by the ER-2, and by POAM III. Between early January and late March, column [O_3*-O_3] equaled 87 DU based on the vortex-averaged sonde data in Figure 12c. The value for column [O_3*-O_3] from the Match approach (Figure 6c) is 88 ± 13 DU for the same date. Although both estimates of column [O_3*-O_3] are based on the same sonde data, they have been calculated in entirely different ways. As noted above, the Match approach is designed to minimize the effects of mixing on the estimated loss. The vortex average approach might, in theory, be affected by flow of air across the edge of the vortex. The good agreement between these two estimates of column [O_3*-O_3] further demonstrates that, for the winter of 1999/2000, transport of extravortex air did not play a significant role in altering the ozone content of the vortex.

[31] The analysis presented here shows that the amount of ozone destroyed by chemistry throughout the column during the Arctic winter of 1999/2000 amounted to 117 ± 14 DU by late March. Chemical processes, in combination with dynamical effects, led to 88 ± 13 DU reduction in the column abundance of O_3 that would have been present in the absence of any chemical loss during late March. The actual column abundance of O_3 in the Arctic vortex was 340 ± 30 DU in late March. In the absence of chemical loss, the column abundance in late March would have been ~430 DU if the motions of air were unchanged.

7. Conclusion

[32] Results from the SOLVE/THESEO 2000 field campaign show that the Arctic vortex during the winter of 1999/2000 was characterized by low temperatures, widespread PSCs, elevated ClO, and considerable chemical loss of ozone. Between early January and late March, loss of 70% of the initial abundance of O_3 occurred in a ~1 km layer near 18 km altitude. This is the largest local loss of ozone ever reported for the Arctic. Loss of more than 50% of initial O_3 occurred over a 3 km broad region. Chemistry alone destroyed 117 ± 14 DU of ozone in the column. Chemistry, in combination with dynamical effects, led to a reduction in the column abundance of ozone by 88 ± 13 DU (~26% of the observed column abundance of O_3 in March 2000) compared to the amount of O_3 that would have been present without chemistry, if the motions of air were unchanged.

[33] **Acknowledgments.** We thank the THESEO 2000 core group, the SOLVE project scientists, and all personnel associated with the project management for making this campaign possible. We thank the innumerable people that made this study possible due to their dedication: the ground staff at the ozonesonde stations and at ESRANGE, the ER-2 and DC-8 personnel, and the ER-2 and DC-8 pilots. We thank the European Centre for Medium-Range Weather Forecasts for supplying the meteorological data. The ozonesondes used in THESEO 2000 were supported through the EC Environment Programme under contracts EVK2-CT-1999-00047 and through numerous national projects. The SOLVE effort was supported by the Upper Atmospheric Research Program, the Atmospheric Chemistry, Modeling and Analysis Program, and the Atmospheric Effects of Aviation Program of the U.S. National Aeronautics and Space Administration. The POAM III experiment is supported by the U.S. Office of Naval Research and NASA. Research at the Jet Propulsion Laboratory, California Institute of Technology, is performed under contract with the U.S. National Aeronautics and Space Administration. Work at the Alfred Wegener Institute was supported by the BMBF under the project 07ATC08.

References

Austin, J., N. Butchart, and K. Shine, Possibility of an Arctic ozone hole in a doubled-CO_2 climate, *Nature*, *360*, 221–225, 1992.

Becker, G., R. Müller, D. S. McKenna, M. Rex, and K. S. Carslaw, Ozone loss rates in the Arctic stratosphere in the winter 1991/1992: Model calculations compared with Match results, *Geophys. Res. Let.*, *25*, 4325–4328, 1998.

Becker, G., R. Müller, D. S. McKenna, M. Rex, K. S. Carslaw, and H. Oelhaf, Ozone loss rates in the Arctic stratosphere in the winter 1994/1995: Model simulations underestimate results of the Match analysis, *J. Geophys. Res.*, *105*, 15,175–15,184, 2000.

Bevilacqua, R. M., C. P. Aellig, and J. E. Rosenfield, POAM II ozone observations in the Antarctic ozone hole in 1994, 1995, and 1996, *J. Geophys. Res.*, *102*, 23,643–23,658, 1997.

Beyerle, G., R. Neuber, O. Schrems, F. Wittrock, and B. Knudsen, Multiwavelength lidar measurements of stratospheric aerosols above Spitsbergen during winter 1992/1993, *Geophys. Res. Lett.*, *21*, 57–60, 1994.

Bremer, H., M. von König, A. Kleinböhl, H. Küllmann, K. Künzi, K. Bramstedt, J. P. Burrows, K.-U. Eichmann, M. Weber, and A. P. H. Goede, Ozone depletion observed by Airborne Submillimeter Radiometer during the Arctic winter 1999/2000, *J. Geophys. Res.*, *107*, 10.1029/2001JD000546, in press, 2002.

Chipperfield, M. P., Multiannual simulations with a three-dimensional chemical transport model, *J. Geophys. Res.*, *104*, 1781–1806, 1999.

Chipperfield, M. P., and R. L. Jones, Relative influence of atmospheric chemistry and transport on Arctic ozone trends, *Nature*, *400*, 551–554, 1999.

Greenblatt, J. B., et al., Defining the polar vortex edge from an N_2O: potential temperature correlation, *J. Geophys. Res.*, *107*, 10.1029/2001JD000575, in press, 2002a.

Greenblatt, J. B., et al., Tracer-based determination of vortex descent in the 1999/2000 Arctic winter, *J. Geophys. Res.*, *107*, 10.1029/2001JD000937, in press, 2002b.

Hansen, G., T. Svenoe, M. P. Chipperfield, A. Dahlback, and U.-P. Hoppe, Evidence of substantial ozone depletion in winter 1995/1996 over northern Norway, *Geophys. Res. Lett.*, *24*, 799–802, 1997.

Hanson, D. R., and K. Mauersberger, Laboratory studies of the nitric acid trihydrate: Implications for the south polar stratosphere, *Geophys. Res. Lett.*, *15*, 855–858, 1988.

Hofmann, D. J., and T. Deshler, Evidence from balloon measurements for chemical depletion of stratospheric ozone in the Arctic winter of 1989–90, *Nature*, *349*, 300–305, 1991.

Hoppel, K., R. M. Bevilacqua, G. Nedoluha, C. Deniel, F. Lefevre, J. D.

Lumpe, M. D. Fromm, C. E. Randall, J. E. Rosenfield, and M. Rex, POAM III observations of arctic ozone loss for the 1999/2000 winter, *J. Geophys. Res.*, *107*, 10.1029/2001JD000476, in press, 2002.

Knudsen, B., et al., Ozone depletion in and below the Arctic vortex for 1997, *Geophys. Res. Lett.*, *25*, 627–630, 1998.

Lucke, R. L., et al., The Polar Ozone and Aerosol Measurement (POAM) III instrument and early validation results, *J. Geophys. Res.*, *104*, 18,785–18,799, 1999.

Manney, G. L., et al., Chemical depletion of ozone in the Arctic lower stratosphere during winter 1992–93, *Nature*, *370*, 429–434, 1994.

Michelsen, H. A., G. L. Manney, M. R. Gunson, and R. Zander, Correlations of stratospheric abundances of NO_y, O_3, N_2O, and CH_4 derived from ATMOS measurements, *J. Geophys. Res.*, *103*, 2777–2780, 1998.

Müller, R., et al., Severe chemical ozone loss in the Arctic during the winter of 1995–1996, *Nature*, *389*, 709–712, 1997.

Pierson, J. M., et al., An investigation of ClO photochemistry in the chemically perturbed Arctic vortex, *J. Atmos. Chem.*, *32*, 61–81, 1999.

Plumb, R. A., D. W. Waugh, and M. P. Chipperfield, The effects of mixing on tracer relationships in the polar vortices, *J. Geophys. Res.*, *105*, 10,047–10,062, 2000.

Proffitt, M. H., et al., Ozone loss in the Arctic polar vortex inferred from high altitude aircraft measurements, *Nature*, *347*, 31–36, 1990.

Ray, E. A., F. L. Moore, J. W. Elkins, D. F. Hurst, P. A. Romashkin, G. S. Dutton, and D. W. Fahey, Descent and mixing in the 1999/2000 northern polar vortex inferred from in situ tracer measurements, *J. Geophys. Res.*, *107*, 10.1029/2001JD000961, in press, 2002.

Rex, M., et al., Prolonged stratospheric ozone loss in the 1995–96 Arctic winter, *Nature*, *389*, 835–838, 1997.

Rex, M., et al., In situ measurements of stratospheric ozone depletion rates in the Artic winter 1991/1992: A Lagrangian approach, *J. Geophys Res.*, *103*, 5843–5853, 1998.

Rex, M., et al., Chemical ozone loss in the Arctic winter 1994/95 as determined by the Match technique, *J. Atmos. Chem.*, *32*, 35–39, 1999.

Rex, M., et al., Arctic and Antarctic ozone layer observations—Chemical and dynamical aspects of variability and long-term changes in the polar stratosphere, *Polar Res.*, *19*(2), 193–204, 2000.

Richard, E. C., K. C. Aikin, A. E. Andrews, B. C. Daube, C. Gerbig, S. C. Wofsy, P. A. Romashkin, D. F. Hurst, E. A. Ray, and F. L. Moore, Severe chemical ozone loss inside the Arctic polar vortex during winter 1999–2000 inferred from in situ airborne measurements, *Geophys. Res. Lett.*, *28*, 2197–2200, 2001.

Salawitch, R. J., et al., Chemical loss of ozone in the Arctic polar vortex in the winter of 1991–92, *Science*, *261*, 1146–1149, 1993.

Salawitch, R. J., et al., Chemical loss of ozone during the Artic winter of 1999/2000: An analysis based on balloon-borne observations, *J. Geophys. Res.*, *107*, 10.1029/2001JD000620, in press, 2002.

Santee, M. L., G. L. Manney, N. J. Livesey, and J. W. Waters, UARS Microwave Limb Sounder observations of denitrification and ozone loss in the 2000 Arctic late winter, *Geophys. Res. Lett.*, *27*, 3213–3216, 2000.

Schoeberl, M. R., et al., Stratospheric constituent trends from ER-2 profile data, *Geophys. Res. Lett.*, *17*, 469–472, 1990.

Shindell, D. T., D. Rind, and P. Lonergang, Increased polar stratospheric ozone losses and delayed eventual recovery owing to increasing greenhouse-gas concentrations, *Nature*, *392*, 589–592, 1998.

Sinnhuber, B.-M., et al., Large loss of total ozone during the Arctic winter of 1999/2000, *Geophys. Res. Lett.*, *27*, 3473–3476, 2000.

Solomon, S., Stratospheric ozone depletion: A review of concepts and history, *Rev. Geophys.*, *37*, 275–316, 1999.

Vömel, H., D. W. Toohey, T. Deshler, and C. Kroger, Sunset observations of ClO in the arctic polar vortex and implications for ozone loss, *Geophys. Res. Lett.*, *28*, 4183–4186, 2001.

von der Gathen, P., et al., Observational evidence for chemical ozone depletion over the Arctic winter 1991–92, *Nature*, 375, 1995.

Woyke, T., et al., A test of our understanding of the ozone chemistry in the Arctic polar vortex based on in situ measurements of ClO, BrO, and O_3 in the 1994/1995 winter, *J. Geophys Res.*, *104*, 18,755–18,768, 1999.

H. Deckelmann, R. Neuber, M. Rex, A. Schulz, and P. von der Gathen, Alfred Wegener Institute for Polar and Marine Research, P.O. Box 600149 D-14401 Potsdam, Germany. (hdec@AWI-Potsdam.de; neuber@awi-potsdam.de; mrex@awi-Potsdam.de; aschulz@AWI-Potsdam.de; gathen@AWI-Potsdam.de)

J. Flesch, R. L. Herman, J. J. Margitan, R. J. Salawitch, G. D. C. Scott, B. Sen, C. G. C. Toon, and R. Webster, Jet Propulsion Laboratory, California Institute of Technology, 4800 Oak Grove Drive, Pasadena, CA 91109, USA. (gregory.j.flesch@jpl.nasa.gov; rherman@igor.jpl.nasa.gov; jjm@caesar.jpl.nasa.gov; rjs@caesar.jpl.nasa.gov; dcscott@igor.jpl.nasa.gov; bhaswar.sen@jpl.nasa.gov; toon@mark4sun.jpl.nasa.gov; chris.r.webster@jpl.nasa.gov)

N. R. P. Harris, European Ozone Research Coordinating Unit, 14 Union Road, Cambridge CB2 1HE, UK. (neil.harris@atm.ch.cam.ac.uk)

B. R. Bojkov and G. O. Braathen, NILU, Instituttveien 18, P.O. Box 100, N-2007 Kjeller, Norway. (bojan@nilu.no; geir@nilu.no)

M. Chipperfield and B.-M. Sinnhuber, University of Leeds, Leeds, LS2 9JT, UK. (martyn@lec.leeds.ac.uk; bms@env.leeds.ac.uk)

R. Alfier and E. Reimer, Meteorological Institute, FU Berlin, C.-H.-Becker Weg 6-10, D-12165 Berlin, Germany. (alfier@strat25.met.fu-berlin. de; reimer@zedat.fu-berlin.de)

R. Bevilacqua and K. Hoppel, Naval Research Laboratory, Code 7220, Washington, D.C. 20375, USA. (bevilacq@poamb.nrl.navy.mil; hoppel@poamb.nrl.navy.mil)

M. Fromm and J. Lumpe, Computational Physics, Inc., 8001 Braddock Road, Springfield, VA 22151, USA. (fromm@poama.nrl.navy.mil; lumpe@cpi.com)

H. Bremer, A. Kleinböhl, H. Küllmann, K. Künzi, and M. von König, Institute of Environmental Physics, University of Bremen, P.O. Box 330 440, D-28334 Bremen, Germany. (holger@clox.physik.uni-bremen.de; kleinb@clox.physik.uni-bremen.de; harry@schalk.physik.uni-bremen.de; kunzi@physik.uni-bremen.de; miriam@iup.physik.uni-bremen.de)

D. Toohey, Program in Atmospheric and Oceanic Science, University of Colorado, Boulder, PAOS/311 UCB, Boulder, CO 80309, USA. (toohey@colorado.edu)

H. Vömel, Cooperative Institute for Research in Environmental Sciences (CIRES), Campus Box 216, University of Colorado, Boulder, CO 80309, USA. (hvoemel@cmdl.noaa.gov)

K. Aikin, J. W. Elkins, D. F. Hurst, F. L. Moore, E. A. Ray, E. Richard, and P. Romashkin, National Oceanic and Atmospheric Administration, Boulder, CO 80303, USA. (aikin@al.noaa.gov; jelkins@cmdl.noaa.gov; dhurst@cmdl.noaa.gov; fmoore@cmdl.noaa.gov; eray@cmdl.noaa.gov; richard@al.noaa.gov; promashkin@cmdl.noaa.gov)

H. Jost, J. B. Greenblatt, M. Loewenstein, and J. R. Podolske, NASA Ames Research Center, Moffett Field, CA 94035, USA. (hjost@mail.arc.nasa.gov; jgreenblatt@mail.arc.nasa.gov; mloewenstein@mail.arc.nasa.gov; jpodolske@mail.arc.nasa.gov)

P. Wennberg, Division of Geological and Planetary Sciences, California Institute of Technology, Pasadena, CA 91125, USA. (wennberg@gps.caltech.edu)

M. Allart, KNMI, P.O. Box 201, N-3730 AE De Bilt, Netherlands. (allaart@knmi.nl)

H. Claude, DWD, Observatory Hohenpeißenberg, Albin-Schwaiger-Weg 10, D-82383 Hohenpeißenberg, Germany. (claude@mohp.dwd.d400.de)

J. Davies and H. Fast, Atmospheric Environment Service, 4905 Dufferin Street, Downsview, ON, M3H 5T4, Canada. (jonathan.davies@ec.gc.ca; hans.fast@ec.gc.ca)

W. Davies, Department of Physics, University of Wales, Aberystwyth, SY23 3BZ Wales, UK. (wdd@aber.ac.uk)

H. de Backer, Royal Meteorological Institute, Ringlaan 3, B-1180 Brussels, Belgium. (hugo@oma.be)

H. Dier, Meteorologisches Observatorium Lindenberg, D-15864 Lindenberg, Germany. (dier@mol.dwd.d400.de)

V. Dorokhov, CAO, Pervomajskaya Street 3, Dolgoprudny, Moscow Region, 141700, Russia. (vdor@ozone.mipt.ru)

Y. Kondo, Research Center for Advanced Science and Technology, University of Tokyo, 4-6-1 Komaba, Meguro, Tokyo 153-8904, Japan. (kondo@atmos.rcast.u-tokyo.ac.jp)

E. Kyrö, MWM, Centre of Aerology, Zegrzynska Str. 38, 05-119 Legionowo, Poland. (esko.kyro@fmi.fi)

Z. Litynska, Institute of Meteorology and Water Management, Centre of Aerology, Zegrzynska Str. 38, 95-119 Legionowo, Poland. (zenoblit@pol.pl)

I. S. Mikkelsen, Danish Meteorological Institute, Lyngbyvej 100, DK-2100 Copenhagen Oe, Denmark. (ism@dmi.min.dk)

M. J. Molyneux, UK Met Office OP2C, London Road, Bracknell, Berkshire, RG11 2SZ, UK. (mjmolyneux@meto.gov.uk)

E. Moran and V. Yushkov, IMS, Valentia Observatory, Cahirciveen, Co. Kerry, Ireland. (eoinm@valentia.iol.ie; vvcao@ozone.mipt.ru)

T. Nagai, Meteorological Research Institute, 1-1, Nagamine, Tsukuba, Ibaraki 305-0052, Japan. (tnagai@mri-jma.go.jp)

H. Nakane, National Institute for Environmental Studies, 16-2 Onogawa, Tsukuba, Ibaraki 305-0053, Japan. (nakane@nies.go.jp)

C. Parrondo, INTA, Torrejon de Argoz, Madrid, Spain. (parrondosc@inta.es)

F. Ravegnani, C.N.R. Fisbat Institute, Via Gobetti 101, Bologna, Italy. (fabrizio@o3.fisbat.bo.cnr.it)

P. Skrivankova, Czech Hydrometical Institute, Na Sabatce 17, 14306 Prague, Czech Republic. (skrivankova@chmi.cz)

P. Viatte, SMI, Les Invuardes, CH-1530 Payerne, Switzerland. (pvi@sap.sma.ch)

GEOPHYSICAL RESEARCH LETTERS, VOL. 30, NO. 1, 1008, doi:10.1029/2002GL016008, 2003

On the unexplained stratospheric ozone losses during cold Arctic Januaries

M. Rex,[1] R. J. Salawitch,[2] M. L. Santee,[2] J. W. Waters,[2] K. Hoppel,[3] and R. Bevilacqua[3]

Received 30 July 2002; revised 27 September 2002; accepted 25 October 2002; published 7 January 2003.

[1] Using a combination of data from Match, POAM II, POAM III and MLS we show that the chemical loss rate of Arctic O_3 during January of four cold winters (1992, 1995, 1996, and 2000) is consistently faster than can be accounted for by assuming complete activation of reactive chlorine and standard reaction kinetics. However, O_3 loss rates measured during late February and early March 1996 are shown to be consistent with observations of ClO. The faster than expected O_3 loss rates during January are shown to occur when air parcels are illuminated at high solar zenith angles (SZAs between ~85 and 94°), and to result in cumulative O_3 loss of ~0.5 ppmv. The cause of the rapid January O_3 loss is unclear, but may be related to a photolytic process at high SZA that is poorly represented by current photochemical models. *INDEX TERMS:* 0340 Atmospheric Composition and Structure: Middle atmosphere—composition and chemistry; 1610 Global Change: Atmosphere (0315, 0325); 3337 Meteorology and Atmospheric Dynamics: Numerical modeling and data assimilation; 9315 Information Related to Geographic Region: Arctic region. **Citation:** Rex, M., R. J. Salawitch, M. L. Santee, J. W. Waters, K. Hoppel, and R. Bevilacqua, On the unexplained stratospheric ozone losses during cold Arctic Januaries, *Geophys. Res. Lett.*, *30*(1), 1008, doi:10.1029/2002GL016008, 2003.

1. Introduction

[2] Proper understanding of the timing and extent of chemical depletion of Arctic O_3 is a prerequisite for developing reliable assessments of future ozone abundances. Early studies suggested consistency between *observed* rates of chemical O_3 loss (hereafter referred to as O_3*loss_obs*) and *modeled* loss rates (O_3*loss_mdl*) based on measured concentrations of ClO and BrO and relevant laboratory kinetics [e.g., *Salawitch et al.*, 1990]. These studies focused primarily on February to March and were limited by large (e.g., factor of two) uncertainties in O_3*loss_obs* [*Schoeberl et al.*, 1990].

[3] Several recent studies suggest that observed rates of chemical loss of Arctic O_3 are considerably faster than expected during mid-winter [e.g., *Becker et al.*, 1998; *Hansen et al.*, 1997; *Deniel et al.*, 1998].

[4] Using a combination of data from the Match technique, POAM II, POAM III and the Microwave Limb Sounder (MLS), we show that Arctic ozone loss during cold Arctic Januaries is consistently faster than is currently understood. Our study focuses on four cold Arctic winters that experienced significant chemical ozone depletion during January.

2. Chemical Loss of Arctic Ozone: January

[5] Figure 1 shows values of O_3 *loss_obs* on isentropic surfaces of the lower stratosphere found by the Match technique. These measurements are based on data collected by ozonesondes from dozens of stations in a coordinated manner that allows air masses to be sampled multiple times as they traverse the vortex [e.g., *Rex et al.*, 1998, 1999]. The loss rates are expressed in ppbv/sunlit hour SVA <~95°.

[6] Chemical loss of O_3 per sunlit hour peaks in January of all winters due to greater abundances of ClO_x [*Rex et al.*, 1997, 2002]. Data for January 1995 and 2000 are shown for the isentropic surfaces that experienced the largest ozone loss rates (490 and 500 K respectively). For 1992 and 1996, sufficient numbers of ozonesonde observations are not available to precisely define loss rates above 475 K. Therefore, for those years, ozone loss rates at the 475 K level are given in Figure 1.

[7] We have used a photochemical box model to calculate the level of ClO_x (ClO + 2 × ClOOCl) that would be required to account for the observed O_3 loss rates along Match trajectories. In the model we use a simple theoretical framework for the representation of the diurnal variation of ClO, ClOOCl, OClO, BrO, BrCl, and atomic O [*Salawitch et al.*, 1993]. Values of BrO are found by specifying the sum, BrO + BrCl, as a function of potential temperature such that observed mixing ratios of BrO in the Arctic vortex [*Avallone et al.*, 1995] are reproduced. Measurements of O_3 from Match are also specified along each trajectory. The calculations assume constant ClO_x along each Match trajectory, account for the effects of variations in temperature and solar insolation and use kinetic parameters from JPL00-3 [*Sander et al.*, 2000]. Use of the *Bloss et al.* [2001] rate for ClO + ClO + M has little effect on our model calculations because a faster rate titrates ClO into ClOOCl and the increase in O_3 loss due to the ClO + ClO cycle is nearly balanced by a slowing down of the BrO + ClO cycle.

[8] The level of ClO_x necessary to account for the observed ozone loss rates in January exceeds 5 ppbv for each winter analyzed. This is larger than 3.7 ppbv, the total amount of inorganic chlorine present in the stratosphere [*WMO*, 1998]. Ozone loss rates for January found by assuming ClO_x equals 3.7 ppbv are also shown in Figure 1. The failure to fully account for O_3 *loss_obs*, even assuming complete activation of ClO_x, is robust for reasonable uncertainties in the reaction coefficients of the primary ozone loss cycles (ClO + ClO and BrO + ClO). These analyses suggest

---

[1] Alfred Wegener Institute for Polar and Marine Research, Potsdam, Germany.

[2] Jet Propulsion Laboratory, California Institute of Technology, Pasadena, California, USA.

[3] Naval Research Laboratory, Washington, DC, USA.

Copyright 2003 by the American Geophysical Union.
0094-8276/03/2002GL016008$05.00

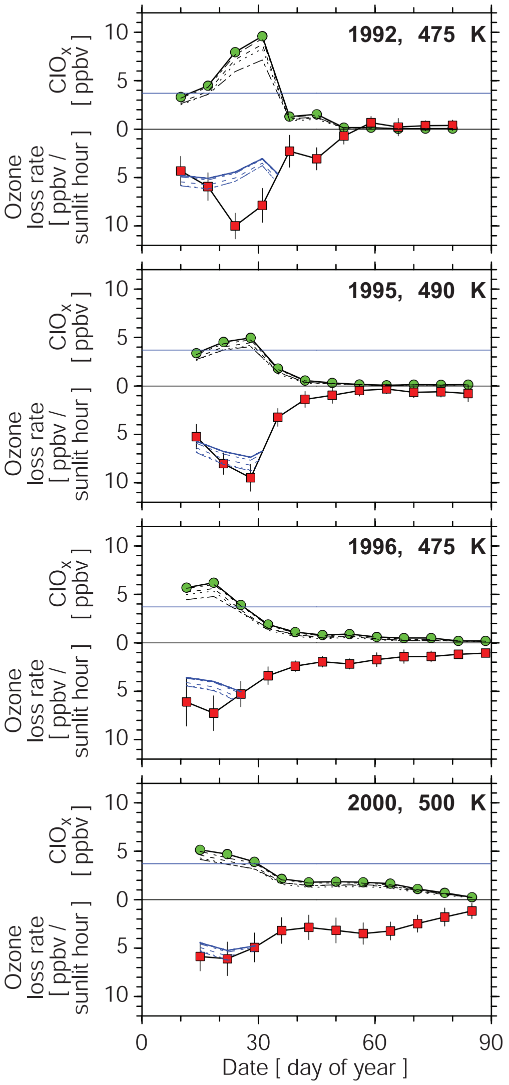

Figure 1. Chemical loss rate of O_3 (O_3 *loss_obs*) in the Arctic vortex based on Match (red boxes; error bars are 1σ uncertainty). The abundance of ClO_x necessary to account for O_3 *loss_obs* (green dots) and an estimate of O_3 *loss_mdl* for January of each year assuming ClO_x = 3.7 ppbv (horizontal blue line) are also shown. Dashed lines: BrO_x based on measurements of BrO by Pfeilsticker et al. (private communication) (run 1). Dotted lines: These values for BrO_x plus 20% (run 2). Dash-dotted lines: J_{Cl2O2} plus 50% (run 3). Dash-dot-dotted lines: $k_{ClO+ClO}$ plus 30% (run 4). Run 2 and 3 are the lines farthest from the base run, run 4 lies closest to it.

that loss of O_3 in January occurs by a process that is not well represented by current models.

[9] Observed ozone loss rates exceed the maximum possible modeled loss rate (assuming ClO_x = 3.7 ppbv) by 2σ to 3σ for late January 1992 and by 1σ to 2σ for parts of mid to late January of other years.

[10] The model calculations depend on the abundance of BrO_x, the photolysis rate of Cl_2O_2 (J_{Cl2O2}) and the constant rate for the reaction ClO + ClO + M ($k_{ClO+ClO}$). We have varied these parameters within reasonable limits, i.e. for BrO the highest measurements of bromine reported for the Arctic so far (Pfeilsticker et al., private communication) plus 20%, these runs were designed to encompass uncertainties in both BrO and $K_{BrOTClO}$ for $k_{ClO+ClO}$ the uncertainty given in JPL00-3 (which encompasses the values reported by *Bloss et al.* [2001]), and for J_{Cl2O2} the recommended value ±50%. The results of some of these sensitivity studies are given in Figure 1. For some of the points in January the discrepancy is larger than the combined uncertainties of the model results and the observations. Our assessment that this discrepancy is significant is based also on the consistent observation of faster than expected ozone loss rates for all cold Januaries during the past decade. However, the uncertainty for J_{Cl2O2} given in JPL00-3 at 50 hPa is about a factor of three. Using the upper limit of J_{Cl2O2} based on this uncertainty, all measurements fall within the model uncertainty, with the exception of two points in January 1992. But increasing J_{Cl2O2} by a factor of three would not be consistent with analysis of ClO measurements at high SZA [e.g. *Avallone and Toohey*, 2001; *Vömel et al.*, 2001], which suggest that the 50% used here is a more realistic estimate for the uncertainty. Finally, the Match observation of essentially zero rates of chemical O_3 loss for January of warm winters (e.g., 1998 and 1999) [*Schulz et al.*, 2001], when higher levels of planetary wave activity pose greater challenges to the Match approach than for cold winters, increases our confidence in the validity of the observed January loss rates shown here.

[11] A bivariate linear regression has been applied to the data to determine whether sunlight exposure is associated with chemical ozone loss [*Rex et al.*, 1999]. Ozone depletion is found only for the sunlit segments along the trajectories (Figure 2). No significant change in O_3 is found for complete darkness. The consistency of these results for four winters suggests that the unaccounted for ozone loss process is photolytic.

[12] The accumulated loss of ozone can be calculated on surfaces that follow the diabatic descend of air [*Rex et al.*, 1997]. For 1994/1995 and 1999/2000 a vertical profile of the overall loss at the end of January (Figure 3) can be derived from the Match results. Accumulated O_3 loss measured by POAM II and POAM III for January 1995, 1996, and 2000, found by allowing vortex averaged ozone to descend using calculated cooling rates [*Hoppel et al.*, 2002], compares well with Match observations considering the respective uncertainties (Figure 3). Significant chemical removal of O_3 during January has been reported by other techniques. Accumulated chemical loss of 0.5 ppmv of ozone at 465 K was observed by MLS during January 1995 (Figure 3), in excellent quantitative agreement with ozone reductions found by Match [*Harris et al.*, 2002].

[13] In January 2000 accumulated loss of O_3 was (~0.22 ± 0.13 ppmv) at the cruise altitude of the NASA ER-2 aircraft during January, consistent with the finding of little or no chemical loss of ozone (0.0 ± 0.15 ppmv) from ER-2 observations during January 2000 [*Richard et al.*, 2001].

3. February and March

[14] Changes in ozone per sunlit hour are smaller in February and March compared to January because of partial

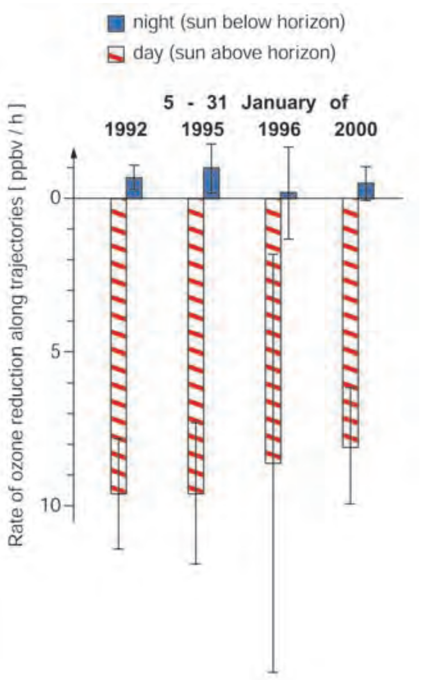

Figure 2. Rate of change of ozone along Match trajectories during sunlit conditions and during dark periods based on bivariate regressions for data collected between 5 and 31 January of each year for the set of matches used in Figure 1. Error bars are 1σ statistical uncertainties. During January 1996 a smaller number of ozone soundings have been performed and the uncertainty of the bivariate analysis is much larger.

recovery of ClO_x to the $ClNO_3$ reservoir [*Rex et al.*, 1997, 2002]. In this section, we use MLS observations of ClO to calculate loss rates along the Match trajectories, and compare them to Match estimates of O_3 *loss_obs*.

[15] 1996 is the only year for which Match observations of rapid ozone loss overlapped with sufficiently dense MLS observations of ClO to allow the reconstruction of ClO_x along the Match trajectories. MLS observations during rapid ozone loss in other years were not available due to the monthly yaw of the Upper Atmospheric Research Satellite (UARS) or were not sufficiently dense due to difficulties with the MLS scan mechanism in later years.

[16] We have reconstructed the abundance of ClO_x along the Match trajectories by interpolating between mixing ratios of ClO_x that have been inferred from MLS measurements of ClO close to the respective trajectories. We use Version 5 MLS retrievals, which provide a better definition of the vertical distribution of ClO than previous MLS retrievals [*Livesey et al.*, 2002]. O_3 *loss_mdl* was calculated along each Match trajectory at 475 K for this time period. All other assumptions (i.e., BrO_x, O_3) are as previously described.

[17] Excellent agreement is found between the observed and modeled loss rates for late February/early March 1996 (Figure 4). The ozone loss per sunlit hour) is considerably smaller than during January. Abundances of ClO_x inferred from MLS ClO along Match trajectories range from ∼1.2 to 2.6 ppbv. Most importantly, the Match trajectories spend a considerably smaller portion of their overall sunlit time at high SZA (e.g., between ∼85 and 94°) than during January.

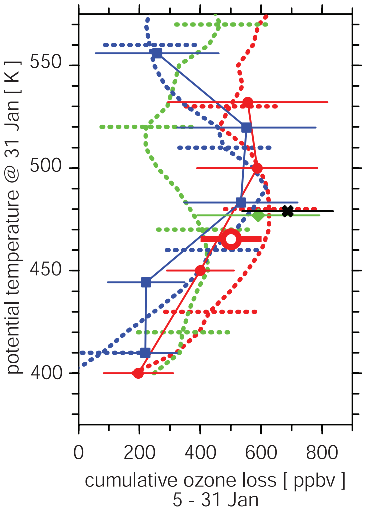

Figure 3. Accumulated chemical loss of O_3 versus potential temperature for 5–31 January of 1992 (black), 1995 (red), 1996 (green), and 2000 (blue), as derived by various methods: Match (solid lines with solid markers), MLS (single open marker) [*Harris et al.*, 2002] and POAM (dotted lines). For the latter an ozone versus PV relation was derived from measurements made during day 32 ± 2 days. The vortex average ozone profile was calculated based on these relations at various heights. The ozone loss was then estimated by comparing this profile with subsided vortex average profiles calculated with the same approach for day 5 ± 2 days. Error bars represent 1σ uncertainties.

4. Discussion

[18] Standard photochemical models predict relatively slow rates of polar O_3 loss at high SZA (e.g., between 85 and 94°) because strong attenuation of UV light, due to the high O_3 slant columns, limits the photolysis rate of ClOOCl and hence the overall rate of O_3 loss by the ClO + ClO and BrO + ClO cycles.

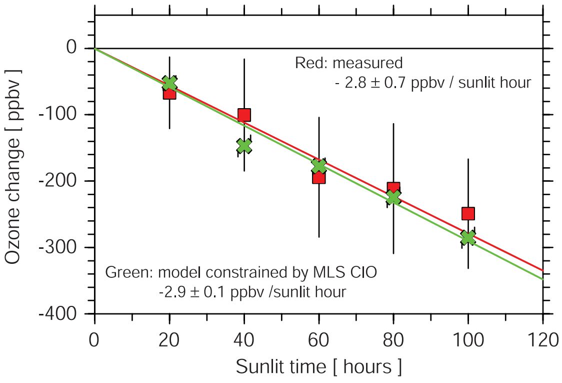

Figure 4. The chemical loss of O_3 measured by Match between 20 February and 3 March 1996 at 475 K versus the amount of sunlight exposure along each Match trajectory (red squares) and the computed reduction in O_3 along the same trajectory based on MLS Version 5 measurements of ClO (green crosses). Error bars are 1σ sigma standard deviations.

[19] Longwave photolysis of ClOOCl by an unknown state in the near IR (wavelengths > 800 nm, which is optically thin even at high SZA) could principally provide a strong enhancement to the abundance of Cl and ClO during twilight and hence faster ozone loss. However, in-situ observations of ClO provide evidence that ClOOCl does not photolyze at an appreciable rate in the near IR [*Avallone and Toohey*, 2001; *Vömel et al.*, 2001; R. M. Stimpfle, private comm., 2002].

[20] O_3 could also be lost by reactions on the surface of PSCs (polar stratospheric clouds). The upper limit for the reaction probability of this process, 2.5×10^{-4} on the surface of nitric acid trihydrate [*Sander et al.*, 2000], suggests that this process could contribute significantly to ozone loss in January. For each January considered here, air was exposed to considerable amounts of PSCs during both day and night. Our finding that loss of ozone occurs only during sunlit periods suggests that, if direct loss on PSC surfaces is responsible, such loss must be driven by photons.

[21] Observations indicate that BrO does not fall off with increasing SZA near sunset as rapidly as expected [*Wahner and Schiller*, 1992; *Avallone and Toohey*, 2001]. But it is not clear how enhanced BrO in twilight could lead to appreciable increases in chemical loss rates since ClO is observed to decline with increasing SZA essentially as expected [*Vömel et al.*, 2001 at sunrise. Observations of a burst of ClO at sunrise [*Pierson et al.*, 1999] and unusually high amounts of BrO at twilight [*Avallone and Toohey*, 2001] suggest that halogen chemistry at high SZA is not fully understood. Perhaps loosely bound higher oxides of ClOOCl contribute to the rapid ozone loss found in January, either by reaction with BrO or in other yet unidentified ozone loss cycles [*Sander et al.*, 1989]. Better understanding of the photochemistry of this time period requires more extensive observations at high SZA, and appropriate potential temperature levels (e.g., 480 to 520 K), of BrO, other radicals, and a variety of chlorine species to test the budget and partitioning of halogens in the stratosphere.

5. Concluding Remarks

[22] The consistent inability to fully account for observed ozone loss rates during cold Arctic Januaries suggests the existence of a currently unknown ozone loss mechanism. Detailed analyses suggest that this loss process involves a photolytic step. The lack of measurable loss during warm winters indicates that the process is related to ClO_x and/or PSCs. Observed ozone loss later during winter is in good agreement with model results based on observed ClO, suggesting that the unknown ozone loss mechanism is most important at high SZA and low temperatures typical of January conditions.

[23] During cold Arctic Januaries we find cumulative ozone loss of about 0.5 ppmv. This is modest for winters with massive ozone depletion. For such Arctic winters, loss of ozone predominantly occurs during February and March by known catalytic processes that operate efficiently under conditions of high solar illumination. Nonetheless, the January discrepancy demands further investigation because reliable assessments of future Arctic ozone depletion require a full understanding of all significant processes that affect ozone.

[24] **Acknowledgments.** We have benefited from public discussion of this material at the Arctic Ozone Workshop held in Potsdam, Germany during March 2002. Research at the Jet Propulsion Laboratory (JPL), California Institute of Technology, is performed under contract with the National Aeronautics and Space Administration. This work was initiated when M. Rex was at JPL, supported by the NASA UARS Guest Investigator Program. Work at the Alfred Wegener Institute was supported by the BMBF under the project AFO 2000/07ATC08.

References

Avallone, L. M., and D. W. Toohey, Tests of halogen photochemistry using in situ measurements of ClO and BrO in the lower polar stratosphere, *J. Geophys. Res.*, *106*, 10,411–10,421, 2001.

Avallone, L. M., D. W. Toohey, and K. R. Chan, In situ measurements of BrO during AASE II, *Geophys. Res. Lett.*, *22*, 831, 1995.

Becker, G., et al., Ozone loss rates in the Arctic stratosphere in the winter 1991/92: Model calculations compared with Match results, *Geophys. Res. Lett.*, *25*, 4325–4328, 1998.

Bloss, W. J., et al., Kinetics of the ClO self reaction and 210 nm absorption cross section of the ClO dimer, *J. Phys. Chem. A.*, *105*, 11,226–11,239, 2001.

Deniel, C., et al., Arctic chemical ozone depletion during the 1994–1995 winter from POAM II observations and the REPROBUS 3D model, *J. Geophys. Res.*, *103*, 19,231–19,244, 1998.

Hansen, G., et al., Evidence of substantial O_3 depletion in winter 1995/96 over Norway, *Geophys. Res. Lett.*, *24*, 799–802, 1997.

Harris, N. R. P., et al., Comparison of empirically derived ozone losses in the Arctic vortex, *J. Geophys. Res.*, in press, 2002.

Hoppel, K., et al., POAM III observations of Arctic ozone loss for the 1999/2000 winter, *J. Geophys. Res.*, *25*, in press, 2002.

Livesey, N. J., et al., The UARS Microwave Limb Sounder version 5 data set: Theory, characterization and validation, submitted to *J. Geophys. Res.*, 2002.

McKinney, K. A., J. M. Pierson, and D. W. Toohey, A winter time in-situ profile of BrO between 17 and 27 km in the Arctic vortex, *Geophys. Res. Lett.*, *24*, 853, 1997.

Pierson, J. M., K. A. McKinney, D. W. Toohey, J. Margitan, U. Schmidt, A. Engel, and P. A. Newman, An investigation of ClO photochemistry in the chemically perturbed Arctic vortex, *J. Atmos. Chem.*, *32*, 61, 1999.

Rex, M., et al., Prolonged stratospheric ozone loss in the 1995–96 Arctic winter, *Nature*, *389*, 835–838, 1997.

Rex, M., et al., In situ measurements of stratospheric ozone depletion rates in the Arctic winter 1991/1992: A Lagrangian approach, *J. Geophys. Res.*, *103*, 5843–5853, 1998.

Rex, M., et al., Chemical ozone loss in the Arctic winter 1994/95 as determined by Match, *J. Atmos. Chem.*, *32*, 35–59, 1999.

Rex, M., et al., Chemical depletion of Arctic ozone in winter 1999/2000, *J. Geophys. Res.*, in press, 2002.

Richard, E., et al., Severe chemical ozone loss inside the Arctic polar vortex during winter 1999–2000 inferred from in situ airborne measurements, *Geophys. Res. Lett.*, *28*, 2197–2200, 2001.

Salawitch, R. J., et al., Loss of ozone in the Arctic vortex for the winter of 1989, *Geophys. Res. Lett.*, *17*, 561–564, 1990.

Salawitch, R. J., et al., Chemical loss of ozone in the Arctic polar vortex in the winter of 1991–92, *Science*, *261*, 1146–1149, 1993.

Sander, S. P., R. R. Friedl, and Y. L. Yung, Rate of formation of the ClO dimer in the polar stratosphere: Implications for ozone loss, *Science*, *245*, 1095–1098, 1989.

Sander, S. P., et al., Chemical kinetics and photochemical data for use in stratospheric modeling, JPL Public. 00-3, Pasadena, CA, 2000.

Schoeberl, M. R., et al., Stratospheric constituent trends from ER-2 profile data, *Geophys. Res. Lett.*, *17*, 469–472, 1990.

Schulz, A., et al., Arctic ozone loss in threshold conditions: Match observations in 1997/98 and 1998/99, *J. Geophys. Res.*, *106*, 7495–7504, 2001.

Vömel, H., D. W. Toohey, T. Deshler, and C. Kröger, Sunset observations of ClO in the Arctic polar vortex and implications for ozone loss, *Geophys. Res. Lett.*, *28*, 4183–4186, 2001.

M. Rex, Alfred Wegener Institute for Polar and Marine Research, Potsdam, Germany.

R. J. Salawitch, M. L. Santee, and J. W. Waters, Jet Propulsion Laboratory, California Institute of Technology, Pasadena, CA, USA.

K. Hoppel and R. Bevilacqua, Naval Research Laboratory, Washington, DC, USA.

GEOPHYSICAL RESEARCH LETTERS, VOL. 31, L04116, doi:10.1029/2003GL018844, 2004

Arctic ozone loss and climate change

M. Rex,[1] R. J. Salawitch,[2] P. von der Gathen,[1] N. R. P. Harris,[3]
M. P. Chipperfield,[4] and B. Naujokat[5]

Received 15 October 2003; revised 5 December 2003; accepted 21 January 2004; published 28 February 2004.

[1] We report the first empirical quantification of the relation between winter-spring loss of Arctic ozone and changes in stratospheric climate. Our observations show that ~15 DU additional loss of column ozone can be expected per Kelvin cooling of the Arctic lower stratosphere, an impact nearly three times larger than current model simulations suggest. We show that stratospheric climate conditions became significantly more favorable for large Arctic ozone losses over the past four decades; i.e., the maximum potential for formation of polar stratospheric clouds increased steadily by a factor of three. Severe Arctic ozone loss during the past decade occurred as a result of the combined effect of this long-term climate change and the anthropogenic increase in stratospheric halogens. *INDEX TERMS:* 0340 Atmospheric Composition and Structure: Middle atmosphere—composition and chemistry; 0370 Atmospheric Composition and Structure: Volcanic effects (8409); 1620 Global Change: Climate dynamics (3309); 1610 Global Change: Atmosphere (0315, 0325); 3349 Meteorology and Atmospheric Dynamics: Polar meteorology. **Citation:** Rex, M., R. J. Salawitch, P. von der Gathen, N. R. P. Harris, M. P. Chipperfield, and B. Naujokat (2004), Arctic ozone loss and climate change, *Geophys. Res. Lett.*, *31*, L04116, doi:10.1029/2003GL018844.

1. Arctic Ozone Loss During the Past Decade

[2] We have analyzed about 2000 ozonesoundings within the Arctic polar vortex to quantify chemical loss of ozone for ten recent winters. Figure 1 shows the evolution of the vortex averaged ozone profile over the course of these winters.

[3] Air masses inside the polar vortex are relatively isolated from air at lower latitudes and, over the time scale of weeks, they cool radiatively and their potential temperature decreases, inducing downward transport of ozone rich air. To account for this effect, in Figure 1 the ozone mixing ratio has been plotted versus spring equivalent potential temperature (eΘ). eΘ is the potential temperature a given air mass reached by the end of March. The calculation of eΘ is based on radiative transport calculations [*Shine*, 1987] as described in *Rex et al.* [2002]. Hence, the changes in ozone profiles shown in Figure 1 during the course of an Arctic winter provide a measure of chemical removal of ozone [*Rex et al.*, 2002]. Chemical ozone loss derived with this approach agrees well (within about 20%) with results from other techniques [*Harris et al.*, 2002].

[4] We have estimated the impact of chemical loss on total column ozone (ΔO_3) from the data in Figure 1. The vortex averaged profiles of ozone loss have been determined as the differences between the end of March (red) and the early January (blue) curves in Figure 1. These have been converted into concentration versus altitude profiles, using the vortex averaged temperature and pressure profiles from late March. The total column loss was calculated as the vertical integral of the loss profiles between 14 and 24 km altitude [see *Rex et al.*, 2002, for details]. The lower limit of this range ($\Theta \approx 380$ K) is close to the bottom of the well isolated part of the polar vortex. The results shown in Figure 1 indicate that for most winters ozone loss at this level is small. Also, the effect of any chemical loss in the vertical region below 14 km on the total ozone column in the Arctic would be limited because of rapid exchange with mid latitude air. Formation of PSCs above the vertical range considered here is unlikely and consequently significant chemical loss of ozone is not expected above 24 km. The estimated uncertainty of ΔO_3 is ~10–15 DU [*Rex et al.*, 2002], mainly due to uncertainties in the calculated cooling rates and potential impact of mixing across the vortex edge. Column ozone loss exhibited significant year-to-year variability during the past decade (Figure 2a, red bars), even though total halogen abundances hardly varied [*WMO*, 2003]. Total column ozone in the Arctic during late March typically ranges from 300–500 DU (average values for the last ten days in March calculated from all ozonesonde observations for the region covered by the polar vortex). Our results indicate that chemical loss of column ozone, which has varied between 0 and about 100 DU during the past decade (Figure 2), has contributed about half of the observed year to year variability of total column ozone.

2. Relation Between Ozone Loss and PSC Formation Potential

[5] We calculated the stratospheric volume where conditions were cold enough for the existence of PSCs from meteorological analyses provided by the European Centre for Medium-Range Weather Forecasts (ECMWF). Figure 2a shows the average value of the potential PSC volume over the period mid-December to end of March (V_{PSC}). V_{PSC} was calculated between $\Theta = 400$ and 550 K using the NAT equilibrium temperature and standard profiles for HNO_3 and H_2O (see *Rex et al.* [2002] for details). Observations of the location of PSCs agree well with this definition for V_{PSC} [*Rex et al.*, 2002]. The degree of Arctic ozone loss and V_{PSC} are closely related (Figure 2b). The slope of a linear fit is

---

[1] Alfred Wegener Institute for Polar and Marine Research, Potsdam, Germany.
[2] Jet Propulsion Laboratory, California Institute of Technology, Pasadena, CA, USA.
[3] European Ozone Research Coordinating Unit, Cambridge, UK.
[4] School of the Environment, University of Leeds, Leeds, UK.
[5] Free Univ. of Berlin, Meteorological Institute, Berlin, Germany.

Copyright 2004 by the American Geophysical Union.
0094-8276/04/2003GL018844$05.00

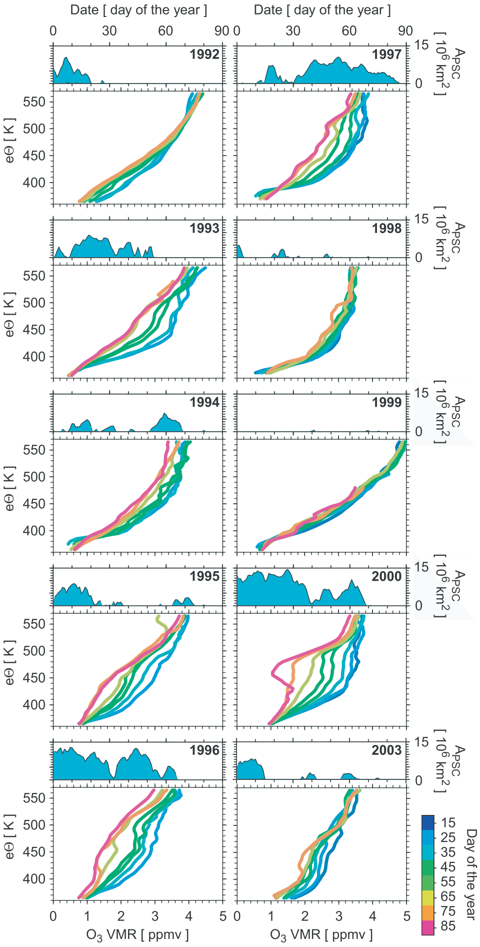

Figure 1. Blue shaded areas: Geographical area covered by temperatures below T_{NAT} (A_{PSC}) on the surface eΘ = 460 K for ten winters between 1992 and 2003 (for winter 2001 our approach to derive ozone loss is not applicable, because the vortex break up overlapped a period of significant ozone loss; in 2002 the number of ozone sondes launched was not sufficient for our analysis). Colored curves: Evolution of the vortex averaged ozone mixing ratio versus eΘ through the same winters.

2.1 ± 0.2 DU per 10^6 km^3, and the correlation coefficient is 0.96.

[6] The compactness of the empirical relation between ΔO_3 and V_{PSC} is quite striking. One could expect that ΔO_3 may also be influenced by a variety of other factors, such as the presence of volcanic aerosols [e.g., *Deshler et al.*, 1996], the degree of denitrification [e.g., *Rex et al.*, 1997; *Waibel et al.*, 1999], the timing of the PSC periods during winter, and the location of PSCs within the Arctic vortex.

[7] Large concentrations of volcanic aerosol from the eruption of Mt. Pinatubo were present in the Arctic stratosphere during the first half of the 1990s [*Thomason et al.*, 1997]. We find that the deviations of ΔO_3 from the linear fit tend to relate to the abundance of aerosols, in a manner consistent with expectation and observations from the Antarctic [*Deshler et al.*, 1996]. However the deviations are hardly larger than the estimated uncertainty of the measured ozone loss (inset in Figure 2b). The slope of the fit through the data points is not significantly impacted by the aerosol effect. It becomes 2.2 ± 0.1 DU per 10^6 km^3 if the measured ozone loss is corrected by 14 DU × log (ρ_a $\mu m^{-2} cm^3$), where ρ_a denotes the surface area density of the stratospheric aerosol. The correlation coefficient between the corrected ΔO_3 and V_{PSC} is 0.99.

[8] The observations show that variability in the other conditions mentioned above has not introduced much scatter into the relation between ΔO_3 and V_{PSC}, probably because these factors correlate with V_{PSC} or cancel to a certain degree. For example, the degree of denitrification may correlate with V_{PSC}, because extensive and persistent exposure of air to PSCs is required for Arctic denitrification to occur [*Fahey et al.*, 2001]. The location of the low temperature regions may have a limited impact on ΔO_3. When the low temperatures are near the edge of the polar vortex (baroclinic situation), the lifecycle of individual PSC particles is short and denitrification is less likely [e.g., *Santee et al.*, 1998], reducing ΔO_3. But, in the baroclinic situation, larger fractions of air inside the Arctic vortex circulate through the low temperature region and are processed by PSCs, thus increasing levels of reactive chlorine (ClO_x) and ΔO_3. The timing of the PSC events may have a limited impact because faster ozone loss later during late winter (due to more sunlight) is offset by the more rapid deactivation of ClO_x due to faster photolysis of HNO_3. Quantitative photochemical model studies are required to study these effects and to

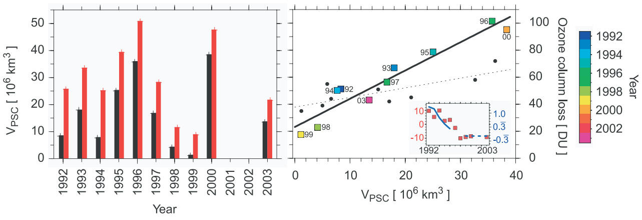

Figure 2. (a) Variation of V_{PSC} (black columns) and ΔO_3 (red columns) through the ten winters shown in Figure 1. ΔO_3 was estimated from the data shown in Figure 1 between day 15 and day 85 of each year. Days 25 and 75 were chosen as start or end date of the integration for years when the well isolated vortex established late (1994, 1999) or broke up early (1992, 1998, 2003). In these cases ozone loss is not expected during the omitted ten days. (b) Scatter plot of ΔO_3 versus V_{PSC}. Measurements are shown by colored squares. Black points are results from the SLIMCAT model (ΔO_3 as calculated from SLIMCAT vs. V_{PSC} based on UK Met Office data that is used in SLIMCAT. The small inset shows the deviations of measured ΔO_3 from the linear fit (in DU; red points, left hand scale). The solid blue line in the inset shows the logarithm of the aerosol surface area density (in $\mu m^2 cm^{-3}$) at 15.5 km estimated from SAGE II data for 60 to 70°N [*Thomason et al.*, 1997]. *Deshler et al.* [1996] showed that the additional polar ozone loss due to the Pinatubo aerosol correlated linearly with the logarithm of the aerosol surface area density. The dashed blue line represents typical background values of surface area estimated from data measured before 1991.

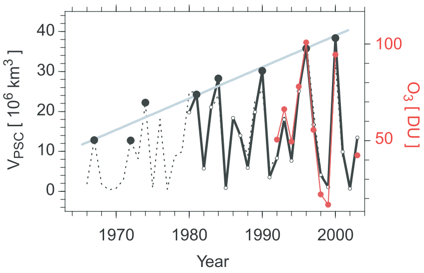

Figure 3. Evolution of V_{PSC} over the past 37 years composed from ECMWF data (solid black line) and data from the FU-Berlin (dashed line). The latter is available only on the 50 and 30 hPa pressure surfaces which are close to the 470 and 540 K potential temperature surfaces. To estimate V_{PSC} from this data, we have used $A_{PSC} = 0.8 \times A_{PSC}(50\ \text{hPa}) + 0.2 \times A_{PSC}(30\ \text{hPa})$ to estimate the average PSC extent between between 400 and 550 K, where A_{PSC} denotes the average horizontal extent of temperatures low enough for PSCs to exist. During the overlapping time period, we find that 5.06 km × A_{PSC} is a very good approximation for V_{PSC} from ECMWF data. The gray line represents a linear fit through the maximum values of V_{PSC} during five year intervals. Also shown is ΔO_3 for the years 1992 to 2003 (red line), scaled such that V_{PSC} represents the best fit through ΔO_3.

fully understand the compactness of the observed relation shown in Figure 2.

3. Impact of Climate Change on Arctic Ozone Loss

[9] The linear quantitative empirical relation between ΔO_3 and V_{PSC} shown in Figure 2b allows us to assess the impact of changes in stratospheric temperature on Arctic ozone loss. For the years shown in Figure 2 we have applied a wide range of temperature offsets to the meteorological data and found that V_{PSC} would have increased by $7.7 \pm 2.6 \times 10^6$ km^3 per Kelvin of uniform cooling throughout the vortex. In combination with the slope of ΔO_3 versus V_{PSC} from Figure 2b, this implies that about 15 DU additional ozone loss can be expected per Kelvin average cooling of the Arctic stratosphere. This is the first empirical measure of the relation between enhanced polar ozone loss and stratospheric cooling induced by climate change, and is only valid for the range of V_{PSC} shown in Figure 2.

[10] The empirical relation between ΔO_3 and V_{PSC} represents a principal diagnostic for assessing the ability of models to predict the evolution of polar ozone under different climate scenarios. This diagnostic allows the validation of both full chemistry chemical transport models (CTMs) and coupled chemistry-climate general circulation models (CCMs). The diagnostic can also be used to calibrate parametrizations of polar ozone loss used in CCMs with simplified chemistry.

[11] Calculations of ΔO_3 versus V_{PSC} from the SLIMCAT CTM [*Chipperfield and Jones*, 1999] for the winters 1992 to 2000 are compared to the observed relation in Figure 2b. Currently, many models tend to underestimate the chemical loss of Arctic ozone during cold winters [*WMO*, 2003], an effect most likely related to problems with the current schemes used to parametrize denitrification [*Davies et al.*, 2002] and to unexplained ozone losses during cold Arctic Januaries [*Becker et al.*, 1998; *Rex et al.*, 2003]. Conversely, the SLIMCAT model overestimates ozone loss during warm winters, suggesting that the effect of small, localized areas of temperatures below the thermodynamic PSC existence threshold is overestimated in the model, because of the equilibrium treatment of PSC occurrence (i.e., PSCs are instantaneously formed in the model once temperatures fall below T_{NAT}). The slope of a fit through the SLIMCAT model results for ΔO_3 vs. V_{PSC} is 0.71 ± 0.23 DU per 10^6 km^{-3}, a value nearly a factor of three smaller than observed. The model suggests only about 5.5 DU additional ozone loss would occur per Kelvin cooling of the Arctic stratosphere. Our observations indicate that the impact of potential, future stratospheric cooling on Arctic ozone loss is about three times larger than this model value.

[12] The observations also indicate that chemical loss is a significant cause of the observed year to year variability of the Arctic ozone column. Based on SLIMCAT results *Chipperfield and Jones* [1999] concluded that, compared to dynamical variability, year-to-year changes in Arctic chemical ozone loss does not play a major role in the interannual variability of late winter column ozone. In contrast, the observations presented here indicate that chemistry contributed about half of the interannual variability. Figure 2 shows that the conclusion of Chipperfield and Jones is affected by the fact that SLIMCAT largely underestimates the year to year variability in the chemical loss term.

[13] The long term evolution of the climate in the Arctic stratosphere has been the subject of active recent research [e.g., *Ramaswamy et al.*, 2001]. These studies generally focused on minimum or average temperatures and concluded that observations indicate a slight cooling over the past decades, which is barely significant. *Pawson and Naujokat* [1999] found that the average area extent of PSC conditions has been increasing over the past decades. Our results show that V_{PSC} is the relevant climate parameter that drives the evolution of polar ozone loss.

[14] Figure 3 shows a time series for V_{PSC} over the past 38 years, based on meteorological data from the ECMWF and from the FU-Berlin stratospheric analyses, together with the evolution of ΔO_3 over the past decade. The severity of extreme ozone loss events in the Arctic is controlled by the cold Arctic winters; i.e., those that define the upper limit of the year-to-year variability of V_{PSC}. These winters reveal significant change in Arctic stratospheric climate over the past four decades. The value of maximum V_{PSC} during five year intervals has increased steadily, by about a factor of three, since the late 1960s. A linear fit through the solid points in Figure 3 has a slope of $7.86 \pm 0.86 \times 10^6$ km^3 per decade. The basic conclusion of a large, steady rise in the maximum value of V_{PSC} does not depend on the length of the time interval. The slope is 6.16 ± 1.9, 7.88 ± 0.96 and $7.38 \pm 1.30 \times 10^6$ km^3 per decade if maximum values of V_{PSC} during 4, 6, and 10 year intervals are chosen instead. Also, the slope does not significantly depend on the end points of the analyzed periods or potential differences of the two meteorological data sets; e.g., the slopes are 9.3 ± 2.8 and $6.6 \pm 1.3 \times 10^6$ km^3 per

decade for the first half (based on FU-Berlin data alone) and the second half (based on ECMWF data alone) of the period respectively. These results demonstrate that the severe Arctic ozone losses reported for some winters during the 1990s [*WMO*, 2003] were not only the result of increased stratospheric halogen loading compared to earlier decades, but also resulted from a long term change in the climate of the Arctic stratosphere.

[15] It is currently not clear what caused the change in climatic conditions in the Arctic polar vortex. Cooling of the polar stratosphere is qualitatively consistent with the direct radiative impact from increased levels of greenhouse gases (GHG) in the atmosphere [e.g., *WMO*, 2003]. However, the indirect effect of changes in the dynamical structure of the stratosphere related to increased GHG forcing also may impact the wintertime polar temperatures [e.g., *Shindell et al.*, 1998; *Langematz*, 2000]. The range of results from current climate models used to study the effect of increasing GHG forcing on the temperatures in the polar stratosphere is broad, ranging from a slight increase in temperatures to severe cooling [*WMO*, 2003]. Hence, it is currently not possibly to unambiguously attribute the climate change observed in Figure 3 to increased GHG forcing. Another factor that could play a role is long term internal variability of the climate system. Model calculations suggest, however, that changes in radiative forcing due to decreased ozone alone are not sufficient to cause the observed decline in the temperature of the Arctic lower stratosphere [*Rosier and Shine*, 2000; *Langematz*, 2000].

[16] The empirical relation between ΔO_3 and V_{PSC} presented here does not appear to be well represented by current chemistry models. The relation between ΔO_3 and V_{PSC} may not be valid for larger values of V_{PSC} than have been observed. It is therefore imperative to develop a theoretical understanding of this relation as a prerequisite for reliably predicting the future evolution of Arctic ozone in a changing stratosphere characterized by rising abundances of GHGs and declining levels of chlorine.

[17] **Acknowledgments.** Ozonesonde data were provided by M. Allart, M. Alpers, B. R. Bojkov, G. O. Braathen, J. Cisneros, H. Claude, J. Davies, W. Davies, H. De Backer, H. Dier, V. Dorokhov, H. Fast, S. Godin, B. Johnson, Y. Kondo, E. Kyrö, Z. Litynska, I. S. Mikkelsen, M. J. Molyneux, E. Moran, G. Murphy, T. Nagai, H. Nakane, C. Parrondo, F. Ravegnani, F. J. Schmidlin, P. Skrivankova, C. Varotsos, C. Vialle, P. Viatte, V. Yushkov, and C. Zerefos. Meteorological data were provided by ECMWF, UKMO, and the FU-Berlin. We thank J. Margitan and J. Notholt for comments. Work at AWI was supported by the BMBF within the AFO2000 program (FKZ 07ATC08), at JPL under contract with the NASA, at EORCU by the EC DG Research CRUSOE II, EVK2-CT-2001-20012, and the SLIMCAT modeling by the U.K. NERC. The measurements were carried out as part of the EU campaigns EASOE, SESAME and THESEO.

References

Becker, G., et al. (1998), Ozone loss rates in the Arctic stratosphere in the winter 1991/92: Model calculations compared with Match results, *Geophys. Res. Lett.*, *25*(23), 4325–4328.

Chipperfield, M. P., and R. L. Jones (1999), Relative influences of atmospheric chemistry and transport on Arctic ozone trends, *Nature*, *400*, 551–554.

Davies, S., et al. (2002), Modeling the effect of denitrification on Arctic ozone depletion during winter 1999/2000, *J. Geophys. Res.*, *108*(D5), doi:10.1029/2001JD000445.

Deshler, T., B. J. Johnson, and B. Nardi (1996), Correlations between ozone loss and volcanic aerosol at altitudes below 14 km over McMurdo Station, Antarctica, *Geophys. Res. Lett.*, *23*(21), 2931–2934.

Fahey, D., et al. (2001), The detection of large HNO_3-containing particles in the winter Arctic stratosphere, *Science*, *291*, 1026.

Harris, N. R. P., et al. (2002), Comparison of empirically derived ozone losses in the Arctic vortex, *J. Geophys. Res.*, *107*(D20), doi:10.1029/2001JD000482.

Langematz, U. (2000), An estimate of the impact of observed ozone losses on stratospheric temperature, *Geophys. Res. Lett.*, *27*(14), 2077–2080.

Pawson, S., and B. Naujokat (1999), The cold winters of the middle 1990s in the northern lower stratosphere, *J. Geophys. Res.*, *104*(D12), 14,209–14,222.

Ramaswamy, V., et al. (2001), Stratospheric temperature trends: Observations and model simulations, *Rev. Geophys.*, *39*(1), 71–122.

Rex, M., et al. (1997), Prolonged stratospheric ozone loss in the 1995/96 Arctic winter, *Nature*, *389*, 835–838.

Rex, M., et al. (2002), Chemical loss of Arctic ozone in winter 1999/2000, *J. Geophys. Res.*, *107*(D20), 8276, doi:10.1029/2001JD000533.

Rex, M., et al. (2003), On the unexplained stratospheric ozone losses during cold Arctic Januaries, *Geophys. Res. Lett.*, *30*(1), 1008, doi:10.1029/2002GL016008.

Rosier, S. M., and K. P. Shine (2000), The effect of two decades of ozone change on stratospheric temperatures as indicated by a general circulation model, *Geophys. Res. Lett.*, *27*(17), 2617–2620.

Santee, M. L., et al. (1998), UARS Microwave Limb Sounder HNO_3 observations: Implications for Antarctic polar stratospheric clouds, *J. Geophys. Res.*, *103*(DD11), 13,285–13,314.

Shindell, D. T., D. Rind, and P. Lonergan (1998), Increased polar stratospheric ozone losses and delayed eventual recovery owing to increasing greenhouse-gas concentrations, *Nature*, *392*, 589–592.

Shine, K. P. (1987), The middle atmosphere in the absence of dynamical heat fluxes, *Q. J. Royal Meteorol. Soc.*, *113*, 476, 603–633

Thomason, L. W., L. R. Poole, and T. Deshler (1997), A global climatology of stratospheric aerosol surface area density deduced from Stratospheric Aerosol and Gas Experiment II measurements: 1984–1994, *J. Geophys. Res.*, *102*(DD7), 8967–8976.

Waibel, A. E., et al. (1999), Arctic ozone loss due to denitrification, *Science*, *283*, 2064–2069.

WMO (2003), Scientific Assessment of Ozone Depletion: 2002, ISBN 92-807-2261-1.

M. P. Chipperfield, School of the Environment, University of Leeds, Leeds, UK.

N. R. P. Harris, European Ozone Research Coordinating Unit, Cambridge, UK.

B. Naujokat, Free Univ. of Berlin, Meteorological Institute, Berlin, Germany.

M. Rex and P. von der Gathen, Alfred Wegener Institute for Polar and Marine Research, Potsdam, Germany. (mrex@awi-potsdam.de)

R. J. Salawitch, Jet Propulsion Laboratory, California Institute of Technology, Pasadena, CA, USA.

GEOPHYSICAL RESEARCH LETTERS, VOL. 33, L10812, doi:10.1029/2005GL025466, 2006

Toward a better quantitative understanding of polar stratospheric ozone loss

K. Frieler,[1] M. Rex,[1] R. J. Salawitch,[2] T. Canty,[2] M. Streibel,[3] R. M. Stimpfle,[4]
K. Pfeilsticker,[5] M. Dorf,[5] D. K. Weisenstein,[6] and S. Godin-Beekmann[7]

Received 12 December 2005; revised 20 March 2006; accepted 31 March 2006; published 27 May 2006.

[1] Previous studies have shown that observed large O_3 loss rates in cold Arctic Januaries cannot be explained with current understanding of the loss processes, recommended reaction kinetics, and standard assumptions about total stratospheric chlorine and bromine. Studies based on data collected during recent field campaigns suggest faster rates of photolysis and thermal decomposition of ClOOCl and higher stratospheric bromine concentrations than previously assumed. We show that a model accounting for these kinetic changes and higher levels of BrO can largely resolve the January Arctic O_3 loss problem and closely reproduces observed Arctic O_3 loss while being consistent with observed levels of ClO and ClOOCl. The model also suggests that bromine catalysed O_3 loss is more important relative to chlorine catalysed loss than previously thought.

Citation: Frieler, K., M. Rex, R. J. Salawitch, T. Canty, M. Streibel, R. M. Stimpfle, K. Pfeilsticker, M. Dorf, D. K. Weisenstein, and S. Godin-Beekmann (2006), Toward a better quantitative understanding of polar stratospheric ozone loss, *Geophys. Res. Lett.*, *33*, L10812, doi:10.1029/2005GL025466.

1. Introduction

[2] Proper quantitative understanding of polar stratospheric O_3 destruction, including the relative contributions of bromine and chlorine species, is a prerequisite for reliable predictions of future polar ozone. The topic has become especially exigent as many independent studies indicate measured O_3 loss is consistently underestimated by current stratospheric chemistry models, particularly during cold Arctic Januaries [e.g., *Hansen et al.*, 1997; *Becker et al.*, 1998; *Deniel et al.*, 1998, *Rex et al.*, 2003, *Rex et al.*, 2004]. The discrepancies lie outside of uncertainties related to heterogeneous chlorine activation [e.g., *Rex et al.*, 2003]. This suggests the possibility of unknown O_3 loss processes, especially under cold mid-winter conditions, or that established catalytic processes are more efficient than currently thought.

2. Tools

[3] We use Match results for the cold Arctic winters 1994/95, 1995/96, 1999/00, 2000/01, 2002/03 and the Antarctic winter 2003 to test our quantitative understanding of measured O_3 loss. We have not reprocessed data for the Arctic winter 1991/92, because only a rudimentary Match analysis was carried out and these data are generally less reliable. Following *Rex et al.* [2003], a photochemical box model is run along trajectories identical to those studied within the Match campaigns. To quantify chemical O_3 loss independent from transport effects, the Match technique is based on a regression analysis of pairs of ozonesonde measurements of the same air parcel sampled at different times.

[4] Here, we use the model system described by *Rex et al.* [2003] to calculate the amount of ClO_x ($ClO + 2 \times ClOOCl$) (“necessary ClO_x”) needed to reproduce the measured O_3 loss rate. The model has two updates. First, by specifying HO_2 concentrations as a function of SZA [*Hanisco et al.*, 2002], the model now accounts for O_3 loss due to cycles limited by $ClO + HO_2$ and $BrO + HO_2$, in addition to loss by the ClO + ClO, BrO + ClO and O + ClO cycles. These two new cycles contribute $\sim$2% to total O_3 loss. Second, the integration scheme has changed [e.g., *Canty et al.*, 2005]. While the old model version represented the diurnal variation of all species assuming a zonal flow (balance of 24 hour avg. production and loss), the new model fully integrates the chemical equations along air mass trajectories. The resulting difference in calculated O_3 loss rates is less than 5%. Thus, the updated version of the model is consistent with results given by *Rex et al.* [2003].

[5] Since *Rex et al.* [2003], a number of atmospheric observations have appeared suggesting an alternative description of ClO-ClOOCl kinetics and increased levels of stratospheric bromine. Here, we quantify the effect of these observations on chemical O_3 loss for the Arctic and Antarctic vortices using four different sets of model parameters. The “reference run” uses JPL 2002 kinetics [*Sander et al.*, 2003] and a BrO_x ($BrO + BrCl$) profile for the Arctic vortex, Feb. 2000, found by the AER 2D model assuming only CH_3Br + halons supply stratospheric bromine. The BrO_x profile ranges from 11 to 13 pptv at the 450 to 525 K potential temperature (Θ) levels, respectively, and is similar to a profile calculated by the 3D CTM Mimosa-CHIM (see auxiliary material[1]).

---

[1] Research Department, Alfred Wegener Institute for Polar and Marine Research, Potsdam, Germany.
[2] Jet Propulsion Laboratory, California Institute of Technology, Pasadena, California, USA.
[3] European Ozone Research Coordinating Unit, Department of Chemistry, University of Cambridge, Cambridge, UK.
[4] Department of Chemistry and Chemical Biology, Harvard University, Cambridge, Massachusetts, USA.
[5] Institut für Umweltphysik, University of Heidelberg, Heidelberg, Germany.
[6] Atmospheric and Environmental Research, Inc., Lexington, Massachusetts, USA.
[7] Service d'Aeronomie-CNRS, Université Pierre et Marie Curie, Paris, France.

Copyright 2006 by the American Geophysical Union.
0094-8276/06/2005GL025466$05.00

[1] Auxiliary material is available at ftp://ftp.agu.org/apend/gl/2005gl025466.

[6] The "new kinetics" run uses values of the ClOOCl absorption cross section (σ_{ClOOCl}) and the ClO-ClOOCl equilibrium constant (K_{EQ}) based on recent atmospheric observations of [ClO] and [ClOOCl]. *Stimpfle et al.* [2004], using daytime observations during cold Arctic conditions, showed that dimer photolysis (J_{ClOOCl}) may be occurring significantly faster than calculated using JPL 2002 values of σ_{ClOOCl}. Assuming the JPL 2002 rate constant for formation of ClOOCl, they demonstrated consistency between atmospheric observations and J_{ClOOCl} found using σ_{ClOOCl} from the laboratory study of *Burkholder et al.* [1990]. Nighttime measurements of [ClO] and [ClOOCl] were used to suggest that K_{EQ} is smaller than the JPL 2002 recommendation and is in better agreement with the *Cox and Hayman* [1988] value, leading to a higher [ClO] to [ClOOCl] ratio during darkness. Lower values of K_{EQ} are also supported by stratospheric observations provided by *von Hobe et al.* [2005] and *Berthet et al.* [2005] and a recent laboratory measurement by *Plenge et al.* [2005]. For the "new kinetics" simulation, we use values of σ_{ClOOCl} from *Burkholder et al.* [1990] extrapolated to 450 nm as described by *Stimpfle et al.* [2004] and K_{EQ} from *Cox and Hayman* [1988].

[7] We show results for a BrO_x profile based on a DOAS measurement of BrO over Kiruna, Sweden (68°N) on Feb. 18, 2000 [*Fitzenberger*, 2000; *Dorf*, 2005]. The BrO_x profile ranges from 19 to 21 ppt between 450 and 500 K. This is nearly 50% larger than both model BrO_x profiles that assume supply of Br_y from CH_3Br + halons, likely reflecting a ~6 pptv contribution to stratospheric inorganic bromine (Br_y) from short lived bromocarbons and tropospheric BrO [e.g., *Pfeilsticker et al.*, 2000]. Higher values of BrO, similar to the Arctic DOAS profile used here, have been reported by independent aircraft and balloon observations of BrO [*Salawitch et al.*, 2005]. Further discussion of BrO and details of how we have accounted for small temporal variations in Br_y are given in the auxiliary material. For clarity, results using JPL 2002 kinetics and the DOAS BrO_x profile are not shown, since they differ only slightly from the "new kinetics" run. Results are shown for a "combined run" that uses "new kinetics" and the DOAS BrO_x profile.

3. Improvements with Respect to the "January Ozone Loss Problem"

[8] The "reference run" (Figure 1, black lines) shows that, for January of all presented Arctic winters and July of the Antarctic winter, the amount of "necessary ClO_x" to match observed chemical O_3 loss rates (top half of each box) exceeds ~3.7 ppbv, the maximum amount of total stratospheric chlorine [*World Meteorological Organization* (*WMO*), 2003]. For 3 of the 6 winters, O_3 loss rates calculated on the basis of ClO_x = 3.7 ppbv ("maximum possible ozone loss", shown in lower half of each box only for the time period when nearly complete chlorine activation might be expected) underestimate the observed O_3 loss by more than the 1σ uncertainty of the measurements. This suggests our current representation of known O_3 loss cycles is insufficient to account for observed loss rates.

[9] Figure 1 shows that changes to J_{ClOOCl} and K_{EQ} ("new kinetics") increase "maximum possible ozone loss" by ~20% (blue dashed lines). This effect is due to higher J_{ClOOCl}; the extrapolation of the ClOOCl cross sections longward of 410 nm plays no significant role in this result. The overall effect of the new K_{EQ} is a slight decrease in modeled O_3 loss (~2%). The impact remains small if K_{EQ} is taken from "Fit 2" of *von Hobe et al.* [2005], the lowest reported value of K_{EQ}.

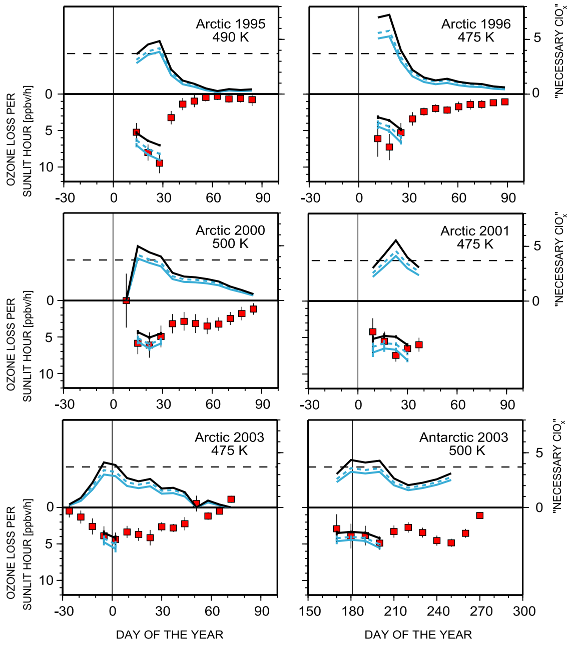

Figure 1. Chemical O_3 loss rate in the polar vortex based on Match (red boxes; error bars are 1σ uncertainty). The abundance of ClO_x necessary to account for the measured O_3 loss ("necessary ClO_x") and the modeled O_3 loss assuming ClO_x = 3.7 ppbv ("maximum possible ozone loss") are shown in the upper and lower parts of each plot, respectively. The dashed line in the upper part of each plot marks the level of 3.7 ppbv ClO_x. Maximum possible ozone loss is shown only for the time periods where nearly complete chlorine activation is likely to occur. Black lines: reference run (JPL 2002 kinetics + AER BrO_x); dashed blue lines: "new kinetics" (J_{ClOOCl} from *Burkholder et al.* [1990] and K_{EQ} from *Cox and Hayman* [1988]) + AER BrO_x; solid blue lines: "new kinetics" + BrO_x derived from DOAS BrO measurements.

[10] Results from a model run that uses "new kinetics" and DOAS BrO_x ("combined run") are shown by solid blue lines in Figure 1. This simulation leads to a ~30–40% increase in ozone loss relative to the reference run and largely resolves the discrepancy between maximum possible ozone loss and measured loss. Present uncertainties in BrO_x derived from DOAS BrO lead to a ~7% uncertainty in "maximum possible ozone loss".

[11] The selection of different Θ levels for Figure 1 is driven by the availability of reliable Match data between 475 and 500 K. For Arctic 2002/03 and Antarctic 2003 we also modeled the 500 and 475 K levels, respectively. Results are similar to those shown in Figure 1. The "combined run" is not sufficient to fully resolve the discrepancy for 1991/92 reported by *Rex et al.* [2003] (not shown). A discrepancy at the 1σ to 2σ level remains for two points during that year.

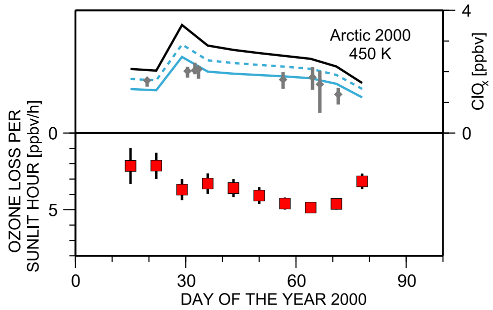

Figure 2. Chemical O_3 loss rate in 1999/2000, 450K, based on Match (red boxes; error bars are 1σ uncertainty). The lines represent the necessary ClO_x to account for measured O_3 loss, where the colors/line types correspond to the same model runs as described in Figure 1. Gray diamonds: mean value of all ClO_x measurements at 450 ± 10 K, for the 8 ER-2 flights that remained entirely inside the vortex, vertical bars represent the maximum and minimum of the considered ClO_x data.

However, the overall picture is that modeled maximum possible ozone loss rates for the "combined run" are within the statistical and systematic uncertainties of the observed rates for nearly all time periods considered.

[12] These results should not be interpreted as evidence for complete, quantitative understanding of polar O_3 loss because the calculations are based on upper limits of ClO_x. A more meaningful comparison of modeled and measured ozone loss rates is described in the following section, which considers measurements of ClO_x at the 450 K level of the Arctic winter 1999/2000. Similar measurements of ClO_x are not available for higher Θ levels considered in Figure 1.

4. Arctic Winter 1999/00, 450 K: "Necessary ClO_x" in Comparison to Measured ClO_x

[13] A stringent test of our quantitative understanding of chemical O_3 loss is provided by comparing measured ClO_x to calculated "necessary ClO_x" needed to account for observed ozone loss rates. Here, we use a time series of ClO_x based on measurements of [ClO] and [ClOOCl] from *Stimpfle et al.* [2004], for Arctic winter 1999/00. We compare measurements near Θ = 450 K (e.g., ClO_x collected between 440 and 460 K) to results from the Match analysis at 450 K. We selected data from 8 flights within the Arctic vortex, during the period Jan. 20 to Mar. 12, 2000. For each individual flight, the average of all ClO_x measurements at 450 ± 10 K is compared to the "necessary ClO_x" derived from measured ozone loss rates. The air masses encountered by the aircraft are representative of vortex conditions sampled by Match (see auxiliary material).

[14] Figure 2 shows that to explain the measured O_3 loss rates, the "reference run" based on JPL 2002 kinetics and BrO_x from CH_3Br + halons needs significantly more ClO_x (black line) than was observed. During late Jan./early Feb., the discrepancies are larger than the 20% uncertainty of the ClO_x measurements [*Stimpfle et al.*, 2004]. The amount of ClO_x needed to account for measured O_3 loss on the basis of the "new kinetics" (dashed blue line) is also higher than the observations, but is just within the uncertainty range. Results using DOAS BrO_x and JPL 2002 kinetics are almost indistinguishable from the "new kinetics" run. Nearly perfect agreement between measured ClO_x and "necessary ClO_x" is found for the "combined run" (solid blue line). Figure 2 demonstrates that use of a faster photolysis rate for ClOOCl (consistent with atmospheric observations of [ClO] and [ClOOCl]) and higher bromine loading (consistent with a ∼6 pptv source of Br_y from species other than CH_3Br + halons) provides an overall good quantitative explanation of Arctic ozone loss rates.

[15] *Rex et al.* [2003] noted the tendency for models to underestimate observed chemical loss of Arctic O_3, particularly during cold Januaries. They speculated that changes to ClO-ClOOCl kinetics and BrO_x, similar to those considered here, could largely resolve the discrepancy. The calculations shown in this paper are given greater credence by numerous studies related to ClO-ClOOCl kinetics [*Stimpfle et al.*, 2004; *Berthet et al.*, 2005; *Plenge et al.*, 2005; *von Hobe et al.*, 2005] and stratospheric Br_y [*WMO*, 2003; *Canty et al.*, 2005; *Dorf*, 2005; *Salawitch et al.*, 2005] that have appeared since *Rex et al.* [2003] was completed. Hence, this work builds upon and advances the speculation of our earlier study.

5. Relative Importance of the BrO + ClO Cycle

[16] To calculate the relative importance of each O_3 loss cycle in the model, we use all Match measurements between Jan. 10 to Feb. 10 (Arctic, all years) and Jul. 10 to Aug. 10 (Antarctic, 2003) to calculate O_3 loss per sunlit hour for these winter periods. The model was run along trajectories, with ClO_x adjusted to reproduce the measured O_3 loss rates for the three combinations of kinetic parameters and BrO_x considered above (Figure 3, top). We calculate O_3 loss per sunlit hour for the 5 catalytic cycles and then derive the relative fraction of each cycle to the total modeled loss rate

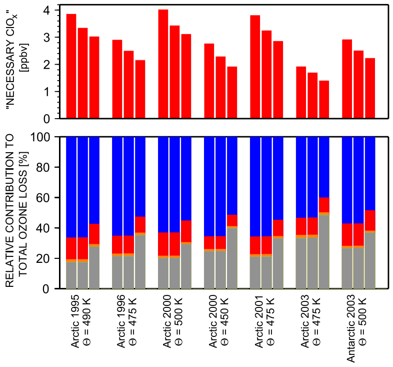

Figure 3. (top) Level of ClO_x needed to account for observed O_3 loss for the "reference run" (JPL 2002 kinetics, AER BrO_x) (1st bar of each grouping), the "new kinetics run" (2nd bar), and the "combined run" (3rd bar). Each grouping of columns represents results of model runs executed along the Match trajectories available between Jan. 10 and Feb. 10 (Arctic) and Jul. 10 and Aug. 10 (Antarctic), respectively. (bottom) Relative importance of the ClO + ClO cycle (blue), the BrO + ClO cycle (gray), the ClO+O cycle (red), and the HOCl cycle (orange) to total O_3 loss. The contribution from the HOBr cycle was calculated but is too small to represent. Groupings are the same as for Figure 3 (top).

(Figure 3, bottom), which by definition equals the measured O_3 loss rate.

[17] The kinetics changes considered here do not alter the relative importance of the BrO + ClO cycle (the increase in J_{ClOOCl}, which dominates the "new kinetics" run, results in faster O_3 loss by all cycles). Even using K_{EQ} of *von Hobe et al.* [2005], the effect on the relative importance of BrO + ClO is negligible. In contrast, use of DOAS BrO_x increases the relative importance of the BrO + ClO cycle by ∼10–15%. Hence, the BrO+ClO contribution to total O_3 loss ranges from ∼27 to 48% for the "combined run", in comparison to 17 to 33% for the "reference run". The relative importance of the BrO + ClO cycle increases with decreasing ClO_x. This explains the differences between results for winter 2000/01 compared to winter 2002/03, where chlorine activation derived from measured O_3 loss rates is much lower.

6. Concluding Remarks

[18] We show that use of a faster value for J_{ClOOCl} and abundances of BrO_x derived from a measured BrO profile increase calculated polar O_3 loss rates by up to 40%, resulting in overall consistency between observed O_3 loss rates and upper limits for O_3 loss based on an assumption of a completely activated vortex (e.g., $ClO_x \approx 3.7$ ppbv). Levels of ClO_x needed to account for observed O_3 loss rates at $\Theta = 450$ K are shown to be in remarkably good agreement with measurements of ClO_x for the Arctic winter of 999/00. The faster value of J_{ClOOCl} is based on a laboratory study [*Burkholder et al.*, 1990] and is consistent with measured partitioning of ClO and ClOOCl [*Stimpfle et al.*, 2004] and the JPL 2002 rate constant for the ClO self reaction. The DOAS BrO_x profile is ∼6 pptv higher than a model profile based on supply of Br_y from only CH_3Br + halons, consistent with other estimates of contributions to Br_y from short lived bromocarbons and tropospheric BrO [*Pfeilsticker et al.*, 2000; *Salawitch et al.*, 2005]. Further laboratory observations of the ClOOCl cross section, extending to 450 nm, are needed to assess the accuracy of J_{ClOOCl}. Also, further atmospheric observations of BrO are needed to better define levels of BrO_x in the polar vortices.

[19] This study suggests that previous discrepancies between measured and modeled polar O_3 loss rates might be resolved by greater efficiency of known catalytic cycles, rather than by the introduction of new chemical loss processes. These results could represent an important "bridge" between analysis of atmospheric observations and computationally expensive 3D model descriptions of climate chemistry interactions used to predict future levels of polar ozone.

[20] **Acknowledgments.** We thank R. Lehmann for helpful discussions. Research at the Jet Propulsion Laboratory, California Institute of Technology, and at the Atmospheric and Environmental Research, Inc., is performed under contract with the National Aeronautics and Space Administration. Work at AWI was supported by the BMBF (project AFO 2000/07ATC08) and EC DG, Research under the projects QUOBI (EVK2-2001-00129) and SCOUT-03 (505390-GOCE-CT-2004). Work at the Univ. of Heidelberg was supported by the BMBF (project 50FE0017).

References

Becker, G., R. Müller, D. S. McKenna, M. Rex, and K. S. Carslaw (1998), Ozone loss rates in the Arctic stratosphere in the winter 1991/92: Model calculations compared with Match results, *Geophys. Res. Lett.*, *25*, 4325–4328.

Berthet, G., P. Ricaud, F. Lefèvre, E. Le Flochmoën, J. Urban, B. Barret, N. Lautié, E. Dupuy, J. De La Noë, and D. Murtagh (2005), Nighttime chlorine monoxide observations by the Odin satellite and implications for the ClO/Cl_2O_2 equilibrium, *Geophys. Res. Lett.*, *32*, L11812, doi:10.1029/2005GL022649.

Burkholder, J. B., et al. (1990), Ultraviolet absorption cross sections of Cl_2O_2 between 210 and 410 nm, *J. Phys. Chem.*, *94*, 687–695.

Canty, T., et al. (2005), Nighttime OClO in the winter Arctic vortex, *J. Geophys. Res.*, *110*, D01301, doi:10.1029/2004JD005035.

Cox, R. A., and G. D. Hayman (1988), The stability and photochemistry of dimers of the ClO radical and implications for Antarctic ozone depletion, *Nature*, *332*, 796–800.

Deniel, C., R. M. Bevilacqua, J. P. Pommereau, and F. Lefèvre (1998), Arctic chemical ozone depletion during the 1994–1995 winter deduced from POAM II satellite observations and the REPROBUS three-dimensional model, *J. Geophys. Res.*, *103*, 19,231–19,236.

Dorf, M. (2005), Investigations of inorganic stratospheric bromine using balloon borne DOAS measurements and model simulations, doctoral dissertation, Univ. of Heidelberg, Heidelberg, Germany.

Fitzenberger, R. (2000), Investigation of the stratospheric inorganic bromine budget for 1996–2000: Balloon borne measurements and model comparison, doctoral dissertation, Univ. of Heidelberg, Heidelberg, Germany.

Hanisco, T. F., J. B. Smith, R. M. Stimpfle, D. M. Wilmouth, J. G. Anderson, E. C. Richard, and T. P. Bui (2002), In situ observations of HO_2 and OH obtained on the NASA ER-2 in the high-ClO conditions of the 1999/2000 Arctic polar vortex, *J. Geophys. Res.*, *107*(D20), 8283, doi:10.1029/2001JD001024.

Hansen, G., T. Svenøe, M. P. Chipperfield, A. Dahlback, and U. Hoppe (1997), Evidence of substantial ozone depletion in winter 1995/96 over Northern Norway, *Geophys. Res. Lett.*, *24*, 799–802.

Pfeilsticker, K., W. T. Sturges, H. Bösch, C. Camy-Peyret, M. P. Chipperfield, A. Engel, R. Fitzenberger, M. Müller, S. Payan, and B.-M. Sinnhuber (2000), Lower stratospheric organic and inorganic bromine budget for the arctic winter 1998/99, *Geophys. Res. Lett.*, *27*, 3305–3308.

Plenge, J., et al. (2005), Bond strength of chlorine peroxide, *J. Phys. Chem. A*, doi:10.1021/jp044142h.

Rex, M., R. J. Salawitch, M. L. Santee, J. W. Waters, K. Hoppel, and R. Bevilacqua (2003), On the unexplained stratospheric ozone losses during cold Arctic Januaries, *Geophys. Res. Lett.*, *30*(1), 1008, doi:10.1029/2002GL016008.

Rex, M., R. J. Salawitch, P. von der Gathen, N. R. P. Harris, M. P. Chipperfield, and B. Naujokat (2004), Arctic ozone loss and climate change, *Geophys. Res. Lett.*, *31*, L04116, doi:10.1029/2003GL018844.

Salawitch, R. J., D. K. Weisenstein, L. J. Kovalenko, C. E. Sioris, P. O. Wennberg, K. Chance, M. K. W. Ko, and C. A. McLinden (2005), Sensitivity of ozone to bromine in the lower stratosphere, *Geophys. Res. Lett.*, *32*, L05811, doi:10.1029/2004GL021504.

Sander, S. P., et al. (2003), Chemical kinetics and photochemical data for use in atmospheric studies, *Evaluation No. 14, JPL Publication 02–25*, Jet Propul. Lab., Pasadena, Calif.

Stimpfle, R. M., D. M. Wilmouth, R. J. Salawitch, and J. G. Anderson (2004), First measurements of ClOOCl in the stratosphere: The coupling of ClOOCl and ClO in the Arctic polar vortex, *J. Geophys. Res.*, *109*, D03301, doi:10.1029/2003JD003811.

von Hobe, M., et al. (2005), A re-evaluation of the ClO/Cl_2O_2 equilibrium constant based on stratospheric in situ observations, *Atmos. Chem. Phys.*, *5*, 693.

World Meteorological Organization (WMO) (2003), Scientific assessment of ozone depletion: 2002, *Global Ozone Research and Monitoring Project—Report No. 47*, 498 pp., Geneva, Switzerland.

T. Canty and R. J. Salawitch, Jet Propulsion Laboratory, California Institute of Technology, Pasadena, CA 91109, USA.

M. Dorf and K. Pfeilsticker, Institut für Umweltphysik, University of Heidelberg, D-69120 Heidelberg, Germany.

K. Frieler and M. Rex, Research Department, Alfred Wegener Institute for Polar and Marine Research, Telegrafenberg A45, D-14401 Potsdam, Germany. (kfrieler@awi-potsdam.de)

S. Godin-Beekmann, Service d'Aeronomie-CNRS, Université Pierre et Marie Curie, F-75252, Paris Cedex 05, France.

R. M. Stimpfle, Department of Chemistry and Chemical Biology, Cambridge, MA 02138, USA.

M. Streibel, European Ozone Research Coordinating Unit, Department of Chemistry, University of Cambridge, Cambridge CB2 1EW, UK.

D. K. Weisenstein, Atmospheric and Environmental Research, Inc., Lexington, MA 02421–3136, USA.

GEOPHYSICAL RESEARCH LETTERS, VOL. 33, L23808, doi:10.1029/2006GL026731, 2006

Arctic winter 2005: Implications for stratospheric ozone loss and climate change

M. Rex,[1] R. J. Salawitch,[2] H. Deckelmann,[1] P. von der Gathen,[1] N. R. P. Harris,[3]
M. P. Chipperfield,[4] B. Naujokat,[5] E. Reimer,[5] M. Allaart,[6] S. B. Andersen,[7]
R. Bevilacqua,[8] G. O. Braathen,[9] H. Claude,[10] J. Davies,[11] H. De Backer,[12]
H. Dier,[13] V. Dorokhov,[14] H. Fast,[11] M. Gerding,[15] S. Godin-Beekmann,[16]
K. Hoppel,[8] B. Johnson,[17] E. Kyrö,[18] Z. Litynska,[19] D. Moore,[20] H. Nakane,[21]
M. C. Parrondo,[22] A. D. Risley Jr.,[23] P. Skrivankova,[24] R. Stübi,[25] P. Viatte,[26]
V. Yushkov,[14] and C. Zerefos[27]

Received 27 April 2006; revised 26 May 2006; accepted 12 September 2006; published 8 December 2006.

[1] The Arctic polar vortex exhibited widespread regions of low temperatures during the winter of 2005, resulting in significant ozone depletion by chlorine and bromine species. We show that chemical loss of column ozone (ΔO_3) and the volume of Arctic vortex air cold enough to support the existence of polar stratospheric clouds (V_{PSC}) both exceed levels found for any other Arctic winter during the past 40 years. Cold conditions and ozone loss in the lowermost Arctic stratosphere (e.g., between potential temperatures of 360 to 400 K) were particularly unusual compared to previous years. Measurements indicate ΔO_3 = 121 ± 20 DU and that ΔO_3 versus V_{PSC} lies along an extension of the compact, near linear relation observed for previous Arctic winters. The maximum value of V_{PSC} during five to ten year intervals exhibits a steady, monotonic increase over the past four decades, indicating that the coldest Arctic winters have become significantly colder, and hence are more conducive to ozone depletion by anthropogenic halogens. **Citation:** Rex, M., et al. (2006), Arctic winter 2005: Implications for stratospheric ozone loss and climate change, *Geophys. Res. Lett.*, *33*, L23808, doi:10.1029/2006GL026731.

1. Introduction

[2] Chemical loss of Arctic ozone for particular winters exhibits large variability, driven by variations in temperature. However, the volume of air cold enough to allow for the existence of polar stratospheric clouds (PSCs) in the Arctic vortex, averaged over winter (V_{PSC}), exhibits a compact, near linear relation with chemical loss of column ozone (ΔO_3) [*Rex et al.*, 2004; *Tilmes et al.*, 2004].

[3] The Arctic winter of 2005 was unusually cold. The geographical extent of temperatures below the PSC formation threshold (A_{PSC}) at particular potential temperature (Θ) levels was high for a broad vertical region of the polar vortex. For Θ of 475 to 500 K, the evolution of A_{PSC} largely followed the previous record values from winter 2000 (see auxiliary material[1]). Below 400 K, daily values of A_{PSC} reached record levels for many weeks and the winter average was 50 to 60% larger than previously observed. For 2005, V_{PSC} (vertical integral of A_{PSC}) reached a value 25% larger than the previous record value from winter 2000.

[4] Here, we quantify ΔO_3 using a variety of techniques. The relation between ΔO_3 and V_{PSC} is examined. Finally, a time series for V_{PSC} is shown that indicates the coldest Arctic stratosphere winters, during the past forty years, have become progressively colder.

2. Ozone Loss Estimates for Winter 2005

[5] Different approaches and data sets are used to characterize chemical ozone loss during the Arctic winter 2005.

---

[1] Research Unit Potsdam, Alfred Wegener Institute for Polar and Marine Research, Potsdam, Germany.
[2] Jet Propulsion Laboratory, California Institute of Technology, Pasadena, California, USA.
[3] European Ozone Research Coordinating Unit, University of Cambridge, Cambridge, UK.
[4] School of Earth and Environment, University of Leeds, Leeds, UK.
[5] Meteorological Institute, Freie Universität Berlin, Berlin, Germany.
[6] Royal Netherlands Meteorological Institute, De Bilt, Netherlands.
[7] Danish Meteorological Institute, Copenhagen, Denmark.
[8] Naval Research Laboratory, Washington, DC, USA.
[9] Norwegian Institute for Air Research, Kjeller, Norway.
[10] Deutscher Wetterdienst, Meteorologisches Observatorium Hohenpeißenberg, German Weather Service, Hohenpeißenberg, Germany.
[11] Meteorological Service of Canada, Toronto, Ontario, Canada.
[12] Royal Meteorological Institute of Belgium, Brussels, Belgium.
[13] Meteorological Observatory Lindenberg, Lindenberg, Germany.
[14] Central Aerological Observatory, Moscow, Russia.
[15] Leibniz-Institut für Atmosphärenphysik, Kühlungsborn, Germany.
[16] Service d'Aéronomie, CNRS, Institut Pierre-Simon Laplace, Paris, France.
[17] Earth System Research Laboratory, NOAA, Boulder, Colorado, USA.
[18] Sodankyla Meteorological Observatory, Sodankylä, Finland.
[19] Institute of Meteorology and Water Management, Centre of Aerology, Legionowo, Poland.
[20] Met Office, Exeter, UK.
[21] Asian Environmental Research Group, National Institute for Environmental Studies, Tsukuba, Japan.
[22] Instituto Nacional de Tecnica Aerospacial, Madrid, Spain.
[23] Science Applications International Corporation, Hampton, Virginia, USA.
[24] Czech Hydrometeorological Institute, Prague, Czech Republic.
[25] Swiss Meteorological Aerological Station, Payerne, Switzerland.
[26] Federal Office of Meteorology and Climatology, MeteoSwiss, Payerne, Switzerland.
[27] Laboratory of Climatology and Atmospheric Environment, University of Athens, Greece.

Copyright 2006 by the American Geophysical Union.
0094-8276/06/2006GL026731$05.00

We consider estimates based on regression analysis of data from the northern hemisphere ozone sonde station network (hereafter, ozonesondes) for air parcels sampled at different times (Match) [e.g., *Rex et al.*, 1999] and estimates based on the ‘‘vortex average descent’’ approach, applied to measurements by the SAGE III [*Randall et al.*, 2005] and POAM III [*Hoppel et al.*, 2002] satellite instruments. First, we describe the morphology of ozone near 450 K, which was notably different than for other cold Arctic winters.

2.1. Ozone Distribution and Evolution

[6] Figure 1 shows the evolution of ozone inside the Arctic polar vortex (defined by the region enclosed by the maximum gradient in potential vorticity versus equivalent latitude) on the 450 K equivalent potential temperature (eΘ) surface, from mid-December 2004 to March 2005, as observed by sondes, SAGE III, and POAM III. The quantity eΘ represents the value of Θ an air mass would achieve on 31 March using calculated, vortex average descent rates [*Rex et al.*, 2004]. The top plot shows the time evolution of Θ for the eΘ = 450 K surface. In the absence of chemical loss and mixing, O_3 should be conserved on an eΘ surface. Figure 1e shows the evolution of vortex averaged ozone on the eΘ = 450 K surface for the winter of 2005 from sondes, SAGE III and POAM III, compared to the same quantity as observed by sondes for the winter of 2000 [from *Rex et al.*, 2002]. The data show a steady decline of ozone within the vortex between late January and early March. About 1.5 ppmv ozone was lost during the winter.

[7] The initial ozone field inside the polar vortex was characterized by relatively low ozone mixing ratios in the core of the vortex (inner 30% of the vortex area). Due to this horizontal gradient, inhomogeneities in sampling can result in uncertainties of ozone loss estimates from the vortex average [*Hoppel et al.*, 2002] or the tracer relation [*Tilmes et al.*, 2004] approaches. The sampling of the vortex by the three instruments used in this study is shown in Figures 1b–1d. Overall the sampling was quite homogenous for all instruments, with the exception of a ten day period in late January, when the sampling from the sondes was biased towards the core of the vortex (Figure 1b). A temporary dip in vortex averaged ozone from the sondes occurs at this time but has no impact on our overall ozone loss estimates. The fact that ozone loss estimates from all these instruments

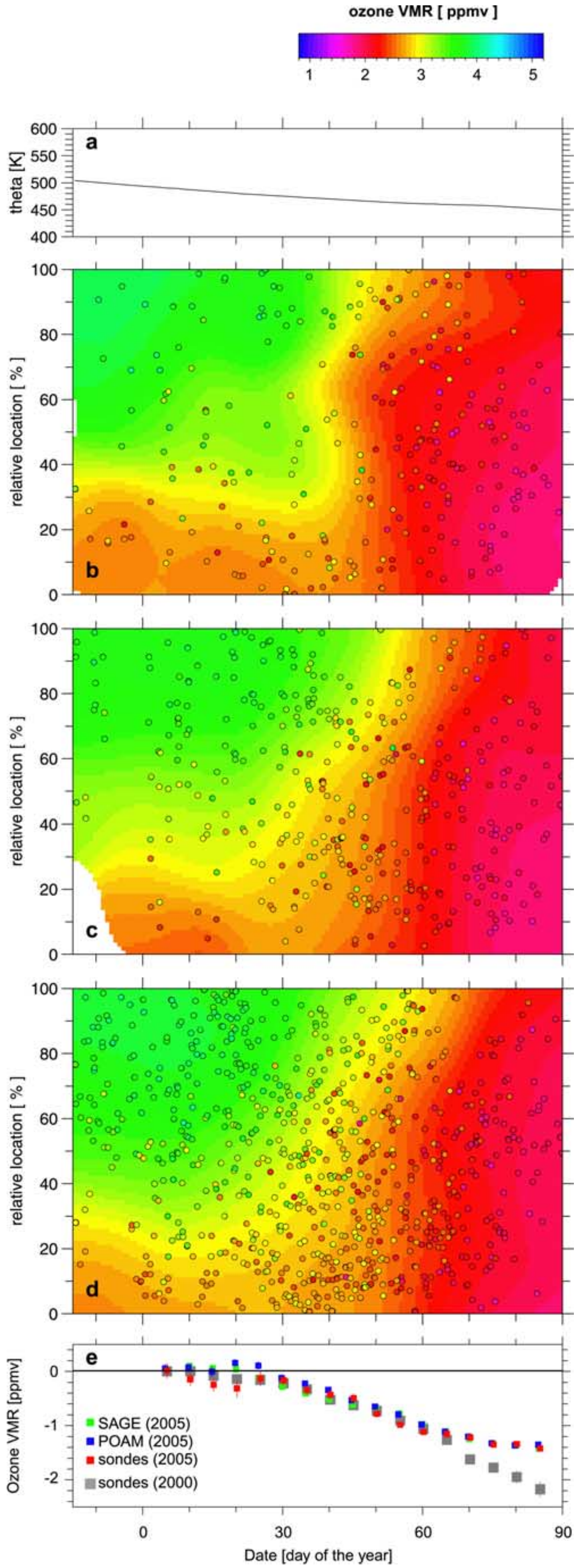

Figure 1. (a) Time evolution of Θ on the eΘ = 450 K surface. Measured ozone inside the Arctic vortex as a function of time and location relative to the vortex core, for the eΘ = 450 K surface, from (b) sondes, (c) SAGE III, and (d) POAM III. Circles indicate time, location and O_3 of actual measurements. Location relative to the vortex core (relative location = 0%) and vortex edge (relative location = 100%) found using equivalent latitude, allowing for daily variations in vortex size [see *Rex et al.*, 1999]. Contour shading calculated by averaging over the closest measurements, gaussian weighted by distance in date/relative location space. (e) Time evolution of vortex averaged ozone mixing ratio on the eΘ = 450 K surface, from sondes, SAGE III, and POAM III (as indicated) for 2005 and from sondes for the Arctic winter of 2000.

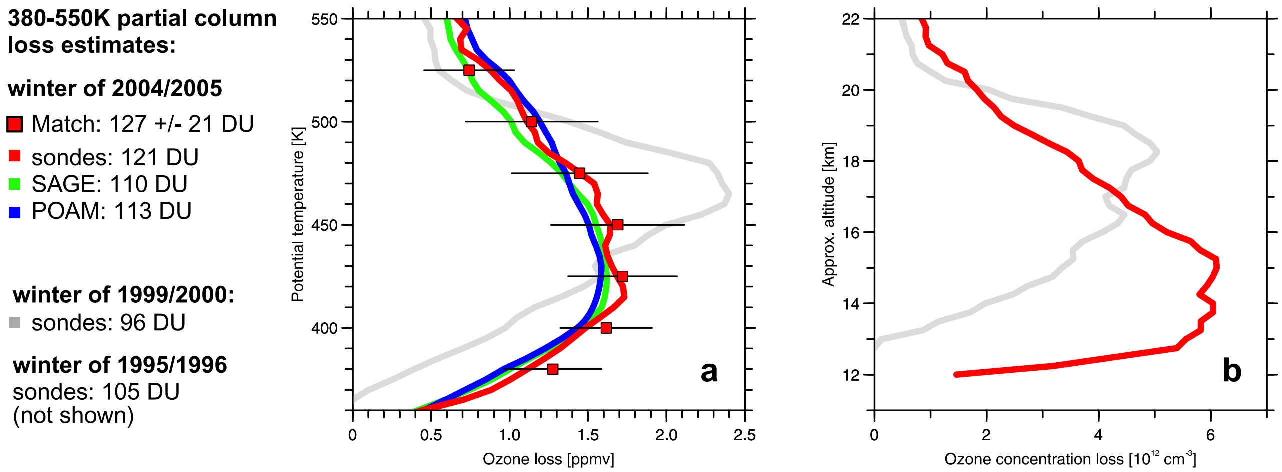

Figure 2. (a) Accumulated ozone loss mixing ratio (ppmv) between 5 Jan and 25 March, versus eΘ, from the vortex averaged sonde method for the winters of 2005 and 2000. Also shown are ozone losses from Match and from the time evolution of vortex averaged ozone from SAGE III and POAM III. Error bars from Match represent 1σ statistical uncertainties; additional systematic uncertainties are in the order of 20%. (b) Same as Figure 2a, except ozone loss concentration is shown from the vortex averaged sonde method for 2005 and 2000. Tabulation of chemical loss of column ozone by the various methods is also given.

agree well (Figure 1e) increases our confidence that sampling issues do not have a significant impact on our results.

2.2. Ozone Loss Profiles

[8] Figure 2a compares the vertical profile of ozone loss at the end of the winter derived from Match with results from the vortex average approach. We find a broad vertical range of ozone loss around 1.5 ppmv between Θ of 400 and 450 K. Good agreement is found at all Θ levels, further increasing our confidence that sampling or mixing issues have not influenced our results. With Match we can separate ozone changes during dark sections along the air mass trajectories from changes that occurred during sunlit portions of the trajectories [*Rex et al.*, 1999]. Figure S2 of the auxiliary material shows that changes in ozone during dark portions of the trajectories are small and if anything positive, suggesting dynamical effects did not significantly impact our estimates of ozone loss and would only lead to an underestimation of the loss rates.

[9] Figure 2a also shows the ozone loss profile for the winter of 2000 found using the vortex averaged descent approach. The maximum ozone loss for the 2005 winter, in terms of mixing ratios, was smaller than the record value reached in a narrow vertical region for the winter of 2000. This is consistent with the finding of *Manney et al.* [2006].

2.3. Total Column Loss

[10] The quantity most relevant for the biosphere is total ozone column. Losses of total column ozone are driven by the vertical distribution of the change in ozone concentration, shown in Figure 2b. The loss of total column ozone that occurred from 5 January to 25 March 2005, between eΘ levels of 380 and 550 K, was 121 DU. This quantity is based on the vertical integral of the vortex averaged sonde data points in Figure 2b; the uncertainty of this estimate is ~20 DU. Similar ozone loss is found by other instruments and from Match (Figure 2). Compared to winter 2000, the ozone loss profile in 2005 extended to lower altitudes, where ozone concentrations are large. Loss of column ozone for the winter of 2005 exceeds those measured during the winters of 1996 (105 DU) and 2000 (96 DU), which are the largest losses recorded previously (all values for eθ between 380 and 500 K). Hence, the winter of 2005 had a larger chemical loss of column ozone than any other winter during the past 40 years, although the uncertainty of the loss for this winter overlaps with the uncertainty of the loss for two previous cold winters.

[11] Quantifications of ozone losses in the vertical region below 400 K are sensitive to mixing issues (exchange of air across the edge of the polar vortex) and uncertainties in the calculated diabatic subsidence rates. The good agreement between results from Match and from the vortex average approach at 380 K (Figure 2a) suggests that mixing did not have a major impact on our ozone loss estimates at these levels. Also, we have not diagnosed substantial ozone losses in this vertical region for most previous winters (and for none of the warm winters), suggesting that the approach does not tend to produce artifacts. The larger ozone losses observed at these levels for winter 2005 are consistent with the fact that low temperatures extended to lower altitudes in this winter, compared to the previous cold winters. Note that ozone loss estimates near the bottom of the vortex are generally less reliable [e.g., *Knudsen et al.*, 1998]. Hence, the uncertainties of the loss estimates for the region below 400K are generally larger than those for the region above. But our overall conclusions still hold if the analysis is restricted to Θ levels above 400 K (auxiliary material[1]).

3. Arctic Ozone Loss and Climate Change

[12] Based on data from the vortex average approach, *Rex et al.* [2004] reported a compact relationship between ΔO_3 and V_{PSC}. This relation was confirmed by an analysis of HALOE data using the tracer relation approach [*Tilmes et*

---

[1] Auxiliary material data sets are available at ftp://ftp.agu.org/apend/gl/2006gl026731. Other auxiliary material files are in the HTML.

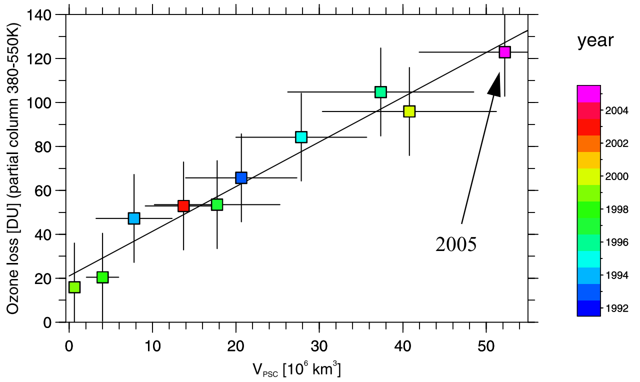

Figure 3. ΔO_3 versus V_{PSC} for Arctic winters between 1993 and 2005 (no values for the warm winters of 2001, 2002, 2004 due to major mid-winter warmings and/or lack of sufficient ozone sonde measurements). Value for 2005 is indicated. Values for other winters from *Rex et al.* [2004], except all values are calculated between eΘ levels of 380 and 550 K. V_{PSC} is found using temperatures from ECMWF, H_2O = 5 ppmv, and an observed profile of HNO_3 [*Rex et al.*, 2002]. The Figure is very similar if FU-Berlin data is used up to 2002 (no FU-Berlin data available after 2002). Error bars for ΔO_3 represent an upper limit of 20 DU uncertainty and for V_{PSC} uncertainty due to 1 K uncertainty in temperature. The line indicates a linear least squares fit to the points and has a slope of 15.6 DU/K cooling, based on 7.7 × 10^6 km^3 additional V_{PSC} per Kelvin uniform cooling [*Rex et al.*, 2004]. The correlation coefficient is 0.98 with a statistical significance larger than 99.9% and an uncertainty of +0.02/−0.14 (the autocorrelation of both time series was considered for the estimation of the significance by reducing the degrees of freedom according to standard statistics; a Monte-Carlo approach was used to estimate the uncertainty: 99.9% of correlation coefficients exceed 0.84, calculated for 1000 data sets with random noise added to ΔO_3 and V_{PSC}, corresponding to the uncertainty of the individual points).

al., 2004]. The observations of ΔO_3 and V_{PSC} for the winter 2005 lie along an extension of the near linear relation between these quantities observed for prior winters (Figure 3).

[13] Figure 4 shows the evolution of V_{PSC} over the past four decades. The unusually cold Arctic winter 2005 extends the long term upward trend of maximum values of V_{PSC} over the past ~forty years described by *Rex et al.* [2004]. A linear fit through the solid points in Figure 4, which represent maximum values of V_{PSC} for 5 year intervals, has a slope of 9.9 ± 1.1 × 10^6 km^3 per decade, similar to the slope given by *Rex et al.* [2004]. The conclusion of a large, steady rise in the maximum value of V_{PSC} does not depend on the length of the time interval or the end points chosen for the analysis (auxiliary material). The strong relation between ΔO_3 and V_{PSC} indicates V_{PSC} is the relevant parameter for relating changes in stratospheric temperature to ozone loss. Indeed, the notion of "coldest Arctic winters getting colder" can be overlooked in analyses of temperature trends [e.g., *Manney et al.*, 2005].

[14] It is unclear why the Arctic vortex has recently exhibited severely cold winters. To explore the robustness of the observed trend, we have generated 10^6 random permutations of the V_{PSC} data set in a Monte-Carlo simulation, ensuring that the random data sets have the same probability density function as the original data. Table 1 gives the probabilities to observe a trend equal to or larger than the observed trend of the cold winters (prob1). A second entry, prob2, is based on the same Monte-Carlo simulations. It gives the probability of observing a trend equal to or larger than the observed trend, with the additional constraint that the uncertainty of the slope is equal to or smaller than the uncertainty of the observed trend. The trend estimates and probabilities are given for 5 and 10 year intervals for the selection of the maximum values of V_{PSC} (details for all intervals between 4 and 10 years are in the auxiliary material). The calculation is repeated assuming: (a) a 1K warm bias of the old radiosonde data (second column); (b) use of the FU-Berlin data alone up to 2002 (again assuming a 1K warm bias for the early data) and V_{PSC} from ECMWF for the remaining years reduced by the maximum difference between the FU-Berlin data and the ECMWF data during the 22-year overlap period (third column); (c) as (b) but adding random noise corresponding to an additional 1K 2σ statistical uncertainty of the temperature data, before calculating the trend (fourth column). Table 1 shows it is very unlikely (well below 1% probability) that the observed trend toward colder winters is a purely random event or is caused by inconsistencies in the meteorological data sets.

[15] Chemistry climate models (CCMs) provide insight into processes controlling the temperature of the Arctic vortex, but results from various studies are contradictory. *Shindell et al.* [1998] suggested decreases in planetary wave activity reaching the mid-latitude stratosphere due to increased westerly winds in the subtropics would lead to stronger, colder Arctic vortices due to climate change associated with rising greenhouse gases (GHGs). *Schnadt et al.* [2002], however, showed a CCM coupled to an oceanic model resulted in a tendency for future warmer, less stable Arctic vortices, a consequence of increased

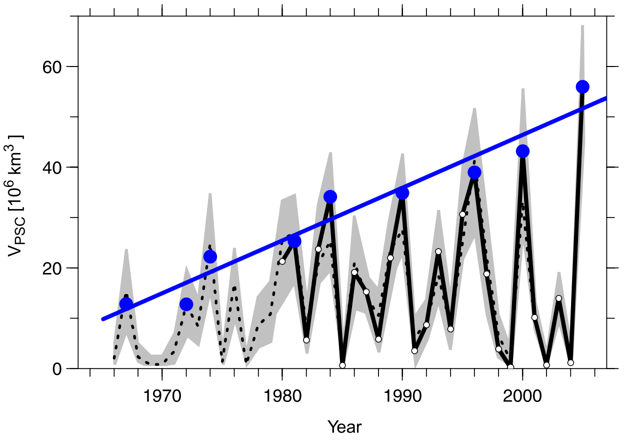

Figure 4. V_{PSC} over the past 40 years from ECMWF data (solid line) and FU-Berlin data (dashed line). See *Rex et al.* [2004] for a discussion of the FU-Berlin data. V_{PSC} has been calculated between 380 and 550 K for all years. The gray shading represents uncertainty of V_{PSC} due to 1 K uncertainty of the long term stability of radiosonde temperatures.

Table 1. Trend Estimates and Probability for Occurrence of Estimated Trend in Random Data

	Original	1K Radiosonde Trend (Assuming Warm Bias for Old Sondes[a])	1K Radiosonde Trend + ECMWF Data Reduced	1K Radiosonde Trend + 1K Statistical Uncertainty + ECMWF Data Reduced
		Interval 5 years		
Original trend, $10^6 km^3$/year	0.99 ± 0.11	0.80 ± 0.13	0.60 ± 0.15	0.60 ± 0.15
prob1/prob2, %	0.04/<0.0001	0.4/0.002	0.8/0.03	0.9/0.04
		Interval 10 years		
Original trend, $10^6 km^3$/year	1.03 ± 0.14	0.73 ± 0.14	0.59 ± 0.21	0.59 ± 0.21
prob1/prob2, %	0.04/0.004	0.4/0.03	0.5/0.3	0.7/0.3

[a] See text.

planetary wave activity associated with rising sea surface temperatures, contradicting earlier CCM calculations that suggested a tendency to future colder, more stable Arctic vortices [*Austin et al.*, 1992].

[16] The increased variability of Arctic stratospheric temperature conditions during recent years [*Manney et al.*, 2005] could indicate that the mechanism described by *Shindell et al.* [1998] acts efficiently during periods of relatively weak dynamic activity, hence during stratospheric conditions that are closer to radiative equilibrium. According to this mechanism, increasing GHGs lead to a stronger meridional temperature gradient during such periods and vertically propagating waves are deflected more equatorwards, leading to further cooling at high latitudes for such situations. On the other hand, an overall increase in momentum flux from the troposphere [*Schnadt et al.*, 2002] could make these conditions less frequent. While quite speculative, this combination of behaviors could be the cause of relatively few cold winters in recent years, but an increase in the severity of the winters that are cold.

[17] We lack a fundamental understanding of the factors responsible for the rise in maximum value of Arctic V_{PSC} shown in Figure 4. Nonetheless, the extension of this time series to a new record value for V_{PSC} in the winter of 2005 is cause for concern. If climate forcing from increasing GHGs plays a role in rising maximum V_{PSC}, the tendency toward colder Arctic winters will likely continue. In this case, Arctic ozone loss could continue to get worse until around the year 2020, when declining levels of anthropogenic halogens will eventually reduce chemical loss [*Knudsen et al.*, 2004]. A reliable assessment of future levels of Arctic ozone will not be possible until the observed tendency toward colder Arctic winters is understood.

[18] **Acknowledgments.** Meteorological data were provided by ECMWF and FU-Berlin. This work was supported by the BMBF (DYCHO, FKZ07ATC08) and by the EC (project SCOUT-O3). Ozonesondes were partially funded by the EC (project QUOBI). Research at the Jet Propulsion Laboratory, California Institute of Technology, is performed under contract with the National Aeronautics and Space Administration. We thank T. Nagai and C. Trepte for providing ozone data for this study and E. Weatherhead for helpful discussions.

References

Austin, J., N. Butchart, and K. P. Shine (1992), Possibility of an Arctic ozone hole in a doubled CO_2 climate, *Nature*, *360*, 221–225.

Hoppel, K., R. Bevilacqua, G. Nedoluha, C. Deniel, F. Lefèvre, J. Lumpe, M. Fromm, C. Randall, J. Rosenfield, and M. Rex (2002), POAM III observations of arctic ozone loss for the 1999/2000 winter, *J. Geophys. Res.*, *107*(D20), 8262, doi:10.1029/2001JD000476.

Knudsen, B. M., et al. (1998), Ozone depletion in and below the Arctic vortex for 1997, *Geophys. Res. Lett.*, *25*, 627–630.

Knudsen, B. M., et al. (2004), Extrapolating future Arctic ozone losses, *Atmos. Chem. Phys.*, *4*, 1849–1856.

Manney, G. L., K. Krüger, J. L. Sabutis, S. A. Sena, and S. Pawson (2005), The remarkable 2003–2004 winter and other recent warm winters in the Arctic stratosphere since the late 1990s, *J. Geophys. Res.*, *110*, D04107, doi:10.1029/2004JD005367.

Manney, G. L., M. L. Santee, L. Froidevaux, K. Hoppel, N. J. Livesey, and J. W. Waters (2006), EOS MLS observations of ozone loss in the 2004–2005 Arctic winter, *Geophys. Res. Lett.*, *33*, L04802, doi:10.1029/2005GL024494.

Randall, C. E., et al. (2005), Reconstruction and simulation of stratospheric ozone distributions during the 2002 austral winter, *J. Atmos. Sci.*, *62*, 748–764.

Rex, M., et al. (1999), Chemical ozone loss in the Arctic winter 1994/95 as determined by the Match technique, *J. Atmos. Chem.*, *32*, 35–59.

Rex, M., et al. (2002), Chemical depletion of Arctic ozone in winter 1999/2000, *J. Geophys. Res.*, *107*(D20), 8276, doi:10.1029/2001JD000533.

Rex, M., R. J. Salawitch, P. von der Gathen, N. R. P. Harris, M. P. Chipperfield, and B. Naujokat (2004), Arctic ozone loss and climate change, *Geophys. Res. Lett.*, *31*, L04116, doi:10.1029/2003GL018844.

Schnadt, C., et al. (2002), Interaction of atmospheric chemistry and climate and its impact on stratospheric ozone, *Clim. Dyn.*, *18*, 501–517.

Shindell, D. T., D. Rind, and P. Lonergan (1998), Increased polar stratospheric ozone losses and delayed eventual recovery owing to increasing greenhouse-gas concentrations, *Nature*, *392*, 589–592.

Tilmes, S., et al. (2004), Ozone loss and chlorine activation in the Arctic winters 1991–2003 derived with the tracer-tracer correlations, *Atmos. Chem. Phys.*, *4*, 2181–2213.

M. Allaart, KNMI, Postbus 201, NL-3730 AE, De Bilt, Netherlands.

S. B. Andersen, Danish Meteorological Institute, Lyngbyvej 100, DK-20100 Copenhagen, Denmark.

R. Bevilacqua and K. Hoppel, Naval Research Laboratory, Code 7227, Washington, DC 20375-5320, USA.

G. O. Braathen, NILU, N-2027 Kjeller, Norway.

M. P. Chipperfield, School of Earth and Environment, University of Leeds, Leeds LS2 9JT, UK.

H. Claude, Met. Obs. Hohenpeißenberg, German Weather Service, Albin-Schwaiger-Weg 10, D-82383 Hohenpeißenberg, Germany.

J. Davies and H. Fast, Met. Service of Canada, 4905 Dufferin Street, Toronto, ON, Canada M3H 5T4.

H. De Backer, Royal Meteorological Institute of Belgium, B01180 Brussels, Belgium.

H. Deckelmann, M. Rex, and P. von der Gathen, Research Unit Potsdam, Alfred Wegener Institute for Polar and Marine Research, P.O. Box 600149, D-14401 Potsdam, Germany. (mrex@awi-potsdam.de)

H. Dier, MOL, Am Observatorium 12, D-15848 Tauche/OT Lindenberg, Germany.

V. Dorokhov and V. Yushkov, CAO, Dolgoprudny, Moscow, Russia.

M. Gerding, IAP, D-18225 Kühlungsborn, Germany.

S. Godin-Beekmann, Service d'Aéronomie, CNRS, Institut Pierre-Simon Laplace, UPMC-b102, 4 Place Jussieu, P-75252 Paris Cedex 05, France.

N. R. P. Harris, European Ozone Research Coordinating Unit, University of Cambridge, Cambridge CB2 1EW, UK.

B. Johnson, Earth System Research Laboratory, NOAA, 325 Broadway, Boulder, CO 80305, USA.

E. Kyrö, SMO, Sodankylä, Finland.

Z. Litynska, MWM, Centre of Aerology, Zegrzynska 39, PL-05119 Legionowo, Poland.

D. Moore, Met Office, FitzRoy Road, Exeter EX1 3PB, UK.

H. Nakane, Asian Environmental Research Group, NIES, 16-2, Onogawa, Tsukuba, Ibaraki 305-8506, Japan.

B. Naujokat and E. Reimer, Met. Institute, Freie Universität Berlin, C.-H.-Becker-Weg 6-10, D-12165 Berlin, Germany.

M. C. Parrondo, INTA, Crta de Ajalvir km 4, E-28850 Torrejon de Ardoz, Madrid, Spain.

A. D. Risley Jr., SAIC, One Enterprise Parkway, Suite 270, Hampton, VA 23666, USA.

R. J. Salawitch, Jet Propulsion Laboratory, California Institute of Technology, Pasadena, CA 91109, USA.

P. Skrivankova, Czech Hydrometeorological Institute, Na Sabatce 17, 143 06 Praha 4, Czech Republic.

R. Stübi, Swiss Meteorological Aerological Station, CH-1530 Payerne, Switzerland.

P. Viatte, Federal Office of Meteorology and Climatology, MeteoSwiss, CH-1530 Payerne, Switzerland.

C. Zerefos, Laboratory of Climatology and Atmospheric Environment, University of Athens, GR-15784 Athens, Greece.

GEOPHYSICAL RESEARCH LETTERS, VOL. 35, L01807, doi:10.1029/2007GL031740, 2008

Polar stratospheric chlorine kinetics from a self-match flight during SOLVE-II/EUPLEX

R. Schofield,[1] K. Frieler,[1,2] I. Wohltmann,[1] M. Rex,[1] M. von Hobe,[3] F. Stroh,[3]
G. Koch,[4] T. Peter,[4] T. Canty,[5,6] R. Salawitch,[5,6] and C. M. Volk[7]

Received 20 August 2007; revised 17 October 2007; accepted 27 November 2007; published 11 January 2008.

[1] In-situ measurements of ClO made onboard the Geophysica aircraft on 30 January 2003 in the Arctic afford a novel approach to constrain the kinetic parameters governing polar stratospheric chlorine chemistry using atmospheric observations. The self-match flight pattern, i.e. sampling individual air masses twice at different zenith angles, was utilized by simulating the evolution of ClO mixing ratios between two 'matching' points using a photochemical model and optimizing the model parameters to fit the observations within a retrieval framework. Our results suggest a ClO/ClOOCl thermal equilibrium constant K_{eq} a factor of 5 smaller and a ratio J/k_f a factor of 2 larger than the values based on the JPL recommendations. This concurs with other studies based on observed ClO_x partitioning and corroborates that our understanding of stratospheric chlorine chemistry is incomplete, particularly in the light of the most recent laboratory experiments pointing to a J/k_f ratio almost an order of magnitude below the JPL recommendation.

Citation: Schofield, R., K. Frieler, I. Wohltmann, M. Rex, M. von Hobe, F. Stroh, G. Koch, T. Peter, T. Canty, R. Salawitch, and C. M. Volk (2008), Polar stratospheric chlorine kinetics from a self-match flight during SOLVE-II/EUPLEX, *Geophys. Res. Lett.*, *35*, L01807, doi:10.1029/2007GL031740.

1. Introduction

[2] Ozone loss in the cold polar stratosphere is largely attributed to the chlorine catalytic cycle involving ClO dimer formation [*Molina and Molina*, 1987]:

$$\mathrm{ClO + ClO + M} \underset{k_b}{\overset{k_f}{\rightleftharpoons}} \mathrm{ClOOCl + M} \tag{1}$$

$$\mathrm{ClOOCl} + h\nu \xrightarrow{J} \mathrm{Cl + ClOO} \tag{2}$$

$$\mathrm{ClOO + M \rightarrow Cl + O_2 + M} \tag{3}$$

$$\begin{array}{c} 2 \times [\mathrm{Cl + O_3 \rightarrow ClO + O_2}] \\ \hline \mathrm{2O_3 \rightarrow 3O_2} \end{array} \tag{4}$$

with the thermal equilibrium constant given by $K_{eq} = k_f/k_b$. K_{eq} is temperature dependent - at lower temperatures the equilibrium shifts towards ClOOCl. J is primarily controlled by the solar zenith angle (SZA).

[3] Measurements of ClO by in-situ and remote sensing methods have been used to test our understanding of the kinetics of this catalytic cycle. Table 1 summarizes these studies in terms of scale factors relative to current JPL06 laboratory based recommendations [*Sander et al.*, 2006]. To explain existing ClO measurements it is required that J/k_f (essential for determining ozone loss) be equal to or greater than JPL06 and K_{eq} be between $0.15-0.5 \times$ JPL06.

[4] The recent laboratory measurements of K_{eq} and k_b by *Plenge et al.* [2005] and *Bröske and Zabel* [2006], respectively, are consistent with a smaller value of K_{eq}. On the other hand, the most recent laboratory studies of k_f by *Boakes et al.* [2005] and the ClOOCl photolysis cross-section measured by *Pope et al.* [2007] indicate a larger value of k_f and a smaller value of J compared to JPL06 and thus seem to contradict the larger J/k_f ratios implied by the atmospheric studies listed in Table 1. These discrepancies suggest that our quantitative understanding of the chemical mechanisms controlling chlorine partitioning in the polar stratosphere is incomplete, compromising our ability to quantitatively account for observed ozone depletion [*von Hobe et al.*, 2007].

[5] Here we present a novel approach to constrain these kinetic parameters made possible by the 'self-match' flight during SAGE III Ozone Loss and Validation Experiment (SOLVEII)/European Polar Stratospheric Cloud and Lee Wave Experiment (EUPLEX). The flight design, photochemical model, and retrieval algorithm used to obtain J/k_f and K_{eq} are described in section 2. In section 3 the results and uncertainties are discussed and compared to previous studies.

2. Data and Analysis

[6] The Geophysica aircraft flew on 30 January 2003 out of Kiruna, Sweden (11:44–14:37 UTC). This airplane flew isentropically, sampling airmasses twice in a self-match pattern (Figure 1). For each airmass ClO was measured at two distinct SZAs near sunset, for otherwise constant conditions. The photolysis of ClOOCl slows as the Sun sets, altering the partitioning between ClO and ClOOCl. No

---

[1] Alfred Wegener Institute for Polar and Marine Research, Potsdam, Germany.

[2] Now at Department of Medical Statistics and Clinical Epidemiology, Charité Universitätsmedizin Berlin, Berlin, Germany.

[3] Institute for Chemistry and Dynamics of the Geosphere 1: Stratosphere (ICG-1), Forschungszentrum Jülich, Jülich, Germany.

[4] Institute for Atmospheric and Climate Science, ETH Zürich, Zürich, Switzerland.

[5] Jet Propulsion Laboratory, California Institute of Technology, Pasadena, California, USA.

[6] Now at Department of Atmospheric and Oceanic Science, University of Maryland, College Park, Maryland, USA.

[7] Institut für Atmosphäre und Umwelt, J. W. Goethe-Universität, Frankfurt am Main, Germany.

Copyright 2008 by the American Geophysical Union.
0094-8276/08/2007GL031740$05.00

Table 1. Scale Factors Relative to JPL06 for Previous Observation/Model Comparisons, Under the Conditions of the Match Flight[a]

Reference	Range	Study Temperature	Platform (Mission) Latitude
Brune et al. [1990]	$0.25K_{eq}$	200 K	NASA ER-2 (AASE I) 68°N
Pierson et al. [1999]	$<0.3K_{eq}$	200 K	Balloon (SESAME/AASE I) 68°N
Avallone and Toohey [2001]	$<0.47-0.49K_{eq}$	188–209 K	NASA ER-2 (AASE I and II) 68°N
Stimpfle et al. [2004]	$\sim 0.5K_{eq}$	189–202 K	NASA ER-2 (SOLVE/THESEO-2000) 68°N
von Hobe et al. [2005]	$0.04-0.48K_{eq}$	192–216 K	M55-Geophysica (EUPLEX) 68°N
Berthet et al. [2005]	$0.15-0.5K_{eq}$	200–220 K	Satellite (ODIN) < 80°N
This work	$0.2^{+0.4}_{-0.1}K_{eq}$	200–207 K	M55-Geophysica (EUPLEX) 68°N
Shindell and de Zafra [1996]	$0.9-1.8J/k_f$	190 K	Ground-based Microwave 78°S (1993)
Solomon et al. [2002]	$1.0-1.7J/k_f$	-	Ground-based Microwave 77°S
Vogel et al. [2003]	$\sim 1.08J/k_f$	190–210 K	Balloon (SOLVE/THESEO-2000) 68°N
Stimpfle et al. [2004]	$\sim 1.4-1.8J/k_f$	189–202 K	NASA ER-2 (SOLVE/THEOSEO-2000) 68°N
von Hobe et al. [2007]	$\sim 1.2-1.7J/k_f$	198–208 K	M55-Geophysica (March 2005) 48–58°N
This work	$(1.9-3.9J/k_f)^{+1.8}_{-0.9}$	200–207 K	M55-Geophysica (EUPLEX) 68°N

[a] Conditions of the match flight are SZA = 83°–94°, T = 200–207 K, and θ = 430 K.

polar stratospheric clouds or large dynamical disturbances capable of significantly altering ClO_x ($ClO + 2ClOOCl$) occurred along the air mass trajectories.

2.1. ClO Observations

[7] The in-situ ClO measurements were made by the HALOX instrument [*von Hobe et al.*, 2005], based on the chemical conversion resonance fluorescence technique [*Brune et al.*, 1989]. Precision, resulting mainly from random noise, varied from 4 to 8%. The accuracy is estimated to be ~16%; 12.5% constant and up to 10% sloping (varying with time) error components.

2.2. Trajectory Calculation and Match Identification

[8] Trajectories were calculated (for details see *Wohltmann and Rex* [2007]) backwards for 48 hours and forward for 24 hours for each individual ClO measurement along the outgoing flight path. Trajectories were generated using a 4th order Runge-Kutta method applied to ECMWF operational data as input for wind and temperature with a 1 minute integration step. An isentropic vertical coordinate was used, assuming no diabatic motion. Wind and temperature were linearly interpolated to the position of the trajectory.

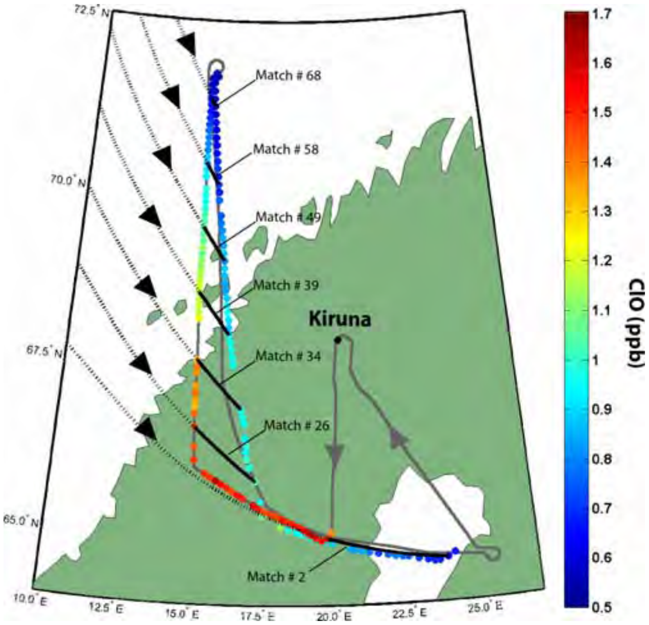

Figure 1. Map of the self-match flight path (grey curve). Colored points: all 72 match pairs ($\theta \sim 430$ K) (colorscale: ClO value). Dotted black lines: back trajectories for seven of the match pairs for this flight. Solid black lines: trajectories linking the outbound and inbound match points.

[9] A match point [*Rex et al.*, 1998] was found by minimizing the distance between the trajectory and inbound flight measurement points in time (1 minute intervals). This distance, the match radius, was never larger than 20 km (see Figure 2). The outbound leg was 85 minutes long, enabling 72 matches to be identified.

2.3. Photochemical Box Model

[10] The photochemical box model described in detail by *Salawitch et al.* [1993] formed the basis of the forward model function, simulating the diurnal variation of ClO, ClOOCl, OClO, BrO, BrCl and atomic O. The model was initialized for 24 hours with ClO_x assigned a priori and Br_y from the AER 2D model (only long-lived species). The chemical model was run along the trajectory for 48 hours (1 minute steps) until the first match point was reached (the outbound ClO value). The chemistry was calculated further along the trajectory until the second match point (the inbound ClO value) was reached.

2.4. Retrieval

[11] The state vector (**x**) describing what we wish to retrieve from the 72 ClO matches (**y**) was constructed with the kinetic parameters describing K_{eq} (log A and B as given by JPL06), and a multiplicative scale factor for J relative to the J value calculated with JPL06 ClOOCl cross-sections (J_{scale}). Additionally **x** contained the ClO_x value for each match pair. ClO_x was assumed to be constant for a given match, but allowed to vary between matches. The state space was explored by fixing k_f between 0.35 and 1.8 × k_f JPL06.

[12] The forward model function $\boldsymbol{F}$ finds ClO at the match points when supplied with the state vector kinetic parameters and ClO_x (section 2.3). The sensitivity of the modeled ClO to the state vector was explored by calculating weighting functions **K** numerically as the response in the forward model to perturbing the parameter of interest ($d\boldsymbol{F}/d\mathbf{x}$) (see auxiliary material).[1]

---

[1] Auxiliary materials are available in the HTML. doi:10.1029/2007GL031740.

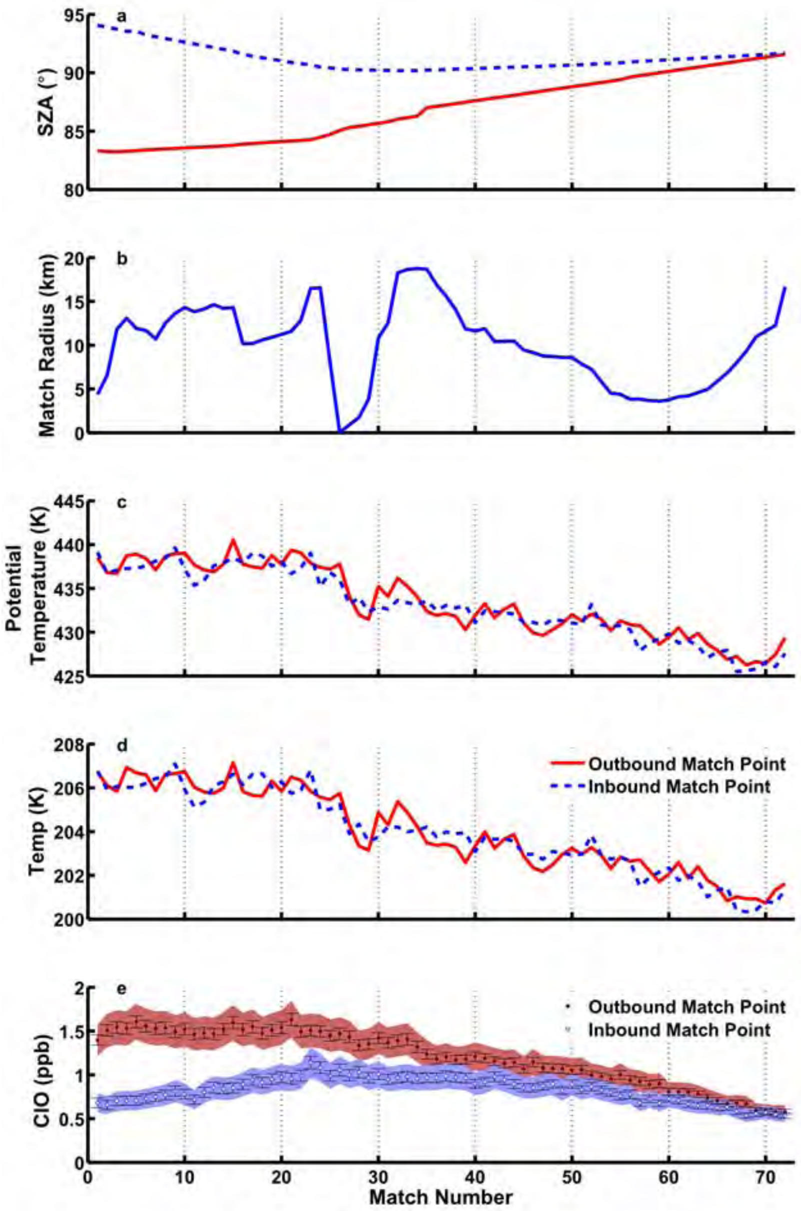

Figure 2. The (a) SZA, (b) match radius, (c) potential temperature, and (d) temperature for the outbound (solid red line) and inbound (dotted blue line) flight legs for each match pair. (e) The ClO observational data with error-bars indicating the precision error and the shaded region the total error (precision plus systematic).

[13] An iterative solution to Bayes Theorem minimized the root mean square difference between the model and the measured values of ClO [*Rodgers*, 2000]:

$$\hat{\mathbf{x}}_{i+1} = \mathbf{x}_a + \left(\mathbf{S}_a^{-1} + \mathbf{K}_i^T \mathbf{S}_\epsilon^{-1} \mathbf{K}_i\right)^{-1} \mathbf{K}_i^T S_\epsilon^{-1} \cdot \left[\mathbf{y} - F(\hat{\mathbf{x}}_i) + \mathbf{K}_i(\hat{\mathbf{x}}_i - \mathbf{x}_a)\right] \qquad (5)$$

This inversion weights the state vector solution according to the measurement precision covariance (S_ϵ) and the a priori state ($\mathbf{x}_a$) covariance ($\mathbf{S}_a$).

[14] Air masses were sampled over sunset, for which the ClO_x system was neither at thermal nor photolytic equilibrium. Therefore, interdependence is high between the parameters describing K_{eq}, J and ClO_x (and forward model parameter k_f). For example, without reaching a daytime equilibrium the same diurnal slope can be explained with more ClO_x but a slower photolysis. Similarly, k_f and J are related; a stronger rate of dimer formation can be balanced by faster photolysis. Thus a priori information was required to constrain the retrieval.

[15] A priori values for K_{eq} and J_{scale} were taken from JPL06. For ClO_x we retrieved for two a priori constraint cases. First; ClO_x = 2.0 ppb, obtained considering the dimer measurements of HALOX [*von Hobe et al.*, 2005] scaled by 1.4 as suggested by *von Hobe et al.* [2007] (see auxiliary material).

[16] For the second a priori case: ClO_x = 2.7 ppb approximating ‘complete activation’ of all available Cl_y (total chlorine). We estimate a mean value of $Cl_y \simeq 2.7$ ppb for the matches, based on the relation between Cl_y

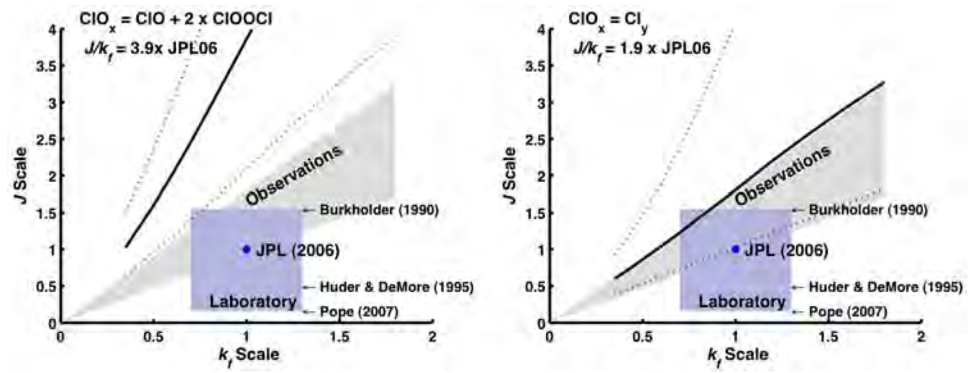

Figure 3. (left) The match-retrieved scale factors for k_f and J given the ClO_x a priori 'dimer' assumption (see text). (right) Same but assuming ClO_x 'total activation' assumption a priori. Black lines: self-match flight. Dashed lines: uncertainties (upper) plus systematic and (lower) minus systematic, respectively. Light grey area: region consistent with previous observational/modeling studies. Light blue area: region consistent with laboratory studies.

and θ inferred from HAGAR measurements (see auxiliary material).

[17] $\mathbf{S_a}$ was constructed using the following uncertainties: JPL06 error for K_{eq}, 0.9 for J_{scale} and 0.5 ppb for ClO_x. The retrievals resulted in an a priori weighting for K_{eq} and J_{scale} of 2% and 7% respectively from averaging kernel considerations. The uncertainties on the retrieved quantities were calculated by repeating the analysis with the measurements modified by their systematic uncertainties. These uncertainty limits represent bounds outside which the model is in no way consistent with the measurements.

3. Results and Discussion

[18] The SZA, match radius, potential temperature, and temperature for the outbound and inbound flight legs are displayed for each match in Figure 2. The ClO measurements with their precision and systematic errors are also displayed for the outbound and inbound flight legs.

3.1. Retrieved Kinetic Parameters

[19] Retrievals were run as outlined in section 2.4. For each retrieval the measurements were well described by the model, with absolute residuals less than 0.15 ppb (see auxiliary material).

[20] Figures 3 and 4 display the results from all retrievals expressed as scale factors of JPL06 kinetic parameters. Figure 3 displays the retrieved values for J against k_f. Only when the 'total activation' a priori constraint where $ClO_x \simeq Cl_y$ is applied does the slope approach that of previous studies using atmospheric observations, with best agreement seen at the lower uncertainty range of our work. This 'total activation' case (Figure 3, right) provides the lower limit constraint on J/k_f of 1.0 × JPL06. When ClO_x is constrained using the ClOOCl measurements (a priori $ClO_x = 2.0$ ppb), then a lower limit for J/k_f of 2.1 × JPL06 is found. The results for the 2 cases shown in Figure 3 give estimates for J/k_f of 1.9 and 3.9 × JPL06, respectively. This lies outside the range of values derived previously from observational/modeling studies. Note that neither this work nor any previous work is consistent with the combination of the most recent laboratory studies of *Pope et al.* [2007] ($0.16 \times J_{\mathrm{JPL06}}$) and *Boakes et al.* [2005] ($k_f = 1.3 \times k_f$ JPL06) giving a ratio of 0.13 × J/k_f JPL06.

[21] Figure 4 displays the retrieved relationship between K_{eq} and k_f with respect to JPL06. The error range is valid for all values of ClO_x. This figure illustrates the $K_{eq} = 0.2^{+0.4}_{-0.1} \times$ JPL06 result that is found when k_f is constrained to lie within the laboratory estimates. This range of K_{eq} is independent of the dimer measurements which have been used in previous estimates of K_{eq} from observations [*Stimpfle et al.*, 2004; *von Hobe et al.*, 2005]. Additionally, if the dimer measurements are considered (a priori = 2.0 ppb for ClO_x), the values retrieved for J_{Scale} are given by the colors on the central curve (refer to Figure 3 for clearer k_f vs J information illustration). The error limits (dashed lines) consider the systematic error in the measurements. Even considering measurement errors, the retrieved K_{eq} and k_f do not agree with JPL06. The relationship of K_{eq} and k_f is virtually unaltered with the 'total activation' assumption, however the relationship between k_f and J is dramatically different (see Figure 3).

4. Conclusions

[22] Using ClO measurements from the self-match flight carried out during the SOLVE II/EUPLEX campaign, the match technique was combined with a retrieval formalization to study the chlorine dimer catalytic cycle in the activated polar stratosphere. Using JPL06 as a normalizing standard, the relationship between K_{eq}, k_f and J was retrieved.

[23] We found no combination of retrieved kinetic parameters (within measurement errors) consistent with JPL06 for K_{eq} and k_f. When k_f is constrained within limits from previous laboratory work then K_{eq} is a factor of $0.2^{+0.4}_{-0.1} \times K_{eq}$ JPL06. This result, independent of the dimer measurement, supports the conclusions of previous analyses of atmospheric observations [*Brune et al.*, 1990; *Pierson et al.*, 1999; *Avallone and Toohey*, 2001; *Stimpfle et al.*, 2004; *von Hobe et al.*, 2005; *Berthet et al.*, 2005] and the recent laboratory observations of K_{eq} and k_b [*Plenge et al.*, 2005; *Bröske and Zabel*, 2006] of a smaller K_{eq} than the current JPL06 recommendations. Furthermore, we determined a lower limit for the ratio of J/k_f of 1.0 × J/k_f JPL06 when simply limiting ClO_x to be below Cl_y. Additionally, when the dimer measurements were used to constrain ClO_x this lower limit becomes 2.1 × J/k_f JPL06, higher than other

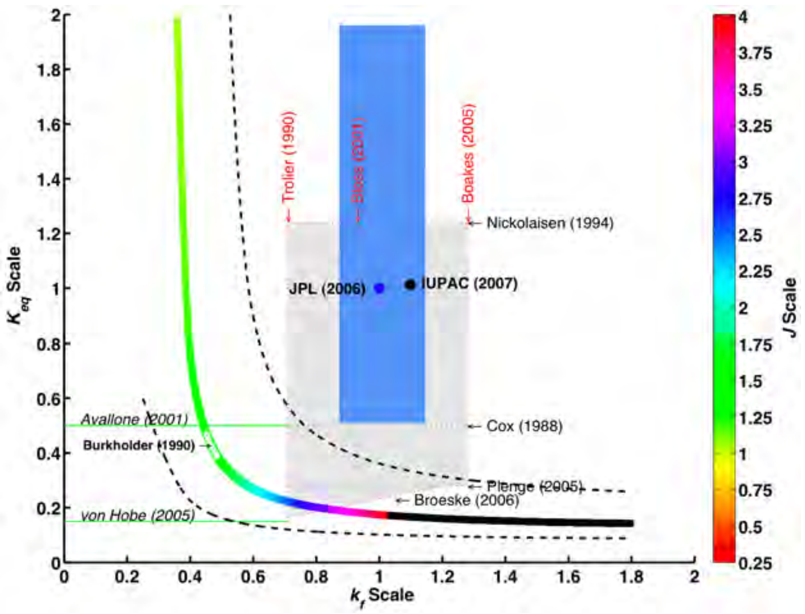

Figure 4. Thick colored curve: match-retrieved scale factors (relative to JPL06) for K_{eq} for varying k_f. The color scale: J_{Scale} for the a priori constraint $ClO_x = 2.0$ ppb ('dimer' case) (J_{Scale} above 4 is black). Dashed curves: the addition (lower), and subtraction (upper) of measurement systematic error. Grey shaded region: region consistent with laboratory studies. Green lines: observationally based K_{eq} estimates (see Table 1 for more details). Blue shaded region: uncertainty range for current JPL06 recommendations. IUPAC (2007) refers to *Atkinson et al.* [2007].

observational estimates. In all cases we find no combination of kinetic parameters that can simultaneously explain our observations of ClO and a value of J found using the *Pope et al.* [2007] cross-sections.

[24] **Acknowledgments.** We thank all those involved in the Geophysica deployment in the VINTERSOL-EUPLEX project, funded by the European Commission (EVK2-2001-00084). R. Schofield thanks the Alexander von Humboldt Stiftung's Research Award allowing this work to be conducted. Research at Jet Propulsion Laboratory, California Institute of Technology, is performed under contract with the National Aeronautics and Space Administration.

References

Atkinson, R., et al. (2007), Evaluated kinetic and photochemical data for atmospheric chemistry: volume III. Gas phase reactions of inorganic halogens, *Atmos. Chem. Phys.*, *7*, 981–1191.

Avallone, L. M., and D. W. Toohey (2001), Tests of halogen photochemistry using in situ measurements of ClO and BrO in the lower polar stratosphere, *J. Geophys. Res.*, *106*, 10,411–10,421.

Berthet, G., P. Ricaud, F. Lefèvre, E. Le Flochmoën, J. Urban, B. Barret, N. Lautié, E. Dupuy, J. De La Noë, and D. Murtagh (2005), Nighttime chlorine monoxide observations by the Odin satellite and implications for the ClO/Cl_2O_2 equilibrium, *Geophys. Res. Lett.*, *32*, L11812, doi:10.1029/2005GL022649.

Bloss, W. J., S. L. Nickolaisen, R. J. Salawitch, R. R. Friedl, and S. P. Sander (2001), Kinetics of the ClO self-reaction and 210 nm absorption cross section of the ClO dimer, *J. Phys. Chem.*, *105*, 11,226–11,239.

Boakes, G., W. H. H. Mok, and D. M. Rowley (2005), Kinetic studies of the ClO plus ClO association reaction as a function of temperature and pressure, *Phys. Chem. Chem. Phys.*, *7*, 4102–4113.

Bröske, R., and F. Zabel (2006), Thermal decomposition of ClOOCl, *J. Phys. Chem.*, *110*, 3280–3288.

Brune, W. H., J. G. A. Anderson, and K. R. Chan (1989), In situ observations of ClO in the Antarctic: ER-2 aircraft results from 54°S to 72°S latitude, *J. Geophys. Res.*, *94*, 16,649–16,663.

Brune, W. H., D. W. Toohey, J. G. Anderson, and K. R. Chan (1990), In situ observations of ClO in the Arctic stratosphere: ER-2 aircraft results from 59° to 80°N latitude, *Geophys. Res. Lett.*, *17*, 505–508.

Burkholder, J. B., J. J. Orlando, and C. J. Howard (1990), Ultraviolet-absorption cross-sections of Cl_2O_2 between 210 and 410 nm, *J. Phys. Chem.*, *94*, 687–695.

Cox, R. A., and G. D. Hayman (1988), The stability and photochemistry of dimers of the ClO radical and implications for Antarctic ozone depletion, *Nature*, *332*, 796–800.

Huder, K. J., and W. B. DeMore (1995), Absorption cross-sections of the ClO dimer, *J. Phys. Chem.*, *99*, 3905–3908.

Molina, L. T., and M. J. Molina (1987), Production of Cl_2O_2 from the self-reaction of the ClO radical, *J. Phys. Chem.*, *91*, 433–463.

Nickolaisen, S. L., R. R. Friedl, and S. P. Sander (1994), Kinetics and mechanism of the ClO + ClO reaction: Pressure and temperature dependences of the bimolecular and termolecular channels and thermal decomposition of chlorine peroxide, *J. Phys. Chem.*, *98*, 155–169.

Pierson, J. M., K. A. McKinney, D. W. Toohey, J. J. Margitan, U. Schmidt, and A. Engel (1999), An investigation of ClO photochemistry in the chemically perturbed Arctic vortex, *J. Atmos. Chem.*, *32*, 61–81.

Plenge, J., S. Kühl, B. Vogel, R. Müller, F. Stroh, M. von Hobe, R. Flesch, and E. Rühl (2005), Bond strength of chlorine peroxide, *J. Phys. Chem.*, *109*, 6730–6734.

Pope, F. D., J. C. Hansen, K. D. Bayes, R. R. Friedl, and S. P. Sander (2007), The ultraviolet absorption spectrum of chlorine peroxide, ClOOCl, *J. Phys. Chem. A.*, *111*, 4322–4342.

Rex, M., et al. (1998), In situ measurements of stratospheric ozone depletion rates in the Arctic winter 1991/1992: A lagrangian approach, *J. Geophys. Res.*, *103*, 5843–5853.

Rodgers, C. D. (2000), *Inverse Methods for Atmospheric Sounding, Theory and Practice*, 1st ed., World Sci., Singapore.

Salawitch, R. J., et al. (1993), Chemical loss of ozone in the Arctic polar vortex in the winter of 1991–1992, *Science*, *261*, 1146–1149.

Sander, S. P., et al. (2006), Chemical kinetic and photochemical data for use in atmospheric studies, *Tech. Rep. 15*, Jet Propul. Lab., Pasasdena, Calif.

Shindell, D. T., and R. L. de Zafra (1996), Chlorine monoxide in the Antarctic spring vortex: 2. A comparison of measured and modeled diurnal cycling over McMurdo station, 1993, *J. Geophys. Res.*, *101*, 1475–1487.

Solomon, P., B. Connor, J. Barret, T. Mooney, A. Lee, and A. Parrish (2002), Measurements of stratospheric ClO over Antarctica in 1996–2000 and implications for ClO dimer chemistry, *Geophys. Res. Lett.*, *29*(15), 1708, doi:10.1029/2002GL015232.

Stimpfle, R. M., D. M. Wilmouth, R. J. Salawitch, and J. G. Anderson (2004), First measurements of ClOOCl in the stratosphere: The coupling of ClOOCl and ClO in the Arctic polar vortex, *J. Geophys. Res.*, *109*, D03301, doi:10.1029/2003JD003811.

Trolier, M., R. L. Mauldin, and A. R. Ravishankara (1990), Rate coefficient for the termolecular channel of the self-reaction of ClO, *J. Phys. Chem.*, *94*, 4896–4907.

Vogel, B., J. Grooß, R. Müller, T. Deshler, J. Karhu, D. S. McKenna, M. Müller, D. Toohey, G. C. Toon, and F. Stroh (2003), Vertical profiles of activated ClO and ozone loss in the Arctic vortex in January and March 2000: In situ observations and model simulations, *J. Geophys. Res.*, *108*(D22), 8334, doi:10.1029/2002JD002564.

von Hobe, M., J. U. Grooß, R. W. Müller, S. Hrechanyy, U. Winkler, and F. Stroh (2005), A re-evaluation of the ClO/Cl_2O_2 equilibrium constant based on stratospheric in-situ observations, *Atmos. Chem. Phys.*, *5*, 693–702.

von Hobe, M., R. J. Salawitch, T. Canty, H. Keller-Rudek, G. K. Moortgat, J. U. Grooß, R. Müller, and F. Stroh (2007), Understanding the kinetics of the ClO dimer cycle, *Atmos. Chem. Phys.*, *7*, 3055–3069.

Wohltmann, I., and M. Rex (2007), Improvement of vertical and residual velocities in pressure or hybrid sigma-pressure coordinates in analysis data in the stratosphere, *Atmos. Chem. Phys. Discuss.*, *7*, 13,401–13,416.

T. Canty and R. Salawitch, Department of Atmospheric and Oceanic Science, University of Maryland, College Park, 2403 Computer and Space Sciences Building, College Park, MD 20742, USA.

K. Frieler, Department of Medical Statistics and Clinical Epidemiology, Charité Universitätsmedizin Berlin, Campus Mitte, D-10098 Berlin, Germany.

G. Koch and T. Peter, Institute for Atmospheric and Climate Science, ETH Zürich, CH-8093 Zürich, Switzerland.

M. Rex, R. Schofield, and I. Wohltmann, Alfred Wegener Institute for Polar and Marine Research, Telegrafenberg A43, D-14473 Potsdam, Germany. (robyn.schofield@awi.de)

F. Stroh and M. von Hobe, Institute for Chemistry and Dynamics of the Geosphere 1: Stratosphere (ICG-1), Forschungszentrum Jülich, D-52425 Jülich, Germany.

C. M. Volk, Institut für Atmosphäre und Umwelt, J. W. Goethe-Universität, Georg Voigt Strasse 14, D-60325 Frankfurt am Main, Germany.

GEOPHYSICAL RESEARCH LETTERS, VOL. 35, L17801, doi:10.1029/2008GL034250, 2008

Relative importance of dynamical and chemical contributions to Arctic wintertime ozone

S. Tegtmeier,[1,2] M. Rex,[1] I. Wohltmann,[1] and K. Krüger[3]

Received 6 April 2008; revised 25 June 2008; accepted 17 July 2008; published 3 September 2008.

[1] We present the first complete budget of the interannual variability in Arctic springtime ozone taking into account anthropogenic chemical and natural dynamical processes. For the winters 1991/1992 to 2003/2004 the Arctic chemical ozone loss is available from observations. This work investigates the dynamical supply of ozone to the Arctic polar vortex due to mean transport processes for the same winters. The ozone supply is quantified in a vortex-averaged framework using estimates of diabatic descent over winter. We find that the interannual variability of both dynamical ozone supply and chemical ozone loss contribute, in equal shares, to the variability of the total ozone change. Moreover, together they explain nearly all of the interannual variability of Arctic springtime column ozone. Variability in planetary wave activity, characterized by the Eliassen-Palm flux at 100 hPa, contributes significantly to the variability of ozone supply, chemical ozone loss and total springtime ozone. **Citation:** Tegtmeier, S., M. Rex, I. Wohltmann, and K. Krüger (2008), Relative importance of dynamical and chemical contributions to Arctic wintertime ozone, *Geophys. Res. Lett.*, *35*, L17801, doi:10.1029/2008GL034250.

1. Introduction

[2] Vortex averages of Arctic column ozone exhibit pronounced interannual variability in late winter and spring [*World Meteorological Organization* (*WMO*), 2003], which is in contrast to a much smaller degree of interannual variability in autumn [e.g., *Rex et al.*, 2000]. Therefore, the variability of the Arctic ozone layer in spring results from the variability of winter processes. A reliable prediction and identification of the ozone recovery in a future climate is limited by our understanding of these processes [*WMO*, 2007]. Changes in the abundance of ozone are driven by chemical and dynamical processes, i.e.

$$\Delta O_{3,\mathrm{tot}} = \Delta O_{3,\mathrm{chem}} + \Delta O_{3,\mathrm{trans}} \qquad (1)$$

where $\Delta O_{3,\mathrm{tot}}$ denotes the fall to spring change in mean total ozone inside the Arctic polar vortex. $\Delta O_{3,\mathrm{chem}}$ denotes the chemical loss of total ozone, i.e. the difference in observed spring total ozone and total ozone that would have been present in spring in the absence of chemical loss, all else being equal [*Rex et al.*, 2002]. $\Delta O_{3,\mathrm{trans}}$ denotes the change in total ozone that results from transport processes.

[3] Past research has focussed mainly on chemical ozone destruction. Several approaches to estimate the chemical loss term and its interannual variability have been developed [*Harris et al.*, 2002, and references therein]. As a consequence, estimates of $\Delta O_{3,\mathrm{chem}}$ are available for the winters 1991/1992 to the present [e.g., *Rex et al.*, 2002; *WMO*, 2007] with uncertainties around 20% [*Harris et al.*, 2002].

[4] Chemistry explains just one component of the interannual variability of Arctic ozone. The other component results from the variability of dynamically driven transport processes and consists of: (a) the transport of ozone due to meridional mixing across the vortex edge, and (b) the transport of ozone due to mean transport by the residual circulation (i.e. the transport of ozone by advection in contrast to the transport by two-way mixing). Mixing is not related to net mass flux but it can contribute to the flux of ozone due to the meridional gradient in ozone mixing ratios. The degree of isolation of the polar vortex from air in midlatitudes and therefore the relative importance of irreversible meridional transport across the vortex edge varies from year to year. Generally the polar vortex is considered to be relatively isolated with a steep gradient in potential vorticity at the edge of the polar vortex constituting an effective barrier to mixing [*WMO*, 2003, section 3.2.1.3, and references therein].

[5] The supply of ozone to the polar vortex due to mean transport is driven by the residual circulation. The theoretical basis of the residual circulation has been laid out by the Transformed Eulerian Mean theory [e.g., *Andrews and McIntyre*, 1976; *Holton et al.*, 1995]. The transport of ozone by the residual circulation has been determined to be an important contributor to the interannual variability of ozone at all latitudes [e.g., *Fusco and Salby*, 1999; *Randel et al.*, 2002]. However, so far the transport of ozone to the polar vortex has not been quantitatively estimated.

[6] The polar branch of the residual circulation results in diabatic descent within the polar vortex. By using diabatic heating rates from radiative transfer calculations, estimates of the diabatic descent have been derived for selected winters [e.g., *Manney et al.*, 1994; *Rosenfield and Schoeberl*, 2001] or in the form of a multi-year time series (1957–2004) [*Tegtmeier et al.*, 2008] (hereinafter referred to as T08).

[7] In this study the vortex-averaged diabatic descent from T08 is used to estimate the dynamical supply of ozone produced by mean transport. The ozone supply is quantified for recent winters, where estimates of the chemical loss term are available. We calculate the fraction of interannual Arctic ozone variability caused by dynamical transport, and that

---

[1] Alfred Wegener Institute for Polar and Marine Research, Potsdam, Germany.

[2] Now at Environment Canada, Toronto, Ontario, Canada.

[3] IFM-GEOMAR, Kiel, Germany.

Copyright 2008 by the American Geophysical Union.
0094-8276/08/2008GL034250$05.00

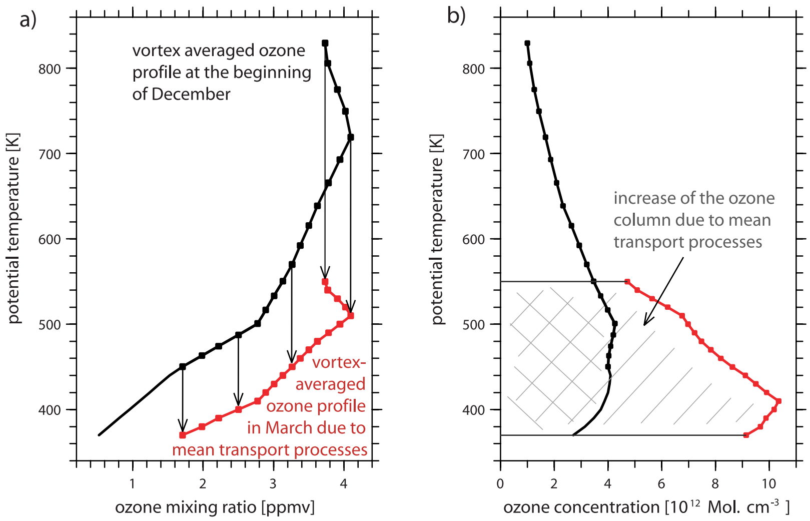

Figure 1. Profiles of (a) ozone mixing ratio and (b) ozone concentration at the beginning of the winter 2000/2001 based on observations (black) and at the end of the winter 2000/2001 resulting from our model calculations (red). The vortex-averaged diabatic descent for the winter 2000/2001 is shown by vertical arrows for five levels.

caused by chemical ozone depletion. The relationships between Eliassen-Palm (EP)-flux and change in total ozone during winter, dynamical supply of ozone, and chemical loss of ozone are investigated.

2. Method

[8] The stratospheric residual circulation transports ozone rich air from lower latitudes into the polar vortex. At the same time, air masses below 400 K with low ozone mixing ratios are transported equatorwards. These processes produce a net dynamical supply of ozone to the polar vortex. The meridional transport leads to adiabatic compression and heating in the polar vortex, which then induces vertical transport. In the isentropic coordinate system, this vertical transport is described by diabatic descent rates. We use the T08 time series of the total winter diabatic descent to quantify the increase of total ozone due to these transport processes in a vortex-averaged framework.

[9] The vortex-averaged descent estimation is based on reverse domain filling trajectory calculations coupled with diabatic heating rate calculations carried out in the polar stratosphere of the NH winters. Input data for temperature and horizontal wind fields are obtained from the European Centre for Medium-Range Weather Forecasts (ECMWF) reanalysis (ERA40) [*Uppala et al.*, 2005] and after 1999 from the ECMWF operational analysis [*Simmons et al.*, 2005]. For December 1995 and 1996 an unrealistic vertical oscillatory temperature structure is found in the Arctic stratosphere in ERA40 [*Uppala et al.*, 2005]. These oscillations might influence the calculated diabatic descent. Therefore these two winters are distinguished from the other winters in the presentation of results to follow.

[10] A vortex-averaged ozone mixing ratio profile for the beginning of each winter is calculated from the ozone dataset CATO [*Brunner et al.*, 2006] as an average of mid November to mid December ozone profiles. CATO provides a homogeneous data set for the years of interest and doesn't suffer from the limited availability of sonde data in the polar vortex in early winter. The edge of the vortex is defined based on the criterion of *Nash et al.* [1996] using the Rossby-Ertel potential vorticity. Figure 1a shows, as an example, the vortex-averaged ozone profile at the beginning of the winter 2000/2001. During the winter the air masses experience diabatic descent. If there would be no chemical ozone loss and no meridional mixing the descending air masses would maintain their corresponding values of ozone mixing ratio. To separate the influence of mean transport from the effects of chemical loss and meridional mixing, we treat the ozone mixing ratio as a conserved quantity. We use the T08 vortex-averaged diabatic descent from beginning of December to mid March to assign each air mass (with its corresponding fixed ozone mixing ratio) to the potential temperature which it would possess near the end of the vortex descent in mid March. The diabatic descent is given for 19 vertical levels between Θ_e = 370 and 550 K. Θ_e is defined as the potential temperature an air mass reaches in spring [*Rex et al.*, 2006]. The new vortex-averaged ozone profile estimated with our method is therefore given by 19 data points between Θ_e = 370 and 550 K. Figure 1a shows example vortex-averaged descent for five levels for the winter 2000/2001, connecting the initial (December, black line) and resulting (mid March, red line) ozone profile.

[11] In order to estimate the influence of the diabatic descent on the total ozone column the corresponding ozone concentration profiles at the beginning and end of the winter are calculated (Figure 1b). The profile estimated for the end of the winter would match the real vortex-averaged ozone profile if there were no chemical ozone loss and no meridional mixing but only mean transport processes. The influence of the mean transport is apparent in the larger values of ozone concentration at the end of the winter.

[12] Based on the two ozone concentration profiles, the partial ozone column between Θ_e = 370 and 550 K at the beginning of winter (marked area bounded by the black curve in Figure 1b) and at the end of winter (entire marked area bounded by the red curve in Figure 1b) are calculated. The difference between the two partial ozone columns equals the dynamical ozone supply by mean transport

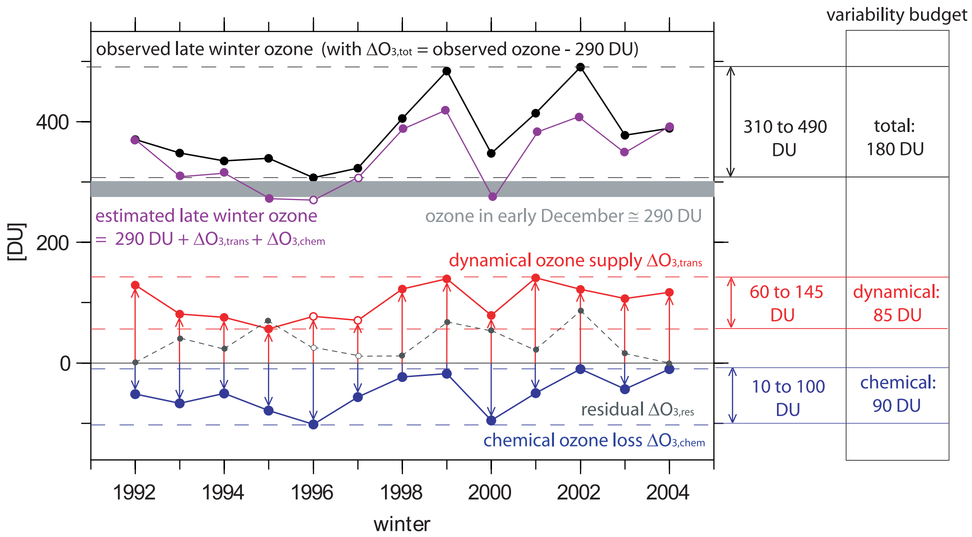

Figure 2. Interannual variability of the observed late winter ozone column (black), the dynamical supply of ozone to the polar vortex (red) and the chemical loss of ozone over the winter (blue) for the winters 1991/1992 to 2003/2004. The range of variability for the three quantities is given on the right hand side. Estimated late winter ozone column (violet) and residual between observed and estimated late winter ozone (dashed grey) are shown for the same years. Results for the winters 1995/1996 and 1996/1997 are marked by open circles.

processes within the region between Θ_e = 370 and 550 K. We do not take into account the net ozone supply above Θ_e = 550 which we consider to be small since ozone profiles at the beginning and end of winter converge quickly above 550 K. Furthermore, we do not take into account the ozone supply below Θ_e = 370 K. Since the polar vortex below 370 K is very unstable, it is not possible to estimate the vortex-averaged descent. However, diabatic descent rates below 370 K are quite small [e.g., *Greenblatt et al.*, 2002] and the main influence of the diabatic descent on total ozone is seen between Θ_e = 370 and 550 K.

[13] Based on this approach we calculate the dynamical ozone supply to the polar vortex between Θ_e = 370 and 550 K caused by mean transport for the winters 1991/1992 to 2003/2004 not taking into account any meridional mixing. For simplicity we will refer to this dynamical ozone supply term as the change in total ozone that results from transport processes $\Delta O_{3,\mathrm{trans}}$.

3. Interannual Variability of Dynamical and Chemical Contributions

[14] The calculated time series of the dynamical ozone supply $\Delta O_{3,\mathrm{trans}}$ for the winters 1991/1992 to 2003/2004 is displayed as red line in Figure 2. The blue and the black line of Figure 2 show the chemical loss of ozone over the winter [*Rex et al.*, 2006] and the observed late winter ozone inside the polar vortex, respectively. All three quantities have been estimated based on the same vortex definition. The time series of observed total ozone is derived from the data set of the NH ozonesonde station network used by *Rex et al.* [2006], applying the same method to estimate the vortex-average. While the procedures used to estimate the dynamical ozone supply and the chemical ozone loss have been applied to slightly different time periods, the quantities produced are valid estimates of the respective terms from December to March. The violet line in Figure 2 shows the late winter ozone estimated as the sum of the chemical ozone loss, the dynamical ozone supply and an approximation of the December total ozone column: 290 DU. The chemical loss and the dynamical supply show a very similar year-to-year variability and together explain a large fraction of the observed fall to spring change in total ozone. The residual change in total ozone $\Delta O_{3,\mathrm{res}}$ may be attributed to transport of ozone due to meridional mixing and dynamical supply above or below the Θ_e = 370 to 550 K region. The residual term $\Delta O_{3,\mathrm{res}}$ can be estimated as

$$\Delta O_{3,\mathrm{res}} = \Delta O_{3,\mathrm{tot}} - \left(\Delta O_{3,\mathrm{chem}} + \Delta O_{3,\mathrm{trans}}\right), \tag{2}$$

and is influenced by the errors of the dynamical supply and the chemical loss. $\Delta O_{3,\mathrm{res}}$ is displayed as dashed grey line in Figure 2 and shows a mean of 38 DU and a standard deviation σ_{res} of 29 DU. The values of $\Delta O_{3,\mathrm{res}}$ are mainly positive, due to not taking into account the processes below Θ_e = 370 K.

[15] The chemical ozone loss varies between −10 and −100 DU with a mean of −50 DU and a standard deviation σ_{chem} of 29 DU. The dynamical ozone supply is characterized by positive values between 60 and 145 DU with a mean of 101 DU and a standard deviation σ_{trans} of 28 DU. Both time series show nearly the same standard deviation and therefore the variability of late winter ozone is influenced in equal shares by the variability of dynamical supply and chemical loss. Winters with a maximum dynamical ozone supply (e.g., 1998/1999) show nearly no chemical ozone loss, whereas winters with little dynamical ozone supply (e.g., 1999/2000) are characterized by strong chemical ozone destruction. This reflects the fact that the dynamical supply and the chemical loss are both strongly correlated with dynamically driven temperature anomalies

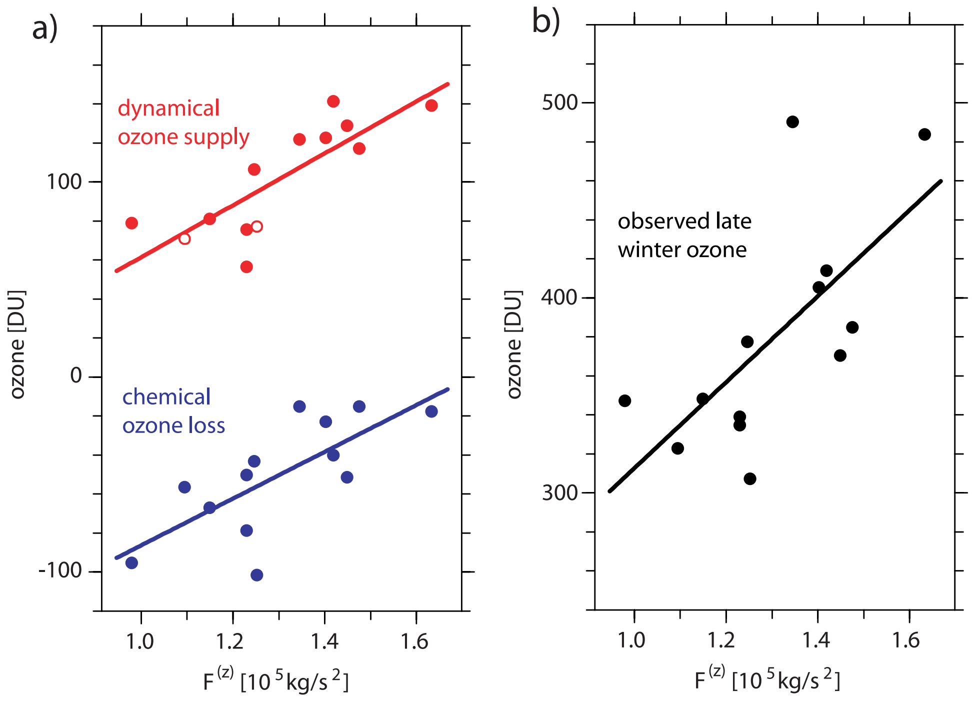

Figure 3. Correlation between the EP-flux and (a) the dynamical supply of ozone (red) and the chemical loss of ozone (blue) and (b) the observed late winter ozone (black). Results for the dynamical supply of ozone for 1995/1996 and 1996/1997 are marked by open circles.

in the polar vortex. The connection between dynamical supply and chemical loss is confirmed by the high correlation coefficient of 0.7 between the two time series. Coefficients greater than 0.55 are statistically significant at the 95% confidence level.

[16] The observed total change in ozone during winter varies between 10 and 190 DU with a standard deviation σ_{tot} of 55 DU. The interannual variability of the fall to spring change in ozone can be explained by the variability of the component time series, and the interaction between them:

$$\sigma^2_{\mathrm{tot}} = \sigma^2_{\mathrm{trans}} + \sigma^2_{\mathrm{chem}} + 2 \cdot \mathrm{cov}_{\mathrm{trans,chem}} + \mathrm{res} \tag{3}$$

with $\mathrm{res} = \sigma^2_{\mathrm{res}} + 2 \cdot (\mathrm{cov}_{\mathrm{trans,res}} + \mathrm{cov}_{\mathrm{chem,res}})$, where $\mathrm{cov}_{\mathrm{x,y}}$ denotes the covariance between the time series x and y. We find no connection between $\Delta O_{3,\mathrm{res}}$ and either $\Delta O_{3,\mathrm{trans}}$ or $\Delta O_{3,\mathrm{chem}}$, reflected by low correlation coefficients of -0.15 and -0.19, respectively. Therefore, the term res is relatively small and represents only a small fraction of the total variance of the fall to spring change in ozone σ^2_{tot}. The main part of the variance σ^2_{tot} results from the term $\sigma^2_{\mathrm{trans}} + \sigma^2_{\mathrm{chem}} + 2 \cdot \mathrm{cov}_{\mathrm{trans,chem}}$. Consequently, a large fraction of the variability of the fall to spring change in ozone is explained by the variability of the dynamical ozone supply, the variability of the chemical ozone loss and the connection between these two time series.

4. Correlations With EP-Flux

[17] The residual circulation is driven by planetary waves which can be characterized by the EP-flux entering the stratosphere. Atmospheric wave activity causes stratospheric temperature anomalies as illustrated by the strong correlation between polar temperatures and the vertical component of the EP-flux [*Newman et al.*, 2001]. Deviations of the temperature from radiative equilibrium cause diabatic descent, as reflected by a strong correlation between diabatic descent and both temperature and EP-flux (T07). Therefore we expect to find a close connection between the strength of wave activity and the dynamical ozone supply. Additionally, the polar temperature has a strong influence on ozone chemistry and we also expect to find a close connection between wave activity and chemical ozone loss. Since dynamical supply of ozone and chemical loss of ozone are both strongly influenced by the EP-flux and together explain most of the variability of the fall to spring change in ozone, there must exist a strong correlation between EP-flux and total springtime Arctic ozone, as first shown by *Randel et al.* [2002]. We will focus on demonstrating the connections between EP-flux and the three time series: $\Delta O_{3,\mathrm{trans}}$, $\Delta O_{3,\mathrm{chem}}$ and total ozone in spring.

[18] The EP-flux is taken at 100 hPa, averaged from December to February over 45°N to 75°N. The data are obtained from ERA40 and after 1999 from the ECMWF operational analysis. The upper portion of Figure 3a shows a scatter plot of the dynamical ozone supply and the vertical component of the EP-flux, $F^{(z)}$. The plot illustrates the correlation between $\Delta O_{3,\mathrm{trans}}$ and EP-flux, as expected. For strong wave activity, high values of dynamical ozone supply are found, whereas low values of $F^{(z)}$ are associated with weak ozone supply. The high correlation coefficient of 0.81 confirms the influence of atmospheric wave activity on the dynamical ozone supply. The lower portion of Figure 3a

displays a similar scatter plot for the chemical loss of ozone and EP-flux. For a stronger wave activity with higher values of $F^{(z)}$ we find less chemical ozone destruction, whereas small values of $F^{(z)}$ lead to strong ozone destruction in a cold and stable polar vortex. The correlation coefficient here ($r = 0.73$) is slightly less strong than the correlation coefficient between $\Delta O_{3,\mathrm{trans}}$ and EP-flux.

[19] Finally we examine the connection between EP-flux and the total ozone column in late winter (Figure 3b). As expected we find a clear correlation ($r = 0.68$) where high values of $F^{(z)}$ are associated with high values of total ozone in spring. The correlation coefficient is smaller than correlation coefficients between $F^{(z)}$ and the dynamical supply or the chemical loss. Since the amount of total ozone in spring is influenced by the residual term, which is not correlated with $F^{(z)}$, we expect a lower correlation coefficient for the total ozone column.

5. Conclusions

[20] The influence of mean transport processes by the residual circulation on the total ozone column in spring is quantified. The net dynamical supply of ozone caused by these transport processes is estimated based on vortex-averaged diabatic descent for the winters 1991/1992 to 2003/2004. Together with the chemical loss term, which is available for the same winters, the estimated dynamical ozone supply explains a large fraction of the observed fall to spring change in ozone. The dynamical ozone supply and the chemical ozone loss influence in equal shares the interannual variability of total ozone in late winter. Additionally, nearly all of the interannual variability of the fall to spring change in ozone is explained by the variability of the dynamical supply, the variability of the chemical loss and the connection between these two time series.

[21] Variability in planetary wave activity, characterized by the EP-flux entering the stratosphere, contributes significantly to the variability of both the net transport of ozone through the residual circulation and the chemical ozone loss during winter, and therefore to the variability of total ozone at the end of winter. This is confirmed by high correlation coefficients between the four time series.

[22] The calculated time series of the dynamical ozone supply can provide a useful diagnostic to validate the influence of transport on total ozone in spring in coupled Chemistry-Climate Models. Continuing the time series for the most recent NH winters and for SH winters can be investigated in a future study.

[23] **Acknowledgments.** We thank D. Brunner for providing the ozone data-set CATO and the ECMWF for providing their operational and reanalysis data. The work has been supported by the EC under contract 505390-GOCE-CT-2004 (SCOUT-O3).

References

Andrews, D. G., and M. E. McIntyre (1976), Planetary waves in horizontal and vertical shear: The generalised Eliassen-Palm relation and the mean zonal acceleration, *J. Atmos. Sci.*, *33*, 2031.

Brunner, D., J. Staehelin, H.-R. Künsch, and G. E. Bodeker (2006), A Kalman filter reconstruction of the vertical ozone distribution in an equivalent latitude–potential temperature framework from TOMS/GOME/SBUV total ozone observations, *J. Geophys. Res.*, *111*, D12308, doi:10.1029/2005JD006279.

Fusco, A. C., and M. L. Salby (1999), Interannual variations of total ozone and their relationship to variations of planetary wave activity, *J. Clim.*, *12*, 1619.

Greenblatt, J. B., et al. (2002), Tracer-based determination of vortex descent in the 1999/2000 Arctic winter, *J. Geophys. Res.*, *107*(D20), 8279, doi:10.1029/2001JD000937.

Harris, N. R. P., M. Rex, F. Goutail, B. M. Knudsen, G. L. Manney, R. Müller, and P. von der Gathen (2002), Comparison of empirically derived ozone losses in the Arctic vortex, *J. Geophys. Res.*, *107*(D20), 8264, doi:10.1029/2001JD000482.

Holton, J. R., P. H. Haynes, M. E. McIntyre, A. R. Douglass, R. B. Rood, and L. Pfister (1995), Stratosphere–troposphere exchange, *Rev. Geophys*, *33*, 403.

Manney, G. L., R. W. Zurek, A. O'Neill, and R. Swinbank (1994), On the motion of air through the stratospheric polar vortex, *J. Atmos. Sci.*, *51*, 2973.

Nash, E. R., P. A. Newman, J. E. Rosenfield, and M. R. Schoeberl (1996), An objective determination of the polar vortex using Ertel's potential vorticity, *J. Geophys. Res.*, *101*, 9471.

Newman, P., E. Nash, and J. Rosenfield (2001), What controls the temperature of the Arctic stratosphere during the spring?, *J. Geophys. Res.*, *106*, 19,999.

Randel, W., F. Wu, and R. Stolarski (2002), Changes in column ozone correlated with the stratospheric EP flux, *J. Meteorol. Soc. Jpn.*, *80*, 849.

Rex, M., et al. (2000), Arctic and Antarctic ozone layer observations: Chemical and dynamical aspects of variability and long-term changes in the polar stratosphere, *Polar Res.*, *19*, 193.

Rex, M., et al. (2002), Chemical depletion of Arctic ozone in winter 1999/2000, *J. Geophys. Res.*, *107*(D20), 8276, doi:10.1029/2001JD000533.

Rex, M., et al. (2006), Arctic winter 2005: Implications for stratospheric ozone loss and climate change, *Geophys. Res. Lett.*, *33*, L23808, doi:10.1029/2006GL026731.

Rosenfield, J. E., and M. R. Schoeberl (2001), On the origin of polar vortex air, *J. Geophys. Res.*, *106*, 33,485.

Simmons, A., et al. (2005), ECMWF analyses and forecasts of stratospheric winter polar vortex breakup: September 2002 in the Southern Hemisphere and related events, *J. Atmos. Sci.*, *62*, 668.

Tegtmeier, S., K. Krüger, I. Wohltmann, K. Schoellhammer, and M. Rex (2008), Variations of the residual circulation in the Northern Hemispheric winter, *J. Geophys. Res.*, doi:10.1029/2007JD009518, in press.

Uppala, S., et al. (2005), The ERA-40 re-analysis, *Q. J. R. Meteorol. Soc.*, *131*, 2961.

World Meteorological Organization (WMO) (2003), Scientific assessment of ozone depletion 2002, *Rep. 47*, Global Ozone Res. Monit. Proj., Geneva, Switzerland.

World Meteorological Organization (WMO) (2007), Scientific assessment of ozone depletion 2006, *Rep. 50*, Global Ozone Res. Monit. Proj., Geneva, Switzerland.

K. Krüger, IFM-GEOMAR, Düsternbrooker Weg 20, D-24105 Kiel, Germany.

M. Rex and I. Wohltmann, Alfred Wegener Institute for Polar and Marine Research, Telegrafenberg A43, D-14473 Potsdam, Germany.

S. Tegtmeier, Environment Canada, 4905 Dufferin Street, Toronto, ON M3H 5T4, Canada. (susann@atmosp.physics.utoronto.ca)

Atmos. Chem. Phys., 8, 265–272, 2008
www.atmos-chem-phys.net/8/265/2008/
© Author(s) 2008. This work is licensed
under a Creative Commons License.

Atmospheric
Chemistry
and Physics

Improvement of vertical and residual velocities in pressure or hybrid sigma-pressure coordinates in analysis data in the stratosphere

I. Wohltmann and M. Rex

Alfred Wegener Institute for Polar and Marine Research, Potsdam, Germany

Received: 6 September 2007 – Published in Atmos. Chem. Phys. Discuss.: 13 September 2007
Revised: 28 November 2007 – Accepted: 9 December 2007 – Published: 21 January 2008

Abstract. Stratospheric vertical winds from analysis data in pressure (p) or hybrid pressure (σ-p) coordinates, for use in e.g. chemical transport models (CTMs) or trajectory models, often suffer both from excessive noise and errors in their mean magnitude, which in turn can introduce errors in important dynamical quantities like vertical mixing or constituent transport with the residual circulation. Since vertical velocities cannot be measured directly, they are inferred from other quantities, typically from horizontal wind divergence, that is the mass continuity equation. We propose a method to calculate the vertical wind field from the thermodynamic energy equation in p or σ-p vertical coordinates that substantially reduces noise and overestimation of the residual circulation. It is completely equivalent to the approach using potential temperature (θ) as a vertical coordinate and diabatic heating rates as vertical velocities, which has already been demonstrated to give superior results to the continuity equation. It provides a quickly realizable improvement of the vertical winds, when a change of the vertical variable would cause an inadequate effort (e.g. in CTMs). The method is only applicable for stably stratified regions like the stratosphere.

1 Introduction

Analysis and reanalysis data from e.g. the European Centre for Medium-Range Weather Forecasts (ECMWF) (Uppala et al., 2005), the United Kingdom Meteorological Office (UKMO) (Swinbank and O'Neill, 1994) or the NASA Goddard Earth Observation System (GEOS) (Schoeberl et al., 2003) often suffer from noisy and biased vertical winds based on the continuity equation in p coordinates. In turn, too much vertical dispersion and mixing or problems with the residual circulation and the mean age of air are introduced (e.g. Uppala et al., 2005). While there are promising developments in new datasets as the ERA-Interim reanalysis (Monge-Sanz et al., 2007), there is a need to improve the analysis data in these aspects.

Vertical wind is an issue in CTMs, which use these data to run the dynamical part of the model. For example, a too young age of air and a too rapid residual circulation are reported for CTMs using GEOS analysis data (and even General Circulation Model (GCM) data) in Hall et al. (1999) or for TM3 in Bregman et al. (2003) (ECMWF forecast data) and van Noije et al. (2004) (ECMWF ERA-40). Excessive vertical dispersion and problems with the age of air are reported in Schoeberl et al. (2003) for the GEOS Finite Volume Data Assimilation System (FVDAS) and UKMO. Models like SLIMCAT (Chipperfield, 2006) (UKMO or ECMWF) or IMATCH (Mahowald et al., 2002) are not affected in the same way, since they use θ coordinates and calculate vertical movements by diabatic heating rates. Indeed, a better performance of this θ coordinate approach in comparison to the continuity equation in p or σ-p coordinates has been demonstrated for trajectory calculations, CTMs and even for the internally consistent wind and temperature fields of GCMs (Eluszkiewicz et al., 2000; Mahowald et al., 2002; Schoeberl et al., 2003; Chipperfield, 2006). These improvements carry over to the winds from the thermodynamic equation in p or σ-p coordinates, as we will show shortly. In addition to CTMs, there are many other studies, like trajectory calculations (e.g. Fueglistaler et al., 2005), which rely on vertical winds from analysis data and could benefit from improved vertical velocities.

The calculation of reliable vertical winds is a longstanding topic in numerical weather prediction (e.g. Krishnamurti and Bounoua, 1996). Several methods have been proposed to calculate vertical wind fields in p coordinates: The "kinematic" method (vertical wind w from the continuity equation), the "adiabatic" or "diabatic" method (w from the thermodynamic energy equation), the

---

Correspondence to: I. Wohltmann
(iwohltmann@awi-potsdam.de)

"vorticity" method (w from the vorticity equation) and the omega equation (a combination of several equations that avoids time derivatives). We choose the diabatic method here, since it is ideally suited for the stratosphere. In addition, it is possible to derive winds for analyses with a low upper boundary (e.g. the NCEP reanalysis, Kistler et al., 2001) if the radiative transfer above this boundary is sufficiently constant, which is difficult with the continuity equation.

2 Eulerian vertical winds

Usually, vertical wind is obtained from the continuity equation

$$\nabla \cdot (\rho_0 \mathbf{u}) = 0 \tag{1}$$

which describes the conservation of mass in p coordinates. $\mathbf{u}{=}(u, v, w)$ is the vector of zonal wind u, meridional wind v and vertical wind w in spherical coordinates. All following equations will use log-pressure height $z{=}-H \log(p/p_0)$ as vertical coordinate (p pressure, p_0 reference pressure, $H{=}RT_0/g$ scale height, R gas constant, T_0 reference temperature, g gravitational acceleration), for which $\rho_0{=}p_0/(RT_0)\exp(-z/H)$ is the air density. Solving for w gives

$$w(z) = \frac{1}{\rho_0(z)} \int_z^{z_\infty} \rho_0(z') \nabla_h \cdot \mathbf{u}_h(z') \, \mathrm{d}z' \tag{2}$$

where $\nabla_h \cdot \mathbf{u}_h(z){=}\left[\partial_\lambda u(z) + \partial_\varphi (v(z)\cos\varphi)\right]/(a\cos\varphi)$ is the horizontal wind divergence in spherical coordinates (λ longitude, φ latitude, a earth radius, ∂ Eulerian derivative). z_∞ is the log-pressure height of the highest given altitude level. The upper boundary condition is assumed to be $w(z_\infty){=}0$ here. If u and v are given, w can be calculated.

However, the continuity equation is not the only conservation equation one can use to determine the vertical wind. At the same time, energy needs to be conserved by the first law of thermodynamics, expressed by the near conservation of potential temperature $\theta{=}T(p_0/p)^{2/7}$ (with T temperature), which can only be changed by radiative heating Q

$$\frac{\mathrm{D}\theta}{\mathrm{D}t} = Q \tag{3}$$

$\mathrm{D}/\mathrm{D}t$ is the Lagrangian derivative. Solving for w gives

$$w = (Q - \partial_t \theta - \frac{u}{a\cos\varphi}\partial_\lambda \theta - \frac{v}{a}\partial_\varphi \theta)/\partial_z \theta \tag{4}$$

If Q, T, u and v are given, w can be calculated (note that we do not use Eq. (4) in this study, but the method presented in the next section). Q is obtained by a radiative transfer model, which needs T profiles as input data. Since we divide by the static stability $\partial_z \theta$, the equation can only be used in stably stratified regions like the stratosphere. For short time-scales, the diabatic component $Q/\partial_z \theta$ of the wind can usually be neglected, while it is the most important term on time-scales of several months.

In theory, Eqs. (2) and (4) obviously should give identical results. However, since u, v and T are measured quantities prone to errors and data are discretized and interpolated, Eqs. (2) and (4) will not be fulfilled at the same time in practice. This also means that mass is not conserved if Eq. (4) or the approach in the next section is used to calculate vertical winds. To ensure conservation of mass, a procedure similar to that presented in Weaver et al. (2000) can be used to correct the horizontal wind by adjusting the divergence to be zero while conserving the vorticity of the wind field (see Appendix B for explicit equations). We do not follow this approach here, since the implied changes to the horizontal wind are rather small.

3 Semi-lagrangian approach

Equation (4) substantially reduces noise in the vertical wind fields, but is not sufficient for long-time integrations and an accurate determination of the residual circulation. Since Eq. (4) basically represents an advection problem in an Eulerian framework, a criterion identical to the Courant-Friedrichs-Lewy criterion $u\Delta t{\leq}\Delta x$ applies as a necessary condition for a stable solution, where u is the advection velocity, Δx is the grid spacing and Δt is the time step of the analysis. Since the time step at which the data is obtained is typically 6 h and the grid spacing typically 2.5°, this condition is usually not fulfilled for available analysis data, especially at high latitudes (the time step and grid spacing of the underlying model of the analysis are usually much higher, but cannot be used due to computational constraints). Note also that since there is no exact constraint to a certain θ level as in an application with θ levels as vertical coordinate, the trajectories/air masses tend to drift away from the correct θ level even if only small systematic errors are present in the vertical wind. Error sources are e.g. the approximation of derivatives by finite differences or interpolation errors. Hence, we use a Semi-Lagrangian approach, where we calculate forward and backward trajectories in a θ coordinate system starting/ending at the analysis grid points in the p or σ-p coordinate system and use the pressure difference between the start and end points of the trajectories (divided by the travel time of the trajectories) as a direct measure for the vertical wind.

In the examples given here, vertical winds are calculated for every grid-point in longitude, latitude and time, but for a staggered grid in the p or σ-p coordinate, with the new grid points centered in log-pressure between the old levels, which greatly improves the long-term stability of the trajectories in the vertical direction (see Appendix B). At every four-dimensional grid-point, a 12 h forward and a 12 h backward

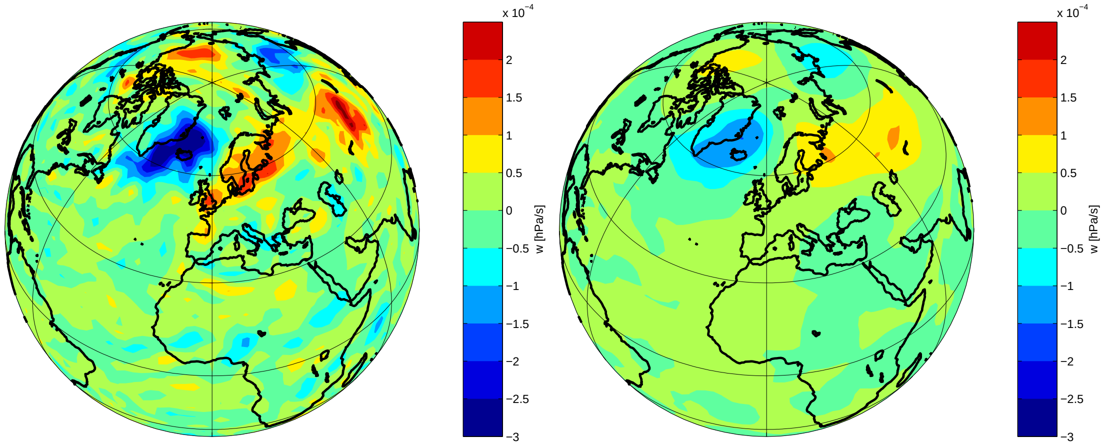

Fig. 1. Vertical wind from ERA-40 reanalysis data on standard pressure levels, calculated with two different methods. Left panel: Vertical wind field at 50 hPa from the continuity equation as provided by ECMWF, averaged over 1 January 2000 00:00–24:00 h (UTC) (to compare better with the right panel). Right panel: Vertical wind field from the thermodynamic equation and the Semi-Lagrangian approach for the staggered level between 30 and 50 hPa and 1 January 12:00 h (UTC).

trajectory in θ coordinates are started. The pressure difference between the latest date of the forward trajectory and the earliest date of the backward trajectory divided by 24 h is the vertical wind at the grid-point. Potential temperature on the isentropic forward and backward trajectories is only allowed to change by radiative heating. The 24 h period was determined empirically as a compromise between the temporal resolution of the winds and the stability of the method, which gets worse for shorter time periods.

The isentropic trajectory model uses a 4th order Runge-Kutta method for integration with a 10 min time step. Spherical coordinates are used, but poleward of 85°, the projection is switched to a polar projection to avoid the singularities at the poles. Wind and temperature values are interpolated linearly in longitude, latitude, the logarithm of θ and time to the position of the trajectory at every time step. Pressure is determined from the interpolated temperature and θ by solving $\theta = T(p_0/p)^{2/7}$ for p. Tests with cubic interpolation showed no significant differences in the results.

Note that the original meteorological data set, which is given either at σ-p or p levels, is not transformed to an intermediate data set with several fixed θ levels as vertical coordinate here, which would introduce additional and unnecessary interpolations. Instead, the trajectory model calculates θ at each original grid point of the meteorological data set and interpolates locally to the isentrope where the trajectory currently is located (see Appendix C).

4 Results and discussion

The left panel of Fig. 1 shows a vertical wind field derived from the continuity equation, as provided by the ECMWF ERA-40 reanalysis (50 hPa taken from the standard pressure levels, horizontal 2.5°×2.5° grid, 1 January 2000 averaged over 00:00–24:00 h UTC to better compare with the right panel). The right panel shows a field calculated from the thermodynamic equation with the Semi-Lagrangian method that closely simulates the wind field in the left panel (calculated with ERA-40 temperature and wind data at the same day at 12:00 h UTC with 12 h back- and forward trajectories, staggered level between 30 and 50 hPa). It is obvious that the right panel is considerably less noisy.

It could be argued that the scatter is real and that the left panel is the correct one. However, the vertical winds in the left panel would correspond to heating rates of several K/day after subtraction of the part of the wind that is caused by adiabatic movements. Such heating rates can be ruled out as unphysical (see also Eluszkiewicz et al., 2000). In addition, the vertical mixing caused by these winds would be much larger than observed (see discussion of diffusion coefficients below).

The method is now tested with ERA-40 σ-p model level data (60 levels) with a horizontal resolution of 2°×2°. After calculating the Eulerian vertical winds with the Semi-Lagrangian method using these ERA-40 data, the original vertical winds from ERA-40 are replaced on a staggered grid, while keeping the horizontal winds and temperature. This data set is used to drive several test runs with a trajectory model using the pressure of the model levels as coordinate (THERMO-P hereafter, red dots in the following figures). In addition, results are compared with trajectory runs with the original vertical winds from the continuity equation in the same coordinate system (CONT-P, blue dots) and with the potential temperatures of the model levels as the coordinate and heating rates as vertical velocities (Q-THETA, green dots).

Heating rates are obtained directly from the ERA-40 archive and are based on the radiative transfer model in use by ECMWF (Morcrette et al., 1998), which uses climatological ozone and prognostic water vapor profiles in the stratosphere. Note that there are known temperature biases and fluctuations compared to measurements in ERA-40 data (Uppala et al., 2005), which could affect the heating rates.

The isobaric trajectory model using vertical winds (used for the THERMO-P and CONT-P cases) is largely identical to the isentropic trajectory model using heating rates (used for the calculation of the Semi-Lagrangian thermodynamic winds and the Q-THETA case). The only difference is that the vertical interpolation is in the logarithm of p and not in the logarithm of θ.

As a first example we start forward trajectory runs at the equator. For all runs, 1440 trajectories are started at 0° N on 1 January 2000 (00:00 h UTC), equally spaced in longitude in 0.25° steps at the 475 K isentropic level. Trajectories are integrated for 20 days.

To test the long-term stability of the method first, we run this setup with a prescribed artificial constant heating rate of 0 K/day. Results after 20 days show an average of 475.5 K and a standard deviation of 3.4 K over all trajectory end-points. A run with 1 K/day heating shows an average of 495.7 K and a standard deviation of 3.2 K. Integration periods of up to 100 days show similar results. This demonstrates the stability of the method.

Figure 2 (left) shows results for the three combinations of vertical coordinates and velocities described above. The Lagrangian mean over the difference of the vertical start and end positions of the trajectories is a direct measure for the vertical residual velocity of the tropical upward branch of the Brewer-Dobson circulation (Andrews et al., 1987). Results are shown in Table 1. The difference between the continuity equation and the thermodynamic equation is noticeable. The mean upward velocity is 15.5 K in 20 days for CONT-P and 10.2 K in 20 days for THERMO-P. Q-THETA shows a change of 8.9 K, comparable to THERMO-P. The table also contains calculations based on standard pressure level data instead of model level data (everything else being the same). The difference between the continuity and thermodynamic equation is much less pronounced here, which demonstrates that many other parameters, like the number of levels, can significantly influence the results.

Additionally, the table shows the results when averaging the CONT-P vertical winds over 24 h (running average over 5 analysis time steps) to concur with the 24 h trajectories of the THERMO-P case. Results for the CONT-P vertical winds averaged over 24 h and horizontally over the nearest 9 grid points (including the original point) are also shown in the table, since it could be argued that there is additional spatial smoothing in the THERMO-P winds from the interpolation to the trajectory points. This has only a moderate effect on the mean upward velocity, which is now 13.3 K or 17.1 K. The mean upward velocity is consistently higher in the CONT-P runs than in the other runs.

Results for the vertical residual velocity from the trajectory calculations are compared to observed vertical velocities in geopotential height (Mote et al., 1998) and potential temperature (Hall and Waugh, 1997), inferred from the tape recorder signal in tropical stratospheric water vapor mixing ratios. Typical heating rates in the tropical stratosphere are in the order of 10 K in 20 days (e.g. Hall and Waugh, 1997), which compares well with the THERMO-P and Q-THETA cases, while the three σ-p CONT-P cases are about 50% higher on average. Comparison with Mote et al. (1998) is only possible for standard pressure levels, since the model level data contains no geopotential. CONT-P shows a mean change of 378 gpm in geopotential height, while THERMO-P shows a change of 397 gpm and Q-THETA shows a change of 342 gpm. Mote et al. (1998) give long-term mean vertical speeds of 0.2 mm/s at altitudes of about 20 km for HALOE data, corresponding to 345 gpm in 20 days. Niwano et al. (2003) also suggests a value near 0.2 mm/s. All values agree roughly within the uncertainties of the observations and our calculations.

The runs can also be used to derive the vertical eddy diffusion coefficient K_z, since K_z and the standard deviation σ of the end-points of the trajectories are related by $K_z=\sigma^2/(2t)$, where t is the integration time (this follows from Fick's law with a delta function as initial condition). Table 1 shows observed values derived from the tape recorder signal in comparison to the values inferred from the trajectory runs. The vertical diffusion coefficients derived from the continuity equation are more than two orders of magnitude larger than observed and are clearly outside the possible range of K_z values compatible with the observed tape recorder signal (Hall and Waugh, 1997; Mote et al., 1998). The diffusion coefficients from the isentropic and thermodynamic runs are much closer to reality. They somewhat underestimate the observed values, perhaps due to missing sub-grid processes.

The result for the both CONT-P cases with averaged winds is surprising: The standard deviation of the end-points of the trajectories is only slightly reduced compared to the run with the instantaneous winds, and gives a K_z only 20%–40% smaller than for the CONT-P run with instantaneous winds. In contrast, the standard deviation of the vertical winds itself (on a given level and date as in Fig. 1) is reduced by about a factor of 2 in the 24 h averaged case, as expected. This points to spurious fluctuations with longer time scales than 24 h in the vertical wind field or other systematic problems. However, it is not related to the much larger amplitude of the vertical winds in the CONT-P case compared to the Q-THETA case, which could lead to more interpolation error. The larger amplitude is caused by the adiabatic component of the wind, which is large compared to the diabatic component. However, this wind component is also present in the THERMO-P case, which shows a much smaller K_z.

Note that it is very difficult to decide what would be a fair

Table 1. Performance of different representations of the vertical wind field. Vertical velocities are derived from the continuity equation (CONT-P) in pressure coordinates, the thermodynamic equation (THERMO-P) in pressure coordinates or from heating rates (Q-THETA) in θ coordinates (all coordinates are interpolated both from standard pressure levels p or model levels σ-p). For CONT-P on model levels, results are given for three cases: instantaneous vertical winds directly from the analysis data, winds averaged over 24 h (running average over 5 analysis time steps) and winds averaged over 24 h and additionally spatially over the nearest 9 grid points. 2nd and 3rd column: Mean ascent (1–21 January 2000) in the tropics based on geopotential height or potential temperature (from Fig. 2, left). 4th and 5th column: Eddy diffusion coefficients K_z based on geopotential height or potential temperature (from Fig. 2, left). 6th column: Mean descent (26 November 1999 to 5 March 2000) in the polar vortex in potential temperature (from Fig. 2, right). All values are compared to observations: [a]Hall and Waugh (1997), [b]Mote et al. (1998), [c]Greenblatt et al. (2002).

	Ascent tropics (K)	(m)	K_z tropics (K^2/d)	(m^2/s)	Descent vortex (K)
Observed	10[a]	345[b]	0.3[a]	0.02[b]	63[c]
CONT-P p (instantaneous)	9.8	378.2	37.3	0.47	205.7
CONT-P σ-p (instantaneous)	15.5	–	54.7	–	186.6
CONT-P σ-p (24 h)	13.3	–	42.2	–	180.9
CONT-P σ-p (24 h+spatial)	17.1	–	32.2	–	258.1
THERMO-P p	11.7	396.9	0.24	0.001	91.4
THERMO-P σ-p	10.2	–	0.25	–	44.0
Q-THETA p	10.0	342.4	0.009	0.002	73.1
Q-THETA σ-p	8.9	–	0.04	–	47.5

comparison between the CONT-P winds and the THERMO-P winds, since the method of calculation is fundamentally different and involves different interpolations and averages at different locations and dates. For example, there is an average over several pressure levels and several derivatives in the divergence operator in the continuity equation, which should also be considered. However, the question how well our method performs in comparison to approaches actually used in existing models is more important than a completely fair comparison in the end.

Figure 2 (right) shows results of backward trajectory runs in the polar vortex as a second example. For all runs, trajectories are initialized on a 2.5°×2.5° grid inside the polar vortex at the 450 K isentropic level. The polar vortex is defined as the area inside the 20 PVU contour of Lait's modified potential vorticity (θ_0=420 K) (Lait, 1994). Trajectories start on 5 March 2000 (12:00 h UTC) and run for 100 days until 26 November 1999. The winter 1999/2000 is selected because it is one of the few winters in which tracer measurements are available for comparison.

The plot shows the position of the trajectories on 26 November 1999 (12:00 h UTC) as a function of modified PV and θ. Only trajectories inside the 20 PVU contour on 1 January 2000 and inside the 15 PVU contour on 26 November 1999 are shown (basically trajectories that stayed inside the vortex). The trajectories show a much larger vertical dispersion in the case of the continuity equation again.

The Lagrangian mean over the difference of the vertical start and end positions of all trajectories is now a measure for the vertical residual velocity of the polar downward branch of the Brewer-Dobson circulation. The mean downward velocity from 26 November 1999 to 5 March 2000 shows relatively large differences between the three σ-p CONT-P runs ($\Delta\theta$=187, 181, 258 K), which may be related to the spurious oscillations in ERA-40 data in the polar stratosphere (Uppala et al., 2005). However, the most obvious difference is between the CONT-P runs and the THERMO-P run ($\Delta\theta$=44 K). Results for the averaged vertical velocity are compared to descent rates inferred from tracer measurements of N_2O (Greenblatt et al., 2002). N_2O tracer measurements conducted around 26 November 1999 (solid black line, θ=513 K) and around 5 March 2000 (dashed black line, θ=450 K) give a change of $\Delta\theta$=63 K. In comparison to this value, the value from the THERMO-P run is far more realistic than the values from the CONT-P runs, which overestimate the descent rates by a factor of 3. The Q-THETA run ($\Delta\theta$=48 K) compares well with the THERMO-P run, but both runs show values slightly too small compared to the observations. Again, there are noticeable differences if standard pressure level data is used in all runs (Table 1).

This article was inspired by the question in how far the use of vertical wind fields from continuity affected water vapor transport into the stratosphere in Fueglistaler et al. (2005). Figure 3 shows results of backward trajectory runs started on 29 February 2000 at 400 K on a 2°×2° grid between 30° N/S and run until they reached the 365 K level for all three wind fields discussed above. The upper panel shows position and temperature of the coldest point along each trajectory while the lower panel shows the distribution of residence times of the trajectories between 365–375 K. While the cold point locations remain relatively unaffected (small change in the stratospheric water vapor obtained by freeze drying), mean

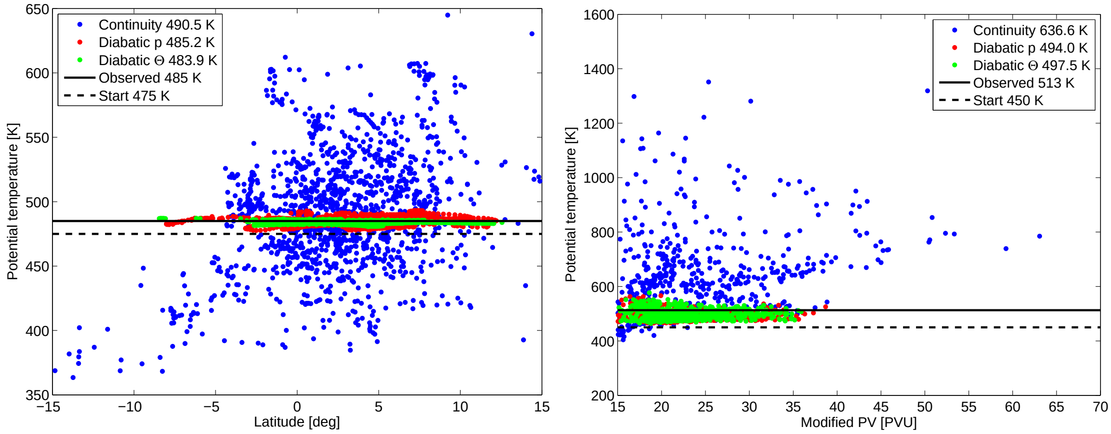

Fig. 2. Trajectory runs driven with different vertical wind fields. Left: Position of 1440 forward trajectories started at 1 January 2000 (00:00 h UTC) on the equator after 20 days, for winds from the continuity equation in pressure coordinates (blue dots), from the thermodynamic equation in pressure coordinates (red dots) and from heating rates in θ coordinates (green dots). Right: Position of backward trajectories on 26 November 1999 (12:00 h UTC) started at 450 K inside the polar vortex on a 2.5° grid on 5 March 2000 (12:00 h UTC).

residence times differ by a factor of 2, which directly affects chemical and microphysical processing.

5 Conclusions

We propose a new method to calculate vertical wind fields from analysis data based on the thermodynamic equation. It substantially reduces overestimation of the residual circulation and spurious noise that usually leads to an overestimation of vertical diffusion by several orders of magnitude (compared to wind fields based on the continuity equation as usually given in analysis data). In contrast, temporal or spatial averaging of the winds from the continuity equation does not significantly improve their performance.

The method proposed here is thought mainly for the application in chemical transport modelling or trajectory models, which use off-line meteorological data and could increase the quality of such models. The method is easily applied in existing models by just exchanging the vertical wind field that is used as input data without changing any model code. On request, we will provide vertical wind fields for modelling studies (see email address). The examples show the importance of a correct representation of vertical wind fields in modelling studies, which will remain an issue in the future.

Appendix A

Correction of horizontal winds

It may be desirable to conserve mass and energy at the same time. This is possible if we correct the horizontal wind for mass conservation after calculating the vertical wind from the thermodynamic equation. These corrections are small compared to the magnitude of the horizontal wind, so that we do not run into inconsistencies by changing the horizontal wind field too much. The following method is similar to that proposed in Weaver et al. (2000), which is not given there in mathematical detail.

Let us call the new winds $\mathbf{u}^N=(u^N, v^N, w^N)$ (with w^N as the vertical wind from the thermodynamic equation and u^N, v^N as the corrected horizontal winds we are looking for) and the old winds $\mathbf{u}=(u, v, w)$ (with w as the vertical wind from the continuity equation and u and v as the horizontal winds from the analysis). For both wind vectors, mass should be conserved

$$\nabla \cdot (\rho_0 \mathbf{u}) = 0 \quad \nabla \cdot (\rho_0 \mathbf{u}^N) = 0 \tag{A1}$$

This condition is not sufficient to determine the new wind field. In addition, we demand that the curl of the wind field is not changed

$$\nabla \times \mathbf{u} = \nabla \times \mathbf{u}^N \tag{A2}$$

In our case, u, v, w and w^N are given, while u^N and v^N are unknown. If $u'=u^N-u$, $v'=v^N-v$ and $w'=w^N-w$ are the differences between the wind fields, u' and v' are unknown and w' is given. We need two equations to solve for the two variables u' and v'. The first one is deduced from Eq. (A1) and states that for the two-dimensional divergence

$$\nabla_h \cdot (u', v') = D \tag{A3}$$

where

$$D = -\partial_z(\rho_0 w')/\rho_0 = -\nabla \cdot (u, v, w^N) \tag{A4}$$

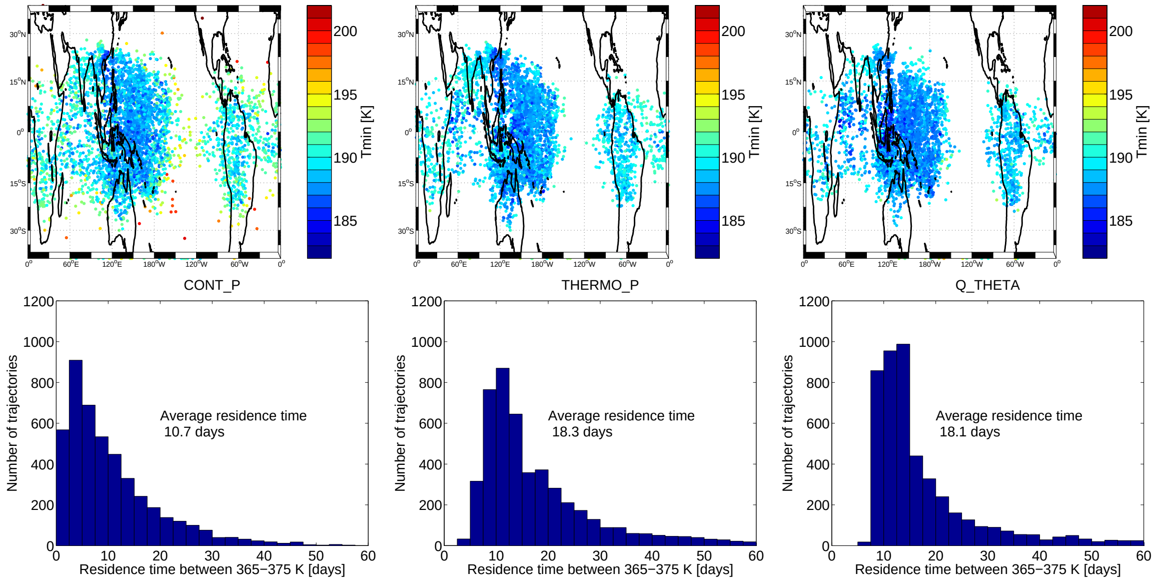

Fig. 3. Upper panel: Cold point locations and temperatures for the CONT-P, THERMO-P and Q-THETA winds and backward trajectories started on 29 February 2000 at 400 K on a 2° × 2° grid between 30° N/S. Lower panel: Distribution of residence times between 365–375 K for the same winds.

is a known function. The second one is deduced from Eq. (A2) and states that the two-dimensional curl (z element of the three-dimensional curl) is zero

$$\nabla \times (u', v') = 0 \tag{A5}$$

It follows that (u', v') can be written as the gradient of a scalar field ψ

$$\nabla \psi = (u', v') \tag{A6}$$

which gives a differential equation for ψ

$$\Delta \psi = D \tag{A7}$$

This is a Poisson equation on the surface of a sphere, which has to be solved by one of the standard methods for boundary value problems. After solving for ψ, u' and v' can be determined by derivation

$$u' = \frac{\partial_\lambda \psi}{a \cos \varphi} \qquad v' = \frac{\partial_\varphi \psi}{a} \tag{A8}$$

Appendix B

The staggered grid

The staggered grid greatly improves the stability of the method and reduces systematic errors in the wind field that cause air masses to drift from the correct isentrope. The reason for this is that the number of vertical levels involved in the calculation is reduced. For example, the vertical wind at the staggered grid-point between the original levels i and $i+1$ will very likely be calculated only with the pressure, wind and temperature values at the levels i and $i+1$, because the isentropic trajectory used to calculate the wind will stay between these levels. If the wind would be calculated directly at the level i, values from levels $i-1$, i and $i+1$ would be involved in the calculation. If now a trajectory is started using the calculated thermodynamic winds, it will use wind fields involving less levels. For example, if the trajectory oscillates around original level i, it will use winds from the staggered level between i and $i+1$ and between $i-1$ and i, which are calculated only with values from levels $i-1$, i and $i+1$. If the thermodynamic vertical winds were on the original levels, the trajectory would use winds from $i-1$, i and $i+1$, which would be calculated with values from levels $i-2$ to $i+2$. Since the vertical grid is often quite coarse, this can encompass a vertical range of considerable depth.

Appendix C

Interpolation in the trajectory model

In the isentropic trajectory model, the original meteorological data set (given on σ-p or p levels) is not transformed to an intermediate data set with several fixed θ levels as vertical coordinate, which would introduce additional and unnecessary interpolations. Instead, data on the isentrope is directly interpolated from the original grid-points, which preserves the original resolution of the data set.

Let the grid be $(\lambda_i, \varphi_j, \eta_k, t_l)$ with η as the values of the vertical σ-p coordinate and i, j, k, l as indices for the grid dimensions. Let $(\lambda, \varphi, \theta, t)$ be the current position of the trajectory. Now, indices for the interpolation in longitude, latitude and time are determined as usual, such that $\lambda_i \leq \lambda < \lambda_{i+1}$, $\varphi_j \leq \varphi < \varphi_{j+1}$ and $t_l \leq t < t_{l+1}$. For the eight combinations $(\lambda_i, \varphi_j, t_l)$, $(\lambda_{i+1}, \varphi_j, t_l), \ldots, (\lambda_{i+1}, \varphi_{j+1}, t_{l+1})$ vertical indices $k_1, \ldots, k_8$ for interpolating in η are determined separately by looking where the isentrope crosses the model levels, e.g. for $(\lambda_i, \varphi_j, t_l)$ the index is determined by $\theta(\lambda_i, \varphi_j, \eta_{k_1}, t_l) \leq \theta < \theta(\lambda_i, \varphi_j, \eta_{k_1+1}, t_l)$. That is, the vertical coordinate is not only dependent on a vertical index and has fixed values, but it also depends on the horizontal position and time.

Now, linear interpolation is used to obtain interpolated values, starting with the interpolation in the vertical coordinate. For example, for the interpolation of temperature at $(\lambda_i, \varphi_j, t_l)$ to θ:

$$
\begin{aligned}
&T(\lambda_i, \varphi_j, \theta, t_l) = \log\theta(\lambda_i, \phi_j, \eta_{k_1}, t_l) \qquad \text{(C1)}\\
&\quad + \frac{T(\lambda_i, \varphi_j, \eta_{k_1+1}, t_l) - T(\lambda_i, \varphi_j, \eta_{k_1}, t_l)}{\log\theta(\lambda_i, \varphi_j, \eta_{k_1+1}, t_l) - \log\theta(\lambda_i, \varphi_j, \eta_{k_1}, t_l)}\\
&\quad \cdot(\log\theta - \log\theta(\lambda_i, \varphi_j, \eta_{k_1}, t_l))
\end{aligned}
$$

The same method is applied in the isobaric trajectory model by just replacing θ by p.

Acknowledgements. We thank P. Haynes and K. Krüger for helpful suggestions. We thank ECMWF for providing reanalysis data. This work is supported by the European Community through the SCOUT-O3 project.

Edited by: K. Hamilton

References

Andrews, D. G., Holton, J. R., and Leovy, C. B.: Middle Atmosphere Dynamics, Academic Press, 1987.

Bregman, B., Segers, A., Krol, M., Meijer, E., and van Velthoven, P.: On the use of mass-conserving wind fields in chemistry-transport models, Atmos. Chem. Phys., 3, 447–457, 2003, http://www.atmos-chem-phys.net/3/447/2003/.

Chipperfield, M. P.: New version of the TOMCAT/SLIMCAT off-line chemical transport model: Intercomparison of stratospheric tracer experiments, Quart. J. Roy. Meteorol. Soc., 132, 1179–1203, doi:10.1256/qj.05.51, 2006.

Eluszkiewicz, J., Hemler, R. S., Mahlman, J. D., Bruhwiler, L., and Takacs, L. L.: Sensitivity of age-of-air calculations to the choice of advection scheme, J. Atmos. Sci., 57, 3185–3201, 2000.

Fueglistaler, S., Bonazzola, M., Haynes, P. H., and Peter, T.: Stratospheric water vapor predicted from the Lagrangian temperature history of air entering the stratosphere in the tropics, J. Geophys. Res., 110, D08107, doi:10.1029/2004JD005516, 2005.

Greenblatt, J. B., Jost, H.-J., Loewenstein, M., Podolske, J. R., Hurst, D. F., Elkins, J. W., Schauffler, S. M., Atlas, E. L., Herman, R. L., Webster, C. R., Bui, T. P., Moore, F. L., Ray, E. A., Oltmans, S., Vömel, H., Blavier, J.-F., Sen, B., Stachnik, R. A., Toon, G. C., Engel, A., Müller, M., Schmidt, U., Bremer, H., Pierce, R. B., Sinnhuber, B.-M., Chipperfield, M., and Lefèvre, F.: Tracer-based determination of vortex descent in the 1999/2000 Arctic winter, J. Geophys. Res., 107, 8279, doi:10.1029/2001JD000937, 2002.

Hall, T., Waugh, D., Boering, K., and Plumb, R.: Evaluation of transport in stratospheric models, J. Geophys. Res., 104, 18 815–18 839, 1999.

Hall, T. M. and Waugh, D.: Tracer transport in the tropical stratosphere due to vertical diffusion and horizontal mixing, Geophys. Res. Lett., 24, 1383–1386, 1997.

Kistler, R. E., Kalnay, E., Collins, W., Saha, S., White, G., Woollen, J., Chelliah, M., Ebisuzaki, W., Kanamitsu, M., Kousky, V., van den Dool, H., Jenne, R., and Fiorino, M.: The NCEP-NCAR 50-year reanalysis: Monthly means CD-ROM and documentation, Bull. Amer. Meteorol. Soc., 82, 247–268, 2001.

Krishnamurti, T. N. and Bounoua, L.: An Introduction to Numerical Weather Prediction Techniques, CRC Press, 1996.

Lait, L. R.: An alternative form for potential vorticity, J. Atmos. Sci., 51, 1754–1759, 1994.

Mahowald, N. M., Plumb, R. A., Rasch, P. J., del Corral, J., Sassi, F., and Heres, W.: Stratospheric transport in a three-dimensional isentropic coordinate model, J. Geophys. Res., 107, 4254, doi:10.1029/2001JD001313, 2002.

Monge-Sanz, B. M., Chipperfield, M. P., Simmons, A. J., and Uppala, S. M.: Mean age of air and transport in a CTM: Comparison of different ECMWF analyses, Geophys. Res. Lett., 34, L04801, doi:10.1029/2006GL028515, 2007.

Morcrette, J.-J., Clough, S. A., Mlawer, E. J., and Iacono, M. J.: Impact of a validated radiative transfer scheme, RRTM, on the ECMWF model climate and 10-day forecasts, ECMWF Tech. Memo., 252, 1–47, 1998.

Mote, P. W., Dunkerton, T. J., McIntyre, M. E., Ray, E. A., Haynes, P. H., and Russell III, J. M.: Vertical velocity, vertical diffusion, and dilution by midlatitude air in the tropical lower stratosphere, J. Geophys. Res., 103, 8651–8666, 1998.

Niwano, M., Yamazaki, K., and Shiotani, M.: Seasonal and QBO variations of ascent rate in the tropical lower stratosphere as inferred from UARS HALOE trace gas data, J. Geophys. Res., 108, 4794, doi:10.1029/2003JD003871, 2003.

Schoeberl, M. R., Douglass, A. R., Zhu, Z., and Pawson, S.: A comparison of the lower stratospheric age spectra derived from a global circulation model and two data assimilation systems, J. Geophys. Res., 108, doi:10.1029/2002JD002652, 2003.

Swinbank, R. and O'Neill, A.: A stratosphere-troposphere data assimilation system, Mon. Weather Rev., 122, 686–702, 1994.

Uppala, S. M., Kållberg, P., Simmons, A. J., et al.: The ERA-40 reanalysis, Quart. J. Roy. Meteorol. Soc., 131, 2961–3012, doi:10.1256/qj.04.176, 2005.

van Noije, T. P. C., Eskes, H. J., van Weele, M., and van Velthoven, P.: Implications of the enhanced Brewer-Dobson circulation in ERA-40 for the stratosphere-troposphere exchange of ozone in global chemistry-transport models, J. Geophys. Res., 109, D19308, doi:101029/2004JD004586, 2004.

Weaver, C. J., Douglass, A. R., and Rood, R. B.: Lamination frequencies as a diagnostic for horizontal mixing in a 3D transport model, J. Atmos. Sci., 57, 247–261, 2000.

Geosci. Model Dev., 2, 153–173, 2009
www.geosci-model-dev.net/2/153/2009/
© Author(s) 2009. This work is distributed under
the Creative Commons Attribution 3.0 License.

Geoscientific
Model Development

The Lagrangian chemistry and transport model ATLAS: validation of advective transport and mixing

I. Wohltmann and M. Rex

Alfred Wegener Institute for Polar and Marine Research, Potsdam, Germany

Received: 25 June 2009 – Published in Geosci. Model Dev. Discuss.: 3 July 2009
Revised: 15 September 2009 – Accepted: 2 October 2009 – Published: 2 November 2009

Abstract. We present a new global Chemical Transport Model (CTM) with full stratospheric chemistry and Lagrangian transport and mixing called ATLAS (Alfred Wegener InsTitute LAgrangian Chemistry/Transport System). Lagrangian (trajectory-based) models have several important advantages over conventional Eulerian (grid-based) models, including the absence of spurious numerical diffusion, efficient code parallelization and no limitation of the largest time step by the Courant-Friedrichs-Lewy criterion. The basic concept of transport and mixing is similar to the approach in the commonly used CLaMS model. Several aspects of the model are different from CLaMS and are introduced and validated here, including a different mixing algorithm for lower resolutions which is less diffusive and agrees better with observations with the same mixing parameters. In addition, values for the vertical and horizontal stratospheric bulk diffusion coefficients are inferred and compared to other studies. This work focusses on the description of the dynamical part of the model and the validation of the mixing algorithm. The chemistry module, which contains 49 species, 170 reactions and a detailed treatment of heterogeneous chemistry, will be presented in a separate paper.

1 Introduction

Chemical Transport Models are commonly based on a fixed spatial grid and include an Eulerian advection scheme for the transport of chemical species (e.g. SLIMCAT, Chipperfield, 2006). Although much effort has been put into the development of advection schemes that minimize numerical diffusion (e.g. Prather, 1986), numerical diffusion is in principle unavoidable in Eulerian models.

In the context of this paper, numerical diffusion is defined as any process that is triggered by the model calculations and behaves like a diffusive process acting on the chemical species in the model. Typically, numerical diffusion will be spurious and unrealistic, e.g. present in every grid cell with the same magnitude. We do not consider processes as numerical diffusion here which are deliberately introduced into the model, e.g. to mimic the observed diffusion. Eulerian approaches suffer from numerical diffusion because they contain an advection step that transfers information between different grid cells. Usually, this step is connected to averaging over several grid points, which introduces diffusion on the spatial scale of the grid resolution at the temporal scale of the model time step. An example is the interpolation of species to trajectory end points in Semi-Lagrangian approaches.

Since diffusion is very small in the stratosphere, numerical diffusion in Eulerian models is always much larger than the real atmospheric diffusion (e.g. Konopka et al., 2005), leading to problems like excessive mixing across atmospheric mixing barriers. Particularly at the low resolutions typically required for long runs (e.g. where the CTM module is coupled to a General Circulation Model, GCM, as part of a Chemistry Climate Model, CCM), numerical diffusion can lead to problems in the representation of the polar vortices and hence the Antarctic ozone hole. With an Eulerian model it is difficult to maintain the steep gradients of species at the boundary of the ozone hole, which are not only relevant for a proper representation of ozone depletion, but also for the radiative and dynamical feedback from the ozone hole on climate processes. We have therefore developed a Lagrangian CTM that can be used as a stand alone model or as module in a CCM system.

Lagrangian models have several advantages over Eulerian models:

- There is no numerical diffusion. Actually, some explicit form of diffusion has to be included in Lagrangian models to obtain realistic results, which gives

---

Correspondence to: I. Wohltmann
(ingo.wohltmann@awi.de)

the opportunity to model the real atmospheric diffusion on a physical basis.

- The model architecture allows for an efficient parallelization of code and runs fast on low-cost computers.
- The time step of the integration of the transport equations can be chosen freely. There is no limitation of the largest time step by the Courant-Friedrichs-Lewy criterion.
- Mixing ratios of inert tracers are conserved by design (no negative mixing ratios by transport).
- Transport of additional species does not add to computing time.

In addition, our specific model is free of any grid in the vertical or horizontal. The absence of numerical diffusion, the conservation of mixing ratios and the fact that transport of additional species does not add to computing time are basically due to the fact that the Lagrangian time derivative of mixing ratios is zero in the absence of local sources and sinks, while the Eulerian derivative contains an advection term. Despite these obvious advantages, only very few global Lagrangian chemical transport models with explicit mixing exist so far (e.g. Collins et al., 1997; Fairlie et al., 1999). The most prominent examples are the CLaMS model (McKenna et al., 2002; Konopka et al., 2004, 2007) and the ATTILA model (Reithmeier and Sausen, 2002), which has recently been coupled to the General Circulation Model ECHAM (Stenke et al., 2009).

The main focus of this model version is on a proper representation of the chemistry and transport of the stratosphere, although a basic troposphere is included. Hence, the validation focusses on the stratosphere. It is planned to extend the model to the troposphere in the future.

Both resolution and trajectory time step can be chosen freely, so the model can be used both for highly resolved process studies and long-term runs over several decades. One of the specific advantages of Lagrangian models is that they allow to study the fine filamentary structures that are usually below the resolution of conventional Eulerian models and that disappear rapidly due to numerical diffusion. This is possible since the information over the small scale behaviour of tracers is contained in the large-scale wind fields (Batchelor regime in fluid dynamics, see Haynes and Vanneste, 2004).

The main concept of the model is similar to the CLaMS 3-D model (Konopka et al., 2004), which has a more sophisticated mixing parameterization compared to models like e.g. ATILLA or Collins et al. (1997). However, ATLAS is a completely new model developed from scratch, which has no code in common with CLaMS. Some changes and improvements are introduced to the transport and mixing approach of CLaMS here, and their impact on the results is elucidated. The method of validation presented in Konopka et al. (2004) is also analyzed, and some changes are proposed for a more robust calculation of the validation parameters. Finally, the model is used to infer values for the effective horizontal and vertical diffusion coefficients for the stratosphere, and results are compared with other studies.

Section 2 contains the basic model description. Section 2.1 gives an overview of the model concept. Sections 2.2 and 2.3 describe the model implementation. While Sect. 2.3 gives a detailed treatment of the mixing algorithm, Sect. 2.2 describes the other relevant features of the model. The validation of the mixing algorithm is presented in Sect. 3. Results for diffusion coefficients are discussed in Sect. 4. Conclusions are given in Sect. 5.

2 Model description

2.1 Model concept

The model design is based upon a modular approach. This allows a flexible configuration and easy exchange of components. The basic layout of the model is shown in Fig. 1.

Transport and chemistry in the model are driven by external meteorological fields. These can be provided either by a General Circulation Model (GCM module in the sketch, red box) or by existing analysis data like ECMWF ERA Interim (Simmons et al., 2006).

With this input, a large number of trajectories, each symbolizing an air parcel, is initialized and advected for some hours (filling the domain of the complete atmosphere) (trajectory module, green box). Chemistry is calculated on every trajectory like in a box model (chemistry module, yellow box).

Since there is no numerical diffusion in a Lagrangian model, some form of mixing has to be introduced to obtain realistic trace gas distributions. This has the advantage that mixing can be modeled from physical considerations and that the strength of mixing can be adjusted to observed values, while numerical diffusion cannot be controlled in strength and location. Every few hours, a mixing step is introduced (mixing module, orange box). In this step, new air parcels are added and existing air parcels are merged in regions of large flow deformation (shear and strain) to keep the density of air parcels constant. The actual mixing is accomplished by averaging the chemical species on the new or merged air parcels. As a side effect, adding and merging parcels also ensures that voids and crowded regions are avoided. After the mixing step, the model continues with the advection step again. A detailed justification of the validity of the mixing approach can be found in Sect. 2 of McKenna et al. (2002) and, shortly recapitulated, in Sect. 2.3.2.

2.2 Basic model features

The initial air parcels are distributed randomly over the model domain by drawing uniformly distributed random

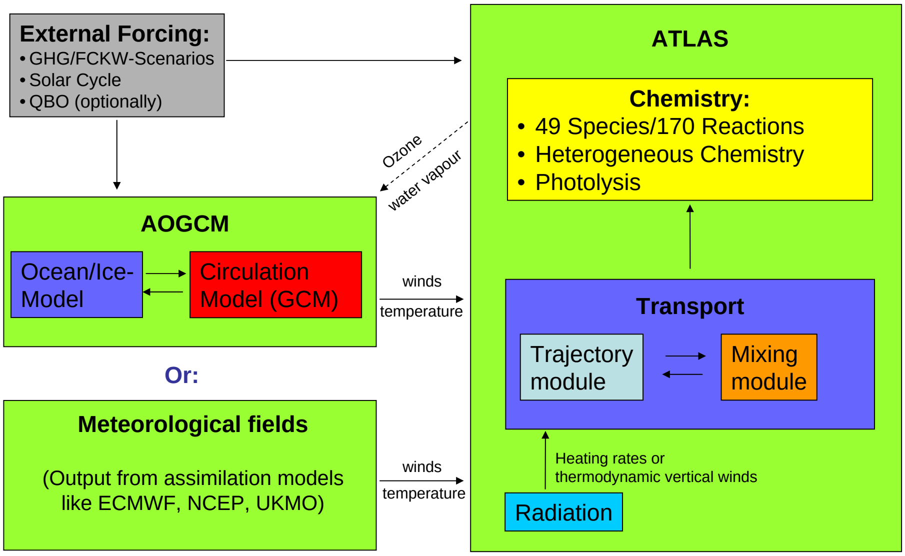
External Forcing:
• GHG/FCKW-Scenarios
• Solar Cycle
• QBO (optionally)
ATLAS
Chemistry:
• 49 Species/170 Reactions
• Heterogeneous Chemistry
• Photolysis
Ozone
water vapour
AOGCM
Ocean/Ice-Model
Circulation Model (GCM)
winds
temperature
Transport
Trajectory module
Mixing module
Or:
Meteorological fields
(Output from assimilation models like ECMWF, NCEP, UKMO)
winds
temperature
Heating rates or thermodynamic vertical winds
Radiation

Fig. 1. Model concept.

numbers for longitude, the cosine of latitude and the vertical coordinate. The initial value of the random generator can be set to a fixed value to obtain reproducible results.

Every air parcel contains variables for a configurable number of chemically active species and additionally, for a configurable number of chemically inert tracers.

The vertical coordinate is limited by an upper and lower boundary, which can be chosen freely. The number of air parcels is then chosen such that a predefined initial resolution r_0 is obtained (defined by the mean horizontal parcel distance in layers of the vertical depth Δz introduced in Sect. 2.3.3). While it is possible to set the lower boundary to the surface, the model does only contain a basic representation of the troposphere, mainly used to provide the stratosphere with tropospheric source gases. Several components that would be necessary for a realistic representation of the troposphere are currently not implemented, like tropospheric chemistry, clouds or a treatment of sub-scale convection.

The trajectory module is based on the parallel trajectory code used in Wohltmann and Rex (2008). Time step and integration method (e.g. 4th order Runge-Kutta) are freely configurable. The vertical coordinate system and the associated vertical winds can be set to four different options:

- Pressure as vertical coordinate and vertical winds taken from the input files of the analysis data or GCM, which usually means winds that satisfy mass conservation by the continuity equation.
- Pressure and vertical winds from the thermodynamic equation (satisfying conservation of thermal energy) as in Wohltmann and Rex (2008).
- Potential temperature and heating rates (satisfying conservation of thermal energy).
- A hybrid coordinate that transforms from a pressure coordinate at the surface to a potential temperature coordinate in the stratosphere, as defined in Konopka et al. (2007). The hybrid winds transform from analysis winds in pressure coordinates to heating rates.

The model contains a lower and an upper boundary layer. The depth of the boundary layers is again based on Δz (Sect. 2.3.3). All parcels in these boundary layers are deleted in every model step and replaced by newly initialized parcels. The reinitialization of the parcels is necessary to avoid that holes or volumes with parcels outside the model boundary appear due to the large-scale motion. Parcels outside the model domain are deleted. Tracers and chemical species are interpolated from the old parcel positions to the new parcels where possible. Where not possible, tracers and chemical species are set to climatological values. This may e.g. be the case where the downward branch of the Brewer-Dobson circulation produces volumes void of any parcels directly below the upper boundary.

A tropopause is needed for several purposes in the model. It is set to the 2 PVU potential vorticity surface in the extratropics (dynamical tropopause) and to the 375 K potential temperature surface in the tropics.

The model code is platform independent and can run in parallel on a simple personal computer network connected via the internet. Main modules are implemented in Matlab and time critical code in C. Extensive use of free software libraries is made, the most important ones are Qhull for the triangulation, KPP (Kinetic Preprocessor) for the chemistry module and a Matlab implementation of a parallel MPI like interface based on exchange via ssh.

2.3 Mixing algorithm

The basic idea of the mixing algorithm is identical to the approach used in the CLaMS 3-D model (Konopka et al., 2004). The algorithm is as follows:

- For every air parcel, determine all air parcels that are, in a certain sense (see Sect. 2.3.1 below), next neighbors of that air parcel.
- Advect air parcels with trajectory model and optionally calculate chemistry.
- If the distance between a particular air parcel and one of its former next neighbors (prior to advection) exceeds a critical distance r_+ after advection, insert a new air parcel in the middle between the original air parcel and the neighbor, the new mixing ratio is the mean of the mixing ratios of the air parcel and its neighbor. Do that for every neighbor.
- Determine next neighbors again.
- If the distance between a particular air parcel and several of its neighbors is lower than a critical distance r_-, merge all of these neighbors and the air parcel itself to a new air parcel, the new mixing ratio is the mean of the old mixing ratios. All merged air parcels are removed immediately and can only contribute to one new air parcel.
- Advance to next mixing step.

2.3.1 Next neighbors

Next neighbors are determined by Delaunay triangulation: the air parcels are connected by a mesh of triangles (2-D case) or tetrahedrons (3-D case), such that the circumcircles of any triangle (or circumspheres of any tetrahedron) are empty (e.g. O'Rourke, 1998). Air parcels that are directly connected in the mesh are considered next neighbors. Depending on the model resolution, we use two different methods, which are outlined in Fig. 2:

- Global layer approach (CLaMS): for high model resolutions (r_0<150 km), the algorithm also applied in CLaMS 3-D (Konopka et al., 2004) is used. The atmosphere is divided into a set of layers. In each layer, the vertical coordinate of the air parcels is ignored and a global 2-D triangulation on the surface of a sphere is performed to obtain the next neighbors. The vertical depth Δz of the layers is determined with one of the methods described in Sect. 2.3.3 to obtain realistic vertical diffusion coefficients and mixing (with z as the log-pressure altitude for the pressure coordinate and appropriate definitions for the potential temperature and hybrid coordinates). A staggered set of layers is used in every second mixing step to avoid a clustering of the air parcels in the vertical direction by the averaging of the vertical coordinate in new and merged air parcels (see Sect. 2.3.4).
- Local layer approach (ATLAS): for low model resolutions (r_0≥150 km), a new method is introduced. The main difference to the global layer approach is that we use a local layer with a limited horizontal extent for every air parcel, which is vertically centered on every single air parcel. The advantage of this approach is that it is less diffusive and gives superior results with the same mixing parameters (see Sect. 3.5). Conceptually, it is also a more realistic approximation to atmospheric mixing, since air parcels that are vertically close, but in adjacent layers do not mix in the CLaMS approach in contrast to the ATLAS approach. Unfortunately, the approach is computationally too expensive for very high resolutions.

  As in the global layer approach, the air parcels tend to cluster vertically in the local layer approach. We add a random component to the vertical coordinate of newly inserted or merged air parcels to avoid the generation of artificial layers in the local layer approach. The addition of the random component is explained in more detail in Sect. 2.3.4.

  In the first step of the method, a global 3-D triangulation is carried out to get a preliminary set of next neighbors for every air parcel (for some details, see Appendix A). The list of next neighbors is then extended by the second neighbors (next neighbors of next neighbors) to get a cloud of air parcels around every original air parcel (the obvious approach to include all air parcels below a given distance to the original parcel in the cloud is computationally to expensive).

  Now, all air parcels outside an interval $\left[z-\Delta z_{\mathrm{low}}, z+\Delta z_{\mathrm{upp}}\right]$ are deleted from the list of neighbors to center the air parcels in the local layer. The vertical mixing depth $\Delta z = \Delta z_{\mathrm{low}} + \Delta z_{\mathrm{upp}}$ is determined as described in Sect. 2.3.3. The remaining parcels and the original air parcel are now treated with a local 2-D triangulation ignoring the vertical coordinate to get a final list of next neighbors. In contrast to the global layer approach, a new 2-D triangulation is necessary for every single air parcel, but the number of points in each triangulation is much lower.

In principle, the final next neighbors could also be obtained directly from the 3-D triangulation. However, there is no constraint on the minimum vertical distance in this approach: newly inserted air parcels will tend to introduce new layers of air parcels with a lower mean vertical distance between parcels than in the last mixing step. These parcels would shield the old parcels that are a little bit further away in the 3-D triangulation and cause a finer mesh in the vertical. This

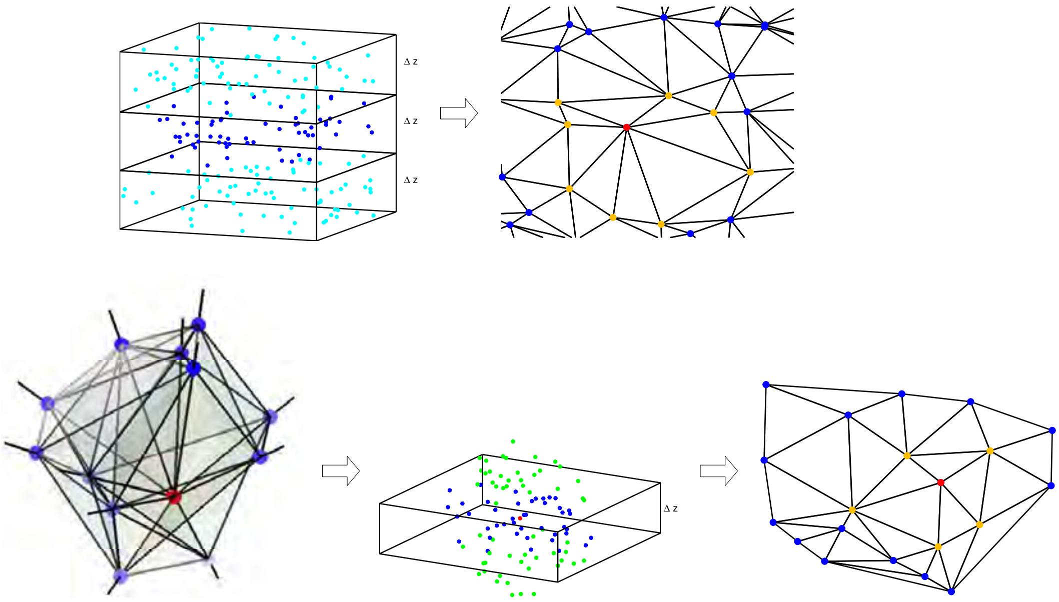

Fig. 2. Sketch of the two methods for finding next neighbors. Top: in the CLaMS approach the atmosphere is divided into layers (left, blue and cyan dots denote the air parcels). In every layer, the z coordinate is ignored and a global 2-D triangulation is performed to find the next neighbors (right, view from above, in the example the orange parcels are the next neighbors of the red parcel, clipped lines symbolize the global triangulation without boundaries). Bottom: in the ATLAS approach, a global 3-D triangulation is performed (left, clipped lines again symbolize the global triangulation) and in a first step, next and second neighbors are determined for each air parcel (middle, in the example all parcels are next or second neighbors of the red parcel). All parcels outside a vertical depth Δz are sorted out (green parcels). The remaining blue parcels are triangulated locally in 2-D ignoring the z coordinate (right).

problem will get worse in every mixing step. In the 2-D triangulation, all these air parcels will tend to end up in the same layer and increase the density of parcels and hence, the number of parcels below the critical distance r_- for merging.

Note that there is no fixed model grid at all in the ATLAS triangulation approach. There are neither distinct layers nor a horizontal grid in the model. The (virtual) model layers in the following discussion just mean all points within a certain interval $[z-\Delta z_{\mathrm{low}}, z+\Delta z_{\mathrm{upp}}]$ with z chosen freely and the vertical extent chosen to get an appropriate density of points in the horizontal. This is done in the post-processing of the model results and completely independent from the model parameterization.

2.3.2 Horizontal parameterization of mixing

Since the stratosphere is stably stratified, vertical turbulence is small and it is mainly the two-dimensional horizontal chaotic advection that will produce fine horizontal filaments and fractal structures in tracers on different scales. In conjunction with the vertical wind shear, sloping structures with large horizontal-to-vertical aspect ratios will be created (Haynes and Anglade, 1997). These structures will get smaller by the rapid scale collapse induced by the large-scale flow (but maintain their aspect ratio) and finally be dissipated by molecular diffusion and with the help of small-scale turbulence (e.g. by breaking gravity waves), which mixes the structures down to the molecular scale (e.g. McKenna et al., 2002; Legras et al., 2005; Balluch and Haynes, 1997; Wilson, 2004). This turbulence is intermittent in space and time due to the stable nature of the stratosphere.

The mixing concept is based on the assumption that mixing by small-scale turbulence predominantly occurs in regions of large flow deformation, e.g. in regions of large vertical shear or horizontal strain. The basic idea is to use the Lyapunov exponent to determine the critical distances r_+ and r_-. It can be shown that large values of the Lyapunov exponent are directly related to large shear or strain rates (McKenna et al., 2002).

The Lyapunov exponent λ is a measure for the rate of separation of trajectories that are initially in close neighborship. In a simplified sense, it can be defined for trajectories by

$$\mathrm{d}r = \lambda r \,\mathrm{d}t \tag{1}$$

where r is the initial separation of the trajectories at t=0 and r+dr is the separation of the trajectories at t=dt. If the flow exceeds a critical value λ_c of the Lyapunov exponent, we will insert a point. If integrating over a time Δt with constant λ_c and initial separation r_0, this corresponds to using a critical distance $r_+ = r_0 \exp(\lambda_c \Delta t)$. λ_c is a free parameter of the model and has to be optimized by comparison of model results with observations. The same is true for the length of the mixing time step Δt. r_0 determines the model resolution and can be chosen freely (it is identical to the r_0 used in the initialization). To relate r_- to r_+, we note that for incompressible flow, a small circle of radius r_0 will be deformed into an ellipse with the same area after a sufficiently small time Δt. If the minor and major axes are r_- and r_+, that means $r_0^2 = r_+ r_-$ and we get

$$r_\pm = r_0 \exp(\pm\lambda_c \Delta t) \tag{2}$$

avoiding another free parameter in the model. In a typical shear flow, r_+ will apply to diffusion along the trajectory and r_- to diffusion orthogonal to it.

The mixing concept ensures that mixing in the model predominantly takes place where the flow deformation is large. This is in broad agreement with observed mixing barriers like the polar vortex edge and observed well-mixed regions like the surf zone, which are indeed situated where deformation is small or large, respectively (e.g. Haynes and Shuckburgh, 2000).

λ_c controls the intensity of mixing (in terms of the percentage of mixed parcels per time interval). The lower λ_c is set, the more air parcels are affected by mixing. In conjunction with r_0, which specifies the horizontal distance affected by one mixing event, λ_c determines the horizontal diffusion coefficient K_h (for an explicit equation, see Sect. 2.3.5). Hence, λ_c is a crucial parameter to adapt the strength of mixing in the model to observed values.

The parameter r_0 does not need to be the actual resolution r_0^{eff} of the model, since there is no constraint on the total number of parcels in the model. While the initialization starts with a mean parcel distance of r_0, the number of parcels will change as long as the number of inserted parcels and the number of deleted parcels do not agree. Eventually, an equilibrium will be reached where this is the case. The equilibrium value for the effective resolution (defined by the mean parcel distance) is close to r_0 both for small values of λ_c (high mixing intensity leads to high grid adaption frequency) and high values of λ_c (no mixing cannot alter the number of parcels), but lower inbetween (see Fig. 3).

Reasonable values of Δt are limited to a range from approximately 6 to 24 h. For too short mixing times, the mixing step gets computationally too expensive. For too long mixing times, neighbor relationships are not conserved and the non-linearity of the flow prevents the application of the mixing algorithm. Δt is no crucial parameter in the parameterization, since validation results only weakly depend on the product $\lambda_c \Delta t$.

2.3.3 Vertical diffusion coefficient

The actual magnitude of vertical diffusion enters into the model through the depth Δz of the layer mixed in one mixing time step, which is directly related to the vertical diffusion coefficient: the greater the diffusion coefficient, the broader the layer mixed in a given time period. Turbulent diffusion in the stratosphere is dominated by vertical diffusion processes, since the horizontal-to-vertical aspect ratio α of tracer structures in the stratosphere is large (about 250) (Haynes and Anglade, 1997). Tracer filaments will be mixed to background values in vertical direction over the whole horizontal extent of the filament quickly, while in the same time period, horizontal diffusion will only affect the outer edges of the filament. For this reason, the apparent (effective) horizontal diffusion is much larger than the actual horizontal diffusion and directly dependent on the vertical diffusion and aspect ratio by $\alpha^2 = K_h / K_z$.

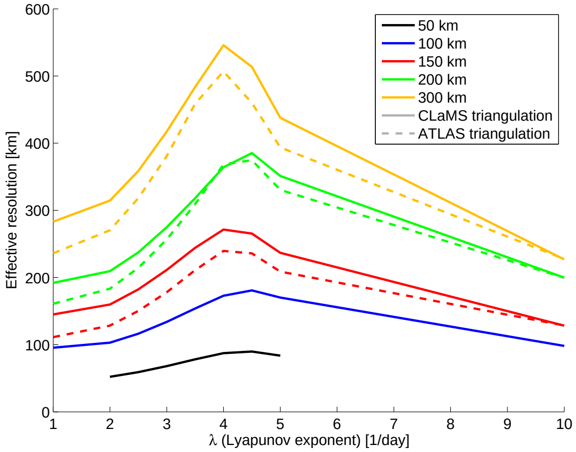

Fig. 3. Effective resolution for different values of the critical Lyapunov exponent λ_c (axis) and resolution r_0 (colors).

The standard deviation σ of the vertical positions of air parcels that start at the same vertical coordinate z after a time Δt is related to the vertical diffusion coefficient by

$$K_z = \frac{\sigma^2}{2\Delta t} \tag{3}$$

This and a normal distribution of the air parcels follows from Fick's second law with a delta function as initial condition. In this sense, if $K_z = \Delta z^2 / (8\Delta t)$, a layer of approximately $\Delta z = 2\sigma$ (containing 69% of the air parcels) is mixed after Δt, which gives the possibility to estimate the mixing layer depth from the diffusion coefficient.

Note that the log-pressure altitude $z = H \log(p_0/p)$, H scale height, is used in all derivations in this section, which do directly apply to the pressure coordinate system. For the potential temperature and hybrid coordinates, Δz is transformed into appropriate quantities in a last step.

A first guess of the vertical diffusion coefficient is obtained from a climatology K_z^{clim} that is a function of log-pressure height (Fig. 4). We denote the diffusion coefficient as K_z^{clim} here to discriminate it from the effective vertical diffusion coefficient K_z^{eff} that is actually applied in the model (see the following paragraphs). The climatology below 50 km is taken from Massie and Hunten (1981), while the part between 50 km and 80 km is following an exponential increase (e.g. Shimazaki and Wuebbles, 1973). In the troposphere, the coefficient is set to a constant value of 10 m^2/s. The boundary between the troposphere and the stratosphere is determined by the altitude of the tropopause. In the stratosphere below 15 km, the coefficient is set to a constant value of 0.58 m^2/s. There is considerable uncertainty in the values of the vertical diffusion coefficient up to the present day (e.g. Wilson, 2004; Legras et al., 2005), and our parameterization, which is based on some rather old, but easily available data, fits well into the published range of values. Note also that the climatology was derived from tracer data by neglecting advective transport, which may introduce uncertainty. Since the climatology is scaled in the following, only the shape and not the absolute values are of importance anyway.

Alternatively, the vertical diffusion coefficient can be set proportional to entropy (the approach taken by CLaMS, Konopka et al., 2007) or to a constant value. Actually, the shape of the diffusion profile based on entropy is quite similar to our approach (Fig. 4, red line), which makes the choice of the method a matter of philosophy rather than being of practical implications.

The vertical mixing depth Δz is obtained individually for each air parcel in the ATLAS triangulation approach. Ideally, Δz would be obtained from

$$\Delta z(z) = \sqrt{8 K_z^{\mathrm{clim}}(z) \Delta t} \tag{4}$$

where z is the log-pressure altitude of the air parcel. However, the equation actually used is

$$\Delta z(z) = \frac{2r_0}{\alpha(20\mathrm{km})} \sqrt{\frac{K_z^{\mathrm{clim}}(z)}{K_z^{\mathrm{clim}}(20\mathrm{km})}} \tag{5}$$

$\alpha(20\mathrm{km})$ is another free parameter of the model and defines the aspect ratio between the vertical scale Δz and the horizontal scale r_0 of the model in the lower stratosphere. This follows from the above equation with z=20 km:

$$\alpha(20\mathrm{km}) = 2r_0/\Delta z(20\mathrm{km}) \tag{6}$$

The factor 2 is due to the fact that in a layer of depth Δz with uniformly distributed points, the mean distance of any two points will be $\Delta z/2$.

The reason for skipping the (physically correct) dependency on Δt and introducing the dependency on r_0 is that it is important to match the horizontal and the vertical scale of the model. The mean horizontal distance between air parcels in a layer of depth Δz must be of the order $r_0(z)=\alpha(z)\Delta z(z)/2$ to ensure that mixing events affecting a certain distance in the vertical do affect an area of the correct horizontal extent and vice versa, as given by α. A simple example may illustrate that: a typical filament in the stratosphere could have a thickness of 1 km and a horizontal extent of 250 km, corresponding to an aspect ratio of 250. If the vertical diffusion coefficient would mix a layer of 1 km in 12 h to background values, it would also mix the structure of 250 km extent horizontally to background values in that time. A filament of thickness 2 km needs to have a width of 500 km and will need correspondingly longer to be mixed. If the horizontal and vertical resolution of the model would be decoupled, the mixing in the model would not work anymore in a realistic way.

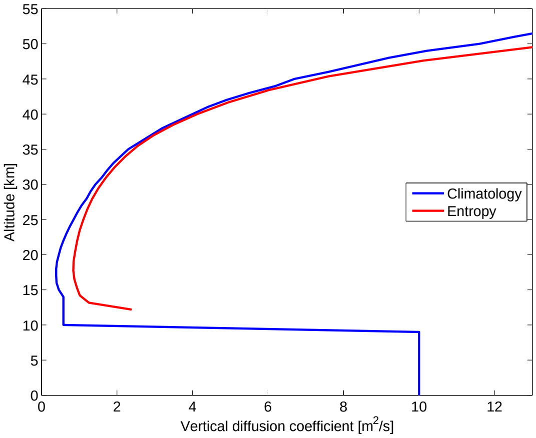

Fig. 4. Vertical diffusion coefficient climatology.

If Eq. (4) would be used for the vertical resolution and the aspect ratio would still be respected, the horizontal resolution would be no free parameter and e.g. $r_0(20\,\mathrm{km})=\alpha(20\,\mathrm{km})\Delta z(20\,\mathrm{km})/2$. With Δz as small as inferred from the vertical diffusion coefficient climatology (e.g. $\Delta z \approx 450$ m and $r_0 \approx 55$ km for K_z=0.58 m^2/s and Δt=12 h), the number of air parcels and model layers would increase to values computationally too expensive. That is, the method used in the model overestimates the effective vertical diffusion coefficient due to computational constraints. Note that CLaMS effectively implements the layer thickness in an equivalent way and suffers from the same problem. This can be partly compensated by setting λ_c to high values, which reduces the number of mixing events. However, while this will lower the effective bulk diffusivity of the model, every single mixing event will still take place over a vertical distance that is too large.

Finally, Δz is split into an upper part Δz_{upp}, which we use to search for all points between z and $z+\Delta z_{\mathrm{upp}}$ and a lower part Δz_{low} to search for points between z and $z-\Delta z_{\mathrm{low}}$. The simplest approach would be to set both values to $\Delta z/2$. In our approach, Δz_{low} and Δz_{upp} can take different values. First, if the interval $[z-\Delta z(z)/2, z]$ crosses the tropopause, Δz_{low} is set such that the interval ends at the tropopause. The same is done with Δz_{upp} and the interval $[z, z+\Delta z(z)/2]$. To avoid problems in other regions where K_z changes rapidly with altitude, Δz_{low} is calculated as half of the mean value of $\Delta z(z')$ between z and $z-\Delta z(z)/2$,

$$\Delta z_{\mathrm{low}}(z) = \frac{1}{2} \frac{\int_{z-\Delta z(z)/2}^{z} \Delta z(z')\,dz'}{\Delta z(z)/2} \tag{7}$$

An analoguous aproach is taken with Δz_{upp}.

Equation (5) can be interpreted as introducing an effective $\alpha(z)$ by

$$\Delta z(z) = 2r_0/\alpha(z)$$

and

$$\alpha(z) = \alpha(20\,\mathrm{km})\sqrt{K_z^{\mathrm{clim}}(20\,\mathrm{km})/K_z^{\mathrm{clim}}(z)}.$$

This implies a higher effective aspect ratio at altitudes with a lower Δz and vice versa. Very probably, this ad hoc assumption of the variation of $\alpha(z)$ with altitude is not compatible with the real atmospheric variation, but this variation follows from the horizontal resolution of the model held constant with altitude. In future versions, that may be changed to allow a varying horizontal resolution. For the following validation the effect is small, since the model is compared to measurements around 20 km altitude.

2.3.4 Inserting new parcels

If a new air parcel is inserted, its coordinates are calculated as follows: the longitude and latitude of the new air parcel are calculated by transforming all longitudes and latitudes of the old air parcels to cartesian coordinates with a local orthographic projection, and averaging the x and y coordinates. The result is transformed back.

In the CLaMS approach, the vertical coordinate is the average of the old vertical coordinates. This would lead to a clustering of the air parcels in the middle of each layer with fixed layers: the average of some random numbers from an interval will typically be close to the middle of the interval and is bounded by the original numbers. This increases the number of air parcels near the middle of the layer in every mixing step and leads to a positive feedback which results in the generation of layers in the vertical distribution of parcels. For this reason, a staggered set of vertical layers is used in every second mixing step in the CLaMS global layer approach. However, this approach still cannot avoid a certain clustering of the parcels into layers (Fig. 5).

Somewhat surprisingly, there is the same problem in the ATLAS local layer approach of triangulation, if the CLaMS method of averaging is used. Although there are no predefined layers, the same process can be triggered once there is a small random initial deviation from a uniform vertical distribution of the air parcels: the deviation will tend to be amplified in the next mixing steps by the feedback described above. This results in a process of self-organisation of the vertical coordinate values, where neighboring layers of enhanced parcel density are in concurrence for the parcels in-between.

It is necessary to work against this effect to avoid the formation of pronounced vertical layers and associated problems with vertical mixing. Since there is no possibility of a staggered set of layers as in the CLaMS approach, a random number is added to the average of the vertical coordinates in every newly inserted or merged air parcel to achieve a more uniform vertical distribution of air parcels (Fig. 5). The random number is chosen from an interval $\left[-\Delta z_{\mathrm{low}}, \Delta z_{\mathrm{upp}}\right]$, with these values again calculated as in Sect. 2.3.3. In most cases, the addition of the random component only slightly increases the diffusivity.

Since there is still a certain vertical clustering of the air parcels in the CLaMS global layer triangulation approach with simple vertical averaging, we also add a random number to the vertical coordinate in the CLaMS triangulation approach by default. This modified CLaMS approach is the only computationally feasible method for higher resolutions, if we want to achieve a distribution as uniform as possible also here. A discussion of the differences of the approaches in the results is given in Sect. 3.5.

2.3.5 The effective large-scale diffusion in the model

It is possible to estimate the diffusion coefficient from the mean distance Δr of any two points in a Gaussian distribution of air parcels as the one used for Eq. (3). It turns out that $\Delta r^2 = 2\sigma^2$ and hence the estimate is

$$K = \frac{\Delta r^2}{4\Delta t} \tag{8}$$

According to this equation, we estimate the diffusion coefficent in the model for every newly inserted or merged parcel. For comparison with other published values of the diffusion coefficient, the diffusion coefficient averaged over a certain geographical area and not for an individual air parcel is needed. Hence, a mean diffusion coefficient is calculated for every mixing step by averaging over the diffusion coefficients of the air parcels in a given area. Parcels not affected by mixing are assigned a coefficient of zero.

It is possible to derive equations that provide some insight on how the diffusion behaves if we change the free model parameters r_0, λ_c, α and Δt, see also Fig. 5 of Konopka et al. (2003). If two air parcels are mixed in the r_+ or r_- step, the horizontal diffusion that the newly inserted air parcel experiences can be roughly estimated to

$$K_{\mathrm{h}\pm}^{\mathrm{eff}} \approx \frac{r_\pm^2}{4\Delta t} = \frac{r_0^2}{4\Delta t}\exp(\pm 2\lambda_c \Delta t) \tag{9}$$

and the vertical diffusion to

$$K_z^{\mathrm{eff}} \approx \frac{(\Delta z/2)^2}{4\Delta t} = \frac{r_0^2 K_z^{\mathrm{clim}}(z)}{4\alpha(20\,\mathrm{km})^2 K_z^{\mathrm{clim}}(20\,\mathrm{km})\Delta t} \tag{10}$$

since the typical distances between the air parcels that contribute to the new parcel are $r_\pm$ and $\Delta z/2$. It is obvious that the diffusivity of the model increases for decreasing resolution, just because every single mixing event occurs over a larger distance. For decreasing λ_c (more mixing), $K_{\mathrm{h}+}^{\mathrm{eff}}$ (diffusion in flow direction) decreases, while $K_{\mathrm{h}-}^{\mathrm{eff}}$ (diffusion orthogonal to flow direction) increases. For the spatially averaged diffusion and also for the average diffusion that a single

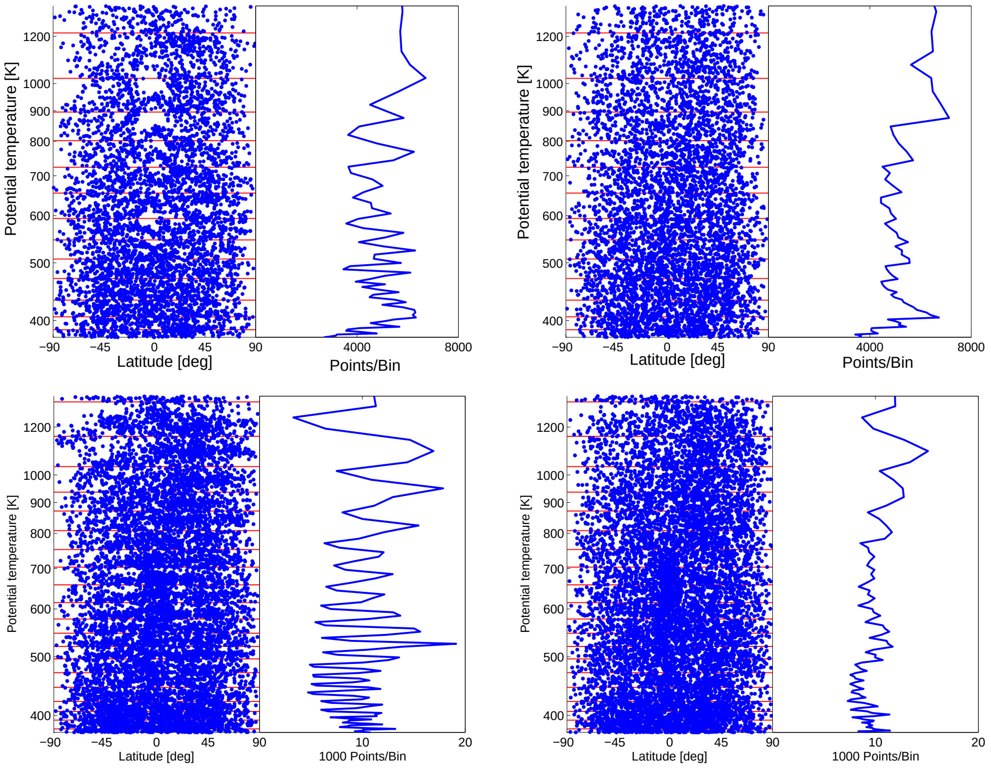

Fig. 5. Vertical distribution of air parcels for the ATLAS triangulation approach (top) or the CLaMS triangulation approach (bottom) and the random vertical coordinate off (left) or on (right). Results of a model run with r_0=150 km (top) or r_0=100 km (bottom), λ_c=2 d^{-1} after 4.5 months. The scatter plot shows the distribution of air parcels in the potential temperature-latitude plane (ignoring longitude). Only a subset of all air parcels is shown to make the clustering visible. The blue line shows the vertical density of the points (as the number of points per the local value of the layer depth Δz). Red lines are the layers of the CLaMS approach.

parcel experiences over a large number of mixing steps, the percentages of added and merged parcels also matters (see Fig. 11). These are also a function of the mixing parameters, particularly of λ_c, where lower values correspond to higher percentages of mixed parcels and a higher average diffusion coefficient (and vice versa). Supplementary to the analysis in Konopka et al. (2003), we find that the increase of diffusivity with lower λ_c in CLaMS and ATLAS is not only due to the increase in K_{h-}^{eff}, but that the higher percentage of mixed parcels contributes significantly. Note that the vertical and horizontal diffusion can be varied independently from each other within certain limits, since λ_c appears only in the horizontal diffusion coefficients and α only in the vertical.

2.3.6 Additional patchyness from noise in the wind fields

In principle the strength of mixing between air parcels can be tuned to the real atmospheric mixing. But in practice random motions from noise in the driving wind fields and their Eulerian discretization result in spurious random transport of air masses. This contributes to unavoidable excessive dispersion even in a purely Lagrangian transport approach, which generates spurious transport across mixing barriers and steep tracer gradients. This results in the artificial generation of small scale structure and patchyness in the tracer fields. The mixing in the model has to be tuned to keep this patchyness at realistic levels. Hence, the mixing in the Lagrangian model will always tend to overestimate the real diffusion in the stratosphere somewhat, though to a much lesser degree than an Eulerian model. Eulerian models suffer from noise and discretization in the driving wind fields in a similar way, but additional numerical diffusion largely dominates these effects such that they do not become visible.

3 Validation and tuning

3.1 Introduction

The validation of ATLAS is based on the same aircraft data set that is used in the validation of CLaMS 3-D in Konopka et al. (2004) in order to facilitate direct comparisons: the model is validated by comparing a passive methane and a passive Halon-1211 tracer to values measured during the SOLVE/THESEO 2000 campaign in the Northern Hemisphere winter 1999/2000 (Newman et al., 2002). A number of model runs is started with different mixing parameterizations. Each run simulates the period from 1 November 1999 to 15 March 2000. The methane and Halon tracers are initialized at 1 December. Between January and March, the model tracers are compared to in-situ measurement data from several high altitude flights conducted during the campaign that are able to temporally resolve fine tracer structures.

We will first describe the setup of the model runs and show some examples for model results. A quantitative validation will then be done by defining parameters for the agreement of the modeled and observed tracer-tracer relationships and the agreement of the spatial roughness of model and observations.

3.2 Setup

The model runs use the hybrid coordinate and are driven by meteorological data from the ECMWF ERA Interim reanalysis (Simmons et al., 2006, 2007) on 60 model levels (6 h temporal resolution, $2^\circ \times 2^\circ$ horizontal resolution). Heating rates (clear sky) are also taken from ERA Interim. ERA Interim data in the stratosphere has improved considerably compared to the ERA-40 reanalysis (Simmons et al., 2006, 2007), and, without any modifications, produces good agreement with observations in the following. Vertical diffusion coefficients are taken from the built-in climatology. The trajectory model uses a 4th order Runge-Kutta method for integration and a time step of 30 min. A change of the time step to 10 min does not lead to any significant improvements in the results.

Model runs are performed for all combinations of the resolutions r_0=50, 100, 150, 200 and 300 km and critical Lyapunov exponents λ_c=1, 2, 2.5, 3, 3.5, 4, 4.5, 5, and 10 d^{-1}. The number of air parcels ranges between 10^4 (300 km) and 10^7 (50 km). All runs at and below 150 km resolution are started both with the CLaMS and the ATLAS method of finding the next neighbors. For higher resolutions, only the CLaMS method can be used. Δt is set to 12 h and α to 250. Additionally, runs with fixed r_0 (100 km) and λ_c (3 d^{-1}) are started for different values of Δt or α. The effect of switching the random vertical coordinate on or off is also studied.

The lower model boundary is at the hybrid level 350 K and the upper boundary is around 1500 K. The number of virtual levels of the model (in the sense of the number of mixing depths Δz one needs to stack on top of each other to span the model domain) is 8 for 300 km resolution, 12 for 200 km, 16 for 150 km, 24 for 100 km, and 48 for 50 km.

The model is started on 1 November 1999, while the tracers are initialized on 1 December. This is done to avoid any spin-up effects in the mixing: usually, the equilibrium number of air parcels is lower than the number of air parcels the model is initialized with. This leads to a spin-up phase where more points are deleted in every model cycle than inserted, which in turn alters the mixing properties of the air parcels in an unrealistic way.

Outside the polar vortex, the methane tracer is initialized with monthly mean HALOE data from November and December 1999 (weighted equally) as a function of pressure and equivalent latitude φ_E (Grooß and Russell III, 2005). Inside the lower vortex ($\varphi_E > 64^\circ$ N, $\theta < 712$ K), an OMS balloon profile from the LACE instrument measured at 19 November is used (Ray et al., 2002), since HALOE is not able to measure in high latitudes and darkness. The profile is corrected for the descent between 19 November and 1 December, as inferred from a model run driven by the heating rates described above. The profile above 712 K in the vortex is a profile from the highest equivalent latitude bin of HALOE scaled to match the LACE values below. The Halon-1211 tracer is initialized by a methane to Halon-1211 tracer-tracer relationship measured at the OMS balloon flight.

The model results for the methane tracer are compared to measurements of the ACATS-IV (Romashkin et al., 2001), ALIAS (Webster et al., 1994) and Argus (Loewenstein et al., 2002) instruments on 11 flights of the ER-2 aircraft between 20 January and 12 March (Newman et al., 2002). The Halon-1211 model results are compared to ACATS measurements on the same flights. Flights started from Kiruna (Sweden) and probed the stratospheric polar vortex and surf zone. Halon and methane measurements from ACATS are available every 70 s, corresponding to a resolution of about 20 km, while ALIAS and Argus measurements are available every 2 s (about 1 km resolution). Wherever possible, we use the high resolution data, tracer-tracer relationships and Halon plots use the low resolution.

3.3 Examples

Figure 6 shows model results and measurements for the 27 January flight as an example. Results are shown for 50 km resolution and optimal mixing parameters (λ_c=3 d^{-1}, α=250, Δt=12 h, see Sect. 3.5). Only the highest tested resolution of 50 km is able resolve the fine filamentary structures at the edge of the polar vortex. The flight crosses the vortex boundary twice at a mean flight level of 50–60 hPa and contains a dive to 100 hPa around 12:00 UTC. For the comparison, the flight path is transformed to the position of the probed air parcels at 12:00 UTC by calculating short forward or backward trajectories starting at every measurement. Model results at 12:00 UTC are interpolated to the transformed measurement positions by averaging the mixing ratios over the next model neighbors of every measurement location, with a 2-D triangulation performed in the same way as in the mixing step of the model. The model values in the average are weighted according to their distance to the measurement: the weight is 1 for distances smaller than $2r_0$ and decreases linearly to zero at $3.5r_0$.

Panels a and b show measurements and model results for methane and Halon as a function of time, while Panels c and d show the same as a function of pressure. The agreement of the modeled and observed methane and Halon-1211 values is

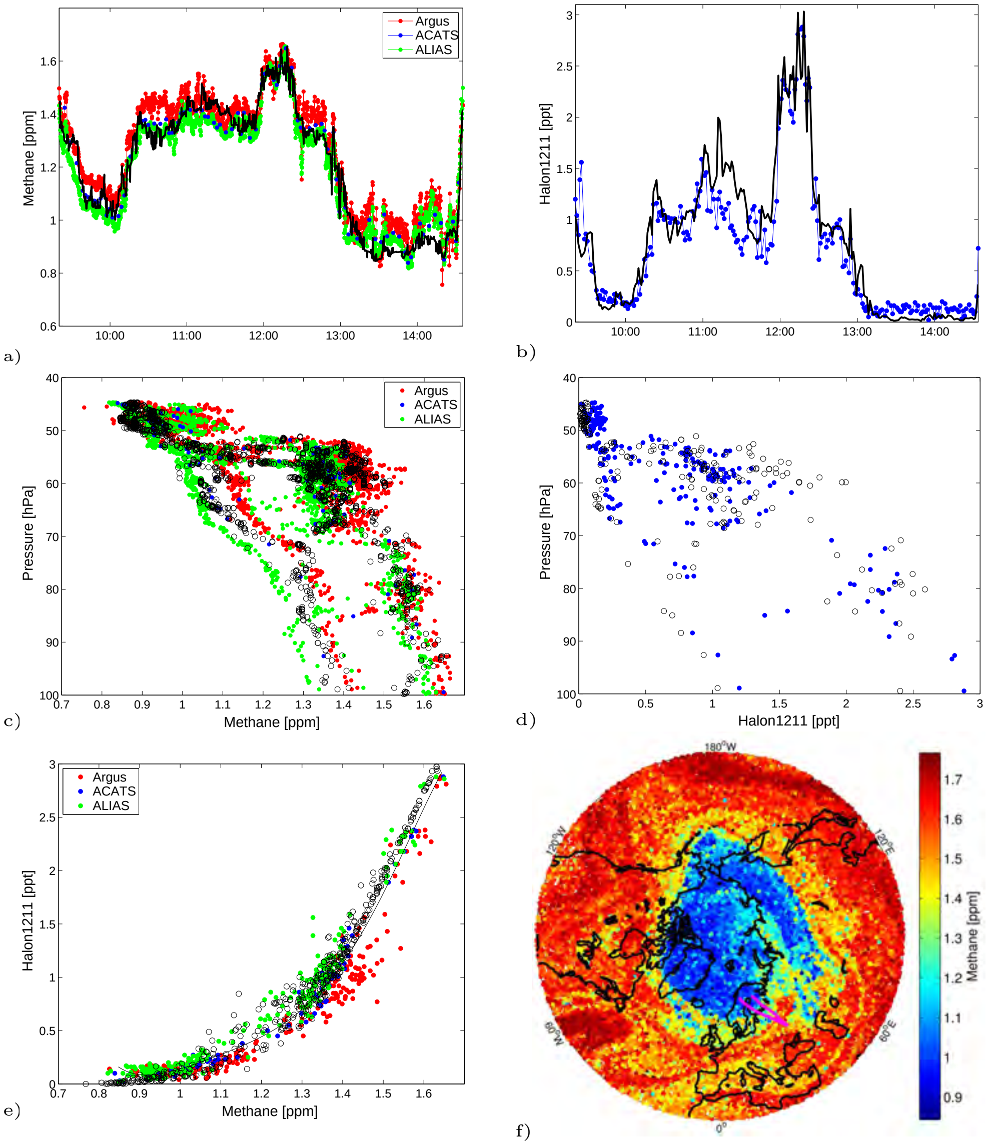

Fig. 6. Example comparison of model results (r_0=50 km, λ_c=3 d^{-1}) and flight data for 27 January, 12:00 UTC: **(a)** Measured methane mixing ratios (red: Argus, blue: ACATS, green: ALIAS) and modeled methane mixing ratios (black line) as a function of flight time (UTC), **(b)** Measured Halon-1211 mixing ratios (blue: ACATS) and modeled Halon-1211 mixing ratios (black line) as a function of flight time, **(c)** Methane mixing ratio as a function of pressure (colored dots: measurements, black circles: model values), **(d)** Halon-1211 mixing ratio as a function of pressure, **(e)** Tracer-tracer relationship of methane and Halon-1211, **(f)** Modeled tracer field for the Northern Hemisphere for all air parcels (dots) between 432–444 K. The magenta line denotes the positions of the air parcels probed by the flight at 12:00 UTC. All model values have been interpolated from the nearest model parcels to the transformed flight path.

quite good, both for the gradient across the vortex edge and the vertical structure. Inner and outer vortex air masses can clearly be distinguished both in the model and the observations below 70 hPa and the gradual transition from inner to outer vortex values above 70 hPa is also matched quite well by the model. The modeling of Halon is challenging, since the mixing ratios of Halon very sharply drop to zero above 50 hPa. Hence, the location of the drop is a good test for the accuracy of the heating rates, the accuracy of the winds and the mixing parameterization. Panel e shows the modeled and observed tracer-tracer relationships, which we will use later to validate the model. Panel f shows the methane tracer field at the flight level, with the polar vortex characterized by low methane values.

The interpolation to the probed air parcels of the flight will inevitably lead to additional diffusion in the model results, and different approaches for finding corresponding model values show considerable differences in the results, see also Konopka et al. (2003). Figure 7 shows the remarkable differences for the flight on 11 March, which crossed a filament

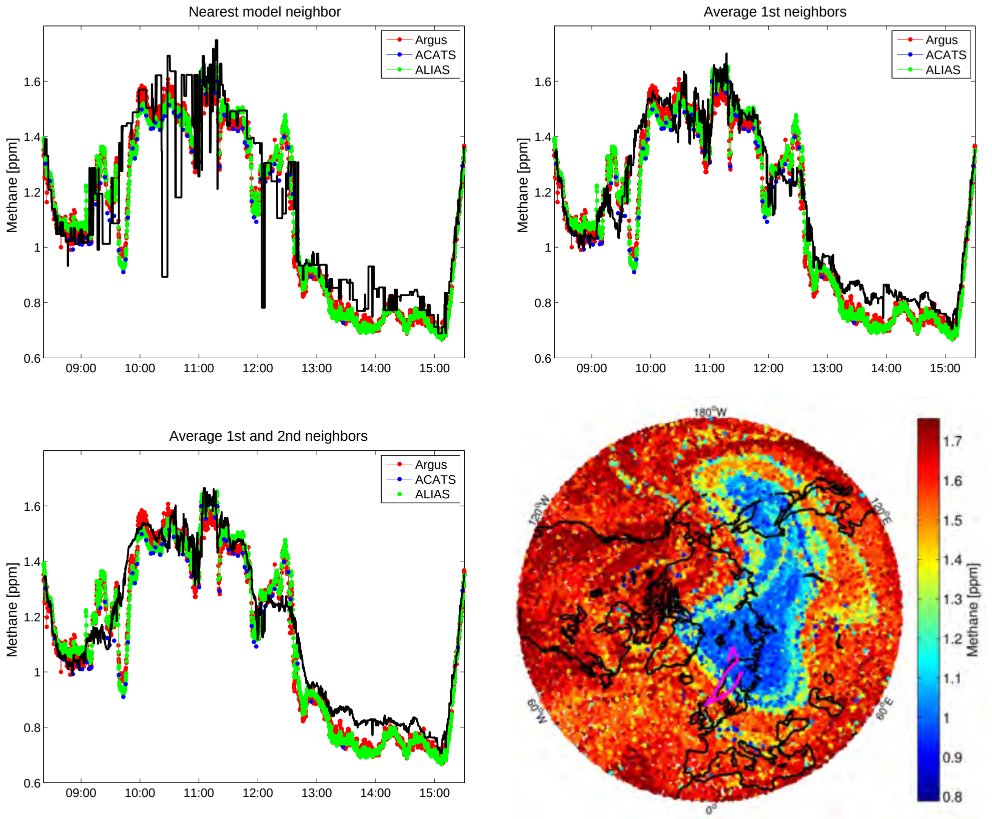

Fig. 7. Different methods of the interpolation to the flight path. Measured methane mixing ratios (colored dots) and modeled methane mixing ratios (black line) as a function of flight time (UTC) for the 11 March flight (λ_c=3 d^{-1}, r_0=50 km): for the nearest model neighbor of the measurement (upper left), the average of the first neighbors (upper right) and the average of the first and second neighbors (lower left). More averaging means a better agreement in areas of low gradients (due to reduced scatter), while less averaging better preserves fine filament structures. Lower right: modeled tracer field for the Northern Hemisphere for all air parcels (dots) between 432–444 K.

of extra-vortex air inside the vortex twice during the flight. While the filament is clearly visible if using only the nearest model neighbor to each measurement as the corresponding model value (free of any interpolation), it is more difficult to see for the average over the next neighbors and barely visible for the average over the next and second neighbors. On the other hand, parts of the flight where gradients are low show a better agreement with more averaging in the interpolation. This effect gets more prominent if λ_c is further increased (not shown). In this sense, the interpolation must be considered as an integral part of the modeling. Hence, for the actual validation, we try to find measures free of any additional interpolation.

Figure 8 demonstrates how the results change if the mixing parameter λ_c is varied. The left column shows an example where the mixing in the model is stronger than observed, leading to a mixing curve in the model that is on the concave side of the observed mixing curve. The middle panel shows an example for optimal mixing parameters and the right panel shows an example for too low mixing, where the modeled mixing curve is on the convex side of the observed curve.

3.4 Validation measures

The quality of the model runs is judged by calculating a parameter ε for the agreement of the modeled and the observed tracer-tracer relationships for every run. Likewise, a parameter γ for the agreement of the spatial "roughness" of the observed and modeled tracer fields is calculated for every run.

While the parameter ε is a straightforward measure for the mixing intensity of the model, the parameter γ needs some explanation. For low mixing intensities (high λ_c), the model fields show scatter and filaments, where the measurements do not show any. There are two possible reasons for this: first, tracer structures that would be mixed to background values in reality are not mixed in the model due to the low mixing intensity. But additionally, the spurious transport described in Sect. 2.3.6 generates small scale structure and leads to the same effect, see also Legras et al. (2005). The two parameters ε and γ give some possibility to distinguish between the two effects: spurious transport generates small scale structure and hence has an effect on γ. But these transport effects do not result in changes in the tracer relationships that are the

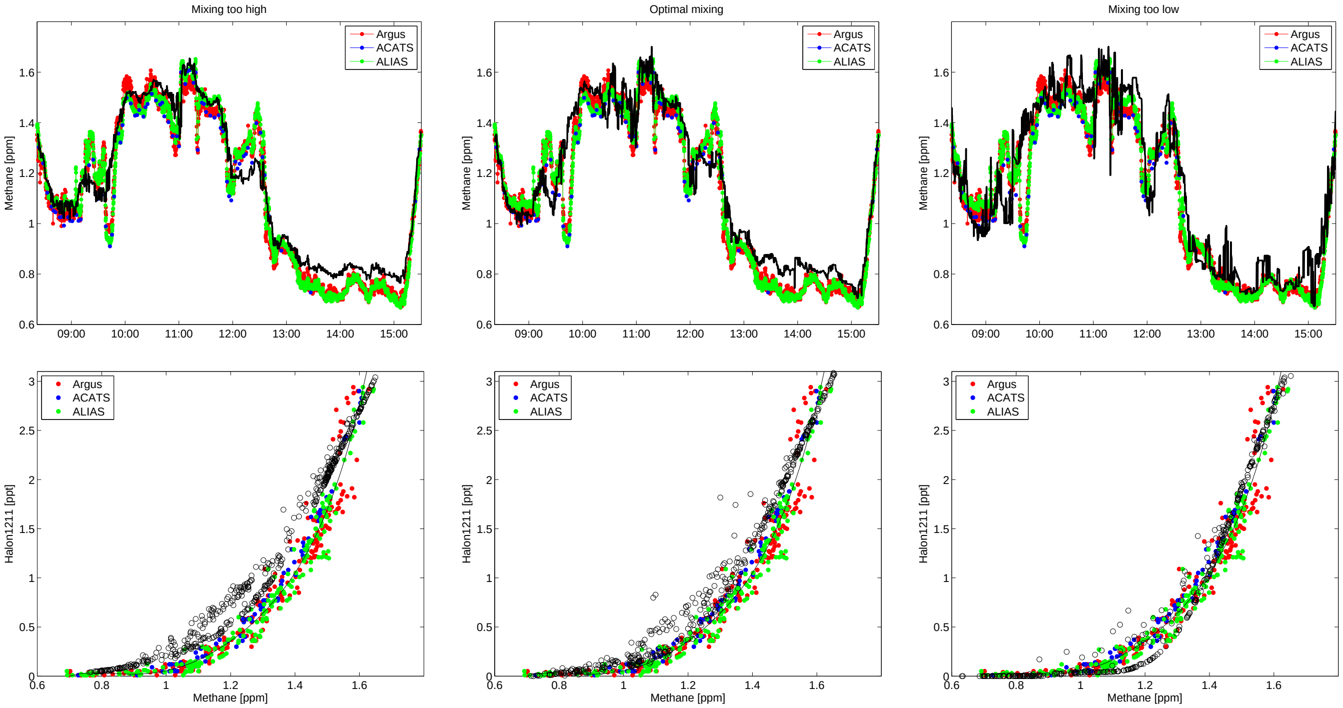

Fig. 8. Change of results when varying λ_c. Top: measured methane mixing ratios (colored dots) and modeled methane mixing ratios (black line) as a function of flight time (UTC) for 11 March 2000, r_0=50 km and λ_c=2 d^{-1} (left, too much mixing), λ_c=3 d^{-1} (middle, best agreement with observations) and λ_c=5 d^{-1} (right, almost no mixing). Bottom: same for the tracer-tracer relationship.

basis for ε in first approximation, since the artificial filaments will be mixed with the same intensity as any filament. Any exaggeration of model mixing used to balance the generation of patchyness and to tune γ to values close to observations results in deviations of modeled and observed tracer relationships which show up in ε.

In the following, we will denote the ith methane measurement with m_i (counting over all flights without resetting the counter), and the corresponding Halon-1211 measurement with h_i.

The parameter ε for the comparison of the mixing intensity is defined by the sum of the distances in tracer-tracer space of the measurement pairs $(m_i^{\text{observed}}, h_i^{\text{observed}})$ to the corresponding model pairs $(m_i^{\text{model}}, h_i^{\text{model}})$ in Konopka et al. (2004). That is,

$$\varepsilon = \sum_{i=1}^{N} (m_i^{\text{observed}} - m_i^{\text{model}})^2 + (h_i^{\text{observed}} - h_i^{\text{model}})^2.$$

A sketch of the method is shown in Fig. 9 (left). Since the absolute magnitude of the sum for methane and the sum for Halon-1211 is very different, relative differences are taken in Konopka et al. (2004)

$$\varepsilon = \sum_{i=1}^{N} \left(1 - \frac{m_i^{\text{model}}}{m_i^{\text{observed}}}\right)^2 + \left(1 - \frac{h_i^{\text{model}}}{h_i^{\text{observed}}}\right)^2 \qquad (11)$$

where N is the total number of measurements over all flights. Small values mean a good agreement between the mixing intensity of the model and the observations. Corresponding model pairs $(m_i^{\text{model}}, h_i^{\text{model}})$ are found by looking for the nearest model neighbor to the measurement location in Konopka et al. (2004) to avoid interpolation to the measurement location. Interpolation would cause additional mixing and may considerably alter the tracer-tracer correlation curve (e.g. by introducing spurious mixing lines, not shown).

There are some possibilities to improve this definition: first, for mixing ratios near zero (as it is the case for Halon-1211 in several parts of the flights), the relative differences go to infinity, and some single measurements can errorneously dominate the overall sum due to measurement error.

Secondly, errors in the wind fields used to drive the model can cause the position of some filament in the model to be shifted from its position in the observations to a slightly different place. This would cause a large distance of the corresponding (m_i, h_i) pairs in tracer-tracer space (where one pair is in the filament and the other is not). However, the mixing intensity could still be right, that is the modeled mixing ratios in the filament would match the observed tracer mixing ratios and the filament would have the right extent and shape. Hence, in a model with perfect mixing but slight systematic errors in the driving wind fields, the mixing curve of the model would still look exactly like the observed mixing curve. Since ε should only measure the mismatch in mixing intensity and not displacements of the filaments, this is not optimal. Konopka et al. (2004) argues that for too low

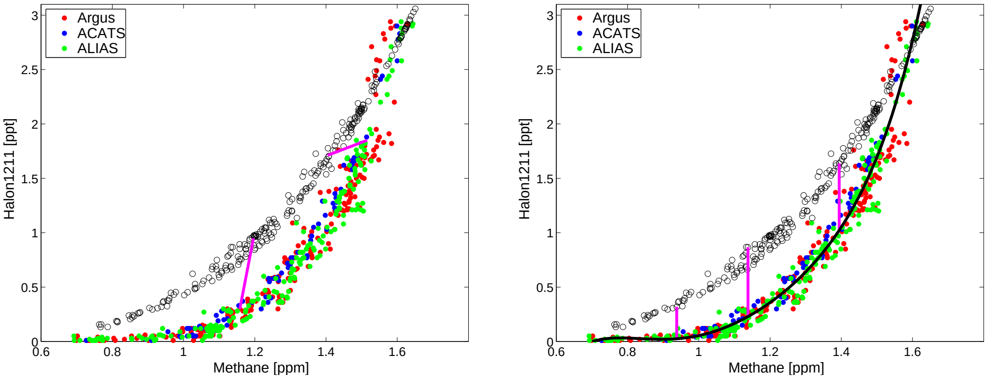

Fig. 9. Sketch of the two methods for calculating the parameter ε. Left: in the definition of Konopka et al. (2004), ε is the sum of the distances of corresponding individual points in the Halon-methane tracer-tracer space. Right: in this work ε is the sum of the distances of modeled values of Halon-1211 to a curve fitted through the observed Halon-1211 values as a function of observed methane.

mixing intensities, spurious filaments that would be mixed in the real atmosphere would also cause large distances of corresponding points in tracer-tracer space, which outweigh the effect of displaced filaments in ε. We argue that the key measure of mixing properties of the model is the shape of the tracer-tracer relation and not the point-to-point distances between model and observations in tracer-tracer space and use an approach that results in a clearer separation of the roughness effect (which is not only caused by too low mixing, but also by the random errors in wind fields) and the effect of displaced filaments from the mismatch in mixing intensity in tracer-tracer space. Hence, we try to put the roughness effect only into γ and try to define ε such that it is only affected by the mixing intensity.

A suitable definition minimizes if the shape of the mixing curve of the model gets more and more similar to the shape of the observed mixing curve. We also look for a definition that allows us to take the model values directly to avoid interpolation. This can be accomplished by the absolute differences of the modeled Halon-1211 values to a curve fitted through the observed Halon-1211 as a function of observed methane. A sketch of the method is shown in Fig. 9 (right). The sum of these differences is largely proportional to the area between the mixing curves of the model and the observations. The observed methane is taken from the average of the three instruments. To obtain the absolute difference, we evaluate the fit function at the modeled methane value. That is

$$\varepsilon = \frac{1}{M}\sum_{j=1}^{M} |h_j^{\text{model}} - \hat{h}_{k(j)}^{\text{obs}}(m_j^{\text{model}})| \qquad (12)$$

where $k(j)$ is the flight number belonging to the modeled value j and $\hat{h}_k^{\text{obs}}$ is a polynomial fit through the observed tracer-tracer relationship of flight k. Since we use a continuous curve for the observed tracer-tracer relationship, we do not need to use a single corresponding value m_i^{model} for every measurement m_i^{observed}. Instead, we use all model air parcels that are next neighbors of the measurement locations, from the 2-D triangulation used in the mixing step and with Δz centered at the measurement location. This method gives us a cloud of air parcels along the flight path. This is indicated here by using j for i as the index and M for N for the number of points. A potential disadvantage of the method is that it can only be applied to data only containing one compact mixing curve (and no additional mixing lines).

In some cases individual methane values in the model are outside of the range of the measured methane values, where the fitted curve is valid. In this case, we do not use these values, so that ε is not based on exactly the same set of points for some model runs. The validity of this approach is verified by extending the mixing curves with a best guess of the likely missing methane values and calculating the parameter again (these tests were not used for the validation). Results are almost identical. The best guess is simply obtained by extending the data of the tracer curves with methane and Halon-1211 data from the third flight for the 5 other flights at the end of January or start of February, since it has the largest range of methane values. The flights at the end of February and in March are extended with data from the eighth flight.

The parameter γ for the roughness of the field in Konopka et al. (2004) is defined in two steps: the sum of the absolute differences of successive methane measurements is

$$\Delta_{\text{observed}} = \sum_{i=1}^{N-1} |m_{i+1}^{\text{observed}} - m_i^{\text{observed}}| \qquad (13)$$

The same can be done for the model values of methane. The ratio of the measured and modeled Δ is

$$\gamma = \frac{\Delta_{\text{model}}}{\Delta_{\text{observed}}} \qquad (14)$$

Values near 1 are defined as the optimum. With this definition the magnitude of the roughness will depend on the spatial scale of the structures we are looking at. It will make a difference if the measurement locations are 1 km or 20 km apart. More importantly, it will also make a difference if the model air parcels are 50 km or 300 km apart. In this sense, γ is not a very robust measure of the roughness. Hence, we use a definition of γ that compares the roughness $\Delta_{\mathrm{observed}}$ and Δ_{model} at the spatial scale of the model resolution and is robust to changes in the spatial distance of the measurements.

Our approach compares the standard deviations of the modeled and observed methane values at the spatial scale of the effective model resolution: we determine the next model neighbors of each measurement i (exactly as described for the other parameter ε) and calculate the standard deviation σ_i of the modeled methane values for each set of next neighbors (avoiding any interpolation). Now, all standard deviations are averaged to give a mean standard deviation σ_{model}. In addition, we calculate the mean distance of the points in every set of next neighbors and compute its average $\bar{d}$. Now, we look for all pairs $(m_i^{\mathrm{observed1}}, m_i^{\mathrm{observed2}})$ of measurements which are separated by a distance within $[\bar{d}-\Delta d, \bar{d}+\Delta d]$, with Δd=5 km. It can be shown that the standard deviation of this set of points is given by the following equation:

$$\sigma_{\mathrm{observed}} = \sqrt{\frac{1}{2N}\sum_i^N (m_i^{\mathrm{observed1}} - m_i^{\mathrm{observed2}})^2} \tag{15}$$

where N is the number of pairs. Now, we define

$$\gamma = \frac{\sigma_{\mathrm{model}}}{\sigma_{\mathrm{observed}}} \tag{16}$$

in equivalence to Eq. (14). Theoretically, a term for the statistical measurement error in the observed values needs to be considered, since the standard deviation of the observations will not only be caused by real variations of the mixing ratio but also by measurement noise. This would cause an offset σ_{bias} to $\sigma_{\mathrm{observed}}$ and the denominator would be $\sqrt{\sigma_{\mathrm{observed}}^2 - \sigma_{\mathrm{bias}}^2}$. However, it turns out that this correction is negligible.

It is important to note that our γ gives us only a measure for the deviation of the model variability from what we would expect from the observations at the given model resolution. There is no penalty if small filaments just do not appear in coarser model resolutions. In this sense it gives a relative but not absolute measure for the expected variability.

Note that our definition of ε and γ does not imply a perfect agreement of the observed and modeled time series along the flight path if $\varepsilon = 0$ and γ=1. For example, all filaments could be displaced by a small distance between the modeled and observed time series along the flight path in this case.

3.5 Validation results

Figure 10 shows the results for the parameters γ and ε for different model resolutions r_0 and different values of the critical Lyapunov exponent λ_c (for a comparison of our definition of ε and γ and the one given in Konopka et al., 2004, see Appendix B).

For a given r_0, data points show more intense mixing to the left (low values of λ_c) and less intense mixing to the right (high values of λ_c). λ_c=10 d^{-1} is virtually identical with no mixing at all ($\lambda_c \rightarrow \infty$).

The agreement of the modeled tracer-tracer relationship with the observed one generally improves with increasing λ_c. For higher resolutions it does only reach a shallow minimum at roughly λ_c=3 d^{-1} to λ_c=4 d^{-1} (see also Fig. 12), which compares well with the value λ_c=3 d^{-1} given in Konopka et al. (2004). This basically means that the observed mixing is extremely low and very anisotropic: the ratio between r_+ and r_- is larger than 20 for these values of λ_c. Switching mixing off in the model is actually not a bad option for optimizing ε. Indeed, the observed tracer-tracer relationships on the first flight on 20 January and the last flight on 12 March are very similar, indicating that mixing in the real stratosphere is extremely low.

Generally, the agreement of the tracer-tracer relationships improves with higher resolution r_0 if λ_c is held constant. This is due to the fact that the model gets more diffusive with increasing distance between the mixed air parcels.

Where the triangulation approach of the ATLAS model is applicable (dashed lines), it is generally less diffusive than the CLaMS approach (solid lines), see also Fig. 14. For the same set of mixing parameters, the results of the ATLAS triangulation approach are superior to the CLaMS approach. One likely reason for that is that the number of mixed parcels is lower in the ATLAS approach than in the CLaMS approach for the same λ_c (Fig. 11). This is due to the lower average vertical distance between mixed air parcels: the maximum distance of two mixed air parcels is Δz in the CLaMS approach (if both are at the edges of the layer), but only $\Delta z/2$ in the ATLAS approach (since one of the parcels is by definition at the center of the local layer). A possibility to work against that in the CLaMS approach would be to increase λ_c until the percentage of mixed parcels is low enough. However, there would still be qualitative differences between the approaches. E.g., if an air parcel is situated at the boundary of a layer in the CLaMS approach, it is possible that it does not mix with a vertically close parcel just because it is in the adjacent layer. In this respect, the ATLAS approach behaves qualitatively more like in the real atmosphere. In fact, there are some runs with the ATLAS approach for 150 km resolution, which show a lower ε than any run with the CLaMS approach in the same resolution, no matter what λ_c is used.

However, note that for coarse resolutions (say 300 km) the mixing process in the ATLAS as well as the CLaMS approach will become unrealistic. The diffusion coefficients of single mixing events will become unrealistically large and that can only be compensated by setting λ_c to large values to obtain realistic bulk diffusivities (see Sect. 4). But this will still be a better option for long-term runs in coarse resolutions than using an Eulerian approach.

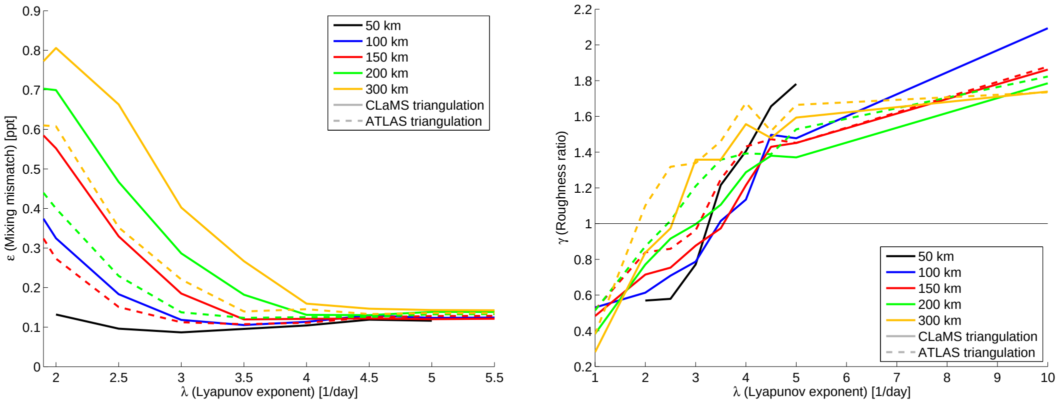

Fig. 10. Mixing mismatch and tracer roughness. Left: the parameter ε for the difference of the modeled and observed tracer-tracer relationship for different values of the critical Lyapunov exponent λ_c (axis) and resolution r_0 (colors). Solid lines show results for the triangulation approach of CLaMS, dashed lines show results for the triangulation approach of ATLAS. Right: same for the parameter γ for the tracer roughness ratio.

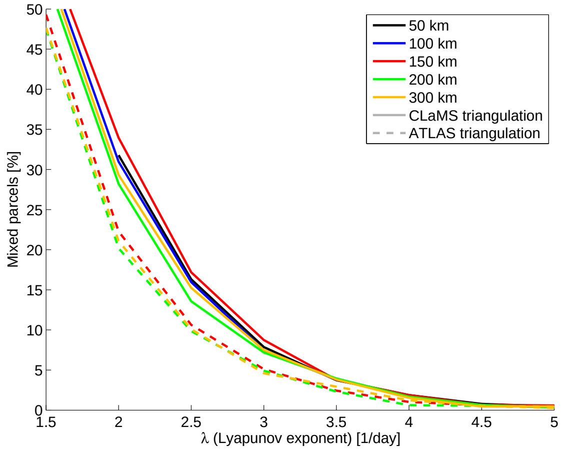

Fig. 11. Percentage of mixed parcels for different values of the critical Lyapunov exponent λ_c (axis) and resolution r_0 (colors).

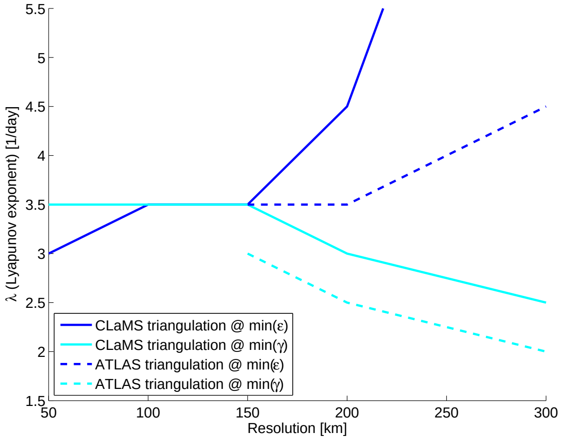

Fig. 12. Critical Lyapunov exponents where the mixing mismatch ε minimizes (blue) and the roughness ratio γ is closest to one (cyan). Solid lines show the CLaMS triangulation approach, dashed lines show the ATLAS triangulation approach.

For all resolutions, the roughness ratio γ increases more or less uniformly with decreasing λ_c (the model fields are too smooth for low values of λ_c and too rough for high values of λ_c), see Fig. 10 (right). The optimal value for λ_c based only on $\gamma \approx 1$ is about 2 d^{-1} to 3.5 d^{-1} for all resolutions and both triangulation approaches.

Since the effect of random errors in the wind fields and numerical discretization shows up mainly in the roughness ratio γ and not in the mixing mismatch ε (because the artificial filaments would still be mixed with the right intensity), γ should optimize at lower values of λ_c (at higher mixing intensity) than ε. Figure 12 shows that this is in fact what is observed in most validation runs. It shows the λ_c values where the ε curves minimize (blue) and γ is closest to one (cyan). Note however that the minima are shallow and that some uncertainty is introduced by this. In addition, the ATLAS triangulation approach is optimal at smaller values of λ_c than the CLaMS approach, possibly since it is less diffusive and needs more mixing in the model to obtain optimal results. The values at 300 km should not be taken too seriously, since the minimum of ε is at the highest tested λ_c of 10 d^{-1} here. Often, it will be unavoidable to find a compromise in optimizing γ and ε, i.e. to fight the patchyness by setting the mixing intensity to slightly higher values than suggested by ε (lower values for λ_c).

The results are not very sensitive to the value of the aspect ratio α. Values between 200 and 500 give comparable results to 250. As long as the product $\lambda_c \Delta t$ stays constant, the results are also not very sensitive to the mixing time step Δt. Values of 6 h and 24 h give comparable results to 12 h. These results are also confirmed by the validation of the CLaMS model (Konopka et al., 2004, 2005).

Figure 13 shows that the effect of adding the random vertical coordinate is small in the range of the minimum ε values both for the ATLAS and CLaMS triangulation. However, switching the random vertical coordinate off does decrease the diffusivity for the lowest λ_c values in the ATLAS triangulation approach. This is very likely due to the vertical clustering into layers of enhanced parcel density that sets in if the random coordinate is switched off and the mixing intensity is high. This effectively suppresses vertical mixing and lowers the effective diffusion coefficient to values which are normally observed at higher λ_c values. That is, while improving the vertical homogeneity of the model, the random coordinate has either negligible effects on the diffusivity (high λ_c) or is just necessary for a realistic behaviour of vertical mixing in the ATLAS approach (low λ_c).

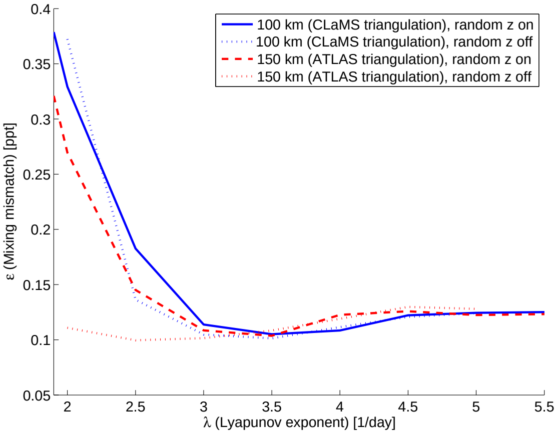

Fig. 13. Effect of adding a random number to the vertical coordinate of newly inserted parcels. The solid blue line shows ε for 100 km resolution, the CLaMS triangulation and the random vertical coordinate on, the dashed red line for 150 km, the ATLAS triangulation and the random vertical cordinate on. Dotted lines are the same with the random vertical coordinate off.

4 Estimation of diffusion coefficients

It is desirable that the diffusion coefficients obtained with the optimal mixing parameters are in the range of other estimates. However, there are few direct and independent estimates of diffusion coefficients (e.g. from radar measurements, like Fukao et al., 1994, see also Wilson, 2004). Most estimates (including ours) are based on indirect methods as the reconstruction of observed tracer filaments, profiles or tracer-tracer relationships, usually with a diffusion component and sometimes a Langrangian transport component, e.g. by a simple 1-D diffusion model for the mean vertical profile (Massie and Hunten, 1981), numerical models for strain and diffusion of filaments (Balluch and Haynes, 1997; Waugh et al., 1997), or by averaging stochastic back trajectories (Legras et al., 2005). In contrast to e.g. Balluch and Haynes (1997), the information about the diffusion coefficient comes mainly from the tracer-tracer relationship in our method and not from reconstructing fine filaments, which are only resolved in the highest resolutions. A general problem of a comparison are the large differences in the methods. Some are local (radar on the 100 m scale), some give bulk estimates, some are Eulerian, some Lagrangian, some direct and some indirect.

Figure 14 shows the effective mean (bulk) vertical and horizontal diffusion coefficients north of 60° N at 430 K as a function of λ_c and r_0, calculated as in Sect. 2.3.5. Vertical diffusion coefficients obtained from the studies mentioned above are also shown for comparison. The modeled vertical diffusion coefficient increases with lower λ_c, which is due to the increasing number of mixing events, and increases with coarser resolution, which is due to increasing distances between mixed parcels. Figure 15 shows the value of the vertical diffusion coefficient at the optimal values of ε and γ in the same manner as in Fig. 12. The vertical diffusion coefficient takes values between 0.07 m^2/s and 0.36 m^2/s for the optimal ε and the CLaMS triangulation approach, and values between 0.02 m^2/s and 0.1 m^2/s for the optimal ε and the ATLAS triangulation approach. The optimal γ shows vertical diffusion coefficients that are probably too large, if compared with the estimates from the other studies. These values are increased due to errors in the wind fields. In summary, our results suggest a value of about 0.1 m^2/s for the vertical diffusivity. As noted, the estimated bulk diffusivities will probably be more realistic for high resolutions, since the diffusivities of single mixing events are probably too large for coarser resolutions.

Our estimate agrees well with the value 0.1 m^2/s given for the lower stratospheric surf zone in Legras et al. (2005). Values from the radar measurements (0.1 m^2/s to 0.5 m^2/s for Fukao et al., 1994) tend to be larger than other estimates. Also the Massie and Hunten (1981) value of 0.58 m^2/s at 22 km seems to be relatively large. As estimated in Sect. 2.3.3, values like these would roughly correspond to a minimum width of a filament of 50 km before it disappears. One reason might be that the effects of the large-scale advection by the Brewer-Dobson circulation are not considered in studies like Massie and Hunten (1981). On the other hand, the estimate of Balluch and Haynes (1997) (0.01 m^2/s to 0.001 m^2/s) and of Legras et al. (2005) for the inner vortex (0.01 m^2/s) are on the lower side of our estimate. Differences can at least partly be explained by the likely dependence on season and location (e.g. single filaments in Balluch and Haynes, 1997, or the average north of 60° N in our approach compared to the separate values for surf zone and vortex in Legras et al., 2005).

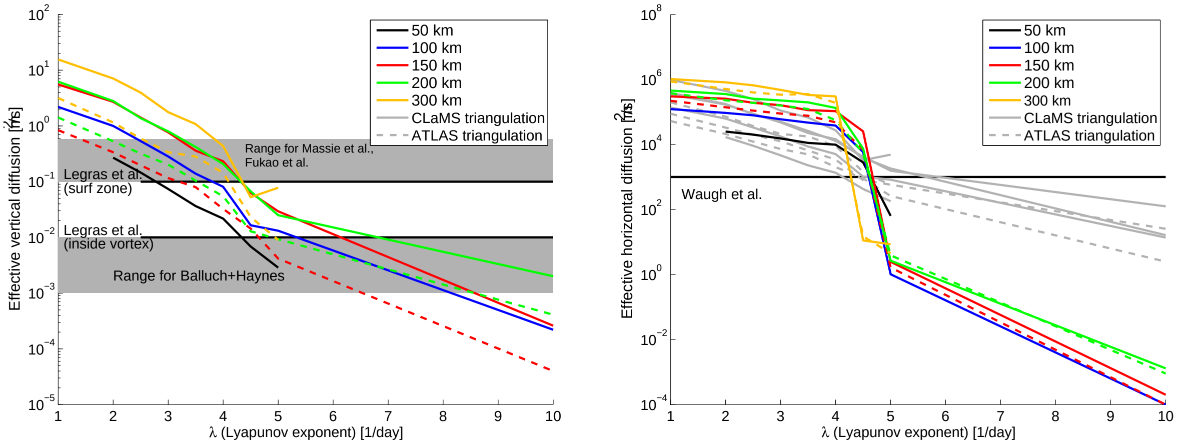

Fig. 14. Left: effective vertical diffusion coefficient north of 60° N at a layer around 430 K for different values of the critical Lyapunov exponent λ_c (axis) and resolution r_0 (colors). Solid lines show results for the triangulation approach of CLaMS, dashed lines show results for the triangulation approach of ATLAS. Shaded areas and solid black lines show vertical diffusion coefficients from other studies for comparison: Massie and Hunten (1981), Fukao et al. (1994), Balluch and Haynes (1997), Legras et al. (2005). Values for λ_c=10 d^{-1} and r_0=300 km are zero and not shown. Right: same for the effective horizontal diffusion coefficient. Grey lines are the vertical diffusion coefficients from the left panel scaled by α^2. Solid black line shows estimate from Waugh et al. (1997).

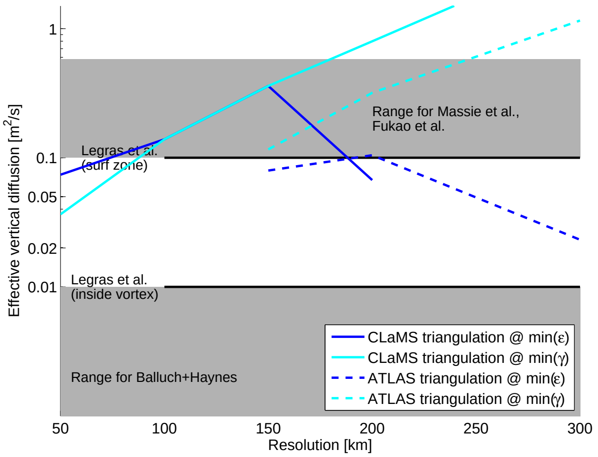

Fig. 15. Value of the vertical diffusion coefficient where the mixing mismatch ε minimizes (blue) and the roughness ratio γ is closest to one (cyan). Solid lines show the CLaMS triangulation approach, dashed lines the ATLAS triangulation approach. Shaded areas and solid black lines show vertical diffusion coefficients from other studies for comparison as in Fig. 14.

The right panel of Fig. 14 shows the horizontal diffusion coefficient, which ideally should be a scaled version of K_z, since Haynes and Anglade (1997) claims K_h=$\alpha^2 K_z$. The grey lines show the vertical diffusion coefficients from the left panel scaled by α^2. In general, the agreement is quite good for values smaller than λ_c=5 d^{-1}, although the horizontal diffusion coefficients are somewhat larger than expected from K_z (note the logarithmic scale). This could be interpreted as the effective aspect ratio of the model being somewhat larger than 250. The modeled horizontal diffusion coefficient also increases with lower λ_c, which is now not only due to the increasing number of mixing events, but also modified by the increasing diffusivity orthogonal to the flow direction and the decreasing diffusivity in flow direction (Sect. 2.3.5). Waugh et al. (1997) gives a value of 10^3 m^2/s for the horizontal diffusion coefficient, which seems to be somewhat lower than our effective diffusion coefficients. The sharp drop in the horizontal diffusion at λ_c values of 5 d^{-1} and 10 d^{-1} is due to the fact that only very few mixing events occured at these values and that all events were merging events (r_-), while at lower λ_c values, also r_+ events occured, which have a much larger diffusion coefficient (at the same mixing parameters). That hints at the fact that the mixing in the model will get unrealistic at these large values of λ_c.

5 Conclusions

The new global Chemical Transport Model (CTM) ATLAS with Lagrangian transport and mixing was presented. In this paper, we focussed on a basic model description and the presentation and validation of the transport and mixing module of the model. In conjunction with a projected second part concentrating on the chemistry module, the paper is thought to serve as the reference citation for the model.

The ability of the transport and mixing model to reproduce observed tracer data and fine-scale tracer structure has been successfully demonstrated. Excellent agreement to observed structures up to scales of typical polar vortex filaments can be reached with suitable settings of the free parameters of the model, which were extensively tested and validated.

The results of the validation suggest a vertical diffusion coefficient on the order of 0.1 m^2/s in the high-latitude lower stratosphere, which fits well into other estimates. However, the vertical diffusion coefficient remains a parameter that can only be estimated with large uncertainty, ranging from 0.5 m^2/s to 0.001 m^2/s in the literature cited here.

The model makes heavy use of concepts developed for the CLaMS model, and consequently part of the study focussed on comparison with that model. Generally, results seem to be of comparable quality and the changes introduced in ATLAS were demonstrated to improve the results (new concept for identifying the neighbors for the mixing process) or to have little effect (effect of random vertical coordinate in the CLaMS triangulation, diffusion coefficient climatology versus entropy-based diffusion coefficient).

As always, time and space did not permit to study all aspects of the model and the validation. For example, since the diffusivity of the atmosphere will vary in time and space, it would be interesting to validate the model with data from other geographical regions or seasons, e.g. to see if the model is also able to reproduce mixing lines in cases of strong mixing events (i.e. in the case of fast anomalous mixing, compared to the constant mixing which is slowly lifting the correlation curve on the concave side). It would also be illuminative to compare the validation results of the Lagrangian model to the results an Eulerian transport code would give.

Future plans with the model include the improvement of the representation of the troposphere, and in the long run, the full coupling to a Atmosphere Ocean General Circulation Model.

Appendix A

Some details of the ATLAS triangulation method

The 3-D triangulation is performed in cartesian space, that is the spherical coordinates are transformed to cartesian coordinates before triangulation with a given radius of the Earth of a=6371 km. Since the large aspect ratio α of the shallow atmosphere would produce very flat tetrahedrons and severe numerical problems in the triangulation, the atmosphere is scaled by a factor of 250 before triangulation. That is

$$\begin{aligned} x &= (a+250z')\cos\varphi\cos\lambda \\ y &= (a+250z')\cos\varphi\sin\lambda \qquad \text{(A1)} \\ z &= (a+250z')\sin\varphi \end{aligned}$$

where z' is log-pressure altitude, λ longitude, φ latitude, x, y, z cartesian coordinates. Finally, an artificial point is inserted at the center of the Earth to avoid that the triangulation creates tetrahedrons in the Earth's interior. This point is later removed from all neighbor relationships. A visualization of the method is shown in Fig. A1.

The 3-D triangulation is only needed to produce a cloud of points surrounding the original point, which includes all points that could possibly be a neighbor of the original point in the final 2-D triangulation. Empirically it is found that including the first and second neighbors makes the cloud large enough for this purpose.

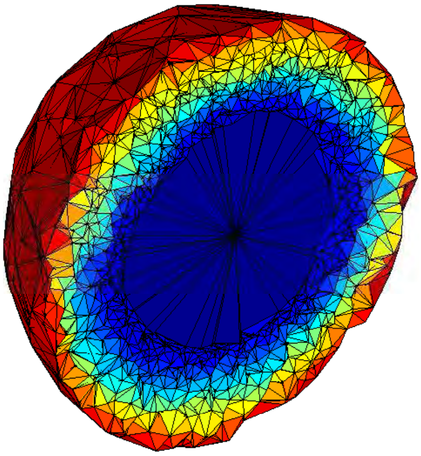

Fig. A1. 3-D triangulation of air parcels on the globe in the ATLAS triangulation method. Edges connecting air parcels are shown as black lines, colors denote an arbitrary altitude scale for better visualization. The sphere is cut into two halfes, with one half removed, to allow for a look into the interior of the triangulation.

Appendix B

Comparison of the different definitions of ε and γ

Figure B1 shows ε calculated by Eq. (11) (originally from Konopka et al., 2004) for comparison with our definition of the parameter by Eq. (12) in Fig. 10 (left). ε according to Eq. (11) (with corresponding model points obtained by nearest neighbors) shows more scatter than our ε. In addition, some of the lines for different resolutions are cutting across each other (note that Fig. 11 in Konopka et al. (2004) uses a smoothed version of the curves). However, it is reassuring that the general conclusions are still the same if using Eq. (11).

Figure B2 shows the ATLAS γ (Eq. 16) for r_0=100 km as reference, and γ as defined by Eq. (14) based on three different methods for finding the corresponding model point m_i^{model} to the measurement: nearest model neighbor of the measurement and two methods of interpolation, namely average over the next neighbors and average over the next and second neighbors. While the method without averaging (nearest neighbor) shows too much variability for all λ_c and never reaches the optimal value 1, the method with the most averaging (first and second neighbors) shows relatively small values at large values of λ_c, since it tends to smear out filaments that are actually in the model data and introduces spurious mixing. The blue lines show the results if the low resolution measurements of ACATS are used (about 20 km

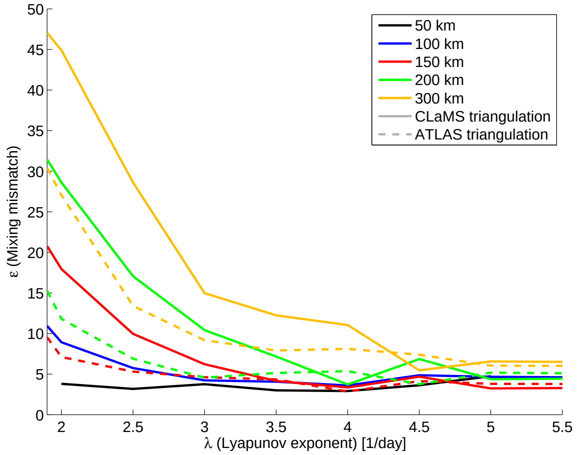

Fig. B1. The parameter ε as defined in Eq. (11) (originally from Konopka et al., 2004) with nearest neighbors as corresponding model points, for comparison with ε as defined in Eq. (12) shown in Fig. 10 (left).

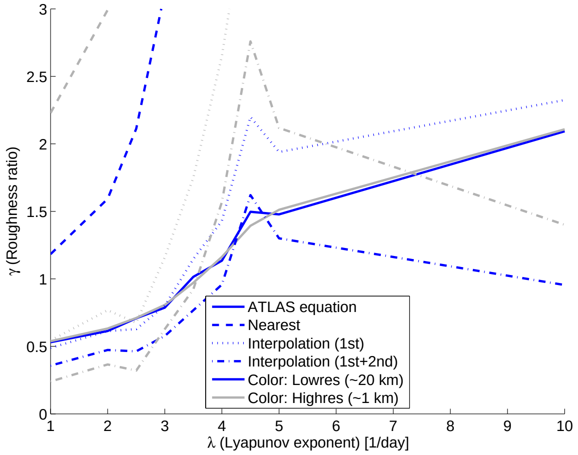

Fig. B2. The parameter γ only for r_0=100 km. The solid lines show the definition for γ from this study (Eq. 16), the different dashed lines show the definition of γ in Konopka et al. (2004) (Eq. 14) with different approaches to obtain the model points m_i^{model}: nearest neighbor of measurement, average over first neighbors of the measurement, average over first and second neighbors. The blue lines show results if only using the ACATS measurements (about 20 km resolution) and the grey lines if only using the Argus and ALIAS measurements (about 1 km resolution).

resolution) and the grey lines show the results if the high resolution measurements of Argus and ALIAS are used (about 1 km resolution). While the γ obtained by Eq. (16) remains virtually unchanged by resolution changes, the other methods are fairly sensitive to them.

Acknowledgements. We thank ECMWF for providing reanalysis data, R. Salawitch for providing the merged ER-2 data files, R. Lehmann for help in deriving some of the equations, J. W. Elkins (NOAA) for providing the ACATS-IV and LACE data, H. Jost (NASA Ames Research Center) for providing the Argus data, C. R. Webster (Jet Propulsion Laboratory, California Institute of Technology) for providing the ALIAS data and J.-U. Grooß and J. M. Russell III for providing HALOE data. Work at AWI was supported by the EC DG Research through the SCOUT-O3 project.

Edited by: P. Jöckel

References

Balluch, M. G. and Haynes, P. H.: Quantification of lower stratospheric mixing processes using aircraft data, J. Geophys. Res., 102, 23487–23504, 1997.

Chipperfield, M. P.: New version of the TOMCAT/SLIMCAT offline chemical transport model: intercomparison of stratospheric tracer experiments, Q. J. Roy. Meteor. Soc., 132, 1179–1203, 2006.

Collins, W. J., Stevenson, D. S., Johnson, C. E., and Derwent, R. G.: Tropospheric ozone in a global-scale three-dimensional Lagrangian model and its response to NO_X emission controls, J. Atmos. Chem., 26, 223–274, 1997.

Fairlie, T. D., Pierce, R. B., Al-Saadi, J. A., Grose, W. L., Russell III, J. M., Proffitt, M. H., and Webster, C. R.: The contribution of mixing in Lagrangian photochemical predictions of polar ozone loss over the Arctic in summer 1997, J. Geophys. Res., 104, 26597–26609, 1999.

Fukao, S., Yamanaka, M. D., Ao, N., Hocking, W. K., Sato, T., Yamamoto, M., Nakamura, T., Tsuda, T., and Kato, S.: Seasonal variability of vertical eddy diffusivity in the middle atmosphere. 1. Three-year observations by the middle and upper atmosphere radar, J. Geophys. Res., 99, 18973–18987, 1994.

Grooß, J.-U. and Russell III, J. M.: Technical note: A stratospheric climatology for O_3, H_2O, CH_4, NO_x, HCl and HF derived from HALOE measurements, Atmos. Chem. Phys., 5, 2797–2807, 2005, http://www.atmos-chem-phys.net/5/2797/2005/.

Haynes, P. and Anglade, J.: The vertical scale cascade in atmospheric tracers due to large-scale differential advection, J. Atmos. Sci., 54, 1121–1136, 1997.

Haynes, P. and Shuckburgh, E.: Effective diffusivity as a diagnostic of atmospheric transport, J. Geophys. Res., 105, 22777–22794, 2000.

Haynes, P. and Vanneste, J.: Stratospheric tracer spectra, J. Atmos. Sci., 61, 161–178, 2004.

Konopka, P., Grooß, J.-U., Günther, G., McKenna, D. S., and Müller, R.: Weak impact of mixing on chlorine deactivation during SOLVE/THESEO 2000: Lagrangian modeling (CLaMS) versus ER-2 in situ observations, J. Geophys. Res., 108, 8324, doi:10.1029/2001JD000876, 2003.

Konopka, P., Steinhorst, H.-M., Grooß, J.-U., Günther, G., Müller, R., Elkins, J. W., Jost, H.-J., Richard, E., Schmidt, U., Toon, G., and McKenna, D. S.: Mixing and ozone loss in the 1999–2000 Arctic vortex: Simulations with the three-dimensional Chemical Lagrangian Model of the Stratosphere (CLaMS), J. Geophys. Res., 109, D02315, doi:10.1029/2003JD003792, 2004.

Konopka, P., Spang, R., Günther, G., Müller, R., McKenna, D. S., Offermann, D., and Riese, M.: How homogeneous and isotropic is stratospheric mixing? Comparison of CRISTA-1 observations with transport studies based on the Chemical Lagrangian Model of the Stratosphere (CLaMS), Q. J. Roy. Meteor. Soc., 131, 565–579, 2005.

Konopka, P., Günther, G., Müller, R., dos Santos, F. H. S., Schiller, C., Ravegnani, F., Ulanovsky, A., Schlager, H., Volk, C. M., Viciani, S., Pan, L. L., McKenna, D.-S., and Riese, M.: Contribution of mixing to upward transport across the tropical tropopause layer (TTL), Atmos. Chem. Phys., 7, 3285–3308, 2007, http://www.atmos-chem-phys.net/7/3285/2007/.

Legras, B., Pisso, I., Berthet, G., and Lefèvre, F.: Variability of the Lagrangian turbulent diffusion in the lower stratosphere, Atmos. Chem. Phys., 5, 1605–1622, 2005, http://www.atmos-chem-phys.net/5/1605/2005/.

Loewenstein, M., Jost, H., Grose, J., Eilers, J., Lynch, D., Jensen, S., and Marmie, J.: Argus: a new instrument for the measurement of the stratospheric dynamical tracers, N_2O and CH_4, Spectrochim. Acta A, 58, 2329–2345, 2002.

Massie, S. T. and Hunten, D. M.: Stratospheric eddy diffusion coefficients from tracer data, J. Geophys. Res., 86, 9859–9868, 1981.

McKenna, D. S., Konopka, P., Grooß, J.-U., Günther, G., Müller, R., Spang, R., Offermann, D., and Orsolini, Y.: A new Chemical Lagrangian Model of the Stratosphere (CLaMS) 1. Formulation of advection and mixing, J. Geophys. Res., 107, 4309, doi:10.1029/2000JD000114, 2002.

Newman, P., Harris, N. R. P., Adriani, A., Amanatidis, G. T., Anderson, J. G., Braathen, G. O., Brune, W. H., Carslaw, K. S., Craig, M. S., DeCola, P. L., Guirlet, M., Hipskind, R. S., Kurylo, M. J., Küllmann, H., Larsen, N., Mégie, G. J., Pommereau, J.-P., Poole, L. R., Schoeberl, M. R., Stroh, F., Toon, O. B., Trepte, C. R., and Roozendael, M. V.: An overview of the SOLVE-THESEO 2000 campaign, J. Geophys. Res., 107, 8259, doi:10.1029/2001JD001303, 2002.

O'Rourke, J.: Computational Geometry in C, Cambridge University Press, 1998.

Prather, M. J.: Numerical advection by conservation of second-order moments, J. Geophys. Res., 91, 6671–6681, 1986.

Ray, E. A., Moore, F. L., Elkins, J. W., Hurst, D. F., Romashkin, P. A., Dutton, G. S., and Fahey, D. W.: Descent and mixing in the 1999–2000 northern polar vortex inferred from in situ tracer measurements, J. Geophys. Res., 107, 8285, doi:10.1029/2001JD000961, 2002.

Reithmeier, C. and Sausen, R.: ATTILA: Atmospheric tracer transport in a Lagrangian model, Tellus B, 54, 278–299, 2002.

Romashkin, P. A., Hurst, D. F., Elkins, J. W., Dutton, G. S., Fahey, D. W., Dunn, R. E., Moore, F. L., Myers, R. C., and Hall, B. D.: In situ measurements of long-lived trace gases in the lower stratosphere by gas chromatography, J. Atmos. Ocean. Tech., 18, 1195–1204, 2001.

Shimazaki, T. and Wuebbles, D. J.: On the theoretical model for vertical ozone density distributions in the mesosphere and upper stratosphere, Pure Appl. Geophys., 106–108, 1446–1463, 1973.

Simmons, A. J., Uppala, S. M., Dee, D., and Kobayashi, S.: ERA-Interim: New ECMWF reanalysis products from 1989 onwards, ECMWF News Lett., 110, 25–35, 2006.

Simmons, A. J., Uppala, S. M., and Dee, D.: Update on ERA-Interim, ECMWF News Lett., 111, 5 pp., 2007.

Stenke, A., Dameris, M., Grewe, V., and Garny, H.: Implications of Lagrangian transport for simulations with a coupled chemistry-climate model, Atmos. Chem. Phys., 9, 5489–5504, 2009, http://www.atmos-chem-phys.net/9/5489/2009/.

Waugh, D. W., Plumb, R. A., Elkins, J. W., Fahey, D. W., Boering, K. A., Dutton, G. S., Volk, C. M., Keim, E., Gao, R.-S., Daube, B. C., Wofsy, S. C., Loewenstein, M., Podolske, J. R., Chan, K. R., Proffitt, M. H., Kelly, K. K., Newman, P. A., and Lait, L. R.: Mixing of polar vortex air into middle latitudes as revealed by tracer-tracer scatterplots, J. Geophys. Res., 102, 13119–13134, 1997.

Webster, C. R., May, R. D., Trimble, C. A., Chave, R. G., and Kendall, J.: Aircraft (ER-2) laser infrared absorption spectrometer (ALIAS) for in-situ stratospheric measurements of HCI, N_2O, CH_4, NO_2, and HNO_3, Appl. Optics, 33, 454–472, 1994.

Wilson, R.: Turbulent diffusivity in the free atmosphere inferred from MST radar measurements: a review, Ann. Geophys., 22, 3869–3887, 2004, http://www.ann-geophys.net/22/3869/2004/.

Wohltmann, I. and Rex, M.: Improvement of vertical and residual velocities in pressure or hybrid sigma-pressure coordinates in analysis data in the stratosphere, Atmos. Chem. Phys., 8, 265–272, 2008, http://www.atmos-chem-phys.net/8/265/2008/.

Geosci. Model Dev., 3, 585–601, 2010
www.geosci-model-dev.net/3/585/2010/
doi:10.5194/gmd-3-585-2010
© Author(s) 2010. CC Attribution 3.0 License.

Geoscientific
Model Development

The Lagrangian chemistry and transport model ATLAS: simulation and validation of stratospheric chemistry and ozone loss in the winter 1999/2000

I. Wohltmann, R. Lehmann, and M. Rex

Alfred Wegener Institute for Polar and Marine Research, Potsdam, Germany

Received: 11 May 2010 – Published in Geosci. Model Dev. Discuss.: 1 June 2010
Revised: 28 September 2010 – Accepted: 21 October 2010 – Published: 1 November 2010

Abstract. ATLAS is a new global Lagrangian Chemistry and Transport Model (CTM), which includes a stratospheric chemistry scheme with 46 active species, 171 reactions, heterogeneous chemistry on polar stratospheric clouds and a Lagrangian denitrification module. Lagrangian (trajectory-based) models have several important advantages over conventional Eulerian models, including the absence of spurious numerical diffusion, efficient code parallelization and no limitation of the largest time step by the Courant-Friedrichs-Lewy criterion. This work describes and validates the stratospheric chemistry scheme of the model. Stratospheric chemistry is simulated with ATLAS for the Arctic winter 1999/2000, with a focus on polar ozone depletion and denitrification. The simulations are used to validate the chemistry module in comparison with measurements of the SOLVE/THESEO 2000 campaign. A Lagrangian denitrification module, which is based on the simulation of the nucleation, sedimentation and growth of a large number of polar stratospheric cloud particles, is used to model the substantial denitrification that occured in this winter.

1 Introduction

Although Lagrangian models have several advantages over grid-based Eulerian models (e.g. no numerical diffusion, no negative species concentrations by transport, easy parallelization), only few Lagrangian CTMs are in use so far, including the STOCHEM (e.g. Collins et al., 1997), ATTILA (e.g. Reithmeier and Sausen, 2002) and CLaMS (e.g. Konopka et al., 2004) models. ATLAS is a new global Lagrangian CTM with a focus on the stratosphere.

This is the second part of the model description of the ATLAS model, which focusses on the stratospheric chemistry module. The implementation of transport and mixing was already described in Wohltmann and Rex (2009). The model architecture of ATLAS shares a number of concepts with the CLaMS 3-D model (see Konopka et al., 2004, 2007 for general aspects and McKenna et al., 2002 and Grooß et al., 2002, 2005 for the chemistry), but ATLAS is an independently developed model with no code in common with CLaMS.

Figure 1 shows the basic layout of the model. A large number of trajectories, each representing an air parcel, is initialized and advected for some hours (filling the domain of the complete atmosphere) (trajectory module, light blue box). Chemistry is simulated on every trajectory like in a box model (chemistry module, yellow box), followed by the calculation of the growth and sedimentation of polar stratospheric cloud particles (brown box). Every few hours, a mixing step is introduced (mixing module, orange box), where air parcels are mixed in regions of large flow deformation (determined by Lyapunov exponent) to obtain a realistic diffusion of species.

The stratospheric chemistry module is based on a box model with a rather extensive set of 171 reactions and 46 active species and includes a detailed treatment of heterogeneous chemistry on polar stratospheric clouds based on the module by Carslaw et al. (1995). The implementation of the denitrification module is based on the DLAPSE particle model of Carslaw et al. (2002). The system of differential equations is solved by a stiff solver with a variable time step without using the concept of chemical families.

Model runs covering the Arctic winter 1999/2000 driven by winds and temperatures from ECMWF ERA Interim reanalysis data (Simmons et al., 2006) are conducted to assess the performance of the chemistry and denitrification modules. The winter of 1999/2000 has been chosen for several reasons: thanks to the SOLVE/THESEO 2000 measurement

---

Correspondence to: I. Wohltmann
(ingo.wohltmann@awi.de)

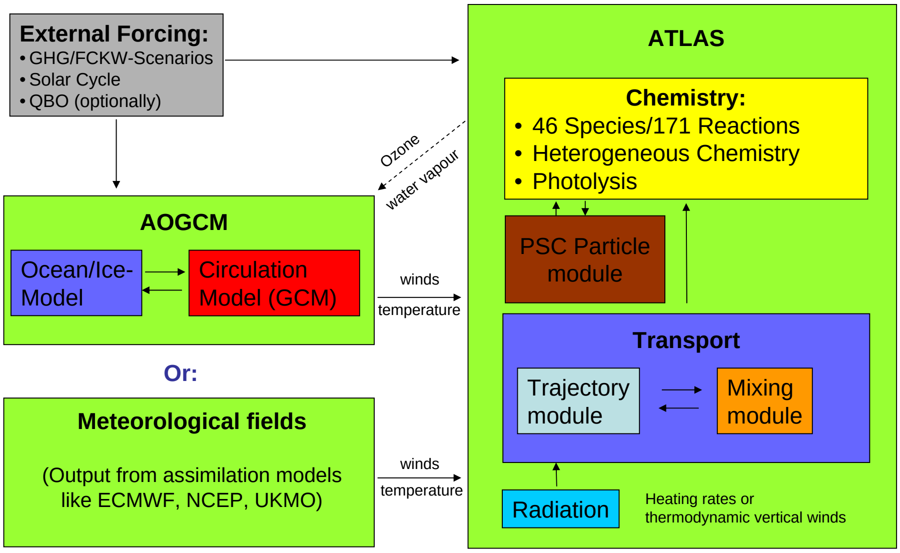
External Forcing:
• GHG/FCKW-Scenarios
• Solar Cycle
• QBO (optionally)
ATLAS
Chemistry:
• 46 Species/171 Reactions
• Heterogeneous Chemistry
• Photolysis
Ozone
water vapour
AOGCM
Ocean/Ice-Model
Circulation Model (GCM)
winds
temperature
PSC Particle module
Transport
Trajectory module
Mixing module
Or:
Meteorological fields
(Output from assimilation models like ECMWF, NCEP, UKMO)
winds
temperature
Radiation
Heating rates or thermodynamic vertical winds

Fig. 1. Model concept.

Table 1. Species considered in the chemistry scheme.

Category	Species
Long-lived	CH_4, H_2O, N_2O, CO_2, CO, H_2
Halogen sources	CFC-11, CFC-12, CFC-113, HCFC-22, CH_3Cl, CH_3Br, CCl_4, CH_3CCl_3, Halon-1211, Halon-1301
Oxygen	O_3, $O(^3P)$, $O(^1D)$
Nitrogen	NO, NO_2, NO_3, N_2O_5, HNO_3, HO_2NO_2, N
Hydrogen	H, OH, HO_2, H_2O_2, CH_2O
Chlorine	Cl, Cl_2, ClO, OClO, Cl_2O_2, HCl, HOCl, $ClONO_2$, $ClNO_2$
Bromine	Br, BrCl, BrO, HBr, HOBr, $BrONO_2$
Fixed	O_2, N_2

campaign (Newman et al., 2002), there is an unrivalled wealth of measurements available, which is beneficial both for initialization and validation. In addition, the winter was one of the coldest stratospheric winters on record, with one of the largest amounts of ozone loss measured so far (e.g. Rex et al., 2002). It was also one of the few winters where substantial denitrification occured in the Northern Hemisphere (Popp et al., 2001), which prolonged the period of stratospheric ozone loss, and it saw the discovery of the so-called "NAT rocks" (large nitric acid trihydrate particles) as the probable cause for this denitrification (Fahey et al., 2001).

A detailed description of the chemistry module and the Lagrangian denitrification module is given in Sect. 2. The setup of the performed model runs is described in Sect. 3. Results of model runs covering the winter 1999/2000 are presented in Sect. 4 and compared to observations. Conclusions are given in Sect. 5. Additionally, a Supplement is provided with the paper, which includes figures of all comparisons of model data to measurements performed for this study.

2 Model description

The chemistry module is based on the stratospheric box model of the Alfred Wegener Institute (see model comparison by Krämer et al., 2003; Lehmann, 2004). It contains 46 active species and 2 fixed species, which are shown in Table 1. The model incorporates 171 reactions, including 42 photolysis reactions (Table 2), 122 gas phase reactions (Table 3) and 7 heterogeneous reactions (Table 4). Note that several equations are given as net equations summarizing the products of an intermediate chain of reactions (in this case, the number of N and O atoms on the left and right hand side of the equation may also differ. These are taken implicitly from the fixed species N_2 and O_2).

Table 2. List of photolysis reactions.

Reaction		
$O_2 + h\nu$	$\rightarrow$	$O(^3P) + O(^3P)$
$O_3 + h\nu$	$\rightarrow$	$O(^3P) + O_2$
$H_2O + h\nu$	$\rightarrow$	$OH + H$
$N_2O + h\nu$	$\rightarrow$	$N_2 + O(^1D)$
$CH_4 + h\nu$	$\rightarrow$	$CO + 2\,H_2O$
$NO_2 + h\nu$	$\rightarrow$	$NO + O(^3P)$
$HNO_3 + h\nu$	$\rightarrow$	$NO_2 + OH$
$HOCl + h\nu$	$\rightarrow$	$Cl + OH$
$HO_2NO_2 + h\nu$	$\rightarrow$	$HO_2 + NO_2$
$HO_2NO_2 + h\nu$	$\rightarrow$	$OH + NO_3$
$ClONO_2 + h\nu$	$\rightarrow$	$Cl + NO_3$
$ClONO_2 + h\nu$	$\rightarrow$	$ClO + NO_2$
$N_2O_5 + h\nu$	$\rightarrow$	$NO_2 + NO_3$
$N_2O_5 + h\nu$	$\rightarrow$	$NO + NO_3 + O(^3P)$
$O_3 + h\nu$	$\rightarrow$	$O(^1D) + O_2$
$H_2O_2 + h\nu$	$\rightarrow$	$OH + OH$
$OClO + h\nu$	$\rightarrow$	$ClO + O(^3P)$
$Cl_2O_2 + h\nu$	$\rightarrow$	$Cl + Cl + O_2$
$HCl + h\nu$	$\rightarrow$	$Cl + H$
$Cl_2 + h\nu$	$\rightarrow$	$Cl + Cl$
$CO_2 + h\nu$	$\rightarrow$	$CO + O(^3P)$
$ClNO_2 + h\nu$	$\rightarrow$	$Cl + NO_2$
$BrONO_2 + h\nu$	$\rightarrow$	$BrO + NO_2$
$BrONO_2 + h\nu$	$\rightarrow$	$Br + NO_3$
$BrCl + h\nu$	$\rightarrow$	$Br + Cl$
$HOBr + h\nu$	$\rightarrow$	$Br + OH$
$CH_2O + h\nu$	$\rightarrow$	$H + CO + HO_2$
$CH_2O + h\nu$	$\rightarrow$	$H_2 + CO$
$NO + h\nu$	$\rightarrow$	$N + O(^3P)$
$BrO + h\nu$	$\rightarrow$	$Br + O(^3P)$
$NO_3 + h\nu$	$\rightarrow$	$NO_2 + O(^3P)$
$NO_3 + h\nu$	$\rightarrow$	$NO + O_2$
CFC-11 $+ h\nu$	$\rightarrow$	3 Cl + products
CFC-12 $+ h\nu$	$\rightarrow$	2 Cl + products
CFC-113 $+ h\nu$	$\rightarrow$	3 Cl + products
HCFC-22 $+ h\nu$	$\rightarrow$	Cl + products
$CH_3Cl + h\nu$	$\rightarrow$	Cl + products
$CCl_4 + h\nu$	$\rightarrow$	4 Cl + products
$CH_3CCl_3 + h\nu$	$\rightarrow$	3 Cl + products
Halon-1211 $+ h\nu$	$\rightarrow$	Br + Cl + products
Halon-1301 $+ h\nu$	$\rightarrow$	Br + products
$CH_3Br + h\nu$	$\rightarrow$	Br + products

All rate constants are set to the recommendations in the JPL 2006 catalogue (Sander et al., 2006) and its 2009 update (Sander et al., 2009).

The system of differential equations needed for the time integration has been created from the list of reactions using the Kinetic PreProcessor (KPP) (Sandu and Sander, 2006). The chemistry module uses a stiff solver for solving the differential equations, so no grouping in families is needed to allow for large integration time steps. The stiff solver is based on the Numerical Differentiation Formulas (NDFs) and uses an automatic adaptive time step (Shampine and Reichelt, 1997). A constraint on positive mixing ratios is built directly into the solver. The box model runs are parallelized.

2.1 Photolysis

Photolysis rates are interpolated from a 4-D look-up table as a function of pressure, temperature, solar zenith angle and overhead ozone column. Overhead ozone is calculated interactively from the ozone mixing ratios of the model. The photolysis table is based on absorption cross sections from JPL 2006 (Sander et al., 2006), except for Cl_2O_2, which are from Burkholder et al. (1990). The radiative transfer model TUV (Madronich and Flocke, 1999) is used to compute the photolysis rates. The table allows solar zenith angles of up to 98° to account for photochemistry under twilight conditions in the polar night.

2.2 Heterogeneous chemistry

The heterogeneous chemistry module is based on the equilibrium scheme by Carslaw et al. (1995). Three types of aerosols are considered: liquid ternary H_2SO_4-HNO_3-H_2O solutions, solid nitric acid trihydrate (NAT) particles and solid water ice particles.

The existence and composition of ternary solutions is calculated according to Carslaw et al. (1995). H_2SO_4 (assumed to be completely in the liquid phase) is taken from a simple climatology with a constant bell shaped profile relative to the mean tropopause which peaks at 0.5 ppb and has a vertical half width of about 5 km. The initial number density of droplets for ternary solutions is set to $10\,\mathrm{cm}^{-3}$. Surface area densities of the liquid aerosols can either be calculated in the module from the input parameters (assuming a lognormal distribution of droplet radii) or can be prescribed from measurements. A surface area density climatology based on SAGE data including volcanic aerosols is included in the model (Eyring et al., 2008). Ternary solutions are formed between 240 K and the formation temperature of ice.

NAT particles form if the saturation mixing ratio of HNO_3 over NAT is exceeded by a factor determined from a given supersaturation. Similarly, ice particles form if the saturation mixing ratio of H_2O over ice is exceeded by a given factor. Saturation mixing ratios (respectively formation temperatures T_{NAT} and T_{ice}) are calculated from the expressions in Hanson and Mauersberger (1988) and Marti and Mauersberger (1993). If NAT and liquid particles coexist, NAT particles are formed from the supercooled ternary solution droplets and the number density of the droplets and the available H_2SO_4 is adjusted accordingly. NAT surface area densities are calculated from the available HNO_3 by assuming a particle number density of $1\,\mathrm{cm}^{-3}$ and a uniform particle radius. Below T_{ice}, water ice clouds form in addition

Table 3. List of gas phase reactions.

Reaction			Reaction		
$\mathrm{O(^3P) + O(^3P) + M}$	$\rightarrow$	$\mathrm{O_2 + M}$	$\mathrm{CH_2O + Cl}$	$\rightarrow$	$\mathrm{HCl + CO + HO_2}$
$\mathrm{O(^3P) + O_2 + M}$	$\rightarrow$	$\mathrm{O_3 + M}$	$\mathrm{OH + HCl}$	$\rightarrow$	$\mathrm{H_2O + Cl}$
$\mathrm{O(^3P) + O_3}$	$\rightarrow$	$\mathrm{O_2 + O_2}$	$\mathrm{ClO + NO_2 + M}$	$\rightarrow$	$\mathrm{ClONO_2 + M}$
$\mathrm{O(^1D) + N_2}$	$\rightarrow$	$\mathrm{O(^3P) + N_2}$	$\mathrm{O(^3P) + ClONO_2}$	$\rightarrow$	$\mathrm{ClO + NO_3}$
$\mathrm{O(^1D) + O_2}$	$\rightarrow$	$\mathrm{O(^3P) + O_2}$	$\mathrm{ClO + HO_2}$	$\rightarrow$	$\mathrm{HOCl + O_2}$
$\mathrm{O(^1D) + O_3}$	$\rightarrow$	$\mathrm{O_2 + O_2}$	$\mathrm{OH + HOCl}$	$\rightarrow$	$\mathrm{H_2O + ClO}$
$\mathrm{O(^1D) + N_2 + M}$	$\rightarrow$	$\mathrm{N_2O + M}$	$\mathrm{O(^3P) + HOCl}$	$\rightarrow$	$\mathrm{OH + ClO}$
$\mathrm{O(^1D) + H_2O}$	$\rightarrow$	$\mathrm{OH + OH}$	$\mathrm{Cl + NO_2 + M}$	$\rightarrow$	$\mathrm{ClNO_2 + M}$
$\mathrm{O(^1D) + CH_4}$	$\rightarrow$	$\mathrm{OH + CH_2O + HO_2}$	$\mathrm{Cl + HOCl}$	$\rightarrow$	$\mathrm{OH + Cl_2}$
$\mathrm{O(^1D) + H_2}$	$\rightarrow$	$\mathrm{OH + H}$	$\mathrm{ClO + OH}$	$\rightarrow$	$\mathrm{HCl + O_2}$
$\mathrm{H + O_2 + M}$	$\rightarrow$	$\mathrm{HO_2 + M}$	$\mathrm{ClO + ClO}$	$\rightarrow$	$\mathrm{Cl + OClO}$
$\mathrm{H + O_3}$	$\rightarrow$	$\mathrm{OH + O_2}$	$\mathrm{ClO + ClO}$	$\rightarrow$	$\mathrm{Cl_2 + O_2}$
$\mathrm{O(^3P) + OH}$	$\rightarrow$	$\mathrm{O_2 + H}$	$\mathrm{ClO + ClO + M}$	$\rightarrow$	$\mathrm{Cl_2O_2 + M}$
$\mathrm{OH + O_3}$	$\rightarrow$	$\mathrm{HO_2 + O_2}$	$\mathrm{Cl_2O_2 + M}$	$\rightarrow$	$\mathrm{ClO + ClO + M}$
$\mathrm{HO_2 + O_3}$	$\rightarrow$	$\mathrm{OH + O_2 + O_2}$	$\mathrm{OClO + OH}$	$\rightarrow$	$\mathrm{HOCl + O_2}$
$\mathrm{O(^3P) + HO_2}$	$\rightarrow$	$\mathrm{OH + O_2}$	$\mathrm{Cl + OClO}$	$\rightarrow$	$\mathrm{ClO + ClO}$
$\mathrm{OH + HO_2}$	$\rightarrow$	$\mathrm{H_2O + O_2}$	$\mathrm{OClO + O(^3P)}$	$\rightarrow$	$\mathrm{ClO + O_2}$
$\mathrm{OH + H_2}$	$\rightarrow$	$\mathrm{H_2O + H}$	$\mathrm{OClO + NO}$	$\rightarrow$	$\mathrm{NO_2 + ClO}$
$\mathrm{H + HO_2}$	$\rightarrow$	$\mathrm{OH + OH}$	$\mathrm{Cl_2 + O(^1D)}$	$\rightarrow$	$\mathrm{Cl + ClO}$
$\mathrm{H + HO_2}$	$\rightarrow$	$\mathrm{H_2 + O_2}$	$\mathrm{Cl + Cl_2O_2}$	$\rightarrow$	$\mathrm{Cl_2 + Cl + O_2}$
$\mathrm{H + HO_2}$	$\rightarrow$	$\mathrm{H_2O + O(^3P)}$	$\mathrm{Cl + NO_3}$	$\rightarrow$	$\mathrm{ClO + NO_2}$
$\mathrm{H_2 + O(^3P)}$	$\rightarrow$	$\mathrm{OH + H}$	$\mathrm{ClO + NO_3}$	$\rightarrow$	$\mathrm{Cl + NO_2 + O_2}$
$\mathrm{NO + HO_2}$	$\rightarrow$	$\mathrm{NO_2 + OH}$	$\mathrm{O(^1D) + HCl}$	$\rightarrow$	$\mathrm{OH + Cl}$
$\mathrm{HO_2 + HO_2}$	$\rightarrow$	$\mathrm{H_2O_2 + O_2}$	$\mathrm{Cl_2 + OH}$	$\rightarrow$	$\mathrm{HOCl + Cl}$
$\mathrm{OH + H_2O_2}$	$\rightarrow$	$\mathrm{H_2O + HO_2}$	$\mathrm{Cl + ClONO_2}$	$\rightarrow$	$\mathrm{Cl_2 + NO_3}$
$\mathrm{OH + CO}$	$\rightarrow$	$\mathrm{CO_2 + H}$	$\mathrm{Cl + HO_2}$	$\rightarrow$	$\mathrm{ClO + OH}$
$\mathrm{OH + CO}$	$\rightarrow$	$\mathrm{CO_2 + HO_2}$	$\mathrm{Cl + H_2O_2}$	$\rightarrow$	$\mathrm{HCl + HO_2}$
$\mathrm{H_2O_2 + O(^3P)}$	$\rightarrow$	$\mathrm{OH + HO_2}$	$\mathrm{O(^3P) + HCl}$	$\rightarrow$	$\mathrm{OH + Cl}$
$\mathrm{OH + OH}$	$\rightarrow$	$\mathrm{O(^3P) + H_2O}$	$\mathrm{OH + ClONO_2}$	$\rightarrow$	$\mathrm{HOCl + NO_3}$
$\mathrm{OH + OH + M}$	$\rightarrow$	$\mathrm{H_2O_2 + M}$	$\mathrm{Br + O_3}$	$\rightarrow$	$\mathrm{BrO + O_2}$
$\mathrm{O(^3P) + NO_2}$	$\rightarrow$	$\mathrm{NO + O_2}$	$\mathrm{BrO + O(^3P)}$	$\rightarrow$	$\mathrm{Br + O_2}$
$\mathrm{O_3 + NO}$	$\rightarrow$	$\mathrm{NO_2 + O_2}$	$\mathrm{BrO + NO}$	$\rightarrow$	$\mathrm{NO_2 + Br}$
$\mathrm{N + NO}$	$\rightarrow$	$\mathrm{N_2 + O(^3P)}$	$\mathrm{BrO + ClO}$	$\rightarrow$	$\mathrm{OClO + Br}$
$\mathrm{N + O_2}$	$\rightarrow$	$\mathrm{NO + O(^3P)}$	$\mathrm{BrO + ClO}$	$\rightarrow$	$\mathrm{Br + Cl + O_2}$
$\mathrm{O_3 + NO_2}$	$\rightarrow$	$\mathrm{NO_3 + O_2}$	$\mathrm{BrO + ClO}$	$\rightarrow$	$\mathrm{BrCl + O_2}$
$\mathrm{NO_2 + NO_3 + M}$	$\rightarrow$	$\mathrm{N_2O_5 + M}$	$\mathrm{BrO + BrO}$	$\rightarrow$	$\mathrm{Br + Br + O_2}$
$\mathrm{OH + NO_2 + M}$	$\rightarrow$	$\mathrm{HNO_3 + M}$	$\mathrm{Br + HO_2}$	$\rightarrow$	$\mathrm{HBr + O_2}$
$\mathrm{HO_2 + NO_2 + M}$	$\rightarrow$	$\mathrm{HO_2NO_2 + M}$	$\mathrm{Br + OClO}$	$\rightarrow$	$\mathrm{BrO + ClO}$
$\mathrm{HO_2NO_2 + M}$	$\rightarrow$	$\mathrm{HO_2 + NO_2 + M}$	$\mathrm{Br + CH_2O}$	$\rightarrow$	$\mathrm{HBr + CO + HO_2}$
$\mathrm{HNO_3 + OH}$	$\rightarrow$	$\mathrm{H_2O + NO_3}$	$\mathrm{OH + HBr}$	$\rightarrow$	$\mathrm{H_2O + Br}$
$\mathrm{OH + HO_2NO_2}$	$\rightarrow$	$\mathrm{H_2O + NO_2 + O_2}$	$\mathrm{BrO + NO_2 + M}$	$\rightarrow$	$\mathrm{BrONO_2 + M}$
$\mathrm{N_2O_5 + M}$	$\rightarrow$	$\mathrm{NO_2 + NO_3 + M}$	$\mathrm{BrO + HO_2}$	$\rightarrow$	$\mathrm{HOBr + O_2}$
$\mathrm{O(^1D) + N_2O}$	$\rightarrow$	$\mathrm{N_2 + O_2}$	$\mathrm{HBr + O(^1D)}$	$\rightarrow$	$\mathrm{Br + OH}$
$\mathrm{O(^1D) + N_2O}$	$\rightarrow$	$\mathrm{NO + NO}$	$\mathrm{BrO + OH}$	$\rightarrow$	$\mathrm{Br + HO_2}$
$\mathrm{O(^3P) + NO_3}$	$\rightarrow$	$\mathrm{NO_2 + O_2}$	$\mathrm{HBr + O(^3P)}$	$\rightarrow$	$\mathrm{Br + OH}$
$\mathrm{OH + NO_3}$	$\rightarrow$	$\mathrm{NO_2 + HO_2}$	$\mathrm{BrONO_2 + O(^3P)}$	$\rightarrow$	$\mathrm{BrO + NO_3}$
$\mathrm{HO_2 + NO_3}$	$\rightarrow$	$\mathrm{NO_2 + OH + O_2}$	$\mathrm{H + NO_2}$	$\rightarrow$	$\mathrm{NO + OH}$
$\mathrm{HO_2 + NO_3}$	$\rightarrow$	$\mathrm{HNO_3 + O_2}$	$\mathrm{N + NO_2}$	$\rightarrow$	$\mathrm{N_2O + O(^3P)}$
$\mathrm{NO_2 + O(^3P) + M}$	$\rightarrow$	$\mathrm{NO_3 + M}$	$\mathrm{OClO + O_3}$	$\rightarrow$	$\mathrm{ClO + O_2 + O_2}$
$\mathrm{NO + O(^3P) + M}$	$\rightarrow$	$\mathrm{NO_2 + M}$	$\mathrm{O(^1D) + O_3}$	$\rightarrow$	$\mathrm{O(^3P) + O(^3P) + O_2}$
$\mathrm{NO + NO_3}$	$\rightarrow$	$\mathrm{NO_2 + NO_2}$	$\mathrm{ClO + O_3}$	$\rightarrow$	$\mathrm{Cl + O_2 + O_2}$
$\mathrm{CH_4 + OH}$	$\rightarrow$	$\mathrm{CH_2O + HO_2}$	$\mathrm{CFC\text{-}11{+}O(^1D)}$	$\rightarrow$	$\mathrm{3\,Cl + products}$
$\mathrm{OH + CH_2O}$	$\rightarrow$	$\mathrm{CO + HO_2 + H_2O}$	$\mathrm{CFC\text{-}12{+}O(^1D)}$	$\rightarrow$	$\mathrm{2\,Cl + products}$
$\mathrm{O(^3P) + CH_2O}$	$\rightarrow$	$\mathrm{CO + HO_2 + OH}$	$\mathrm{CFC\text{-}113 + O(^1D)}$	$\rightarrow$	$\mathrm{3\,Cl + products}$
$\mathrm{Cl + O_3}$	$\rightarrow$	$\mathrm{ClO + O_2}$	$\mathrm{HCFC\text{-}22 + O(^1D)}$	$\rightarrow$	$\mathrm{Cl + products}$
$\mathrm{ClO + O(^3P)}$	$\rightarrow$	$\mathrm{Cl + O_2}$	$\mathrm{HCFC\text{-}22 + OH}$	$\rightarrow$	$\mathrm{Cl + products}$
$\mathrm{ClO + NO}$	$\rightarrow$	$\mathrm{NO_2 + Cl}$	$\mathrm{CH_3Cl + OH}$	$\rightarrow$	$\mathrm{Cl + products}$
$\mathrm{Cl + CH_4}$	$\rightarrow$	$\mathrm{HCl + CH_2O + HO_2}$	$\mathrm{CCl_4 + O(^1D)}$	$\rightarrow$	$\mathrm{4\,Cl + products}$
$\mathrm{Cl + H_2}$	$\rightarrow$	$\mathrm{HCl + H}$	$\mathrm{CH_3CCl_3 + OH}$	$\rightarrow$	$\mathrm{3\,Cl + products}$
$\mathrm{Cl + HO_2}$	$\rightarrow$	$\mathrm{HCl + O_2}$	$\mathrm{CH_3Br + O(^1D)}$	$\rightarrow$	$\mathrm{Br + products}$
$\mathrm{ClO + OH}$	$\rightarrow$	$\mathrm{Cl + HO_2}$	$\mathrm{CH_3Br + OH}$	$\rightarrow$	$\mathrm{Br + products}$

Table 4. List of heterogeneous reactions. The cloud types on which the reactions happen are indicated (STS = supercooled ternary solution, NAT = nitric acid trihydrate).

Reaction			STS	NAT	Ice
$ClONO_2 + H_2O$	$\rightarrow$	$HOCl + HNO_3$	x	x	x
$ClONO_2 + HCl$	$\rightarrow$	$Cl_2 + HNO_3$	x	x	x
$N_2O_5 + H_2O$	$\rightarrow$	$HNO_3 + HNO_3$	x	x	x
$N_2O_5 + HCl$	$\rightarrow$	$ClNO_2 + HNO_3$		x	x
$HOCl + HCl$	$\rightarrow$	$Cl_2 + H_2O$	x	x	x
$BrONO_2 + H_2O$	$\rightarrow$	$HOBr + HNO_3$	x		
$HOBr + HCl$	$\rightarrow$	$BrCl + H_2O$	x		

to NAT clouds. Surface area densities are calculated from the available H_2O by assuming a particle number density of $0.01\,\mathrm{cm}^{-3}$ and a uniform particle radius. The fractions of HNO_3, H_2O and HCl contained in the cloud particles are not available for gas phase reactions.

2.3 Lagrangian denitrification

The model contains a Lagrangian denitrification module based on the DLAPSE model (Carslaw et al., 2002), which is implemented in the ATLAS model in a way similar to Grooß et al. (2005). Denitrification removes nitrogen by sedimenting PSC particles and can lead to additional ozone loss by impeding deactivation of chlorine into $ClONO_2$. Denitrification in 1999/2000 was presumably caused by large NAT particles with radii above 10 µm (Fahey et al., 2001). The scheme is based on the sedimentation of these NAT particles and not on the sedimentation of ice particles with co-condensed NAT or the sedimentation of smaller NAT particles, since both approaches would not be effective enough to explain the observed denitrification.

The denitrification module uses an independent second set of Lagrangian parcels for representing the particles, in addition to the air parcels that are used for transport and chemistry. Particles are created with a constant nucleation rate where NAT formation is possible and are allowed to sediment and change size in the following time steps until they eventually evaporate. These particles exist in the model in addition to the particles that are formed in the heterogenous chemistry module (these are usually smaller with typical radii of 1 µm). The coexistence of both particle modes is necessary to allow for a sufficient chlorine activation on the large surface area of the small mode and denitrification due to the Lagrangian particles at the same time. The small mode is assumed not to grow and sediment due to the depletion of HNO_3 where these particles exist.

After every mixing step, new NAT particles are initialized at the positions of all air parcels of the model which are below the formation temperature of NAT (the procedure is somewhat different from Grooß et al. (2005), which uses more particles). Any of these particles is representative for a much larger number of real NAT particles, since the number of simulated particles needs to stay at a manageable level. This is considered by a scaling factor if interaction with the background nitric acid field is done. Particles are initialized with a uniform initial radius and are transported with the trajectory module of the model. Horizontal velocities are taken from the wind fields of the analysis, while the vertical velocities are the sum of the terminal fall velocities of the particles and the vertical velocities of the analysis. Terminal fall velocities $\mathrm{d}z/\mathrm{d}t$ of the particles are calculated from the particle radii r by $\mathrm{d}z/\mathrm{d}t = Cr^2$, where C depends on the viscosity of air and the crystal mass density of NAT. Particle growth is calculated by $\mathrm{d}r/\mathrm{d}t = G/r$ where G is a growth factor depending on the supersaturation of HNO_3 with respect to NAT. If the calculated radius drops below zero, the particle evaporates. Details on the calculation of the fall velocities and the growth factor can be found in Appendix A.

For interaction with the background HNO_3 field, the four air parcels of the model which form the enclosing tetrahedron of the particle are determined. At each of these four air parcels, it is assumed that a number density n_{NAT} of NAT particles with the properties of the enclosed particle is present. If an air parcel is adjacent to several particles, the number densities are added. n_{NAT} is the scale factor mentioned above and is a free parameter of the model which has to be tuned to observations. Note that the choice of air parcels is handled differently in Grooß et al. (2005). HNO_3 in the gas phase is depleted if the NAT particle has grown in the last time step and set free if it decreased in size. A nucleation rate can be estimated from n_{NAT} by multiplying it with four (for the four air parcels affected in each step) and dividing it by the mixing time step of the model.

The denitrification module is called after the chemistry module has calculated the evolution of the species for the length of the mixing time step (the chemistry module includes the equilibrium model of the heterogeneous chemistry module, which uses the total HNO_3 not contained in the Lagrangian particles and partitions it into the gas phase and the solid phase for the small particles of the equilibrium model). The initial background HNO_3 for the denitrification module is taken from the final total mixing ratio produced by the chemistry module (and not contained in the Lagrangian particles). Then the denitrification module is run for the length of the mixing time step (process splitting). Finally, HNO_3 contained in the Lagrangian particles and the total background HNO_3 is adjusted according to the results of the denitrification module.

If small particles are formed in the equilibrium model, they would leave exactly the saturation mixing ratio of HNO_3 in the gas phase. That would impede the growth of the Lagrangian particles, since the growth factor G would be zero in this case. The total and not the gas phase HNO_3 is used as the available HNO_3 in the denitrification model to avoid this behaviour. Under typical circumstances, when more HNO_3

than the saturation mixing ratio is available, a part of the available background HNO_3 is put into the Lagrangian particles in every mixing time step, while the gas phase HNO_3 is constantly forced to the saturation mixing ratio, leaving less and less HNO_3 for the small particles of the equilibrium model. That is, the combination of the equilibrium module and the particle module tends to transform particles from the small mode to the large mode with a time constant dependent on G and n_{nat}.

This simplified scheme seems a reasonable compromise for two reasons: First, the exact mechanisms of the formation of the large and small NAT particle modes are still unknown. Second, the chlorine activation on the small mode and the denitrification due to the large mode are normally sufficiently fast (on the order of some days) for details of the exact timing not to matter for ozone loss and most of the chemistry.

2.4 Freeze drying

The only microphysical process apart from PSC formation and sedimentation considered in the model is freeze drying of water vapor at the tropical tropopause. It is assumed that all water vapor above the saturation mixing ratio is condensed and immediately removed from the air parcel by sedimentation.

3 Model setup

3.1 Setup

Model runs are driven by meteorological data from the ECMWF ERA Interim reanalysis (Simmons et al., 2006, 2007) on 60 model levels (6 h temporal resolution, $2° \times 2°$ horizontal resolution). Horizontal model resolution (as the initial mean separation of air parcels) is 150 km. Vertical resolution is 1–2 km (in log-pressure altitude). The runs use the hybrid pressure-potential temperature coordinate of the model (Wohltmann and Rex, 2009), which is almost a pure potential temperature coordinate in the stratosphere. Heating rates (clear sky) from ERA Interim are used as the vertical velocity. The lower model boundary is at the hybrid level 350 K and the upper boundary at 1900 K. Mixing strength by the Lyapunov exponent is set to $3\,\mathrm{d}^{-1}$ (optimal mixing, see Wohltmann and Rex, 2009) and the mixing time step to 12 h. The run is started on 1 November 1999 and ends on 16 March 2000. Chemical species are initialized on 1 December. Chemical species at the lower and upper boundary are re-initialized every 12 h, as described in Wohltmann and Rex (2009).

In addition to the chemical species, two tracers are initialized. A passive ozone tracer is initialized with the ozone values of 1 December, but no chemistry acts on the tracer in the following. The difference between the passive ozone tracer and the chemically active ozone is then a measure for chemical ozone depletion. In an equivalent way, a passive NO_y tracer is set up by adding up all nitrogen-containing species (except for N_2O). The difference between this tracer and NO_y is then a measure for denitrification by sedimenting particles, since the number of N atoms in NO_y cannot be changed by chemistry (except by reactions with N_2O).

A run with Lagrangian denitrification and a run without denitrification are started for comparison. n_{NAT} is set to 2.34×10^{-5} particles per cm^3, which corresponds to a nucleation rate of 7.8×10^{-6} particles per h and cm^3 (as in Grooß et al., 2005). No further sensitivity analyses are performed for this study, which focusses on the model description. The initial radius of the NAT particles is set to 0.1 µm.

A supersaturation of 5 is assumed necessary for the formation of the small NAT mode. The value is estimated from test runs by comparing measurements of HNO_3 on flights of the ER-2 aircraft (see below) to the equilibrium values of HNO_3 over NAT that should be present according to the measured temperatures and modeled water vapour.

3.2 Measurements used for initialization and comparison

A large number of measurements from many different instruments on different platforms is used to initialize the model in the following. Additionally, model results are compared to a similarly diverse collection of measurements. The following section gives an overview over the used data.

16 flights of the ER-2 high-altitude aircraft in altitudes of up to 20 km were performed during the campaign between 6 January and 16 March 2000. Flights between 20 January and 12 March started from Kiruna (Sweden) and probed the stratospheric polar vortex and surf zone, while the other flights were transfer and test flights. Table 5 shows the instruments onboard the ER-2 that are used for comparison and Table 6 shows a time table of the campaign.

ACATS-IV is a gas chromatograph measuring every 70–140 s (Romashkin et al., 2001), while Argus and ALIAS are tunable diode laser instruments measuring with a high time resolution of 2 s (Loewenstein et al., 2002; Webster et al., 1994). These three instruments observe several long-lived species (CFCs, Halons, N_2O, CH_4). The instrument measuring ozone is a dual-beam UV-absorption ozone photometer (Proffitt and McLaughlin, 1983). Water vapor is observed by a tunable diode laser instrument from JPL (May, 1998; Herman et al., 2002) and a fluorescence instrument from Harvard (Weinstock et al., 1994). The NOAA NO_y instrument measures NO and NO_y (that is, all reactive nitrogen reduced to NO on a catalysator) by chemiluminescence (Fahey et al., 1989, 2001). The instrument uses two different inlets with different sample characteristics with respect to aerosol particle size. Here, data of the rear inlet are used, which samples the gas phase and particles with a diameter of less than about 2 µm. Note that the instrument oversamples particles compared to the ambient air. HNO_3 in the gas phase

Table 5. Measurements used for initialization and comparison.

Platform	Instrument	Species	Citation
ER-2	ACATS-IV	N_2O, CH_4, CFC-11, CFC-12, CFC-113, Halon-1211, CH_3CCl_3, CCl_4	Romashkin et al. (2001)
ER-2	Argus	N_2O, CH_4	Loewenstein et al. (2002)
ER-2	ALIAS	N_2O, CH_4	Webster et al. (1994)
ER-2	Harvard H2O	H_2O	Weinstock et al. (1994)
ER-2	JPL JLH	H_2O	May (1998); Herman et al. (2002)
ER-2	Harvard CO2	CO_2	Boering et al. (1994)
ER-2	NOAA O3	O_3	Proffitt and McLaughlin (1983); Richard et al. (2001)
ER-2	Harvard ClONO2	$ClONO_2$, NO_2, ClO, Cl_2O_2	Stimpfle et al. (1999, 2004)
ER-2	NOAA NOy	NO_y in gas and solid phase (see text), NO	Fahey et al. (1989, 2001)
ER-2	Cal. Tech. CIMS	gas phase HNO_3	Dhaniyala et al. (2003) McKinney et al. (2004)
ER-2	Harvard HOx	OH, HO_2	Hanisco et al. (2002)
OMS remote	JPL Mark IV	H_2O, O_3, N_2O, CO, CH_4, NO, NO_2, HNO_3, HCl, ClO, CH_2O, HOCl, H_2O_2, N_2O_5, $ClONO_2$, CH_3Cl, CFC-11, CFC-12, CCl_4, HCFC-22, CFC-113	Toon (1991)
OMS remote	JPL SLS	O_3, HCl, ClO, N_2O, HNO_3	Stachnik et al. (1992)
OMS in-situ	NOAA LACE	CFC-11, CFC-12, Halon-1211, N_2O, H_2, CH_4	Ray et al. (2002)
Triple	Cryogenic WAS	N_2O, CH_4, Cl_y	Grooß et al. (2002)
–	Ozone sondes	O_3	
UARS	HALOE	O_3, CH_4, H_2O, HCl, NO_x	Grooß and Russell III (2005)
SCISAT-1	ACE FTS	HNO_3, CO	K. Walker, personal communication, 2010; Jones et al. (2010)

is measured by a chemical ionization mass spectrometer (CIMS) instrument (Dhaniyala et al., 2003; McKinney et al., 2004). The Harvard $ClONO_2$-NO_2-ClO-Cl_2O_2 instrument (Stimpfle et al., 1999, 2004) is composed of a laser-induced resonance fluorescence instrument for measuring NO_2 and a resonance fluorescence instrument for ClO. Cl_2O_2 and $ClONO_2$ are measured by thermal dissociation into ClO. The Harvard HO_x instrument measures OH by laser-induced fluorescence (Hanisco et al., 2002). HO_2 is transformed to OH by chemical titration. CO_2 is observed by infrared absorption (Boering et al., 1994).

Measurement uncertainties are typically a few percent for most instruments and are not shown in the subsequent plots. For some instruments the accuracies are not negligible and indicated by thin lines. This applies to the ClO (34% at 2σ), Cl_2O_2 (42%), $ClONO_2$ (42%) and NO_2 (20%) measurements (Stimpfle et al., 2004) and the OH (26%) and HO_2 (40%) measurements (Hanisco et al., 2002). Measurements are typically made every few seconds for most instruments. Exceptions are ACATS-IV (70–140 s), CIMS (alternates between gas phase and solid measurements every 3 min), ClO (35 s), Cl_2O_2 and $ClONO_2$ (more than 35 s).

Several balloon ascents are used for initialization and comparison. There were two balloon ascents of the OMS balloon with remote sensing measurements from the solar occultation Mark IV interferometer (Toon, 1991) and the Submillimeter Limb Sounder (SLS) instrument (Stachnik et al., 1992) on 3 December 1999 (used for initialization and comparison) and 15 March 2000 (used for comparison). Measured species can be found in Table 5. The OMS balloon was launched with an in-situ payload including the LACE instrument on 19 November 1999 (used for initialization) and 5 March 2000 (used for comparison). Cryogenic whole air sampler measurements on Triple balloon ascents on 27 January 2000 and 1 March are used for initialization (Grooß et al., 2002).

Measurements of the HALOE solar occultation instrument onboard the UARS satellite were used both for initialization and comparison. Measurements of the solar occultation ACE FTS interferometer instrument onboard the SCISAT-1 satellite were also used for initialization. Additionally, a number of ozone sondes from the stations Ny-Ålesund (high latitudes, Spitzbergen), Hohenpeissenberg (mid-latitudes, Germany) and Paramaribo (Suriname) and Samoa (tropics, SHADOZ data set, see Thompson et al., 2003) are used for comparison.

Table 6. Time table of the measurements.

Date	Activity
19 Nov	OMS balloon in-situ
3 Dec	OMS balloon remote
6 Jan	ER-2 (pre-campaign)
9 Jan	ER-2 (pre-campaign)
11 Jan	ER-2 (pre-campaign)
14 Jan	ER-2 (transfer)
20 Jan	ER-2 (vortex)
23 Jan	ER-2 (vortex)
27 Jan	ER-2 (across vortex edge) Triple balloon
31 Jan	ER-2 (vortex)
2 Feb	ER-2 (vortex)
3 Feb	ER-2 (vortex)
26 Feb	ER-2 (vortex)
1 Mar	Triple balloon
5 Mar	ER-2, OMS balloon in-situ
7 Mar	ER-2 (vortex)
11 Mar	ER-2 (across vortex edge)
12 Mar	ER-2 (vortex)
15 Mar	OMS balloon remote
16 Mar	ER-2 (transfer)

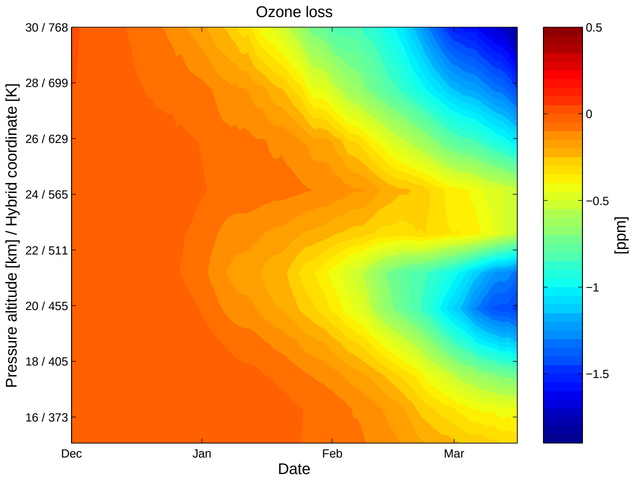

Fig. 2. Vortex-averaged ozone loss as function of model date and altitude. Difference between the passive ozone tracer and the modeled ozone averaged over all air parcels inside the inner vortex boundary according to the Nash criterion (Nash et al., 1996) and over several hybrid coordinate (i.e. potential temperature) intervals equivalent to the mixing depth of the model. Before 24 December 1999, the Nash criterion is not applicable and replaced by a constant value of 67° equivalent latitude.

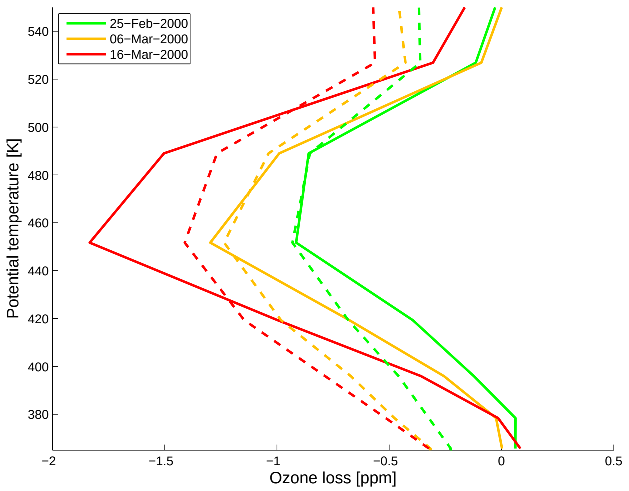

Fig. 3. Vortex-averaged ozone loss profiles for selected dates from measurements of ozone sondes treated by the vortex-average method (Rex et al., 2002, solid lines) and from the vortex-averaged results of the model (as in Fig. 2, but different vortex edge criterion, dashed lines). Results of the vortex-average method are convoluted to the altitude resolution of the model. The vortex edge criterion is identical to the one in Rex et al. (2002), both for model and measurements (40, 41, and 40 units of normalized PV, respectively).

3.3 Initialization

The long-lived species H_2O, CH_4, O_3 and HCl are initialized from monthly mean HALOE data of November and December 1999 as a function of equivalent latitude φ_E and pressure (Grooß and Russell III, 2005). All NO_x from the monthly mean HALOE data set is put into NO. Since HALOE is not able to measure in high latitudes and darkness, the CH_4 profiles inside the vortex ($\varphi_E > 64°$ N) are replaced by a single constant OMS in situ balloon profile from the LACE instrument determined on 19 November 1999 (Ray et al., 2002). O_3 and HCl in the vortex are replaced in the same way by measurements of the Mark IV instrument (Toon, 1991) on the OMS remote sensing balloon flight on 3 December 1999. N_2O is initialized from a N_2O-CH_4 tracer-tracer relationship derived from ER-2 and Triple balloon data (Grooß et al., 2002). HNO_3 and CO are taken from a climatology (2004–2009 mean) based on ACE FTS data as a function of pressure and equivalent latitude (K. Walker, personal communication, 2010; Jones et al., 2010). HNO_3 inside the vortex is taken from the Mark IV measurement (see above). $ClONO_2$ outside the vortex is initialized in two steps: first Cl_y is calculated from a Cl_y-CH_4 relationship from ER-2 and Triple data (Grooß et al., 2002), where Cl_y is deduced from the sum of the measured organic source gases. $ClONO_2$ is then calculated as the difference between HCl and Cl_y. Negative values are set to zero. Maximum Cl_y values obtained in this way are 3.4 ppb. $ClONO_2$ inside the vortex is again taken from the Mark IV instrument.

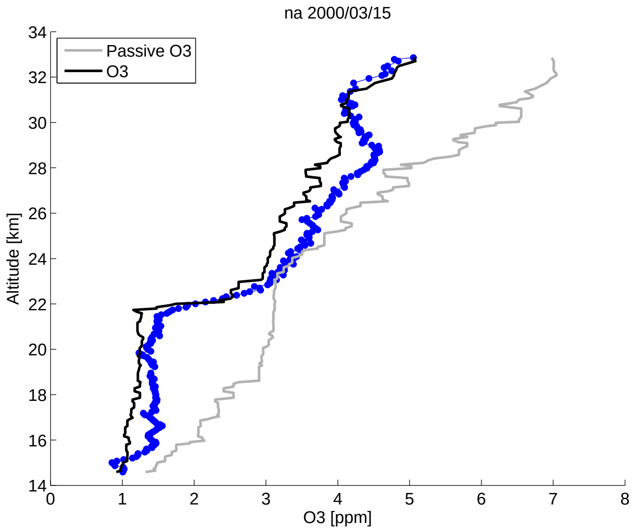

Fig. 4. Ozone sonde measurement from Ny-Ålesund, Spitzbergen on 15 March 2000 (blue dots) compared to modeled ozone values (black line). The grey line shows the passive ozone tracer to indicate the amount of ozone loss.

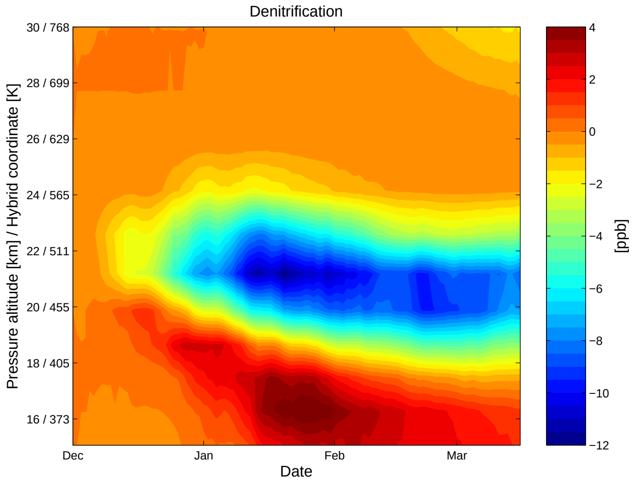

Fig. 5. Vortex-averaged denitrification as the difference of the passive NO_y tracer and modeled NO_y, averaged as in Fig. 2.

$BrONO_2$ is assumed to contain all Br_y, which is taken from a Br_y-CH_4 relationship from ER-2 data in Grooß et al. (2002), with Br_y again deduced from the measured organic source gases. The relationship does also contain a contribution from some short-lived source gases of 2–3 ppt. The relationship is only valid for methane values smaller than 1.64 ppm, for values between 1.64 and 1.8 ppm, Br_y values are decreased from 6 ppt to 0 ppt. The obtained Br_y is scaled by a constant factor to give maximum Br_y values of 19.9 ppt to agree with Differential Optical Absorption Spectroscopy (DOAS) measurements of BrO (Dorf et al., 2008).

CFC-11, CFC-12 and Halon-1211 are initialized by CH_4 tracer relationships derived from the LACE instrument on the OMS balloon flight on 19 November 1999 (Ray et al., 2002). Other CFCs and related species (CFC-113, HCFC-22, CCl_4, CH_3CCl_3, CH_3Cl, CH_3Br, Halon-1301) are initialized from their tropospheric mixing ratios and an age-of-air tracer. If the age of air is t_{age}, the current date is t and the tropospheric mixing ratio is x_{tropo}, the stratospheric mixing ratio is

$$x_{\mathrm{strato}} = (1 - f(t_{\mathrm{age}}))x_{\mathrm{tropo}}(t - t_{\mathrm{age}}) \tag{1}$$

The fractional release factor f is the fraction of the source gas released into other substances. Age of air is taken from the t_{age}-N_2O relationships described in Woodbridge et al. (1995) and Andrews et al. (2001). Mixing ratios are calculated using both age-of-air relationships and averaging the results. Fractional release factors as a function of age of air are taken from Laube et al. (2010). Tropospheric mixing ratios are from input files of the CCMVal project (Eyring et al., 2008), which are based on WMO (2007). CO_2 is initialized with the same method and $f = 0$, tropospheric mixing ratios are taken from CCMVal based on IPCC (2001). All other species are set to zero.

4 Model results

In the next section, model results are compared to observations and results from other studies. The comparison includes the most important chemical families: oxygen species (ozone and ozone loss), nitrogen species (NO_y, NO_x, denitrification), chlorine species (ClO_x and Cl_y), hydrogen species (HO_x) and long-lived source gases. Only an exemplary subset of all comparisons conducted for this study is shown. A complete list of figures can be found in the Supplement, including the flight parameters (flight path, altitude, solar zenith angle and so on) for the balloons and ER-2 flights.

In the following, model results coincident to the measurements are obtained as follows: a short backward trajectory is calculated starting at the location and time of the measurement and ending at the time of the last model output before the measurement (model fields are saved every 12 h). Typically, trajectories are started every 10 s along the flight path for the ER-2 measurements. Mixing ratios of all chemical species are interpolated from the neighboring air parcels of the model to the end location (i.e. earliest time) of the trajectory as initialization for the chemistry model. Now, the chemical box model is used to calculate the chemical evolution forward in time on the trajectory. The last computed value of each chemical species (coincident with the measurement date) is used as the model value to compare with. This procedure is needed since some of the shorter-lived species change substantially in the time period between model output and measurement date.

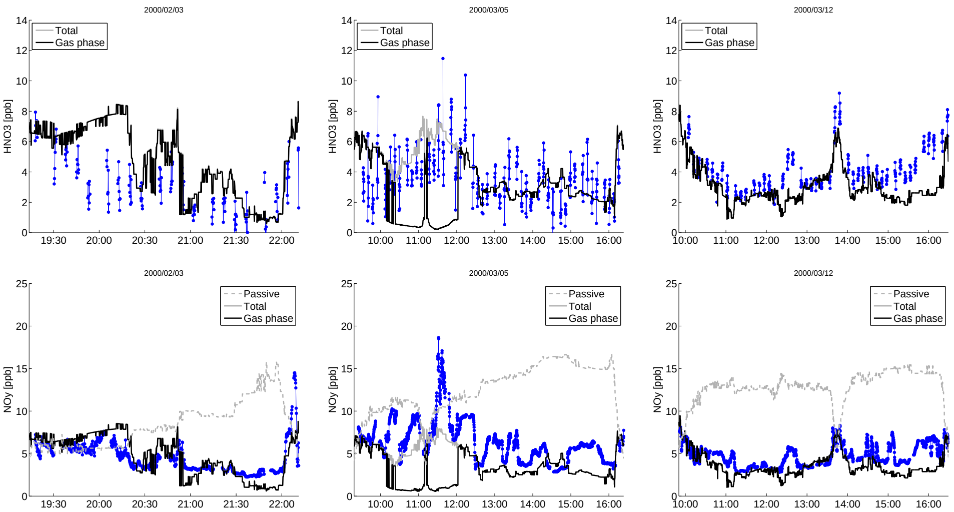

Fig. 6. HNO_3 (top) and NO_y (bottom) as a function of flight time (UTC) from measurements of selected ER-2 flights (3 February, 5 March, 12 March) (blue dots) compared to modeled values (lines). NO_y measurements give the total (solid and gas phase, for details see text) values, HNO_3 measurements show only the gas phase. The black line shows the model values for the gas phase, the grey line the total (solid not in the Lagrangian particles and gas phase) values and the dashed grey line the passive NO_y tracer.

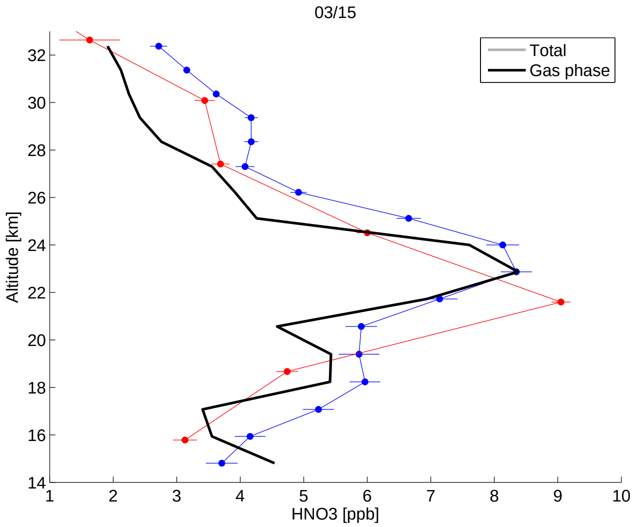

Fig. 7. HNO_3 profile from the OMS balloon launch on 15 March 2000 measured by the Mark IV instrument (blue) and the SLS instrument (red). The black line shows the modeled profile. Note that Mark IV and SLS are remote sensing instruments viewing into opposite directions and that the mixing ratios of the species are interpolated to the Mark IV tangent points.

4.1 Ozone loss

Figure 2 shows the vortex-averaged ozone loss of the model for the run including denitrification. Ozone loss sets in about the beginning of January and develops a pronounced double-peak structure in altitude. While the lower peak is clearly due to ozone loss by halogens set free by heterogeneous reactions, the upper peak is probably due to NO_x induced loss. The lower peak shows maximum loss values of 1.5 ppm averaged over the layer from 433 K to 471 K in mid-March (approximately 50% ozone loss). The run without denitrification shows maximum loss values of 1.25 ppm, corresponding to about 17% additional loss (0.25 ppm) by denitrification (not shown). Figure 3 shows the observed ozone loss deduced from ozone sondes by the vortex-average method and convoluted to the altitude resolution of the model (Rex et al., 2002) in comparison to the simulated ozone loss. The simulated ozone loss is generally in good agreement with the observations. Only for the latest date in mid-March, the sharp peak of 1.9 ppm in the observations is smeared out somewhat in the simulation.

Comparison of the modeled ozone to individual ozone sondes or ozone measurements on the ER-2 flights generally shows good agreement (see Fig. 4 for a sounding from Ny-Ålesund, Spitzbergen, on 15 March and the Supplement for more examples). There is some discrepancy between the results of the vortex-average method from Rex et al. (2002) and the direct comparison to measurements: if anything, the comparison with individual sondes and ER-2 flights shows a slight overestimation of the loss by the model. This might be due to different heating rates and different initialization of the passive ozone profile in the model and in the vortex-average method. In addition, passive ozone in the vortex-average method is assumed not to be affected by mixing, while the passive ozone in the model can be changed by

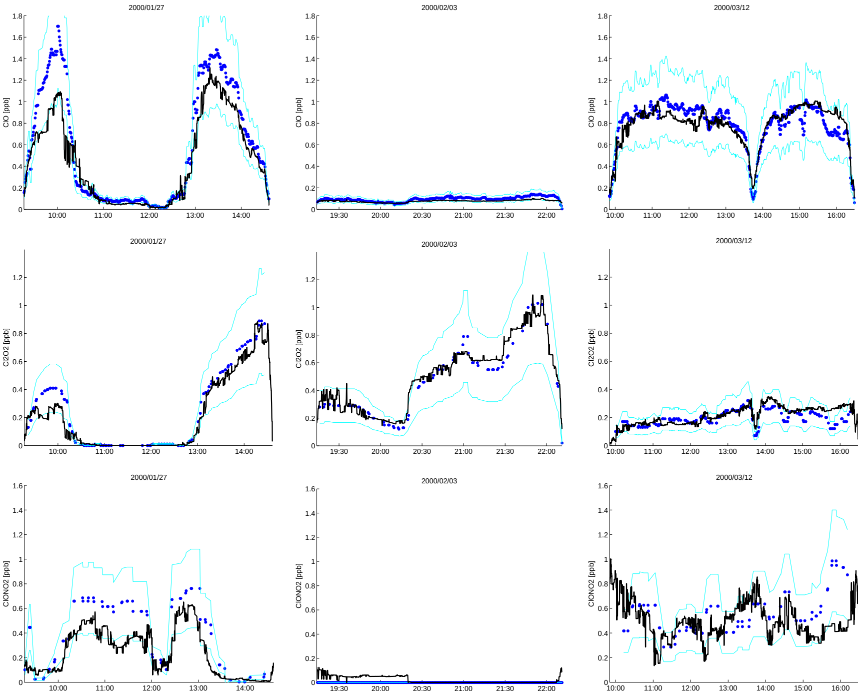

Fig. 8. ClO (top), Cl_2O_2 (middle) and $ClONO_2$ (bottom) as a function of flight time (UTC) from measurements of selected ER-2 flights (27 January, 3 February, 12 March) (blue dots, cyan lines show 2σ accuracy) compared to modeled values (black lines).

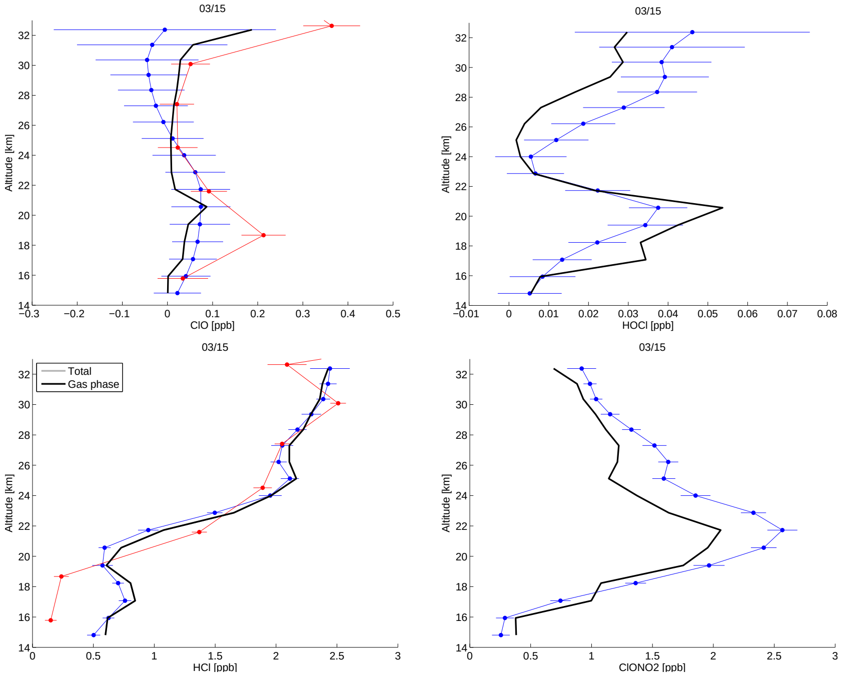

Fig. 9. ClO and its reservoirs HOCl, HCl and $ClONO_2$ from data of the OMS balloon launch on 15 March 2000. Measurements of the Mark IV instrument (blue, with error bars), the SLS instrument (red) and modeled values (black lines) are shown for comparison. Note that Mark IV and SLS are remote sensing instruments viewing into opposite directions and that the mixing ratios of the species are interpolated to the Mark IV tangent points.

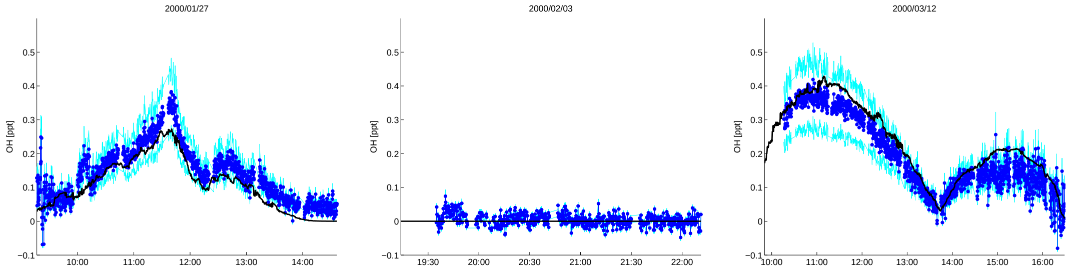

Fig. 10. OH as a function of flight time (UTC) from measurements of selected ER-2 flights (27 January, 3 February, and 12 March) (blue dots, cyan lines show 2σ accuracy) compared to modeled values (black lines).

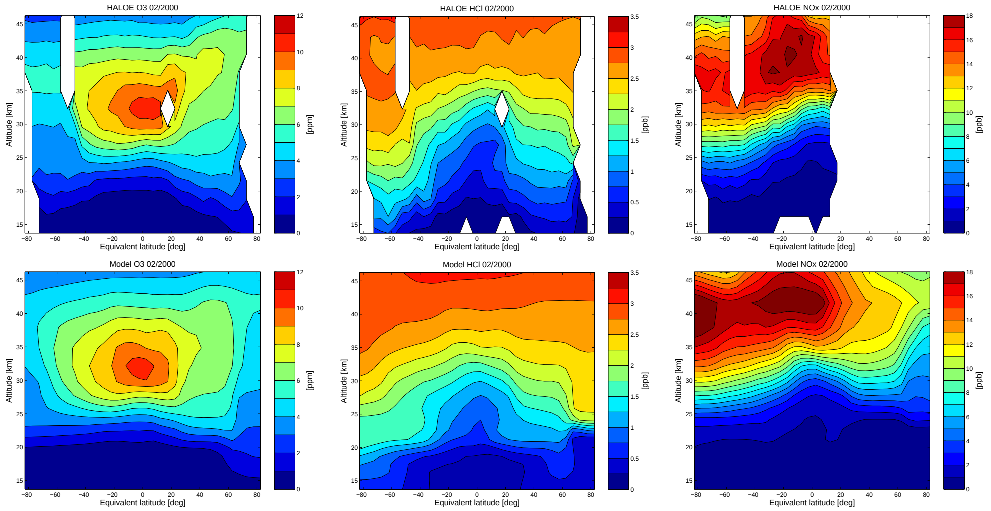

Fig. 11. Zonal and monthly mean mixing ratios for O_3, HCl and NO_x as a function of pressure altitude and equivalent latitude for February 2000. Top: HALOE measurements, bottom: modeled values.

mixing from outside the vortex (see Grooß et al., 2008). There is also some variation of ozone loss with equivalent latitude in the model results, with highest values of 1.7 ppm ozone loss in the vortex core in mid-March (not shown). A direct estimate of ozone loss from the ER-2 flights by tracer correlations gives a loss of 1.8 ± 0.3 ppm (Richard et al., 2001). The general overestimation of ozone loss on both sides of the ozone loss peak could be due to a slightly too high vertical diffusivity in the model.

The agreement of simulated and observed ozone loss is very encouraging if compared with similar results from other models. The current version of the Eulerian model SLIMCAT captures the magnitude of the observations relatively well, but shows considerable differences in the shape of the profile (Chipperfield et al., 2005, their Fig. 2, note the different period 15 January to 25 March). The MIMOSA-CHIM model (Tripathi et al., 2006) shows an ozone loss of 1.9 ppm at 475 K at the end of March (and about 1.75 ppm in mid March). Magnitude and shape of the ozone loss profile (their Fig. 1) and ER-2 comparisons (their Fig. 2) are in good agreement with our results.

In general, the ozone loss estimate from our model seems to be on the low side of the loss estimates from the other models presented here. The modeled additional ozone loss by denitrification of 17% (0.25 ppm) is in good agreement with Tripathi et al. (2006) (23% and 0.2–0.4 ppm).

The vortex-average method is not applicable to the upper peak, but ozone sonde measurements inside the vortex show good agreement with the model results up to 35 km. As an example, the sounding from Ny-Ålesund on 15 March is shown in Fig. 4.

4.2 Denitrification and nitrogen species

Figure 5 shows the modeled denitrification. Denitrification begins in early December and reaches peak values of 12 ppb in January in the layer from 471–507 K. The denitrified layer typically extends over the levels from 433–594 K. Below the denitrified layer, renitrification is strongest (with maximum values of about 4.5 ppb) at altitudes of about 371–386 K. The vertical extent and magnitude of denitrification in the model are in good agreement with the results of the denitrification study by Popp et al. (2001), which used ER-2 and Mark IV measurements (see also the direct comparison below). The denitrification scheme typically produces maximum particle radii of 10 µm at altitudes between 16–18 km, somewhat smaller than observed by Fahey et al. (2001).

Figure 6 shows selected ER-2 measurements of NO_y and HNO_3 and Fig. 7 shows HNO_3 profiles from the Mark IV and SLS instruments on an OMS balloon ascent on 15 March 2000. The agreement between the modeled and observed NO_y and HNO_3 is quite reasonable, given the facts that there are considerable uncertainties in PSC formation and denitrification mechanisms and that the model was not tuned to the observations by sensitivity studies.

Note that the flight on 5 March shows no activity of polar stratospheric clouds, while the model formed PSCs. The flight on 5 March shows signs of supersaturation with respect to NAT. The assumed constant supersaturation of 5 in the model can only be an approximation to the complex formation processes of the clouds and it is difficult to find a value that matches all measurements. Some smaller discrepancies occur for the flights on 26 February, 5 March, and 7 March and species like gas phase HNO_3 (underestimation), $ClONO_2$ (underestimation) and ClO_x (slight overestimation), see Supplement.

NO and NO_2 are generally near zero inside the vortex in the model at the ER-2 flight altitude, in agreement with the measurements (see Supplement).

4.3 ClO_x and its reservoirs

In general, the modeled evolution of both active chlorine (ClO, Cl_2O_2) and its reservoir gases (HCl, $ClONO_2$, HOCl) agrees with the measurements inside the error bars. However, there are some indications in the ER-2 and Mark IV data that $ClONO_2$ might be a little bit too low.

Figure 8 shows measurements of ClO, Cl_2O_2 and the reservoir species $ClONO_2$ from selected ER-2 flights and Fig. 9 shows measurements of ClO, HOCl, HCl and $ClONO_2$ of the Mark IV and the SLS instrument from the OMS balloon ascent on 15 March 2000. The flight on 27 January crossed the vortex edge, showing that the difference between vortex and surf zone is modeled well. The flight on 3 February shows measurements in darkness with high mixing ratios of the night-time reservoir Cl_2O_2 and low mixing ratios of ClO, while the flight on 12 March took place in daylight and shows deactivation of chlorine into $ClONO_2$. More comparisons can be found in the Supplement.

4.4 HO_x

Measured and modeled values of HO_x agree inside the error bars of the measurements for most of the ER-2 flights. Figure 10 shows comparisons of modeled OH values to measurements from selected ER-2 flights. HO_2 shows a similarly good agreement (see Supplement).

4.5 Long-lived species

All major long-lived species (N_2O, CH_4, H_2O, CO_2, CFC-11, CFC-12) are reproduced very well, both at all ER-2 flights and at all vertical profiles of the balloon flights (see Supplement). The agreement for CH_4 and Halon-1211 has already been demonstrated in Wohltmann and Rex (2009). This gives confidence that the ERA Interim reanalysis driving the runs (and the formulation of the model) reproduce the general circulation in a sufficiently good quality. Differences of the chemical species between model and measurements are therefore likely due to problems in the chemistry module or measurement error.

4.6 Agreement outside the polar vortex

The data situation outside the vortex is somewhat worse than for polar measurements. Comparison of the modeled values with global zonal mean HALOE data, tropical ozone sondes and the precampaign ER-2 test flights show that the model is able to simulate the global large scale features of the chemical species correctly, albeit some of the species show larger differences outside the vortex due to the inferior initialization (see Supplement). As an example, Fig. 11 shows zonal and monthly mean mixing ratios of O_3, HCl and NO_x from HALOE measurements compared to model results for February 2000.

5 Summary

The model run with denitrification shows an excellent agreement with ER-2 aircraft, balloon and other measurements during the SOLVE/THESEO 2000 campaign. This is true both for long-lived tracers and species from all important chemical families, including ozone, chlorine species, nitrogen species and hydrogen species.

A maximum ozone loss of 1.5 ppm or 50% averaged over 433–471 K and the polar vortex is simulated in mid-March, including an additional loss of 0.25 ppm (17%) due to denitrification. The simulated ozone loss is in good agreement with observations.

The denitrification module produces a pronounced denitrification of up to 12 ppb and particles of maximum sizes of 10 µm (which are somewhat smaller particles than observed). Given the fact that no sensitivity studies with respect to denitrification and heterogeneous chemistry were conducted for this model description paper, the agreement with HNO_3 and NO_y measurements from the ER-2 is surprisingly good.

No major differences between model and observations are found in this study, indicating that Chemical Transport Models of the stratosphere could have reached a state of maturity.

There are still considerable uncertainties remaining (e.g. in the formation mechanisms of polar stratospheric clouds or in denitrification mechanisms), but often the model results are relatively insensitive to them (e.g. to the exact mechanisms of chlorine activation, as long as it is sufficiently fast).

Appendix A

Details of the denitrification scheme

If not indicated otherwise, equations are taken from Carslaw et al. (2002). New particles are initialized at the positions of all model air parcels below T_{NAT} at every mixing time step with a uniform initial radius r_0. Particles are advected by the same wind field that acts on the air parcels. Additionally, the vertical velocity is modified by the terminal fall velocity of the particle, which for spherical particles in the Stokes regime is given by

$$\frac{\mathrm{d}z}{\mathrm{d}t} = \frac{2g\rho_{\mathrm{NAT}}C_{\mathrm{C}}r^2}{9\eta} \tag{A1}$$

where g is acceleration due to gravity, $\rho_{\mathrm{NAT}} = 1.62 \times 10^3\,\mathrm{kg\,m^{-3}}$ is the mass density of NAT (of the solid, not per volume of air) (Mann et al., 2003),

$$C_{\mathrm{C}} = 1 + \frac{\lambda}{r}\left(1.257 + 0.4\exp\left(\frac{-1.1r}{\lambda}\right)\right) \tag{A2}$$

is the Cunningham slip correction factor ($\lambda = k_{\mathrm{B}}T/(4\sqrt{2}\pi r_{\mathrm{air}}^2 p)$ mean free path of molecules, $r_{\mathrm{air}} \approx 3\times10^{-10}$ m radius of air molecule, k_{B} the Boltzmann constant, T temperature) and

$$\eta = 18.27 \times 10^{-6}\frac{T_0 + C}{T + C}\left(\frac{T}{T_0}\right)^{3/2} \tag{A3}$$

is the viscosity of air in Pa s ($C = 120$ K, $T_0 = 291.15$ K) (White, 1991). The growth of a NAT particle is given by

$$\frac{\mathrm{d}r}{\mathrm{d}t} = \frac{G}{r} \tag{A4}$$

where G is a growth factor. Integration gives that the radius of the particle is changed by

$$\Delta r = \sqrt{r^2 + 2G\Delta t} - r \tag{A5}$$

in every time step Δt of the trajectory model (every 30 min). If r gets negative, it is assumed that the particle evaporated and it is deleted. G is given by

$$G = \frac{D^*_{\mathrm{HNO_3}} m_{\mathrm{NAT}}}{\rho_{\mathrm{NAT}} k_{\mathrm{B}} T}\left(p_{\mathrm{HNO_3}} - p^{\mathrm{NAT}}_{\mathrm{HNO_3}}\right) \tag{A6}$$

where $D^*_{\mathrm{HNO_3}}$ is a modified diffusion coefficient of HNO_3 in air, $m_{\mathrm{NAT}} = 117 \times 1.66 \times 10^{-27}$ kg is the mass of a NAT molecule, $p_{\mathrm{HNO_3}}$ the partial pressure of HNO_3 and $p^{\mathrm{NAT}}_{\mathrm{HNO_3}}$ the saturation pressure of HNO_3 over NAT. $D^*_{\mathrm{HNO_3}}$ is a diffusion coefficient modified for non-continuum effects for small particles comparable to the mean free path,

$$D^*_{\mathrm{HNO_3}} = \frac{D_{\mathrm{HNO_3}}}{1 + 4D_{\mathrm{HNO_3}}/(\bar{c}_{\mathrm{HNO_3}} r)} \tag{A7}$$

where $\bar{c}_{\mathrm{HNO_3}} = \sqrt{8k_{\mathrm{B}}T/(\pi m_{\mathrm{HNO_3}})}$ is the mean molecular speed ($m_{\mathrm{HNO_3}} = 63 \times 1.66 \times 10^{-27}$ kg mass of HNO_3 molecule) and

$$D_{\mathrm{HNO_3}} = 0.113\left(\frac{T}{T_0}\right)^{1.94}\left(\frac{p_0}{p}\right) \tag{A8}$$

the diffusion coefficient of HNO_3 in air in $\mathrm{cm^2\,s^{-1}}$ ($p_0 = 1013.25$ hPa, $T_0 = 273$ K) (Wofsy et al., 1990).

The change of HNO_3 mixing ratio in an air parcel if assuming a NAT particle number density n_{NAT} in that parcel is

$$-\frac{4}{3}\pi\left((r+\Delta r)^3 - r^3\right)\rho_{\mathrm{NAT}}\frac{n_{\mathrm{NAT}} k_{\mathrm{B}} T}{m_{\mathrm{NAT}}\, p} \tag{A9}$$

The HNO_3 mixing ratio is changed according to this equation in the four air parcels of the model that form the enclosing tetrahedron of the NAT particle (obtained by triangulation) in every trajectory time step. HNO_3 is either depleted or set free depending on the sign of the equation.

Supplementary material related to this article is available online at: http://www.geosci-model-dev.net/3/585/2010/gmd-3-585-2010-supplement.pdf.

Acknowledgements. We thank ECMWF for providing reanalysis data, R. Salawitch (U. Maryland) for providing the merged ER-2 data files, R. Stimpfle (Harvard U.) for providing ER-2 ClO, $ClONO_2$ and Cl_2O_2 data, K. Perkins (Harvard U.) for providing NO_2 data, D. Fahey (NOAA, National Oceanic and Atmospheric Administration) for providing ER-2 NO_y and NO data, P. Wennberg (Cal. Tech.) for providing ER-2 CIMS HNO_3 data, T. Hanisco (Harvard U.) for providing ER-2 HO_x data, C. R. Webster (JPL, Jet Propulsion Laboratory, California Institute of Technology) for providing the ALIAS data, R. Herman (JPL) for providing ER-2 JLH H_2O data, R. Spackman and E. Weinstock (Harvard U.) for providing ER-2 Harvard H_2O data, S. Wofsy (Harvard U.) for providing ER-2 CO_2 data, E. Richard (NOAA) for providing ER-2 O_3 data, G. C. Toon (JPL) for providing Mark IV data, R. Stachnik (JPL) for providing SLS data, H. Claude (DWD) for the Hohenpeissenberg ozone sonde data, A. M. Thompson, H. Kelder, S. Oltmans and the SHADOZ programme for the Samoa and Paramaribo ozone sonde data, V. Eyring and the CCMVal activity for providing forcing data (greenhouse gases, CFCs, halons and surface area densities), J. W. Elkins (NOAA) for providing ACATS-IV and LACE data, H. Jost (NASA Ames Research Center) for providing the Argus data, K. Walker (U. Toronto) for providing ACE FTS data (The Atmospheric Chemistry Experiment (ACE), also known as SCISAT, is a Canadian-led mission mainly supported by the Canadian Space Agency), J.-U. Grooß and J. M. Russell III for providing HALOE data and ER-2 and Triple balloon tracer relationships. Work at AWI was supported by the EC DG research through the SHIVA project (SHIVA-226224-FP7-ENV-2008-1) and the SCOUT-O3 project.

Edited by: P. Jöckel

References

Andrews, A. E., Boering, K. A., Daube, B. C., Wofsy, S. C., Loewenstein, M., Jost, H., Podolske, J. R., Webster, C. R., Herman, R. L., Scott, D. C., Flesch, G. J., Moyer, E. J., Elkins, J. W., Dutton, G. S., Hurst, D. F., Moore, F. L., Ray, E. A., Romashkin, P. A., and Strahan, S. E.: Mean ages of stratospheric air derived from in situ observations of CO_2, CH_4, and N_2O, J. Geophys. Res., 106, 32295–32314, 2001.

Boering, K. A., Daube, B. C., Wofsy, S. C., Loewenstein, M., Podolske, J. R., and Keim, E. R.: Tracer-tracer relationships and lower stratospheric dynamics: CO_2 and N_2O during SPADE, Geophys. Res. Lett., 21, 2567–2570, 1994.

Burkholder, J. B., Orlando, J. J., and Howard, C. J.: Ultraviolet absorption cross sections of chlorine oxide (Cl_2O_2) between 210 and 410 nm, J. Phys. Chem.-US, 94, 687–695, 1990.

Carslaw, K. S., Luo, B., and Peter, T.: An analytical expression for the composition of aqueous HNO_3-H_2SO_4 stratospheric aerosols including gas phase removal of HNO_3, Geophys. Res. Lett., 22, 1877–1880, 1995.

Carslaw, K. S., Kettleborough, J. A., Northway, M. J., Davies, S., Gao, R.-S., Fahey, D. W., Baumgardner, D. G., Chipperfield, M. P., and Kleinböhl, A.: A vortex-scale simulation of the growth and sedimentation of large nitric acid hydrate particles, J. Geophys. Res., 107, 8300, doi:10.1029/2001JD000467, 2002.

Chipperfield, M. P., Feng, W., and Rex, M.: Arctic ozone loss and climate sensitvity: updated three-dimensional model study, Geophys. Res. Lett., 32, 11813, doi:10.1029/2005GL022674, 2005.

Collins, W. J., Stevenson, D. S., Johnson, C. E., and Derwent, R. G.: Tropospheric ozone in a global-scale three-dimensional Lagrangian model and its response to NO_x emission controls, J. Atmos. Chem., 26, 223–274, 1997.

Dhaniyala, S., Flagan, R. C., McKinney, K. A., and Wennberg, P. O.: Novel aerosol/gas inlet for aircraft-based measurements, Aerosol Sci. Tech., 37, 828–840, 2003.

Dorf, M., Butz, A., Camy-Peyret, C., Chipperfield, M. P., Kritten, L., and Pfeilsticker, K.: Bromine in the tropical troposphere and stratosphere as derived from balloon-borne BrO observations, Atmos. Chem. Phys., 8, 7265–7271, doi:10.5194/acp-8-7265-2008, 2008.

Eyring, V., Chipperfield, M., Giorgetta, M. A., Kinnison, D. E., Manzini, E., Matthes, K., Newman, P. A., Pawson, S., Shepherd, T. G., and Waugh, D. W.: Overview of the new CCMVal reference and sensitivity simulations in support of upcoming ozone and climate assessments and the planned SPARC CCMVal report, SPARC News Lett., 30, 20–26, 2008.

Fahey, D. W., Kelly, K. K., Ferry, G. V., Poole, L. R., Wilson, J. C., Murphy, D. M., Loewenstein, M., and Chan, K. R.: In situ measurements of total reactive nitrogen, total water and aerosol in a polar stratospheric cloud in the Antarctic, J. Geophys. Res., 94, 11299–11315, 1989.

Fahey, D. W., Gao, R. S., Carslaw, K. S., Kettleborough, J., Popp, P. J., Northway, M. J., Holecek, J. C., Ciciora, S. C., McLaughlin, R. J., Thompson, T. L., Winkler, R. H., Baumgardner, D. G., Gandrud, B., Wennberg, P. O., Dhaniyala, S., McKinney, K., Peter, T., Salawitch, R. J., Bui, T. P., Elkins, J. W., Webster, C. R., Atlas, E. L., Jost, H., Wilson, J. C., Herman, R. L., Kleinböhl, A., and von König, M.: The detection of large HNO_3-containing particles in the winter Arctic stratosphere, Science, 291, 1026–1031, 2001.

Grooß, J.-U. and Russell III, James M.: Technical note: A stratospheric climatology for O_3, H_2O, CH_4, NO_x, HCl and HF derived from HALOE measurements, Atmos. Chem. Phys., 5, 2797–2807, doi:10.5194/acp-5-2797-2005, 2005.

Grooß, J.-U., Günther, G., Konopka, P., Müller, R., McKenna, D. S., Stroh, F., Vogel, B., Engel, A., Müller, M., Hoppel, K., Bevilacqua, R., Richard, E., Webster, C. R., Elkins, J. W., Hurst, D. F., Romashkin, P. A., and Baumgardner, D. G.: Simulation of ozone depletion in spring 2000 with the Chemical Lagrangian Model of the Stratosphere (CLaMS), J. Geophys. Res., 107, 8295, doi:10.1029/2001JD000456, 2002.

Grooß, J.-U., Günther, G., Müller, R., Konopka, P., Bausch, S., Schlager, H., Voigt, C., Volk, C. M., and Toon, G. C.: Simulation of denitrification and ozone loss for the Arctic winter 2002/2003, Atmos. Chem. Phys., 5, 1437–1448, doi:10.5194/acp-5-1437-2005, 2005.

Grooß, J.-U., Müller, R., Konopka, P., Steinhorst, H.-M., Engel, A., Möbius, T., and Volk, C. M.: The impact of transport across the polar vortex edge on Match ozone loss estimates, Atmos. Chem. Phys., 8, 565–578, doi:10.5194/acp-8-565-2008, 2008.

Hanisco, T. F., Smith, J. B., Stimpfle, R. M., Wilmouth, D. M., Anderson, J. G., Richard, E. C., and Bui, T. P.: In situ observations of HO_2 and OH obtained on the NASA ER-2 in the high-ClO conditions of the 1999/2000 Arctic polar vortex, J. Geophys. Res., 107, 8283, doi:10.1029/2001JD001024, 2002.

Hanson, D. and Mauersberger, K.: Laboratory studies of the nitric acid trihydrate: Implications for the south polar stratosphere, Geophys. Res. Lett., 15, 855–858, 1988.

Herman, R. L., Drdla, K., Spackman, J. R., Hurst, D. F., Popp, P. J., Webster, C. R., Rosmashkin, P. A., Elkins, J. W., Weinstock, E. M., Gandrud, B. W., Toon, G. C., Schoeberl, M. R., Jost, H., Atlas, E. L., and Bui, T. P.: Hydration, dehydration, and the total hydrogen budget of the 1999/2000 winter Arctic stratosphere, J. Geophys. Res., 107, 8320, doi:10.1029/2001JD001257, 2002.

IPCC: Climate Change 2001: The scientific basis. Contribution of working group I to the third assessment report of the Intergovernmental Panel on Climate Change, Cambridge University Press, Cambridge, UK and New York, NY, USA, 2001.

Jones, A., Walker, K. A., Jin, J., Taylor, J. R., Boone, C. D., Bernath, P. F., Manney, G. L., McLeod, S., and Hughes, R.: A description of the ACE-FTS global climatological datasets, in preparation, 2010.

Konopka, P., Steinhorst, H.-M., Grooß, J.-U., Günther, G., Müller, R., Elkins, J. W., Jost, H.-J., Richard, E., Schmidt, U., Toon, G., and McKenna, D. S.: Mixing and ozone loss in the 1999–2000 Arctic vortex: simulations with the three-dimensional Chemical Lagrangian Model of the Stratosphere (CLaMS), J. Geophys. Res., 109, D02315, doi:10.1029/2003JD003792, 2004.

Konopka, P., Günther, G., Müller, R., dos Santos, F. H. S., Schiller, C., Ravegnani, F., Ulanovsky, A., Schlager, H., Volk, C. M., Viciani, S., Pan, L. L., McKenna, D.-S., and Riese, M.: Contribution of mixing to upward transport across the tropical tropopause layer (TTL), Atmos. Chem. Phys., 7, 3285–3308, doi:10.5194/acp-7-3285-2007, 2007.

Krämer, M., Müller, R., Bovensmann, H., Burrows, J., Brinkmann, J., Röth, E. P., Grooß, J.-U., Müller, R., Woyke, T., Ruhnke, R., Günther, G., Hendricks, J., Lippert, E., Carslaw, K. S., Peter, T., Zieger, A., Brühl, C., Steil, B., Lehmann, R., and McKenna, D. S.: Intercomparison of stratospheric chemistry models under polar vortex conditions, J. Atmos. Chem., 45, 51–77, 2003.

Laube, J. C., Engel, A., Bönisch, H., Möbius, T., Sturges, W. T., Braß, M., and Röckmann, T.: Fractional release factors of long-lived halogenated organic compounds in the tropical stratosphere, Atmos. Chem. Phys., 10, 1093–1103, doi:10.5194/acp-10-1093-2010, 2010.

Lehmann, R.: An algorithm for the determination of all significant pathways in chemical reaction systems, J. Atmos. Chem., 47, 45–78, 2004.

Loewenstein, M., Jost, H., Grose, J., Eilers, J., Lynch, D., Jensen, S., and Marmie, J.: Argus: a new instrument for the measurement of the stratospheric dynamical tracers, N_2O and CH_4, Spectrochim. Acta A, 58, 2329–2345, 2002.

Madronich, S. and Flocke, S.: The role of solar radiation in atmospheric chemistry, in: Handbook of Environmental Chemistry, edited by: Boule, P., Springer-Verlag, Heidelberg, 1–26, 1999.

Mann, G.W., Davies, S., Carslaw, K. S., and Chipperfield, M. P.: Factors controlling Arctic denitrification in cold winters of the 1990s, Atmos. Chem. Phys., 3, 403–416, doi:10.5194/acp-3-403-2003, 2003.

Marti, J. and Mauersberger, K.: A survey and new measurements of ice vapor pressure at temperatures between 170 and 250 K, Geophys. Res. Lett., 20, 363–366, 1993.

May, R. D.: Open-path, near-infrared tunable diode laser spectrometer for atmospheric measurements of H_2O, J. Geophys. Res., 103, 19161–19172, 1998.

McKenna, D. S., Grooß, J.-U., Günther, G., Konopka, P., and Müller, R.: A new Chemical Lagrangian Model of the Stratosphere (CLaMS) 2. Formulation of chemistry scheme and initialization, J. Geophys. Res., 107, 4256, doi:10.1029/2000JD000113, 2002.

McKinney, K. A., Wennberg, P. O., Dhaniyala, S., Fahey, D. W., Northway, M. J., Künzi, K. F., Kleinböhl, A., Sinnhuber, M., Küllmann, H., Bremer, H., Mahoney, M. J., and Bui, T. P.: Trajectory studies of large HNO_3-containing PSC particles in the Arctic: evidence for the role of NAT, Geophys. Res. Lett., 31, L05110, doi:10.1029/2003GL018430, 2004.

Nash, E. R., Newman, P. A., Rosenfield, J. E., and Schoeberl, M. R.: An objective determination of the polar vortex using Ertel's potential vorticity, J. Geophys. Res., 101, 9471–9478, 1996.

Newman, P., Harris, N. R. P., Adriani, A., Amanatidis, G. T., Anderson, J. G., Braathen, G. O., Brune, W. H., Carslaw, K. S., Craig, M. S., DeCola, P. L., Guirlet, M., Hipskind, R. S., Kurylo, M. J., Küllmann, H., Larsen, N., Mégie, G. J., Pommereau, J.-P., Poole, L. R., Schoeberl, M. R., Stroh, F., Toon, O. B., Trepte, C. R., and Roozendael, M. V.: An overview of the SOLVE-THESEO 2000 campaign, J. Geophys. Res., 107, 8259, doi:10.1029/2001JD001303, 2002.

Popp, P. J., Northway, M. J., Holecek, J. C., Gao, R. S., Fahey, D. W., Elkins, J. W., Hurst, D. F., Romashkin, P. A., Toon, G. C., Sen, B., Schauffler, S. M., Salawitch, R. J., Webster, C. R., Herman, R. L., Jost, H., Bui, T. P., Newman, P. A., and Lait, L. R.: Severe and extensive denitrification in the 1999–2000 Arctic winter stratosphere, Geophys. Res. Lett., 28, 2875–2878, 2001.

Proffitt, M. H. and McLaughlin, R. J.: Fast-response dual-beam UV-absorption ozone photometer suitable for use on stratospheric balloons, Rev. Sci. Instrum., 54, 1719–1728, 1983.

Ray, E. A., Moore, F. L., Elkins, J. W., Hurst, D. F., Romashkin, P. A., Dutton, G. S., and Fahey, D. W.: Descent and mixing in the 1999–2000 northern polar vortex inferred from in situ tracer measurements, J. Geophys. Res., 107, 8285, doi:10.1029/2001JD000961, 2002.

Reithmeier, C. and Sausen, R.: ATTILA: atmospheric tracer transport in a Lagrangian model, Tellus B, 54, 278–299, 2002.

Rex, M., Salawitch, R. J., Harris, N. R. P., von der Gathen, P., Braathen, G. O., Schulz, A., Deckelmann, H., Chipperfield, M., Sinnhuber, B.-M., Reimer, E., Alfier, R., Bevilacqua, R., Hoppel, K., Fromm, M., Lumpe, J., Küllmann, H., Kleinböhl, A., Bremer, H., von König, M., Künzi, K., Toohey, D., Vömel, H., Richard, E., Aikin, K., Jost, H., Greenblatt, J. B., Loewenstein, M., Podolske, J. R., Webster, C. R., Flesch, G. J., Scott, D. C., Herman, R. L., Elkins, J. W., Ray, E. A., Moore, F. L., Hurst, D. F., Romashkin, P., Toon, G. C., Sen, B., Margitan, J. J., Wennberg, P., Neuber, R., Allart, M., Bojkov, B. R., Claude, H., Davies, J., de Backer, H., Dier, H., Dorokhov, V., Fast, H., Kondo, Y., Kyrö, E., Litynska, Z., Mikkelsen, I. S., Molyneux, M. J., Moran, E., Nagai, T., Nakane, H., Parrondo, C., Ravegnani, F., Skrivankova, P., Viatte, P., and Yushkov, V.: Chemical depletion of Arctic ozone in winter 1999/2000, J. Geophys. Res., 107, 8276, doi:10.1029/2001JD000533, 2002.

Richard, E. C., Aikin, K. C., Andrews, A. E., Daube, Jr., B. C., Gerbig, C., Wofsy, S. C., Romashkin, P. A., Hurst, D. F., Ray, E. A., Moore, F. L., Elkins, J. W., Deshler, T., and Toon, G. C.: Severe chemical ozone loss inside the Arctic polar vortex during winter 1999–2000 inferred from in situ airborne measurements, Geophys. Res. Lett., 28, 2197–2200, 2001.

Romashkin, P. A., Hurst, D. F., Elkins, J. W., Dutton, G. S., Fahey, D. W., Dunn, R. E., Moore, F. L., Myers, R. C., and Hall, B. D.: In situ measurements of long-lived trace gases in the lower stratosphere by gas chromatography, J. Atmos. Oceanic Technol., 18, 1195–1204, 2001.

Sander, S. P., Friedl, R. R., Ravishankara, A. R., Golden, D. M., Kolb, C. E., Kurylo, M. J., Molina, M. J., Moortgat, G. K., Finlayson-Pitts, B. J., Wine, P. H., Huie, R. E., and Orkin, V. L.: Chemical kinetics and photochemical data for use in atmospheric studies, Evaluation Number 15, JPL Publication 06-2, Jet Propulsion Laboratory, California Institute of Technology, Pasadena, available at: http://jpldataeval.jpl.nasa.gov (last access: May 2010), 2006.

Sander, S. P., Friedl, R. R., Abatt, J., Barker, J. R., Burkholder, J. B., Golden, D. M., Kolb, C. E., Kurylo, M. J., Moortgat, G. K., Wine, P. H., Huie, R. E., and Orkin, V. L.: Chemical kinetics and photochemical data for use in atmospheric studies, Evaluation Number 16, JPL Publication 09-31, Jet Propulsion Laboratory, California Institute of Technology, Pasadena, available at: http://jpldataeval.jpl.nasa.gov (last access: May 2010), 2009.

Sandu, A. and Sander, R.: Technical note: Simulating chemical systems in Fortran90 and Matlab with the Kinetic PreProcessor KPP-2.1, Atmos. Chem. Phys., 6, 187–195, doi:10.5194/acp-6-187-2006, 2006.

Shampine, L. F. and Reichelt, M. W.: The MATLAB ODE Suite, SIAM J. Sci. Comput., 18, 1–22, 1997.

Simmons, A. J., Uppala, S. M., Dee, D., and Kobayashi, S.: ERA-Interim: new ECMWF reanalysis products from 1989 onwards, ECMWF News Lett., 110, 25–35, 2006.

Simmons, A. J., Uppala, S. M., and Dee, D.: Update on ERA-Interim, ECMWF News Lett., 111, 5, 2007.

Stachnik, R. A., Hardy, J. C., Tarsala, J. A., and Waters, J. W.: Submillimeterwave heterodyne measurements of stratospheric ClO, HCl, O_3 and HO_2: first results, Geophys. Res. Lett., 19, 1931–1934, 1992.

Stimpfle, R. M., Cohen, R. C., Bonne, G. P., Voss, P. B., Perkins, K. K., Koch, L. C., Anderson, J. G., Salawitch, R. J., Lloyd, S. A., Gao, R. S., DelNegro, L. A., Keim, E. R., and Bui, T. P.: The coupling of $ClONO_2$, ClO, and NO_2 in the lower stratosphere from in situ observations using the NASA ER-2 aircraft, J. Geophys. Res., 104, 26705–26714, 1999.

Stimpfle, R. M., Wilmouth, D. M., Salawitch, R. J., and Anderson, J. G.: First measurements of ClOOCl in the stratosphere: the coupling of ClOOCl and ClO in the Arctic polar vortex, J. Geophys. Res., 109, D03301, doi:10.1029/2003JD003811, 2004.

Thompson, A. M., Witte, J. C., McPeters, R. D., Oltmans, S. J., Schmidlin, F. J., Logan, J. A., Fujiwara, M., Kirchhoff, V. W. J. H., Posny, F., Coetzee, G. J. R., Hoegger, B., Kawakami, S., Ogawa, T., Johnson, B., Vömel, H., and Labow, G.: Southern Hemisphere Additional Ozonesondes (SHADOZ) 1998–2000 tropical ozone climatology 1. Comparison with Total Ozone Mapping Spectrometer (TOMS) and ground-based measurements, J. Geophys. Res., 108, 8238, doi:10.1029/2001JD000967, 2003.

Toon, G. C.: The JPL MklV interferometer, Opt. Photonics News, 2, 19–21, 1991.

Tripathi, O. P., Godin-Beekmann, S., Lefèvre, F., Marchand, M., Pazmiño, A., Hauchecorne, A., Goutail, F., Schlager, H., Volk, C. M., Johnson, B., König-Langlo, G., Balestri, S., Stroh, F., Bui, T. P., Jost, H. J., Deshler, T., and von der Gathen, P.: High resolution simulation of recent Arctic and Antarctic stratospheric chemical ozone loss compared to observations, J. Atmos. Chem., 55, 205–226, doi:10.1007/s10874-006-9028-8, 2006.

Webster, C. R., May, R. D., Trimble, C. A., Chave, R. G., and Kendall, J.: Aircraft (ER-2) laser infrared absorption spectrometer (ALIAS) for in-situ stratospheric measurements of HCI, N_2O, CH_4, NO_2, and HNO_3, Appl. Optics, 33, 454–472, 1994.

Weinstock, E. M., Hintsa, E. J., Dessler, A. E., Oliver, J. F., Hazen, N. L., Demusz, J. N., Allen, N. T., Lapson, L. B., and Anderson, J. G.: New fast response photofragment fluorescence hygrometer for use on the NASA ER-2 and the Perseus remotely piloted aircraft, Rev. Sci. Instrum., 65, 3544–3554, 1994.

White, F. M.: Viscous Fluid Flow, McGraw-Hill, New York, 1991.

WMO: World Meteorological Organization (WMO)/United Nations Environment Programme (UNEP), Scientific assessment of ozone depletion: 2006, Global Ozone Research and Monitoring Project – Report No. 50, 2007.

Wofsy, S. C., Gobbi, G. P., Salawitch, R. J., and McElroy, M. B.: Nucleation and growth of $HNO_3 \cdot 3H_2O$ particles in the polar stratosphere, J. Atmos. Sci., 47, 2004–2012, 1990.

Wohltmann, I. and Rex, M.: The Lagrangian chemistry and transport model ATLAS: validation of advective transport and mixing, Geosci. Model Dev., 2, 153–173, doi:10.5194/gmd-2-153-2009, 2009.

Woodbridge, E. L., Elkins, J. W., Fahey, D. W., Heidt, L. E., Solomon, S., Baring, T. J., Gilpin, T. M., Pollock, W. H., Schauffler, S. M., Atlas, E. L., Loewenstein, M., Podolske, J. R., Webster, C. R., May, R. D., Gilligan, J. M., Montzka, S. A., Boering, K. A., and Salawitch, R. J.: Estimates of total organic and inorganic chlorine in the lower stratosphere from in situ and flask measurements during AASE II, J. Geophys. Res., 100, 3057–3064, 1995.

ARTICLE

doi:10.1038/nature10556

Unprecedented Arctic ozone loss in 2011

Gloria L. Manney[1,2], Michelle L. Santee[1], Markus Rex[3], Nathaniel J. Livesey[1], Michael C. Pitts[4], Pepijn Veefkind[5,6], Eric R. Nash[7], Ingo Wohltmann[3], Ralph Lehmann[3], Lucien Froidevaux[1], Lamont R. Poole[8], Mark R. Schoeberl[9], David P. Haffner[7], Jonathan Davies[10], Valery Dorokhov[11], Hartwig Gernandt[3], Bryan Johnson[12], Rigel Kivi[13], Esko Kyrö[13], Niels Larsen[14], Pieternel F. Levelt[5,6,15], Alexander Makshtas[16], C. Thomas McElroy[10], Hideaki Nakajima[17], Maria Concepción Parrondo[18], David W. Tarasick[10], Peter von der Gathen[3], Kaley A. Walker[19] & Nikita S. Zinoviev[16]

Chemical ozone destruction occurs over both polar regions in local winter–spring. In the Antarctic, essentially complete removal of lower-stratospheric ozone currently results in an ozone hole every year, whereas in the Arctic, ozone loss is highly variable and has until now been much more limited. Here we demonstrate that chemical ozone destruction over the Arctic in early 2011 was—for the first time in the observational record—comparable to that in the Antarctic ozone hole. Unusually long-lasting cold conditions in the Arctic lower stratosphere led to persistent enhancement in ozone-destroying forms of chlorine and to unprecedented ozone loss, which exceeded 80 per cent over 18–20 kilometres altitude. Our results show that Arctic ozone holes are possible even with temperatures much milder than those in the Antarctic. We cannot at present predict when such severe Arctic ozone depletion may be matched or exceeded.

Since the emergence of the Antarctic ‘ozone hole’ in the 1980s[1] and elucidation of the chemical mechanisms[2–5] and meteorological conditions[6] involved in its formation, the likelihood of extreme ozone depletion over the Arctic has been debated. Similar processes are at work in the polar lower stratosphere in both hemispheres, but differences in the evolution of the winter polar vortex and associated polar temperatures have in the past led to vastly disparate degrees of springtime ozone destruction in the Arctic and Antarctic. We show that chemical ozone loss in spring 2011 far exceeded any previously observed over the Arctic. For the first time, sufficient loss occurred to reasonably be described as an Arctic ozone hole.

Arctic polar processing in 2010–11

In the winter polar lower stratosphere, low temperatures induce condensation of water vapour and nitric acid (HNO_3) into polar stratospheric clouds (PSCs). PSCs and other cold aerosols provide surfaces for heterogeneous conversion of chlorine from longer-lived reservoir species, such as chlorine nitrate ($ClONO_2$) and hydrogen chloride (HCl), into reactive (ozone-destroying) forms, with chlorine monoxide (ClO) predominant in daylight[5,7].

In the Antarctic, enhanced ClO is usually present for 4–5 months (through to the end of September)[8–11], leading to destruction of most of the ozone in the polar vortex between ~14 and 20 km altitude[7]. Although ClO enhancement comparable to that in the Antarctic occurs at some times and altitudes in most Arctic winters[9], it rarely persists for more than 2–3 months, even in the coldest years[10]. Thus chemical ozone loss in the Arctic has until now been limited, with largest previous losses observed in 2005, 2000 and 1996[7,12–14].

The 2010–11 Arctic winter–spring was characterized by an anomalously strong stratospheric polar vortex and an atypically long continuously cold period. In February–March 2011, the barrier to transport at the Arctic vortex edge was the strongest in either hemisphere in the last ~30 years (Fig. 1a, Supplementary Discussion).

The persistence of a strong, cold vortex from December through to the end of March was unprecedented. In the previous years with most ozone loss, temperatures (T) rose above the threshold associated with chlorine activation (T_{act}, near 196 K, roughly the threshold for the potential existence of PSCs) by early March (Fig. 1b, Supplementary Figs 1, 2). Only in 2011 and 1997 have Arctic temperatures below T_{act} persisted through to the end of March, sporadically approaching a vortex volume fraction similar in size to that in some Antarctic winters (Fig. 1b). In 1996–97, however, the cold volume remained very limited until mid-January and was smaller than that in 2011 at most times during late January through to the end of March (Fig. 1b, Supplementary Figs 1, 2).

Daily minimum temperatures in the 2010–11 Arctic winter were not unusually low, but the persistently cold region was remarkably deep (Supplementary Figs 1, 2). Temperatures were below T_{act} for more than 100 days over an altitude range of ~15–23 km, compared to a similarly prolonged cold period over only ~20–23 km altitude in 1997; below ~19 km altitude, $T < T_{\mathrm{act}}$ continued for ~30 days longer in 2011 than in 1997 (Supplementary Fig. 1b). In 2005, the previous year with largest Arctic ozone loss[7], $T < T_{\mathrm{act}}$ occurred for more than 100 days over ~17–23 km altitude, but all before early March.

The winter mean volume of air in which PSCs may form (that is, with $T < T_{\mathrm{act}}$), V_{psc}, is closely correlated with the potential for ozone loss[7,15–17]. In 2011, V_{psc} (as a fraction of the vortex volume) was the largest on record (Fig. 1c). Both large V_{psc} and cold lingering well into spring are important in producing severe chemical loss[7,15,16], and 2010–11 was the only Arctic winter during which both conditions have been met. Much lower fractional V_{psc} in 1997 than in 1996, 2000, 2005 or 2011 (Fig. 1c) is consistent with less ozone loss that year[16,17].

---

[1] Jet Propulsion Laboratory, California Institute of Technology, Pasadena, California 91109, USA. [2] New Mexico Institute of Mining and Technology, Socorro, New Mexico 87801, USA. [3] Alfred Wegener Institute for Polar and Marine Research, D-14473 Potsdam, Germany. [4] NASA Langley Research Center, Hampton, Virginia 23681, USA. [5] Royal Netherlands Meteorological Institute, 3730 AE De Bilt, The Netherlands. [6] Delft University of Technology, 2600 GA Delft, The Netherlands. [7] Science Systems and Applications, Inc., Lanham, Maryland 20706, USA. [8] Science Systems and Applications, Inc., Hampton, Virginia 23666, USA. [9] Science and Technology Corporation, Lanham, Maryland 20706, USA. [10] Environment Canada, Toronto, Ontario, Canada M3H 5T4. [11] Central Aerological Observatory, Dolgoprudny 141700, Russia. [12] NOAA Earth System Research Laboratory, Boulder, Colorado 80305, USA. [13] Arctic Research Center, Finnish Meteorological Institute, 99600 Sodankylä, Finland. [14] Danish Climate Center, Danish Meteorological Institute, DK-2100 Copenhagen, Denmark. [15] Eindhoven University of Technology, 5600 MB Eindhoven, The Netherlands. [16] Arctic and Antarctic Research Institute, St Petersburg 199397, Russia. [17] National Institute for Environmental Studies, Tsukuba-city, 305-8506, Japan. [18] National Institute for Aerospace Technology, 28850 Torrejón De Ardoz, Spain. [19] University of Toronto, Toronto, Ontario, Canada M5S 1A7.

©2011 Macmillan Publishers Limited. All rights reserved

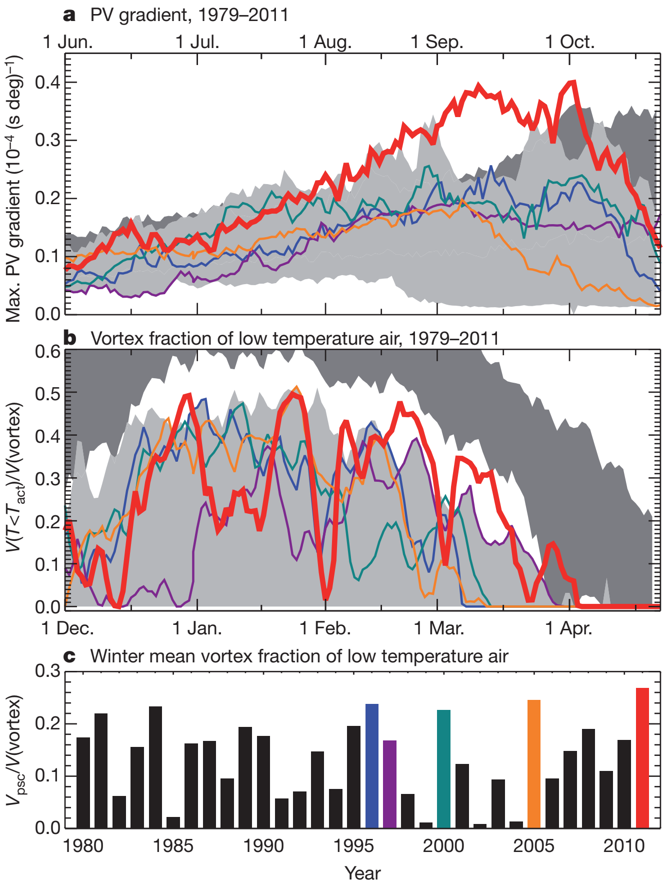

Figure 1 | Meteorology of the Arctic lower stratosphere. a, Vortex strength (as indicated by maximum potential vorticity[49] (PV) gradients) at 460 K potential temperature (~18 km altitude, ~65 hPa level). **b**, Fraction of vortex volume at potential temperatures between 390 and 550 K with a temperature less than the chlorine activation threshold (T_{act}). Light (dark) grey shading shows range of Arctic (Antarctic) values for 1979–2010. Antarctic dates are shifted by six months (top axis in **a**) to show the equivalent season. **c**, Winter mean V_{psc} during the past 32 years, expressed as a fraction of vortex volume. Red, orange, green, purple and blue lines/bars show the 2010–11, 2004–05, 1999–2000, 1996–97 and 1995–96 Arctic winters, respectively.

Factors playing secondary parts in governing interannual variability in ozone destruction, including vortex strength, structure and position relative to the cold region, also favour large loss in 2011 (Supplementary Figs 2, 3, Supplementary Discussion). However, despite the fraction of the vortex with $T < T_{\mathrm{act}}$ and mid-March temperatures sporadically approaching those seen in the Antarctic (Fig. 1b, Supplementary Fig. 1a), even in 2011 temperatures were much higher, and the cold regions much smaller, than those in most Antarctic winters.

Satellite trace-gas and PSC measurements highlight the stark contrast between polar processing in 2010–11 and that in typical Arctic winters, and the parallels with Antarctic conditions (Figs 2, 3). In 2011, PSCs or aerosols were abundant until mid-March (Fig. 3a; consistent with a deep region with $T < T_{\mathrm{act}}$, Fig. 3b), much later than usual in the Arctic[18–20], with vortex-average amounts at some altitudes similar to those in the Antarctic and dramatically larger than the near-zero values at that time in most Arctic winters. Furthermore, PSCs in 2011 spanned an altitude range comparable to that in the Antarctic, an uncommon occurrence in the Arctic[18–20]. Particles in long-lasting PSCs can grow large enough to sediment, resulting in denitrification, permanent removal of HNO_3 from the stratosphere[7,12]. By late March 2011 no PSCs remained (Fig. 3a), yet HNO_3 mixing ratios were much lower than observed in any previous Arctic winter (Fig. 2a). The continuing depression in HNO_3 after PSCs had evaporated indicates denitrification. Albeit less severe than in typical Antarctic winters (Fig. 2b, c, 3c), the extent and degree of denitrification in 2011 were unmatched in the Arctic, approaching the range of Antarctic conditions for the first time.

Decreasing HCl and increasing ClO signify chlorine activation (Fig. 2d–i). Some ClO enhancement has occurred in all recent Arctic winters, but has never been as prolonged and extensive as that in 2011. In late February, high ClO pervaded the sunlit portion of the vortex. The 2011 values vastly exceed the range previously observed in the Arctic from late February through to the end of March. They also briefly lie outside the Antarctic seasonal envelope, primarily because the higher solar zenith angles of the Antarctic measurements used here lead to ~30% lower ClO under fully activated conditions. In late February, HCl values (unaffected by solar zenith angle issues) fall along the lower boundary of the Antarctic envelope, confirming the picture seen in ClO. The vertical extent of chlorine activation was also comparable to that in the Antarctic (Fig. 3d, e).

In previous cold Arctic winters, chlorine was deactivated (converted from ozone-destroying forms into less reactive reservoir species) by mid-March[11]; even in 1997, ClO started to decline by late February (Fig. 2g). In 2011, by contrast, ClO began decreasing rapidly only about a week earlier than is typical in the Antarctic. ClO data in late February 1997 indicate that not only were maximum values lower than those in early March 2011, but also the vertical range of enhancement was shallower, with weaker activation at low altitudes than in 2011 (Fig. 3e), consistent with the higher altitudes and decreasing extent (Figs 1b, 3b, Supplementary Fig. 2) of $T < T_{\mathrm{act}}$.

When chlorine is deactivated, whether it is converted first into HCl or $ClONO_2$ depends sensitively upon HNO_3 and ozone abundances. In the Arctic, chlorine is normally deactivated through initial reformation of $ClONO_2$. In the severely denitrified and ozone-depleted Antarctic vortex, production of $ClONO_2$ is suppressed and that of HCl highly favoured[11,12,21]. In March 2011, the recovery of HCl followed a much more Antarctic-like pathway than has been observed in any other Arctic winter.

The largest Arctic chemical ozone loss was previously observed in 2005, followed closely by 2000 and 1996[7,12–14]. Although low temperatures persisted until the end of March 1997, the ozone loss in that year was far less. No previous year rivals 2011, when the evolution of Arctic ozone more closely followed that typical of the Antarctic (Fig. 2j). Ozone profiles in late March 2011 resemble typical Antarctic late-winter profiles much more strongly than they do the average Arctic one (Fig. 3f). Because mixing in April 2011 (for example, lamination events larger than that shown in Fig. 3f) entrained ozone-rich air into the vortex, the slight decrease in vortex-averaged ozone at a potential temperature of 485 K from 26 March to 20 April (from ~1.8 to ~1.6 p.p.m.v., Fig. 2j) indicates continuing chemical loss during this interval.

Estimates of chemical ozone loss

Chemical loss is difficult to quantify in the Arctic, where transport from above replenishes ozone in the lower stratospheric vortex, obscuring the signature of chlorine-catalysed destruction[12,22,23]. The evolution of the long-lived trace gas nitrous oxide (N_2O) reflects steady downward transport throughout the 2010–11 winter–spring, indicating that subsidence partially masked chemical loss. Horizontal transport can also confound the signature of chemical loss, bringing air into the vortex that has either higher[24] or lower[14] concentrations of ozone, depending on the altitude and latitude from which it originates.

Representative results from two types of chemical loss calculations[24–28] based on balloon-borne and satellite observations are shown in Fig. 4. The differences (up to ~0.4 p.p.m.v. at the end of March 2011) in estimates derived from the various methods and data sets imply some uncertainty in the chemical loss determination. Year-to-year differences in the amount of ozone loss are very similar when obtained from any method/data set combination, however, indicating a high degree of precision in the relative amount of calculated loss

©2011 Macmillan Publishers Limited. All rights reserved

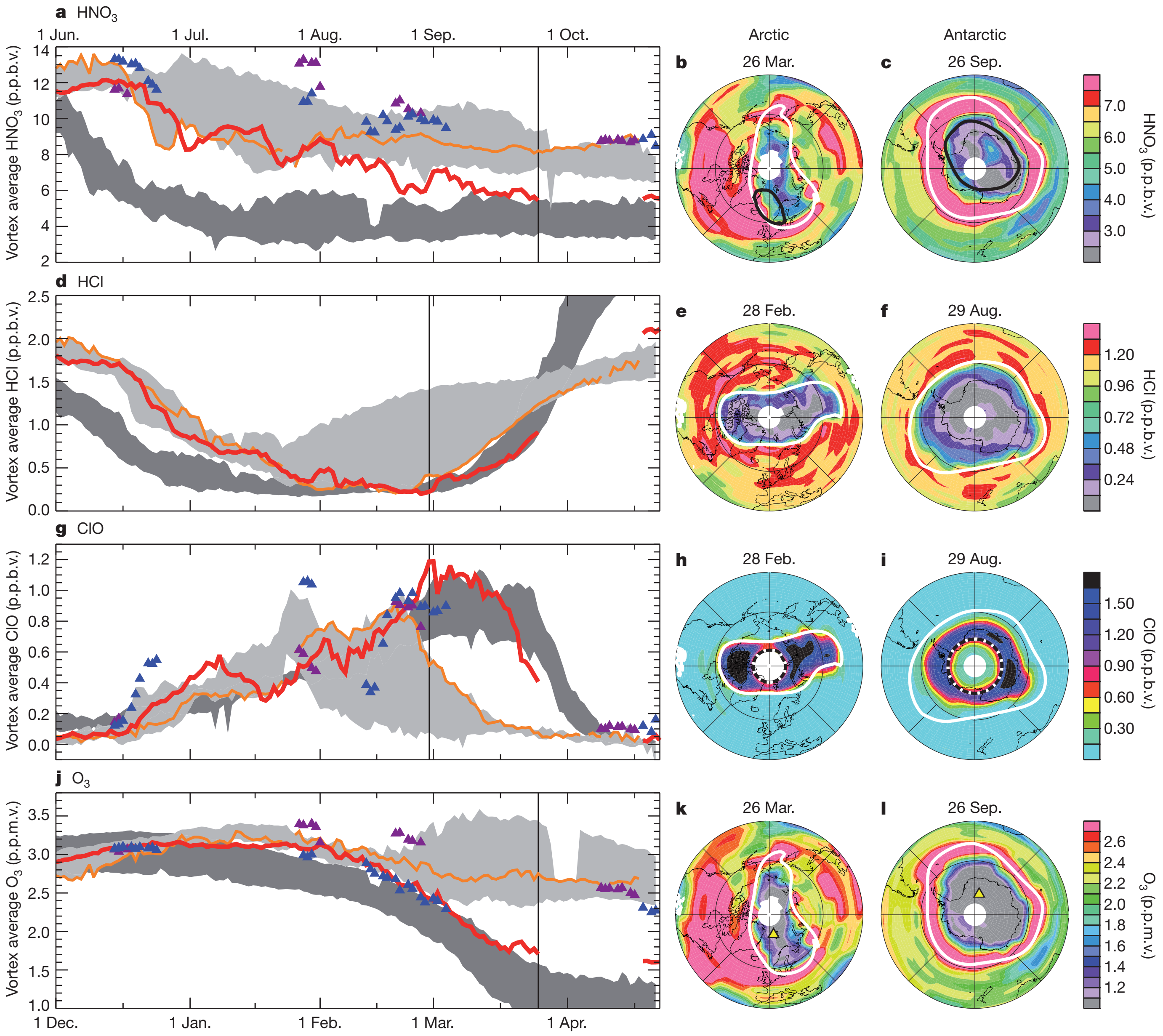

Figure 2 | Chemical composition in the lower stratosphere. **a**–**l**, Maps (right) and vortex-averaged time series (left) at 485 K potential temperature (~20 km, ~50 hPa) for four different gases: HNO_3 (**a**, **b**, **c**), HCl (**d**, **e**, **f**), ClO (**g**, **h**, **i**) and O_3 (ozone; **j**, **k**, **l**); mixing ratios from Aura MLS are shown. Averaging for the time series is done within the white contour shown on the maps. Blue (purple) triangles on time series, 1995–96 (1996–97) values from UARS MLS. Line colours/shading as in Fig. 1, but shading is for Aura MLS measurements from 2005–10. Antarctic dates are shifted by six months (top axis on time series) to show the equivalent season. Vertical lines show dates of maps in 2011 (2010) in the Arctic (Antarctic). Black overlays on HNO_3 maps, T_{act} (~196 K at this level); HNO_3 may be sequestered in PSCs at lower temperatures. Dotted black/white contour on ClO maps, 92° SZA, poleward of which measurements were taken in darkness. Yellow/black triangles on ozone maps, locations of the profiles in Fig. 3.

between different years. Chemical destruction was severe between ~16 and 22 km altitude, with the largest loss exceeding 2.5 p.p.m.v. by 26 March 2011 (Fig. 4a). By 31 March 2011, chemical loss was nearly double that in 2005 from ~18 to above 22 km, and similar to that in 2005 at lower altitudes (Fig. 4b, c). From ~18 to 20 km, more than 80% of the ozone present in January had been chemically destroyed by late March. Chemical removal in 1996 and 2000 started at a rate similar to that in 2011 (Fig. 4c), but ceased by late March; maximum losses in 2000 approached those in 2011, but extended over a much smaller vertical range (Fig. 4b). Loss in 1996, 2000 and 2005 considerably exceeded that in 1997, with greater destruction at lower altitudes in those years contributing more to total column loss[7,12,13]. Chemical loss in 2011 was two to three times larger than that in 1997, and about twice that in 1996 and 2005 above ~16 km; from ~15 to 23 km it was comparable to that in the Antarctic ozone hole in 1985[29]. Single ozone-sonde station measurements in early April 2011 suggest continuing ozone loss (Fig. 4c).

Although the meteorology during March–April was similar in 1997 and 2011, ozone loss was much more pronounced in 2011. Photochemical box model simulations (Supplementary Fig. 4, Supplementary Discussion) elucidate how early winter conditions set the stage for record springtime ozone destruction in 2011. Chlorine activation brought on by enduring cold from December through to the end of February led to ~0.7–0.8 p.p.m.v. lower ozone at the beginning of March 2011 (Figs 2j, 4c). The early onset of continuous cold also facilitated formation of PSC particles large enough to sediment, resulting in ~4 p.p.b.v. less HNO_3 by March in 2011 than in 1997 (Fig. 2a). The degree of denitrification has a profound impact on the severity of springtime Arctic ozone loss[30]. By delaying chlorine deactivation, lower HNO_3 by 1 March was responsible for ~0.6 p.p.m.v. more ozone

©2011 Macmillan Publishers Limited. All rights reserved

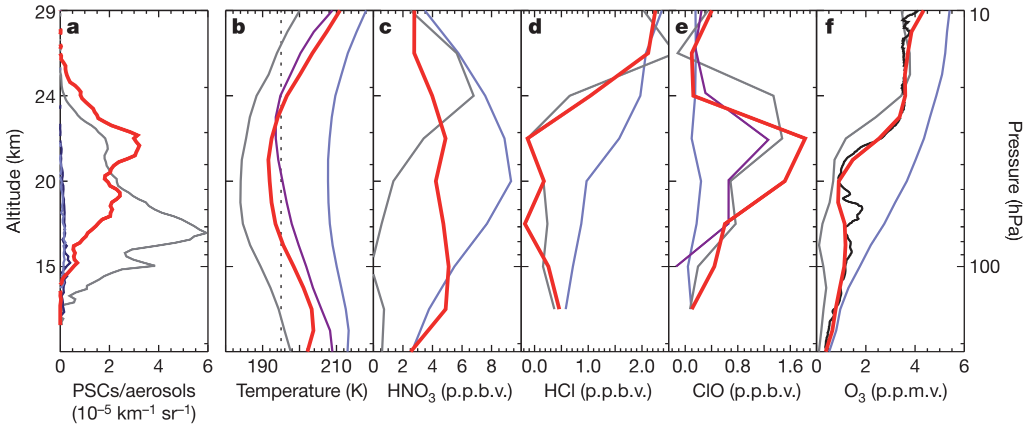

Figure 3 | Vertical composition information. **a**, Red, PSCs/aerosol amounts averaged in the vortex over a week centred around 25 February 2011; dark blue, the average for the same week in 2007–10; grey, the average over the equivalent period (centred on 28 August) for the Antarctic in 2006–10; lavender, the Arctic average for a week centred around 26 March 2011. (In late winter–spring, maximum PSC altitudes are generally higher in the Arctic because early winter PSC activity redistributes HNO_3 and water vapour to lower altitudes in the Antarctic[18]). **b**–**f**, Daily average profiles of MERRA temperatures (**b**) and MLS HNO_3 (**c**), HCl (**d**), ClO (**e**) and ozone (**f**). Red lines, data from a 4° × 15° latitude × longitude box around 79° N, 12° E; in **c**, **f**, taken on 26 March; in **b**, **d**, **e**, on 6 March 2011. Lavender, 7-day average for 2005–10 (1980–2010 for **b**) centred on the same location and days. Grey, profiles in a similar box in the Antarctic (79° S, 12° E) on 26 September for **c**, **f**, and on 8 September 2010 for **b**, **d**, **e**. Dotted black line in **b**, approximate T_{act} (195 K), see text. Purple line in **b**, 7-day average around 6 March 1997, centred on same location. Purple line in **e**, a midday ClO profile from UARS MLS on 26 February 1997 averaged in an 8° × 30° box centred at the same Arctic location. A high-resolution ozone-sonde profile at Ny Ålesund on 26 March 2011 (black in **f**) agrees well with MLS; lamination, a signature of mixing with ozone-rich extra-vortex air, is apparent as a local maximum near 60 hPa.

loss after that date in 2011 than in 1997 (Supplementary Fig. 4, Supplementary Discussion). The effects of denitrification and early-winter loss together account for the disparity in ozone depletion in these two winters (~1.5 p.p.m.v. more loss at 460 K in 2011 than in 1997, Fig. 4c, Supplementary Fig. 4). Loss as severe as that in 2011 thus requires $T < T_{act}$, with consequent chlorine activation and ozone destruction, early in winter (as in 1996, 2000 and 2005, but not in 1997), a cold period and region before March sufficient to allow widespread denitrification, and the persistence of a cold polar vortex into April (as in 1997, but not in 1996, 2000 or 2005).

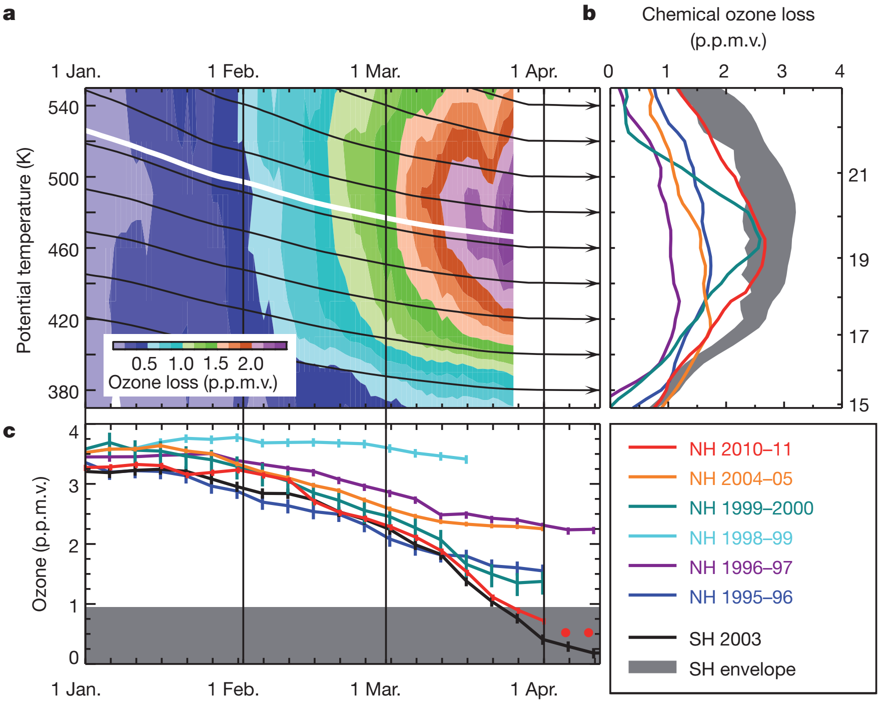

Figure 4 | Chemical ozone loss estimates. **a**, Chemical loss as a function of time and potential temperature from passive subtraction of MLS and ATLAS passively-transported ozone (initialized with December MLS data). **b**, Chemical loss from ozone sondes in unmixed vortex air as a function of 'spring equivalent potential temperature'[48] (black contours in **a**). Shading, Antarctic range defined by 1985 (the first year with profile measurements inside the ozone hole[29]) and 2003 (a recent year with a severe ozone hole). The 2003 Antarctic curve is shifted by six months minus 10 days because ozone sondes that year predominantly sampled the outermost vortex, where ozone loss begins earliest. **c**, Ozone at a spring equivalent potential temperature of 465K (white contour in **a**), near the level of maximum chemical loss. Shading, the region below the minimum reached in the 1985 Antarctic ozone hole. In April 2011 most soundings sampled the disturbed vortex edge; only two were made in air uninfluenced by mixing (red dots). Error bars, 1σ uncertainties based on the scatter of individual ozone-sonde measurements. Line colours as in Fig. 1; 1998–99 (a winter with no ozone loss) is shown in cyan. NH, Northern Hemisphere; SH, Southern Hemisphere.

©2011 Macmillan Publishers Limited. All rights reserved

Column ozone

Total column ozone is a predominant factor determining exposure of Earth's surface to ultraviolet radiation[7,12]. In the context of previous Arctic winters, 2011 was truly remarkable: the fraction of the Arctic vortex in March with total ozone less than 275 Dobson units (DU) is typically near zero, but reached nearly 45% in 2011 (Fig. 5a). Because of the dynamically-driven correlation between total ozone and lower-stratospheric temperature[23,31–34] (Supplementary Discussion), the abiding cold in 1997 and 2011 would have led to lower March total ozone than in other Arctic winters even without chemical loss; dynamical conditions in March–April 1997 particularly favoured low total ozone[33] (Supplementary Discussion). In March 2011, however, the area of low total ozone covered more than twice as much of the vortex as in 1997, and the daily vortex 'ozone deficit' (Supplementary Fig. 5a) was 30–50 DU larger, consistent with the greater chemical loss (Fig. 4). Maximum 2011 vortex fractions of low ozone approached those in early Antarctic ozone holes (Fig. 5a). The close correspondence between the vortex and both low total ozone and the large Arctic total ozone deficit (Fig. 5b, d) implies that low total ozone in March 2011 resulted primarily from chemical loss[31,32] (Supplementary Discussion). The ozone deficit in the Antarctic (Fig. 5e) shows a maximum over 0–90° W, and a minimum over 90–200° E, reflecting a vortex position in 2010 different to that in the reference state (which is less robust than that for the Arctic). Differences in morphology deep in the vortex are, however, minimal. The 2011 Arctic ozone deficit was at least comparable to that in the 2010 Antarctic vortex core at an equivalent time.

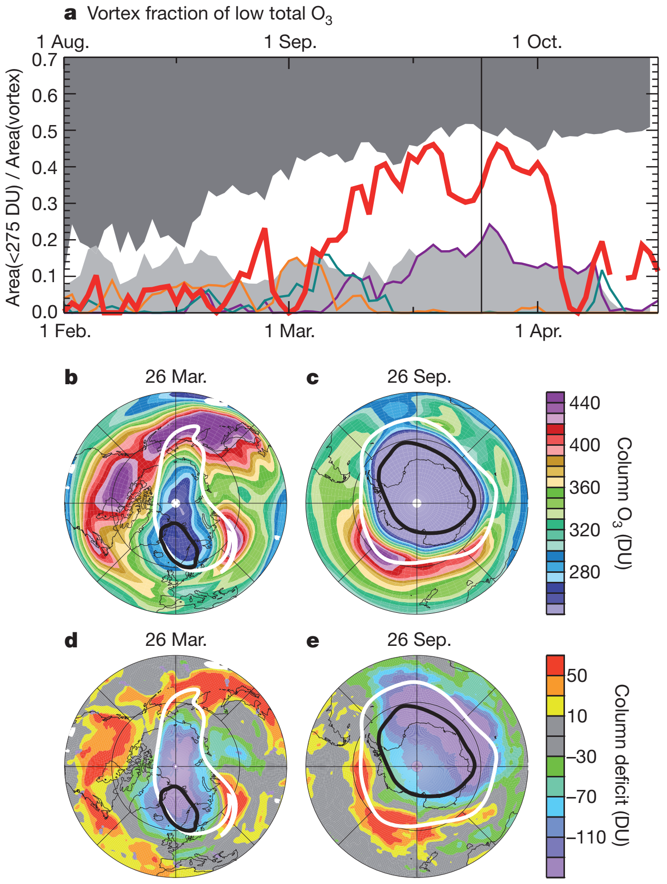

Figure 5 | Total column ozone. **a**, Time series of the fraction of 460 K vortex area with total ozone below 275 Dobson units (DU) in February–April in the Arctic (bottom axis), and in August–October in the Antarctic (top axis). Line colours/shading as in Fig. 1. 2005–2011 values are from OMI; earlier values are from TOMS (Total Ozone Mapping Spectrometer) instruments[50]. Maps show OMI total ozone (**b**, **c**) and ozone deficit (**d**, **e**) in the Arctic (Antarctic) on 26 March 2011 (26 September 2010). Overlays as in Fig. 2 but at 460 K.

An echo of the Antarctic

In the absence of chemical ozone loss, downward transport during winter results in a springtime maximum in total ozone; because this transport is stronger in the Arctic, background ozone levels there are ~100 DU higher than those in the Antarctic[7,23]. Therefore Arctic spring total ozone could, even after chemical destruction comparable to that in an Antarctic ozone hole (commonly defined by values less than 220 DU; refs 7, 12), exhibit only a weak maximum in total ozone rather than a well-defined minimum. Examination of the long-term ozone-sonde record in the Arctic shows that abundances near 250 DU or less are well below typical autumn values, thus appearing as a 'hole' in total ozone. Dynamical processes can result in transient regions of very low total ozone (Supplementary Discussion, Supplementary Figs 5, 6) and/or local minima in lower-stratospheric ozone profiles (for example, via ozone-poor extra-vortex air transported into the polar vortex[14,24]). For an interhemispheric comparison of chemical loss, it is thus important to verify that observed Arctic ozone decreases were primarily related to chemical, rather than dynamical, processes.

Figure 4 shows that the precipitous decline in Arctic ozone in February–March 2011 resulted from chemical loss of similar magnitude to that in the Antarctic in the mid-1980s. Observed ozone between ~15 and 20 km altitude decreased to values matching the minima in early Antarctic ozone holes and those reached at the corresponding time in some recent Antarctic winters (Figs 2j–l; 3f). In late March–early April, most ozone-sonde profiles in the vortex had mixing ratios less than 1 p.p.m.v., with values ~0.7 p.p.m.v. over an approximately 2-km altitude region, and some dipping to 0.5 p.p.m.v. (Supplementary Fig. 7). Minimum total ozone in spring 2011 was continuously below 250 DU for ~27 days (Supplementary Fig. 5b), with a maximal area below that level of $\sim 2 \times 10^6\ \mathrm{km}^2$ (roughly five times the area of Germany or California). Values dropped to ~220–230 DU for about a week in late March 2011.

In these respects, chemical ozone destruction in the 2011 Arctic polar vortex attained, for the first time, a level clearly identifiable as an Arctic ozone hole. On the other hand, although the magnitude of chemical depletion was comparable to that in the Antarctic, total ozone values remained higher and, because the areal extent of the Arctic vortex was much smaller (~60% the size of a typical Antarctic vortex), the low-ozone region was more confined.

The Arctic winter stratosphere exhibits striking interannual variability. The past decade has included the four most dynamically active (hence among the warmest) Arctic winters in the past 32 years (ref. 35) and now the two coldest winters with largest ozone loss[7,12–14], extending the previously noted trend of the coldest winters becoming colder[13,16]. Had implementation of the Montreal Protocol not curbed the increase in stratospheric halogen loading, formation of an Arctic ozone hole would have already become common even in moderately cold winters[36]. Even with the lower anthropogenic halogen levels actually reached, the potential for Antarctic-like ozone loss in the Arctic in the event of a persistently cold winter–spring such as that in 2010–11 has been recognized for decades[5,22]. Despite temperatures that were generally far higher than those in Antarctic winter, Arctic chemical ozone destruction in 2011 rivalled that in some Antarctic ozone holes. The development of an Arctic ozone hole under conditions only slightly more extreme than those in some previous Arctic winters raises the possibility of yet more severe depletion as lower-stratospheric temperatures decrease. More acute Arctic ozone destruction could exacerbate biological risks from increased ultraviolet radiation exposure, especially if the vortex shifted over densely populated mid-latitudes, as it did in April 2011.

Our present understanding of what drives variability in the Arctic winter stratosphere is incomplete. Stratospheric temperatures and vortex evolution depend on the atmosphere's radiative properties and propagation of wave activity[37,38], which are being modified by increasing greenhouse gas concentrations. Day-to-day tropospheric disturbances can lead to stratospheric warming or cooling, depending

©2011 Macmillan Publishers Limited. All rights reserved

on their geographical location and the stratospheric vortex structure, which controls their upward propagation[39,40]. Current climate models do not fully capture either the observed short-timescale patterns of Arctic variability or the full extent of the observed longer-term cooling trend in cold stratospheric winters; nor do they agree on future circulation changes that affect trends in transport[41,42]. Our ability to predict when conditions similar to, or more extreme than, those in 2011 may be realized is thus very limited. Improving our predictive capabilities for Arctic ozone loss, especially while anthropogenic halogen levels remain high, is one of the greatest challenges in polar ozone research. Comprehensive stratospheric data sets, such as those used here, are critical to meeting that challenge.

METHODS SUMMARY

MERRA (Modern Era Retrospective-analysis for Research and Applications[43]) fields are used for temperature and vortex analysis and for vortex averaging of composition measurements. The CALIOP (Cloud-Aerosol Lidar with Orthogonal Polarization) on the CALIPSO (Cloud-Aerosol Lidar and Infrared Pathfinder Satellite Observations) satellite[44] provides PSC/aerosol information.

Trace gas profiles are from the Microwave Limb Sounder (MLS)[45] on NASA's Aura satellite. Only daytime ClO measurements are used. Northern (southern) high latitudes are sampled near midday (in late afternoon), thus the average solar zenith angle (SZA) of MLS Antarctic measurements is $\sim$7° higher than that in the Arctic. Reactive chlorine partitioning shifts away from ClO at higher SZAs[7,12], leading to $\sim$30% lower ClO measured in the Antarctic than in the Arctic under fully activated conditions. An instrument anomaly disrupted MLS measurements from 27 March to 20 April 2011. UARS (Upper Atmosphere Research Satellite) MLS measurements, used for 1995–1996 and 1996–1997 analyses, are sparse because of the UARS yaw cycle and other measurement gaps[26].

Total column ozone is measured by the Dutch-Finnish Ozone Monitoring Instrument (OMI)[46] on Aura. Total ozone 'deficit' is the difference between daily values and a reference that is minimally affected by chemical loss.

Measurements from MLS and the Match network of balloon-borne ozone soundings (ozone sondes)[47] are used to estimate chemical ozone loss in two ways. The difference between calculated 'passive' (influenced only by transport) ozone and observed ozone is computed, with passive ozone obtained using MLS nitrous oxide[14], a 'reverse trajectory' model[25,26], and the ATLAS (Alfred Wegener Institute Lagrangian Chemistry/Transport System) model[27]. Vortex ozone is also examined on the surfaces on which it subsides[12,14,28,48], with descent rates from modelled radiative heating/cooling rates averaged over the polar vortex[48].

Photochemical box model runs were performed using the chemical model from ATLAS[27] to test the sensitivity of ozone loss to initial ozone amounts and denitrification.

Full Methods and any associated references are available in the online version of the paper at www.nature.com/nature.

Received 3 May; accepted 7 September 2011.

Published online 2 October 2011.

1. Farman, J. C., Gardiner, B. G. & Shanklin, J. D. Large losses of total ozone in Antarctica reveal seasonal ClO_x/NO_x interaction. *Nature* **315,** 207–210 (1985).
2. Solomon, S., Garcia, R. R., Rowland, F. S. & Wuebbles, D. J. On the depletion of Antarctic ozone. *Nature* **321,** 755–758 (1986).
3. Molina, L. T. & Molina, M. J. Production of Cl_2O_2 from the self-reaction of the ClO radical. *J. Phys. Chem.* **91,** 433–436 (1987).
4. Anderson, J. G., Brune, W. H. & Proffitt, M. H. Ozone destruction by chlorine radicals within the Antarctic vortex: the spatial and temporal evolution of ClO-O_3 anticorrelation based on *in situ* ER-2 data. *J. Geophys. Res.* **94,** 11465–11479 (1989).
5. Solomon, S. Stratospheric ozone depletion: a review of concepts and history. *Rev. Geophys.* **37,** 275–316 (1999).
6. Schoeberl, M. R. & Hartmann, D. L. The dynamics of the stratospheric polar vortex and its relation to springtime ozone depletions. *Science* **251,** 46–52 (1991).
7. World Meteorological Organization. *Scientific Assessment of Ozone Depletion: 2010* (Report 52, Global Ozone Research and Monitoring Project, 2011).
8. Solomon, P. M. *et al.* High concentrations of chlorine monoxide at low altitudes in the Antarctic spring stratosphere: secular variation. *Nature* **328,** 411–413 (1987).
9. Waters, J. W. *et al.* Stratospheric ClO and ozone from the Microwave Limb Sounder on the Upper Atmosphere Research Satellite. *Nature* **362,** 597–602 (1993).
10. Santee, M. L., Manney, G. L., Waters, J. W. & Livesey, N. J. Variations and climatology of ClO in the polar lower stratosphere from UARS Microwave Limb Sounder measurements. *J. Geophys. Res.* **108,** 4454, http://dx.doi.org/10.1029/2002JD003335 (2003).
11. Santee, M. L. *et al.* A study of stratospheric chlorine partitioning based on new satellite measurements and modeling. *J. Geophys. Res.* **113,** D12307, http://dx.doi.org/10.1029/2007JD009057 (2008).
12. World Meteorological Organization. *Scientific Assessment of Ozone Depletion: 2006* (Report 50, Global Ozone Research and Monitoring Project, 2007).
13. Rex, M. *et al.* Arctic winter 2005: implications for stratospheric ozone loss and climate change. *Geophys. Res. Lett.* **33,** L23808, http://dx.doi.org/10.1029/2006GL026731 (2006).
14. Manney, G. L. *et al.* EOS MLS observations of ozone loss in the 2004–2005 Arctic winter. *Geophys. Res. Lett.* **33,** L04802, http://dx.doi.org/10.1029/2005GL024494 (2006).
15. Harris, N. R. P., Lehmann, R., Rex, M. & von der Gathen, P. A closer look at Arctic ozone loss and polar stratospheric clouds. *Atmos. Chem. Phys.* **10,** 8499–8510 (2010).
16. Rex, M. *et al.* Arctic ozone loss and climate change. *Geophys. Res. Lett.* **31,** L04116, http://dx.doi.org/10.1029/2003GL018844 (2004).
17. Tilmes, S., Müller, R., Engel, A., Rex, M. & Russell, J. M. III. Chemical ozone loss in the Arctic and Antarctic stratosphere between 1992 and 2005. *Geophys. Res. Lett.* **33,** L20812, http://dx.doi.org/10.1029/2006GL026925 (2006).
18. Poole, L. R. & Pitts, M. C. Polar stratospheric cloud climatology based on Stratospheric Aerosol Measurement II observations from 1978 to 1989. *J. Geophys. Res.* **99,** 13083–13089 (1994).
19. Fromm, M. D. *et al.* An analysis of Polar Ozone and Aerosol Measurement (POAM) II Arctic stratospheric cloud observations, 1993–1996. *J. Geophys. Res.* **104,** 24341–24357 (1999).
20. Pitts, M. C., Poole, L. R. & Thomason, L. W. CALIPSO polar stratospheric cloud observations: second-generation detection algorithm and composition discrimination. *Atmos. Chem. Phys.* **9,** 7577–7589 (2009).
21. Douglass, A. R. *et al.* Interhemispheric differences in springtime production of HCl and $ClONO_2$ in the polar vortices. *J. Geophys. Res.* **100,** 13967–13978 (1995).
22. Manney, G. L. *et al.* Chemical depletion of ozone in the Arctic lower stratosphere during winter 1992–93. *Nature* **370,** 429–434 (1994).
23. Tegtmeier, S., Rex, M., Wohltmann, I. & Krüger, K. Relative importance of dynamical and chemical contributions to Arctic wintertime ozone. *Geophys. Res. Lett.* **35,** L17801, http://dx.doi.org/10.1029/2008GL034250 (2008).
24. Rex, M. *et al. In situ* measurements of stratospheric ozone depletion rates in the Arctic winter of 1991/1992: a Lagrangian approach. *J. Geophys. Res.* **103,** 5843–5853 (1998).
25. Manney, G. L. *et al.* Lagrangian transport calculations using UARS data. Part II: ozone. *J. Atmos. Sci.* **52,** 3069–3081 (1995).
26. Manney, G. L. *et al.* Variability of ozone loss during Arctic winter (1991–2000) estimated from UARS Microwave Limb Sounder measurements. *J. Geophys. Res.* **108,** 4149, http://dx.doi.org/10.1029/2002JD002634 (2003).
27. Wohltmann, I., Lehmann, R. & Rex, M. The Lagrangian chemistry and transport model ATLAS: simulation and validation of stratospheric chemistry and ozone loss in the winter 1999/2000. *Geosci. Model Dev.* **3,** 585–601 (2010).
28. von der Gathen, P. *et al.* Observational evidence for chemical ozone depletion over the Arctic in winter 1991–92. *Nature* **375,** 131–134 (1995).
29. Gernandt, H. The vertical ozone distribution above the GDR-research base, Antarctica in 1985. *Geophys. Res. Lett.* **14,** 84–86 (1987).
30. Rex, M. *et al.* Prolonged stratospheric ozone loss in the 1995–96 Arctic winter. *Nature* **389,** 835–838 (1997).
31. Manney, G. L., Froidevaux, L., Santee, M. L., Zurek, R. W. & Waters, J. W. MLS observations of Arctic ozone loss in 1996–97. *Geophys. Res. Lett.* **24,** 2697–2700 (1997).
32. Manney, G. L., Santee, M. L., Froidevaux, L., Waters, J. W. & Zurek, R. W. Polar vortex conditions during the 1995–96 Arctic winter: meteorology and MLS ozone. *Geophys. Res. Lett.* **23,** 3203–3206 (1996).
33. Petzoldt, K. The role of dynamics in total ozone deviations from their long-term mean over the Northern Hemisphere. *Ann. Geophys.* **17,** 231–241 (1999).
34. Hood, L. L., Soukharev, B. E., Fromm, M. & McCormack, J. P. Origin of extreme ozone minima at middle to high northern latitudes. *J. Geophys. Res.* **106,** 20925–20940 (2001).
35. Manney, G. L. *et al.* Aura Microwave Limb Sounder observations of dynamics and transport during the record-breaking 2009 Arctic stratospheric major warming. *Geophys. Res. Lett.* **36,** L12815, http://dx.doi.org/10.1029/2009GL038586 (2009).
36. Newman, P. A. *et al.* What would have happened to the ozone layer if chlorofluorocarbons (CFCs) had not been regulated? *Atmos. Chem. Phys.* **9,** 2113–2128 (2009).
37. Newman, P. A., Nash, E. R. & Rosenfield, J. E. What controls the temperatures of the Arctic stratosphere during the spring? *J. Geophys. Res.* **106,** 19999–20010 (2001).
38. Polvani, L. M. & Saravanan, R. The three-dimensional structure of breaking Rossby waves in the polar wintertime stratosphere. *J. Atmos. Sci.* **57,** 3663–3685 (2000).
39. Orsolini, Y. J., Karpechko, A. Y. & Nikulin, G. Variability of the Northern Hemisphere polar stratospheric cloud potential: the role of North Pacific disturbances. *Q. J. R. Meteorol. Soc.* **135,** 1020–1029 (2009).
40. Woollings, T., Charlton-Perez, A., Ineson, S., Marshall, G. & Masato, G. Associations between stratospheric variability and tropospheric blocking. *J. Geophys. Res.* **115,** D06108, http://dx.doi.org/10.1029/2009JD012742 (2010).
41. Butchart, N. *et al.* Multimodel climate and variability of the stratosphere. *J. Geophys. Res.* **116,** D05102, http://dx.doi.org/10.1029/2010JD014995 (2011).
42. Charlton-Perez, A. *et al.* The potential to narrow uncertainty in projections of stratospheric ozone over the 21st century. *Atmos. Chem. Phys.* **10,** 9473–9486 (2010).
43. Reinecker, M. M. *et al.* MERRA — NASA's modern-era retrospective analysis for research and applications. *J. Clim.* **24,** 3624–3648 http://dx.doi.org/10.1175/JCLI-D-11-00015.1 (2011).

©2011 Macmillan Publishers Limited. All rights reserved

44. Hunt, W. H. *et al.* CALIPSO lidar description and performance assessment. *J. Atmos. Ocean. Technol.* **26,** 1214–1228 (2009).
45. Waters, J. W. *et al.* The Earth Observing System Microwave Limb Sounder (EOS MLS) on the Aura satellite. *IEEE Trans. Geosci. Rem. Sens.* **44,** 1075–1092 (2006).
46. Levelt, P. F. *et al.* The Ozone Monitoring Instrument. *IEEE Trans. Geosci. Rem. Sens.* **44,** 1093–1101 (2006).
47. Rex, M. *et al.* Chemical ozone loss in the Arctic winter 1994/95 as determined by the Match technique. *J. Atmos. Chem.* **32,** 35–59 (1999).
48. Rex, M. *et al.* Chemical depletion of Arctic ozone in winter 1999/2000. *J. Geophys. Res.* **107,** 8276, http://dx.doi.org/10.1029/2001JD000533 (2002).
49. Hoskins, B. J., McIntyre, M. E. & Robertson, A. W. On the use and significance of isentropic potential-vorticity maps. *Q. J. R. Meteorol. Soc.* **111,** 877–946 (1985).
50. McPeters, R. D. *et al.* *Earth Probe Total Ozone Mapping Spectrometer (TOMS) Data Products User's Guide* (NASA Technical Publication 1998-206895, 1998).

Supplementary Information is linked to the online version of the paper at www.nature.com/nature.

Acknowledgements We thank the MLS (especially A. Lambert, D. Miller, W. Read, M. Schwartz, P. Stek, J. Waters), OMI (especially P. K. Bhartia, G. Jaross, G. Labow), CALIPSO and Match science teams, as well as A. Douglass, J. Joiner and the Aura project, for their support. We also thank W. Daffer and R. Fuller for programming assistance at JPL; the many observers whose work went into obtaining the ozone-sonde measurements; the ozone scientists who participated in the discussion of the 2011 Arctic ozone loss and appropriate definition of an Arctic ozone hole (including, but not limited to, N. Harris, G. Bodeker, G. Braathen, M. Kurylo, R. Salawitch); and especially P. Newman and K. Minschwaner for discussions and comments. Meteorological analyses were provided by NASA's Global Modeling and Assimilation Office (GMAO) and by the European Centre for Medium-Range Weather Forecasts. We thank S. Pawson of GMAO for advice on usage of the MERRA reanalysis. Ozone-sonde measurements at Alert, Eureka, Resolute Bay, Churchill and Goose Bay were funded by Environment Canada. Additional ozone sondes were flown at Eureka as part of the Canadian Arctic Atmospheric Chemistry Experiment (ACE) Validation Campaign and were funded by the Canadian Space Agency. Academy of Finland provided partial funding for performing and processing ozone-sonde measurements in Jokioinen and Sodankylä. Ozone soundings and work at AWI were partially funded by the EC DG Research through the RECONCILE project. Work at the Jet Propulsion Laboratory, California Institute of Technology, and at Science Systems and Applications Inc., was done under contract with NASA.

Author Contributions G.L.M. and M.L.S. led analysis of MLS data; M.R. led analysis of ozone-sonde data; G.L.M. led the meteorological data analysis. M.R., G.L.M., N.J.L. and I.W. did chemical ozone loss calculations. R.L. and M.R. performed and analysed chemical box model calculations. M.C.P. and L.R.P. provided CALIPSO/CALIOP data analyses; E.R.N. and P.V. provided TOMS and OMI data analyses. L.F., M.L.S., G.L.M. and N.J.L. provided expertise on MLS data usage; D.P.H., P.V. and P.F.L. provided expertise on OMI data usage. J.D., V.D., H.G., B.J., R.K., E.K., N.L., A.M., C.T.M., H.N., M.C.P., D.W.T., P.v.d.G., K.A.W. and N.S.Z. were responsible for performing and processing ozone-sonde measurements. All authors contributed comments on the manuscript. G.L.M., M.L.S. and M.R. jointly compiled and synthesized the results. G.L.M. and M.L.S. wrote the paper.

Author Information CALIOP data are publicly available at http://eosweb.larc.nasa.gov/PRODOCS/calipso/table_calipso.html, MLS data at http://disc.sci.gsfc.nasa.gov/Aura/data-holdings/MLS, OMI data at http://disc.sci.gsfc.nasa.gov/Aura/data-holdings/OMI/omto3_v003.shtml, and GEOS-5 MERRA analyses through http://disc.sci.gsfc.nasa.gov/mdisc/data-holdings/merra/. The balloon-borne Antarctic ozone-sonde data recorded in 1985 and the following years are publicly available at http://dx.doi.org/10.1594/PANGAEA.547983. Reprints and permissions information is available at www.nature.com/reprints. The authors declare no competing financial interests. Readers are welcome to comment on the online version of this article at www.nature.com/nature. Correspondence and requests for materials should be addressed to G.L.M. (Gloria.L.Manney@jpl.nasa.gov) or M.L.S. (Michelle.L.Santee@jpl.nasa.gov).

©2011 Macmillan Publishers Limited. All rights reserved

METHODS

Data sets. Modern Era Retrospective-analysis for Research and Applications (MERRA)[43] fields, from the Goddard Earth Observing System Version 5.2.0 (GEOS-5) data assimilation system, are used for the temperature and vortex analysis. The Cloud-Aerosol Lidar with Orthogonal Polarization (CALIOP) on the Cloud-Aerosol Lidar and Infrared Pathfinder Satellite Observations (CALIPSO) satellite[44] provides PSC/aerosol information. CALIOP measurements began in April 2006. Trace gas profile measurements are from the Microwave Limb Sounder (MLS)[45] on NASA's Aura satellite, and the predecessor MLS instrument[26] on the Upper Atmosphere Research Satellite (UARS). Total column ozone data are from the Dutch-Finnish Ozone Monitoring Instrument (OMI)[46] on board Aura. The historical total ozone record comprises data from Nimbus-7 and Earth Probe Total Ozone Mapping Spectrometer (TOMS)[50]. Aura MLS and OMI measurements are available from August 2004 through to the present. UARS MLS measurements were obtained from September 1992 through to early 2000, with increasingly sparse sampling in the later years[26]. TOMS data are available beginning in 1979, but no TOMS instrument was taking measurements during the 1995–96 Arctic winter.

Measurements from the Match network of balloon-borne ozone soundings (ozone sondes)[47] are used in some of the chemical ozone loss estimates.

Temperature and vortex analysis. Potential vorticity[49] (PV) is used to define the vortex, with a contour of 'scaled' PV of $1.4 \times 10^{-4}\,\mathrm{s}^{-1}$ (in vorticity units) demarking the vortex edge[51,52]. Vortex strength is diagnosed as the maximum daily gradient in PV as a function of equivalent latitude (the latitude that would enclose the same area between it and the pole as a given PV contour)[51–53]. Scaled PV multiplied by 10^4 is used in the calculation, resulting in units for its gradient of 10^{-4} (s degrees equivalent latitude)$^{-1}$.

The temperature threshold for chlorine activation, T_{act}, is estimated using the formula for nitric acid trihydrate formation[54], which depends on pressure, HNO_3 and H_2O. Climatological HNO_3 and H_2O profiles are used, derived from UARS data. The area with $T < T_{\mathrm{act}}$ is calculated on seven isentropic surfaces in the lower stratosphere: 390, 410, 430, 460, 490, 520 and 550 K; T_{act} on these levels is 197.5, 197.2, 196.8, 196.5, 195.9, 195.3 and 194.5 K, respectively. To get the volume with $T < T_{\mathrm{act}}$ from 380 through 565 K, the areas at each of the seven levels are multiplied by the estimated altitude associated with that layer and summed. The altitude range associated with each layer is obtained from a standard potential temperature profile as a function of altitude derived from high latitude temperature soundings taken during the 1988–89 through to 2001–02 winters (the same profile was used for V_{psc} calculations in refs 13, 16 and 48). These thicknesses are 1.29088, 1.19995, 1.36770, 1.46281, 1.30554, 1.18199 and 1.07382 km for the seven levels listed above. Vortex volume is calculated from vortex area in the same manner. Winter mean V_{psc} is calculated over 16 December through to 15 April. Previous studies have shown that V_{psc} scaled by the vortex area is a good proxy for chlorine activation and ozone loss potential[17]. Additional temperature and vortex diagnostics are described in Supplementary Information.

Polar stratospheric cloud and aerosol information. Particulate backscatter averaged over the polar vortex derived from CALIOP data is used to provide PSC/aerosol information. Total attenuated backscatter at 532 nm, $b(z)$, is one of the basic CALIOP Level 1B data products. $b(z)$ is the sum of the particulate backscatter (due to liquid aerosol and PSCs), $b_{\mathrm{p}}(z)$, and molecular backscatter, $b_{\mathrm{m}}(z)$. $b_{\mathrm{m}}(z)$ is calculated using GEOS-5 molecular density profiles (included in the CALIOP Level 1B data files) and a theoretical value for the molecular scattering cross-section[55]. Profiles of $b_{\mathrm{p}}(z)$ are then produced by subtracting $b_{\mathrm{m}}(z)$ from $b(z)$. Vortex-averaged profiles of $b_{\mathrm{p}}(z)$ are produced by averaging all CALIOP $b_{\mathrm{p}}(z)$ profiles located inside the vortex edge (defined using information available in GEOS-5 Derived Meteorological Product (DMP) files for the nearly-coincident Aura MLS data[52]) over the selected time interval.

MLS trace gas profile measurements and analysis. Trace gas profile measurements of HNO_3, HCl, ClO, ozone and N_2O (a long-lived tracer used to assess descent) are from Aura MLS[45] version 3 retrievals; data quality screening is as recommended in the MLS data quality document[56]. MLS data are retrieved on pressure surfaces; potential temperature as a function of pressure from MLS DMPs[52] calculated from GEOS-5 analyses is used to interpolate to isentropic surfaces. Vortex averages of MLS data are calculated using the $1.4 \times 10^{-4}\,\mathrm{s}^{-1}$ scaled PV contour to define the vortex edge, using PV values from the MLS DMPs[52]. Active chlorine is in the form of ClO mainly during the daytime, and thus measured ClO amounts vary with the solar zenith angle (SZA) at which the measurements are taken. Only daytime ClO measurements are used here. Northern high latitudes are sampled near midday local time, southern high latitudes are sampled in late afternoon, thus the SZA of Aura MLS Antarctic measurements is ~7° higher on average than that in the Arctic. Reactive chlorine partitioning shifts away from ClO at higher SZAs[7,12], leading to ~30% lower ClO measured by Aura MLS in the Antarctic than in the Arctic under fully activated conditions. MLS measurements are unavailable from 27 March through to 20 April 2011 because of an instrument anomaly. Upper Atmosphere Research Satellite (UARS) MLS measurements, used for analysis of 1995–96 and 1996–97, are sparse because of the UARS yaw cycle and other measurement gaps[26]. The time of day of UARS measurements varied through the yaw cycle, in the middle of which no daytime ClO measurements were obtained[10]; thus ClO values shown in 1995–96 and 1996–97 near those dates (including the mid-February 1996 measurements shown in Fig. 2g) are not representative of the degree of chlorine activation.

Chemical loss calculations. Chemical ozone loss is quantified by two methods, both widely used for such calculations[7,12,24–28,47,48]. In the 'passive subtraction' method[25–27], a transport model is used to calculate the evolution of ozone in the absence of chemical changes ('passive' ozone). The difference between passive ozone and observed ozone provides an estimate of chemical loss.

Here, passive ozone is obtained in three different ways. First, MLS observations of N_2O, a long-lived species unaffected by chemical processes, are used to calculate vertical motion, and that estimate of descent is then used to calculate how initial MLS ozone profiles would have evolved in the absence of chemical loss[14]. Second, a 'reverse trajectory' transport model[25,26] is used to transport an initial state based on MLS-observed ozone with no chemistry. Finally, the ATLAS (Alfred Wegener Institute Lagrangian Chemistry/Transport System) chemistry and transport model is run in passive mode[28], initialized with MLS ozone.

Vortex ozone is also examined in relation to the surfaces on which it is subsiding[12,14,28,48]. The descent rates used here are obtained by averaging radiative heating/cooling rates from the radiation calculation used in the ATLAS model over the polar vortex[48]. These rates are then used to examine vortex-averaged MLS and ozone-sonde data on surfaces of 'spring equivalent potential temperature'[48], defined as the potential temperature at which air originating at a given level arrived at the end of March. Since the air descended on these surfaces, ozone would have been constant on each such surface in the absence of chemical loss.

The ozone-sonde data used here are all from electrochemical concentration cell (ECC) sondes, made by different manufacturers. Ozone-sonde data quality was assessed in an intercomparison experiment[57] and is discussed in ref. 47. For chemical loss calculations using ozone-sonde data, the profiles are first examined using a procedure for detecting lamination in the profiles; such lamination (an example is shown in Fig. 3f) is associated with mixing in of extra-vortex air, which may obscure the signature of chemical loss. Profiles that have been significantly altered by mixing processes, as indicated by lamination, are excluded from the vortex averages used in the chemical loss calculations. 2010–11 Arctic ozone-sonde data are provided as Supplementary Information.

Results from the ATLAS model passive subtraction calculations, and from the calculations on spring equivalent potential temperature surfaces using the Match network ozone-sonde data, are shown in Fig. 4; all panels show vortex averages. These results have been compared with the results from the other methods described above. While absolute ozone values obtained from different methods/data sets vary significantly (up to ~0.4 p.p.m.v. at the end of March 2011), the year-to-year variations in chemical loss calculated using all three methods agree closely, indicating a high degree of precision in the relative amount of calculated loss between different years.

The Alfred Wegener Institute chemical box model, also used as the chemical module in ATLAS, simulates 175 reactions between 48 chemical species in the stratosphere[27,58] This model was used to perform conceptual runs (Supplementary Fig. 4), started on 1 March with identical initial mixing ratios of all species except HNO_3 and O_3. For these two species values corresponding to 1997 (3 p.p.m.v. O_3, 10 p.p.b.v. HNO_3) and 2011 (2.2 p.p.m.v. O_3, 6 p.p.b.v. HNO_3) (compare Figs 2a and 4c) were combined to yield four sets of initial conditions. Initial ClO_x was 2 p.p.b.v., corresponding to the vortex-averaged ClO_x derived by ATLAS from MLS ClO measurements on 1 March 2011. An air parcel at 70° N, 460 K potential temperature, with a temperature of 193 K throughout March, was used. Heterogeneous reactions took place on liquid aerosols, rather than solid (nitric acid trihydrate, NAT) PSCs, since the widespread existence of the latter is inconsistent with MLS observations of gas-phase HNO_3 values (Fig. 2a) larger than those the microphysical module predicts if NAT is present. A sensitivity run showed that sporadically occurring solid PSCs did not change the results significantly.

Column ozone and ozone deficit calculation. OMI total ozone data were processed with version 8.5 of the TOMS algorithm and have been extensively validated[59]. TOMS data were processed with version 8 of the algorithm. The OMI and TOMS total ozone data used in this study were averaged on a fixed global $1^\circ \times 1^\circ$ latitude × longitude grid. Averages were computed by area-weighting observations based on the overlap of their instantaneous field-of-view with each grid cell. Only data that satisfy quality criteria based on measurement path length and algorithm diagnostic criteria were included in the averaged samples.

©2011 Macmillan Publishers Limited. All rights reserved

Individual total ozone retrievals included in the samples are expected to have a root-mean-squared error of 1–2%.

Total ozone 'deficit' is calculated as the difference between daily values and a reference that is minimally affected by chemical ozone loss. The reference for the Arctic is the daily mean over all Arctic winters from 1978–79 through to 2009–10, from OMI starting in 2004–05 and from TOMS for earlier years[50]. The Antarctic reference state is the daily mean of TOMS measurements for 1979 through to 1981. Because the Antarctic reference state is based on only three years' data for each day, variations in vortex position are not effectively averaged out; this reference is thus less robust than that for the Arctic, so patterns in daily maps may partially reflect differences in vortex position between the reference and the focus day.

51. Manney, G. L., Zurek, R. W., Gelman, M. E., Miller, A. J. & Nagatani, R. The anomalous Arctic lower stratospheric polar vortex of 1992–1993. *Geophys. Res. Lett.* **21,** 2405–2408 (1994).
52. Manney, G. L. *et al.* Solar occultation satellite data and derived meteorological products: Sampling issues and comparisons with Aura MLS. *J. Geophys. Res.* **112,** D24S50, http://dx.doi.org/10.1029/2007JD008709 (2007).
53. Butchart, N. & Remsberg, E. E. The area of the stratospheric polar vortex as a diagnostic for tracer transport on an isentropic surface. *J. Atmos. Sci.* **43,** 1319–1339 (1986).
54. Hanson, D. & Mauersberger, K. Laboratory studies of the nitric acid trihydrate: implications for the south polar stratosphere. *Geophys. Res. Lett.* **15,** 855–858 (1988).
55. Hostetler, C. A. *et al.* CALIOP algorithm theoretical basis document. Calibration and Level 1 data products (Technical Report, NASA Langley Research Center, 2006); available at ⟨ http://www-calipso.larc.nasa.gov/resources/pdfs/PC-SCI-201v1.0.pdf⟩.
56. Livesey, N. J. *et al.* Version 3.3 Level 2 data quality and description document. (Technical Report JPL D-33509, Jet Propulsion Laboratory, 2010); available at ⟨http://mls.jpl.nasa.gov/data/v3-3_data_quality_document.pdf⟩.
57. Smit, H. G. *et al.* Assessment of the performance of ECC-ozonesondes under quasi-flight conditions in the environmental simulation chamber: insights from the Jülich Ozone Sonde Intercomparison Experiment (JOSIE). *J. Geophys. Res.* **112,** D19306, http://dx.doi.org/10.1029/2006JD007308 (2007).
58. Krämer, M. *et al.* Intercomparison of stratospheric chemistry models under polar vortex conditions. *J. Atmos. Chem.* **45,** 51–77 (2003).
59. McPeters, R. *et al.* Validation of the Aura Ozone Monitoring Instrument total column ozone product. *J. Geophys. Res.* **113,** D15S14, http://dx.doi.org/10.1029/2007JD008802 (2008).

©2011 Macmillan Publishers Limited. All rights reserved